The Design, Theory, and Development of the Flight Envelope for a Twin-Ducted-Fan Jetpack

Michael Aldo Speck

Dissertation submitted to the faculty of the
University of Canterbury,
Christchurch New Zealand,
in partial fulfillment of the requirements for the degree of
Doctor of Philosophy in Mechanical Engineering

30 September 2013

Supervisor: Dr. Mathieu Sellier

Co-Supervisor: Prof. Dr. Ing. Jörg Buchholz

Abstract

In order to improve the flight performance of the Martin Jetpack research was undertaken to investigate the aerodynamic issues that were limiting the P-11A Jetpack's flight envelope. Through research of existing ducted-fan aircraft, a flight model describing the unique aerodynamics of the Martin Jetpack was developed using Matlab®/Simulink® software. The dynamic flight model, which can be ran in real time, includes the reactions from: ducted-fans, aircraft body aerodynamics, control surfaces, gyration and landing gear interactions.

Numerous experiments were designed to quantify and validate assumptions used in the development of the model equations. The experiments took advantage of the small size of the Jetpack by designing and building test apparatuses that measured reactions directly on the actual aircraft. This avoided scaling issues that are traditionally encountered when employing wind tunnels for aerodynamic measurements.

Implementing the experimental results into the model led to the modifications of the existing Jetpack airframe to produce the P-11C Jetpack prototype, which significantly improved the performance of the aircraft. The collected flight data was used to validate the model and good agreement was achieved.

Based on this research a new Jetpack prototype (P-12) was developed that combined the flight performance of the P-11C Jetpack with the ability to carry a man or manned sized payload. The model was used to design the layout and to size the control vanes for the P-12 Jetpack. Further research was performed to design larger rotor and stator blades required for the P-12 Jetpack prototype.

The developed model allows the user to efficiently evaluate various control methodologies and changes to key aerodynamic features of the aircraft to aid in the design and flying of the Martin Jetpack.

The outcome of this research is a better understanding of the ducted-fan technology, and via the development of a Jetpack flight model, correctly applying this understanding to improve the Jetpack's flight performance.

Declaration

I hereby declare that this thesis is my own work and effort and that it has not been submitted anywhere for any award. Where other sources of information have been used, they have been acknowledged. All experiments were designed, led, and analysed by myself. Martin Aircraft Company engineers and technicians helped preform and physically setup the experiments. The tow test experiment was designed and built by myself, while all other experimental setups were fabricated by Martin Aircraft Company staff. The formulation of the Jetpack flight model was developed by myself, while Professor Jörg Buchholz collaborated with myself in rewriting the model in Simulink and improving the simulation performance.

Signature:.....

Michael Aldo Speck

Acknowledgments

This thesis has been an arduous challenge for myself, but has provided me a valuable learning experience. Although my name alone appears as the author, the completion of this thesis must be shared with and credited to, the numerous colleagues, friends, and family that have supported me during the duration of this research.

Firstly, I would like to acknowledge the founder of the Martin Aircraft Company, Glenn Martin. If it were not for his persistent drive the entire concept would have literally never left the ground.

To Martin Aircraft Company, thank you for the greatest of all opportunities to allow me to work on a once in a life time project and to be able to collaborate with such a fantastically talented team.

To the Martin Aircraft Company team, I am grateful that I have had the pleasure to work with such a talented group of people who strive to produce the best. Using open mindedness this team solves, fabricates, and delivers solutions efficiently, which makes me proud to have had the privilege to work with them.

Colin Dodge, you have taught me a great deal from your vast experiences, but most importantly you have reminded me the importance of being practical and open minded during the engineering process. James Bowker, I have enjoyed working with you and your abundant enthusiasm. I hope we can continue working together in the future, and thank you for your proof reading. Bill Clemence, you have shown me how to relate the theoretical and practical worlds of engineering.

I would like to thank my supervisor Dr Mathieu Sellier for his guidance, patience and encouragement, while mentoring me throughout my research, and also a thank you for the hours of proof reading. I can only begin thinking how frustrating it must have been to proof read my thesis. To Professor Jörg Buchholz, for being such a knowledgeable and vibrant teacher. I have learnt a lot from collaborating with you. You and Mathieu have helped to show me the path towards the researcher and engineer that I strive to be.

Thank you to my mother and father for always being there for me, believing and supporting me in all my endeavours. You have given so much of your time and energy in supporting me. I just hope that one day I can repay your kindness. To my girlfriend Judith, you have been such a blessing to me and my well being. You were able to re-energize my spirit and bring the focus needed to finish of this research.

A thank you must also go out to all past and active researchers of ducted-fan aircraft, as my research has been a continuation of their knowledge and lessons. I believe Sir Isaac Newton best describes this with his quote: *"If I have seen further than others, it is by standing upon the shoulders of giants".*

Contents

List of Publications

1. Michael Speck, Jörg Buchholz, Mathieu Sellier. A Mathematical Model of a Twin Ducted-Fan VTOL Jetpack. *Journal of Aerospace Engineering*, 2013.

2. Michael Speck, Jörg Buchholz, Mathieu Sellier. An Applied and Theoretical Approach to the Development of a Twin Ducted Fan VTOL Aircraft. Presented at *the American Helicopter Society Future Vertical Lift Aircraft Design Conference, January 18-20, 2012, San Francisco, California,* 2012.

3. Oliver Grant, A. Swain, K. Stol, Michael Speck. Attitude Hold Attitude Command Control of the Martin Jetpack; A Handling Qualities Assesment. To be presented at *AIAA Science and Technology Forum and Exposition 2014*.

Nomenclature

Main Symbols

a	Speed of sound [m/s], acceleration [m/s^2]
A	Area [m^2]
A_R	Aspect ratio (span/chord)
b	Aerofoil span [m]
B	Number of blades
cmd	Command signal
C	Damping coefficient
C_d	Sectional drag coefficient
C_D	Drag coefficient
C_{Dd}	Ducted-fan drag coefficient
C_{FM}	Figure of Merit
C_l	Sectional lift coefficient
C_L	Lift coefficient
C_{lc}	Load cell capacity
C_{Ld}	Ducted-fan lift coefficient
C_M	Moment coefficient
C_P	Power coefficient
CP	Centre of Pressure
C_Q	Torque coefficient
C_T	Thrust coefficient
d	Duct diameter [m]
D	Drag force [N], characteristic diameter [m]
DCM	Directional cosine matrix
dD	Blade element drag force [N]
dL	Blade element lift force [N]
DL	Disc loading [Pa] (T/S)
dQ	Blade element torque [Nm]

dT	Blade element thrust force [N]
e	Vane to ground clearance [m]
F	Force [N]
F_n	Ducted-fan normal force [N]
g	Acceleration due to gravity [$g = 9.80665\,\mathrm{m/s^2}$]
G	Ground (height above from inertial datum) [m]
h	Elevation (height above ground) [m]
H	Angular momentum [$\mathrm{kgm^2/s}$]
I	Inertia [$\mathrm{kgm^2}$]
J	Advance ratio
K	Spring constant [N/m], control gain
l	Characteristic length [m]
$\mathbf{l}$	Moment arm [m]
L	Lift force [N], moment about x axis [Nm]
m	Mass [kg]
$\dot{m}$	Mass flow rate [kg/s]
M	Moment [Nm], moment about y axis [Nm]
n	Rotational speed [rev/s], load factor
N	Moment about z axis [Nm]
p	Pressure [Pa]
p, q, r	Angler velocity rates about aircraft axes x, y, z [1/s]
P	Power [kW]
P_e	Engine power [kW]
P_F	Power factor
PL	Power loading [s/m](T/P)
Q	Torque [Nm]
r	Radius of blade element [m], turning radius [m]
r_o	Blade root radius [m]
r_t	Blade tip radius [m]

R	Radius [m], Gas constant for air [$R = 287.0531\,\mathrm{J/kg/K}$]
RE	Reynolds Number
$RMSE$	Root mean square error
R_{vane}	Vane-ground interaction factor
s	Distance [m]
S	Swept area [m^2]
t	Time [s], thickness [m]
T	Thrust force [N], temperature [K]
T_M	Thrust margin [N]
T_s	Static thrust force [N]
$\mathbf{u}$	Velocity vector [m/s]
U	Output signal
u, v, w	Velocity components x, y, z direction [m/s]
V	Velocity [m/s], Voltage [V]
V_{air}	Airspeed [m/s]
V_0	Free stream airspeed [m/s]
W	Weight force [N]
x, y, z	Cartesian coordinates

Subscripts and Superscripts

$()_a$	Aileron
$()_{ang}$	Angular
$()_c$	Chord
$()_d$	Ducted-fan
$()_f$	Body or aircraft fixed coordinate system
$()_F$	F series aerofoil
$()^G_{wind}$	Wind gust
$()_{gyr}$	Gyration
$()_i$	Inertial, Earth or global fixed coordinate system, induced flow, inner loop

$()_{lc}$	Load cell
$()_{LG}$	Landing gear
$()_o$	Outer loop
$()_p$	Propeller
$()_r$	Rotor, relative velocity
$()_{rot}$	Rotation
$()_s$	Stator
$()^S_{wind}$	Steady wind
$()_t$	Horizontal tail
$()^T_{wind}$	Turbulent wind
$()_{tc}$	Tail cone
$()_v$	Vertical tail
$()_{x,y,z}$	x, y, z axis, respectively

Greek Letters

α	Angle of attack
β	Sideslip angle
β_1	Inflow angle
β_2	Outflow angle
γ	Ratio of specific heats for air [$\gamma = 1.4$], blade element relative velocity angle, flight path angle
ϵ	Flow expansion, signal error
ϵ_d	Ducted-fan expansion ratio
ζ	Yaw vane setting
η	Pitch vane setting, Efficiency
θ	Pitch attitude, camber angle
ι	F-series additional camber angle
κ	Rated load cell calibration factor
λ	Flow coefficient
μ	Viscosity

ν	Load cell supply voltage
ξ	Roll vane setting
π	Ratio of circle circumference to diameter ($\pi = 3.14159$)
ρ	Air density, $1.225\,\mathrm{kg/m^3}$ at standard conditions
σ	Blade solidity
τ	Throttle setting [%]
υ	Engine time constant [s]
ϕ	Bank angle
Φ	Blade element setting angle
χ	Track angle
ω	Rotational velocity of swirl [1/s]
$\boldsymbol{\omega}$	Angular velocity vector [1/s]
Δ	Change
Φ, Θ, Ψ	The Euler angles
Ω	Angular velocity of rotating components [1/s] or [RPM]

Acronyms

CAD	Computer Aided Design
CFD	Computational Fluid Dynamics
CG	Centre of Gravity
CP	Centre of Pressure
DAQ	Data Acquisition System
EOM	Equations of Motion
INU	Inertial Navigation Unit
ISA	International Standard Atmospheric
LG	Landing Gear
LH	Left Hand side
NACA	National Advisory Committee for Aeronautics
NASA	National Aeronautics and Space Administration
ODE	Ordinary Differential Equation

PWM	Pulse Width Modulation
RAD	Relative Air Density
RAP	Relative Air Pressure
RH	Right Hand side
RSS	Relative Speed of Sound
SAS	Stability Augmentation System
TOM	Takeoff Mass
TOW	Takeoff Weight
UAV	Unmanned Aerial Vehicle
VTOL	Vertical Takeoff and Landing

Visual Symbols

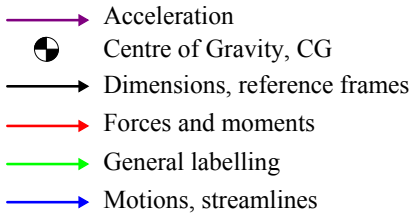

Chapter 1

Introduction

"Anyone who has never made a mistake has never tried anything new."
Stephen Hawking

1.1 The Dream

Since the dawn of mankind, man has dreamed of reaching and exploring the heavens above, but man had to first be patient and learn. This involved researching and testing the universe surrounding us; mathematics first had to be developed as a language to communicate and quantify the newly learnt wonders of the physical world. As time progressed man's knowledge of mathematics, physics, and other sciences accumulated; laying a foundation for new technologies to be developed to further explore the unknown.

On the 21st November 1783 two French brothers Joseph and Etienne Montgolfier left the surface of Earth and flew in a hot air balloon [**?**], Figure 1.1a. Soon after, hot air balloon flights were quickly setting new aeronautical records. However, man could only choose to slowly climb and descend and were largely left to the mercy of the dynamic atmosphere in their balloons. One hundred and twenty years later, in 1903, man obtained controlled flight [1]. This was achieved by Wilber and Orville Wright with their new invention - the aeroplane, Figure 1.1b. This was the proof that man needed to begin the age of aviation. Aeroplane technologies quickly advanced, as ever new and challenging demands were asked from them. Now, the newly produced Airbus A-380, Figure 1.1c, is at the forefront of aeroplane technology. The highly advanced A-380 passenger airliner dwarfs the nearest rival the Boeing 747-400 by carrying up to 853 passengers, in an all economy configuration.

Despite how practical and marvelous the aeroplane is one demand could not be answered - vertical takeoff and landing (VTOL). In 1909 Ludwig Prandtl foresaw this limitation, *"The considerable superiority of the aeroplane with the regard to the ability to fly does not exclude that - with advance in technology - the desired flying machine taking of vertically will come some day".* In the late 1930s Igor Sikorsky proved with his invention, the helicopter [5], that aircraft could takeoff vertically - translate - and then land vertically.

As technologies developed at an ever increasing rate in the latter part of the 20th century, new aircraft types were developed that combined the high speed performance of aeroplanes and the vertical takeoff and landings (VTOL)

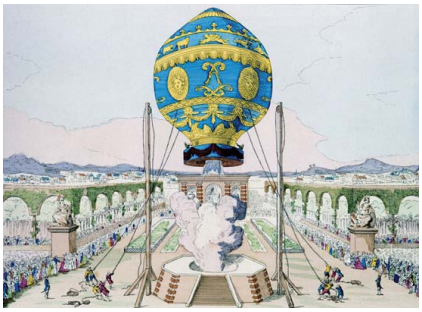

(a) Montgolfier brothers hot air balloon, first recorded human flight [2] (picture credit [3])

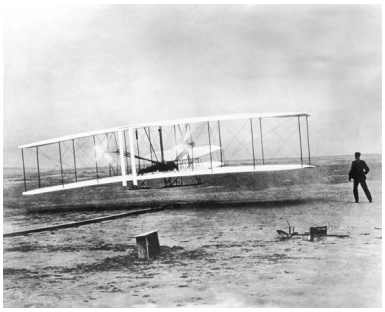

(b) Wright brothers first controlled flight at Kitty Hawk, 17th December 1903, (photo credit [4])

(c) Airbus A380, largest passenger aircraft (photo credit Airbus)

(d) Sikorsky VS-300 helicopter (photo credit Sikorsky Aircraft Corporation)

Figure 1.1: A brief history of aviation milestones

capabilities of helicopters. The pinnacle being the latest fighter aircraft - known as the F-35 Joint Strike Fighter, Figure 1.2a, which has supersonic cruise and VTOL abilities; but out of the seven billion inhabitants of earth, how many will ever get the chance to fly an F-35 Joint Strike Fighter?

With the exception of the F-35 Joint Strike Fighter and Harrier Jump Jet variants, Figure 1.2a and Figure 1.2c, respectively, as well as the problematic and costly V-22 Ospreys, Figure 1.2b, all other production aircraft are either fixed-wing aeroplanes or rotor-wing helicopters. Fixed winged aircraft are economical to operate and in the extreme case of sailplanes are able to soar at no cost. However, aeroplanes are all restricted in that they require a minimum forward speed to create lift and stay aloft. This forward speed requires aeroplanes to have a long clear space for takeoff and landing. Helicopters on the other hand use rotating wings, hence the term *rotor wing*, to generate lift so no longer have the aforementioned restriction. However, helicopters have a higher economic cost and are more vulnerable due to the inherent mechanical complexities.

What has long been dreamt, but still not yet achieved is a simple aircraft that can combine the benefits of the superior speeds of aeroplanes and the VTOL abilities of helicopters into a small, safe, practical package that anyone can fly. Eurocopter has recently shown that its new X-3 demonstrator, Figure 1.2d, which may be the best compromise between the aeroplane and the helicopter yet.

Another possible solution is the jetpack. The jetpack concept is not a recent fictional dream, it was proven in the 1950s when Bell engineer Wendell F. Moore [6] began work on the Bell Rocket Belt, Figure 1.3a. This jetpack

(a) Lockheed-Martin F-35 joint strike fighter (photo credit Lockheed-Martin)

(b) Bell Boeing V-22 Osprey is an example of a tilt-rotor aircraft where wing tip propellers can rotate from vertical to horizontal (photo credit Bell Boeing).

(c) AV-8 Harrier Jump Jet (photo credit US Navy)

(d) Eurocopter X-3 heli-plane (photo credit Eurocopter Group)

Figure 1.2: Unusual VTOL aircraft

used a mono-propellant rocket engine powered by hydrogen peroxide to create thrust for lift and control. One might ask, if the jetpack has been around since the 1950s why are we not all commuting with them already, instead of driving? Simply put, the rocket powered jetpack has one serious flaw; a best flight time of about 30 s with exceptionally high fuel costs.

Recently a new jetpack concept has emerged, the Martin Jetpack. The Martin Jetpack has overcome the inherent problem of the rocket belt needing to carry all of working fluid, by creating a lightweight internal combustion engine that powers two ducted-fans to produce two streams of jetted air. The jetted air is deflected left and right, forwards and backwards to orient and move the Martin Jetpack.

The Martin Jetpack is not alone in the ultra light weight VTOL flight category. Technology advances are making miniature helicopters such as the GEN H-4, Figure 1.3b and the twin rotor NASA Puffin[1] [8], Figure 1.3c, concepts a reality. The recently revealed hover-bike concept by Aerofex, Figure 1.3d, even uses a similar ducted-fan propulsion system to that of the Jetpack. All these aircraft boast similar or better performance (refer to table 1.1) than the P-11A Martin Jetpack, where only time will tell which one succeeds.

1.2 Description of the Martin Jetpack

The Martin Jetpack, Figure 1.4, is a new Vertical Takeoff and Landing (VTOL) aircraft that is under development as a solution for personal flight and/or UAV

[1] Yet to be made and flown

(a) Bell Rocket Belt (photo credit[6])

(b) World's smallest helicopter Gen H-4 (photo credit GEN Corporation)

(c) NASA Puffin concept (photo credit NASA)

(d) Aerofex tandem ducted-fan hover-bike (photo credit De Roche [7])

Figure 1.3: Personal VTOL aircraft

Table 1.1: Advertised flight performance of personal VTOL aircraft

	GEN H-4 [9]	NASA Puffin[8]	P-11A Martin Jetpack[10]
Dry Weight	730 N	1330 N	1310 N
Max Take off weight	1770 N	2350 N	2450 N
Speed	40 m/s	67 m/s	28 m/s
Power	30 kW	45 kW	150 kW

platform with equivalent payload. This aircraft, like other VTOL aircraft, produces a lift force greater than the weight force of the aircraft at zero airspeed allowing it to hover.

(a) P-10 Martin Jetpack in flight (photo credit Martin Aircraft Company)

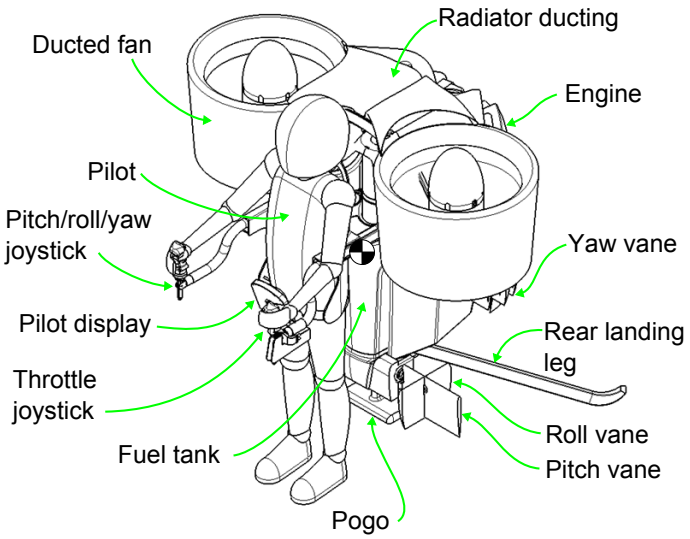

(b) P-11A Martin Jetpack features

Figure 1.4: Martin Jetpack prototypes

The Jetpack was initially intended to be designed to meet the Part 103-Ultra-Light Aircraft Standard [11]. This standard is a sub-part of the United States of America Federal Aviation Regulation and covers the design requirements, airworthiness, and flight restrictions for aircraft that have a takeoff weight less than 1310 N (113 kg). The goal of Martin Aircraft Company is to develop a VTOL jetpack concept that is low cost, intuitive, safe, and functional. Potential uses of the Martin Jetpack proposed by Martin Aircraft Company are:

- Search and rescue
- Military uses, both urban and open warfare
- Thrill seekers activity
- Urban commuter, fly from one high rise building to another
- Compact simple airframe

Propulsion

The lift and thrust force that the Jetpack requires to fly is produced from two ducted-fan propulsion systems. The ducted-fan, also referred to as a shrouded-propeller, consists of three key aerodynamic components: fan, duct, and stator blades, as shown in Figure 1.5. The fan is an assembly of individual rotor blades that are aerodynamically shaped aerofoils much like a propeller or wing and produce a lift force when rotated. During rotation of the fan the rotor blades induce momentum parallel and tangentially to the fan axis to produce

a resultant helical flow. The tangentially induced momentum is referred to as swirl. The axially induced flow component equates to a mass flow rate and according to Newton's laws of motion produces a thrust force. The stator blades are used to recover the induced swirl momentum from the flow by straightening the airflow so that the air leaves the duct, ideally, in a purely axial direction. By removing the swirl momentum from the flow the stators also create a torque opposing the induced torque from the fan, thus creating a torque neutral ducted-fan.

The presence of the duct helps direct and channel the airflow through the fan and stators. This gives the ducted-fan the following benefits over an open propeller/fan:

1. Reduced tip vortices allow greater spanwise loading of the rotor blade, thus improve efficiency.

2. Curvature of airflow around duct leading edge creates additional lift force at hovering and low airspeeds.

3. Duct acts as a natural shield/enclousure around the spinning fan.

4. Duct diffuser angle defines flow expansion.

The ducted-fan system also has nose and tail cones that encourage a smooth and attached airflow through the duct. The hub is located at the centre of the duct and contains the bearing housing that supports the fan shaft. The hub is located and secured by the Jetpack beam and supports the stators blades which are connected to the duct.

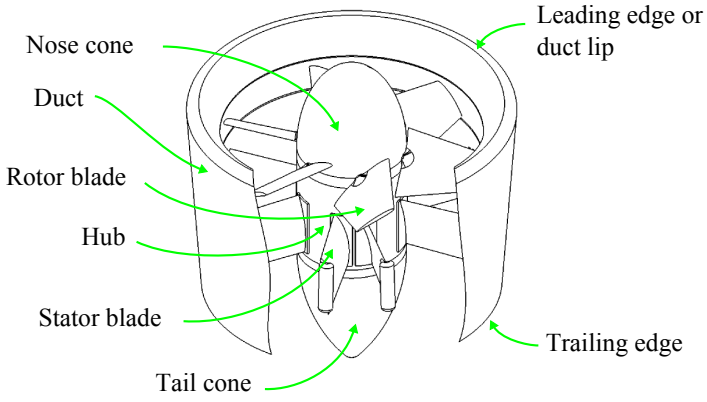

Figure 1.5: Components of the Martin Jetpack ducted fan

Power Plant

The Martin Jetpack ducted-fans are powered by a single two-stroke combustion engine. The 2 L two-stroke engine is arranged as a V4 configuration and develops 150 kW at 6000 RPM. Two belt drives are used to transfer the power from the main drive shaft to each fan shaft. This belt drive arrangement with conventional internal belt teeth means that each fan spins in the same direction, anticlockwise when viewed from above.

Control

The motion of the Jetpack is achieved by tilting the Jetpack and thus the ducted-fans in the desired direction of travel. The exhaust air streams from the ducted-fans are deflected by roll, pitch, and yaw vanes to control the orientation of the Jetpack about the longitudinal x, the lateral y, and the vertical z axes, respectively, refer to Figure 1.6. These vanes are immersed in the high dynamic pressure slipstream of the ducted-fans allowing the aircraft to maintain control independent of the aircraft's airspeed. A fourth control is used to control the rate of climb by varying engine power output, and hence, fan speed.

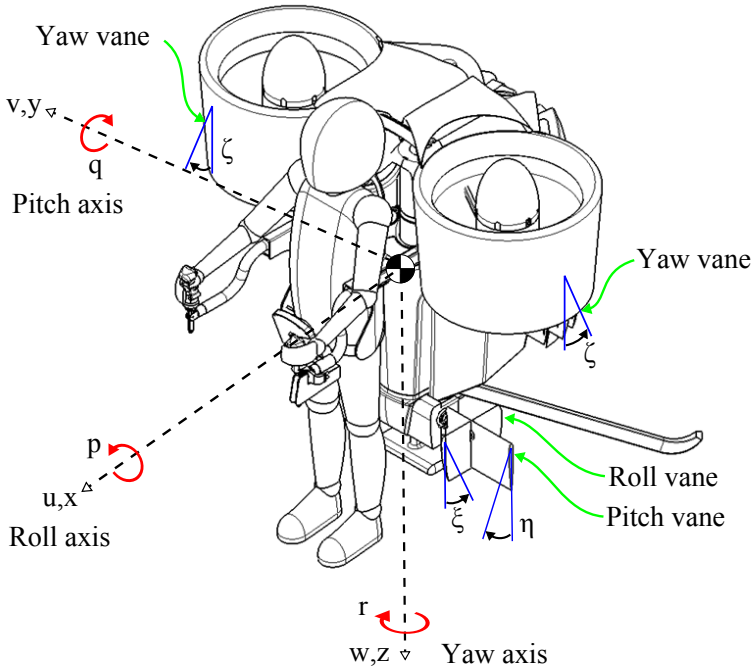

Figure 1.6: Model sign convention

The Jetpack uses an inertial navigation unit (INU) coupled with a flight computer to produce a fly-by-wire system that artificially stabilises the Jetpack, which is similar to that used on UAVs and advanced fighter aircraft. This means the flight computer, using the sensory gyro and attitude information, is actually flying the aircraft and the pilot is simply instructing the flight computer where to go. With this technology, it is proposed by Martin Aircraft Company, that users/pilots will be able to quickly learn how to fly the Jetpack confidently.

P-11 Airframe

The weight of the Jetpack airframe must be minimised to ensure that Jetpack remains functional. This has been achieved by the use of advanced composite design and construction techniques utilizing carbon fiber materials, which offer high stiffness and strength with minimal weight. The airframe of the Jetpack is relatively simple in that only two major components exist that secure all the critical features of the aircraft, which are the beam and the spine. The beam runs laterally across the width of the Jetpack and supports both the left hand

and right ducted-fans, the main drive shaft, and the pilot. The spine, which is bonded to the beam, supports the engine and the landing gear. The output from the engine is transferred to the main shaft by a flexible torque coupler. The rotor blades are secured to the fan hub via an arrangement that allows the rotor blade angle to be adjusted (ground adjustable) as required. Note that in flight the rotor blades are at a fixed pitch. The landing gear consists of a pogo stick style suspension that supports the bulk of the Jetpack's weight and rear legs to stabilise.

Safety Features

Safety features on the Jetpack are still in the development phase. It is proposed that a ballistic parachute, which is under development, will be used in the event an engine failure, as the Jetpack is unable to autorotate. The Martin Aircraft Company are aiming to eliminate the *avoidance curve*, also known as the *dead man's curve*; this curve is well known to helicopter pilots as it represents the speed and altitude combinations where an engine failure would must likely result in death.

Performance of the P-11A Jetpack

Table 1.2 summaries the Jetpack's performance at the onset of this research in June 2009. The performance data is from the P-11A Jetpack prototype and highlights that flying qualities of the Jetpack differ greatly from the intended performance, which stipulates a cruise speed of 28 m/s. This thesis explains in depth why the initial performance of the Jetpack was poor and more importantly shows with theory, experimentation, and flight testing that Jetpack can achieve and exceed the intended performance specifications.

Table 1.2: Jetpack P-11A performance June 2009

Performance	Value
Max speed	< 3 m/s
Wind/turbulence tolerance	Nil
Handling quality	Poor[2]

History of the Martin Jetpack

Numerous Jetpack prototypes have been developed by Martin Aircraft Company. The P-9 Jetpack was developed in the early to mid 2000s. This prototype contained the basic form of the company's Jetpack concept with two ducted-fans located above the centre of gravity and the pilot located at the front. However, this prototype lacked the thrust and power for flight.

The P-10 Jetpack, developed and flown in 2007, improved upon the P-9 Jetpack by using appropriately designed 600 mm diameter ducted-fans and replacing the engine with a custom designed two stroke V4 150 kW engine. This configuration enabled the Jetpack to lift off the ground and sustain a hover, albeit a very difficult to control hover. Mechanical control vanes were fitted to provide roll, pitch, and yaw control. However, pilots significantly relied upon movement of their legs to change the centre of gravity position of aircraft to supplement the control system.

The P-11A Jetpack was developed in 2008 and unveiled to the world at the 2008 Oshkosh air show. The P-11A Jetpack was largely a cosmetic improvement upon the P-10 Jetpack, where a more extensive use of carbon fiber composites were used to lighten the aircraft. The ducted-fans remained the same as per the P-10 Jetpack; while centre of gravity was lowered, in the false belief that this would improve stability. The initial version of the P-11A contained mechanical control linkages, but in 2009 a fly-by-wire system was implemented to stabilise the aircraft allowing for easier manned and remote control flying.

Utilising the research effort, the theoretical understanding, and the experimental results presented within this thesis, Martin Aircraft Company modified the P-11A Jetpack prototype by increasing the centre of gravity position to above the ducts; this was done by inverting the engine. This configuration of the Jetpack was termed the P-11C Jetpack and first flew in mid 2011. The P-11C demonstrated controlled flight up to speeds of 15.8 m/s, making a vast improvement on the aerodynamic capabilities of the previous prototypes.

Further improvements to the control vanes on the P-11C lead to the P-11E configuration, which was flown in early 2012. This configuration has shown the peak aerodynamic performance of the P-11 prototype series allowing for aggressive and responsive flight manoeuvres. The P-11E Jetpack prototype was used as a basis to develop the P-12 Jetpack, which first flew in November 2012. The P-12 Jetpack features a re-designed airframe and larger 800 mm diameter ducted-fans using the same V4 engine as its predecessors. The larger ducted-fans increased the maximum thrust to 3700 N, which is a 42 % improvement on the P-11 Jetpacks. This thrust increase combined with the improved control design has demonstrated the superiority of the P-12 Jetpack, in both payload and manoeuvering performance, compared to its predecessors.

1.3 Motivation

Overall Goal

To be able to accurately describe the Martin Jetpack's flight dynamics and define a safe and high performing flight envelope for the Martin Jetpack.

Reasons for Study

The flight dynamics for an aircraft need to be thoroughly understood for the importance of safety and function. Understanding the flight dynamics using a suitable flight model allows the aeronautical engineer to identify any unstable modes or tendencies, which can then be re-engineered or avoided by restricting flight manoeuvres. The aeronautical engineer produces flight charts that visually communicate the limitations of an aircraft to the pilot. The lines on the charts often form regions or envelopes and represent areas where flight dynamics are proven to be safe and well understood. Hence, any flight beyond these lines is termed *beyond the flight envelope,* and is associated with high risk, as flight is being conducted beyond the known and safe limits. When a new aircraft is developed the flight envelope is generally very small, but as more

is learnt about the aircraft the flight envelope can be progressively extended, termed *expanding the envelope*. The envelope needs to be expanded beyond the aircraft's mission requirements to ensure both safety and performance, and hence, prove the functionality of the product.

Chapter 2

Background

"If you can't explain it simply, you don't understand it well enough."
Albert Einstein

This chapter presents a literature review of historic and the state-of-the-art ducted-fan research for VTOL aircraft applications.

2.1 Ducted-Fan Aircraft

This section describes the aerodynamics, functions, and purpose for various VTOL ducted fan aircraft that have flown throughout history. Each aircraft is briefly analyzed in terms of how the ducted-fan is used and how control of the aircraft type is achieved.

2.1.1 Early Investigations in Ducted-Fans

Ducted-fans or shrouded propellers as they were initially referred to, were first investigated by the Germans in the late 1930s. An early NACA (National Advisory Committee for Aeronautics) technical memorandum [12] by Krüger is actually a translation from German research first published in 1944. The research demonstrates that the shrouded propeller, with its smaller diameter than an open propeller, would be well suited as a rear mounted or *pusher* propulsion system on aircraft. The report contains both wind tunnel measurements up to blade tip velocities of Mach 0.45 and theoretical derivations of the shrouded propeller.

Research into ducted-fans was also initiated by the Australian Council for Aeronautics in the mid 1940s. Patterson produced three reports on ducted-fan design methodologies. The first report [13] explains a detailed design method for a ducted-fan for applications within a duct systems; this report showed that the ratio of axial to swirl velocity was of primary importance in the design of a high efficiency ducted-fan. The second report [14] explains a second approximate design methodology for ducted-fans. The third report [15] describes the design methodology for high efficiency straightener designs.

2.1.2 Hiller VZ-1 Flying Platform

Purpose of Aircraft

The Hiller VZ-1 Flying Platform was developed in mid 1950s and first flew on 27 January 1957. The VZ-1 uses two co axial counter rotating propellers in a single ducted-fan. The concept had originally been progressed by Charles H. Zimmerman, who first experimented with VTOL kinesthetic flight in the early 1950s [16]. Zimmerman's experiment was based on the theory that all a person needed to hover is an upward force equal to the persons weight applied at the feet, much like standing on solid ground. The stability would be controlled by tilting the persons centre of gravity, which for any walking/standing person is intuitive. This theory was successful tested by standing on top of a flying plank propelled by air jets. The four air jets, one located in each corner, were powered by compressed air supplied by a large ground base air receiver. Numerous comments from the test pilots mentioned that they were unaware they had left the ground, such was the stability using unconscious kinesthetic movement.

Figure 2.1: Hiller VZ-1 Flying Platform (photo credit Hiller Aviation Museum)

Control of Aircraft

The patent for the VZ-1 [17] describes how control is achieved. Attitude control for both pitch and roll is achieved by using kinesthetic movement of the pilot. The kinesthetic control uses the pilot's biological sensors to sense the orientation and motion of the platform to intuitively use their muscles to remain up right to create control moments to stabilise; this is inherently done by the pilot in the same manner as standing on a fixed earth surface. Motion of the aircraft was controlled by the pilot tilting in the direction of desired travel, while yaw control was achieved by the use of aerofoil control vanes in the ducted-fan slip stream to create yaw moments.

The setup of the VZ-1 is mechanically very simple, as no additional control system is required, thus resulting in the pinnacle of VTOL aircraft control. However, an investigation by Parlett [18] in 1961 showed that pilots preferred

being seated with a traditional stick control rather than the kinesthetic standing control method.

Issues Encountered

Although the Hiller VZ-1 Flying Platform successfully demonstrated kinesthetic controlled flight, the aircraft lacked in performance. The top flight speed, from various sources, ranges from 4 m/s to 7 m/s, which is far too slow for an aerial vehicle. Higher flight speeds were not possible due to a large positive aerodynamic pitching moment that prevented the aircraft from tilting further into wind, which is required to obtain higher flight speeds. The large ducted-fan normal force and positive pitching moment due to the turning of the free stream airflow through the ducted-fan prevented higher flight speeds from being achieved. If the centre of gravity of the VZ-1 had been increased relative to the ducts, higher flight speeds would have been possible (author's opinion). Although this may have jeopardized the stability of the aircraft.

A theoretical investigation of the Hiller Flying Platform by Ando[19] in 1986 reinforces the fact that the momentum drag[1] and the positive pitching moment provided in-flight stability for the aircraft. The investigation was done by developing an eigenvalue problem and solving it with developed constant stability derivatives. It was also determined by the analysis that if the centre of gravity was slightly changed, by the pilot squatting or standing on tiptoes, the stability of the aircraft may have been lost.

Piasecki VZ-8 Flying Jeep

Purpose of Aircraft

Developed in the late 1950s and early 1960s to address US army requirements, the *Flying Jeep* concepts contained two-ducted-fans in tandem configuration, refer to Figure 2.2. A few variants existed with the Piasecki VZ-8 being the most successful[20].

Figure 2.2: Piasecki VZ-8 Flying Jeep (photo credit Piasecki Aircaft)

Control of Aircraft

The Flying Jeep designs used cyclic control on the fan rotor blades to create attitude control moments, similarly to a helicopter. Control vanes were also

[1]Referred to as the *ducted-fan normal force* within this research.

located in the duct slip streams to produce additional roll control as well as yaw control. The variable/cyclic pitch of the ducted-fans, although adding mechanical complexity, allows for responsive climb control while maintaining a near constant fan speed, which is necessary for gas turbine engines.

Issues Encountered

Two major problems were encountered with the Flying Jeep concept: control and forward speed. The model of the Flying Jeep was shown to be inherently unstable by NASA [21] causing divergent oscillations about both pitch and roll. The pitch oscillation was slower than the roll oscillation due to the aircraft's inertial mass distribution. It was found that artificially induced damping was necessary to get the model to fly. At full scale, experienced pilots were able to deal with the instability [20].

The second problem of the concept was the high angle of forward pitch to achieve only a moderate airspeed, about a mile per hour per degree of forward pitch. With increasing forward speed the aircraft developed increasing nose pitch up moment, which was only slightly improved by the addition of control vanes in the duct slip streams [21]. NASA also tested a model with four ducted-fans, one in each corner, but found that this model also suffered from divergent oscillations, which required damping, and a positive pitch up moment, which increased with increasing forwards airspeed[22].

Doak VZ-4

Purpose of Aircraft

Developed in the 1950s for the US Army, the Doak VZ-4 (Figure 2.3) is the first example of an aircraft with tilting ducted-fans mounted on the wing-tips of a conventional aeroplane. The aircraft utilized the propulsion efficiency of the ducted-fan to produce the thrust necessary for VTOL flight.

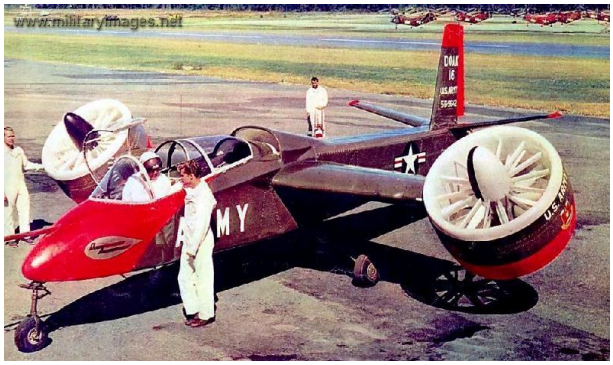

Figure 2.3: Doak VZ-4 (photo credit US Army)

Control of Aircraft

With the ducts in horizontal position and the aircraft flying under wing lift the control of the aircraft was by conventional aeroplane control: ailerons, elevator, and rudder. In transition and hovering flight steerable ducting of the gas turbine exhaust at the tail was used for pitch and yaw control.

Issues Encountered

A report of the flight trials of the Doak VZ-4 described some of the handling issues encountered [23]. Transition from hover to forward flight could be completed within 11 s, however, it required full forward trim to offset the large nose up moment and large control deflections to maintain control, but was still tolerable. The reverse transition, conversion from forward flight to hovering flight, took one minute to complete. This transition had to be completed slowly as the deceleration of the aircraft compounded with the severe nose up pitching moment, which was due to the high duct angles of attack and high airspeed at the beginning of the transition phase. Hence, full use of forward trim and full forward stick input by the pilot were necessary. It was also noted that large control deflections were necessary for hovering and vertical descent to maintain attitude control, suggesting that the control authority should be increased. The report concluded that the Doak VZ-4 could perform takeoffs smoothly with a constant rate of climb, but transition from forward flight to hover was the largest problem.

A NASA wind-tunnel investigation [24, 25] of a semi-span wing-tip mounted ducted-fan, as used on the Doak, was undertaken to determine the appropriate duct angles of attack and power setting for a range of level flight speeds for the Doak. This, combined with the addition of a control vane in the duct slipstream suggested nose up pitching problems encountered on the Doak could be reduced.

NASA performed additional wind-tunnel experiments using the semi-span wing-tip mounted ducted-fan describe above [26, 27]. These wind-tunnel tests discovered that at high angles of attack the lip stall would create a rapid change in pitching moment, which would limit the rate of descent on a wing-tip-mounted ducted-fan aircraft. The reports also showed that the wing supplements the ducted-fan lift during low speed flight.

Bell X-22

Purpose of Aircraft

Development of the Bell X-22 began in the mid 1960s and the first example flew in 1966, but was lost due to a malfunction. A second example was made and had a very successful career as a VTOL research aircraft, although the aircraft never reached its target maximum airspeed of 525 km/h. The Bell X-22 achieved vertical flight by tilting the ducted-fans 90° to the horizontal and then via a transition phase tilting them horizontal for forwards flight.

Control of Aircraft

The success of the Bell X-22 is attributed to the success of the control system used. Control was achieved by using variable pitch on each of the ducted-fans combined with control surfaces in each of the duct slipstreams. The rather elegant control system allows for responsive and powerful control that is necessary to overcome the large nose up pitching moments, which plagued the Doak and Hiller Flying Platform. A NASA wind-tunnel investigation [28] showed that the vanes and differential fore and aft duct incidence angles could be used to control the aircraft.

(a) Bell X-22 in hovering flight with duct mounted pitch control vanes visible (photo credit Bell Textron)

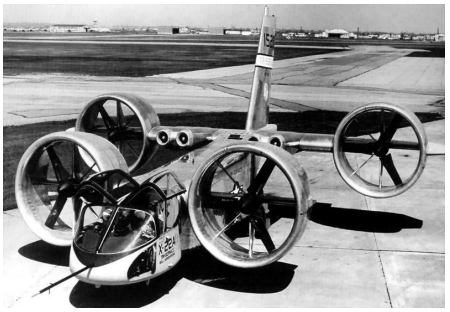

(b) Bell X-22 with ducts positioned for horizontal aeroplane flight (photo credit Bell Textron)

Issues Encountered

Wind-tunnel test on a range of speeds and duct angles of attack from hover through transition into forward flight were preformed on a scaled model of the Bell X-22. These tests showed longitudinal stability problems, but these were corrected by decreasing the destabilising fore wing area and increasing the windward duct lip radius of the front ducts to delay stall until a higher duct angle of attack is reached [29].

A NASA investigation by Giulianetti[30] used a large scale model of the Bell X-22 and examined how ground effect influenced lift and control for both VTOL flight and short takeoff and landing (STOL) scenarios. The report highlighted that the use of control vanes alone in the duct slip stream was not enough to trim the aircraft when the ducts were at angles of attack greater than 50°.

Trek Aerospace Solo Trek

Purpose of Aircraft

The Solo Trek (Figure 2.4) developed by Trek Aerospace was intended to be a solution for a small footprint single pilot VTOL aircraft, with similar performance targets to the Martin Jetpack. However, controlled flight was never publicly demonstrated, and development efforts have stagnated due to lack of funding and progress.

Control of Aircraft

Control of the aircraft was to be achieved by control vanes located in the slipstream of the ducted fans. Additional pitch control was provided by tilting the ducted-fans in pitch. However, at the time of writing no public evidence exists of a successful flight demonstration of the concept, thus there is no validation that the control system is effective.

Issues Encountered

The ducted-fans used in the Solo-Trek were tested in a NASA wind-tunnel for various forward flight conditions with the ducted-fan set to angles of attack close to 90° [31]. It was also shown that the control vanes located in the duct slipstream could produce a sidewards force and moment about the centre of

Figure 2.4: Solo Trek twin ducted fan VTOL aircraft (photo credit Trek Aerospace)

gravity of the aircraft. The report also showed that extending the 10" (254 mm) length duct chord by 5" (127 mm) on the trailing edge had no significant effect on the thrust coefficient.

Aerofex 'Hover-Bike'

Purpose of Aircraft

Aerofex Corporation have recently (publicly released August 2012) developed a hover-bike concept, Figure 1.3d, utilizing two ducted-fans in tandem configuration, much like the VZ-8 Flying Jeeps. The pilot sits between the two fixed-pitch counter-rotating ducted-fans and uses a mix of kinesthetic and control inputs to manoeuvre the aircraft. Full specifications of this aircraft are not available, but the intended purpose is a low cost, mechanically simple aircraft that is intuitive to fly. Potential uses of the aircraft range from first response to border patrol. This design makes use of high-aspect ratio ducted-fans to fly in ground effect, from 1 to 1.5 duct diameters above ground. It is unclear at present whether the concept is intended to fly out of ground effect.

Control of Aircraft

Control of the Aerofex Hover-Bike is achieved by a combination of kinesthetic movement of the pilot and activation of the ejectors. The pilot movement fore and aft, left and right, produces control movements by effectively changing the centre of gravity of the aircraft. With the change in centre of gravity and the fixed location of thrust a moment couple between the net thrust and weight forces is produced. However, Aerofex have discovered this control movement relying on the pilot weight movement, although intuitive, is not effective

enough for the total control of the aircraft. Aerofex have tried other means for generating control moments. Beginning with the state of the art - control vanes and coupling these control vanes with kinesthetic movement of the pilot [32] Aerofex improved kinesthetic control of their aircraft. However, the control vane force was also found to be inadequate for sufficient control while maintaining a low form factor, which is a requirement for their design. A paper by Weir [33] shows that the theoretical optimum location of control vanes in the duct slip stream is between 0.75 to 1.0 rotor diameters below the duct exit plane. Hence, positioning control vanes at their optimum position would leave little clearance between the control vanes and the ground while flying in ground effect, which the Aerofex Hover-Bike .

Consequently, Aerofex have invented and patented [34] a control system using ejectors around the periphery of the duct trailing edges, refer to Figure 2.5. By similar means as to the control vanes, the ejectors are activated by kinesthetic movement [35] of the pilot to produce pitch and roll control moments. The moments are created by closing the ejectors on the side of the intended pitch/roll motion. The difference in thrust created about the aircraft's centre line, when a control vane is deflected, enhances the moment arm between the centre of thrust and the centre of gravity. The centre of gravity also shifts in the opposite direction to the centre of thrust due to pilot weight shift.

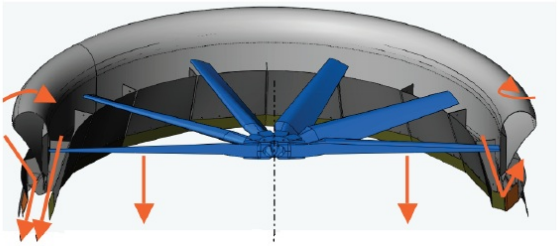

Figure 2.5: Aerofex ducted fan with open and close ejectors. Diagram credit De Roche[7]

Yaw control of the aircraft is achieved by using yaw vanes above the fans. As the yaw vanes are located above the fan the vanes need to be enlarged to provide the same effectiveness as vanes located below the fan where the duct diameter is reduced. The yaw vanes are controlled by the pilot steering the handle bars in the direction of intended yaw/turn, much like a motor bike.

Issues Encountered

At time of writing Aerofex has given little information on the performance details of their hover bike, but has advertised that they are still working on the technology to improve the control of the aircraft against gust and for flight out of ground effect. Only a qualitative description of their of ejector system has published to date [7], so it is difficult to assess whether the ejector system will perform to the desired requirements for the aircraft to be successful. A paper by Fleming [36], which is discussed later, provides pitching moment performance of a low aspect ratio ducted-fan that is fitted with an internal duct deflector with bleed. This device is similar to the ejectors used on the Aerofex Hover Bike.

Urban Aircraft Tandem Ducted-Fans

Purpose of Aircraft

In recent years Urban Aeronautics, an Israeli Company, have been developing a tandem ducted-fan aircraft similar in principle to the the Flying Jeeps of the 1950s and 1960s [37, 38, 39, 40, 41, 42]. Urban Aeronautics have differed their design from those in the past by including two additional forward facing ducted-fans to aid in forwards thrust and overcoming the high nose up pitch tendencies associated with this kind of a design.

Figure 2.6: The Urban Aeronautic Urban Mule tandem ducted fan aircraft (photo credit Urban Aeronautics Ltd)

Control of Aircraft

Control of the aircraft is achieved using an array of control vanes above and below the fan as described in the patents [43, 44, 42, 45]. Little information has been given about the actual and estimated performance of the Urban Aeronautic aircraft.

Issues Encountered

The mesh of control surfaces uses on the Urban Mule would add significant amount of drag thus would require additional thrust to hover. The fundamental problem with this type of design is that conventional control vanes cannot be used as described by [7] as the vane moment arms are restricted to a minimum to maintain a low form factor for the aircraft.

Lockheed F-35B

Purpose of Aircraft

The Lockheed F-35B, Figure 2.7a, is the first example of a ducted-fan in a VTOL application to make it to production. The ducted-fan in the F-35 is used as an additional source of lift on the aircraft and allows for short takeoff and vertical landing (STOVL) operations.

Control of Aircraft

Stabilization of the aeroplane is done by fly-by-wire technology and is used for all modes of flight from conventional aeroplane mode through transition and into hover. The counter-rotating ducted-fan is used for VTOL operations

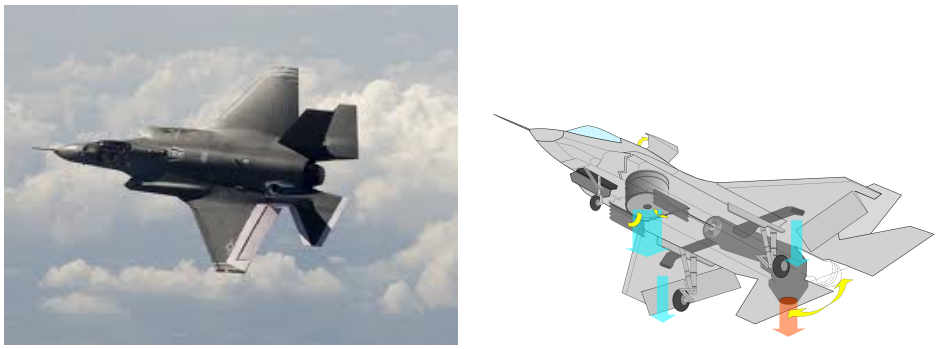

(a) In aeroplane flight mode (photo credit US Air Force)

(b) VTOL configuration, ducted-fan located behind the cockpit (diagram credit Tosaka)

Figure 2.7: Lockheed F-35B

and assists the thrust vectoring from the jet engine exhaust to enable the the F-35B to hover. Additional by-pass air is bleed off to jets located on the wings to provide roll control, as shown on Figure 2.7b.

Single Ducted-Fan MAVs

Purpose of Aircraft

The rapid advancement of micro controllers in the 1990s has paved the way for a resurgence of unmanned aerial vehicles (UAV) and micro aerial vehicles (MAV), which are human transportable UAVs as described in [46]. In this role the ducted-fan system has been a favourite form of propulsion amongst MAV VTOL aircraft designers due to the inherent benefits of the higher static thrust and shielding of fan(s). Numerous designs, such as the Honeywell T-Hawk (Figure 2.8), use counter rotating fans and control vanes located in the duct slipstream. The primary function of these MAVs is to provide ground troops with real time aerial surveillance at the foot soldier level. The foot solider operator uses a ground station (laptop device) to send instructions to the aircraft and receive visual data from the aircraft. Due to the compact size of these single ducted-fan MAVs they are easily transportable and robust, making them ideal for their front line surveillance roles.

A paper by Weir [33] presents high level considerations of a free-flying ducted-fan aircraft and is the basis for modern research efforts on single-ducted-fan VTOL aircraft. The paper states that the optimal position of the control vane within the slip stream of a ducted-fan aircraft is 0.75 duct diameters from the duct trailing edge. Wind tunnel results of a two-thirds scale model subjected to various angles of attack and velocity showed that pitching moments are significant. The presence of roll moments suggests that asymmetric loading of the propeller is present due to retreating and advancing blades. However, these roll moments are an order of magnitude smaller than the pitching moments. The influence of leading edge radius was examined by comparing an annular duct (aerofoil cross-section) with a toroidal shaped duct inlet. It was found that the toroidal configuration gave slightly better lift at low advance ratios due to the increased surface area at the duct inlet.

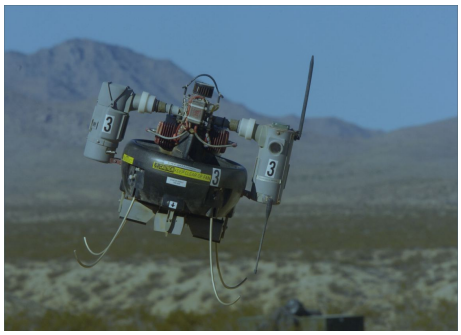

Figure 2.8: Honeywell RQ-16 T-Hawk (photo credit to U.S. Navy)

Control of Aircraft

The control of single-ducted-fan aircraft is typically done with control vanes located in the duct slipstream where tilting of the vanes produces roll, pitch and yaw moments. Synthetic jets have also been investigated to control these ducted-fan aircraft as described in [47, 48]. Synthetic jets are an example of a boundary layer control device, where flow separation and reattachment is controlled by activation of jet flow over various portions of the duct surface.

Synthetic jets are more complex to integrate and control. They require a high pressure air source, which needs additional power. Control vanes provide a mechanically simpler solution, but also have limitations.

Issues Encountered

The resurgence of ducted-fans for MAVs has also brought out the inherent problem of the large nose up pitching moment due to crosswinds. This has initiated further research into the control of ducted-fan aircraft [49, 50, 51, 52, 36, 53].

Fleming [53] performed research on a scale model of a single ducted-fan MAV in conjunction with Honeywell Labs, which later developed the Honeywell T-Hawk, Figure 2.8. Fleming's research highlights the existing problems of ducted-fan VTOL aircraft of high momentum drag and over stabilising duct pitching moment due to asymmetric duct-lip lift when exposed to a crosswind. Fleming's first paper on wind tunnel results of a 10" (254 mm) ducted-fan with a disc loading of 575 Pa showed the presence of momentum drag and the large pitching moment that is well known for VTOL ducted-fans. The baseline pitching moment results of the duct at an angle of attack 90° showed that as airspeed was increased a positive pitching moment developed. However, it reached a maximum value before decreasing and becoming negative. Measurements of pitching moment were performed with control vanes located in the slipstream over a range of airspeeds from 0 knots to 30 knots (15.4 m/s). The results showed that with increasing airspeed the moment produced by vane deflections of 20° and −20° converged to a net negative moment about the duct quarter chord. This convergence of the pitching moment with the control vanes at opposite settings indicates the ineffectiveness of the control vane on the net moment. A simple CFD analysis of the ducted-fan was performed to study the flow path of the duct jet. The results clearly showed that the duct jet deflected with increasing velocity. For a velocity of 20 knots (10.3 m/s) it

was estimated that a 3° to 4° deflection of the jet occurs at the control vanes while at 25 knots (12.9 m/s) the jet deflection angle was estimated to be 17°. This significant deflection of the jet explains the loss of control vane authority measured in the wind-tunnel model.

Subsequent research by Fleming [36] investigated a large number of control concepts with the goal of counteracting the large duct pitching moment. These control concepts focused on producing asymmetric duct pressure distributions, and hence, asymmetric duct-exit velocity profiles that produced a counteracting moment. This was done using a variation of spoilers, duct bypass flow, leading and trailing edge flap devices in addition to the conventional slip stream control vanes, as shown in Figure 2.9. Out of the 14 concepts tested the internal duct deflector with bleed, Figure 2.9d, provided a pitching moment approximately 50% of baseline control vanes. This arrangement was preferred by Fleming due to implementation considerations and the near constant performance of the device versus airspeed. However, the results provided by Fleming were only made at a duct angle of attack of 90°, so further performance testing over a range of angles of attack would be required to determine their suitability on an actual ducted-fan aircraft.

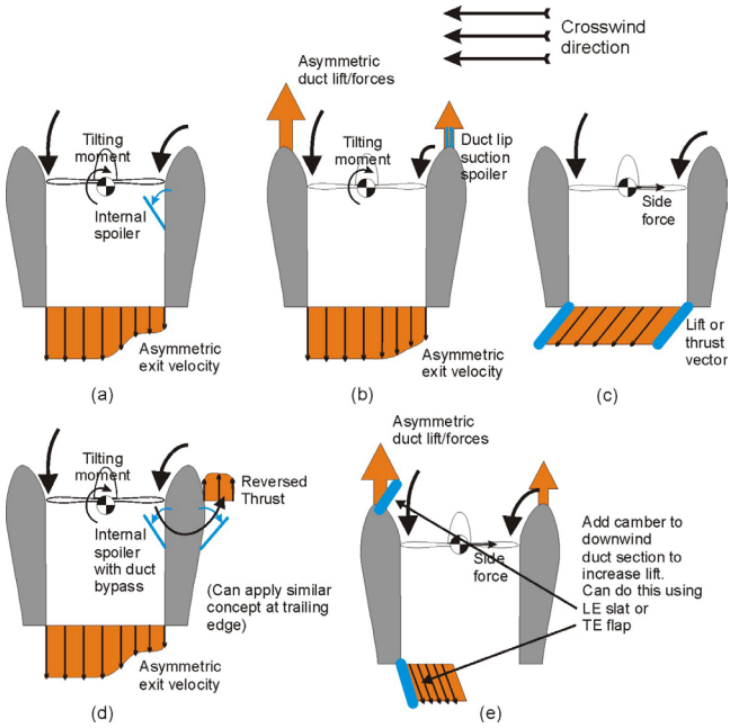

Figure 2.9: Various control effectors investigated by Fleming. Diagram credit Jonathan Fleming [36]

A wind tunnel investigation on a 10" (254 mm) ducted-fan was done by Martin [54], who examined the ducted-fan from 0° to 110° angle of attack and for airspeeds from 0 ft/s to 120 ft/s (36.6 m/s). The tests examined the isolated rotor, isolated duct and combined duct and rotor with two duct shapes with varying duct inlet radii. The results showed that the isolated duct would stall at an angle of attack near 15° and with the addition of the powered propeller stall was delayed until 40°. Decreasing the inlet radius reduced the overall thrust, but improved the stability for cross-wind effects. For both shaped

ducts the blade tip clearance was varied from 1 % to 4.5% of the blade radius which showed that as tip clearance increased the Figure of Merit decreased from 0.66 to 0.46, respectively. The isolated propeller in comparison had a Figure of Merit of 0.44.

A paper and Masters thesis by Graf [46, 55] examined various duct lip shapes and their effect on the pitching moment by wind-tunnel measurement. The wind-tunnel specimen was an existing model used in the development of the Honeywell MAV. Graf used the concept of duct centre of pressure position from the duct leading edge to highlight where the aircraft's centre of pressure should be located to minimise the influence of the momentum drag and asymmetric lift. Graf showed the important result that the duct centre of pressure is not a function of the duct angle of attack between 20° to 90°. Various leading edge devices such as slats and spoilers were tested to measure their performance in mitigating the pitching moment effects. Interestingly, the slats in their open position have a twofold benefit of increasing thrust and limiting the variation of the duct centre of pressure travel movement from 0.14 to 0.18 duct diameters above the duct leading edge for angles of attack from 40° to 90° at 30 ft/s (9.1 m/s).

Other Ducted-Fan aircraft

Numerous other ducted-fan aircraft have been developed, some only to the design stage, such as the four engined ducted-fan aircraft describe in this patent [56], which claims that the thrust lines from the four ducted-fans point to a single point above the centre of gravity to achieve an inherently stable VTOL aircraft. This claim is a contradiction to the qualitative discussion of VTOL aircraft in[57], which describes and reinforces the fact that all heavier than air aircraft are only at best neutrally stable in hover, and that their attitude response is a function of the ratio of control moments to the aircraft inertia.

Ducted-Fans in Wind Tunnels

The technical report by Parlett in 1955 [58] contains aerodynamic measurements of a small, 0.46 m diameter, ducted-fan in a wind tunnel in support of the Hiller VZ-1 Flying Platform. Lift, drag, and pitching moments were measured for a range of wind tunnel airspeeds from 0 m/s to 17 m/s. Measurements were also taken with the propeller removed to show the affect of the duct in isolation.

Results from the test showed that the pitching moment, about the point where the duct quarter-chord plane intersects the duct axis, is a function of duct angle of attack and airspeed. The general trend of the results for an angle of attack of 90° showed that a positive pitching moment would increase with increasing airspeed until a maximum moment occurs, where the pitching moment would then decrease and become negative with increasing airspeed. As the angle of attack diminished towards zero so did the pitching moment. Measurements showed that maximum drag occurs at maximum angle of attack and airspeed, and decreases and becomes negative as the angle of attack tends to zero. Lift measurements were found to increase to a maximum before de-

creasing to zero as the angle of attack decreased from 90° to zero. Static thrust measurements indicated that increasing inlet radius size improved efficiency for the ducted-fan.

A NACA technical report by Taylor in 1958 [59], showed the measured static thrust for a propeller submerged inside a wing (fan-in-wing) for various parameters of: inlet radius, propeller axial position, chord length, diffuser angle, and ground proximity. Results demonstrated that an inlet radius of less than 6 % of the propeller diameter showed marked falls in static thrust. It was found that the axial position of the propeller inside the duct did not have a significant effect on the thrust, unless it was positioned close to the entrance. An improvement in efficiency of 66 % to 74 % was found from increasing the duct chord from 3 % to 103 % of the propeller diameter, respectively. Increasing the diffuser angle from 0° to 7° and 14° increased the static thrust force substantially, as this increased the exit diameter. This report also presented the interesting result that a suction force equal to the out-of-ground-effect static thrust is created when the fan-in-wing is at 25 % of the propeller diameter above the ground. The reason for the suction is that the airflow between the ground and underside of the wing is at a high speed, which according to Bernoulli equation reduces the static pressure below atmospheric. Since the pressure on the top side of the wing is at atmospheric pressure, the pressure difference between the top and bottom sides of the wing produces the negative net thrust force that sucks the fan-in-wing towards the ground. As clearance between the wing and ground is increased the static thrust force rapidly increases towards out-of-ground-effect static thrust force.

Due to the lack of data on large diameter ducted-fans, NASA researchers wind-tunnel tested a 7 ft ducted fan propeller in the Ames 40 ft by 80 ft wind-tunnel [60]. The results showed that the ducted-fan had a 74% efficiency as a propulsion device and that the Figure of Merit was 81%. Reaction measurements for a small range of angles of attack from 0° to 40° are also presented.

A thesis by Pereira [61] investigated a large number of ducted-fan parameters with the aim of studying how these parameters affect a ducted-fan at the micro UAV scale. A 160 mm rotor diameter ducted-fan was studied in 17 configurations and compared to an open propeller in a wind-tunnel. It was found that the addition of the duct could provide up to a 94 % increase in thrust, or a 62 % reduction in power for the same thrust over the baseline open propeller sharing the same diameter. These results exceed the predictions of momentum theory, which as Pereira explains occurs due to the duct reducing non-ideal power losses of the rotor. An optimal diffuser angle of 10° and an optimal chord length equal to 50 % of the rotor diameter was found. Reactions and surface pressure measurements were also recorded for a range of angles of attack from 0° to 90° over a range of advance ratios. The high asymmetry of the pressure readings, in the longitudinal plane reflected the much higher pitching moments of the ducted-fan over the open propeller. The pressure measurements also revealed that the pressure at the duct exit plane does not quite reach atmospheric pressure, which challenges the validity of the momentum theory used in the analysis of a ducted-fan. The thesis also made the comment that ignoring the inherent safety advantages of the ducted-fan, a larger propeller is more likely to give better performance than the smaller

diameter ducted-fan for a given overall aircraft size.

Ducted-Fan CFD Studies

Numerous CFD studies on ducted-fans have been made where the majority of these studies have used the actuator disc model/momentum source to represent the fan, [62, 63, 53, 52, 51, 64]. A CFD study by Alturk [65] describes the CFD methodology for modelling a 127 mm diameter ducted-fan complete with rotor and stator blades in the hovering condition. The k-ω turbulence model was used, and the results were validated against measurement and showed good agreement.

Chang and Rajagopalan [64] developed their own CFD program to model the axis-symmetric ducted-fans in axial flight. Their code was validated against the SoloTrek ducted-fan and Micro-Craft's UAV ducted-fan and showed good relation, within 3 %. However, their code is limited to axial flight conditions.

A paper by Zhao [52] explains how two-dimensional CFD techniques were used to analyze the axial flow performance of a ducted-fan from hovering to cruise flight airspeeds; in the same paper three-dimensional CFD simulations were also performed for an entire ducted-fan MAV aircraft. The CFD simulations showed lift, drag, and pitching moment coefficients for a range of velocities up to 20 m/s and a range of angles of attack from $-16°$ to $16°$. However, for the range of angles of attack studied by Zhao, the free stream velocity is only minimally deflected, hence the well known large ducted-fan pitching moments are not examined, which is a necessity for VTOL ducted fans; the small range of angles of attack also avoid simulating separated flow conditions that occur at higher angles of attack [62]. The Master's thesis by Zhao [51] presents further CFD results with validation from wind tunnel results of a scaled model.

Summary of Ducted Fan Aircraft

An extensive range of vehicles, from small UAVs to large transport aircraft, make use of the ducted-fan. Table 2.1 summarizes the design and performance of more well known VTOL ducted-fan aircraft. It must be noted that, although the ducted-fan has been used on many VTOL aircraft concepts the only commercially available ducted-fan aircraft to date is the Honeywell UAV ducted-fan. Without the ability of wingless ducted-fan aircraft to safely descend due to power loss the ducted fan concept may be forever limited to UAV applications. However, with the improvement of more reliable technologies and the ballistic parachute, future ducted-fan aircraft, such as the Martin Jetpack, may be safely flown and commercially viable.

History has shown that ducted-fan propulsion systems have promise for VTOL aircraft concepts but the aerodynamic behaviour, namely large pitching moments, of the ducted fans in crosswind/high angle or attack flight poses a significant hurdle for the control of ducted-fan aircraft. Without adequate control ducted-fan aircraft cannot function in practical real-life situations.

Table 2.1: Comparison of Ducted Fan Aircraft

Aircraft	Number of ducts	Config.	Control Method	Max/Range of Disk Loadings T/S [Pa]	Max Speed [km/h]	MTOW [N]	Duct Diameter [m]	Power [kW]	Duct Efficiency	MTOW/ Power [N/kW]
Martin Jetpack P-11A	2	Twin	Vanes in slipstream	$4200-4700$	10	2450	0.6	149	0.55	16.4
Martin Jetpack P-12	2	Twin	Vanes in slipstream	$2600-3100$	NA	2649	0.8	149	0.69	14.5
Hiller VZ-1 Flying Platform	2	Tandem	CG movement, yaw vanes	700	$16-25$	2470	2.13	60	0.49	41.2
Piasecki VZ-8 Flying Jeep	2	Tandem	Variable pitch, cyclic and vanes	1700	136	16300	2.5	825	0.36	19.8
Bell X-22	4	Quad	Variable pitch	5500	409	78500	2.13	3800	0.69	20.65
Doak VZ-4	2	Wing tip	Duct tilt, vanes, pitch elevator	6100	370	14200	1.22	626	0.80	22.7
Aerofex Hover Bike	2	Tandem	CG movement, deflectors, yaw vanes	$450-610$	50	2830	1.52	N/A	N/A	N/A
Urban Aeronautics Honeywell T-Hawk	2	Tandem	Cascade vanes	2700	N/A	14800	1.8	720	0.45	19.2
Micro Craft iStar MAV	1	Single	Vanes in slipstream	430	90	82	0.22	0.9	0.31	22.1
	1	Single	Vanes in slipstream	960	N/A	18	0.33	3.72	0.18	19.6

2.2 Qualitative Discussion on Martin Jetpack Aerodynamics

Jetpack Description

The Martin Jetpack uses two ducted-fans in twin configuration to produce both the lift and thrust forces to lift and propel the aircraft through the air. Figure 2.10 shows the major forces of the P-11A Jetpack in trimmed level flight. The key ducted-fan forces of thrust and ducted-fan normal force govern the aerodynamic behaviour the aircraft. The control vanes located in the duct exhaust flow are used to create the control moments to orientate and trim moments to balance the aircraft.

Lift and Propulsion

Lift for the Jetpack is generated in a similar means to a helicopter in that an engine powers rotor blades to create a relative velocity and aerodynamic forces, but unlike a helicopter the Jetpack's fan blades are enclosed by a duct. This forces the air to flow axially through the duct, thus the airflow differs from that of an open helicopter rotor system. The presence of the duct makes the ducted-fan more susceptible to pitching moments than an open propeller/rotor when subjected to cross-wind effects.

Lift on the Jetpack is a function of the fan speed, which is controlled by engine speed. Thus, the rate of change of lift is a function of the rate of change of engine speed. Hence, to ensure the thrust is responsive the engine must have significant excess torque, and the fans, drive system, and engine must have low inertia. A helicopter rotor system in comparison has far too much inertia to

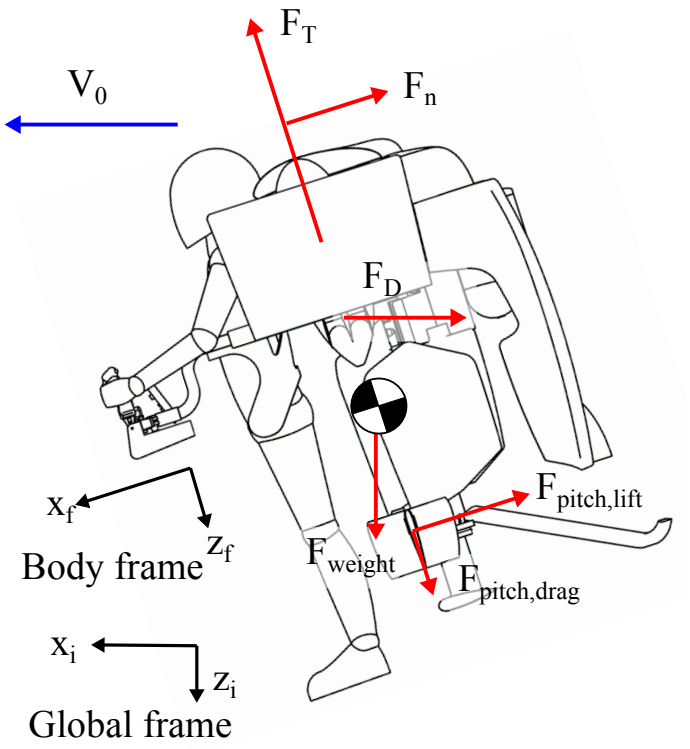

Figure 2.10: Jetpack P-11A in trimmed level flight

allow for engine thrust control, so uses collective pitch to vary the angle of attack of the rotor blades to vary thrust. This can be done quickly allowing for large changes in thrust.

The helicopter has the ability to momentarily output thrust greater than the maximum steady state thrust. This is done by abruptly increasing the angle of attack of the rotor blades and using the angular momentum of the rotor blades to supply extra energy to overcome the increased drag of the rotor blades at the higher angle of attack. The Jetpack in comparison relies on excess thrust/power margin from the hovering requirements to generate manoeuvering thrust.

Control

Similarly to an aeroplane, the Jetpack uses control surfaces located with moment arms from the centre of gravity to generate control moments when deflected, as shown on Figure 2.11. The Jetpack's yaw vanes are similar to ailerons on an aeroplane in that they deflect in opposite directions generating a pure moment. The deflection of the Jetpack pitch and roll vanes produce both a lift force and a moment. This is not ideal as the force causes the Jetpack to accelerate. The helicopter control strategy has the advantage over the Jetpack in that pure moment couples between thrust and weight vectors is created by cyclic variation of the rotor blade angles of attack.

The height and directional control in a a helicopter is coupled as discussed in section B.2, whereas in the in the Jetpack they are uncoupled as the ducted-fans are essentially torque neutral.

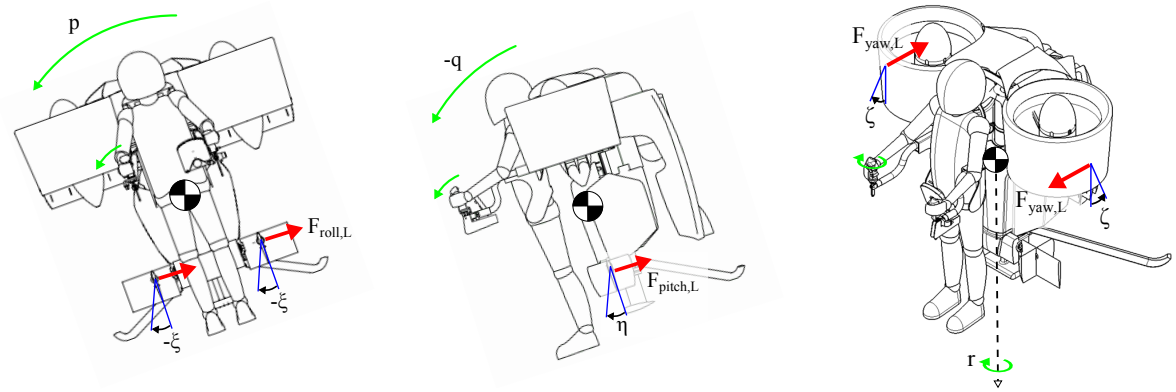

(a) Roll (b) Pitch (c) Yaw

Figure 2.11: Jetpack roll, pitch, and yaw motion due to respective control vane deflection

Stability

Similar to a helicopter in hover, the Jetpack is unstable in pitch and roll, as no restoring moment is created when disturbed. However, since the thrust vector is tilted a motion develops in the direction of tilt, refer to Figure 2.12. This motion produces a restoring moment that will stabilise the Jetpack. However, as little to no damping exists the Jetpack will overshoot the level position and tilt in the opposite direction resulting in acceleration and motion in this direction, which then produces another restoring moment. As little damping exits and the restoring moments and translation speeds are not in-sync, the oscillation becomes unstable.

The Jetpack mass distribution is very dense and closely located to the centre of gravity, thus the moment of inertia of the Jetpack is very small compared to other VTOL aircraft. The small moment of inertia translates to high angular acceleration and rapidly diverging motion. This fast response due to the low moment of inertia requires a fly-by-wire control system to make the Jetpack controllable.

In yaw the Jetpack exhibits neutral static stability and stable dynamic stability due to the momentum drag created by the ducts from motion about the z axis.

Summary

In summary the Jetpack is a mix between a helicopter and an aeroplane. It can produce lift at zero airspeed and thus hover like a helicopter, but uses the simple control system of an aeroplane. The Jetpack is unstable in hover and relies on dynamic motion to create a restoration moment. However, due to the absence of inherent damping the Jetpack is dynamically unstable, resulting in a diverging oscillation. This was experienced with the original manually controlled Martin Jetpack prototypes. To achieve stability in hover the Jetpack uses a fly-by-wire system to artificially introduce restoring and damping moments.

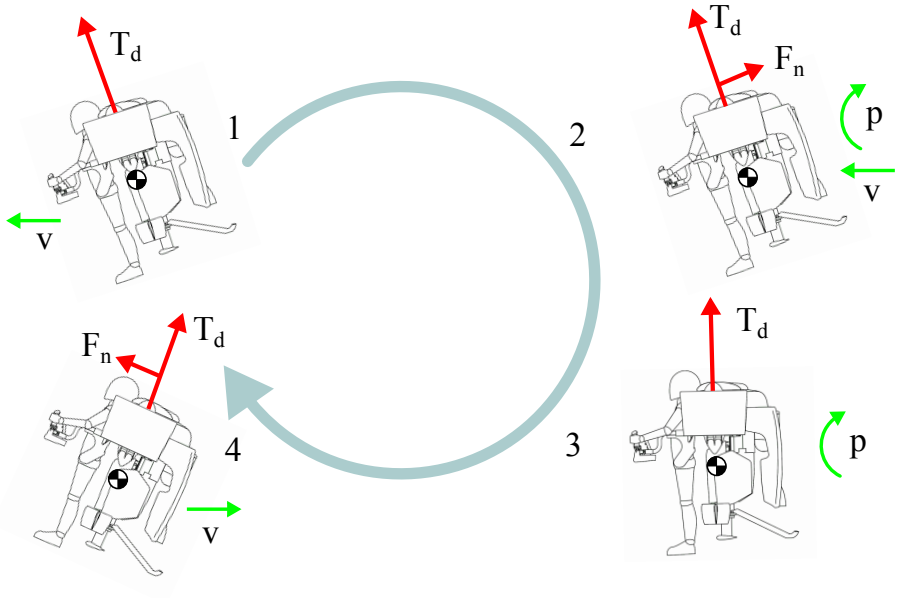

Figure 2.12: Oscillation of the Jetpack in hover due to pitch disturbance.

Chapter 3

Mathematical Derivations

"The greatest enemy of knowledge is not ignorance, it is the illusion of knowledge."
Stephan Hawking

This chapter explains the physics of the key aerodynamic features on the Martin Jetpack via mathematical models. The derivation of actuator disc theory is first presented with validation from thrust measurements. Next, the effect of a cross wind on the ducted-fan is examined, showing the derivation of the ducted-fan normal force. Models for the key concept of duct centre of pressure are developed using various methodologies to produce a range of initial models to capture this complex phenomenon. The development of the control vane moment model for the Jetpack based on conventional aerofoil lift and drag coefficients as a function of angle of attack is shown. The chapter concludes with the presentation of mathematical models of the atmosphere used in the Jetpack model.

3.1 Ducted-Fan Thrust Model

The purpose of a ducted-fan is similar to that of an open propeller, which is to develop thrust to propel the aircraft through the atmosphere. Fundamentally, the thrust force is created by the change in momentum of air through the propeller and/or ducted-fan system. This change in momentum occurs due the rotation of the propeller/fan blades which accelerate air along the axis of rotation. This creates a lower than atmospheric pressure area in-front of the propeller and a higher than atmospheric pressure region behind the propeller producing an abrupt pressure rise across the propeller which is proportional to the thrust generated by the propeller.

The aerodynamics associated with the change of momentum through a propeller is complex and relies on numerous parameters to fully model the phenomena. Fortunately, a simple model (actuator disc theory) exists, which describes the thrust, power, and diameter relationship of a propeller. This model was developed by Rankine and Froude [66] to understand the performance of marine propellers, but can equally well be used for aircraft propellers.

The ducted-fan thrust is the most important aerodynamic force to model in the design of the Jetpack. The thrust model relates the diameter of the duct,

thrust, and power. Hence, this primary model dictates the characteristic size of the ducted-fan required for the given engine power and thrust requirements.

The complete derivations for both an open propeller and a ducted-fan are presented in the following sections and a comparison of the two is shown to highlight the advantages of a ducted-fan for VTOL aircraft applications. The complete derivations are shown as could not be found elsewhere, and are also helpful for the Jetpack model.

Open Propeller Derivation

General Case

The purpose of a propeller is to produce a thrust force. This is accomplished by the pressure rise across the propeller accelerating the fluid, thus creating a change in momentum resulting in a thrust force. Figure 3.1 shows the control volume around an open propeller. The streamlines indicate the airflow passing through the propeller, the outer most stream lines represent the top and bottom boundaries of the control volume, and hence, the boundary between the airflow that is influenced and not influenced by the propeller. It can be seen in Figure 3.1 that the streamlines contract as they approach and depart from the propeller. This is the result of the thrust force inducing a momentum change in the fluid, which causes the fluid to accelerate from the free-stream velocity V_1 to the faster free-stream velocity V_4, where the static pressure returns to atmospheric conditions. The location of V_1 and V_4 are infinitely upstream and downstream from the propeller, respectively. The locations of station 2 and 3 are just upstream and downstream of the propeller plane, respectively and bound the pressure rise across the propeller, as shown of Figure 3.1. The actuator disc theory assumes that the pressure rise across the propeller multiplied by the propeller disc area is equal to the propeller thrust.

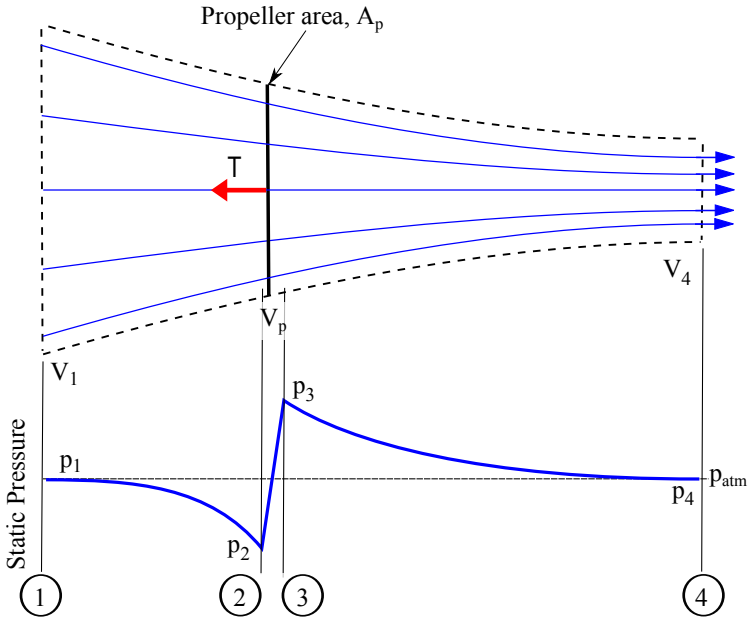

Figure 3.1: Cross section of a control volume around an propeller

Applying the three fundamental physical laws and the actuator disk model

to the propeller control volume shown in Figure 3.1 gives the conservation of mass as:

$$\dot{m} = \rho A_p V_2 = \rho A_p V_3 = \rho A_4 V_4 \tag{3.1.1}$$

the conservation of momentum as:

$$T_p = \dot{m}\Delta V = \dot{m}(V_4 - V_1) \tag{3.1.2}$$

the conservation of energy as:

$$P_p = \frac{1}{2}\dot{m}(V_4^2 - V_1^2) \tag{3.1.3}$$

and the actuator disc model as:

$$T_p = A_p(p_3 - p_2) \tag{3.1.4}$$

Using the condition that the pressures at stations 1 and 4 must equal atmospheric pressure, $p_1 = p_4 = p_{atm}$, the Bernoulli equation (B.1.1) can be applied between stations 1 to 2, and from stations 3 to 4 to get:

$$p_1 + \frac{1}{2}\rho V_1^2 = p_2 + \frac{1}{2}\rho V_2^2 \tag{3.1.5}$$

$$p_3 + \frac{1}{2}\rho V_3^2 = p_4 + \frac{1}{2}\rho V_4^2 \tag{3.1.6}$$

which can be rearranged for:

$$p_2 = p_1 + \frac{1}{2}\rho(V_1^2 - V_2^2) \tag{3.1.7}$$

$$p_3 = p_4 + \frac{1}{2}\rho(V_4^2 - V_3^2) \tag{3.1.8}$$

Using the conservation of mass across the actuator disc, which implies $V_2 = V_3 = V_p$, and substituting equations 3.1.7 and (3.1.8) into the actuator disc model (3.1.4) results in:

$$T_p = A_p(p_4 + \frac{1}{2}\rho(V_4^2 - V_p^2) - (p_1 + \frac{1}{2}\rho(V_1^2 - V_p^2)) \tag{3.1.9}$$

$$T_p = \frac{1}{2}A_p\rho(V_4^2 - V_1^2) \tag{3.1.10}$$

Combining equations (3.1.10) and (3.1.2):

$$\rho A_p V_p(V_4 - V_1) = \frac{1}{2}A_p\rho(V_4^2 - V_1^2) \tag{3.1.11}$$

which reduces to:

$$V_p = \frac{1}{2}(V_1 + V_4) \tag{3.1.12}$$

Thus, the velocity at the propeller is the average between the free-stream and fully developed far-stream velocities. Rearranging for V_4:

$$V_4 = 2V_p - V_1 \tag{3.1.13}$$

Equation (3.1.13) combined with the conservation of mass (3.1.1) shows that the expansion ratio ϵ_p, which is the ratio between the area at station 4, A_4, and the propeller area, A_p, is:

$$\epsilon_p = \frac{A_4}{A_p} = \frac{V_p}{2V_p - V_1} \tag{3.1.14}$$

It can be seen that the expansion ratio ranges between $\frac{1}{2} \leq \epsilon_p < 1$ for the range of free-stream velocities from $V_1 = 0$ to $V_1 = V_p$. Substituting equation 3.1.13 for V_4 into equation (3.1.10):

$$T_p = \frac{1}{2} A_p \rho((2V_p - V_1)^2 - V_1^2) \tag{3.1.15}$$

$$T_p = \frac{1}{2} A_p \rho((4V_p^2 - 2V_1V_p - 2V_1V_p + V_1^2) - V_1^2) \tag{3.1.16}$$

$$T_p = \frac{1}{2} A_p \rho(4V_p^2 - 4V_1V_p) \tag{3.1.17}$$

$$T_p = 2A_p \rho(V_p^2 - V_1V_p) \tag{3.1.18}$$

Equation (3.1.18) can be rearranged into the form of a quadratic equation, $0 = ax^2 + bx + c$, and solved for the unknown term V_p as:

$$0 = V_p^2 - V_1V_p - \frac{T_p}{2\rho A_p} \tag{3.1.19}$$

$$V_p = \frac{V_1 \pm \sqrt{V_1^2 + \frac{2T_p}{\rho A_p}}}{2} \tag{3.1.20}$$

Taking the positive value, as the negative term does not make physical sense, this results in a general equation for the velocity at the actuator disc, and hence, the propeller:

$$V_p = \frac{V_1}{2} + \sqrt{\frac{V_1^2}{4} + \frac{T_p}{2\rho A_p}} \tag{3.1.21}$$

Letting the velocity at the disc V_p equal the sum of the induced velocity V_{pi} and free stream velocity V_1 leads to:

$$V_p = V_{pi} + V_1$$

$$V_{pi} = -\frac{V_1}{2} + \sqrt{\frac{T_p}{2\rho A_p}} \tag{3.1.22}$$

where V_{pi} is termed the *induced velocity* and is the velocity increment due to the presence of thrust from the propeller.

Applying the conservation of energy (3.1.3) and equation (3.1.21) the ideal power required to induce the fluid flow for a given thrust is:

$$P_p = \frac{1}{2}\dot{m}(V_4^2 - V_1^2) = T_pV_p = T_p\left(\frac{V_1}{2} + \sqrt{\frac{V_1^2}{4} + \frac{T_p}{2\rho A_p}}\right)$$

$$P_p = \frac{T_p V_1}{2} + \sqrt{\frac{T_p^2 V_1^2}{4} + \frac{T_p^3}{2\rho A_p}} \tag{3.1.23}$$

Equation (3.1.23) presents the general relationship of power, thrust, and area as a function of free-stream velocity for an open propeller.

Hovering/Static Case
In the case of hovering flight $V_1 = 0$ the power equation (3.1.23) reduces to:

$$P_p = P_{pi} = \sqrt{\frac{T_p^3}{2\rho A_p}} \tag{3.1.24}$$

and the thrust equation (3.1.21) reduces to the induced thrust equation (3.1.22):

$$V_p = V_{pi} = \sqrt{\frac{T_p}{2\rho A_p}} \tag{3.1.25}$$

The far-stream velocity equation 3.1.13 reduces to:

$$V_4 = 2V_p = \Delta V \tag{3.1.26}$$

which shows by conservation of mass that the expansion between the final state at station 4 and at the propeller for the hover condition is $\frac{1}{2}$, as shown by the reduce state of equation 3.1.14 as:

$$\epsilon_p = \frac{A_4}{A_p} = \frac{1}{2} \tag{3.1.27}$$

Ducted-Fan Derivation

Hovering/Static Case
Similar, to a propeller, the purpose of a ducted-fan is to produce thrust, which like the propeller is accomplished by creating a pressure differential across the fan that accelerates the fluid flow. The effect of the duct or shroud on the propeller/fan is to prevent the contraction and rather introduce an expansion of the fluid flow behind the fan to raise the static pressure to the atmospheric pressure at the the duct exit plane. Hence, the presence of the duct defines the flow slipstream and the final condition of the flow at the duct exit. By modifying the expansion ratio, ϵ_d, of a ducted-fan, the performance of the ducted-fan can be altered for a specific purpose. The shape and size of the duct inlet also significantly effects the efficiency and crosswind behaviour.

Following a similar methodology to that used for an open propeller, the derivation for a ducted-fan as shown in Figure 3.2 and presented in [67, 61, 12] is developed from the three fundamental physical laws. Conservation of mass implies:

$$\dot{m} = \rho A_r V_r = \rho A_d V_d \tag{3.1.28}$$

where the subscript r refers to rotor. Assuming air density is constant throughout the control volume mass conservation implies:

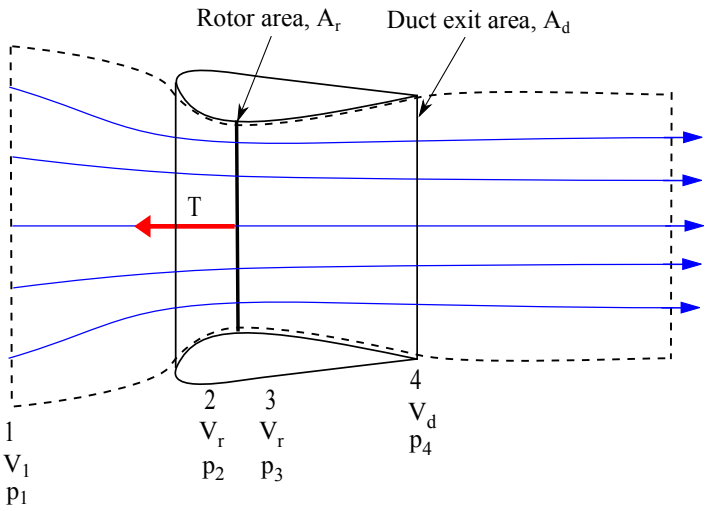

Figure 3.2: Cross section of a control volume around a ducted-fan

$$V_d = V_r \frac{A_r}{A_d} = \frac{V_r}{\epsilon_d} \tag{3.1.29}$$

where the expansion ratio, ϵ_d, is the ratio of duct exit area to rotor area:

$$\epsilon_d = \frac{A_d}{A_r} \tag{3.1.30}$$

Conservation of momentum implies:

$$T_d = \dot{m}\Delta V = \dot{m}V_d = \rho A_r V_r \frac{V_r}{\epsilon_d} = \rho A_r \frac{V_r^2}{\epsilon_d} \tag{3.1.31}$$

which can be rearranged into terms of the velocity at the rotor. For hovering flight this is equal to the induced velocity V_{ri} for a ducted-fan:

$$V_r = V_{ri} = \sqrt{\frac{T_d \epsilon_d}{\rho A_r}} \tag{3.1.32}$$

Using the mass conservation equation (3.1.28) with equation (3.1.32) the ducted-fan velocity V_d can be found to be:

$$V_d = \sqrt{\frac{T_d}{\rho A_d}} \tag{3.1.33}$$

Conservation of Energy implies:

$$P_d = \frac{1}{2}\dot{m}V_d^2 \tag{3.1.34}$$

Substituting equations (3.1.28) and 3.1.29 for V_d results in:

$$P_d = \frac{1}{2}\rho A_r \frac{V_r^3}{\epsilon_d^2} \tag{3.1.35}$$

Substituting in equation 3.1.32 puts the ducted-fan power in terms of thrust and duct diameter as:

$$P_d = \sqrt{\frac{T_d^3}{4\rho A_r \epsilon_d}} = \sqrt{\frac{T_d^3}{\rho \pi d^2}} \tag{3.1.36}$$

Equation (3.1.34) shows the relation between the key ducted-fan parameters of ideal power, P_d, the total thrust of the ducted-fan system, T_d, the fan rotor area, A_r, and the expansion ratio ϵ_d for the hovering flight condition, $V_1 = 0$, which was developed without the need of the actuator disc model. By applying the actuator disc model, $T_r = A_r \Delta p$, to the rotor of the ducted-fan the thrust developed by the fan can be determined. Using the Bernoulli equations between stations 1 and 2, and stations 3 and 4:

$$p_2 = p_1 + \frac{1}{2}\rho(V_1^2 - V_r^2) \tag{3.1.37}$$

$$p_3 = p_4 + \frac{1}{2}\rho(V_d^2 - V_r^2) \tag{3.1.38}$$

and substituting the above equations into the actuator disc model at the hover conditions yields:

$$T_r = A_r \Delta p = A_r(p_3 - p_2) = \frac{1}{2}\rho A_r \frac{V_r^2}{\epsilon_d^2} \tag{3.1.39}$$

The ratio of fan thrust to total thrust developed by the ducted-fan is:

$$\frac{T_r}{T_d} = \frac{\frac{1}{2}\rho A_r \frac{V_r^2}{\epsilon_d^2}}{\rho A_r \frac{V_r^2}{\epsilon_d}} = \frac{1}{2\epsilon_d} \tag{3.1.40}$$

From equation (3.1.40) it can be seen if the fan thrust equals the total thrust that the expansion ratio $\epsilon_d = \frac{1}{2}$. This result shows that the presence of the duct has no effect on the total thrust for this expansion ratio, which is expected as this expansion (contraction in reality) of flow, from the station 3 to station 4, is that described by equation (3.1.13) for an open propeller in the hover condition. This result has the benefit that the equations used for the derivation of the ducted-fan can be equally used for an open propeller by substituting T_p for T_d and $\frac{1}{2}$ for ε_d into equations (3.1.32) and (3.1.34).

Axial Flight Case

For axial flight $V_1 \neq 0$ the rotor induced velocity V_{ri} and far-stream induced velocity ΔV is incremented by V_1. Unlike the open propeller that experiences an increase in the expansion ratio with free-stream velocity, as described by equation (3.1.14), the expansion ratio for a ducted-fan remains constant. Therefore for a ducted-fan in axial flight conservation of mass implies:

$$\dot{m} = \rho A_r V_r = \rho A_d V_d = \rho A_r(V_{ri} + V_1) = \rho A_4(\Delta V + V_1) \tag{3.1.41}$$

Assuming air density is constant throughout the control volume the above implies:

$$\Delta V = V_d - V_1 = \frac{V_r}{\epsilon_d} - V_1 = \frac{V_{ri} + V_1}{\epsilon_d} - V_1 \tag{3.1.42}$$

Conservation of momentum implies:

$$T_d = \dot{m} V_w = \rho A_r V_r \left(\frac{V_r}{\epsilon_d} - V_1 \right) \tag{3.1.43}$$

which can be rearranged in terms of the velocity at the rotor:

$$V_r = \frac{V_1 \epsilon_d}{2} + \sqrt{\frac{V_1^2 \epsilon_d^2}{4} + \frac{T_d \epsilon_d}{\rho A_r}} \tag{3.1.44}$$

Using the actuator disc model the thrust produced by the rotor can be determined to be:

$$T_r = A_r \Delta p = A_r (p_3 - p_2) \tag{3.1.45}$$

Using the Bernoulli equations (3.1.7) and (3.1.8) to relate stations 1 to 2, and stations 3 to 4:

$$T_r = A_r \frac{1}{2} \rho (V_d^2 - V_1^2)$$

By letting $V_d = \Delta V + V_1$ the above reduces to:

$$T_r = A_r \rho \Delta V (\frac{\Delta V}{2} - V_1) \tag{3.1.46}$$

The ratio of fan rotor thrust to total duct thrust for the general case is:

$$\frac{T_r}{T_d} = \frac{A_r \rho \Delta V (\frac{\Delta V}{2} - V_1)}{\dot{m} \Delta V} = \frac{1}{2} (\frac{1}{\epsilon_d} + \frac{V_1}{V_r}) \tag{3.1.47}$$

The power required for axial flight of the ducted-fan by conservation of energy is:

$$P_d = \frac{1}{2} \dot{m} \left(V_d^2 - V_1^2 \right) = T_r V_r = V_r \frac{T_d}{2} (\frac{1}{\epsilon_d} + \frac{V_1}{V_r}) = \frac{3}{4} T_d V_1 + \sqrt{\frac{T_d^2 V_1^2}{16} + \frac{T_d^3}{4 \rho A_r \epsilon_d}} \tag{3.1.48}$$

Comparison of Ducted-Fan to Open Propeller

Hover Flight Comparison

A comparison of the ducted-fan to an open propeller in hover, as performed by [61], can be made by the ratio of equation (3.1.34) to equation (3.1.24) as:

$$\frac{P_d}{P_p} = \frac{\sqrt{\frac{T_d^3}{4 \rho A_r \epsilon_d}}}{\sqrt{\frac{T_p^3}{2 \rho A_p}}} = \frac{1}{\sqrt{2 \epsilon_d}} \left(\frac{T_d}{T_p} \right)^{\frac{3}{2}} \left(\frac{A_p}{A_r} \right)^{\frac{1}{2}} \tag{3.1.49}$$

For equal power and area equation (3.1.49) reduces to:

$$\frac{T_d}{T_p} = \sqrt[3]{2\epsilon_d} \tag{3.1.50}$$

which shows that the ducted-fan of the same power and rotor area as a propeller produces greater thrust. For equal power and thrust equation (3.1.49) reduces to:

$$\frac{A_r}{A_p} = \frac{1}{2\epsilon_d} \tag{3.1.51}$$

$$\frac{d_r}{d_p} = \sqrt{\frac{1}{2\epsilon_d}} \tag{3.1.52}$$

which shows that the ducted-fan of the same power and thrust as a propeller can have a smaller rotor area/diameter.

For equal thrust and area equation (3.1.49) reduces to:

$$\frac{P_d}{P_p} = \frac{1}{\sqrt{2\epsilon_d}} \tag{3.1.53}$$

which shows that the ducted-fan of the same thrust and rotor area as a propeller requires less power at static conditions.

Figure 3.3 shows how the thrust, area, and power ratios, equations (3.1.50) to (3.1.53), vary with the expansion ratio. It can be seen on Figure 3.3 that the benefit of a duct increases with increasing duct expansion ratio. However, in reality an upper limit exists on the expansion ratio due to the onset of flow separation within the duct.

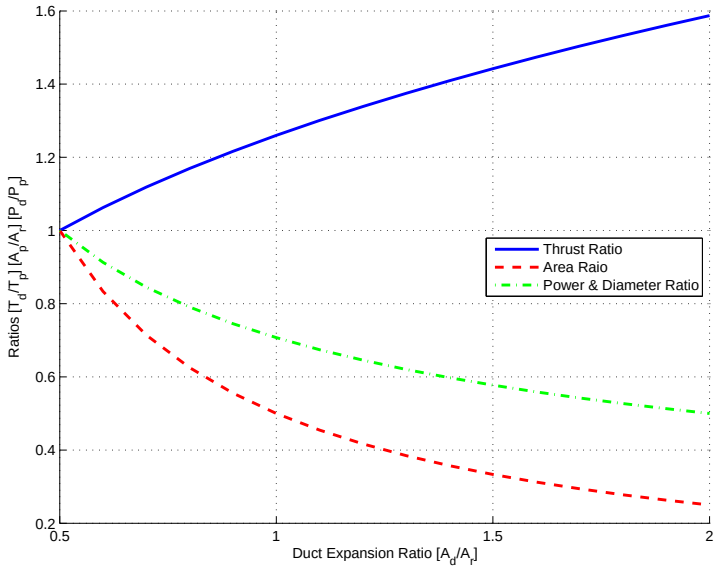

Figure 3.3: Comparison of ducted-fan to open propeller for range of duct expansion ratios, ϵ_d.

Arguably the maximum diameter of the duct should be compared to the open propeller diameter as this is the physical equivalent footprint for the ducted-fan. However, as no theory exists that takes into account this maximum extent of the duct, typically the outside diameter of the duct lip, the duct exit

diameter is used instead. This comparison can be made by substituting in equation (3.1.30) for A_r into equation (3.1.49), which eliminates the expansion ratio to give:

$$\frac{P_d}{P_p} = \frac{1}{\sqrt{2\epsilon_d}} \left(\frac{T_d}{T_p}\right)^{\frac{3}{2}} \left(\frac{A_p \epsilon_d}{A_d}\right)^{\frac{1}{2}} = \frac{1}{\sqrt{2}} \left(\frac{T_d}{T_p}\right)^{\frac{3}{2}} \left(\frac{A_p}{A_d}\right)^{\frac{1}{2}} \tag{3.1.54}$$

Note equation 3.1.54 can also be derived by setting $\epsilon_d = 1$ so that $A_r = A_d$. For equal power and area equation 3.1.54 reduces to:

$$\frac{T_d}{T_p} = \sqrt[3]{2} \approx 1.26 \tag{3.1.55}$$

This thrust ratio gives a practical result that the addition of the duct and supporting features should not increase the aircraft weight by a factor of 1.26 to an open propeller design.

For equal power and thrust equation 3.1.54 reduces to:

$$\frac{A_r}{A_p} = \frac{1}{2} \tag{3.1.56}$$

$$\frac{d_r}{d_p} = \sqrt{\frac{1}{2}} \approx 0.707 \tag{3.1.57}$$

which shows that maintaining the same thrust and power the exit diameter of the ducted-fan exit diameter can be reduced to 0.707 of an open propeller diameter, potentially resulting in a smaller aircraft. A similar result is shown in McCormick[68] who also explains ducted-fan aerodynamics. For this reason the ducted-fan has been extensively studied and used for MAVs, as described in section 2.1.2.

For equal thrust and area equation 3.1.54 reduces to:

$$\frac{P_d}{P_p} = \sqrt{\frac{1}{2}} \approx 0.707$$

which shows that maintaining equal thrust and area the ducted-fan requires only 0.707 of the power of an open propeller in hover. This substantial reduction in power is a fundamental reason why the ducted-fan has been chosen to propel the Martin Jetpack.

Axial Flight Comparison

Comparing the ducted-fan to an open propeller with the same ideal input power and the same rotor/propeller area, it can be seen in Figure 3.4 that at hover the presence of the duct substantially assists the static thrust generation. As airspeed increases the thrust produced by a ducted-fan converges to that produced by an open propeller. This analysis assumes that the duct is producing no parasite drag. However, in reality as airspeed increases so does the drag produced by the duct. Hence, there exists an airspeed where the presence of the duct becomes a disadvantage as the net ducted-fan thrust will be less than that of an open propeller.

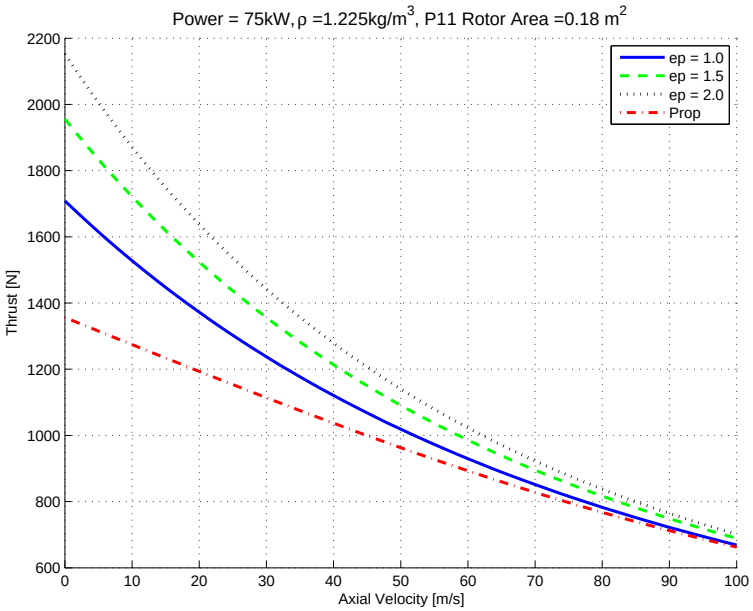

Figure 3.4: Comparison of ducted-fan to open propeller for range axial flight velocities.

Ducted-Fan Froude Efficiency

The axial flight efficiency of a ducted-fan is similar to that of an open propeller and is the ratio of propulsive power to the power added into the fluid (change in kinetic energy of the fluid) and is shown by:

$$\eta_{propulsion} = \frac{P_{propulsion}}{P_{fluid}} = \frac{T_d V_1}{\frac{1}{2}\dot{m}(V_4^2 - V_1^2)} \tag{3.1.58}$$

which can be reduced further by substituting in (3.1.43) for T_d:

$$\eta_{propulsion} = \frac{\rho A_r V_r \left(\frac{V_r}{\epsilon_d} - V_1\right) V_1}{\frac{1}{2}\rho A_r V_r (V_4^2 - V_1^2)} = \frac{V_1}{\frac{1}{2}(V_1 + V_4)} \tag{3.1.59}$$

Equation (3.1.59) is known as the *Froude efficiency* and shows that like a propeller the ducted-fan's ideal efficiency as a propulsion device occurs when there is the smallest possible change in velocities between stations 1 and 4. Hence, for a given amount of thrust the best propulsion efficiency occurs for the largest duct area as this produces the smallest change in velocity between V_1 and V_4.

It can be seen from the Froude efficiency (3.1.59) that as the free stream velocity reduces to zero, the propulsion efficiency becomes zero, so it is not valid for static conditions, such as in hovering flight. Hence, a better efficiency measure for a ducted-fan or propeller in static conditions is the ratio of ideal power to the actual power supplied:

$$\eta_{hover} = \frac{P_{fluid}}{P_{supplied}} \tag{3.1.60}$$

This hover efficiency can only be used as an overall efficiency to compare ducts and propellers of the same size and producing the same thrust, because the

fluid power, P_{fluid}, is the ideal power for the given thrust and area of the propulsion device and changes if thrust and area change.

Non-Dimensionalized Parameters

This section introduces the standard non-dimensional propeller coefficients, as described by Houghton [69], to allow for comparisons to be made between propellers and ducted-fans of various sizes.

Advance Ratio

The advance ratio is the non-dimensionalized distance travelled as a multiple of the propeller diameter, defined as:

$$J = \frac{V}{nD} \tag{3.1.61}$$

where V is the forward velocity of the propeller, n is the number of revolutions per second, so that $\frac{V}{n}$ is the distance traveled per revolution of the propeller, and D is the diameter of the propeller.

Thrust Coefficient

The thrust coefficient, C_T , is the non-dimensionalized thrust force produced by a the propeller. It is non-dimensionalized with respect to the propeller rotation speed and propeller diameter as:

$$C_T = \frac{T}{\rho n^2 D^4} \tag{3.1.62}$$

Figure 3.5 shows how the thrust coefficient changes with increasing diameter for a given blade tip speed and fixed thrust. Using the the duct rotor diameter of 0.528 m the thrust coefficient for the P-11 ducted-fan is shown on Figure 3.5, which shows that the Jetpack produces high thrust for a small propulsion diameter.

Torque Coefficient

Similarly to the thrust coefficient the torque coefficient, C_Q, depends on the same terms, but to maintain non-dimensionality has an additional distance quantity:

$$C_Q = \frac{Q}{\rho n^2 D^5} \tag{3.1.63}$$

where Q is the torque required to spin the propeller. Figure 3.6 shows the P-11 ducted-fan torque coefficient at designed maximum power conditions.

Power Coefficient

The power coefficient, C_P, for a propeller is related to the torque coefficient by a factor of 2π, hence defined as:

$$C_P = 2\pi C_Q = \frac{2\pi Q}{\rho n^2 D^5} = \frac{P}{\rho n^3 D^5} \tag{3.1.64}$$

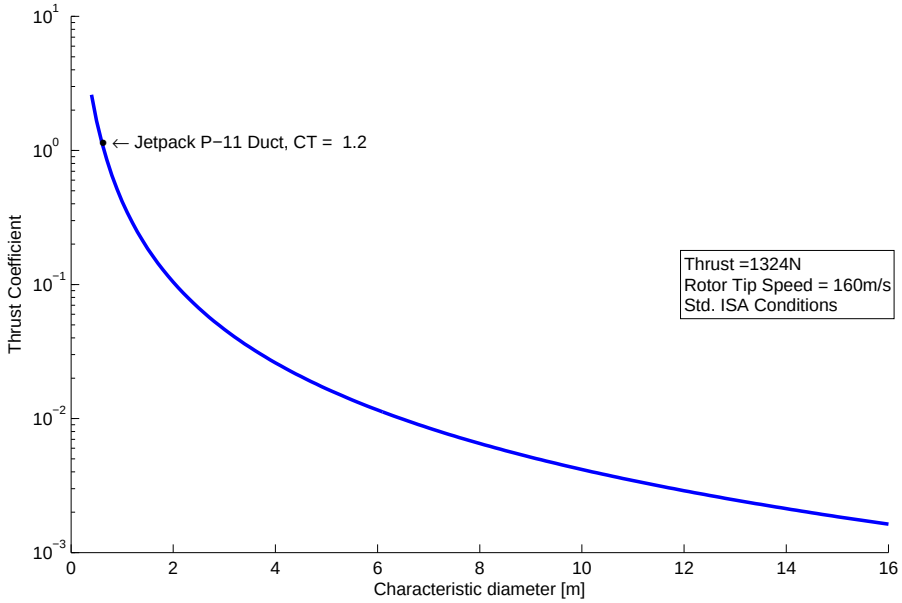

Figure 3.5: Variation of thrust coefficient with diameter for given thrust and rotor blade tip speed.

Figure 3.6 shows how the power and torque coefficients vary with increasing propeller diameter for a constant thrust and rotor tip speed. It can be seen that the Jetpack has both a high power and torque coefficient due to the small diameter of the rotor.

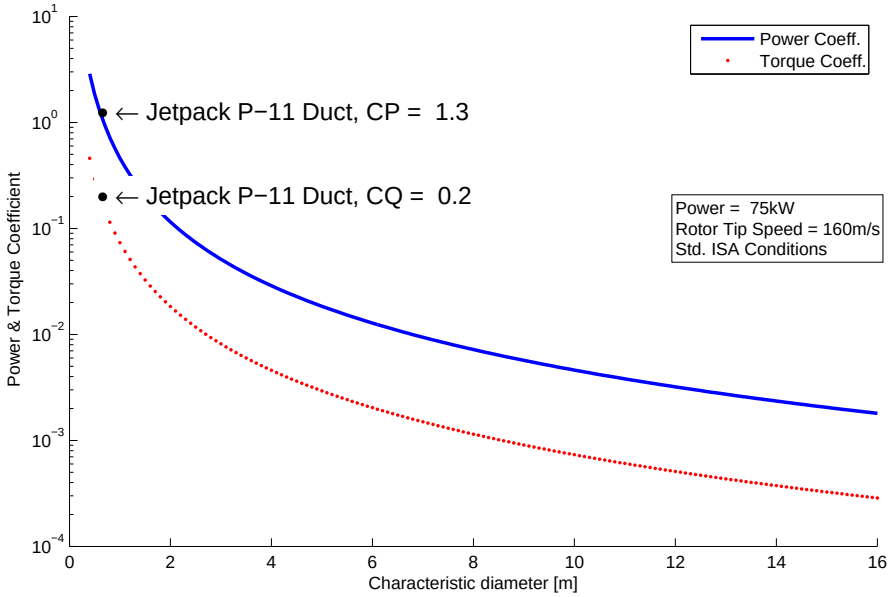

Figure 3.6: Variation of power coefficient with diameter for given power and blade tip speed.

Efficiency

The propulsion efficiency can be worked out based on the ratio of input power needed to turn the propeller:

$$P_{torque} = 2\pi nQ \tag{3.1.65}$$

to the output power delivered to the fluid:

$$P_{propulsion} = TV \tag{3.1.66}$$

where V is the velocity of the duct or propeller traveling through the air. The efficiency is then:

$$\eta = \frac{P_{propulsion}}{P_{torque}} = \frac{TV}{2\pi nQ} = \frac{C_T \rho n^2 D^4 V}{2\pi C_T \rho n^3 D^5} \tag{3.1.67}$$

$$\eta = \frac{1}{2\pi}\frac{C_T}{C_Q}\frac{V}{nD} = \frac{1}{2\pi}\frac{C_T}{C_Q}J = J\left(\frac{C_T}{C_P}\right) \tag{3.1.68}$$

As C_T varies non-linearly with the free stream velocity the propulsion efficiency also varies in a non-linear fashion. The non-dimensionalized efficiency is similar to that described by the Froude efficiency, equation (3.1.59), with the difference that the denominator term, C_P, is the actual power supplied to the propulsion device and not the ideal power supplied to the fluid for the given thrust and area of the propulsion device. As with the Froude efficiency, equation (3.1.59), equation (3.1.68) is only valid for non zero values of free stream velocity V.

Figure of Merit

The *Figure of Merit*, C_{FM}, is a non-dimensionalized performance parameter for comparing the static performance of a propeller, and is calculated as:

$$C_{FMp} = \frac{C_T^{\frac{3}{2}}}{\sqrt{\pi} C_P} \tag{3.1.69}$$

The C_{FM} can also be applied to measure the static performance of a ducted-fan, as done in [60], by including the ratio of fan diameter to duct exit diameter into equation 3.1.69, resulting in:

$$C_{FMd} = \frac{d_r}{d\sqrt{\pi}}\frac{C_T^{\frac{3}{2}}}{C_P} \tag{3.1.70}$$

where d_r is the rotor diameter and d is the duct exit diameter. Figure 3.7 shows how the Figure of Merit changes with increasing diameter. It can be seen that increasing the diameter reduces the Figure of Merit, this is because fixed values of power and thrust are used. In reality when diameter is increased the thrust typically increases as well, which would show an increasing Figure of Merit value.

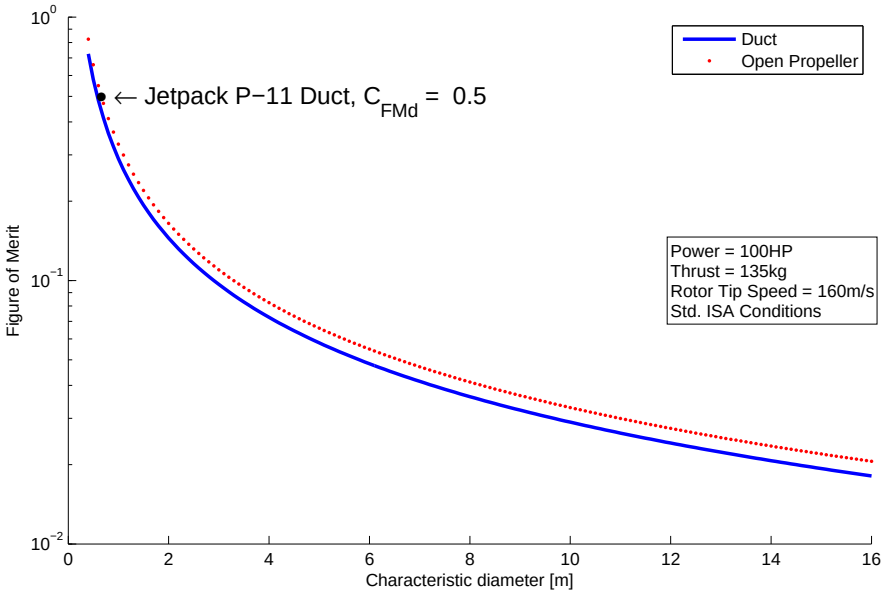

Figure 3.7: Figure of Merit versus diameter for given power, thrust, and rotor blade tip speed.

Dimensionalized Parameters

The use of the non-dimensionalized propeller equations is limited to comparisons of equal propeller areas or thrust loads. These coefficients are best used to compare the same propeller for various operation conditions, i.e. flight velocity, air density, rotation speed, and blade setting angles. As soon as the diameter is changed the coefficients values change making comparison between different sized propellers cumbersome using non-dimensionalized parameters.

Disc Loading

An important parameter of propulsion systems is the *disc loading,* DL, which is a measure of how much lift or thrust force the aerodynamic feature is producing per unit area. The disc loading is defined as:

$$DL = \frac{T}{S} \tag{3.1.71}$$

where T is the thrust force and S is the reference area of the aerodynamic feature. For a VTOL aircraft this is the total rotor or ducted-fan swept area. For a fixed-wing aircraft the reference area is the wing planform area. Table 3.1 from [70] summarizes a range of disc loading for various aircraft propulsion devices, the Martin Jetpack P-11 and P-12 disc loading have also been included as well as disc loadings from MAV ducted-fans.

Power Loading

Another practical aircraft design parameter is the *power loading* PL, which for rotor wing aircraft is the ratio of thrust to power:

Table 3.1: Comparison of Propulsion Disk Loadings

Thrust Device	Range of Disk Loadings T/S [Pa]
Helicopter Rotor	200 to 700
MAV Ducted-Fan	400 to 1000
VTOL Propeller	700 to 2400
STOL Propeller	1400 to 3400
Conventional Propeller	1900 to 4300
Martin Jetpack P-12	2600 to 3100
Martin Jetpack P-11	4200 to 4700
Other Ducted-Fans	4800 to 7200
Lift Engine	24000 to 34000
Turbo Fan	57000 to 72000
Jet Engine	~80000

$$PL = \frac{T}{P} \tag{3.1.72}$$

where P is the power supplied to the propulsion device. Using equations (3.1.34), (3.1.71), and (3.1.72) the power loading can be calculated for the hovering condition as a function of the disc loading as:

$$PL = \frac{1}{\sqrt{\frac{DL}{2\rho}}} \tag{3.1.73}$$

Using equation (3.1.73) Figure (3.8) can be produced, which shows the ideal power loading versus disc loading for static/hovering conditions. It can be seen that the Martin Jetpack P-11 has a very low power loading; and has the lowest in Table 2.1 (assuming that $PL = MTOW/P$), which compares the most well known ducted-fan VTOL aircraft. In contrast to the P-11 Jetpack, the first human powered helicopter, Gamera II [71], to achieve flight of longer than 60 s has an extremely high power loading due to the extremely low disc loading. These parameters are so extreme due to the physical limitations of the human body power output, approximately 460 W for one minute duration. Note also that the Gamera II is above the ideal curve, which is a result of hovering in ground effect.

Although the power loading is dimensional ($\frac{s}{m}$), it is a very useful parameter to compare the effective overall efficiency of one aircraft to another, as the aircraft with a higher power loading requires less power to lift a given weight than one that has a lower power loading. The power loading parameter also allows the aircraft designer to quickly determine how much power is required to lift a given weight, which is a useful parameter for scaling an aircraft design.

3.2 Ducted-Fan Reactions in Crosswind

To model the flight behaviour of an aircraft the key components contributing to the sum of forces and moments of the aircraft need to be accurately modelled. The *sum of forces* tells the story of how the aircraft translates, while the

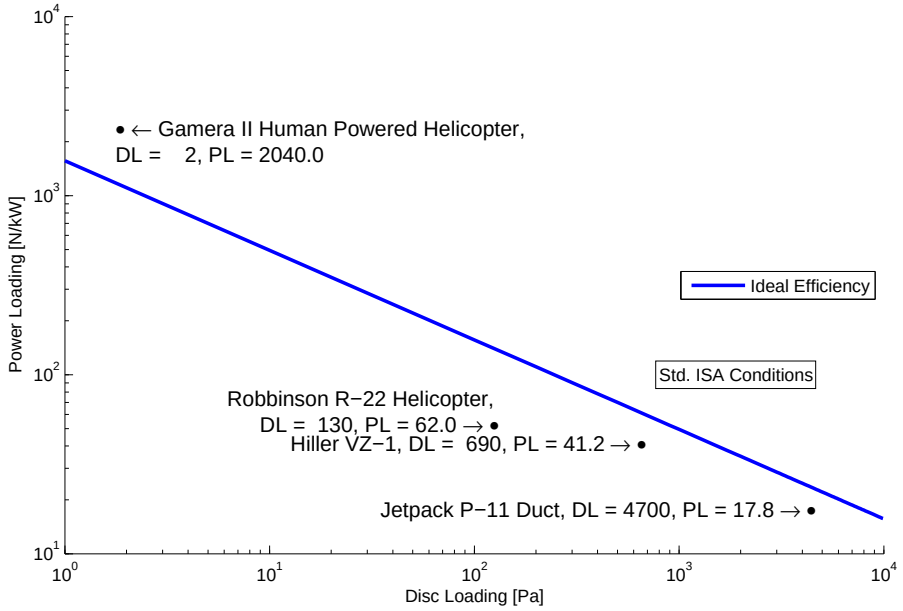

Figure 3.8: Relationship between power and disc loadings for hovering flight at ISA conditions.

sum of moments defines the orientation of the aircraft. In order to get the aircraft to translate in a desired direction the orientation of the aircraft must be controlled. Thus the aircraft moments need to be appropriately modelled to predict the orientation of the aircraft, accurately.

The twin-ducted-fans as the key aerodynamic features of the Jetpack are the major contributors to both forces and moments on the Jetpack. Hence, accurately modelling the duct behaviour is critical to the success of the Jetpack model. To model the ducted-fan the thrust force, the normal force, and the duct pitching moment need to be modelled. The derivation of each of these is explained next.

Ducted-Fan Normal Force

For flight regimes other than hover, vertical climb, and descent there will be a velocity component perpendicular to the duct. This perpendicular velocity component is absorbed by the duct as the ducted-fan has the effect of straightening any perpendicular airflow, as shown in Figure 3.9. Hence, the perpendicular component of the free-stream air momentum is redirected along the axis of the duct. This results in a force being created, *ducted-fan normal force*[1], due to the momentum change of the airflow perpendicular to the duct axis. The orientation of the ducted-fan normal force F_n is shown on Figure 3.9, where it can be seen that this force has a large drag component for VTOL aircraft applications, such as the Martin Jetpack. The ducted-fan normal force is calculated in [49] as:

[1]Also referred to as *ram-drag* or *momentum drag* force amongst ducted-fan aircraft designers [49, 36, 72, 50, 19, 53, 46].

$$F_n = \dot{m}_d V_0 \sin\alpha \tag{3.2.1}$$

where $\dot{m}_d$ is the mass flow through the ducted-fan, calculated from equation (3.1.44). V_0 is the free-stream velocity and α is the angle of attack defined as the angle between the airspeed vector and the duct axis.

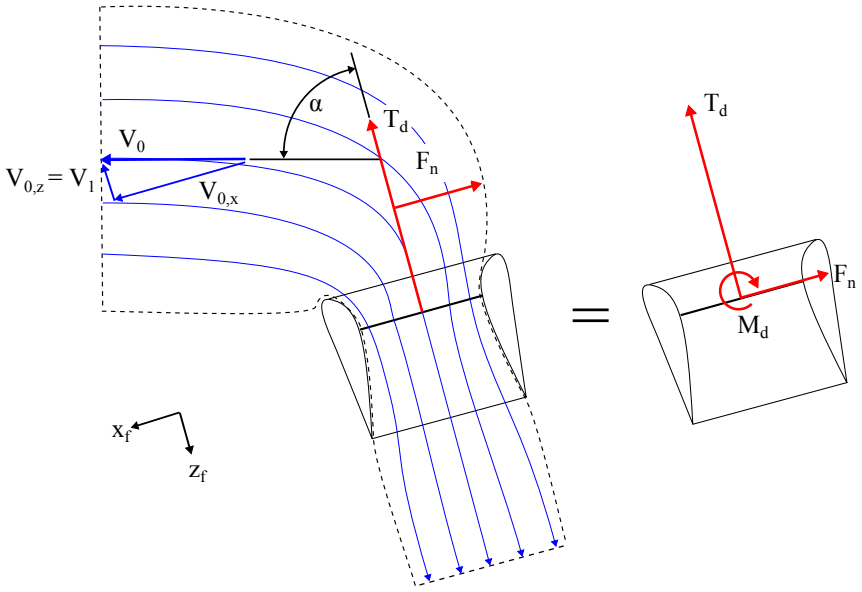

Figure 3.9: Ducted-fan free body diagram

Ducted-Fan Moment

For any aerodynamic body, be it a wing, streamlined, or bluff body, there exists a point where the sum of forces and moments caused by the distribution of the normal and shear stresses can be replaced by a single resultant force vector. The location of this point where the equivalent resultant force vector acts is the *centre of pressure*. Thus, if the centre of pressure, lift, and drag forces are known for a body then the moment for the body can be determined by the cross product of the moment arm and the resultant force as:

$$\mathbf{M} = \mathbf{l} \times \mathbf{F}$$

where $\mathbf{M}$ is the moment about a convenient reference point, $\mathbf{l}$ is the distance vector from the reference point to the centre of pressure and $\mathbf{F}$ is the resultant force.

Using the above concept of centre of pressure and the fact that a simple formula already exists (ducted-fan normal force formula (3.2.1)) for determining the radial duct force it makes sense to model the centre of pressure and apply the known axial and normal forces at this point to determine the pitching moment of a duct. Two methods for determining the centre of pressure are presented. The first assumes a constant position and the second a variable position as a function of duct angle of attack and free stream velocity. The experimental results in Chapter 6 will show that the variable centre of pressure

model is more realistic for the pitch plane and the that fixed centre of pressure fits better to the roll plane.

Fixed Centre of Pressure Model

A simple first pass approach for modelling the ducted-fan moment can be done by assuming that the centre of pressure acts at half a duct diameter above the lip, as shown in Figure 3.10, so that the ducted-fan normal force produces a moment about the duct chord quarter point, as:

$$\mathbf{M}_d = \left[0, 0, \frac{1}{2}d + \frac{1}{4}d_c\right] \times \mathbf{F}_d \tag{3.2.2}$$

where d is duct diameter, d_c is duct chord length, and $\mathbf{F}_d$ is the ducted-fan force vector. However, in reality the centre of pressure of a ducted-fan is a function of the flow conditions, which will be shown in Chapter 6. Figure 3.11 shows the theoretical pitching moment for a single P-11 (600 mm diameter) at nominal flying conditions for a range of airspeed and angle of attack values. It can be seen the moment is linear and increases with airspeed. Maximum pitching moments occur for 90° angle of attack and diminish for angles of tending towards 0° and 180°.

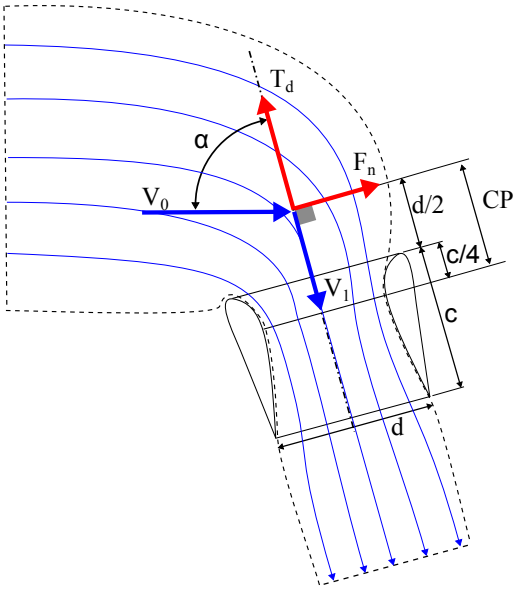

Figure 3.10: Ducted-fan fixed centre of pressure at half a duct diameter above duct lip.

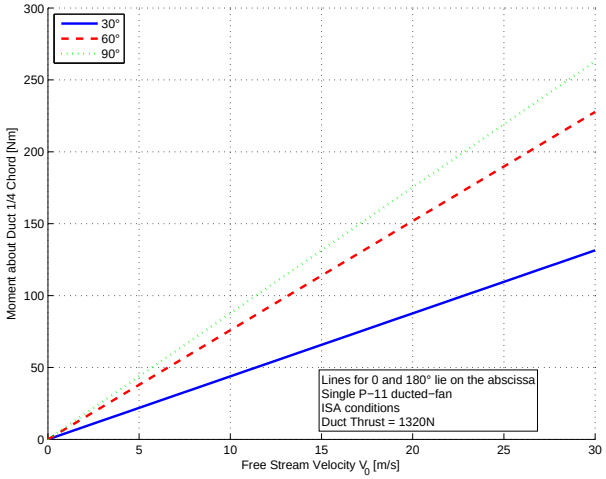

Figure 3.11: Map of duct pitching moment for fixed centre of pressure model

Variable Centre of Pressure Model

A more accurate approach to the location of the duct centre of pressure is to visualize the physical phenomenon of the air mass being sucked through the duct. Assuming that the duct is at some angle of attack to the free stream velocity, then the mass of air being sucked through the duct must turn through some angle (approximately the angle of attack) as the duct redirects the air mass, refer to Figure 3.12. If the air mass in the control volume is replaced with a stream tube and that stream tube reduced to a line that acts at the centre of the tube then two lines or vectors can be drawn at the entrance and exit of the control volume, as shown on the diagram on the right hand side of Figure 3.12. The intersection of these two vectors can be assumed the centre of pressure.

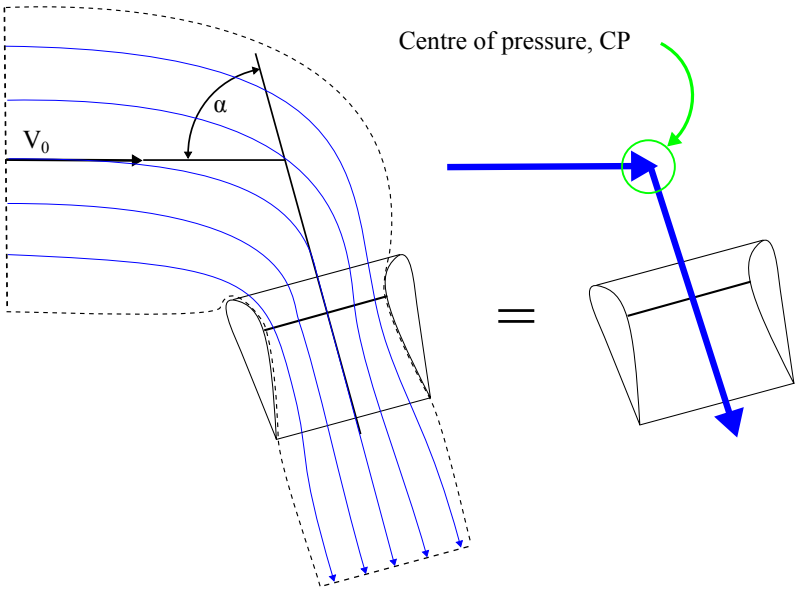

Figure 3.12: Control volume around a ducted-fan at an angle of attack showing equivalent momentum vectors.

If the exit vector is aligned to the duct axis, which can be assumed if the flow is uniform through the duct, the entry vector requires constraints to fully define the location of the centre of pressure. The entry vector position can be defined based on the dependent entry parameters of free stream velocity, mass flow rate, and angle of attack. The entry vector position is used to calculate the turning radius r, which is illustrated in Figure 3.13 and calculated as follows:

$$r = \sqrt{\frac{\dot{m}}{\pi \rho V_0}} \tag{3.2.3}$$

where $\dot{m}$ is the mass flow rate through the duct and V_0 is the free stream velocity.

The ducted-fan centre of pressure CP_d located along the duct axis and measured from the duct quarter chord[2] is, graphically shown on Figure 3.13 and calculated as:

$$CP_d = r \sin \frac{\alpha}{2} \tag{3.2.4}$$

where α is the angle of attack the duct. Using the above formula the pitching moment about the intersection of the duct axis and duct quarter chord line can be modelled by applying the ducted-fan normal force equation, (3.2.1), at the duct centre of pressure, as:

$$\mathbf{M_d} = \mathbf{CP_d} \times \mathbf{F_n} \tag{3.2.5}$$

where the vector $\mathbf{CP_d} = [0, 0, -CP_d]$.

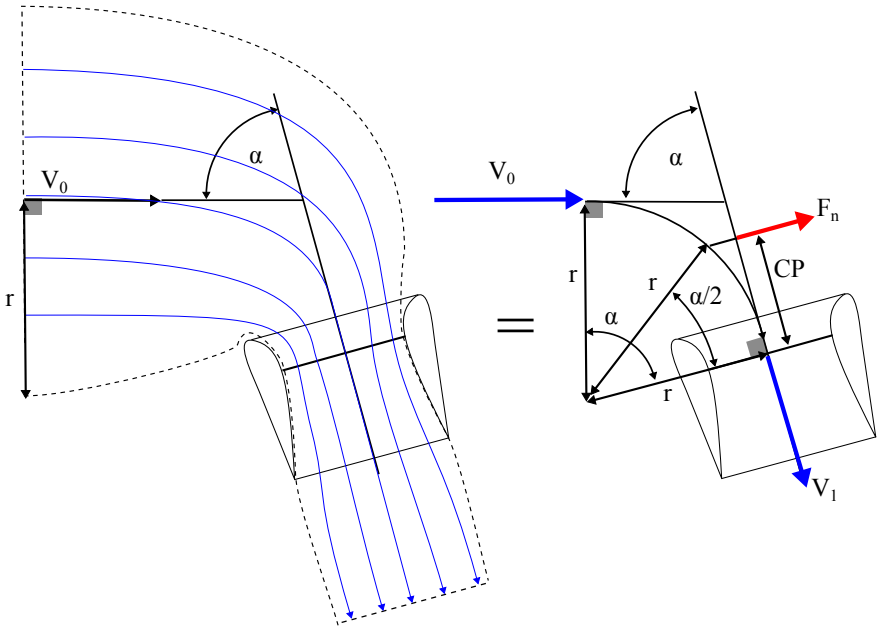

Figure 3.13: Duct centre of pressure derivation based on turning radius r

Applying equations (3.2.3) and (3.2.4) for a range of angles of attack from 0° to 180° and for velocities from 0° to 30 m/s the CP_d and pitching moment maps can be produced, as per Figures 3.14a and 3.14b. Figure 3.14b shows that duct moment is unique for a range of angles of attack from 0° to 180°.

[2]Measured from duct quarter chord as this is historic reference point for ducted-fans.

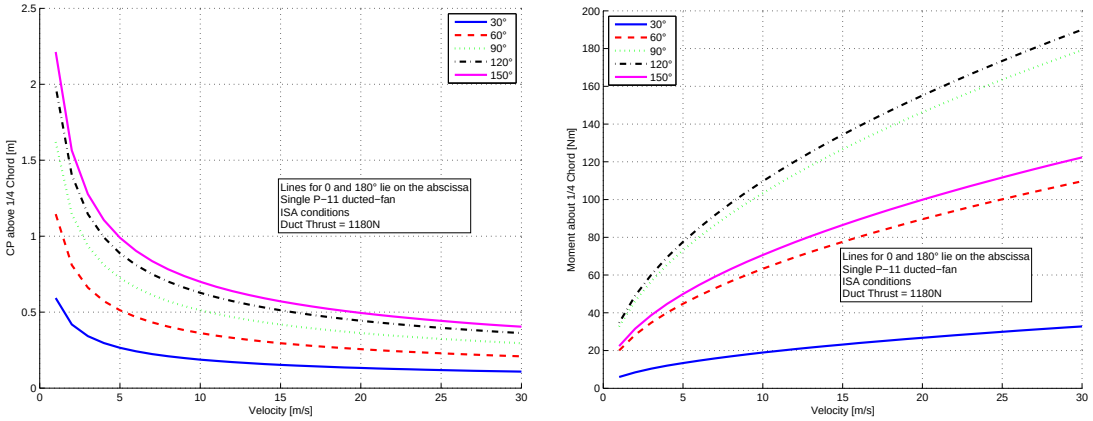

(a) Centre of pressure

(b) Pitching moment

Figure 3.14: Ducted-fan variable centre of pressure model showing centre of pressure movement and pitching moment

3.3 The Control Vanes

This section describes how the control moments for orientating the Jetpack are calculated from deflections of the roll, pitch, and yaw control vanes.

Control Vane Moments

The control vane moment for each control vane is created by the multiple of the control vane force and the respective moment arm, as:

$$\mathbf{M}_{vane} = \mathbf{l}_{vane} \times \mathbf{F}_{vane} \tag{3.3.1}$$

where $\mathbf{M}_{vane}$ is the control moment, $\mathbf{l}_{vane}$ is the distance from the centre of gravity to the location of the resultant control vane force $\mathbf{F}_{vane}$. Equation (3.3.1) shows that to achieve a higher control vane moment either the vane moment arm or the vane lift force needs to increase.

Control Vane Force

The Jetpack control vanes (roll, pitch, and yaw) create a lift force whenever the vane chord is deflected at an angle of attack relative to the airflow. A vane drag force is also present and is a function of the vane angle of attack. Since the vane drag force acts in the opposite direction to the thrust of the ducted-fans it is desirable that the drag force of the vanes be kept to a minimum to avoid excessive loss of overall thrust. The control vane lift and drag force as a function of the vane angle of attack are described by the following equations:

$$L_{vane}\left(\alpha_{vane}\right) = \frac{1}{2}\rho V_{vane}^2 A_{vane} C_{Lvane}\left(\alpha_{vane}\right) \tag{3.3.2}$$

$$D_{vane}\left(\alpha_{vane}\right) = \frac{1}{2}\rho V_{vane}^2 A_{vane} C_{Dvane}\left(\alpha_{vane}\right) \tag{3.3.3}$$

where ρ is the air density, assumed to be ambient air density, as the flow through the duct is assumed to be incompressible as the Mach number is low, $M =\sim 0.15$. The velocity at the vane is V_{vane} and is dependent on the position of vane within the duct wake. The plan area of the control vane is A_{vane}. The terms C_{Lvane} and C_{Dvane} are the lift and drag coefficients of the control vane, and are a function of the control vane angle of attack, α_{vane}.

Duct Exit Velocity

The velocity in the duct wake has significant effects on the performance of the control vanes. The lift force produced for a given control vane geometry is a function of the dynamic pressure that the control vane is exposed to, where the dynamic pressure is proportional to the velocity squared. Figure 3.15 shows the wake velocity map behind P-11 ducted-fan. This map was produced at nominal operating conditions by Martin Aircraft Company. The velocity map clearly shows that two differing velocity streams exist. The high velocity region (indicated by red) occurs for approximately three quarters of the duct exit area and is referred to as *clean airflow*. The area of low velocity airflow is a result of the turbulence created by the wake of the exposed hub support struts and drive belt, refer to Figure 3.16. The wake from the obstructions in this section of the duct reduces the airspeed and mass flow rate, and hence, reduces the effectiveness of the duct to generate lift over this portion of the duct; this portion is referred to as *disturbed airflow*. The drag from these components is clearly evident when one sticks ones hand under the disturbed airflow region of the duct and compares this to the pressure under a non obstructed region.

At the onset of this research the P-11 Jetpack had pitch and roll control vanes located in this disturbed airflow, hence poorly utilizing the capabilities of the control vanes. Figure 3.17 shows dynamic pressure variation with increasing distance from the duct trailing edge along a line located 200 mm from the duct axis. The results show that the dynamic pressure in disturbed airflow is 34 % of the clean airflow. Hence, a control vane positioned in this airflow will produce 34 % of the lift as the same control vane positioned in the undisturbed airflow. This information has lead to the control vanes being position in the high dynamic airflow regions in the ducted-fan wake for the P-11E and P-12 Jetpacks.

Vane Velocity

The Jetpack concept makes use of the high velocity duct-exhaust stream by positioning control vanes within this airflow. The velocity and effectiveness of the control vanes to produce moments is a function of the duct exist velocity. The duct exit velocity is calculated from equation (3.1.32) and using conservation of mass from the rotor to the duct exit plane as:

$$\dot{m}_r = \dot{m}_e = \rho A_r V_r = \rho A_e V_e \tag{3.3.4}$$

Assuming that the duct-exhaust airflow maintains an outer diameter equal to the duct diameter after exiting the duct and that no mass flux occurs through the circumferential area between the duct exit and control vanes.

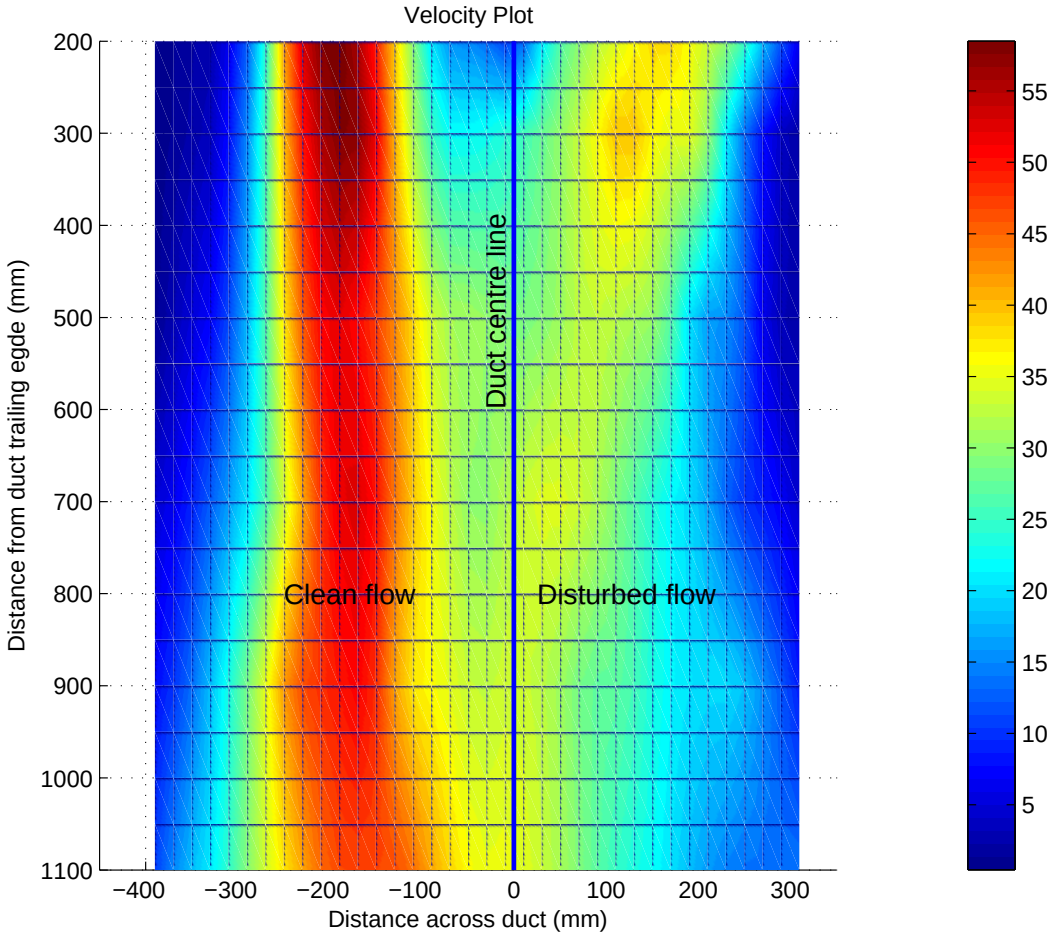

Figure 3.15: Velocity map of wake behind P-11 ducted-fan measured in m/s, courtesy of Martin Aircraft Company. This was produced by extensive grid-pattern hot-wire anemometer measurements combined with interpolation using Matlab^{TM}.

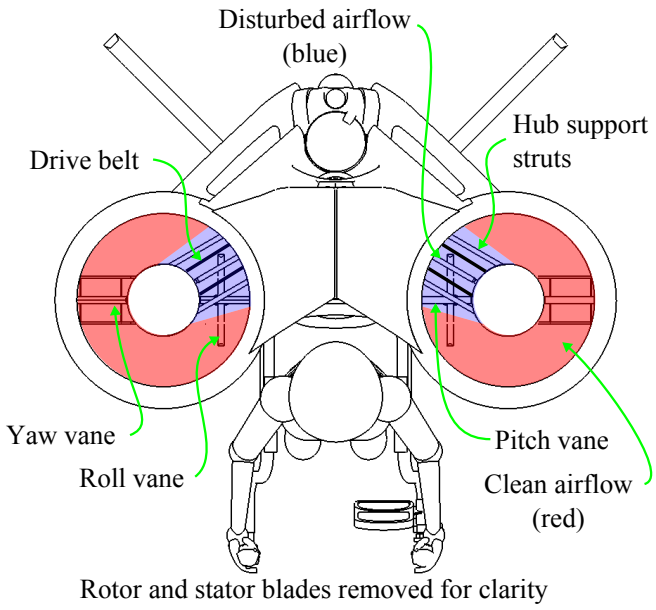

Figure 3.16: Top view of Martin Jetpack P-11A showing Jetpack features in the duct wake.

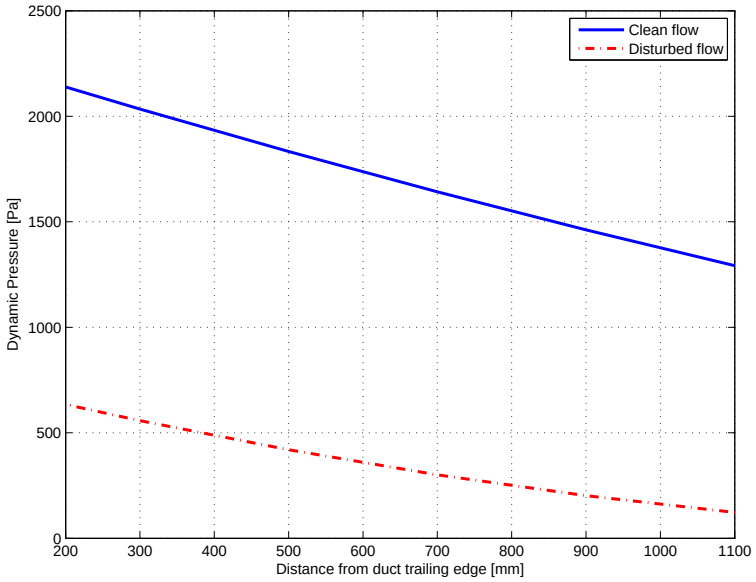

Figure 3.17: Comparison of dynamic pressure between clean and disturbed airflow wakes measured 200 mm from either side of the duct centreline. Dynamic pressure is calculated from the velocity measurements presented in Figure 3.15.

Then the velocity at the control vanes can be calculated using conservation of mass as:

$$V_{vane} = \frac{A_e V_e}{(A_e - A_{tc})} \tag{3.3.5}$$

where A_{tc} is the cross-sectional area of the tail cone at the location of the control vanes.

Effect of Crosswind on Vane

The vane distance from the trailing edge not only affects the duct axial velocity, but also increases the influence of any crosswind acting on the Jetpack. When the Jetpack experiences a crosswind the duct efflux is also subjected to the crosswind. This effectively tilts the duct-exhaust stream in the direction of the crosswind, refer to Figure 3.18. The further away the control vane is located from the duct exit the greater the effect the crosswind will have on the control vane. The crosswind affects the control vane by increasing the angle of attack and thus increases the lift force in such a way that a negative nose down moment is produced to turn the duct towards the crosswind, in a weathercock fashion.

Although this action at first glance seems favourable as it helps to develop a nose pitch moment to counter act the moment produced by the ducted-fan normal force it is actually unfavourable, as the fly-by-wire system is not able recognize that the vane is at a higher angle of attack and has the potential to increase the angle of attack of the vane above the stall angle, which would result in loss of control.

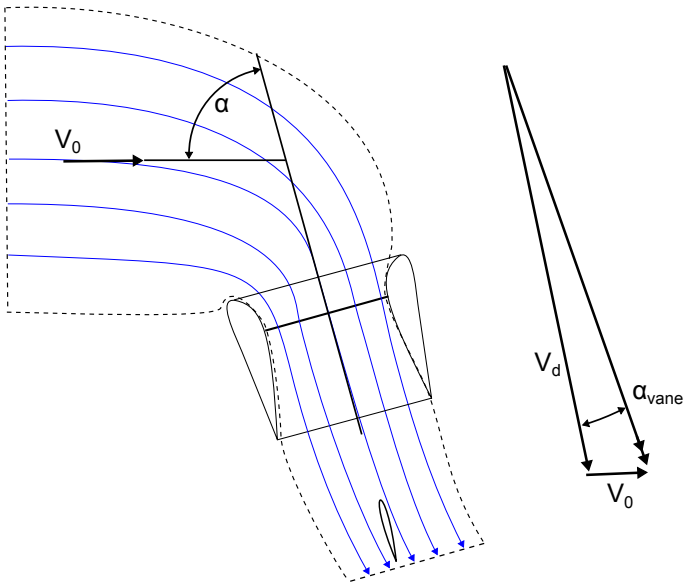

Figure 3.18: Affect of crosswind on control vane

Vane Lift Coefficient

The vane lift coefficient is a function of the vane angle of attack, vane cross-sectional shape, vane aspect ratio, and Reynolds number. Conventionally, an

aircraft designer will use two dimensional aerofoil data and adopt this data to suit a real finite wing based on the aspect ratio of the finite wing. However, as the Jetpack control vanes have very low aspect ratios (ratio of span to chord length), approximately between $A_R = 1$ to 2, the flow over the vanes differs widely from that of the two-dimensional aerofoil data, due to the tip vortices dominating much of the control vane surface. An early paper by Zimmerman [73] found that wings with aspect ratios of between 1 and 1.5 experienced much higher maximum lift coefficients than wings of greater aspect ratio wings. This was due to the tip vortices that cover most of the wing re-energizing the boundary layer and thus delaying flow separation and stall until angles of attack close to 45°. However, these high lift values also greatly increased the drag, they did not exhibit good lift to drag ratio values.

The addition of end-caps and additional aerofoils also affects the aerofoil properties from those of a infinite aerofoil. Hence, lift, and drag data for the Martin Jetpack is experimentally determined by measuring lift and drag forces of control vanes located in the duct-jet stream. Refer to Chapter 5 on experimental methodology used to measure the control vane forces on the Jetpack.

This research has lead to end-caps, as shown on Figure 5.12a, being fitted onto the Jetpack control vanes to improve their performance. The end-caps size was determined from [70] as shown on Figure 3.19, which shows how the effective aspect ratio, A_i, of a wing is increased with increasing end cap height to wing span ratio, $\frac{h}{b}$. Using the end-caps the effective aspect ratio of the control vane is increased, which reduces induced drag and increases the lift curve slope of the wing. Hence, a wing fitted with end-caps will produce more lift at a given angle of attack, below stall angle, than the same wing without end-caps. However, the end-caps are not as efficient as extending the aerofoil by the same surface area as the endcap.

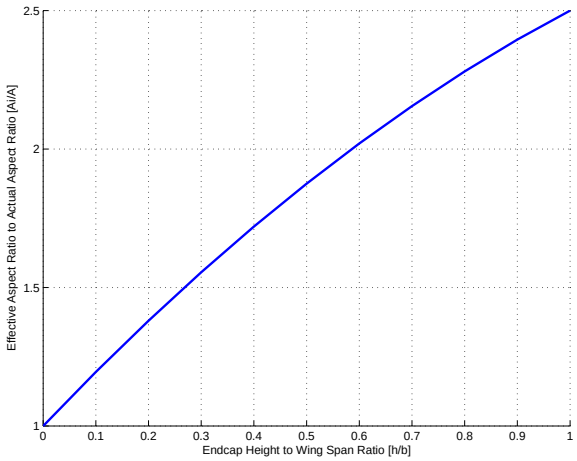

Figure 3.19: Effect of end-caps on wing aspect ratio, as describe by [70].

Vane Area

Equation 3.3.2 shows that the lift force is proportional to the control vane plan area (span multiplied by chord). Assuming the airflow leaving the ducted-fan is a tube equal to the duct diameter, it can been seen that extending the vanes

outside of the tube will have little effect on the vane lift force generated, as the portion outside of the tube experiences little dynamic pressure. Hence, the vane span is limited to the duct diameter.

The vane chord is limited by the vane aspect ratio. It is undesirable to have an aspect ratio below 1.5 as the geometric stall angle becomes much greater, (can exceed 30°[73]), thus the angular range between positive and negative maximum lift is larger. This requires the vane to be driven through a wider arc by the servo, which naturally takes longer, adding a delay into the control system. However, the nature of stall for a low aspect ratio aerofoil is much smoother than for a high aspect ratio aerofoil [74, 75]. This has the practical benefit of allowing the control vane to be deflected closer to the stall angle of attack without the abrupt loss of lift if the stall angle is accidentally exceeded. Low aspect ratio wings are also less efficient than high aspect ratio wings, as they produce much more drag to achieve the same lift.

3.4 Flight Mechanics

This section explains the fundamental flight mechanics based on first principle analysis of the Martin Jetpack. The equations developed in this section give a high level overview of the performance of the Martin Jetpack as an aircraft.

Load Factor

The ratio of lift to weight forces is called *load factor*. The magnitude of the maximum obtainable load factor is an effective measure of the potential of an aircraft to turn, pull out of a dive, or arrest a descent; hence, a useful parameter to grade the manoeuvrability of an aircraft. Table 3.2 shows the minimum design load factor requirements for various fixed and rotor wing aircraft from a structural aspect, but also gives a good indication of the load factors that are possible for each aircraft. Aerobatic aeroplanes have the highest design load factors, as these aircraft are designed to perform aggressive manoeuvres, while aeroplane transport aircraft have the lowest.

Table 3.2: Required FAA minimum design load factors for fixed and rotor wing aircraft

Category	Negative	Positive	Standard
Aeroplane Normal	−1.5	3.8	FAR Part 23[76]
Aeroplane Transport	−1	2.5	FAR Part 25[77]
Aeroplane Aerobatic	−3	6	FAR Part 23[76]
Helicopter normal	−1	3.5	FAR Part 27[78]

An expression for the Jetpack load factor has been developed from the ratio of maximum thrust to the take off weight as:

$$n = \frac{W + T_M}{W} \tag{3.4.1}$$

where T_M is the additional thrust (thrust margin) to the hovering thrust requirement that is equal to the takeoff weight W, and n is the load factor, which is measured in multiples of gravitational acceleration at sea level. Using this

equation Figure 3.20 can be created to give an indication of how the load factor varies with thrust margin and takeoff weight. Table 3.3 shows the calculated load factors for the P-11A, P-11C, and P-12 Jetpack prototypes.

Unlike an aeroplane or helicopter that have direct control over their lift producing aerofoils, by changing the aerofoil angle of attack, the Jetpack increases its load factor by increasing the thrust force from the ducted-fans. Since the ducted-fan thrust is limited by the maximum engine power, the Jetpack's load factor and manoeuvering performance is also restricted by the engine power. Hence, the load factor is smaller when compared to aeroplanes and helicopters, which have their load factors increase quadratically with airspeed. However, the Jetpack does have the benefit over aeroplanes and helicopters that the aircraft structure cannot be aerodynamically overloaded by in-flight forces, as the critical aerofoils (fan blades) can only be substantially loaded by engine power, which is physically restricted.

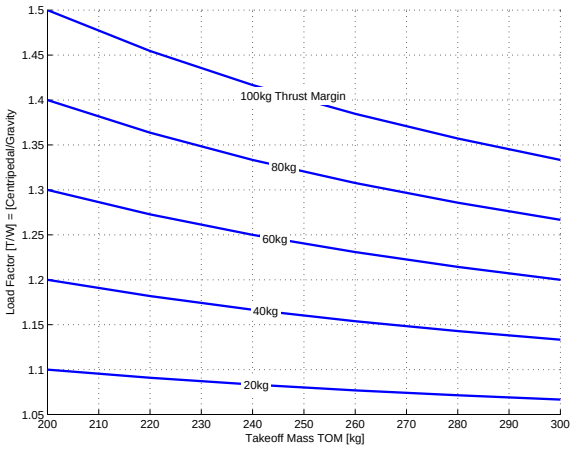

Figure 3.20: Load factor versus takeoff mass

Table 3.3: Load factors for the various Martin Jetpack prototypes

	Design MTOW [N]	Max Thrust [N]	Thrust Margin [N]	Load Factor [n]
P-11A	2450	2650	200	1.08
P-11C	2110	2650	540	1.26
P-12	3140	3630	490	1.15

Manoeuvres Based On Load Factor

Figure 3.21 shows three fundamental manoeuvres that requires a load factor greater than unity, which the Jetpack needs be able to perform.

Pull up

The *pull up* manoeuvre is analogous to that of an aeroplane pulling out of a dive. The load factor must be increased above unity so that a net centripetal

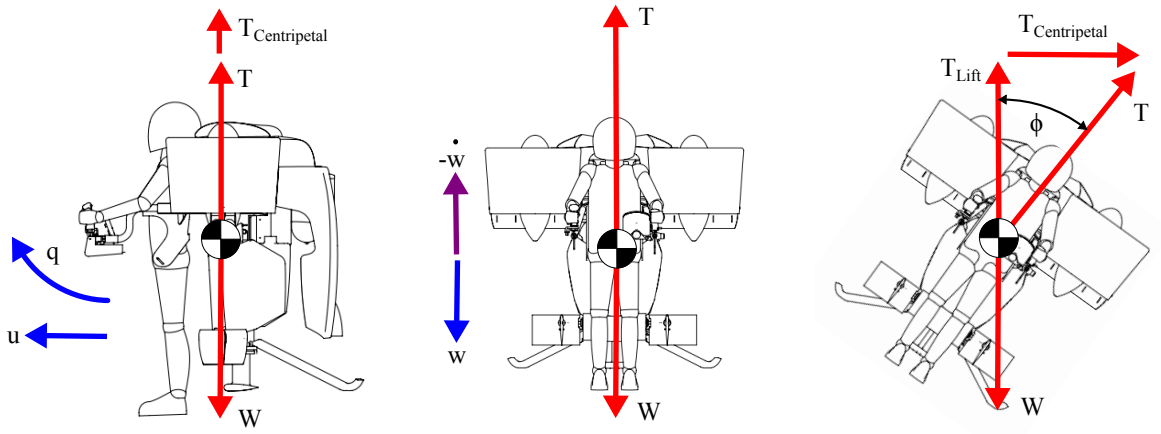

(a) Pull up (b) Descent arrest (c) Banked turn

Figure 3.21: Three fundamental Jetpack manoeuvres requiring load factor greater than unity.

force and acceleration results so that the pull out angular velocity q is induced. The magnitude of the load factor, n, plays an important part in determining limits on the enter velocity u and the pull out radius R. The pull out manoeuvre equation is derived from the analysis of the free body shown in Figure 3.21a as:

$$n = \frac{W + T_{Centripetal}}{W} = \frac{mg}{mg} + \frac{mu^2}{mgR} = 1 + \frac{u^2}{gR} = 1 + \frac{(qR)}{gR} = 1 + \frac{q^2R}{g} \quad (3.4.2)$$

Figure 3.22 shows that for low load factor values the aircraft needs a significantly larger turning radius than an aircraft with a large load factor value. Practically, this means that an aircraft with a low load factor will require significant height to pull out of a dive. For this reason the Jetpack should avoid pull up manoeuvres during descents, as the low load factor will allow the airspeed to build up too quickly, which rapidly increases the pull up radius leading to the dangerous scenario that required altitude to complete the manoeuvre may not be available.

Descent Arrest

The *descent arrest* manoeuvre is a critical manoeuvre for the Jetpack to reduce descending vertical speed, w, by creating an opposing acceleration, $-\dot{w}$. The magnitude of the load factor plays an important role on determining the maximum descent speed and height above the ground that the pilot must begin applying power to reduce the descent rate, in order to avoid impacting into the ground at speed. Using the following kinematic equation calculates the descent arrest height, s_{arrest}, for various initial descent velocities, w, and load factors:

$$s_{arrest} = \frac{w^2}{2g(n-1)} \quad (3.4.3)$$

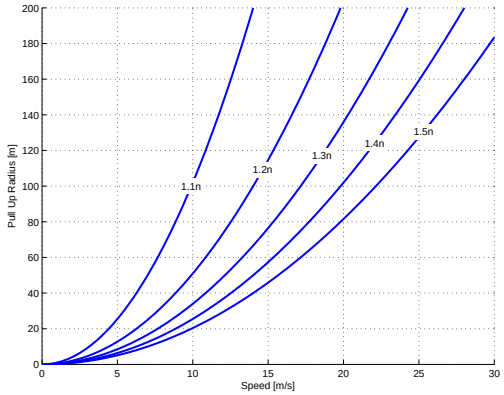

Figure 3.22: Pull up manoeuvre performance

Using this equation Figure 3.23 is produced, which shows the required height above the ground (descent arrest height, s_{arrest}) that full power needs to be delivered to arrest a descent. Results on Figure 3.23 show that arresting distance significantly increases for load factors less than 1.25. This has the implications that descents will need to be planned well in advance.

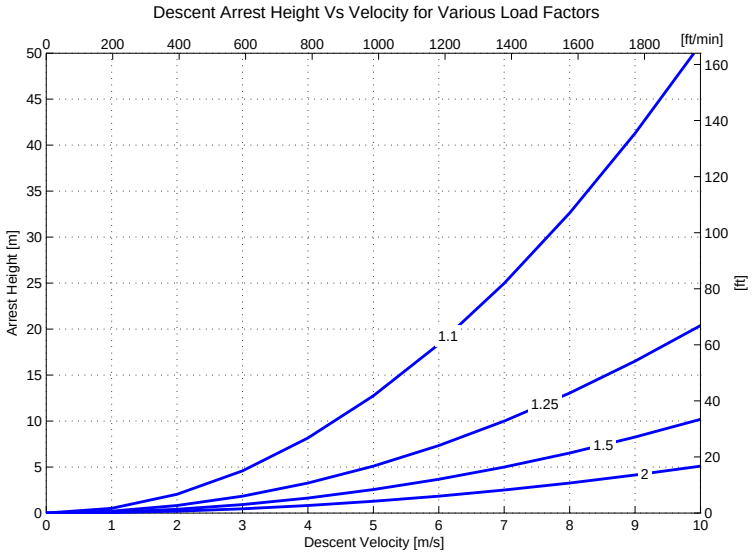

Figure 3.23: Determination of the descent arrest height

Banked Turn

The level flight *banked turn* is a turning manoeuvre that the Jetpack makes when it has a forward airspeed and tilts its lift vector towards the centre of the turn to create a centripetal acceleration to initiate and sustain the turn. For the aircraft to maintain constant altitude and speed during the turn the magnitude of the vertical component of the thrust force must be equal to the weight force, Figure 3.21c. The load factor required for level bank can be derived from Figure 3.21c as a function of the bank angle ϕ as:

$$\phi = \arccos\left(\frac{1}{n}\right) = \arccos\left(\frac{W}{W + T_M}\right) \tag{3.4.4}$$

Solving this equation for a range of bank angles it can be seen in Figure 3.24 that as the bank angle approaches 90° the load factor tends towards infinity, and for bank angles less than 30°only small values of load factor are required, less than 1.25.

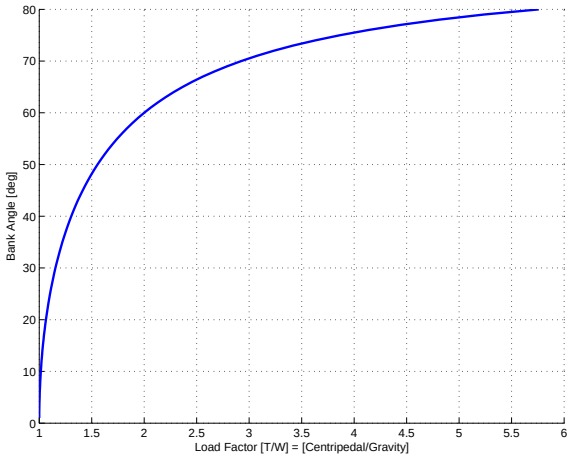

Figure 3.24: Level flight bank angle versus load factor

The centripetal force is a function of aircraft's mass m, velocity u, turn rate $\dot{\Psi}$, and turn radius. For a level bank turn the centripetal force can be derived from Figure 3.21c as a function of the bank angle ϕ as:

$$F_{Centripetal} = \frac{mu^2}{R} = mu\dot{\Psi} = m\dot{\Psi}^2 R = W\tan\phi = W\sqrt{n^2 - 1} \tag{3.4.5}$$

and by dividing through by mass m the centripetal acceleration can be obtained:

$$a_{Centripetal} = \frac{u^2}{R} = u\dot{\Psi} = \dot{\Psi}^2 R = g\tan\phi = g\sqrt{n^2 - 1} \tag{3.4.6}$$

Using the centripetal acceleration equation, the turn rate, Figure 3.25a, and turn radius, Figure 3.25b, can be determined as a function of the airspeed and bank angle independent of the aircraft's mass. These plots give a useful insight as to what bank angles, and hence, load factors are required to achieve a given turn performance. From Figures 3.25a the turn rate quickly diminishes with increasing airspeed; assuming that the Jetpack has a maximum level bank turn angle of 30° it can be seen that at high speeds, 30 m/s, the turn rate is low, 10°/s, and that the turn radius is in excess of 150 m. Unless the Jetpack's load factor is improved better turn performance at high speed will not be possible. Note, the Jetpack can turn tighter and quicker at high speed, but altitude will not be maintained and a height loss will occur.

For low speed flight, less than 10 m/s, acceptable turn rates (greater than 10°/s) and turn radii (less than 20 m) are possible for an assumed maximum

level bank angle of 30°. Hence, the manoeuverability of the Jetpack will be best at low speed where centripetal accelerations are small.

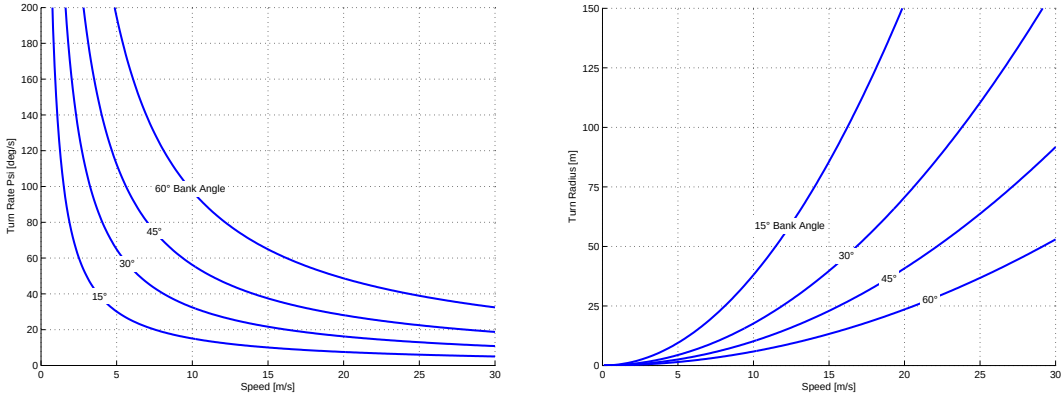

(a) Turn rate versus bank angle

(b) Turn radius versus bank angle

Figure 3.25: Banked level flight

Jetpack Level Flight

Since the purpose of the Jetpack is to be able to fly from one point to another an understanding of the level flight forces acting on the Martin Jetpack is required. The term *level flight* is used to describe the aircraft flying through the air at a constant: heading, attitude, altitude, and airspeed. In hovering flight only two forces act on the Jetpack, the thrust force and the weight force. In level flight an additional two forces occur, the ducted-fan normal force and the parasitic drag force. Assuming that the aircraft is balanced about the y axis, which is the ideal case where no trim moment is required by the pitch vanes, the free body diagram of the Jetpack can be drawn as shown on Figure 3.26.

It can be seen that the parasite drag force, D, opposes the motion V_0 and that the ducted-fan normal force, F_n, has a component that opposes the motion and a component that adds to the lift of the Jetpack. Summing the forces shown in Figure 3.26 for equilibrium flight in the xz plane the following two equations can be made:

$$F_x = 2T\cos\alpha - 2F_n\sin\alpha - D = 0 \tag{3.4.7}$$

$$F_z = -2T\sin\alpha - 2F_n\cos\alpha + W = 0 \tag{3.4.8}$$

where T is the required thrust force per duct ducts, F_n is the ducted-fan normal per duct (calculated by equation (3.2.1)), D is the parasite drag of the aircraft and W is the aircraft weight force. The parasite drag is calculated by conventional drag equation as a function of the dynamic pressure as:

$$D = C_D\frac{1}{2}\rho V_0^2 A \tag{3.4.9}$$

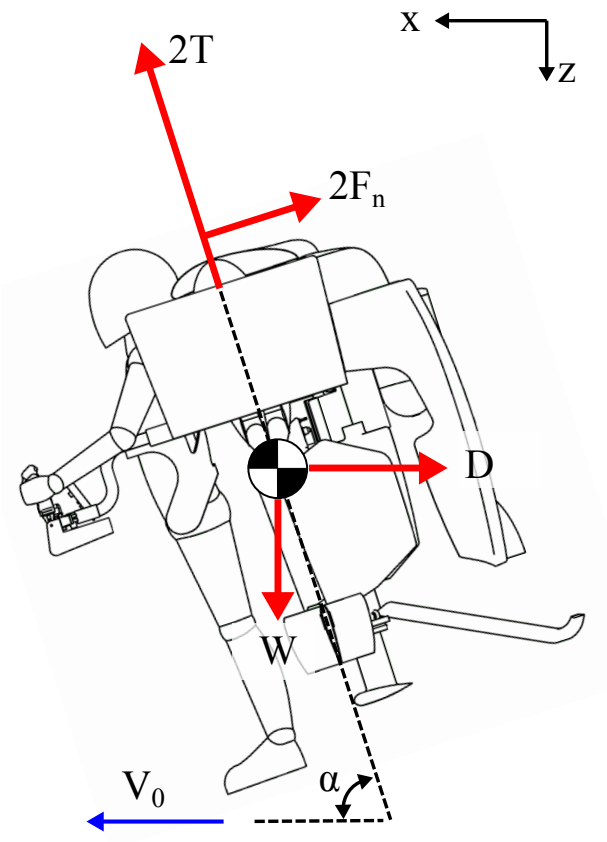

Figure 3.26: Free body diagram of the Jetpack P-11A in ideal trimmed level flight.

where C_D is the drag coefficient, A is the frontal area of the Jetpack, ρ is the air density, and V_0 is the horizontal velocity of the Jetpack. Using the conditions shown in Table 3.4 the equations (3.4.7) to (3.4.8) are solved for a range of pitch attitudes, θ, from 0° to 50°, where $\theta = 90° - \alpha$.

Table 3.4: Ideally trimmed P-11A Jetpack level flight conditions

Condition	Value
W	2450 N
C_D	0.9
A	1.8 m^2
ρ	1.225 kg/m^3
d_r	0.528 m
d	0.6 m

Lift to Drag Ratio Versus Pitch Attitude

The lift to drag ratio explained in section B.1 is commonly extended further to include the aircraft as a whole, where the lift and drag is the net lift and drag on the aircraft. Applying the lift to drag ratio to the whole aircraft allows for easy comparison between aircraft types as well as assessing the efficiency of the aircraft to fly from point A to point B. Figure 3.27 shows that the lift to drag ratio for the Jetpack P-11A diminishes with increasing attitude. The lift to drag ratio for an aircraft in level flight can be written as:

$$\frac{L}{D} = \frac{W}{T_{horizontal}} \tag{3.4.10}$$

where $T_{horizontal}$ is the horizontal component of thrust and is equal and opposite to the drag D, and the lift L is equal and opposite to the weight W. As the Jetpack is able to hover it can fly at very low airspeeds and as such experiences very low drag of both parasite and lift induced (ducted-fan normal force). Hence, the lift to drag ratio tends to infinity as airspeed tends to zero. The decaying lift to drag ratio for increasing attitude occurs as less lift is being produced due to the duct thrust force becoming more horizontal and the drag forces significantly increasing.

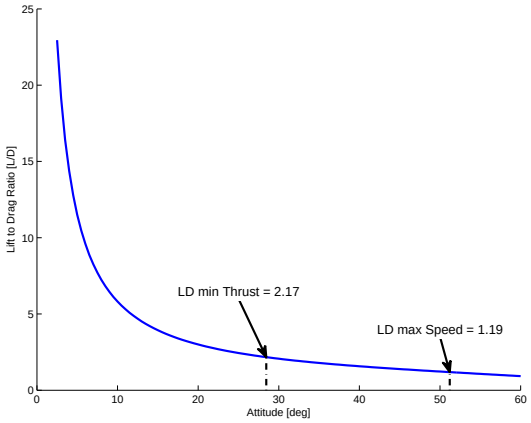

Figure 3.27: Lift to drag ratio versus attitude

Performance Versus Pitch Attitude

Figure 3.28a shows that the speed versus attitude relation is near linear between 0 to 60° pitch attitude with an $R^2 = 0.99821$. This has the benefit that potential control algorithms based on attitude and velocity can be kept simple as the speed to attitude relation is proportional, up to 60° pitch attitude. The maximum speed is determined where the maximum available thrust equals the required thrust, Figure 3.28b. In reality the maximum speed is less than this as the available duct thrust is not a constant, but diminishes with increasing speed. The nature of the diminishing thrust needs to be determined to improve the model.

A minimum thrust below the hovering thrust requirement exists due to the vertical component of the ram-drag force aiding in lift of the Jetpack. In reality additional lift forces may also be present from lift generated from the body and the effects of ducted-fan normal force with speed, but these need to be determined experimentally to evaluate their magnitudes, as no analytical means exists.

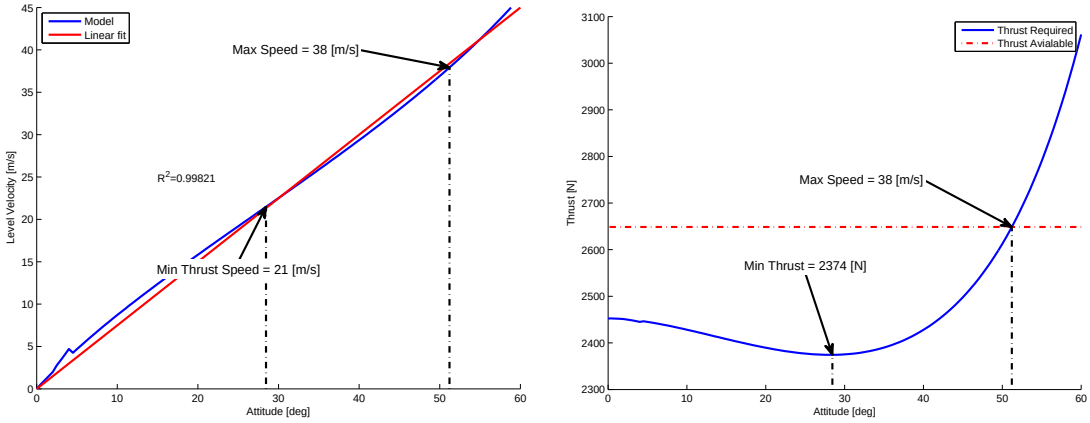

(a) Speed versus attitude

(b) Thrust requirement versus attitude showing locations of minimum thrust and maximum speed.

Figure 3.28: Ideally trimmed level flight performance for the P-11A Jetpack.

Jetpack Trimmed Longitudinal Level Flight

For trimmed level flight the moments about the aircraft's centre of gravity need to be taken into account to ensure the aircraft is balanced. The aircraft is trimmed (in equilibrium) if and only if the overall centre of pressure coincides with the centre of gravity so that there are no net moments about the centre of gravity. For assessing longitudinal level flight an additional moment equation about the y axis, which passes through the centre of gravity, is included in the horizontal and vertical equilibrium equations of (3.4.7) and (3.4.8), respectively, to complete the trim analysis in the longitudinal plane:

$$M_y = 2F_n l_d - 2F_{pitch,L} l_{pitch} + M_d = 0 \tag{3.4.11}$$

where $F_{pitch,L}$ is the net lift force of the pitch vanes, l_{pitch} is the pitch vane moment arm, l_d is the moment arm from the centre of gravity to the duct quarter-chord point, and M_d is the ducted-fan moment calculated using the

variable centre of pressure model described in section 3.2, Figure 3.13. Since the pitch vane force has components in the horizontal and vertical directions equations (3.4.7) and (3.4.8) are expanded to include these effects as:

$$F_x = 2T\cos\alpha - 2F_n\sin\alpha - D - 2F_{pitch,L}\sin\alpha - 2F_{pitch,D}\cos\alpha = 0 \quad (3.4.12)$$

$$F_z = -2T\sin\alpha - 2F_n\cos\alpha + W - 2F_{pitch,L}\cos\alpha + 2F_{pitch,D}\sin\alpha = 0 \quad (3.4.13)$$

where $F_{pitch,D}$ is the pitch vane drag and is calculated from the pitch vane lift $F_{pitch,L}$ using an assumed pitch vane lift to drag ratio, L/D_{pitch}. Using the assumption that the duct centre of pressure varies as a function of free stream velocity and angle of attack, as described in section 3.2, equations (3.4.11) to (3.4.13) are solved for two configurations of the Jetpack; the P-11A Jetpack and a hypothetical P-11A Jetpack that has the centre of gravity positioned approximately to the ducted-fan centre of pressure. For both cases all other parameters remain constant and it is assumed that the drag of the Jetpack acts at the centre of gravity thus produces no moments.

3.4.0.1 P-11A Jetpack

The free body diagram for the P-11A Jetpack as developed by Martin Aircraft and flown up until May 2011 is shown in Figure 3.29. It is evident from Figure 3.29 that the ducted-fan normal force will produce a positive pitching moment. The pitch vane that has a similar moment arm will have to produce a force approximately equal to the ducted-fan normal force to trim the aircraft. Hence, the ducted-fan normal force contributions to the total drag is effectively doubled due to the contribution of the pitch vane force required to trim (balance) the aircraft. Using the conditions shown in table 3.5 the equations (3.4.11) to (3.4.13) are solved to produce Figures 3.30 to 3.31b.

Table 3.5: Additional trimmed flight conditions for P-11A Jetpack

Condition	Value
l_{duct}	0.529 m
$l_{pitvane}$	0.524 m
L/D_{pitch}	5

Pitch Force Required for Trim

Figure 3.30 shows the required pitch force versus the attitude, and hence speed, for trimmed level flight of the P-11A Jetpack. The solid line represents the required pitch force while the dashed line shows the maximum net lift force of the pitch vanes. The point where these two lines intersect is the attitude where the maximum trimmed flight velocity occurs. For flight speeds greater than this value the lift vane force, or more fundamentally the pitch vane moment needs to be increased. The pitch vane moment can be increased by:

1. Increasing the moment arm of the pitch vanes.

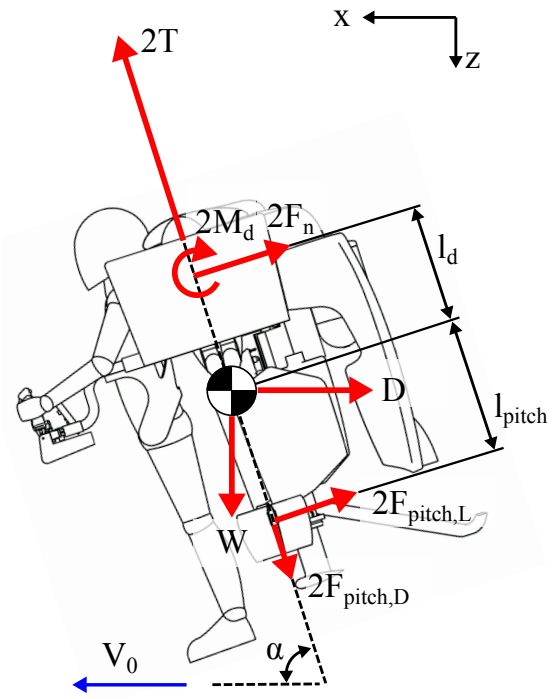

Figure 3.29: Free body diagram of P-11A Jetpack in trimmed level flight.

2. Increasing the size and number of pitch vanes, which effectively increases the pitch force.

Both of the above measures have practical disadvantages. Increasing the moment arm of the pitch vanes cannot practically be done as the vanes will interfere with the ground if extended further during takeoff and landing. Raising the height of the aircraft would allow the vane moment arms to be extended, but this detrimentally reduces the stability of the aircraft on the ground. Extending the control vane moment arm also increases the crosswind effect on the control vanes, which negatively affects the control system, as described in section 3.3.

The excessive pitch force required to trim the aircraft is a clear indication that the P-11A aircraft was fundamentally poorly balanced. From a dynamic aspect, if the Jetpack were to encounter a gust, the abrupt increase in speed would create a large pitch back moment due to the ducted-fan normal force contribution. To balance this the pilot would either have to anticipate the gust, which is unfeasible, or allow the control system to correct the disturbance. The latter is far more practical, but implies a delay due to the time to recognize the disturbance, compute the correct reaction, and apply the action. During this time the Jetpack, due to the overly large ducted-fan normal moment, has greatly increased its pitch back attitude requiring an even larger corrective moment from the control vanes. Hence, the control system quickly becomes saturated trying to control the aircraft leading to loss of control, which may or may not be recoverable.

Since the pitch control vanes are used for both trim and manoeuvering a tradeoff between trim and manoeuvering moments must be made as the maximum pitch vane moment is limited. For example, it can be seen on Figure

3.30 that if airspeed/attitude is increased more control moment is required for trim leaving less control authority for manoeuvering. At maximum speed the control vanes are saturated (at maximum deflection), thus no reserve pitch moment exists for manoeuvering or stabilising the aircraft for any disturbance in pitch. Hence, at this point the P-11A is uncontrollable in pitch and must be flown at airspeeds/attitudes lower than 1.7 m/s or 8° attitude respectively.

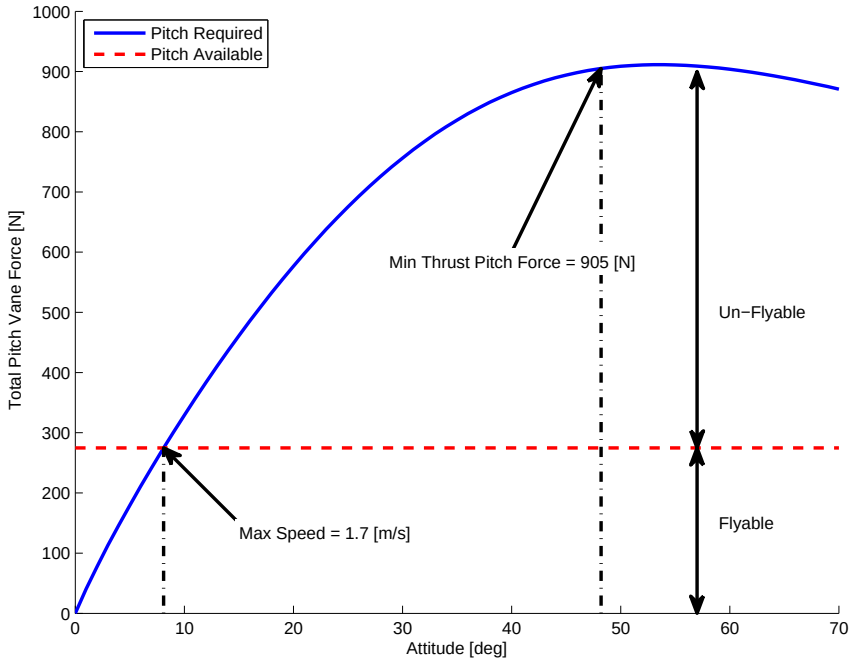

Figure 3.30: Jetpack P-11A trimmed level flight pitch force requirement versus attitude.

Flight Performance

Figure 3.31a shows the Jetpack speed versus attitude. Comparing this figure to Figure 3.28a, which shows the ideal Jetpack (ideally balanced, thus no trim required), it can be seen that the extra drag produced by the required pitch vane force to trim the Jetpack has substantially reduced the possible flight speed over the entire attitude range. Hence, the efficiency of the Jetpack to fly at a given speed has greatly decreased due to the large drag component created by the pitch vane to trim the aircraft. Figure 3.31b shows that the value of minimum thrust is lower and that the velocity of minimum thrust is higher than the ideal Jetpack, which is favourable. However, this minimum thrust airspeed is not reachable as the control authority does not exist to obtain this airspeed.

3.4.0.2 Hypothetical Jetpack P-11A

The trim analysis of the P-11A Jetpack shows that the P-11A Jetpack is poorly balanced, as a result of the large ducted-fan normal moment. By hypothetically arranging the centre of gravity to coincide with the duct centre of pressure, the ducted-fan normal moment can largely be eliminated giving much more authority to the control vanes to develop moments for responsive manoeuvering

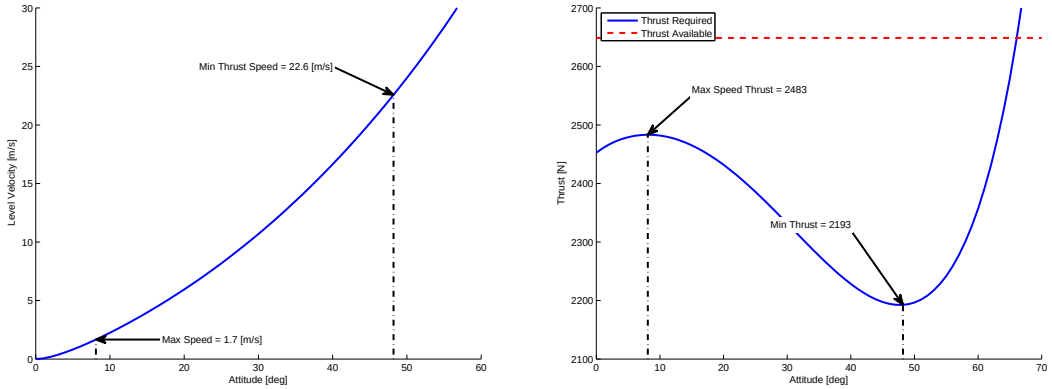

(a) Speed versus attitude

(b) Required thrust versus attitude

Figure 3.31: Trimmed level flight performance for the Martin Jetpack P-11A.

rather than having to trim the aircraft. Using the hypothetical P-11A Jetpack parameters shown in table 3.6, and solving the equations (3.4.11) to (3.4.13) Figures 3.33 to 3.34b are created.

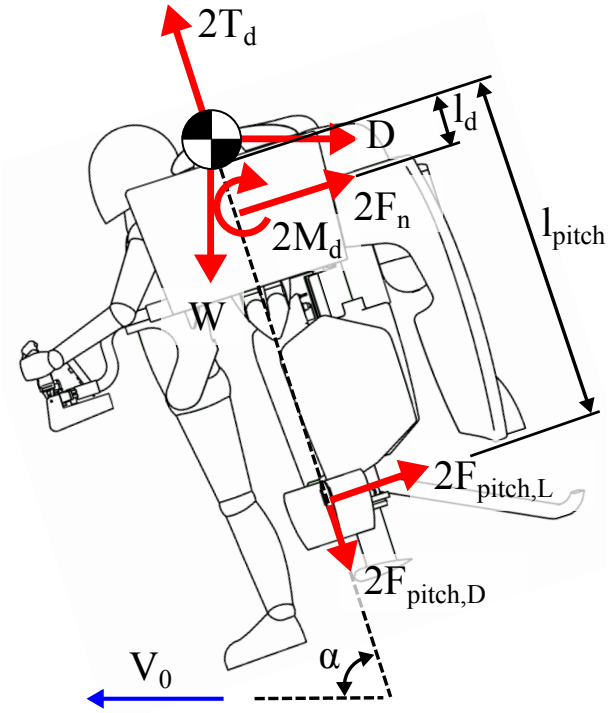

Figure 3.32: Free body diagram of a hypothetical P-11A Jetpack with centre of gravity coinciding with duct centre of pressure.

Table 3.6: Additional trimmed flight conditions of a hypothetical P-11A Jetpack with centre of gravity coinciding with duct centre of pressure.

Condition	Value
l_{duct}	$-0.3\,\mathrm{m}$
$l_{pitvane}$	$0.524\,\mathrm{m}$
L/D_{pitch}	5

Pitch Force Required for Trim

Due to the dynamic nature of the ducted-fan centre of pressure position, as described by equation (3.2.4), the required pitch vane force has a maximum value at approximately 15° of attitude and decreases with increasing attitude beyond this point, as shown on Figure 3.33. Since the required pitch force for trim flight is less than the maximum pitch force available throughout the obtainable level flight speeds (up to 49° of attitude), the pitch vanes are always capable trimming and manoeuvring the Jetpack. Hence, the level speed flight envelope is limited by power/thrust limitations rather than the unfavourable control saturation limits.

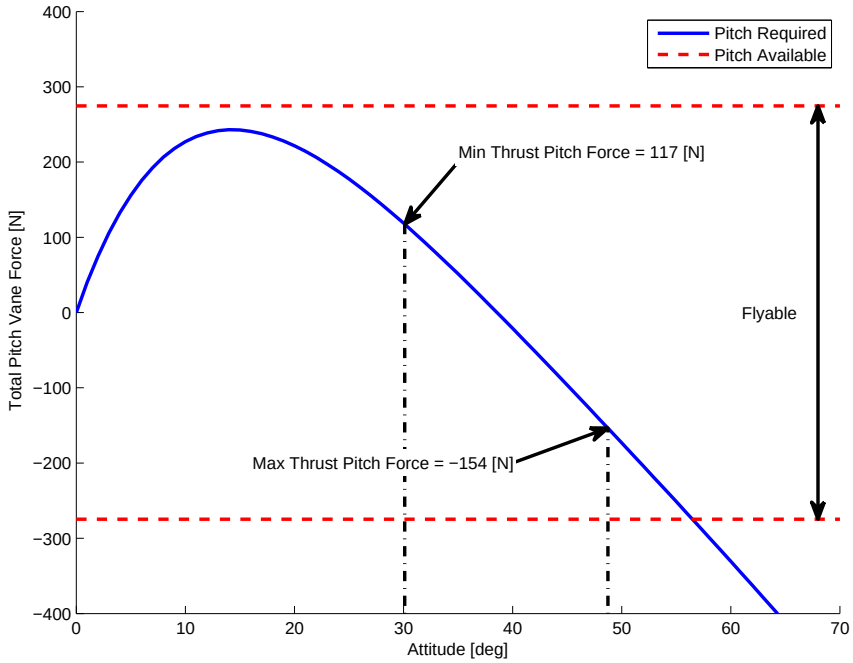

Figure 3.33: Jetpack P-11A trimmed level flight pitch vane force requirement versus attitude with centre of gravity coinciding with duct centre of pressure.

Flight Performance

Comparing Figures 3.28a and 3.34a, it can be seen that velocities throughout the flight range are very similar. Indicating that positioning the centre of gravity closer to the duct centre of pressure should be done to maximize the efficiency of the Jetpack. The minimum thrust value is less than the minimum thrust value of the P-11A as the lift component of the pitch vane force is greatly reduced, and the point of minimum thrust occurs at a much lower pitch attitude, when compared to the P-11A.

Sizing of Control Vanes for Manoeuvering

The control vanes, particularly the pitch control vanes, provide two functions, one to trim the aircraft for steady state flight, and two to create angular motion to change the orientation of the aircraft for manoeuvering. The control moments are created by deflecting the control vanes, as described in section 3.3,

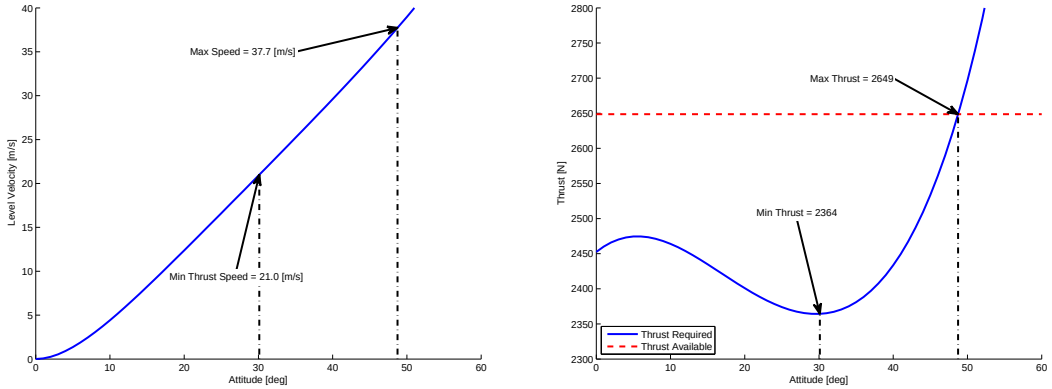

(a) Speed versus attitude

(b) Required thrust versus attitude

Figure 3.34: Trimmed level flight performance for the Martin Jetpack P-11A with centre of gravity coinciding with duct centre of pressure.

and the trim requirements of the control vanes are determined by trim calculations as done in section 3.4, which leaves only the manoeuvering requirements to be determined. Beginning with a fundamental analysis of the desired angular motion, the angular acceleration can be determined via kinematics using Newton's Second law of motion and the inertia value of the Jetpack the required moment for the desired acceleration can be determined.

Adding the trim and manoeuvering control requirements the total required control vane moment can be calculated. From this total moment, the control vane moment arm, plan-form size, and lift coefficient can be determined to complete the control vane design.

Figure 3.35a shows the required angular acceleration needed to achieve both a given angular velocity and angular displacement after a 1 s duration. Utilizing Newton's Second law, in angular terms $M = I\dot{\omega}$, together with an appropriate angular acceleration from Figure 3.35b, and the Jetpack's moment of inertia, the required control vane moment to produce an angular acceleration can be found. Figure 3.35b shows the angular acceleration versus moment for a range of inertia values close to that of the Jetpack's, and in conjunction with Figure 3.35a it can be used to size the control vanes to achieve a desired change in orientation, or angular rate.

Figures 3.35a and 3.35b allow the desired motion to be related to the necessary control moment needed for the manoeuvering. However, this raises the question of what value of motion is desirable. This is highly dependent on the mission objectives of the aircraft, but in short, the faster the change in attitude, the more maneuverable the aircraft is, the more effectively the aircraft can achieve a broader range of mission objectives. The desired motion, or rate of response, can be determined experimentally by flying the aircraft and determining what level of motion is suitable, or the desired motion can be determined from historical data of similar aircraft types.

Table 3.7 from the United States Army Helicopters Standard ADS-33 [79] shows the required motion for various agility categories and levels helicopters and gives a good indication of what the Jetpack should be designed for. As

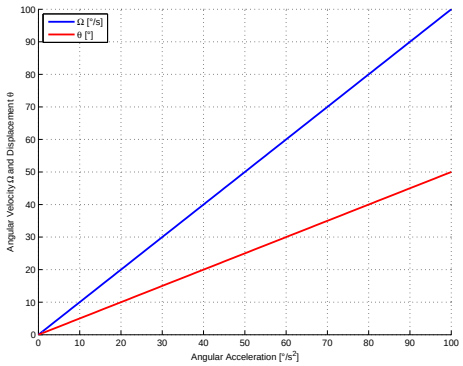

(a) Angular acceleration required for given angular velocity and displacement for a 1 s duration.

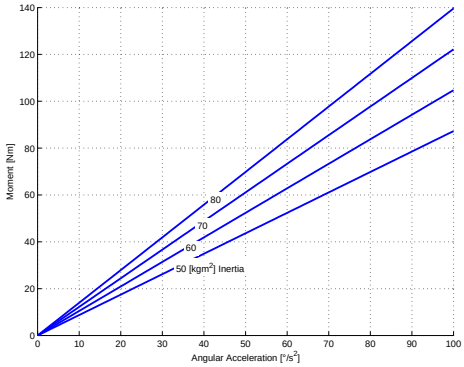

(b) Moment required for angular acceleration for various inertia values.

Figure 3.35: Moment and angular motion relations

the Jetpack has a low inertia for a human lifting aircraft it is expected that the Jetpack should have a high degree of manoeuverability exceeding the values of level one in table 3.7.

Table 3.7: Requirements for large-amplitude attitude changes – hover and low speed. Taken from ADS-33 standard [79]

AGILITY CATEGORY MTE	RATE RESPONSE-TYPES						ATTITUDE COMMAND RESPONSE-TYPES			
	ACHIEVABLE ANGULAR RATE (deg/sec)						ACHIEVABLE ANGLE (deg)			
	LEVEL 1			LEVELS 2 AND 3			LEVEL 1		LEVELS 2 AND 3	
	Pitch	Roll	Yaw	Pitch	Roll	Yaw	Pitch	Roll	Pitch	Roll
Limited Agility Hover Landing Slope Landing	±6	±21	±9.5	±3	±15	±5	±15	±15	±7	±10
Moderate Agility Hovering Turn Pirouette Vertical Maneuver Depart/Abort Lateral Reposition Slalom	±13	±50	±22	±6	±21	±9.5	+20 -30	±60	±13	±30
Aggressive Agility Vertical Remask Acceleration Deceleration Sidestep Target Acquisition and Track Turn to Target	±30	±50	±60	±13	±50	±22	±30	±60	+20 -30	±30

3.5 Summary

This Chapter has introduced and explained the fundamental physics with mathematical derivations for the key aerodynamic features of the Martin Jetpack. Combining these models of the key Jetpack aerodynamic features with the atmospheric model, which includes the influences from wind, a complete flight model describing the dynamic interactions of the Jetpack flight mechanics with the atmosphere can be developed, which will be the topic of the next chapter (Chapter 4).

The effectiveness of the control vanes to develop moments to control the Jetpack is critical for both safe and functional operation of the Jetpack, hence the importance of validating their effectiveness, which is explained in Chapter 5.

Methods of determining the ducted-fan centre of pressure were derived as modelling the ducted-fan centre of pressure and moment versus angle of attack and airspeed is of highest importance in order to correctly design the Jetpack for practical flight. Hence, the assumptions made in developing the ducted-fan pitching moment model, section 3.2, need to be validated to determine their accuracy for the design of the Jetpack, which will be explained in Chapter 6.

The steady state flight equations have highlighted that the P-11A Jetpack is poorly aerodynamically balanced, which resembles the actual performance of P-11A Jetpack, Table 1.2. Fortunately, the fundamental flight mechanics also suggest a possible solution by locating the centre of gravity of the aircraft close to the ducted-fan centre of pressure, in practical terms the centre of gravity should be located slightly above the duct lip.

Chapter 4

The Jetpack Flight Model

"Pure mathematics is, in its way, the poetry of logical ideas."
Albert Einstein

This chapter explains the development of a six degrees of freedom model that describes the flight dynamics of the twin ducted-fan Martin Jetpack. Employing the conventional aircraft modelling methodology, a system of ordinary differential equations (ODEs) that describes the behaviour of the Jetpack is developed. The equations are solved in real-time using Matlab®/Simulink® software to simulate the responses to given inputs.

An accurate flight model of an aircraft allows for a better understanding of the flight behaviour, which leads to a reduced number of test flights and consequently, reduced cost and risk. An accurate model allows designers to investigate the effect of changing model parameters of not just the physical aircraft, but also those of the control system included in the model [50]. For these unique flying machines, which have unfamiliar characteristics, it is prudent to have real-time simulation of the aircraft to allow test pilots to familiarize and train themselves.

This Chapter describes the flight mechanics of a twin ducted-fan aircraft and explains in detail the modelling of the forces and moments contributed by the twin ducted-fans, body aerodynamics, control surfaces, gyration, and landing gear interactions.

4.1 Model Overview

The flight model developed has the form of a state-space system where inputs are fed into the derivative of the state variables resulting in outputs that are fed back into the system. The top level block diagram of the Jetpack Simulink® model is shown in Figure 4.1, which highlights the inputs, state variables, outputs, and feedback of the Jetpack Simulink® model.

The state variables block of the Jetpack model contains the information to describe how the Jetpack reacts to inputs. The state variables block is split into two categories: Jetpack reactions and kinematics. The Jetpack reactions

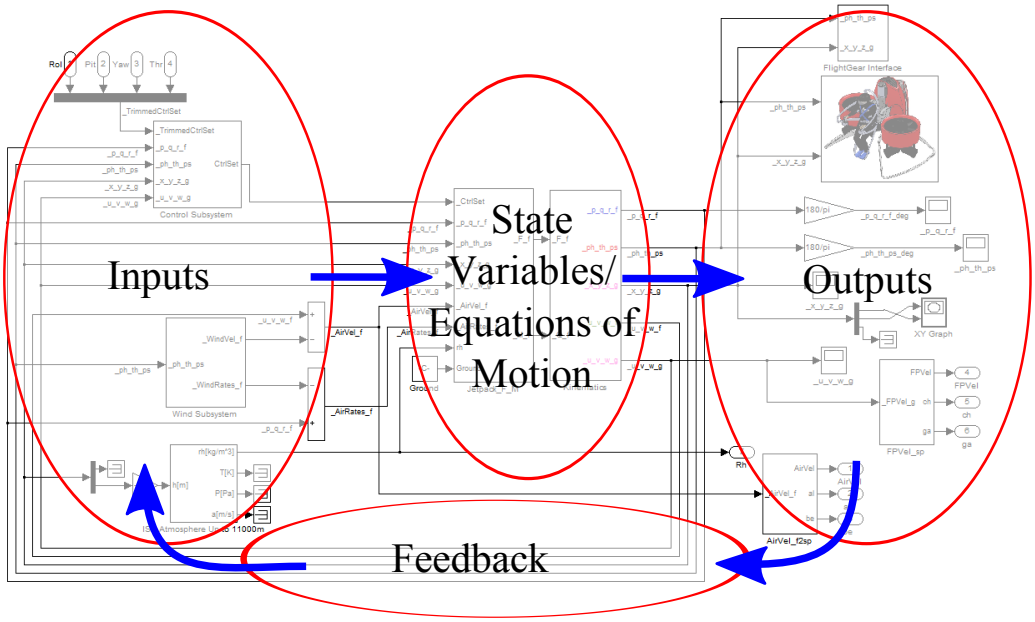

Figure 4.1: Overview of Jetpack Simulink® model,

describe all the external[1] forces and moments that affect the Jetpack. The sum of these becomes the left-hand side of Newton's Second Law of motion $\mathbf{F} = m\mathbf{a}$. The kinematic equations describe how net accelerations relate to the Jetpack's velocity and position, in both translational and angular terms. The kinematic equations and the Jetpack forces and moments create the dynamic equations of motion of the Jetpack.

Equations of Motion

To account for all the accelerations acting on an aircraft Pamadi[80] and Cook[81] state that Newton's Second Law of Motion must be solved with respect to an inertial reference frame. For the three translational degrees of freedom x, y, z Newton's Second Law of Motion is:

$$\mathbf{F}_i = m\left(\frac{\mathrm{d}\mathbf{u}}{\mathrm{d}t}\right)_i \tag{4.1.1}$$

where $\mathbf{F}$ is the force vector, m is the mass, and $\mathbf{u}$ is the velocity vector with the velocity components u, v, w in the x, y, z axis, respectively, measured with respect to the inertial axis indicated by the subscript i. Similarly, for the three rotational degrees of freedom Φ, Θ, Ψ Newton's Second Law of Motion is:

$$\mathbf{M}_i = \left(\frac{\mathrm{d}\mathbf{H}}{\mathrm{d}t}\right)_i = \left(\frac{\mathrm{d}\mathbf{I}}{\mathrm{d}t}\right)_i \boldsymbol{\omega} + \mathbf{I}\left(\frac{\mathrm{d}\boldsymbol{\omega}}{\mathrm{d}t}\right)_i \tag{4.1.2}$$

where $\mathbf{M}$ is the moment, $\mathbf{H}$ is the angular momentum, $\mathbf{I}$ is the inertia tensor of the aircraft, and $\boldsymbol{\omega}$ is the angular velocity vector with the velocity components

[1]The use of the word external refers to the fact that these forces and moments are due to the influence of the various Jetpack features, whereas internal refers to forces and moments produced by inertial and gravitational effects as described by the kinematics.

p, q, r about the x, y, z axis. The subscript i indicates that the time derivatives in equations (4.1.1) and (4.1.2) are measured with respect to the inertial reference frame. Since the inertia tensor $\mathbf{I}$ is described in the inertial reference frame the inertia tensor and its time derivative must be calculated at every time step due to the angular motion of the aircraft. Fortunately, this can be avoided by introducing a second reference frame, the *body frame*, fixed to the aircraft and centred on the aircraft's centre of gravity, so the inertia tensor is constant with respect to the body frame. However, the body frame is not an inertial reference frame, so requires the *moving axis theorem,* as described in [80, 81], to introduce the inertial accelerations into the body frame, where it is convenient to solve the equations of motion. Hence, the translational accelerations with respect to the body frame are:

$$\mathbf{a}_f = \frac{\mathbf{F}_f}{m} - \boldsymbol{\omega}_f \times \mathbf{u}_f + \mathbf{DCMg}_i \tag{4.1.3}$$

where: $\mathbf{F}$ is the net-external force acting on the Jetpack, m is the mass of the aircraft, $\boldsymbol{\omega}$ is the vector of angular rates p, q, r, $\mathbf{DCM}$ is the Euler angle transformation matrix equation 4.1.10, $\mathbf{g}$ is the acceleration due to gravity in the inertial frame ([0, 0, g]), and the subscripts f and i denote the body and inertial reference frames that the vectors are define in. Note, the acceleration due to gravity could have been included as a weight force, $\mathbf{F}_w = m\mathbf{DCMg}$, but this results in an unnecessary computation using the mass term, and eliminates the classification of internal and external forces. The term $\boldsymbol{\omega}_f \times \mathbf{u}_f$ represents the centripetal accelerations of the aircraft with respect to the inertial reference frame due to angular and translational velocities of the aircraft.

Similarly to the translation accelerations, the rotational accelerations with respect to the body frame are:

$$\dot{\boldsymbol{\omega}}_f = \mathbf{I}_f^{-1}(\mathbf{M}_f - \boldsymbol{\omega}_f \times (\mathbf{I}_f \boldsymbol{\omega}_f)) \tag{4.1.4}$$

where $\mathbf{I}$ is the inertia tensor of the Jetpack determined from CAD geometry and mass data, and $\mathbf{M}$ is the net moment. The inertia tensor is defined as:

$$\mathbf{I} = \begin{bmatrix} I_{xx} & -I_{xy} & -I_{xz} \\ -I_{yx} & I_{yy} & -I_{yz} \\ -I_{zx} & -I_{zy} & I_{zz} \end{bmatrix} = \begin{bmatrix} I_{xx} & -I_{xy} & -I_{xz} \\ -I_{xy} & I_{yy} & -I_{yz} \\ -I_{xz} & -I_{yz} & I_{zz} \end{bmatrix}$$

$$\mathbf{I} = \begin{bmatrix} \int (y^2 + z^2)\mathrm{d}m & -\int xy\mathrm{d}m & -\int xz\mathrm{d}m \\ -\int xy\mathrm{d}m & \int (x^2 + z^2)\mathrm{d}m & -\int yz\mathrm{d}m \\ -\int xz\mathrm{d}m & -\int yz\mathrm{d}m & \int (x^2 + y^2)\mathrm{d}m \end{bmatrix} \tag{4.1.5}$$

where the diagonal terms I_{xx}, I_{yy}, I_{zz} are the moments of inertia, and the non-diagonal terms are the products of inertia, which can be further simplified by noting that $I_{xy} = I_{yx}$, $I_{xz} = I_{zx}$ and $I_{yz} = I_{zy}$. SThe term $\boldsymbol{\omega}_f \times (\mathbf{I}_f \boldsymbol{\omega}_f)$ describes the gyroscopic effects due to the rotation of aircraft. For the case of a perfectly symmetrical aircraft the inertia tensor reduces to that of a diagonal matrix, so no gyroscopic angular accelerations are introduced as a result of the angular motion.

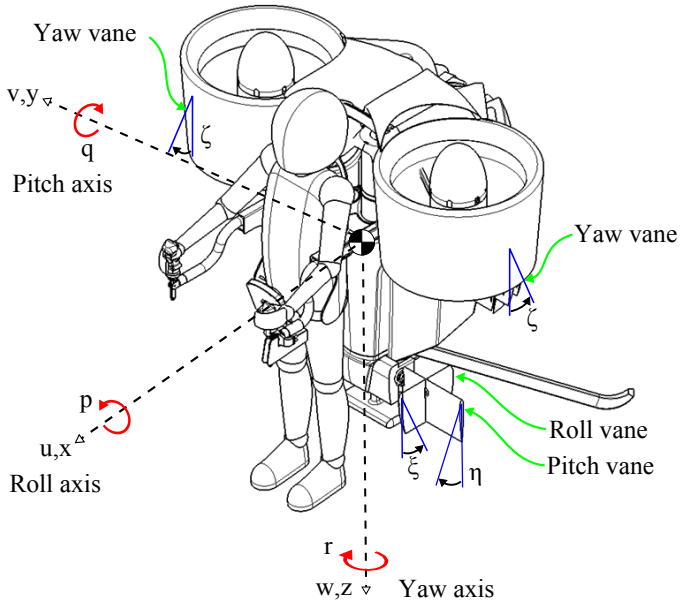

Figure 4.2: The Martin Jetpack P-11A sign convention and key features

The motion and position vectors of the Jetpack, due to the net accelerations calculated from equations (4.1.3) and (4.1.4), are obtained through the kinematic relations:

$$\mathbf{a}_f = \frac{\mathrm{d}\mathbf{u}_f}{\mathrm{d}t} \tag{4.1.6}$$

$$\mathbf{DCM}^{-1}\mathbf{u}_f = \frac{\mathrm{d}\mathbf{x}_i}{\mathrm{d}t} \tag{4.1.7}$$

$$\dot{\boldsymbol{\omega}}_f = \frac{\mathrm{d}\boldsymbol{\omega}_f}{\mathrm{d}t} \tag{4.1.8}$$

$$\mathbf{DCM}_{ang}^{-1}\boldsymbol{\omega}_f = \frac{\mathrm{d}\boldsymbol{\Phi}}{\mathrm{d}t} \tag{4.1.9}$$

where $\mathbf{x}_i$ is position vector of the aircraft with respect to the inertial reference frame, $\boldsymbol{\Phi}$ is the vector of Euler angles Φ, Θ, Ψ, and $\mathbf{DCM}_{ang}^{-1}$ will be defined in equation 4.1.15. Together equations (4.1.3) and (4.1.4) and equations (4.1.6) to (4.1.9) form the system of ordinary differential equations (ODEs) that model how the Jetpack behaves in flight.

Euler Angles

Euler angles are used to relate the orientation of the aircraft's coordinate system, the body frame (x, y, z), to the inertial coordinate system, the inertial frame (x_i, y_i, z_i), via the intermediate coordinate systems (x_1, y_1, z_1) and (x_2, y_2, z_2) [80, 81]. The *directional cosine matrix*, equation (4.1.10), describes the transformation of a vector quantity from the inertial frame to the body frame, and is created by considering the positive right hand rotations of Ψ about the z_g axis, then Θ about y_1 axis, and finally Φ about the x axis, as shown on Figure 4.3.

$$\mathbf{DCM} = \begin{bmatrix} \cos\Theta\cos\Psi & \cos\Theta\sin\Psi & -\sin\Theta \\ \sin\Phi\sin\Theta\cos\Psi - \cos\Phi\sin\Psi & \sin\Phi\sin\Theta\sin\Psi + \cos\Phi\cos\Psi & \sin\Phi\cos\Theta \\ \cos\Phi\sin\Theta\cos\Psi + \sin\Phi\sin\Psi & \cos\Phi\sin\Theta\sin\Psi - \sin\Phi\cos\Psi & \cos\Phi\cos\Theta \end{bmatrix} \tag{4.1.10}$$

$$\begin{bmatrix} x \\ y \\ z \end{bmatrix} = \mathbf{DCM} \begin{bmatrix} x_i \\ y_i \\ z_i \end{bmatrix} \tag{4.1.11}$$

To relate back from the body frame to the inertial frame the reverse calculation is made by inverting the *directional cosine matrix.* As the *directional cosine matrix* is an orthogonal matrix its inverse is also its transpose, so accordingly:

$$\begin{bmatrix} x_i \\ y_i \\ z_i \end{bmatrix} = \mathbf{DCM}^{-1} \begin{bmatrix} x \\ y \\ z \end{bmatrix} = \mathbf{DCM}^{T} \begin{bmatrix} x \\ y \\ z \end{bmatrix} \tag{4.1.12}$$

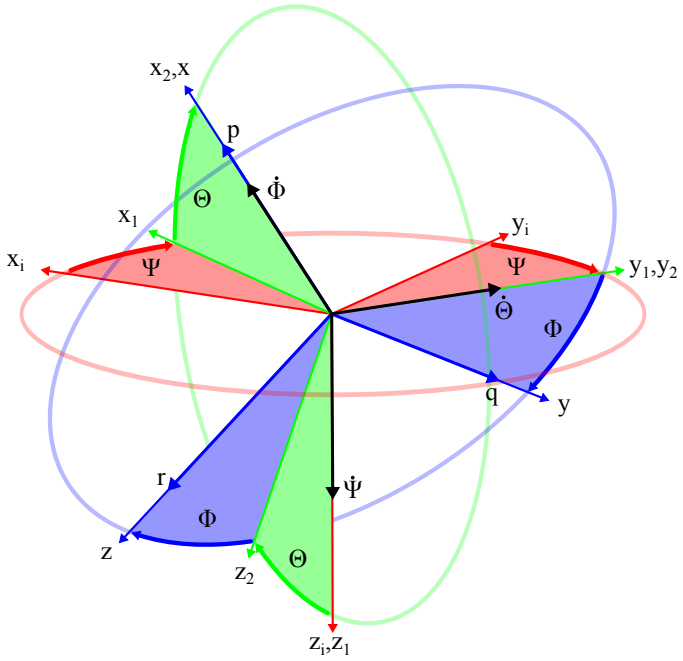

Figure 4.3: Linear and angular-rate Euler transformations from the inertial frame to the body frame. The angular-rate transformation has the rotational quantities $p, q, r, \dot{\Phi}, \dot{\Theta}, \dot{\Psi}$ superimposed on top of the linear Euler transformation, which shows that $\dot{\Phi}, \dot{\Theta}, \dot{\Psi}$ are not orthogonal.

It is also necessary to relate angular quantities from the inertial frame to the body frame. This is done in a similar manner to the translational case, but the transformation matrix is no longer orthogonal, as the angular rotation rates rotate about their intermediate axes, as described in [80] and shown in Figure 4.3. The angular transformation matrix is defined as follows:

$$\mathbf{DCM}_{ang} = \begin{bmatrix} 1 & 0 & -\sin\Theta \\ 0 & \cos\Phi & \sin\Phi\cos\Theta \\ 0 & -\sin\Phi & \cos\Phi\cos\Theta \end{bmatrix} \tag{4.1.13}$$

This leads to the relation between the angular velocity ω in the aircraft fixed axis and the Euler angle rates to be:

$$\begin{bmatrix} p \\ q \\ r \end{bmatrix} = \mathbf{DCM}_{ang} \begin{bmatrix} \dot{\Phi} \\ \dot{\Theta} \\ \dot{\Psi} \end{bmatrix} \tag{4.1.14}$$

As the angular transformation matrix is not orthogonal its inverse, equation 4.1.15, can be undefined for certain conditions, which has the implication that the transformation matrix can be inaccurate. This occurs when $\Theta = \frac{\pi}{2}$ or $\Theta \approx \frac{\pi}{2}$. Hence, whenever the simulated Jetpack has a pitch angle close to $\Theta \approx \frac{\pi}{2}$ results will be inaccurate. Fortunately steady flight at this attitude is not physically achievable by the Martin Jetpack so the model does not have to account for this. This problem can be overcome by using quaternion transformations[80]. The inverse of the Euler angle rates is shown in [80] to be:

$$\mathbf{DCM}_{ang}^{-1} = \begin{bmatrix} 1 & \tan\Theta\sin\Phi & \cos\Phi\tan\Theta \\ 0 & \cos\Phi & -\sin\Phi \\ 0 & \sec\Theta\sin\Phi & \sec\Theta\cos\Phi \end{bmatrix} \tag{4.1.15}$$

which allows for the Euler angle rates to be calculated from the body angular rates as:

$$\begin{bmatrix} \dot{\Phi} \\ \dot{\Theta} \\ \dot{\Psi} \end{bmatrix} = \mathbf{DCM}_{ang}^{-1} \begin{bmatrix} p \\ q \\ r \end{bmatrix} \tag{4.1.16}$$

4.2 Jetpack Forces and Moments

This section explains all the external forces and moments acting on the Jetpack, which include the aerodynamic affects from the ducted-fans, the Jetpack body, and the control vanes, as well as the gyration from rotating components, and landing gear ground interactions. Figure 4.4 shows the key reactions acting on the Jetpack in flight in the longitudinal plane. Similar reactions are experienced in the lateral plane when subjected to motion within this plane. It can be seen that any force not located at the centre of gravity also produces a moment about the centre of gravity. Note, all the aerodynamic constants presented in this chapter will be explained in Chapter 6.

The net reactions are the summation of the individual reactions from all of the features making up the unique layout of the Martin Jetpack. They are is calculated as:

$$\mathbf{F} = \mathbf{F}_{d,RH} + \mathbf{F}_{d,LH} + \mathbf{F}_{control} + \mathbf{F}_{D} + \mathbf{F}_{LG} \tag{4.2.1}$$

$$\mathbf{M} = \mathbf{M}_{d,RH} + \mathbf{M}_{d,LH} + \mathbf{M}_{control} + \mathbf{M}_{D} + \mathbf{M}_{LG} + \mathbf{M}_{gyr} \tag{4.2.2}$$

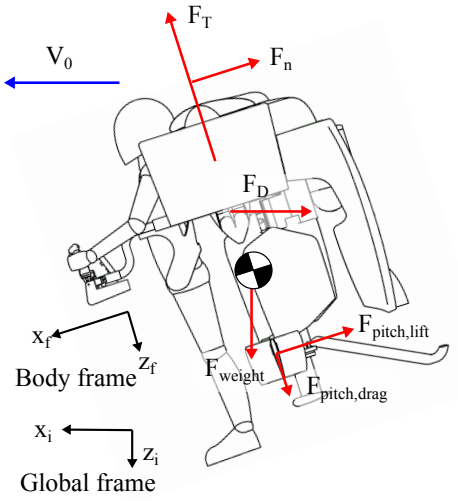

Figure 4.4: Free body diagram showing forces acting on the Jetpack in the longitudinal/pitch plane.

Ducted-Fan Reactions

Ducted-Fan Thrust

The ducted-fan thrust forces are the key forces on the Jetpack. They provide the lift and propulsion force for the aircraft to fly. For a given duct size (diameter), supplied power, and axial velocity the ducted-fan thrust force can be determined by momentum considerations, as per equation (3.1.48) and explained in section 3.1. The Jetpack model determines the power supplied to the ducted-fans from the engine power model in the frequency domain:

$$P_e = P_e(\tau)\frac{1}{\upsilon s + 1}RAD \tag{4.2.3}$$

where $P_e(\tau)$ is found via a look up table as a function of the throttle setting τ, υ is the engine time constant, and RAD is the relative air density as per equation (B.3.6). A first order transfer function is used to model the engine latency due to engine inertia, and the engine time constant τ_e is found by trial to match the actual engine. The relative air density, RAD, is used to correct the engine power for changes in air density, which occur for changes in altitude, air pressure, and air temperature. The ideal ducted-fan power, P_d, for supplied to each ducted-fan is:

$$P_d = \frac{1}{2}\eta_d P_e \tag{4.2.4}$$

where η_d is the duct efficiency and the division by two is the number of ducts on the Jetpack.

The ducted-fan power equation, equation (3.1.48), requires the axial component of the free stream velocity to be found, which is denoted V_1 as defined in Figures 3.2 and 3.9. To find V_1 the relative air velocity at each duct must be found as:

$$\mathbf{V}_{0,d,RH} = \Omega_0 \times \mathbf{l}_{d,RH} + \mathbf{V}_0 \tag{4.2.5}$$

where Ω_0 is the angular air velocity of the Jetpack; $\mathbf{l}_{d,RH}$ is the vector from the CG to right hand duct reference point, which is the intersection of the duct axis and the duct quarter chord plane. $\mathbf{V}_0$ is the translational air velocity of the Jetpack. The velocity component axial to the duct is found by:

$$V_1 = [0, 0, -1] \cdot \mathbf{V}_{0,d,RH} = [0, 0, -1] \cdot [u, v, w]_{d,RH} = -w_{d,RH}$$

where the sign change is required to relate between the Jetpack coordinate system and the definition of V_1 in equation (3.1.48).

For the given duct exit diameter the thrust for each ducted-fan can be determined using equation (3.1.48), where the unknown thrust force is in the form of a cubic equation. The roots of the equation are found using the Matlab® *roots* function, and using logic statements the smallest positive real root is chosen as the ducted-fan thrust force, T_d.

Ducted-Fan Normal Force

The ducted-fan normal force, equation (3.2.1), is projected onto the x axis, as shown on Figure 3.9, as:

$$F_{n,x} = \dot{m}_d V_{0,x} \tag{4.2.6}$$

where $V_{0,x}$ is the airspeed component in the x direction relative to the Jetpack and is calculated as:

$$V_{0,x} = [-1, 0, 0] \cdot \mathbf{V}_{0,d,RH} = [1, 0, 0] \cdot [u, v, w]_{d,RH} = -u_{d,RH} \tag{4.2.7}$$

Similarly the ducted-fan normal force in the y direction is:

$$F_{n,y} = \dot{m}_d V_{0,y} \tag{4.2.8}$$

where $V_{0,y}$ is the airspeed in the y direction relative to the Jetpack and is calculated as:

$$V_{0,y} = [0, -1, 0] \cdot \mathbf{V}_{0,d,RH} = [0, -1, 0] \cdot [u, v, w]_{d,RH} = -v_{d,RH} \tag{4.2.9}$$

Note the subscript RH in the above equations denotes that the equations are evaluated for the right hand ducted-fan. The same equations are also used for the left hand ducted-fan, LH.

Aerodynamic Ducted-Fan Lift Force

It will be seen in Chapter 6 that the ducted-fan lift and drag forces are also dependent on the dynamic pressure. These ducted-fan lift and drag forces are additional to the momentum derived forces, explained in sections 3.1 and 3.2, which model the forces from the redirection of airflow through the ducted-fan. Favourably, the downward momentum of the airflow through the ducted-fan encourages the free stream airflow surrounding the ducted-fan to also be redirected downwards. Consequently, the redirected downward momentum of the surrounding airflow manifests itself as an additional pressure distribution around the aircraft resulting in a lift and drag force proportional to the dynamic pressure. Hence, two equations are developed to model the additional

lift and drag forces; and are termed the *aerodynamic ducted-fan lift force* and *aerodynamic ducted-fan drag force,* respectively.

The ducted-fan dynamic lift force, which is evaluated for each duct, has a similar form to the traditional lift force equation, equation (B.1.6):

$$F_{L,d,x,RH} = C_{L,d,x,RH}\frac{1}{2}\rho V_{x,z,RH}^2 A_d P_F \tag{4.2.10}$$

where $C_{L,d,x,RH}$ is the ducted-fan lift coefficient, $\frac{1}{2}\rho V_{x,z,RH}^2$ is the dynamic pressure at the right hand ducted-fan, A_d is the ducted-fan area calculated from the duct exit diameter, and P_F is the power factor, which is an additional dimensionless term. The power factor is used to scale the aerodynamic ducted-fan lift force in proportion to the engine power as:

$$P_F = \frac{P_e}{P_{e,max}} \tag{4.2.11}$$

where P_e is the engine power and $P_{e,max}$ is the maximum engine power. This scaling of the power is necessary to include the effects of changing power on the dynamic lift force. For example at full power the ducted-fan will induce a higher flow rate through the ducted-fan, and consequently will produce more aerodynamic lift for a given non-zero velocity than when operating at a lower power setting at the same velocity. If no power is supplied then the aerodynamic lift is zero, which is expected as there is no induced momentum through the duct thus no downward accelerated air outside of the ducted-fan.

The ducted-fan lift coefficient, similarly to an aerofoil lift coefficient (section B.1), is dependent on the angle of attack:

$$C_{L,d,x,RH} = C_{L,d,max,x}\sin\alpha_{x,RH} \tag{4.2.12}$$

where $C_{L,d,max,x}$ is a constant identified from experiment, which will be explained in Chapter 6, and α_x is the angle of attack of the ducted-fan to the airspeed component in the xz plane, defined as:

$$\alpha_{x,RH} = \arctan(\frac{\|u_{f,RH}\|}{-w_{f,RH}}) \tag{4.2.13}$$

The airspeed $V_{x,z,RH}$ at the right hand ducted-fan in the xz plane is defined as:

$$V_{x,z,RH} = \sqrt{u_{f,RH}^2 + w_{f,RH}^2} \tag{4.2.14}$$

Equations (4.2.10) to (4.2.14) calculate the dynamic lift of the ducted-fan when a velocity component exists in the xz plane. The same equations are repeated for the velocity component in the yz plane as:

$$F_{L,d,y,RH} = C_{L,d,y}\frac{1}{2}\rho V_{y,z,RH}^2 A_d P_F \tag{4.2.15}$$

$$C_{L,d,y,RH} = C_{L,d,max,y}\sin\alpha_{y,RH} \tag{4.2.16}$$

where $C_{L,d,max,y}$ is a constant identified from experiment and differs from $C_{L,d,max,x}$.

$$\alpha_{y,RH} = \arctan(\frac{\|v_{f,RH}\|}{-w_{f,RH}}) \tag{4.2.17}$$

$$V_{y,z,RH} = \sqrt{v_{f,RH}^2 + w_{f,RH}^2} \tag{4.2.18}$$

To obtain the dynamic lift force from the right hand ducted-fan the lift forces $F_{L,d,x,RH}$ and $F_{L,d,y,RH}$ are transformed from the wind axes to the aircraft axes as:

$$\begin{aligned}\mathbf{F}_{L,d,RH} = [&-F_{L,d,x,RH}\cos\alpha_x, -F_{L,d,y,RH}\cos\alpha_y, \\ &- F_{L,d,x,RH}\sin\alpha_x - F_{L,d,y,RH}\sin\alpha_y]\end{aligned} \tag{4.2.19}$$

Aerodynamic Ducted-Fan Drag Force

Similarly to the aerodynamic ducted-fan lift forces, the aerodynamic ducted-fan drag forces are proportional to the dynamic pressure, as will be shown in Chapter 6. The aerodynamic ducted-fan drag forces are introduced into the model by applying the drag equation, equation (B.1.5) to the ducted-fan as:

$$F_{D,d,x,RH} = C_{D,d,x,RH}\frac{1}{2}\rho V_{x,z,RH}^2 A_d P_F \tag{4.2.20}$$

where $C_{D,d,x,RH}$ is the ducted-fan drag coefficient, $\frac{1}{2}\rho V_{x,z,RH}^2$ is the dynamic pressure at the right hand ducted-fan, and $V_{x,z,RH}$ is defined in equation (4.2.14), A_d is the ducted-fan area and P_F is the power factor as per equation (4.2.11). The ducted-fan drag coefficient, similarly to an aerofoil drag coefficient (section B.1), is dependent on the angle of attack, as described by:

$$C_{D,d,x,RH} = C_{D,d,max,x}\sin\alpha_{x,RH} \tag{4.2.21}$$

where $C_{D,d,max,x}$ is a constant identified from experimentation, which will be explain in Chapter 6, and α_x is the angle of attack of the ducted-fan to the airspeed component in the xz plane, as defined in equation 4.2.13. Equations (4.2.20) to (4.2.21) are repeated for the velocity component in the yz plane as:

$$F_{D,d,y,RH} = C_{D,d,y,RH}\frac{1}{2}\rho V_{y,z,RH}^2 A_d P_F \tag{4.2.22}$$

$$C_{D,d,y,RH} = C_{D,d,max,y}\sin\alpha_{y,RH} \tag{4.2.23}$$

To obtain the dynamic drag force for the right hand ducted-fan the drag forces $F_{D,d,x,RH}$ and $F_{D,d,y,RH}$ need to be transformed from the wind axes to the aircraft axes, which is done by:

$$\begin{aligned}\mathbf{F}_{D,d,RH} = [&-F_{D,d,x,RH}\sin\alpha_x, -F_{D,d,y,RH}\sin\alpha_y, \\ &F_{D,d,x,RH}\cos\alpha_x + F_{D,d,y,RH}\cos\alpha_y]\end{aligned} \tag{4.2.24}$$

Equations (4.2.20) to (4.2.24) are repeated for the left hand ducted-fan, where the subscribe LH is used instead of RH to denote left hand specific variables.

Ducted-Fan Moments

Instead of modelling the ducted-fan moment directly, the ducted-fan centre of pressure is first modelled and then the moment is calculated by the cross product of the centre of pressure and the ducted-fan reaction force; which in component form reduces to the centre of pressure multiplied by the ducted-fan normal force. It will be shown in Chapter 6 that ducted-fan moments and centre of pressure movements behave differently between the yz and xz planes.

Based on the fixed centre of pressure model, as described in section 3.2 with the modifications that will be described in Chapter 6, the ducted-fan centre of pressure in the yz plane can be modelled as:

$$CP_{y,RH} = \begin{cases} CP_{max} \sin \alpha_{y,RH} & 0 \leq \alpha_y \leq 90^\circ \\ CP_{max} & 90^\circ < \alpha_y \end{cases} \tag{4.2.25}$$

where $\alpha_{y,RH}$ is the duct angle of attack with respect to the y air velocity component, and the maximum centre of pressure CP_{max} above the duct quarter chord is calculated as:

$$CP_{max} = \frac{1}{2}d + \frac{1}{4}d_c \tag{4.2.26}$$

where d is the duct diameter and d_c is the duct chord length. The ducted-fan moment in the yz plane about the ducted-fan quarter chord is calculated as:

$$M_{x,RH} = F_{n,y,RH} CP_{y,RH} \tag{4.2.27}$$

where $F_{n,y,RH}$ is the y component of the ducted-fan normal force, and the subscript x indicates that the moment is about the x axis.

It will be shown that the ducted-fan moment in xz plane is dependent on both the velocity and the angle of attack, which can be modelled by the variable centre of pressure model described in section 3.2 and modified according to the results that will be presented in Chapter 6. The centre of pressure model in the xz plane is:

$$CP_{1,RH} = r_{RH} \sin \frac{\alpha_{x,RH}}{2} - CP_{max,RH} \cos \alpha_{x,RH}$$

$$CP_{max,1,RH} = \begin{cases} CP_{max} \sin \alpha_{x,RH} & 0 \leq \alpha_{x,RH} \leq 90^\circ \\ CP_{max} & 90^\circ < \alpha_{x,RH} \end{cases}$$

$$CP_{x,RH} = \begin{cases} CP_{1,RH} & CP_{1,RH} \leq CP_{max,1,RH} \\ CP_{max,1,RH} & CP_{max,1,RH} < CP_{1,RH} \end{cases} \tag{4.2.28}$$

where $r_{,RH}$ is the turning radius as per equation (3.2.3), $\alpha_{x,RH}$ is the duct angle of attack with respect to the x air velocity component, and $CP_{max,RH}$ is defined as per equation (4.2.26). The ducted-fan moment in the xz plane about the ducted-fan quarter chord is calculated as:

$$M_{y,RH} = -F_{n,x,RH} CP_{x,RH} \tag{4.2.29}$$

where $F_{n,x}$ is the x component of the ducted-fan normal force, the negative sign is used is required as per the sign convention, and the subscript y indicates that the moment is about the y axis. The resultant ducted-fan moment is then:

$$\mathbf{M}_{d,RH} = [\ M_{x,RH},\quad M_{y,RH},\quad 0\ ] \tag{4.2.30}$$

Equations (4.2.25) to (4.2.30) are repeated for the left hand ducted-fan, where the subscribe LH is used instead of RH to denote left hand specific variables.

Net Reactions

The resulting ducted-fan force vector is the sum of the momentum based forces ($\left[\ F_{n,x},\quad F_{n,y},\quad -T_d\ \right]$), and ducted-fan dynamic lift and drag forces:

$$\mathbf{F}_{d,RH} = \left[\ F_{n,x,RH},\quad F_{n,y,RH},\quad -T_{d,RH}\ \right] + \mathbf{F}_{L,d,RH} + \mathbf{F}_{D,d,RH} \tag{4.2.31}$$

$$\mathbf{F}_{d,LH} = \left[\ F_{n,x,LH},\quad F_{n,y,LH},\quad -T_{d,RLH}\ \right] + \mathbf{F}_{L,d,LH} + \mathbf{F}_{D,d,LH} \tag{4.2.32}$$

where net ducted-fan forces $\mathbf{F}_{d,RH}$ and $\mathbf{F}_{d,LH}$ are acting at the duct quarter chord point on the right and left hand ducted-fans, respectively, as shown in Figure 3.9. The duct quarter point has be chosen as the reference point where these forces act as this is the historic reference point for circular-wings/ducts, as used in [82, 58]. The net ducted-fan moment about the CG becomes:

$$\mathbf{M}_{d,CG} = \mathbf{l}_d \times \mathbf{F}_d + \mathbf{M}_d \tag{4.2.33}$$

Since there are two ducts, this is done for both right and left-hand ducted-fans as:

$$\mathbf{M}_{d,RH,CG} = \mathbf{l}_{d,RH} \times \mathbf{F}_{d,RH} + \mathbf{M}_{d,RH} \tag{4.2.34}$$

$$\mathbf{M}_{d,LH,CG} = \mathbf{l}_{d,LH} \times \mathbf{F}_{d.LH} + \mathbf{M}_{d,LH} \tag{4.2.35}$$

Control Forces

Various control vane configurations have been used on the Martin Jetpack prototypes throughout their development. The control vane reactions are modelled for each individual vane. For the case of the P-11E and P-12 Jetpacks which use combined pitch-yaw vanes, the pitch signal is superimposed on top of the yaw vane signal, a gain is introduced into the model that adds the contribution of the pitch vane signal onto the yaw vane signal. This gives the model the flexibility to model the control vane layouts for all Jetpack prototypes to date. The control vane force is modelled as explained in section 3.3, the control vane lift and drag coefficients as a function of the vane angle of attack are found by experiment, which is described in Chapter 5.

Vane Position in Duct Wake

Each of the control vane forces is modified by a factor that effectively reduces the dynamic pressure experienced by the vane due to the position of the vane within the duct wake. For the roll, pitch, and yaw vanes the factors ξ_f, η_f, and ζ_f are based on dynamic pressure results shown in section 3.3.

Vane Ground Interaction

It will be shown in Chapter 5 that the control vane forces lose effectiveness as they become closer to the ground during during takeoff and landing, due to the diverging airflow experienced by the control vanes. This reduction in the vane force is incorporated into the model by calculating the clearance between the trailing edge of the control vane and the ground in the direction of the duct axis, as shown on Figure 4.5. The clearance distance is then used to find the vane ground interaction factor, which is used to reduce the vane forces when in proximity to the ground.

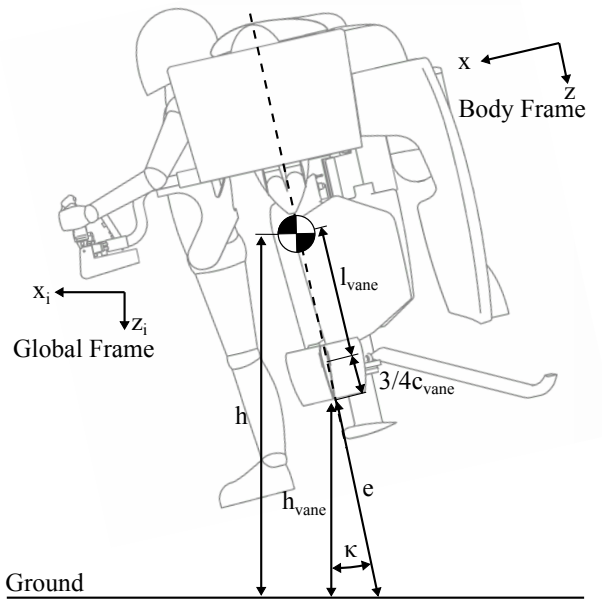

Figure 4.5: Schematic of vectors required to determine control vane clearance for ground interaction model.

The height of the aircraft above the ground is determined as:

$$\mathbf{h}_i = [\ 0 \quad 0 \quad z_i\ ] - [\ 0 \quad 0 \quad G\ ] \tag{4.2.36}$$

$$\mathbf{h}_{vane,i} = \mathbf{h}_i - \mathbf{DCM^{-1}}(\mathbf{l}_{vane} + [\ 0 \quad 0 \quad \tfrac{3}{4}c_{vane}\ ]) \tag{4.2.37}$$

$$e = \frac{\|\mathbf{h}_{vane,i}\|}{\cos\kappa} = \frac{\|\mathbf{h}_{vane,i}\|}{\left(\frac{\mathbf{h}_{vane,i}\bullet\mathbf{b}_i}{\|\mathbf{h}_{vane,i}\|}\right)} \tag{4.2.38}$$

where G is the height of the ground above the inertial datum, $\mathbf{b}_i$ is the unit vector along the negative duct axis in the inertial reference frame, as indicated by the subscript i; and e is the clearance between the vane trailing edge and the ground along a line parallel to the duct axis. Using the experimental data from Chapter 5 the vane ground interaction factor R_{vane} can be found via a look up table, as shown in Appendix G.

$$R_{vane} = f\,(e) \tag{4.2.39}$$

The equations (4.2.36) to (4.2.39) are repeated for each of the control vanes on the Jetpack.

Vane Servo Dynamics

The dynamics of the control vane servos are also included in the Jetpack model to improve the model's realism. Since the servos have a limited power output their performance, namely their speed, is also restricted. This can significantly affect the responsiveness of the Jetpack to control inputs.

To prevent the control vanes from exceeding the mechanical deflection limits, a saturation model is used as described by:

$$\xi = \begin{cases} \xi & -\xi_{max} < \xi < \xi_{max} \\ \xi_{max} & \xi \geq \xi_{max} \\ -\xi_{max} & \xi \leq -\xi_{max} \end{cases} \tag{4.2.40}$$

where ξ and ξ_{max} are the deflection and the maximum deflection of the roll vane, respectively. The limited speed of the roll vane is modelled as:

$$\xi = \begin{cases} \xi & -\xi_{s,max} < \xi_s < \xi_{s,max} \\ \xi_{s,max}\triangle t + \xi & \xi_s \geq \xi_{s,max} \\ -\xi_{s,max}\triangle t + \xi & \xi_s \leq -\xi_{s,max} \end{cases} \tag{4.2.41}$$

where ξ_s is the roll vane speed, $\xi_{s,max}$ is the maximum roll vane speed, and $\triangle t$ is the simulation time step. The roll vane speed ξ_s is calculated as:

$$\xi_s = \frac{\xi - \xi_{t-1}}{\triangle t} \tag{4.2.42}$$

where ξ_{t-1} is the vane deflection from the previous time step. Equations (4.2.40) to (4.2.42) are repeated for the pitch and yaw vanes to obtain the deflection of the control vanes that will be used in the following equations to determine the force produced by each the control vanes.

Roll Vanes

Two roll vanes are used to generate roll moments to orientate the aircraft about the x axis. When deflected from their neutral position ($\xi = 0$), the roll vanes generate an aerodynamic lift force in the y direction and drag forces in the z direction. Due to the perpendicular distance between the roll vane centre of pressure and the aircraft's CG a roll moment is created:

$$\mathbf{F}_{roll,RH} = R_{roll,RH}\xi_f[0, \frac{1}{2}\rho V_{vane}^2 A_{roll} C_{L,vane}(\xi), \frac{1}{2}\rho V_{vane}^2 A_{roll} C_{D,vane}(\xi)] = \mathbf{F}_{roll,LH} \tag{4.2.43}$$

$$\mathbf{M}_{roll,RH} = \mathbf{l}_{roll,RH} \times \mathbf{F}_{roll,RH} \tag{4.2.44}$$

Similarly the left-hand roll vane produces the following moment:

$$\mathbf{M}_{roll,LH} = \mathbf{l}_{roll,LH} \times \mathbf{F}_{roll,LH} \tag{4.2.45}$$

where the position vector $\mathbf{l}_{roll,LH}$ describes the distance from the CG to the centre of pressure of the left hand roll vane.

Pitch Vanes
Similarly to the roll vanes the pitch vanes also create moments about their intended axis, the lateral y axis. The pitch vanes create lift forces in the x direction and drag forces in the z direction.

$$\mathbf{F}_{pitch,RH} = R_{pitch,RH}\eta_f[\frac{1}{2}\rho V_{vane}^2 A_{pitch} C_{L,vane}(\eta), 0, \frac{1}{2}\rho V_{vane}^2 A_{pitch} C_{D,vane}(\eta)] = \mathbf{F}_{pitch,LH} \quad (4.2.46)$$

$$\mathbf{M}_{pitch,RH} = \mathbf{l}_{pitch,RH} \times \mathbf{F}_{pitch,RH} \quad (4.2.47)$$

similarly for the left-hand pitch vane:

$$\mathbf{M}_{pitch,LH} = \mathbf{l}_{pitch,LH} \times \mathbf{F}_{pitch,LH} \quad (4.2.48)$$

Yaw Vanes
The yaw vanes on the Jetpack act differentially to one another, similar to ailerons on an aeroplane, to produce a moment about the z axis. Due to the differential nature of the yaw vanes a moment couple is produced, which is favourable as no net translational accelerations occur as the yaw vane forces oppose each other. Yaw vane force is:

$$\mathbf{F}_{yaw,RH} = R_{yaw,RH}\zeta_f[\ \tfrac{1}{2}\rho V_{vane}^2 A_{yaw} C_{L,vane}(\zeta),\ \ 0,\ \ \tfrac{1}{2}\rho V_{vane}^2 A_{yaw} C_{D,vane}(\zeta)\ ] \quad (4.2.49)$$

$$\mathbf{M}_{yaw,RH} = \mathbf{l}_{yaw,RH} \times \mathbf{F}_{yaw,RH} \quad (4.2.50)$$

similarly for the left-hand yaw vane:

$$\mathbf{F}_{yaw,LH} = R_{yaw,LH}\zeta_f[\ -\tfrac{1}{2}\rho V_{vane}^2 A_{yaw} C_{L,vane}(\zeta),\ \ 0,\ \ \tfrac{1}{2}\rho V_{vane}^2 A_{yaw} C_{D,vane}(\zeta)\ ]$$

$$\mathbf{M}_{yaw,LH} = \mathbf{l}_{yaw,LH} \times \mathbf{F}_{yaw,LH} \quad (4.2.51)$$

Net Control Reactions
The net control forces can now be calculated as the sum of the individual vane forces:

$$\mathbf{F}_{control} = \mathbf{F}_{roll,RH} + \mathbf{F}_{roll,LH} + \mathbf{F}_{pitch,RH} + \mathbf{F}_{pitch,LH} + \mathbf{F}_{yaw,RH} + \mathbf{F}_{yaw,LH} \quad (4.2.52)$$

similarly for the net control moments:

$$\mathbf{M}_{control} = \mathbf{M}_{roll,RH} + \mathbf{M}_{roll,LH} + \mathbf{M}_{pitch,RH} + \mathbf{M}_{pitch,,LH} + \mathbf{M}_{yaw,RH} + \mathbf{M}_{yaw,LH} \quad (4.2.53)$$

Body Aerodynamic Reactions

The aerodynamic forces on the Jetpack body are similar to most aircraft in that the forces are a function of the airspeed. The airspeed is calculated as the difference between ground/inertial speed of the aircraft and the wind speed as:

$$\mathbf{V}_0 = \mathbf{V} - \mathbf{V}_{wind} \tag{4.2.54}$$

where $\mathbf{V}_0$ is the airspeed, $\mathbf{V}$ is the inertial speed, and $\mathbf{V}_{wind}$ is the wind speed.

The Jetpack is considered to be a bluff body, as it is not streamlined, and for this reason it is assumed that the body itself does not create any lift forces. Also, as the Jetpack's intended velocity range is from 0 to 100 km/h, any lift force from the body would be small due to the low dynamic pressure. However, drag forces are significant and are accounted for by the following equation:

$$\mathbf{F}_D = -\frac{1}{2}\rho \begin{bmatrix} C_{D,x} A_x \, \|V_{0,x}\| \, V_{0,x} \\ C_{D,y} A_y \, \|V_{0,y}\| \, V_{0,y} \\ C_{D,z} A_z \, \|V_{0,z}\| \, V_{0,z} \end{bmatrix} \tag{4.2.55}$$

where C_D is the drag coefficient, A is the projected area and V_0 is the airspeed. The subscripts x, y, z denote the axis the aforementioned variables refer to. The moment due to the distance $\mathbf{l}_D$ between the centre of pressure and the centre of gravity is:

$$\mathbf{M}_D = \mathbf{l}_D \times \mathbf{F}_D \tag{4.2.56}$$

Landing Gear Reactions

Takeoff and landing are critical flight phases. Hence, a ground interaction model was added to increase the realism of the Jetpack for pilot-in-the-loop simulations. This was done by modelling each ground contact point as a spring and damper system with the spring force normal to the horizontal ground and damping forces normal and parallel to the ground. The landing gear forces were modelled as a compression-only spring, so that the landing gear force only occurs when the contact point of the landing gear is below ground height, as shown on Figure 4.6. When a contact point is below ground height, ground reaction forces normal and parallel to the surface are calculated. The orientation of these forces are defined in the global frame, as shown on Figure 4.6. The force normal to the surface, $F_{LG,z,g}$, is proportional to the distance h_{LG}. The drag forces, $F_{LG,x,g}$ and $F_{LG,y,g}$, prevent the Jetpack from sliding along the ground are parallel to the surface and in the opposite direction and proportional to the velocity of the Jetpack.

The Jetpack landing gear consists of three contact points, but a forth contact point was added. This extra contact point located at the top of the Jetpack is used to prevent the Jetpack from inverting in the simulation environment. Hence, the forth point gives the Jetpack a simple three dimensional tetrahedral shape in the simulation environment. For each contact point the following was determined:

- The distance of each contact point to ground:

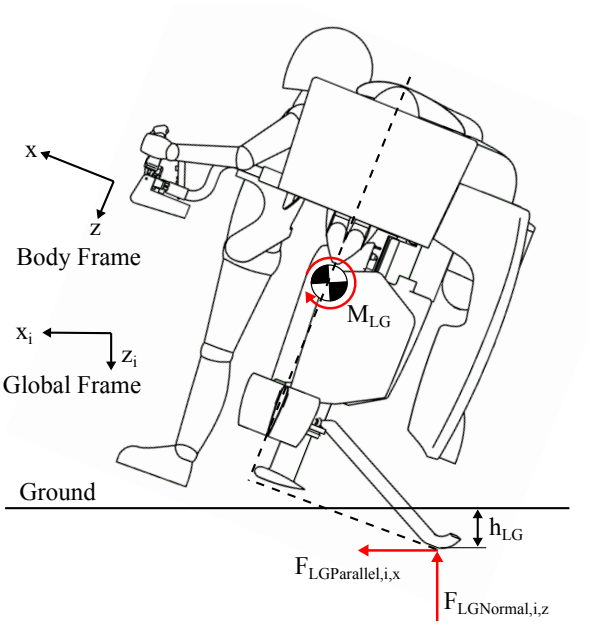

Figure 4.6: Landing gear force on rear contact point

$$h_{LG} = (z_i - \mathbf{l}_{LG,i,z}) - G \tag{4.2.57}$$

where: h_{LG} is the height of the landing gear contact point above ground, z_i is the inertial height of the Jetpack, $\mathbf{l}_{LG,i,z}$ is the z component of the distance vector from the centre of gravity to the landing gear contact point, and *ground* is the height of the ground above inertial frame.

- The velocity of the contact point with respect to ground:

$$\mathbf{V}_{LG,i} = \mathbf{V}_i + \mathbf{DCM}^{-1}(\boldsymbol{\omega} \times \mathbf{l}_{LG}) \tag{4.2.58}$$

where: $\mathbf{V}_{LG,i}$ is the velocity vector of the contact point with respect to the earth fixed axis, $\mathbf{V}_i$ is the velocity of the Jetpack with respect to inertial frame, $\mathbf{DCM}^{-1}$ is the inverse Directional Cosine Matrix, $\boldsymbol{\omega}$ is the vector of angular body rates and $\mathbf{l}_{LG}$ is the distance vector from the CG to the contact point.

- The landing gear force normal to the surface (ground reaction) is given by:

$$F_{LG,z,i} = \begin{cases} -C_z w_{LG,i} - K h_{LG} & h_{LG} > 0 \\ 0 & h_{LG} \leq 0 \end{cases} \tag{4.2.59}$$

where K is a spring constant, C_z is the damping coefficient normal to the ground, and $w_{LG,i}$ is the z component of the landing gear velocity $\mathbf{V}_{LG,i}$. Values of K and C were chosen to give a realistic representation of ground contact.

- The landing gear force parallel to the surface and opposite to the direction of motion (sliding drag) is given by:

$$F_{LG,x,i} = \begin{cases} -C_x u_{LG,i} & h_{LG} > 0 \\ 0 & h_{LG} \leq 0 \end{cases} \tag{4.2.60}$$

where: C_x is the damping coefficient parallel to the ground in the x direction, $u_{LG,i}$ is the x component of the landing gear velocity $\mathbf{V}_{LG,i}$. The force $F_{LG,y,i}$ is calculated using the same formula, but with the subscript x replaced by y with terms of y instead of x, and the velocity $u_{LG,i}$ replaced by velocity $v_{LG,i}$ which is the velocity in the y direction.

The landing gear force for each contact point in terms of the Jetpack body frame is:

$$\mathbf{F}_{LG} = \mathbf{DCM} \left[\begin{array}{ccc} F_{LG,x,i}, & F_{LG,y,i}, & F_{LG,z,i} \end{array} \right] \tag{4.2.61}$$

Moments are calculated for each individual landing gear contact point by multiplying the distance vector from the CG to the contact point with its force as:

$$\mathbf{M}_{LG} = \mathbf{l}_{LG} \times \mathbf{F}_{LG} \tag{4.2.62}$$

The total combined landing gear forces and moments is the sum of the individual landing gear contact forces and moments.

Gyration Forces

The Jetpack has significant rotating inertia (angular momentum), due to the high speed rotation of various components, which include: two fan rotors, drive belts and rotating engine parts. The gyration moment is proportional to the pitch and roll rate on the Jetpack and induces a motion similar to that of a spin top. For example, using the right hand rule, the Jetpack's rotating parts all rotate around the $-z$ axis and if an angular downwards pitching rate, $-q$ about the y axis, is present a gyroscopic reaction moment is induced creating positive roll about the x axis. This motion about the x axis then induces a positive moment about the y axis which in turn produces a negative moment about the x axis. The cyclic motion continues until dampened. To simply summarize: downwards pitch leads to right roll; right roll leads to upwards pitch; upwards pitch to left roll; left roll to downwards pitch to complete the cycle. The effects of gyration are modelled using the gyration equation as presented in [83], as:

$$\mathbf{M}_{gyr} = \boldsymbol{\omega} \times \mathbf{I}_{rot} \boldsymbol{\Omega}_{rot} \tag{4.2.63}$$

where $\boldsymbol{\omega}$ is the Jetpack angular velocity vector $[p, q, r]$; $\mathbf{I}_{rot}$ is the inertia tensor of the rotating parts, as determined from computer aided design (CAD) geometry, and $\boldsymbol{\Omega}_{rot}$ is the angular velocity of the rotating parts.

4.3 Model Inputs

This section describes the various inputs to the Jetpack model.

Flight Control Inputs

Like the actual Jetpack, the model requires four Jetpack control signals for roll, pitch, yaw, and throttle. These signals can be generated by: real-time pilot-

in-the-loop commands, predetermined commands, or by commands external to Simulink®.

Pilot-in-the-Loop Inputs
The pilot-in-the-loop commands are added into the model by using a four axis joystick. The joystick allows for progressive control inputs to be given in a similar fashion as the real Jetpack. The generated joystick signals can either be passed directly to the servo/engine models for manual control, or can first be passed through control algorithms, which use feedback loops to stabilise the aircraft and make it easier to fly, as in reality.

Predetermined Inputs
Predetermined inputs as a function of time can also be used to run the model. The predetermined inputs can either be developed or can be the transient inputs recorded from flight tests. The latter will be used in Chapter 8 to validate the model by using the recorded flight control inputs as the inputs into the model to allow the model outputs to be compared to the recorded test flight data.

External Inputs
The external inputs refer to the inputs generated externally and introduced into the Simulink® model. The external generation of inputs is done for the special case of determining steady-state (trim) solutions of the model, as described in Chapter 7.

Controllers

Due to the unstable or at best neutrally stable [57] response of VTOL aircraft and particularly the Jetpack with its inherently low inertia, a fly-by-wire system with controllers is necessary to introduce artificial stability to achieve controlled flight.

The controllers used in the fly-by-wire system are included in the Jetpack model to stabilise the model. Beneficially, the model allows for various types of controllers to be economically evaluated. The simplest controller found to achieve desirable attitude handling qualities was the rate controller. However, to aid in remote control test flying of the Jetpack a nested controller has been added to the model to reflect the Jetpack prototype.

Rate Controller
The rate controller, Figure 4.7, corrects the aircraft's angular rates p, q, r proportionally to the error between the commanded and the actual rates.

$$\epsilon(t) = cmd(t) - x(t) \tag{4.3.1}$$

where: $\epsilon(t)$ is the error, $cmd(t)$ is the commanded signal from the pilot's joystick, and $x(t)$ is the corresponding rate value representing the aircraft's angular rates p, q, r. The process-point $U(t)$ is calculated in terms of vane

deflections ξ, η, ζ by multiplying the error with an appropriate gain K value as:

$$U(t) = K\epsilon(t) \tag{4.3.2}$$

Tuned gain values K were quickly determined by pilot-in-the-loop-simulations. This was done by running the model in real time and using a joystick to interface pilot inputs into the model while alternating gain values until satisfactory controller performance achieved. Satisfactory performance was deemed achieved when the simulated aircraft responded to pilot inputs in a timely and controller manner.

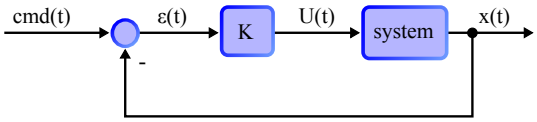

Figure 4.7: Rate controller, used for yaw control

Although the rate controller provides the most direct feel between pilot and aircraft response, to date it is only used for yaw control on the Jetpack. It has not been implemented for roll and pitch attitude as the Jetpack has largely been flown by remote control, where it is beneficial that the aircraft is able to self-stabilise into a hover, which is not possible with the simple rate controller.

Nested Controller

The nested or cascaded controller contains two loops, an outer and an inner loop. The inner loop is used to control faster or higher order dynamics while the outer loop controls the overall system, which is usually a slower dynamic. In the case of the Jetpack model the outer loop controls roll Φ and pitch Θ attitudes, while the inner loop controls the angular roll p and pitch q rates. The error from the outer loop (difference between attitude target and actual attitude, equation (4.3.3)) is processed by the outer loop controller, equation (4.3.4), and produces a rate target, $U_o(t)$. A saturation (limiter), equation (4.3.5), is used to prevent too large a rate target from being passed to the inner loop. The difference between target rate and actual rate, equation (4.3.6), is then processed by the inner controller, equation (4.3.7), to produce the inner process-point $U_i(t)$, which is in terms of roll and pitch vane deflection.

$$\epsilon_o(t) = cmd_o - x(t)_o \tag{4.3.3}$$

$$U_o(t) = K_o\epsilon_o(t) \tag{4.3.4}$$

$$cmd_i(t) = \begin{cases} U_o & |U_o| < Limit_{u,o} \\ Limit_{u,o}\frac{U_o}{|U_o|} & |U_o| > Limit_{u,o} \end{cases} \tag{4.3.5}$$

$$\epsilon_i(t) = cmd_i(t) - \dot{x}(t)_i \tag{4.3.6}$$

$$U_i(t) = K_i \epsilon_i(t) \tag{4.3.7}$$

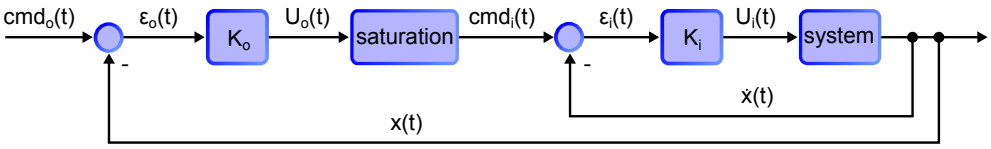

Figure 4.8: Nested controller, used for roll and pitch attitude control

Rate of Climb Controller

The relationship between throttle setting τ and climb rate largely depends on the air density and the aircraft takeoff weight, and changes due to:

- fuel burn
- effects of altitude and temperature on air density
- engine operating conditions
- varying payloads

Hence, the controller used to control the aircraft's rate of climb needs to be able to take into account the changing power requirement for a hover. This is accomplished using the *velocity algorithm*, which is a discrete implementation of the proportional, integral, and differential (PID) controller. The velocity algorithm differs from the previous control algorithms as the current process-point is also used to compute the new process-point. This gives the velocity algorithm the ability to find the floating process-point (throttle setting). The error is first computed as:

$$\epsilon(t) = cmd_o - x(t)_o \tag{4.3.8}$$

The process-point is calculated as:

$$U(t) = K_1\epsilon(t) + K_2(\epsilon(t) - \epsilon(t)_{t-1}) + U(t)_{t-1} \tag{4.3.9}$$

where K_1 and K_2 are the gains, and $U(t)_{t-1}$ is the process-point from the previous time step. A saturation condition is included as the throttle setting is physically limited by maximum and minimum limits.

$$U(t) = \begin{cases} U(t) & \left|U_{(t)}\right| < Limit_{u,o} \\ Limit_{U(t)} \frac{U(t)}{\left|U_{(t)}\right|} & \left|U_{(t)}\right| > Limit_{u,o} \end{cases} \tag{4.3.10}$$

Wind

To simulate the effects of wind on the Jetpack, the wind models described in section B.3 are added into the model. Using equations (B.3.13) and (B.3.14) the airspeed of the Jetpack is determined from the difference between the inertial and wind speeds.

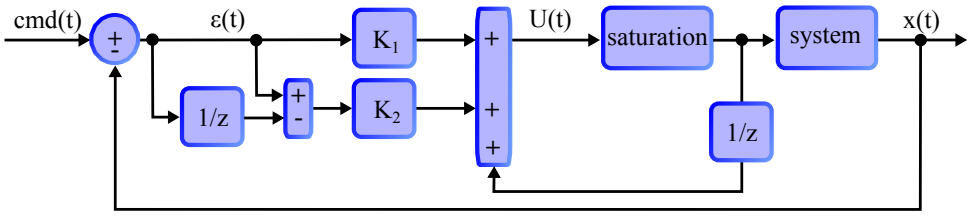

Figure 4.9: Velocity controller, used for throttle/climb rate control

4.4 Model Outputs

The calculated outputs from the Jetpack equations of motion are the goal of the Jetpack model. These outputs contain the position, attitude, translational velocity, and angular velocity information needed to describe the Jetpack's response to given inputs. The Jetpack's response can either by examined as a steady state response, as per Chapter 7, to analyze the flight envelope, or can be examined dynamically to study the dynamic effects and determine the handling quality of the Jetpack.

The outputs as well as every internal variable within the model can also be monitored and exported for analysis, which is useful for assessing how parameters effect the Jetpack's performance. This ability to monitor and quantify the effect of variables is the advantage of the model, as in reality the cost and practicality of measuring the Jetpack parameters is very expensive.

The outputs are fedback in the Jetpack equations of motion via the feedback loops as shown in Figure 4.1 to calculate the next time step. The model also outputs the Jetpack position and orientation to two forms of visual displays in real-time. The real-time ability allows for pilot-in-the-loop flight simulation and has proven to be the an efficient way of assessing the handling qualities of the Jetpack model and tuning the control algorithms. The Matlab® display environment, as shown of Figure 4.10a, displays a simplified Jetpack geometry in a three-dimensional grid space. Although the visual environment is only a grid the Jetpack can easily be simulated and pilot-in-the-loop handing qualities assessed. The FlightGear environment has also be implemented into the model, Figure 4.10b, and allows the Jetpack flight dynamics to be put into a virtual three-dimensional world and to be flown within this environment for greater realism. This environment requires that FlightGear software and a communication link from Simulink® to FlightGear, which is handled by the FlightGear Simulink® block.

4.5 Conclusion and Final Comments

A flight model has been developed from a fundamental approach to model the behaviour of a twin ducted-fan VTOL aircraft, namely the Martin Jetpack. Following the conventional aircraft modelling methodology, unique mathematical formulas were developed to model the physics of the key Jetpack features. This includes modelling the reactions produced by both ducted-fans, the control vanes, the body aerodynamics, and the gyration moment. Landing gear forces are included to allow the Jetpack model to simulate the ground inter-

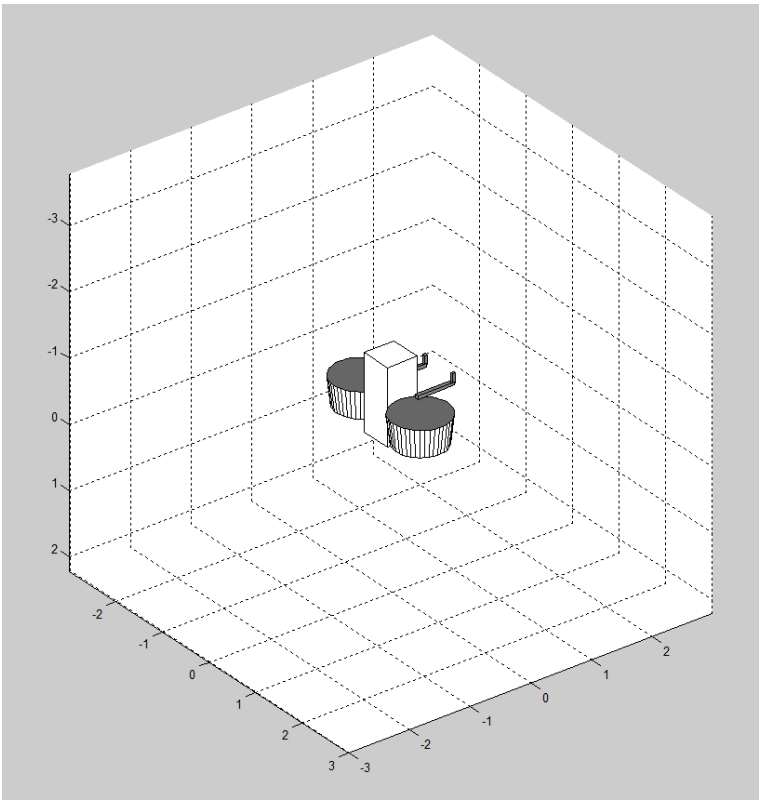

(a) Matlab® environment

(b) FlightGear™ environment showing P-11A Jetpack

Figure 4.10: Visual displays of the Jetpack simulation

action during takeoff and landing, which is a vital phenomenon to simulate. Combining all of these forces and moments and employing Newton's second law of motion, Euler angle transformations, and the kinematic equations, for a six degree of freedom system, a system of ODEs was produced. The ODEs are solved, in real-time, using Matlab®/Simulink® software to simulate the flight behaviour of the Jetpack.

Similarly to the actual Jetpack, the model also requires artificial control to stabilise and obtain humanly controllable flight. It was found that the rate controller is the simplest controller to give desirable handling qualities. A nested attitude-rate controller is also included in the model to reflect the current controller used by the Jetpack.

The model presented includes a novel analytical method to predict the duct centre of pressure as a function of airspeed and angle of attack, which allows for the duct pitching moment to be accurately predicted.

The Jetpack model has also been added into the Martin Aircraft Company four-axis Jetpack flight simulator (Figure 4.11), where the model describes the physical behaviour of the Jetpack, which is used to drive the motion and visual displays for the Jetpack simulator.

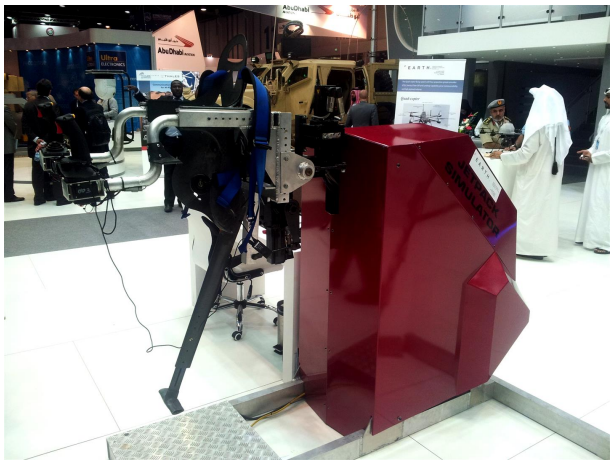

Figure 4.11: The Martin Aircraft Company Jetpack simulator

This Chapter has explained the framework of a six degrees of freedom flight model that can simulate the response of the Martin Jetpack. In order to improve the accuracy of the model various parameters need to be measured. Initially, these parameters were planned to be measured using CFD, however the necessity of Martin Aircraft Company to obtain good data in the shortest time available prompted the use of physical experiments (Chapters 5 and 6) using the Jetpack to improve on the knowledge obtained from free body diagram analysis, and also it was anticipated that the values obtained from direct measurement would more readily apply to the model. The model presented is validated using recorded data from test flights, as described in Chapter 8.

Chapter 5

Static Aerodynamic Experiments

> "I can calculate the motion of heavenly bodies, but not the madness of people."
> *Isaac Newton*

This Chapter explains the series of experiments made using the Jetpack static test apparatus. The static test apparatus suspends the P-11A Jetpack by a pivot that allows the Jetpack to freely rotate in either the roll (yz) or pitch (xz) plane while the Jetpack operates at nominal flying engine power. The Jetpack's rotation about the pivot is constrained by a load cell, which is used to measure the roll or pitch moment generated by the deflection of the control vanes. The following tests were made:

- Pitch vane force versus height
- Roll vane force versus height
- Jetpack moment due to the ducted-fan normal force
- Effect of lowering the pitch vanes
- Servo speed and signal delay

5.1 Roll and Pitch Vane Force

The aim of this experiment is to determine the roll and pitch vane of the P-11A Jetpack, and determine how the vane lift forces change as the Jetpack is positioned closer to the ground. The motivation for these tests is to quantify the roll and pitch vane lift force so that the findings can be included into the Jetpack flight model.

Method

A test apparatus, Figure 5.1, was developed to measure the roll and pitch control vane forces in-situ on the P-11A Jetpack. This was accomplished by a frame that suspends the Jetpack and permits the Jetpack to freely pivot

about an axis in the desired plane, roll or pitch, with a load cell positioned to measure any moment reactions produced. The frame is fastened to the floor to prevent lift off. The test apparatus requires the orientation of the load cell to be changed between testing in the roll and pitch planes, as shown in Figure 5.2.

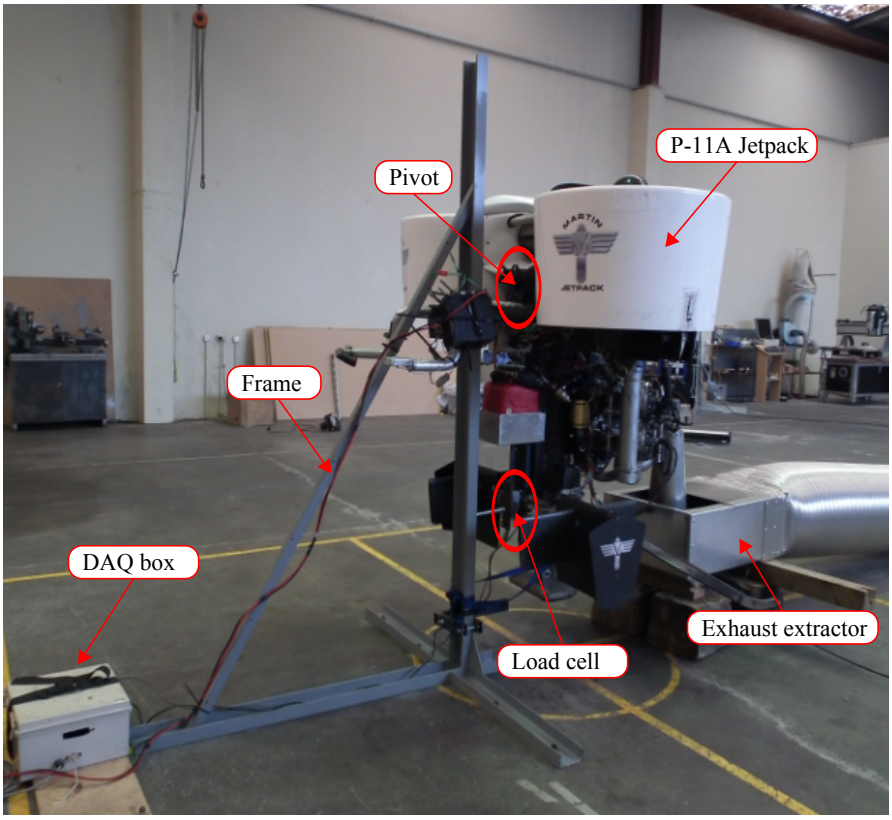

Figure 5.1: Experiment setup with load cell positioned to measure pitch vane force.

A single point load cell[1] measures the varying compression forces between the Jetpack and the apparatus. When the pivot allows freedom in the pitch plane, the low and offset CG position of the Jetpack naturally swings the Jetpacks towards the apparatus. When the pivot is setup for roll a bungee chord is used to pre-load the Jetpack against the test apparatus so that the load cell always experiences a compressive load. The bungee cord gives a constant force on the load cell if the deflection of the load cell during testing is kept small.

Referring to Figure 5.3 it can be seen that multiplying the measured load cell force, F_{LC}, by the distance between the load cell and the pivot point gives the pitch moment. This moment is divided by the distance between the control vanes and the pivot point to calculate the total pitch vane force from both left and right hand pitch vanes. A subsequent division by two results in the individual pitch vane force F_{vane}, as:

$$F_{vane} = \frac{1}{2}\frac{l_{lc}}{l_{Vvane}}F_{lc} \tag{5.1.1}$$

[1]Single point load cells only measure compressive forces.

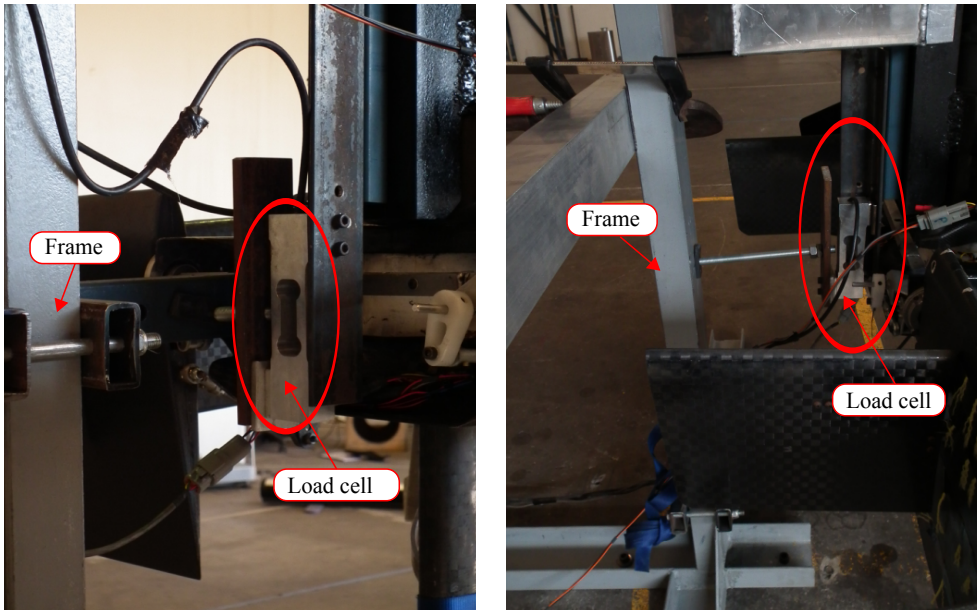

(a) Roll plane (b) Pitch plane

Figure 5.2: Load cell orientations for roll and pitch plane moment measurements

where l_{lc} and l_{vane} are the moment arms from the pivot the to load cell, and from the pivot to the control vane quarter chord point, respectively, as shown in Figure 5.3. The load cell force F_{lc} is calculated as:

$$F_{lc} = \frac{\kappa V}{C_{lc}\nu} \tag{5.1.2}$$

where κ is the rated load cell calibration, C_{lc} is the load cell capacity or design load, ν is the load cell supply voltage, and V is the recorded load cell voltage.

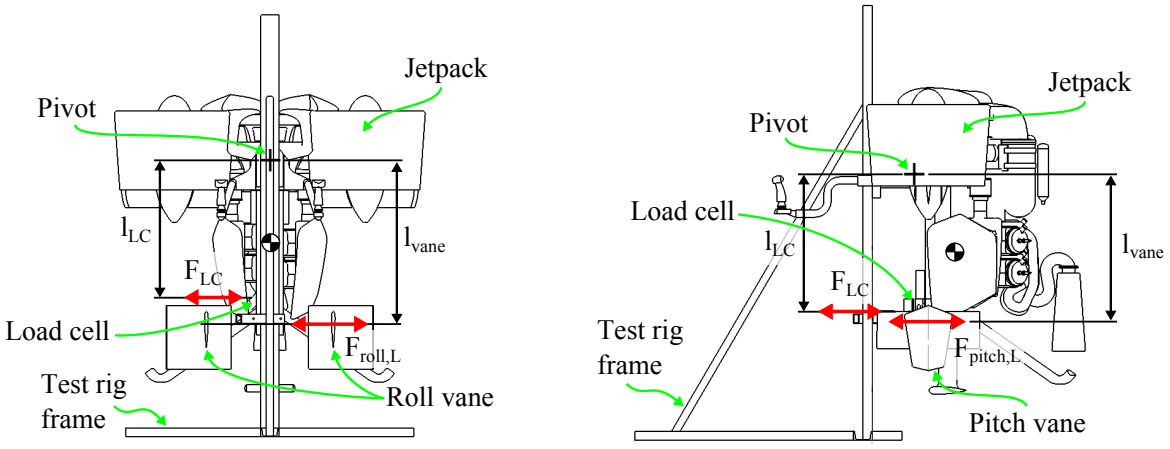

(a) Roll plane (b) Pitch plane

Figure 5.3: Schematic of static test apparatus

Testing Procedure

The test matrix involved measuring the roll and pitch vane forces for Jetpack engine speeds of 5000 RPM to 5750 RPM in approximately 250 RPM increments for Jetpack heights of 0.25 m, 0.5 m, and 1.1 m above the ground, as illustrated in Figure 5.4. All data was recorded in terms of engine speed, which can be related to the fan speed by the engine to fan gear ratio of 34/40.

(a) 0.25 m (b) 0.5 m (c) 1.1 m

Figure 5.4: The three static aerodynamic test heights

For each height and orientation (roll or pitch plane) the test procedure involved starting the Jetpack and warming the engine to operating temperature. The engine was then manually controlled to hold 5000 RPM. A servo driver was used to increment the control vane deflection from neutral to positive stall angle and then reverse the increments until the negative stall angle was achieved. This was repeated for nominal engines speeds of 5250 RPM, 5500 RPM, and 5750 RPM and for the each test height in both the roll and the pitch plane.

Data Analysis

The data acquisition (DAQ) system, based on an Advantec USB-4716 DAQ card, continuously measured the engine speed, the load cell force, and the vane angle of attack during the experiment. This data was analyzed by finding samples at each nominal engine speed and plotting the vane force versus the angle of attack. A third order polynomial was fitted to the measured data points, as shown on Figure 5.5. The third order polynomial was chosen as this is the minimum order polynomial required to show both positive and negative stall points. It is expected that the aerofoil will stall when the angle of attack becomes high enough [74], and that the nature of the stall will be smooth and at a higher angle of attack than for a two-dimensional aerofoil, since the aerofoil is of a low aspect ratio[74, 73].

The spread of raw data shown on Figure 5.5 is attributed to the high vibration of Jetpack during testing. Electronic noise, the cantilever design of the control vanes, mechanical play, and the manual engine control also contribute to the spread of the data. These effects to the data spread were mitigated by taking a large number of data points at a high sample rate (37 Hz). The *goodness of fit* was determined by calculating the *root mean square error,*

$RMSE$, between the raw data and fitted polynomial as described by :

$$RMSE = \sqrt{\frac{\sum_{k=1}^{n} (a_k - b_k)^2}{n}} \tag{5.1.3}$$

where $\mathbf{a} = [a_1, a_2, \ldots a_n]$ and $\mathbf{b} = [b_1, b_2, \ldots b_n]$ are two vectors that the error is being determined for, and n in the number of data pairs. The $RMSE$ is dimensional and tends to zero as the error/spread between vectors a and b decreases, and hence, a fit showing good agreement will have a small value relative to the data. The $RMSE$ value shown in Figure 5.5 is representative for all the fitted polynomials in this Chapter.

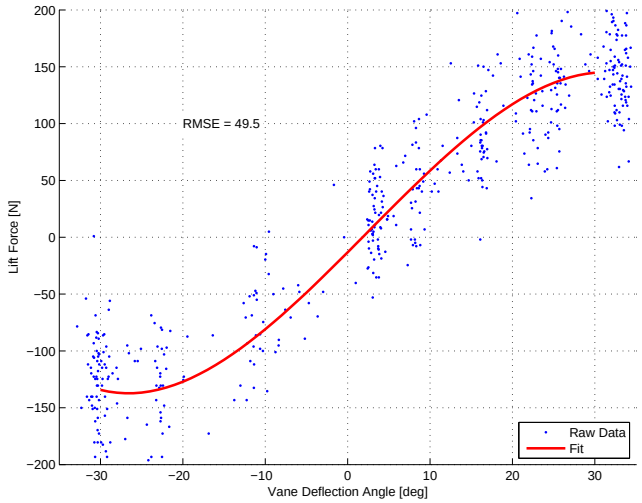

Figure 5.5: Third order polynomial fitted to raw pitch vane data

It is desirable to present aerofoil data by non-dimensional coefficients, so that the aerofoil force becomes a function of the aerofoil: lift coefficient, dynamic pressure, and planform area, as per equation (B.1.6). Using the engine speed relationship from the P-11 600 mm ducted-fan thrust measurements, which will be presented in Chapter 9 Figure 9.15, the lift coefficient for each vane force measurement can be found by calculating the theoretical ducted-fan exit velocity using equations (3.3.5), (3.3.4), and (3.1.44). The lift coefficient is found by using equation (B.1.6) applied to the pitch and roll control vanes where A is the vane planform area, V is the calculated velocity experienced by the vane, ρ is the recorded air density, and L is the measured vane lift force. Using this method plots of the vane lift coefficient versus angle of attack were produced.

Results

All Figures from 5.6 to 5.11 show how the lift vane force changes as a function of the engine speed. Figures 5.6 to 5.8 show the measured pitch vane lift force and calculated pitch vane lift coefficient for Jetpack heights of 0.25 m, 0.5 m, and 1.1 m above the ground. Figure 5.9 shows the lift force and vane coefficient for the pitch vanes extended by 0.2 m. Figures 5.10 and 5.11 show the roll vane force for heights of 0.5 m and 1.1 m above the ground.

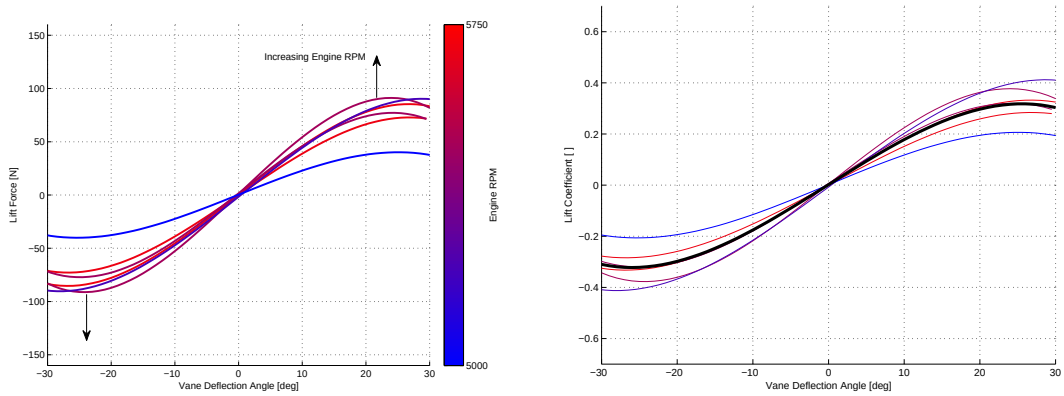

(a) Lift force (b) Lift Coefficient

Figure 5.6: Measured pitch vane force and lift coefficient on P-11A Jetpack at 0.25 m height above ground.

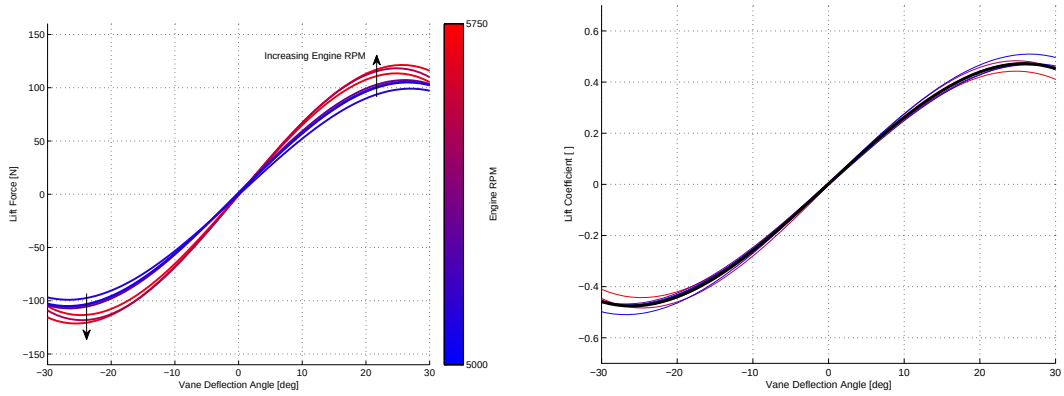

(a) Lift force (b) Lift Coefficient

Figure 5.7: Measured pitch vane force and lift coefficient on P-11A Jetpack at 0.5 m height above ground.

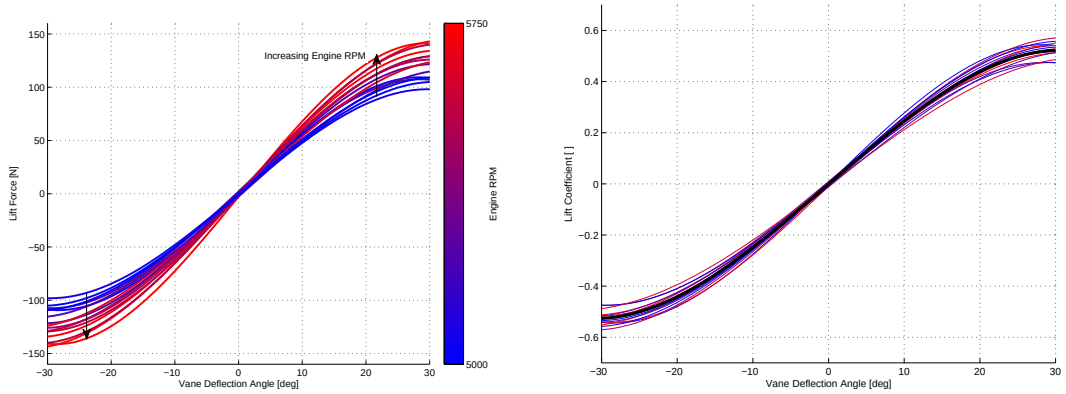

(a) Lift force (b) Lift Coefficient

Figure 5.8: Measured pitch vane force and lift coefficient on P-11A Jetpack at 1.1 m height above ground. Note the black line indicates the average lift coefficient versus angle of attack.

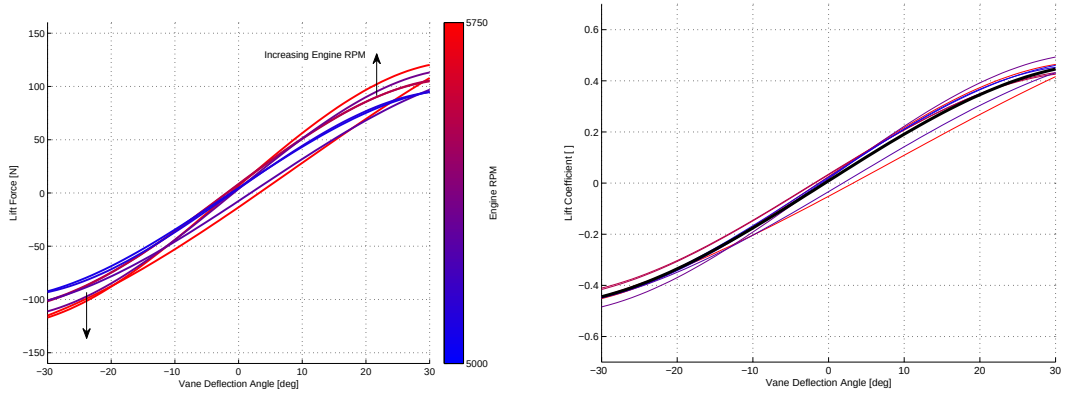

(a) Lift force (b) Lift Coefficient

Figure 5.9: Measured pitch vane force and lift coefficient on P-11A Jetpack at 1.1 m height above ground with pitch vanes extended by 0.2 m from nominal position.

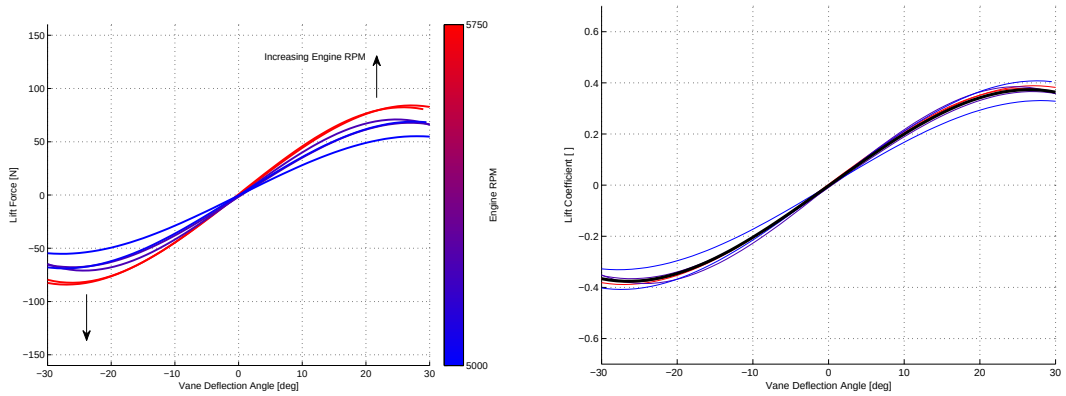

(a) Lift force (b) Lift Coefficient

Figure 5.10: Measured roll vane force and lift coefficient on P-11A Jetpack at 0.5 m height above ground.

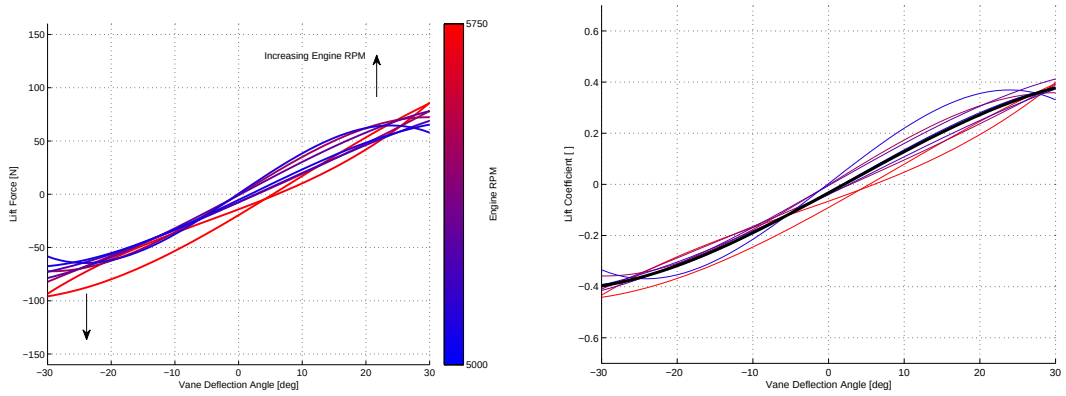

(a) Lift force (b) Lift Coefficient

Figure 5.11: Measured roll vane force and lift coefficient on P-11A Jetpack at 1.1 m height above ground.

Wool tufts were added to one of the pitch vanes to visualize the airflow pattern around the pitch vane. It can be seen in Figure 5.12a that when the pitch is near the neutral position the wool tufts are largely parallel to the vane chord, which shows that the flow is attached. The root of the pitch vane (right-hand edge) shows some leakage of airflow as the tufts wrap around this edge, which indicates that the vane is not at a perfectly neutral position. Figure 5.12b shows the pitch vane at approximately 30° angle of attack. The reversed and turbulent nature of the wool tufts over the entire pitch vane show that the pitch vane is in a deep stall condition, where the flow has separated from the leading edge and remains separated over the entire aerofoil. Strong tip vortices at the root are also noticeable from the spanwise flow indicated by the wool tufts along the root of the pitch vane.

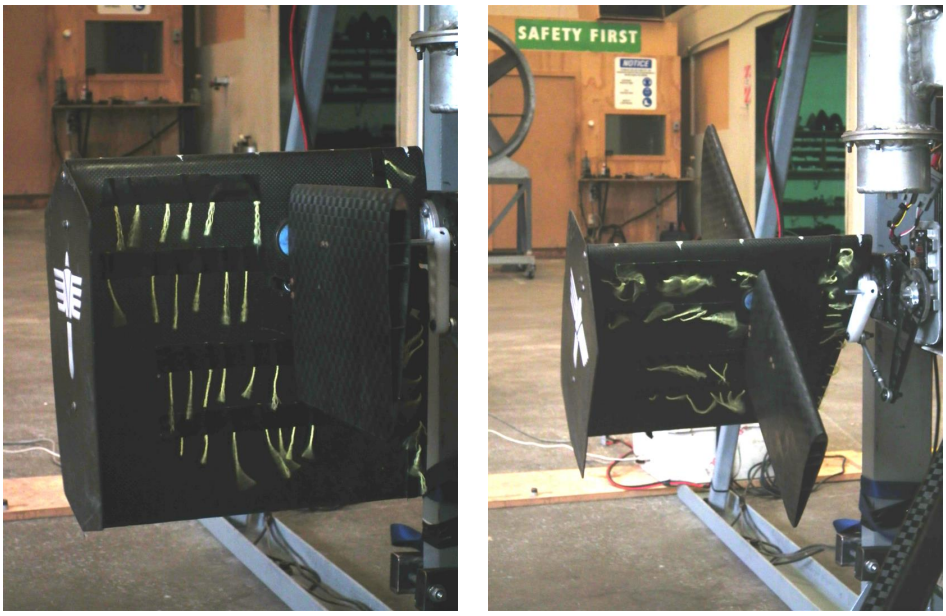

(a) Pitch vane neutral position

(b) Pitch vane approximately 30° angle of attack

Figure 5.12: Tufts photos of pitch vane for Jetpack heights of 0.25 m

Discussion of Results

Lift Coefficient

Figures 5.8b and 5.11b show how the out-of-ground-effect vane lift coefficient varies with angle of attack, as expected for an aerofoil [74]. Within ±10 % of either side of the average lift coefficient, the lift coefficient can be assumed independent of the engine speed, and hence, vane velocity. This result shows that the lift coefficient for the Jetpack control vanes can be assumed to be a function of the angle of attack alone.

Comparing 5.8b and 5.11b it can be seen that the maximum roll vane lift coefficient of 0.40 is less than that of the pitch vanes 0.53, but the stall angles of attack are similar at approximately 30°. A technical report by Zimmerman [73] shows that very low aspect ratio aerofoils, close to an aspect ratio of 1, experience an increase in values of maximum lift coefficients compared to aerofoils with an aspect ratio of 2 and 3. The increased maximum lift coefficient

is attributed to the strong spanwise flow, which re-energizes the boundary layer delaying separation and stall. The measured lift coefficients for the roll and pitch vanes, which have an aspect ratio of 2.65 and 1, respectively, reflect the results found by Zimmerman. However, Zimmerman's results show higher maximum lift coefficients of 1.2 and 1.3 for aspect ratios of 3 and 1, respectively. Using the *disturbed* to *clean* dynamic pressure ratio of 0.34, as determined in section 3.3, within the wake of the ducted-fan and noting that both the roll and pitch vanes are located in this disturb airflow, Zimmerman's lift coefficients can be reduce 0.41 and 0.44 for the roll and pitch vanes, respectively, which closely matches that found in this experiment.

Ground Effect on Control Vanes

Using the mean of the maximum pitch vane lift coefficients from Figures 5.6 to 5.8 and factoring these values with respect to the mean maximum lift coefficient measured at 1.1 m, Figure 5.13 can be created, which shows how the pitch vane lift force degrades as the Jetpack's height above ground reduces. The wake from the ducted-fan diverges radially when impacting the ground forming a divergent region, as shown in Figure 5.14. When the roll and pitch vanes are submerged into this divergent region their effectiveness rapidly reduces. Practically, this results in a reduced ability to produce moments to control the aircraft. This loss of effectiveness has been qualitatively reported by Martin Aircraft Company test pilots, who recommend from experience that flight close to ground should be avoided due to the slow response of the Jetpack from control inputs. The divergent region is practically found by moving a wool tuft wand across the diameter of the ducted-fan efflux at various highs above the ground.

It is assumed that the control vane will have no effect when the Jetpack contacts the ground, and full effect when the Jetpack is above 1.1 m. The assumed degradation of the control vane between ground and 0.25 m height is shown by the dashed line on Figure 5.13.

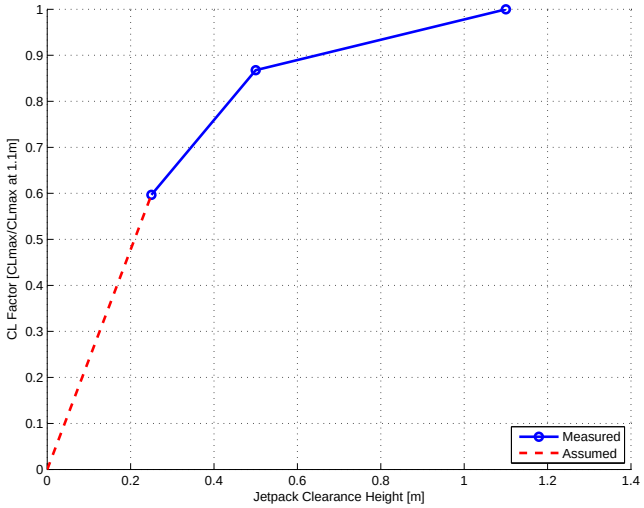

Figure 5.13: Effect of ground clearance on pitch vane force.

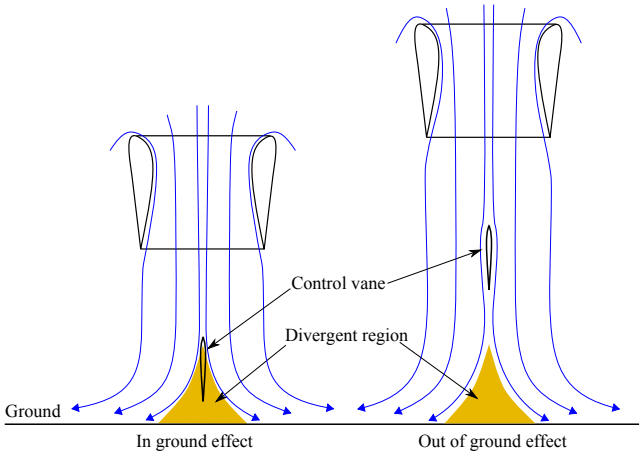

Figure 5.14: Effect of ground clearance on the control vanes

Effect of Lowering Pitch Vanes

Comparing Figures 5.8 and 5.9, which show the out-of-ground-effect pitch vane lift force and coefficient, Figure 5.15 can be produced by factoring the vane force and moment to the maximum vane force and moment produced from the nominal pitch vane position. Lowering vanes by 0.2 m effectively increases the moment arm about the Jetpack centre of gravity from 0.454 m to 0.655 m, an increase of 44 %. However, the effective pitch moment only increases by 22 %, as extending the pitch vanes reduces the force by 18 %.

The nominal position of the vanes on P-11A is 0.725 m from the duct exit plane, and the extended position is 0.926 m. The ratio of control vane distance from duct exit plane to duct exit diameter is 1.21 and 1.54 for the nominal and extended positions, respectively, both of these values are greater than those recommended in [33]. Therein the author recommends that the control vanes for optimal performance should be located between 0.75 to 1.0 duct diameters from the duct exit plane.

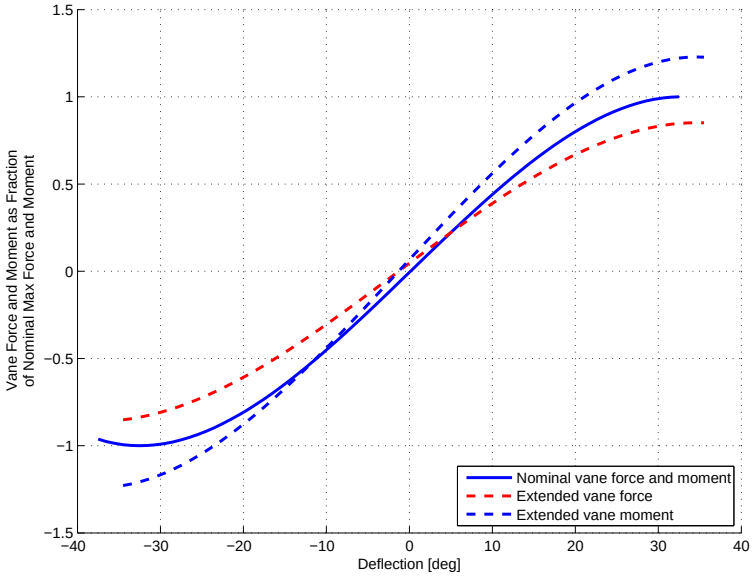

Figure 5.15: Effect of extending the pitch vane moment arm by 0.2 m

Conclusion

The lift coefficient for both the roll and pitch vanes were determined in-situ on the P-11A Jetpack. The maximum out-of-ground-effect lift coefficient was determined to be 0.40 and 0.53 for the roll and pitch vanes, respectively. Comparing the maximum lift coefficients for various Jetpack heights above the ground showed that the maximum lift coefficient reduces to 60 % of the out-of-ground-effect lift coefficient at 0.25 m above the ground. Extending the pitch vanes to improve the control moments showed only a marginal improvement, due to decreased effectiveness of the pitch vanes by increasing the pitch vane moment arm.

The results from the lift coefficient versus angle of attack for both roll and pitch, as well as the vane ground-effect measurements are included in the Jetpack model described in Chapter 4.

5.2 Pitch Vane Servo Load and Speed

This experiment was made to determine the approximate servo rate of the pitch vanes and to measure the amount of delay between the vane deflection and the command signal.

Method

While the P-11A Jetpack was held firmly to the ground and operating at nominal flying power settings, the pilot moved the pitch joystick between maximum and minimum extremities as fast as possible. The pitch vane servo position was recorded by an external potentiometer and the data logged into the Jetpack flight computer, which also simultaneously recorded the pilot pitch command. Direct pitch command was used for this test, hence, no feedback was introduced into the pitch command which could alter the output signal going to the pitch vane servo.

Result

Figure 5.16 shows the recorded pitch vane command signal and pitch vane position versus time. The vane deflection/servo speed was found by measuring the time taken to travel from maximum positive to negative deflection by inspection of Figure 5.16. The mean result of the servo deflection rate was found to be 84.5°/s. Again from inspection of Figure 5.16, the delay between input and output (vane deflection) was found by the time difference between input and output crossing the abscissa to be 0.15 s

5.3 Summary

The results presented in this Chapter combined with data measured by Martin Aircraft Company provides the information to quantify the aerodynamics associated with the control vanes. This Chapter shows how the roll and pitch vane forces were measured and how the dimensionless lift coefficients were derived.

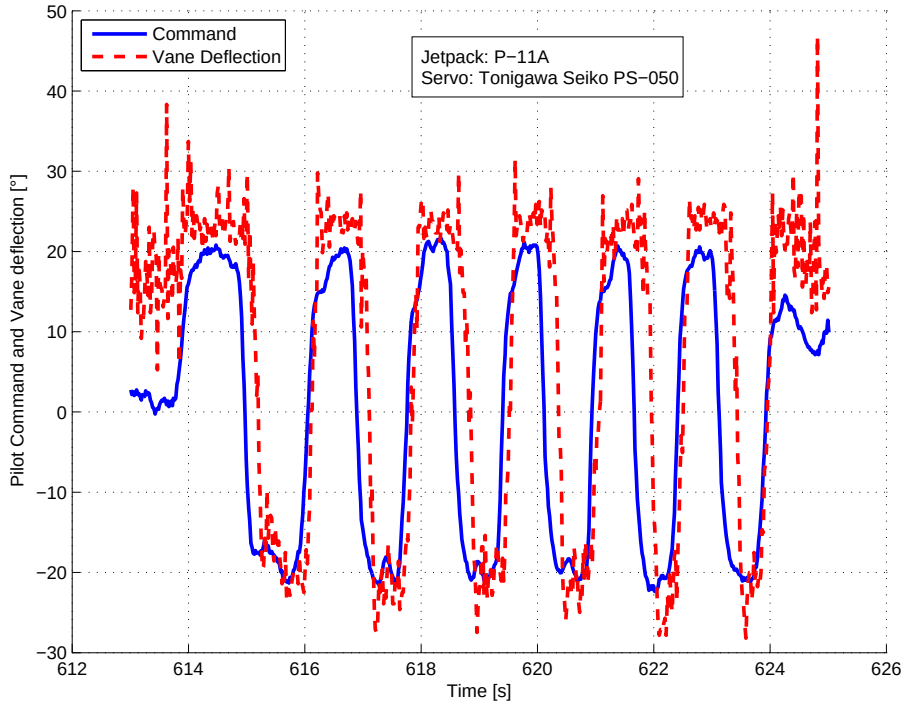

Figure 5.16: Pitch vane input signal and pitch vane deflection versus time on the P-11A Jetpack

The important result of control vane effectiveness as a function of clearance height from the ground was quantified.

Chapter 6

Experimental Determination of Aerodynamic Parameters

"Intelligence is the ability to adapt to change".
Stephen Hawking

This Chapter presents the design, test protocol, and results from extensive tow testing of the Martin P-11A Jetpack. Tow testing involves securing the Jetpack onto an apparatus that allows lift, drag, and pitching moment reactions to be measured while the Jetpack is being towed by a vehicle through the air at various air and engine speeds; refer to Figure 6.1 for an overview of the experimental setup. This method of tow testing allows for a range of roll and pitch angles of attack to be examined, enabling the ducted-fan reactions and centre of pressure movement to be determined as a function of velocity and angle of attack.

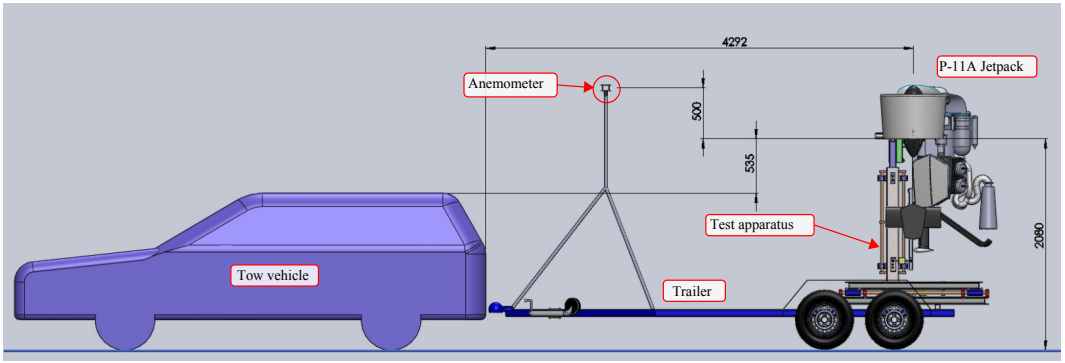

Figure 6.1: Overall experiment setup showing leading dimensions with Jetpack secured at an angle of attack of 90° in the pitch plane.

6.1 Introduction

The design of any aircraft requires an understanding of its response to aerodynamic loads. This is particularly true for vertical take off and landing (VTOL) aircraft that encounter a wide range of flight regimes between hover, no to little dynamic pressure, and high speed flight, high dynamic pressure. This understanding is not only necessary to allow the designer/engineer to make

the aircraft function safely, but also to ensure that the aircraft is aerodynamically optimized, so that the aircraft can meet its mission requirements in a cost effective manner. Aircraft designers typically begin their designs by developing mathematical expressions to describe the behaviour of the aircraft. These expressions can then be used to create a flight model of the aircraft. An accurate aircraft model allows for the flight dynamics and flight envelope to be predicted and optimized through repeated simulations. However, the accuracy of the model is only as good as the equations used to model the aircraft behaviour. Typically, scaled prototype models are physically examined in wind tunnels to obtain aerodynamic coefficients that can be used to improve the expressions of the flight model. However, scaling down an aircraft to fit inside a wind tunnel requires attention to: the scaling of flow conditions, the scaling of aircraft features, and the effects of wind tunnel walls, as described in [84, 85].

Scaling of flow conditions is done by matching the Mach and the Reynolds numbers between the scaled model and prototype aircraft. This places a limit on the scaling factor that can exist while still maintaining a realistic representation of the airflow around the full scale aircraft. The smaller the model the faster the airflow needs to be, to equate the Reynolds number between the prototype and the scaled model. The limiting factor is the wind tunnel airspeed can only be increased to the point where compressibility effects begin to affect the scale model. For compressible flows, the Mach number between prototype and scaled model needs to remain similar to ensure similarity of flow conditions.

Scaling of aircraft features is typically not an issue for fixed-wing aircraft, as the lifting surfaces, wings, remain static and the propulsion systems are generally not included in the scaled model. However, for rotorcraft, where the lifting surfaces and propulsion system are combined, the scaled model also requires scaling of these systems to make them operational at the scale of the model, adding cost and complexity.

The effects the of wind tunnel walls prescribes how much space should occur between the model and wind tunnel walls. The model cannot be too large compared to the wind tunnel cross-section, as the flow around the model will experience an artificially high accelerated airflow, due to the conservation of mass. For VTOL aircraft models at low airspeeds significant cross-sectional space is required to avoid the large downward momentum impinging on the wind tunnel walls and creating additional flows that can affect the model. If the airflow is significantly deflected it will interfere with the wind tunnel walls and effectively simulate ground effect conditions, especially if the scale model is in close proximity to the wind tunnel walls. This can be avoided by either decreasing the size of the model or by testing the scaled model in as large a wind tunnel as possible, as recommend in [85].

The aircraft to be studied is the Martin P-11A Jetpack, which is 1.7 m wide by 1.7 m high and has a duct exit diameter of $d = 0.6$ m and duct axis separation of $1.75d$. These dimensions are small warranting the concept of tow testing, where the full-sized aircraft is towed through the air, instead of producing a scaled model for conventional wind tunnel testing. The major advantage tow testing has over a typical scaled wind tunnel testing is that the

airflow Reynolds numbers are identical. The testing is done at a one-to-one scale and at comparable airspeeds using the actual prototype aircraft, which avoids the complexity of designing and powering a scaled ducted-fan system. A similar methodology is described in [86], where a large 6 ft ducted-propeller was supported in a specially designed vehicle, and driven at various speeds along a runway to measure the aerodynamic reactions.

Of all the aerodynamic components on the Martin Jetpack, the ducted-fans are the most significant; much like the wings are to an aeroplane. The interaction of the free stream airflow around the ducts can produce significant forces and moments in addition to the axial thrust force, as shown in Figure 3.9 and described by [25, 36, 60]. Understanding these forces and moments allows the designer to correctly position the centre of gravity relative to the duct centre of pressure and thus size the control vanes to achieve the required response.

Note, that in this chapter the terms *roll plane* and *pitch plane* are used to identify the planes defined by the yz and xz axes, respectively. Roll and pitch moment are about the x and y axis, respectively.

Ducted-Fan Reactions

To quantify the aerodynamic behaviour of the Jetpack the reactions from the ducted-fans need to be measured. By measuring the lift, drag, and pitching moment of the Jetpack at nominal flying power settings and then measuring again with the engine turned off at the same airspeed two measurements are obtained; the total aerodynamic reactions (*Engine On*) and the passive aerodynamic reactions (*Engine Off*), respectively. The *Engine On* reactions are the reactions the Jetpack experiences in flight, while the *Engine Off* reactions are the reactions due to the presence of the Jetpack body alone. The isolated ducted-fan reactions, which includes both the left and right ducted-fans, are determined by subtracting the *Engine Off* aerodynamic data from the *Engine On* aerodynamic data, as:

$$L_d = L_{EngineOn} - L_{EngineOff} \tag{6.1.1}$$

$$D_d = D_{EngineOn} - D_{EngineOff} \tag{6.1.2}$$

$$M_d = M_{EngineOn} - M_{EngineOff} \tag{6.1.3}$$

In the above equations L, D, and M are the lift force, the drag force, and the pitching moment, respectively.

Ducted-Fan Centre of Pressure

Using the measured ducted-fan lift, drag, and moment data, the ducted-fan centre of pressure can be determined. The centre of pressure is a key location for the aircraft designer, as this is where the centre of mass is best located to minimise the moments produced by the ducted-fans. The position of the ducted-fan centre of pressure (CP) is defined as the point where the pitching moment equates to zero, leaving only a resultant force made up of the ducted-fan lift and drag. Ohanian [87] describes that two schools of thought exist for

the determination of this point. The paradigm preferred by Ohanian assumes that the CP lies on the plane on the fan rotor, and moves fore and aft from the duct axis as a function of the speed/advance-ratio and angle of attack. This allows for the CP^* to be calculated by the thrust force as:

$$CP^* = \frac{M_{\frac{1}{4}}}{T} = \frac{M_{\frac{1}{4}}}{D\sin\alpha + L\cos\alpha} \tag{6.1.4}$$

where D is the drag force, L is the lift force, $M_{\frac{1}{4}}$ is the moment, α is the duct angle of attack and CP^* is the distance from the duct axis to the duct centre of pressure, as shown on Figure 6.2a. Typically, for a duct at an angle of attack of 90° with increasing speed the CP will move fore from the duct axis until a maximum point is reached (duct stall) and then begins to move aft as duct stall progresses. Using this method the CP at zero advance ratio is located at the intersection of the fan plane and duct axis.

The second paradigm, as used by [46], assumes that the position of CP is located along the duct axis and is determined by the ducted-fan normal force as:

$$CP = \frac{M_{\frac{1}{4}}}{F_n} = \frac{M_{\frac{1}{4}}}{D\cos\alpha + L\sin\alpha} \tag{6.1.5}$$

where CP is the distance from the duct quarter chord line to the duct centre of pressure as shown in Figure 6.2b. Again, using the scenario of a duct at an angle of attack of 90°, for a low speeds the CP is located above the duct quarter chord line and moves towards the duct quarter chord with increasing speed as duct stall progresses. However, this approach results in the CP being undefined for zero speed due to the denominator F_n being zero. The latter CP concept is favoured within this research, as this gives a better insight of where the centre of gravity should be positioned to minimise the effects of the moment produced by the ducted-fan normal force throughout the flight envelope.

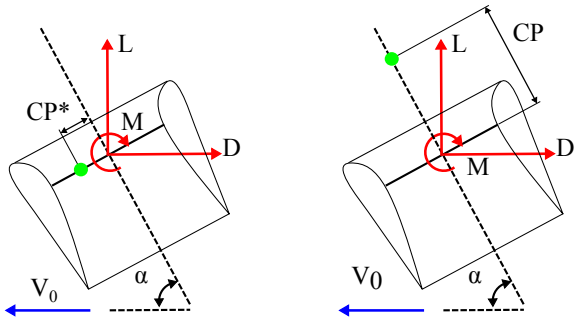

(a) Fan plane (b) Duct axis

Figure 6.2: Schematic of two ducted-fan centre of pressure paradigms, where the duct centre of pressure CP is determined from lift L, drag D, and moment M measurements.

The aim of this Chapter is to quantify the aerodynamic behaviour of the Martin Jetpack during flying conditions. Specifically:

- Determine the ducted-fan aerodynamic lift, drag, moment, and centre of

pressure for both roll and pitch planes.

- Determine the drag coefficients of the Jetpack.
- Determine how the thrust force varies with increasing positive and negative airflows (simulated ascending and descending flight conditions).

Overview of Tow Testing Concept

To avoid the complexities of scaling down the Jetpack to fit into a large enough wind tunnel for aerodynamic testing, a concept was developed where the Jetpack was secured to a trailer (Figure 6.1) and towed at various speeds while the engine was set to nominal flying power output, and hence, effectively creating an inverse wind tunnel. This concept requires the following key components to complete the experiment:

- Tow vehicle. An aerodynamically clean and powerful car, Subaru Legacy GTB wagon (maximum power 206 kW), was chosen to tow the test setup. The Jetpack engine operator, DAQ operator, and tow vehicle driver were all seated within the tow vehicle during test runs.
- Trailer. A tandem axle trailer was used to transport the test apparatus and the Jetpack.
- Test apparatus. This was designed to secure the P-11A Jetpack to the trailer and measure the aerodynamic loads on the Jetpack during testing.
- Aircraft or test specimen. The Martin P-11A Jetpack prototype was the test specimen.
- Anemometer. An ultrasound wind anemometer was used to record the airspeed magnitude and direction.

The tow testing concept introduces several issues that are not present in wind tunnel testing, which included:

- Effects of head and cross winds
- Vibrations from road surface
- Disturbances of the flow in front of the Jetpack by wake of tow vehicle
- Disturbances of the flow in front of the Jetpack by wake of test rig

These issues are mitigated by:

- Measuring airspeed using an ultrasound anemometer, which also measures the presence of any crosswind. Performing test runs on calm days and early in the morning before diurnal winds develop.
- Tests were performed on a flat smooth race track and a large number of data points collected over the sample time. A tandem axle trailer was chosen over a single axle trailer to reduce road vibration.

- The test apparatus was designed to support the Jetpack as high up as possible to minimise the wake from the tow vehicle interfering with the Jetpack. As the ducted-fans are the most significant aerodynamic feature, the apparatus was designed to minimise any aerodynamic disturbance on the ducted-fans by allowing a clearance in excess of 0.5 m between the bottom edge of the ducts and the top of the tow vehicle, as shown on Figure 6.1.

- The test apparatus was designed to minimise flow shielding on the Jetpack by presenting as small a frontal area as possible.

The design of two tow testing experiments are described in this Thesis. The first tow test experiment is a proof-of-concept, which measured the Jetpack forces at a 90° angle of attack in the pitch plane at 5750 RPM for a range of airspeeds, refer to Appendix C for the details on the methodology and the results from this experiment. The second tow test experiment involved a redesigned apparatus that allows for the Jetpack to be examined at a range of roll and pitch angles of attack, the details of this experiment are explained in this chapter.

6.2 Methodology

Design Specifications
A test apparatus was designed to support the Jetpack and allow lift, drag, and moment loads to pass through three independent load cells. This was done to avoid compounding load cell errors between the drag and moment load cells, as per the proof of concept trailer tow test setup described in Appendix C. The frontal area of the test apparatus was kept to a minimum to minimise the aerodynamic influence of the structure on the Jetpack. The structure of the test apparatus was designed to support the expected aerodynamic loads from 0 m/s to 28 m/ and allow for the Jetpack to be orientated for pitch angles of attack from 0° to 180° and roll angles of attack from 45° to 135°.

Description of the Test Apparatus Design
The concept was developed in Solidworks™ CAD (computer aided design) software. The main hurdle in the test apparatus design was creating an allowance to accommodate for both roll and pitch testing. This was solved using two different pivot bearing assemblies that could be interchanged for either roll or pitch testing, as shown of Figure 6.4. Both arrangements allowed for the pivot point to be aligned with the overall thrust line at the centre of ducts, so that thrust variation did not affect moment measurements at static conditions.

The test apparatus concept used a telescopic construction of square hollow sections (SHS) constrained with linear bearings to allow for freedom in the vertical axis (Figure 6.3). The lift load cell was used to constrain the vertical motion of the Jetpack and thus pass the full vertical force through the load cell. The telescoping SHS assembly was positioned upon a frame that had horizontal freedom from linear bearings. The horizontal motion was constrained by the drag load cell, to allow for aerodynamic measurements parallel to the tow

direction. A third load cell, the moment load cell, was used to constrain the rotation of the Jetpack by connecting the Jetpack to the telescoping SHS. The moment was calculated by multiplying the moment load cell force by moment arm, which is the perpendicular distance from the moment load cell to the pivot point. The Jetpack angle of attack is changed by altering the length of the attitude bar (Figure 6.4a), which also changes the moment arm for each angle of attack setting. The sign convention used for positive lift, drag, and moment measurements is shown in Figure 6.5.

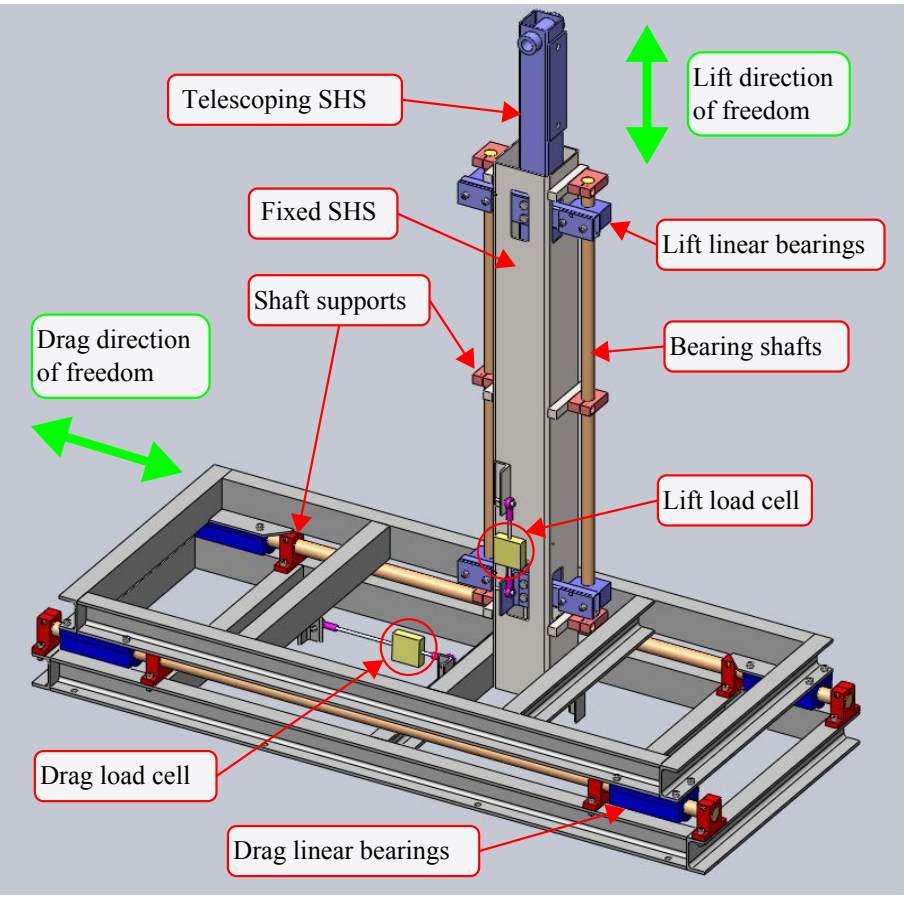

Figure 6.3: CAD model of Jetpack test rig showing key features

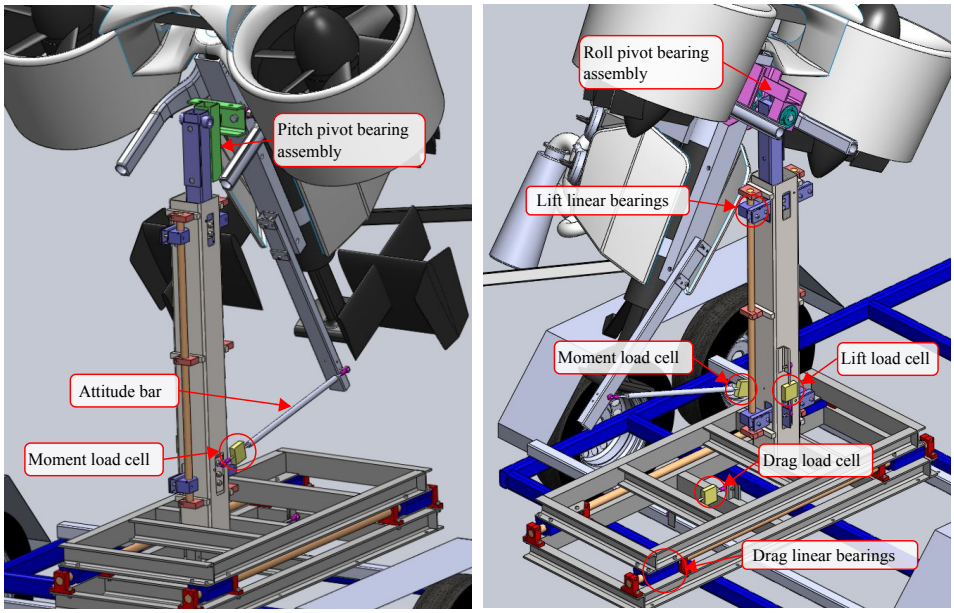

(a) 60° angle of attack in pitch plane (b) 60° angle of attack in roll plane

Figure 6.4: CAD model of Martin Jetpack secured on test apparatus

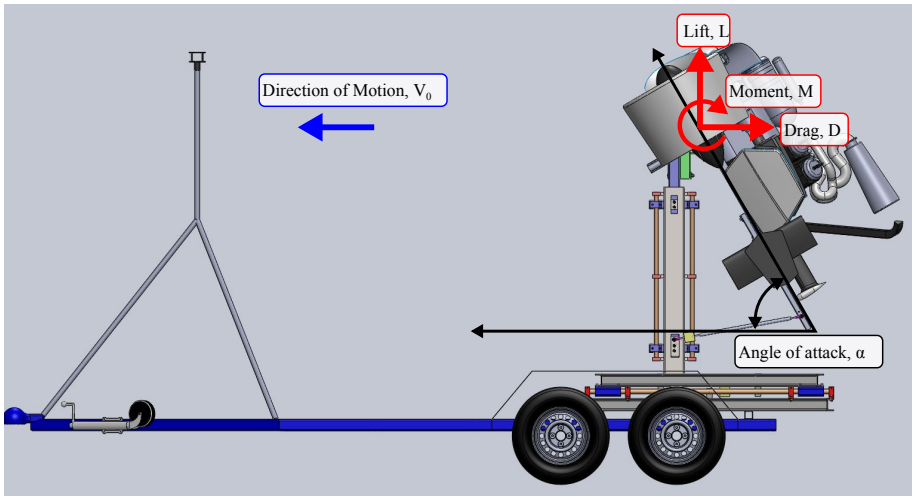

Figure 6.5: CAD model of the test apparatus supporting the Jetpack at a 60° pitch angle of attack, and the sign convention used to describe angle of attack, lift, drag, moment and motion.

It is assumed that the pilot of the Jetpack is not a major contributor to the overall aerodynamics of the Jetpack, as the pilot does not greatly add to the frontal area of the Jetpack, and does not add or remove energy into the airflow. Hence, no provision was made for a pilot/dummy to be included in the experiment, which significantly reduced the complexity of the mechanical design.

Tuft Rig

A tuft rig was made to help visualise the airflow entering the ducted-fan by positioning wool tufts in a grid pattern above and below the duct. The tuft rig was made of 10 mm diameter aluminium tubing to provide a frame to

suspended stainless steel wire to form a grid. Wool tufts of approximately 100 mm long were tied to the wire grid. A small digital video camera, (*Contour HD*) was secured to the end of a 3 m long aluminium tube to film the wool tufts during testing. Best quality results were found when the camera was set to high definition,1280 × 720 p, at 60 frames per second. The reduced frame rate of 30 frames per second at full high definition, 1920 × 1080 p, setting produced blurry results due to the longer exposures of the individual frames.

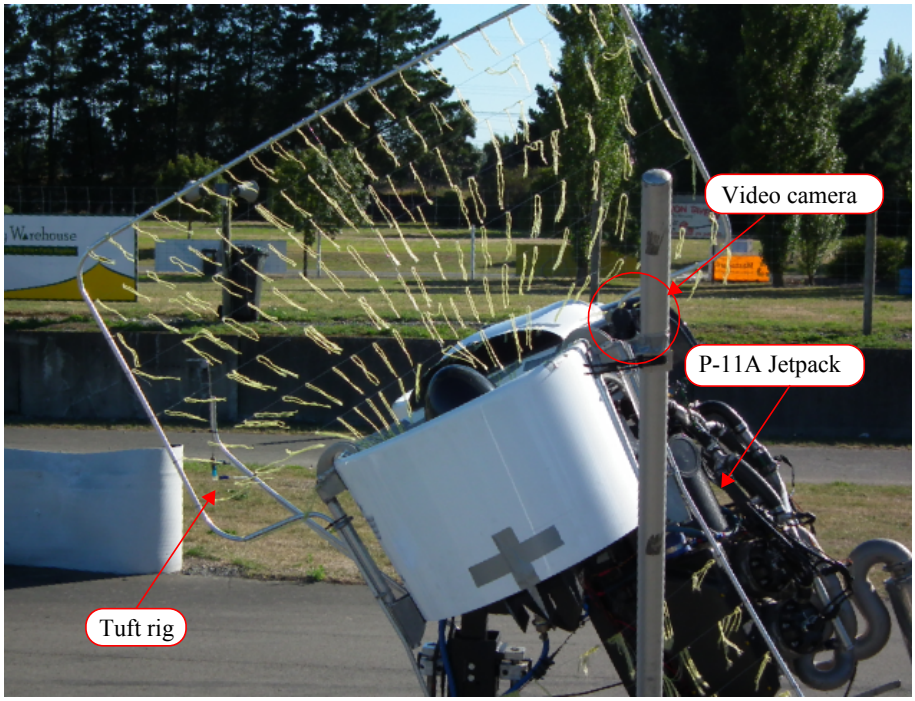

Figure 6.6: Wool tuft rig

Data Acquisition System

The data acquisition system (DAQ) was assembled from a number of components. At the core of the system was an Advantec USB-4716 DAQ card that was used to record the input voltages from the load cells, engine rotational speed sensor, and the event switch. Calibration of all the loads cells was performed by suspending a range of known masses from the load cells and comparing measured results to the corresponding masses to produce a calibration factor for each load cell, and to verify the load cell accuracy and precision.

The DAQ system was used to make the following measurements for each test run:

1. Moment about pivot point measured by a 100 kgf (981 N) shear beam load cell
2. Drag force measured by a 250 kgf (2452 N) shear beam load cell
3. Lift force measured by a 250 kgf (2452 N) shear beam load cell
4. Atmospheric properties: temperature, humidity, and pressure
5. Duct, test apparatus, and road test surface angles

6. Airspeed, measured by an ultrasonic anemometer
7. DAQ supply voltage
8. Tuft movement recorded by a digital video camera

Test Procedure

Test runs were recorded for a range of nominal pitch angles of attack of 0°, 600, 75°, 90°, 105°, 120°, and 180°; as well as nominal roll angles of attack of 60°, 75°, 90°, 105°, and 120°; at engine settings of: 0 RPM, 5500 RPM and 5750 RPM. The following steps describe the testing procedure:

1. Measure atmospheric data using the portable weather station.
2. Measure angles of duct, test rig, and road surface.
3. Warm up Jetpack to normal operating temperature and shut down.
4. Start logging data, DAQ on.
5. Wait 10 s to obtain zero reading.
6. Start Jetpack.
7. Bring Jetpack up to target engine rotation speed (5500 RPM and 5750 RPM) and maintain for 10 s at each engine speed setting to obtain static values.
8. Start the tow vehicle and drive up to test speed and maintain speed.
9. At test speed the engine operator brings the Jetpack up to target engine speed and maintains the engine speed for 5 s to 10 s for each setting.
10. If available race track exists speed is increased to next target speed and step 9 is repeated.
11. If no more race track exists the steps 9 and 10 are repeated on the reverse leg back to the start.
12. Steps 9 to 11 are repeated until all speeds have been measured.
13. Engine is shut down and steps 9 to 12 are repeated at 0 RPM to obtain *Engine Off* aerodynamic data.
14. Save collected data.
15. The above steps are then repeated for each desired angle of attack in both pitch and roll planes.

Note, the *event switch* was pressed by the DAQ operator to stamp the time when the engine and tow vehicle were at their appropriate settings. This was done to help identify the measurement samples and points of interest during testing in the DAQ data.

Data Processing

The data collected from the DAQ system was post-processed using developed Matlab® programs. Since the wind anemometer data (airspeed data) was collected at a sample rate of 4 Hz and the DAQ system recorded the load cell data and engine rotation speed at 60 Hz a synchronization process was performed to match the airspeed data to the DAQ data such that each sample instance has a load cell, engine rotation speed, event switch, and airspeed reading. The synchronization process involved an iterative process; for each DAQ time sample the closest airspeed time sample was found and the corresponding airspeed value was assigned to a new airspeed vector within the DAQ results matrix. The data for each test run was stored in a single matrix, where it could be easily analysed.

Using the *event switch* data, the start and end times of the measured samples were identified. These sample times were used to bracket the DAQ data to obtain the load cell force measurement samples. The measurement samples were plotted against the airspeed, as shown on Figure 6.7. The measurement uncertainty was determined by the combination of the load cell and velocity accuracy, ±1 kgf (±10 N) and ±2 km/h (±0.6 m/s), respectively, and the standard deviation of the measured data points. The large spread in the data is due to the extensive vibrations from the Jetpack engine, and electronic noise recorded by the DAQ system. Second order polynomials were fitted to the data to produce smooth best fit curves to represent the measured data to allow for a convenient means of analysing the data. The second order polynomials were chosen as typically aerodynamic reactions are a function of the dynamic pressure, which has a square relationship with velocity.

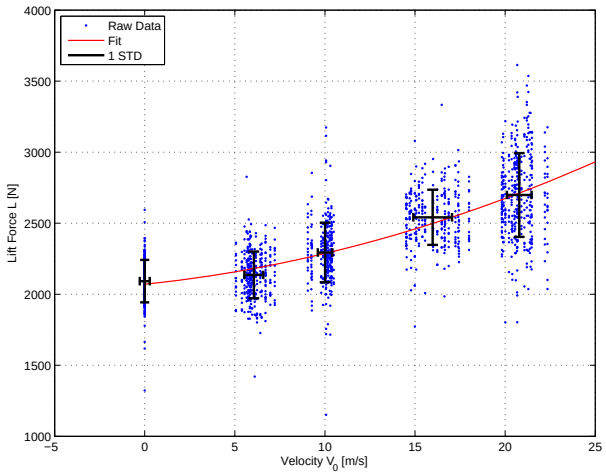

Figure 6.7: Jetpack lift versus velocity at a 60° angle of attack in the pitch plane, at 5750 RPM. The scattered points show each individual reading, the black crosses show the experimental uncertainty, and the solid red line shows the fit of a second order polynomial to the data. The data spread shown in this plot is typical of that recorded from the testing.

Results were also produced in dimensionless form to allow a more generic presentation. The velocity is non-dimensionalized using the advance ratio J defined as:

$$J = \frac{V_0}{nd} \tag{6.2.1}$$

where V_0 is the airspeed in m/s, n is the fan speed in revolutions per second, and d is duct exit diameter in m. The lift and drag forces, L and D, respectively, are non-dimensionalized as a fraction of the static thrust, as:

$$C_{LTs} = \frac{L}{T_s} \tag{6.2.2}$$

$$C_{DTs} = \frac{D}{T_s} \tag{6.2.3}$$

where C_{LTs} and C_{DTs} are the non-dimensionalized lift and drag force, and T_s is the static thrust or lift force at an angle of 90°. The roll and pitch moments, $M_{\frac{1}{4}}$, about the duct quarter point are non-dimensionalized with respect to the duct diameter, d, and static thrust, T_s as:

$$C_{M\frac{1}{4}Ts} = \frac{M_{\frac{1}{4}}}{T_s d} \tag{6.2.4}$$

where $C_{M\frac{1}{4}Ts}$ is the non-dimensionalized moment.

To obtain the moment data about the duct quarter chord point, the measured moment data was transformed using the following transformation, for both the roll and pitch planes:

$$M_{\frac{1}{4}} = M - sLcos\,(\alpha) - sDsin\,(\alpha) \tag{6.2.5}$$

where s is the distance separating the pivot point and the quarter chord point, as shown on Figure 6.8.

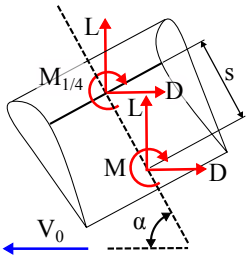

Figure 6.8: Pivot moment to duct quarter chord moment transformation

The measured ducted-fan lift and drag forces are related to the thrust force and ducted-fan normal force by the following transformation:

$$\begin{bmatrix} L \\ D \end{bmatrix} = \begin{bmatrix} \sin\alpha & \cos\alpha \\ -\cos\alpha & \sin\alpha \end{bmatrix} \begin{bmatrix} T \\ F_n \end{bmatrix} \tag{6.2.6}$$

This transformation is used to relate the theoretical ducted-fan predictions to the measured lift and drag forces.

6.3 Results and Discussion

Aerodynamic Reactions *Engine Off*

Figures 6.9 to 6.11 show the aerodynamic lift, drag, and moments in the roll and pitch plane of the Jetpack with the *Engine Off*.

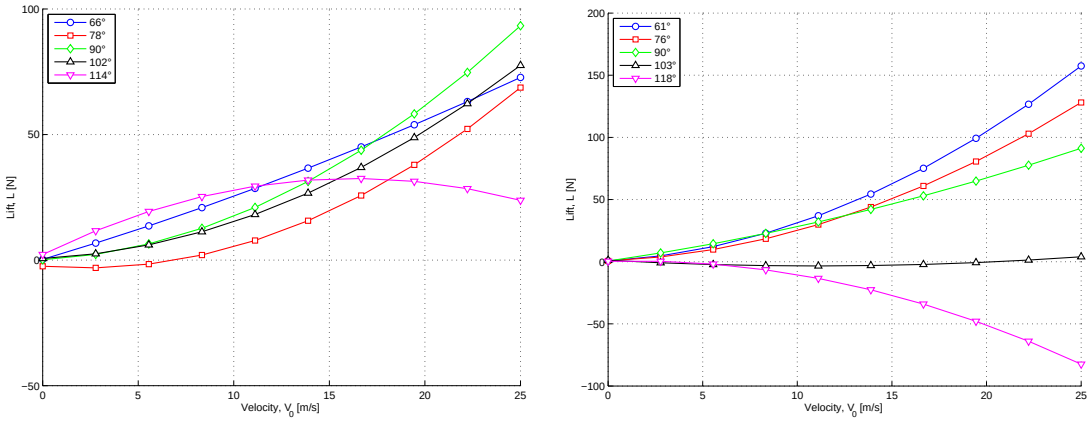

(a) Roll (b) Pitch

Figure 6.9: Measured Jetpack aerodynamic lift at 0 RPM

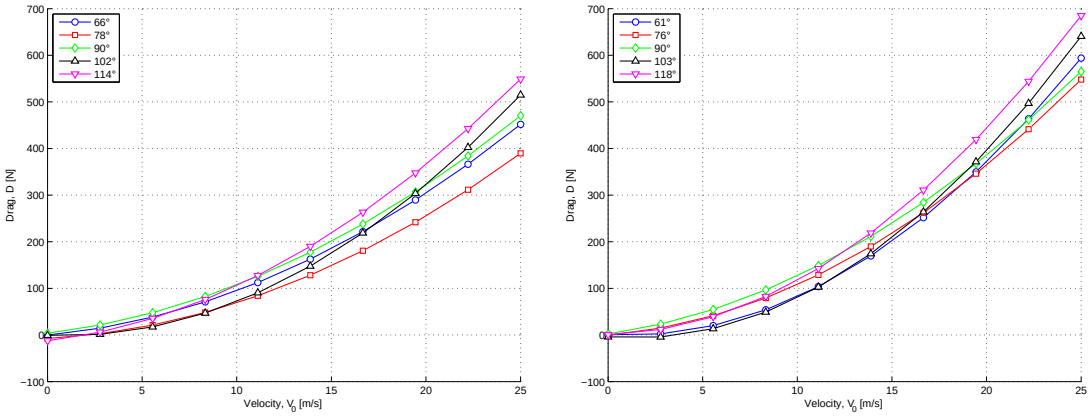

(a) Roll (b) Pitch

Figure 6.10: Measured Jetpack aerodynamic drag at 0 RPM

The *Engine Off* drag data, Figure 6.10, shows that the drag force is an order of magnitude greater than the lift force, hence more significant. Using the drag coefficient equation, (B.1.5), the drag coefficients for each axis can be determined by finding the drag coefficient that creates the best fit to the measured drag data. Figure 6.12 shows the measured and theoretically fitted drag forces for angles of attack of pitch 90°, roll 90°, and pitch 0°, which correspond to the x, y, and z axis, respectively. Drag coefficients of 0.81, 1.05, and 0.94 are found for x, y, and z axis, respectively. These drag coefficients are typical for a bluff body traveling at these speeds [84]. The drag coefficient of 0.81 in the x direction is higher than that found in the first tow test experiment. This difference is attributed to the improved experimental setup of the second tow tests; which has the Jetpack raised higher into the free stream airflow than the initial tow test, and the second test apparatus reduces aerodynamic

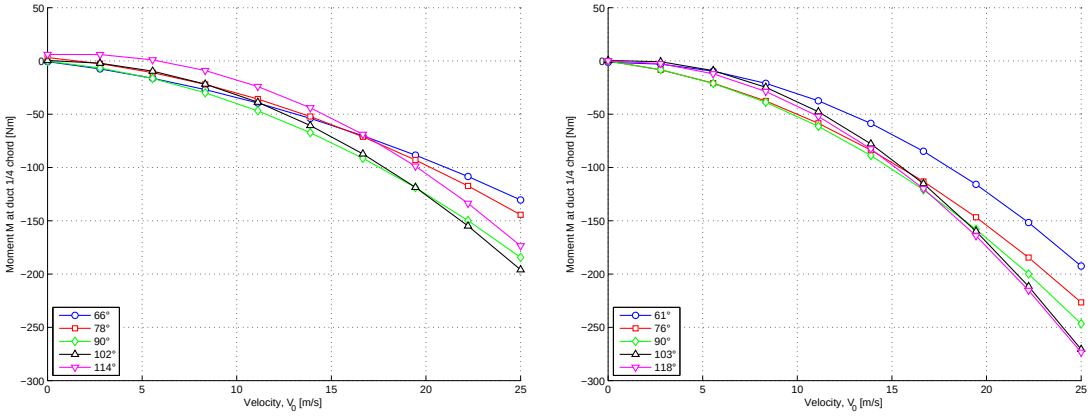

(a) Roll (b) Pitch

Figure 6.11: Measured Jetpack aerodynamic moment at 0 RPM

shielding of the Jetpack. Both of these factors increase the drag force acting on the Jetpack, which results in the higher drag coefficient.

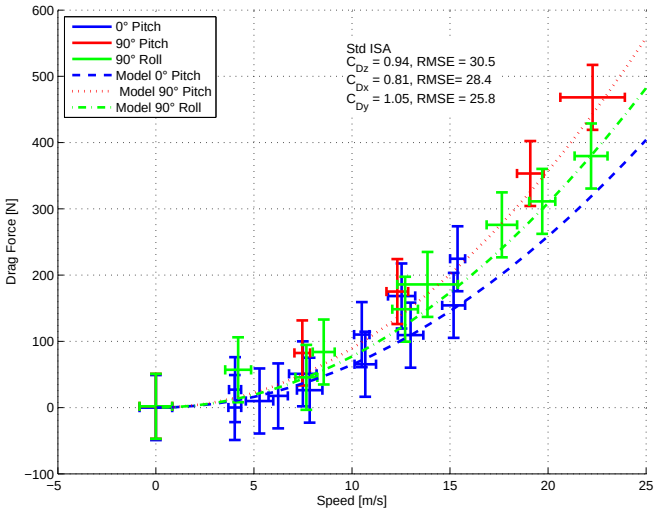

Figure 6.12: Measured Jetpack drag force compared to model predictions for angles of attack of pitch 0°, pitch 90° and roll 90°.

Aerodynamic Reactions *Engine On*

The Jetpack *Engine On* reactions for engine speeds of 5500 RPM to 5750 RPM are shown in Figures D.3 to D.8 in Appendix D. The reactions measured at 5500 RPM are similar to those measured at 5750 RPM data, but are a slightly reduced magnitudes due to reduced engine speed/power.

Ducted-Fan Aerodynamic Reactions

The aerodynamic reactions acting on the ducted-fans are shown on Figures 6.13 to 6.17.

Ducted-Fan Lift

Comparing roll and pitch plane ducted-fan lift forces on Figures 6.13a and 6.13b it can been seen that the roll lift is smaller than the pitch lift. This is attributed to the combination of decreased span and efficiency in the roll plane compared to that in the pitch plane. Referring to Figure 6.14, in the pitch plane the ducted-fans present a span of 2.75 times the duct diameter, or $2.75d$, whereas in the roll plane the ducts span only a single duct diameter to free steam airflow. The increased span in the pitch plane allows for more airflow surrounding the ducted-fans to be deflected downwards creating more lift compared to that of the roll plane. A Jetpack in the roll plane presents less aspect ratio (ratio of span to chord/diameter), and similarly to a wing a lower aspect ratio produces less lift for the same angle of attack, as it is less efficient [74]. Therefore, assuming an aircraft predominately flies in the forwards direction, the twin-ducted-fan (side-by-side) arrangement, Figure 6.14a, is more efficient than the tandem-ducted-fan arrangement, 6.14b.

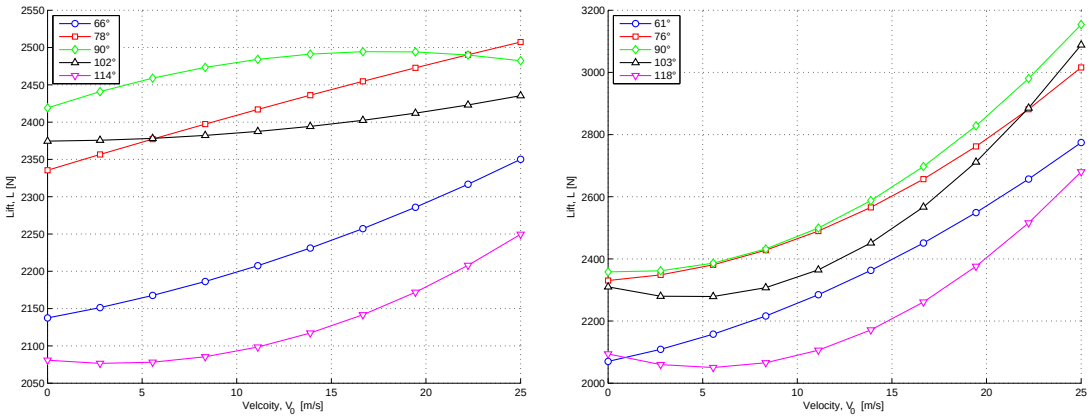

(a) Roll (b) Pitch

Figure 6.13: Measured combined ducted-fan lift for various angles of attack at 5750 RPM

Figures 6.13a and 6.13b show that the ducted-fan lift force increases with airspeed for all angles of attack in both the roll and pitch planes. This increase in lift force, as discovered from the first tow test experiment, is not explained by ducted-fan momentum theory introduced in Chapter 3. However, this additional lift force can be explained by assuming the ducted-fan behaves similarly to a wing, which deflects air downwards as the wing moves through the air. With this assumption, the additional lift force on the ducted-fan can be modelled using the lift force equation (B.1.6) that shows for a given lift coefficient the lift force increases quadratically with velocity, which is in good agreement to the results presented in Figure 6.13b. Applying the lift force equation (B.1.6) to the ducted-fan results in the development of the ducted-fan dynamic-lift equation:

$$F_{L,d} = C_{L,d}\frac{1}{2}\rho V_0^2 A_d \tag{6.3.1}$$

where $C_{L,d}$ is the ducted-fan lift coefficient, $\frac{1}{2}\rho V_0^2$ is the dynamic pressure of the free stream airflow, A_d is the ducted-fan area. The ducted-fan lift coefficient, similarly to an aerofoil lift coefficient (section B.1), is dependent on the angle

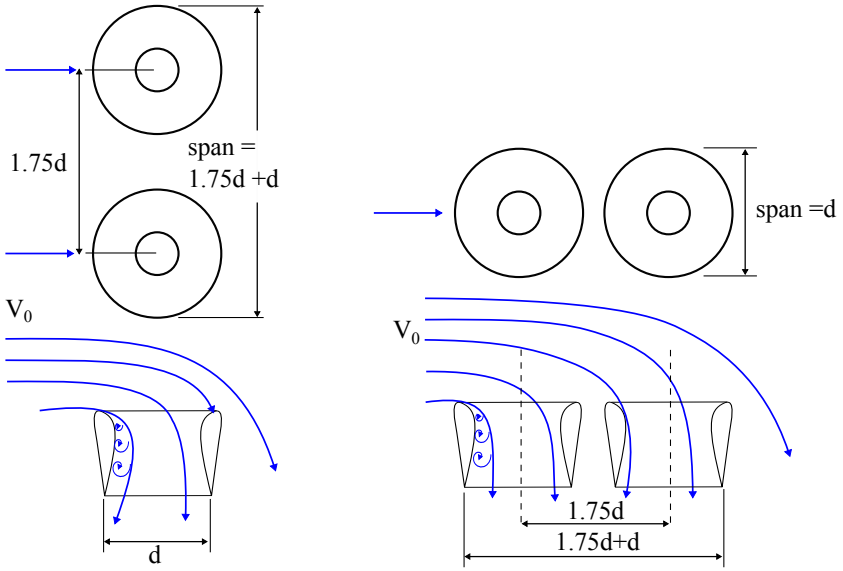

(a) Pitch plane (b) Roll plane

Figure 6.14: Schematic of flow comparisons around ducted-fans in pitch and roll planes

of attack. From the results shown in Figures 6.13a and 6.13b and physical insight, the ducted-fan lift coefficient equates to zero at 0° angle of attack and has a maximum value at 90° angle of attack. Hence, the ducted-fan lift coefficient takes the assumed form of:

$$C_{L,d} = C_{L,d}^{max} P_F \sin\alpha \tag{6.3.2}$$

where α is the angle of attack of the ducted-fan to the free stream airflow; $C_{L,d}^{max}$ is the maximum ducted-fan lift coefficient, which needs to be experimentally identified; and P_F is the power factor, which is an additional dimensionless term. The power factor is used to scale the ducted-fan lift force, which is necessary to include the effects of changing power on the dynamic lift force. For example at full power the ducted-fan will induce a higher flow rate through the ducted-fan and consequently will produce more aerodynamic lift at a given velocity than when operating at a lower power setting at the same velocity. If no power is supplied then the aerodynamic lift is zero, which is expected as there is no induced momentum through the ducted-fan, hence no downward accelerated airflow outside of the ducted-fan. Assuming a linear variation of the ducted-fan lift coefficient with power, then the power factor is calculated as:

$$P_F = \frac{P_e}{P_{e,max}} \tag{6.3.3}$$

where P_e is the engine power and $P_{e,max}$ is the maximum engine power.

Using the results shown in Figures 6.13a and 6.13b, identification of the maximum lift coefficient in both the roll and pitch planes, $C_{L,d,y}^{max}$ and $C_{L,d,x}^{max}$, respectively, is achieved by trial and error. Figures 6.15a and 6.15b compare the modelled ducted-fan lift forces to the experimentally measured forces for a

range of airspeeds and angles of attack. These Figures are produced using the ducted-fan power and normal force equations, (3.1.48) and (3.2.1) as described in Chapter 3, with equations (6.3.1) to (6.3.3) and the identified maximum ducted-fan lift coefficients of $C^{max}_{L,d,y} = 1$ and $C^{max}_{L,d,x} = 4.5$ for the roll and pitch planes, respectively. Note, that only angles from 0° to 90° are shown on the Figures 6.15a and 6.15b as the equation (6.3.2) is symmetrical about 90° angle of attack. Figure 6.15a shows that the model matches the measured data well for roll angle of attack of 66°. However, for angles of attack of 78° and 90° differences occur. This is attributed to differences in static thrust between the model and experimental data, and the different the form the experimental results show for angles of attack of 78° and 90°. Figure 6.15b shows that model matches well for all of the measured angles of attack. Hence, using the momentum equations to model the lift forces produced by the airflow passing through the ducted-fans, with the additional ducted-fan dynamic-lift equation to model the lift force of the deflected airflow outside the ducted-fan, the net in-flight ducted-fan lift force, as a function of angle of attack and airspeed, can be predicted with reasonable confidence.

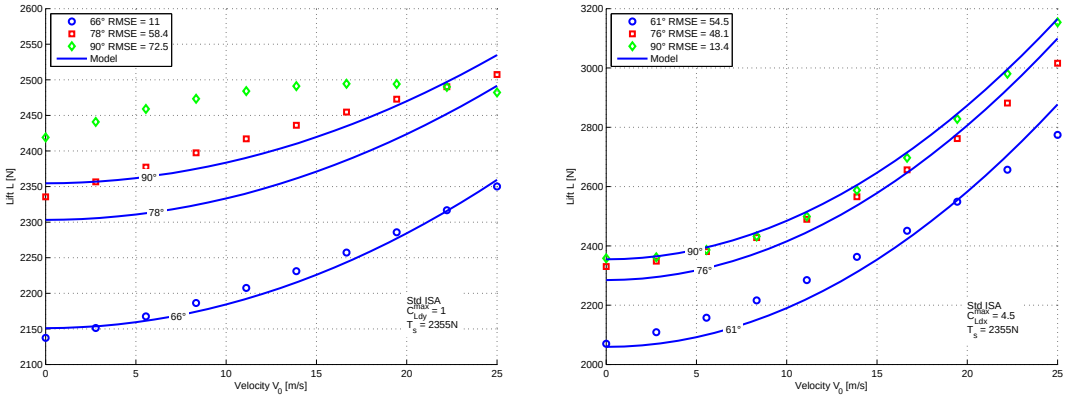

(a) Roll (b) Pitch

Figure 6.15: Combined theoretical ducted-fan lift force for various angles of attack calculated for the equivalent power setting of 5750 RPM. Note *Model* indicates the theoretical modelled result.

Ducted-Fan Drag

The ducted-fan drag forces in both the roll and pitch plane are shown in Figures 6.16a and 6.16b, and show, in general, a near linear trend with increasing speed.

At an angle of 0° and 0 m/s the combined duct drag is at −2350 N, as the ducted-fan static thrust force is acting in the opposite direction to the drag. It can be seen on Figure 6.17 that the combined ducted-fan drag increases linearly with increasing speed. The drag increase is expected for two reasons. Firstly, thrust benefit of the ducted-fan decreases with increasing speed, as the stagnation line moves from outside to inside of the duct leading edge resulting in the duct inlet producing drag rather than thrust, refer to Figure 6.18. Secondly, for a fixed pitch and constant fan rotational speed the thrust from the fan decreases, as the change of momentum through the ducted-fan decreases with increasing speed.

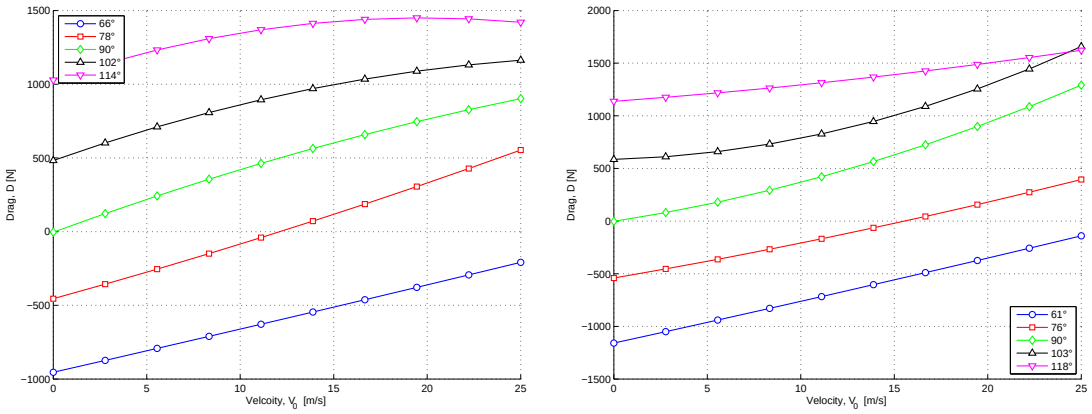

(a) Roll (b) Pitch

Figure 6.16: Measured combined duct drag for various angles of attack at 5750 RPM.

The ducted-fan drag force at an angle of attack 180° (Figure 6.17) shows a slight increase with increasing speed until approximately 8 m/s where the drag force begins to decrease; for speeds greater than approximately 17 m/s the drag force is less than the static thrust. This data shows that for low speed vertical descents the Jetpack will experience a beneficial increase in thrust. However, for high vertical descent speeds above 17 m/s the ducted-fan thrust decreases below static thrust at the same engine speed, which reduces the ability of the Jetpack to arrest the descent. This effect will have the implication that the vertical descent speed of the Jetpack will need to be limited for safe operations. It must also be noted that during testing of the Jetpack at an angle of attack 180°, the Jetpack experienced significant vibration and shaking, which increased with speed, this effect is attributed to the Jetpack being towed through the duct wake. This shaking may cause significant detrimental handling and control issues for the Jetpack during vertical descent. With increasing descent speed it is expected that the rotor blades will being to stall due to the increased back pressure and progress to a condition known as vortex ring state[88], which occurs when helicopters descend vertically into there own downwash.

Similarly, to the development of the ducted-fan dynamic-lift term a ducted-fan dynamic-drag term is also added to the momentum based drag terms, equations (3.1.48) and (3.2.1), to produce a complete model of the ducted-fan drag force. Hence, the momentum equations model the drag forces produced by the airflow passing through the ducted-fans, while the ducted-fan dynamic-drag equation models the drag force of the deflected airflow outside the ducted-fan. The ducted-fan dynamic-drag equation takes the form of the drag equation (B.1.5) as:

$$F_{D,d} = C_{D,d}\frac{1}{2}\rho V_0^2 A_d \tag{6.3.4}$$

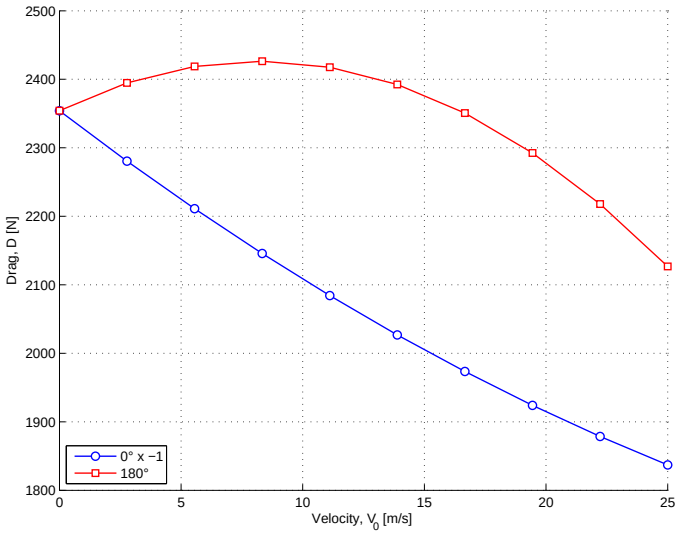

Figure 6.17: Combined duct drag in pitch for angles of attack of 0° and 180° at 5750 RPM. Note that the 0° angle of attack data is presented as the negative of what was measured.

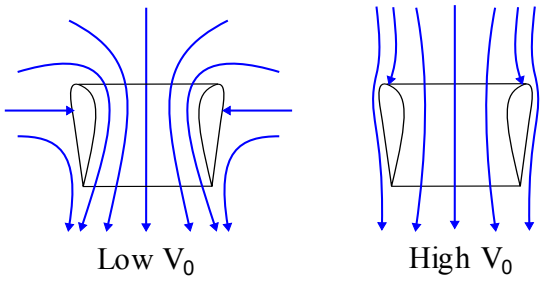

Figure 6.18: Schematic of stream lines around a ducted-fan in axial flight

where $C_{D,d}$ is the ducted-fan drag coefficient, $\frac{1}{2}\rho V_0^2$ is the dynamic pressure of the free stream airflow, A_d is the ducted-fan area. The ducted-fan drag coefficient, similarly to an aerofoil drag coefficient (section B.1), is dependent on the angle of attack. From the results shown in Figures 6.16a and 6.16b, the ducted-fan drag coefficient should equate to zero at 0° angle of attack and have a maximum value at 90° angle of attack. Hence, the ducted-fan lift coefficient takes the form of:

$$C_{D,d} = C_{D,d}^{max} P_F \sin\alpha \tag{6.3.5}$$

where $C_{D,d}^{max}$ is the maximum ducted-fan drag coefficient, which needs to be experimentally identified; and P_F is the power factor as defined by equation (6.3.3).

Performing a parameter identification by trial and error leads to the results shown in Figures 6.19a and 6.19b for the drag coefficients of $C_{D,d,y}^{max} = 0$ and $C_{D,d,x}^{max} = 1$ for the roll and pitch planes, respectively. Note, since $C_{D,d,y}^{max} = 0$ equation (6.3.4) is neglected leaving only the momentum based equations to calculate the ducted-fan drag in the roll plane. The ducted-fan drag model, shown by the solid lines in Figures 6.19a and 6.19b, is in good agreement with experimental data up to 50 km/h, where deviations for angles of attack greater than 90° occur. These deviations are attributed to the non-linear behaviour of the airflow interaction with the ducted-fans at these conditions, where the aircraft begins to experience reversed flow entering the ducted-fans and also interacts with its own wake. It must be noted, that the experimental results for angles of attack of greater than 90° may not replicate the actual flying conditions, due to the unknown effect of ducted-fan efflux impinging the ground and circulating back towards the aircraft during testing, as illustrated in Figure 6.20. For angles of attack of 90° and less the ducted-fan drag model matches reasonably well with $RMSE < 150$ N for both the roll and pitch planes. Note, the $RMSE$ has been calculated by equation (5.1.3) between the model and the curve fitted to the measured data for each angle of attack.

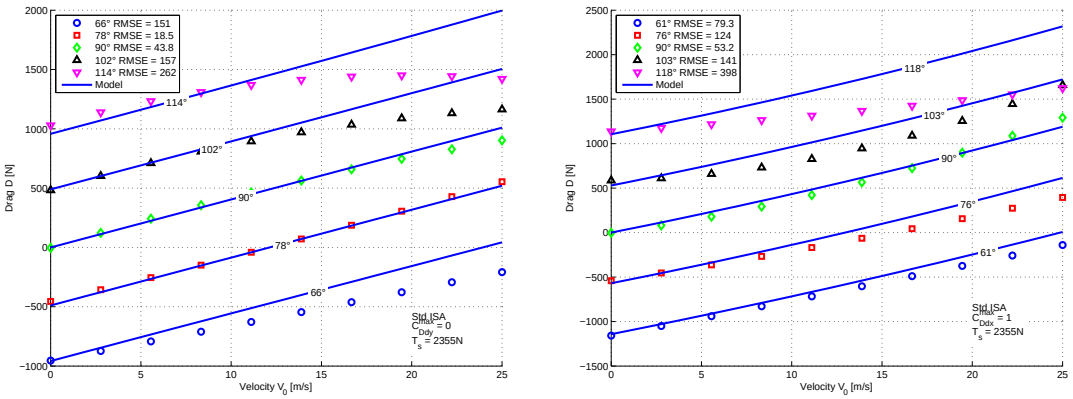

(a) Roll (b) Pitch

Figure 6.19: Combined ducted-fan drag force for various angles of attack calculated for the equivalent power setting of 5750 RPM.

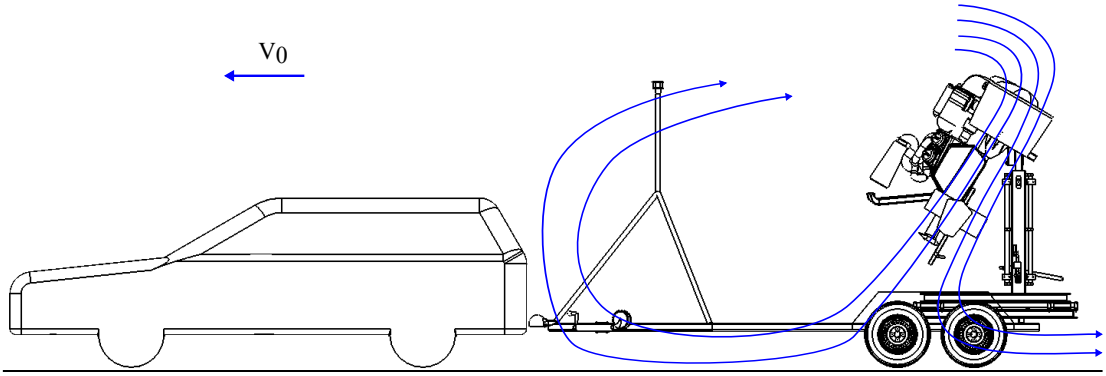

Figure 6.20: Indication of ducted-fan induced flow recirculation effecting Jetpack during tow testing.

Ducted-Fan Moment

Figure 6.21 shows the measured combined ducted-fan moments about the duct quarter chord point for both the roll and pitch planes. The results for the combined ducted-fan moment in the pitch plane (Figure 6.21b) for angles of attack from 60° to 90° show that a maximum pitching moment is reached. It is suspected that this maximum coincides with the onset of flow separation/stall on the ducted-fan leading edge as found and described by Ohanian [87]. Flow separation on the duct leading edge occurs due to the increased centripetal forces pulling the airflow away from the surface at higher airspeeds, as illustrated in Figure 6.22. When separation occurs on the windward-side leading-edge of the duct, the thrust line effectively moves away from the duct axis towards the opposite side; which creates a pitch down moment that counteracts the pitch up moment produced by the ducted-fan normal force. For angles of attack greater than 90° the pitching moment shows a linear relation with increasing speed.

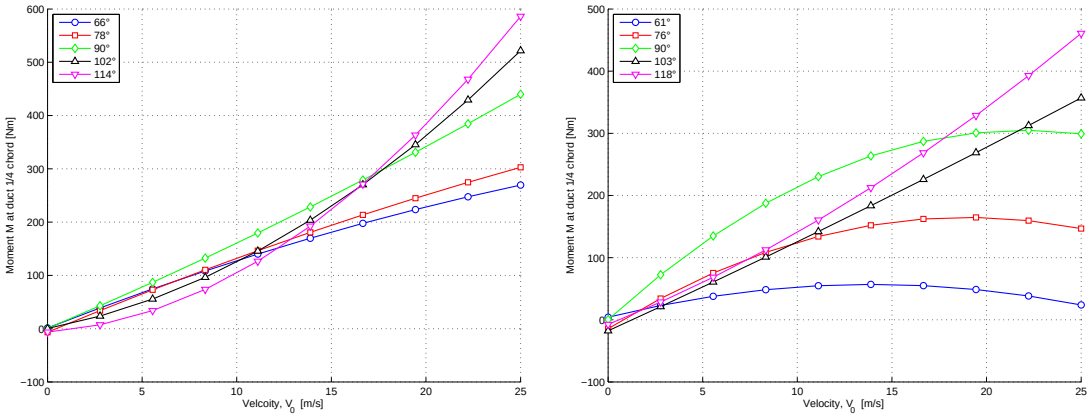

(a) Roll (b) Pitch

Figure 6.21: Measured combined duct moment for various angles of attack at 5750 RPM

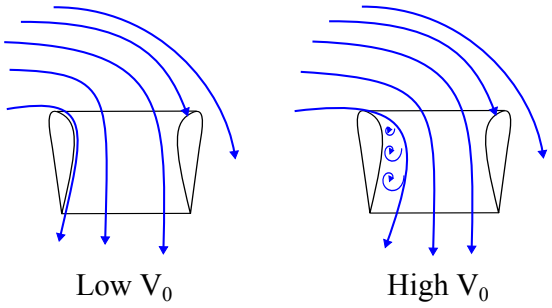

Figure 6.22: Schematic of stream lines around a ducted-fan in crosswind/radial flight

The roll plane ducted-fan moments, Figure 6.21a, show a linear relationship with speed and no indication of a maximum moment, as occurs in the pitch plane, 6.21b. It is assumed that this linear relation is due to the windward duct in roll producing more lift than the leeward duct resulting in a large positive roll moment. This large roll moment is magnified further as the roll angle of attack exceeds 90°. Figures 6.21a and 6.21b show that the behaviour of roll and pitch moments are different about the roll and pitch axis, with generally the roll moments being larger than the pitch moments at higher airspeeds.

Using single ducted-fan moment data found in [86, 87, 89] and comparing this to both roll and pitch moment results it can be seen on Figure 6.23 that the measured results are in good agreement, with $RMSE \leq 0.0423$ when compared to the experimental pitch results, hence, validating the experimental protocol presented. Note, that the measured experimental results have been divided by two as the Jetpack has two ducted-fans.

Ducted-Fan Center of Pressure

Figures 6.24a and 6.24b show how the centre of pressure changes with increasing speed for duct angles of attack ranging from 61° to 118°. For pitch angles from 60° to 105° the centre of pressure decreases towards the quarter chord point with increasing speed. While the centre of pressure at an angle of attack of 118° shows the opposite trend and rapidly increases in a linear manner with increasing speed. Practically, this increase of the centre of pressure with increasing attitude is an unstable behaviour of the ducted-fan. For example if the aircraft is flying in level forwards flight (pitch down) and experiences a sudden pitch up disturbance, the increased angle of attack would increase the centre of pressure and consequently increase the ducted-fan pitching moment, which would further increase the pitch up motion. If the ducted-fan pitching moment exceeds the maximum pitch vane moment then loss of control will occur!

In comparison to the pitch plane the centre of pressure in the roll plane for angles of attack from 66° to 90° remains much more constant, approximately 0.4 m above the ducted-fan quarter chord point throughout the flight envelope. This is a result of the linear nature of the moment in the roll plane where it is believed that the leeward duct does not experience any stall, as the downward deflection of the airflow from the windward ducted-fan helps align the airflow

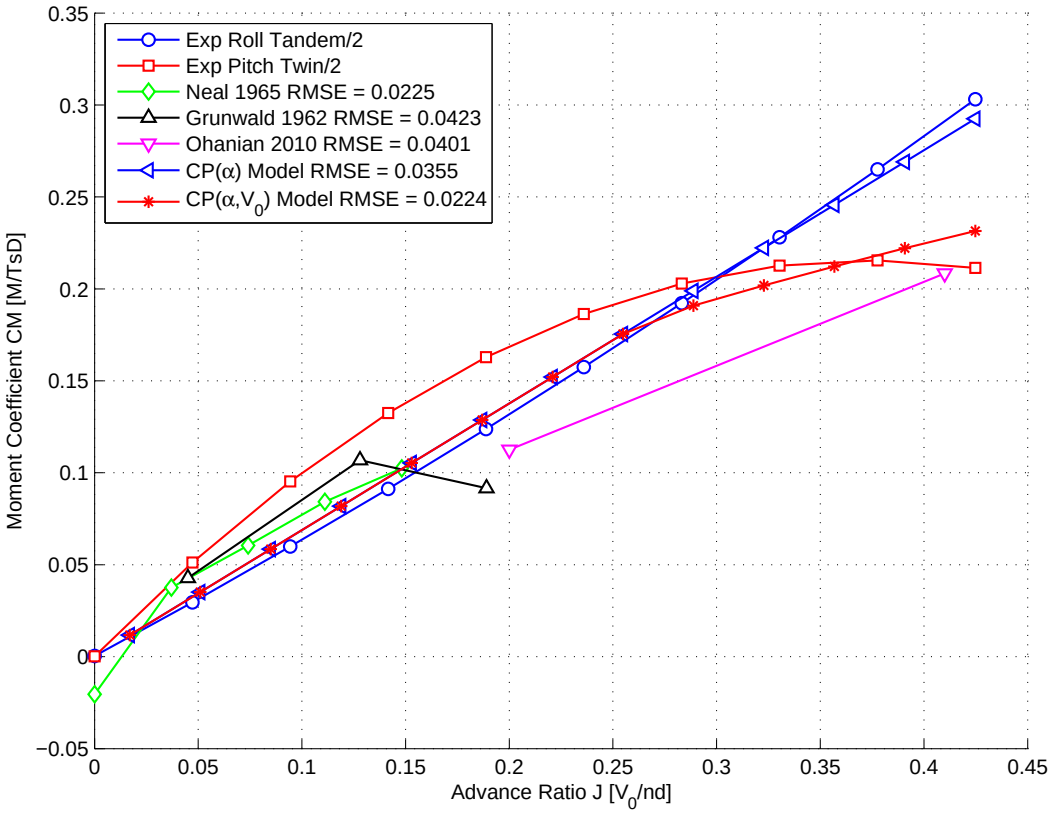

Figure 6.23: Comparison of duct moments at 90° angle of attack

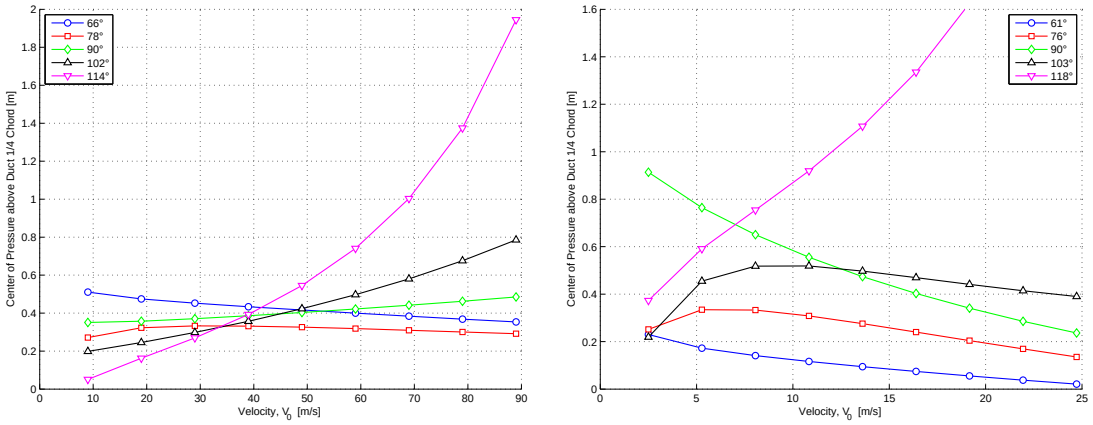

(a) Roll plane (b) Pitch plane

Figure 6.24: Measured ducted-fan centre of pressure movement at 5750 RPM

into the leeward duct, refer to Figure 6.14b. The near constant centre of pressure for the ducts in the roll plane allows for easier identification of where the centre of gravity should be located with respect to the ducted-fan centre of pressure. Similar to the pitch plane the roll centre of pressure also increases rapidly with speed for angles of attack greater than the hover attitude of 90°.

The near constant centre of pressure in the roll plane allows the fixed centre of pressure model, as described in section 3.2, to be modified to match experimental data. From the results shown and physical insight the fixed centre of pressure model is altered to become a function of the angle of attack as:

$$CP_y = \begin{cases} CP_{max} \sin \alpha_y & 0 \leq \alpha_y \leq 90° \\ CP_{max} & 90° < \alpha_y \end{cases} \tag{6.3.6}$$

where the conditional formulation is used to decrease the centre of pressure for angles of attack below 90°, and maintain a constant centre of pressure for angles above 90°; α_y is the duct angle of attack with respect to the y air velocity component; and the maximum centre of pressure CP_{max} above the duct quarter chord is calculated as:

$$CP_{max} = \frac{1}{2}d + \frac{1}{4}d_c \tag{6.3.7}$$

where d is the duct diameter and d_c is the duct chord length. Using this model of the ducted-fan centre of pressure, the moment about the ducted-fan quarter chord point can be calculated as:

$$M_x = F_{n,y} CP_y \tag{6.3.8}$$

where $F_{n,y}$ is the y component of the ducted-fan normal force, and the subscript x indicates that the moment is about the x axis.

The variable centre of pressure model described in section 3.2 is also modified to reflect the measured moment in the pitch plane, as:

$$CP_1 = r \sin \frac{\alpha_x}{2} - CP_{max} \cos \alpha_x \tag{6.3.9}$$

$$CP_{max,1} = \begin{cases} CP_{max} \sin \alpha_x & 0 \leq \alpha_x \leq 90° \\ CP_{max} & 90° < \alpha_x \end{cases} \tag{6.3.10}$$

$$CP_x = \begin{cases} CP_1 & CP_1 \leq CP_{max,1} \\ CP_{max,1} & CP_{max,1} < CP_1 \end{cases} \tag{6.3.11}$$

where r is the turning radius as per equation (3.2.3). α_x is the duct angle of attack with respect to the x air velocity component. CP_{max} is defined as per equation (6.3.7). The first conditional formulation is used to decrease the centre of pressure for angles of attack below 90°, and maintain the maximum centre of pressure for angles above 90°. The second conditional formulation is used to limit the centre of pressure to the maximum centre of pressure, which is necessary as the turning radius r tends to infinity as the free stream air velocity approaches zero. Using this modified variable centre of pressure model, the moment about the ducted-fan quarter chord point can be calculated as:

$$M_y = -F_{n,x} CP_x \tag{6.3.12}$$

where $F_{n,x}$ is the x component of the ducted-fan normal force, the negative sign is used is required as per the sign convection, and the subscript y indicates that the moment is about the y axis.

Figures 6.25 and 6.26 show the ducted-fan centre of pressure and moment models compared to the experimental results. Both roll and pitch show comparable centre of pressure for angles of attack up to and including 90°. Beyond 90° both roll and pitch models under estimate the centre of pressure. Both models show large errors for low velocities below approximately 11 m/s. However, it can be seen on Figure 6.26 that the large deviations at low speeds have little affect on the moment, which has a higher priority, than the centre of pressure to be modelled accurately as the ducted-fan moment strongly dictates the Jetpack behaviour.

Both centre of pressure models, equations (6.3.6) and (6.3.11), capture the physics of the ducted-fan moment by showing reasonable agreement to measured data, as shown in Figure 6.26. For the roll plane equation (6.3.6) models the ducted-fan moment well for angles of attack from 66° to 114° up speeds of 17 m/s. For the 90°angle of attack the model has a very good fit to the data with a $RMSE = 11.5$ Nm. For the pitch plane equation (6.3.11) models the pitching moment well with the $RMSE < 42$ Nm. Also, both centre of pressure models, show good relation compared to the single ducted-fan moments at 90° angle of attack, as shown in Figure 6.23. Hence, both models can now be confidently applied to the Jetpack model to predict the flight behaviour up to airspeeds of 25 m/s.

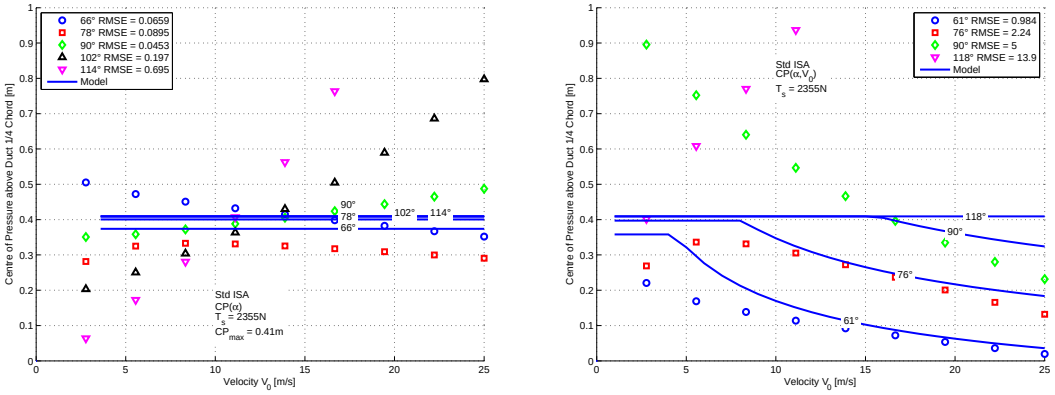

(a) Roll (b) Pitch

Figure 6.25: Ducted-fan centre of pressure for various angles of attack calculated for the equivalent power setting of 5750 RPM.

Direct Experimental Comparison

Using the ducted-fan models, as described in section 6.3, with the identified drag coefficients from section 6.3, the Jetpack aerodynamic model, which includes both ducts and the Jetpack body, can be compared to the measurements from section 6.3, as shown on Figures 6.27 to 6.29. In general, the predicted

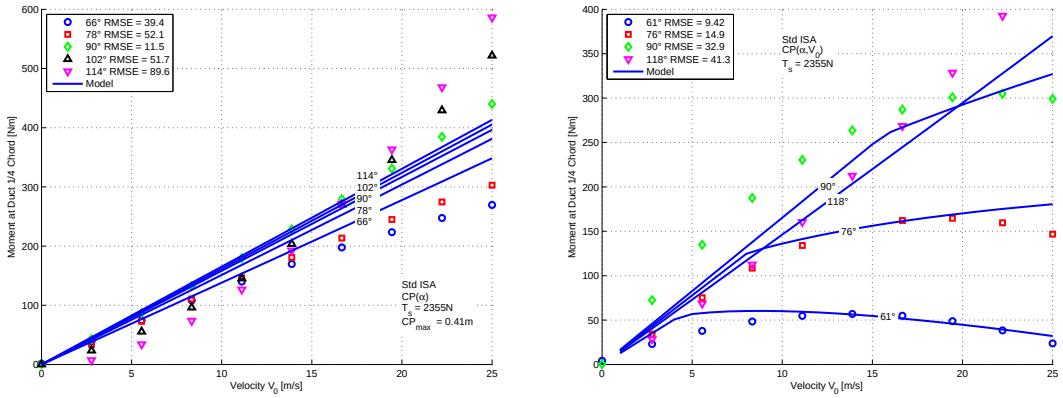

(a) Roll (b) Pitch

Figure 6.26: Ducted-fan moment for various angles of attack calculated for the equivalent power setting of 5750 RPM.

Jetpack aerodynamic reactions compare well to the measured data. This result validates the approach of isolating the combined ducted-fans from the net Jetpack reactions, and developing stand-alone models of the ducted-fans, which are more useful for the aircraft designer as the ducted-fan can be treated in isolation.

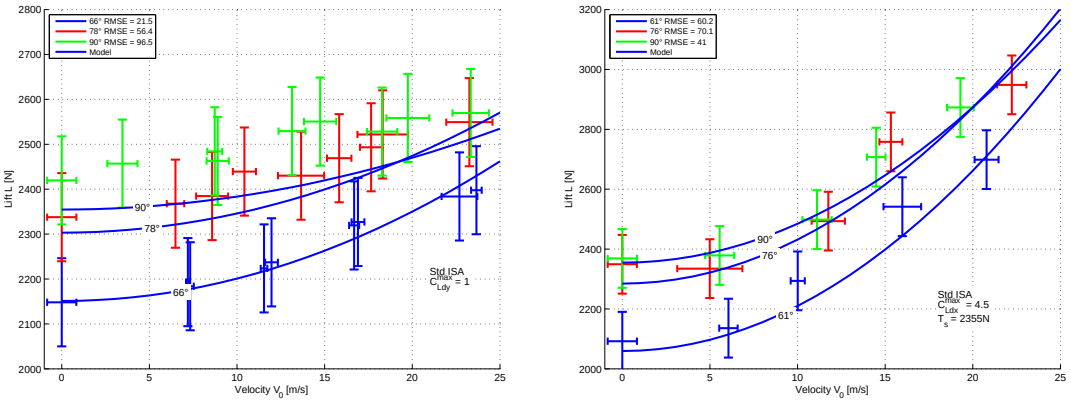

(a) Roll (b) Pitch

Figure 6.27: Comparison of model to measured Jetpack aerodynamic lift at 5750 RPM

Flow Visualization

The wool tuft rig and digital video camera recorded videos of the flow entering the ducted fans. Still images were captured from slow speed playback of the recorded videos. Images were made for all test speeds, attitudes and engine speeds. The images shown in Figures 6.30a to 6.30c show the momentum change of air occurring as the air is redirected downwards when the engine is operating at nominal flying power. Figure 6.30b also shows vapor condensing in an arch connecting one duct to the other. This method of flow visualization

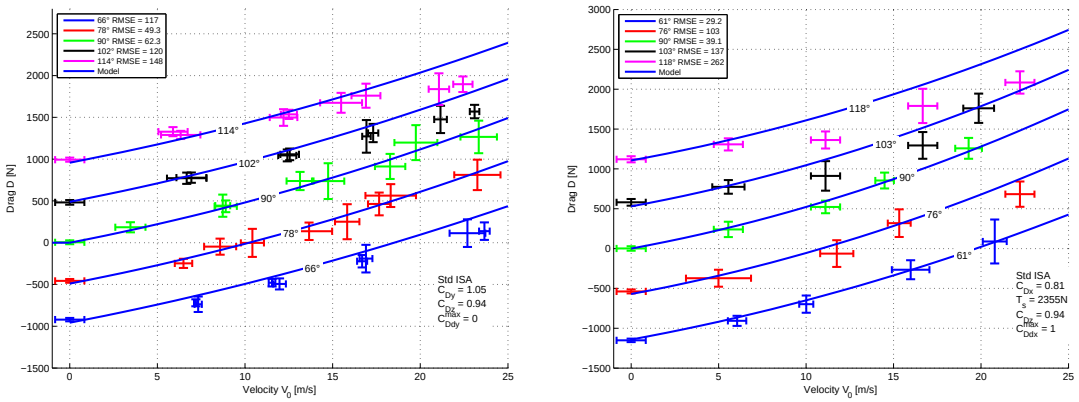

(a) Roll (b) Pitch

Figure 6.28: Comparison of model to measured Jetpack aerodynamic drag at 5750 RPM

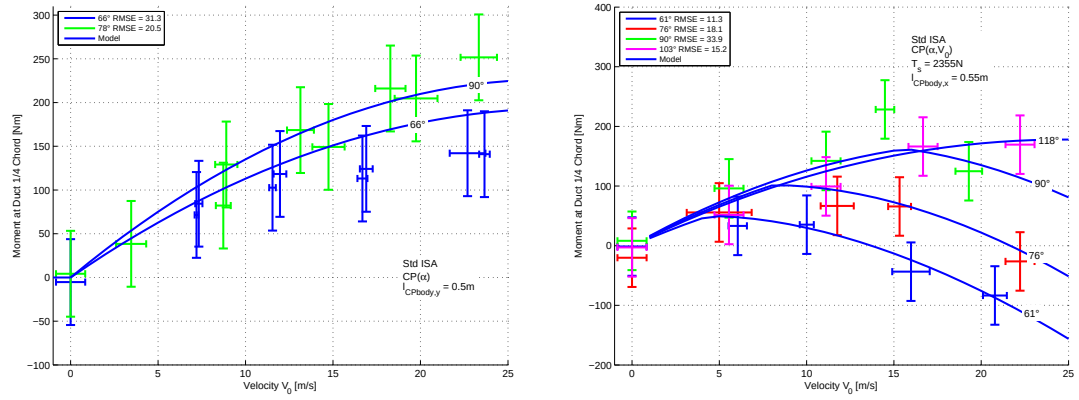

(a) Roll (b) Pitch

Figure 6.29: Comparison of model to measured Jetpack aerodynamic moment at 5750 RPM

produced similar flow maps to those performed by particle image velocimeter in [62] and computational fluid dynamics in [63] and gave a useful means of identifying the flow path entering the ducted-fan.

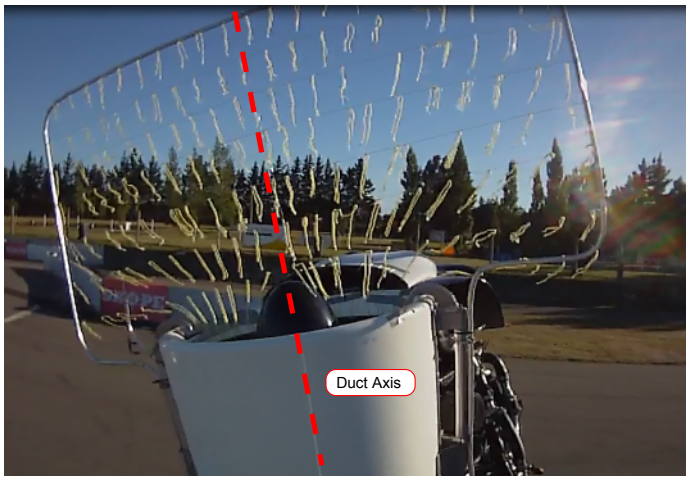

(a) 0 m/s with the engine on

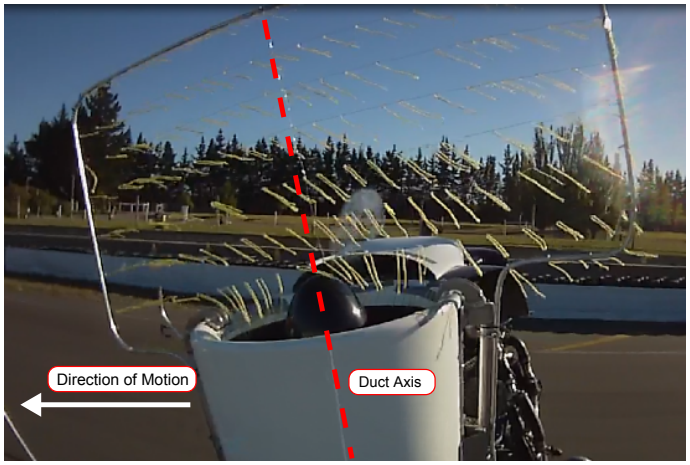

(b) 17 m/s with the engine on

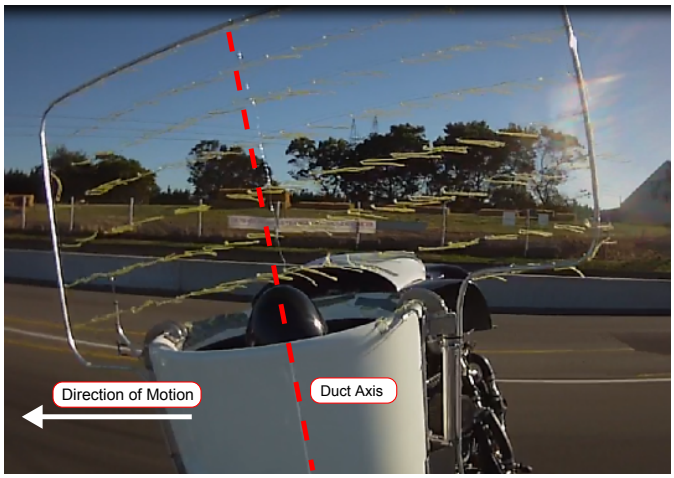

(c) 17 m/s with the engine off

Figure 6.30: Picture of wool tufts at a duct angle of attack of 76°

6.4 Conclusion

A low cost means of acquiring the in-flight forces and moments acting on a Jetpack has been successfully developed, and used to quantify the aerodynamic behaviour of the Jetpack in both the roll and pitch planes. The developed experiment hardware and protocol allows for:

- Complete force resolution in either roll or pitch plane, (measures lift, drag and moment).
- Roll angles of attack from 45° to 135°
- Pitch angles of attack from 0° to 180°
- Measurement of aerodynamic loads up to 28 m/s (100 km/h)
- Measurement of aerodynamic loads of other similarly sized specimens

Results collected from the tow test experiment have been used to determine:

- The aerodynamic drag coefficients for the P-11A Jetpack, which are found to be 0.81, 1.05, and 0.94 for the x, y and z axis, respectively.
- The aerodynamic lift, drag, and moment of the Jetpack and ducted-fans for a range of pitch angles of attack from 0° to 180° and roll angles of attack from 60° to 120°.
- The ducted-fan dynamic lift equation. The maximum ducted-fan dynamic lift coefficients have been found to be 4.5 and 1 for the x and y axis, respectively.
- The ducted-fan dynamic drag equation. The maximum ducted-fan dynamic drag coefficient has been found to be 1 and 0 for both the x and y axes, respectively.
- The necessary modifications to the fixed and variable centre of pressure and moment models.

The experimental quantification of the combined ducted-fan reactions allows for the calculation of the centre of pressure, which provides the ducted-fan aircraft designer with the necessary information to correctly position the ducted-fan relative to the centre of gravity to achieve a successful VTOL ducted-fan design. The centre of pressure plots presented show how the roll centre of pressure remains relatively constant. Whereas, the pitch plane centre of pressure decreases towards the duct quarter chord position with increasing speed; this result suggests that a compromise between the ideal centre of gravity positions in each plane, roll and pitch, needs to be found.

This chapter describes how the ducted-fan centre of pressure movement has been measured on the P-11A Martin Jetpack. This centre of pressure movement along with the ducted-fan lift, drag, and moment reactions gives an understanding of the aerodynamics experienced by the Jetpack in-flight. The data from this experiment can be used to improve the accuracy of the Jetpack model described in Chapter 4, so the model can be used to predict and define the flight envelope of the Jetpack, which is the topic of the next Chapter.

Chapter 7

Flight Envelope Definition

"A well-spent day brings happy sleep."
Leonardo da Vinci

This chapter explains how the flight model described in Chapter 4 is used to develop the flight performance charts, which define the flight capabilities, and hence, the flight envelope, for the Jetpack.

The Jetpack flight model has the form of a state space model containing input, state, state derivative, and output variables related by first order differential equations. Using physical insight various combinations of input, state, state derivative, and output variables are constrained and solved for to find steady state solutions of the model. Steady state solutions or equilibrium points are also known as *trim points*. Solving for these trim points allows for steady state information to be extracted from the model, which gives significant insight into the performance capabilities of the Jetpack. The following information can be found from solving the model for various trim points:

- Landed position (deflection of the landing gear due to self weight)
- Hovering conditions
- Vertical climb conditions
- Longitudinal (forwards and rearwards) level flight conditions
- Lateral (sidewards) level flight conditions
- Longitudinal climb conditions
- Lateral climb conditions
- Yaw turn conditions
- Banked turn conditions

VTOL aircraft, such as the Jetpack, due to their unique ability to fly at zero airspeed have a greater variation in trim points than fixed wing aircraft, which are confined to fly within a small cone governed by the range of flyable angles of attack and angles of side slip, refer to Figure B.33. Figure 7.1 shows the simplified free body diagrams of the aforementioned Jetpack trim points. The

trim points calculated within this Chapter for the P-11C Jetpack used the ducted-fan centre of pressure models described by equations 6.3.6-6.3.8 and equations 6.3.9-6.3.12 to model the roll and pitch moments respectively.

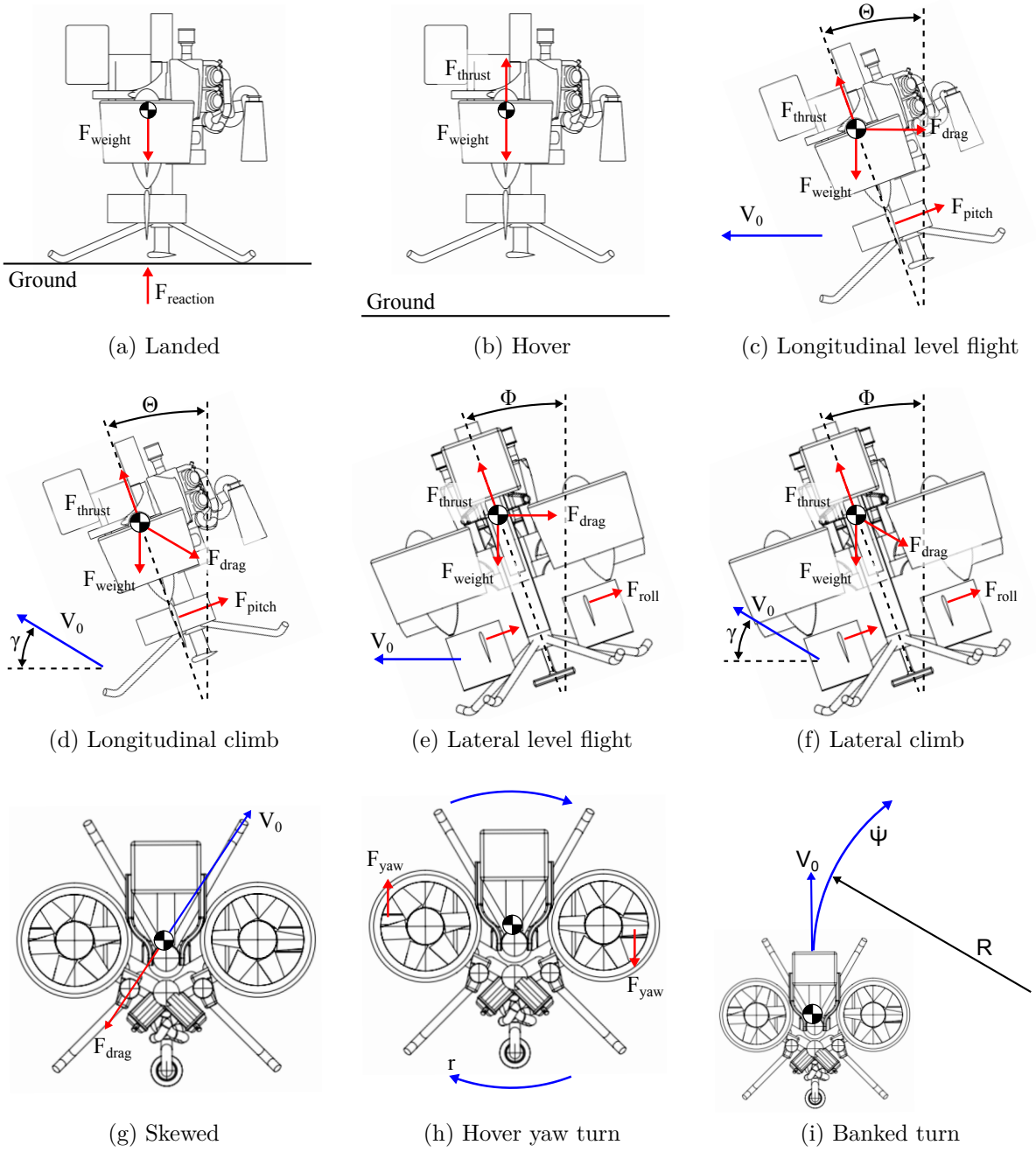

(a) Landed (b) Hover (c) Longitudinal level flight

(d) Longitudinal climb (e) Lateral level flight (f) Lateral climb

(g) Skewed (h) Hover yaw turn (i) Banked turn

Figure 7.1: Free body diagrams of various trimmable Jetpack flight conditions

7.1 Landed Trim Point

The landed trim point, Figure 7.1a, is the simplest trim point. It describes the equilibrium condition between throttle position and landing gear deflection of the Jetpack when stationary on the ground. This trim point determines the position of the Jetpack above the ground when the ground is supporting the weight of the Jetpack and the throttle set at levels below hovering levels (idle

thrust force is being exerted at zero throttle setting). This trim point is a function of the throttle position, which determines the duct thrust force and hence the apparent weight of the Jetpack on the landing gear. The height of the centre of gravity from the ground is a function of the landing gear deflection, which is proportional to the apparent weight of the Jetpack and the landing gear spring constant. The settings used to calculate the landed trim point are shown in 7.1.

Table 7.1: Landed trim point settings

State derivative and output requirements	State and input trim variables with initial guess	Non-zero state and input fixed variables
$\dot{w}_f = 0$	$z_i = 4\,\text{m}$	$\tau = 0$
$\dot{P} = 0$	$P = 120\,\text{kW}$	

Note, for successful trim point calculation we begin with a height value of $z_g < G$, as the landing gear force only exits when the extent of un-sprung landing gear is below ground height, as the landing gear force is a discontinuous function. The trimmed solution is a combination of power, throttle setting, and corresponding height z_i of the CG from the origin.

7.2 Hover Trim Point

The hover trim point, Figure 7.1b, is the simplest flying trim point where the Jetpack is aloft and remains in a stationary upright position with the thrust force opposing the weight force. The hover trim point is actually similar to that of the landed trim point, but instead of the landing gear supporting the weight of the Jetpack the thrust force from the ducted-fans does. Hence, the difference between the landed and hovering trim point is that the height z_i is fixed and the throttle setting becomes the variable. The hover trim point is a function of the weight, throttle setting, and air density. Since altitude is a function of air density the relationship between hovering altitude and weight can be found, as shown on Figure 7.2.

The limiting variable is the maximum throttle setting of 100 %. Thus a maximum performance curve exists as a function of the maximum weight and altitude at maximum throttle setting. Determining the maximum hovering height versus weight with a thrust margin (excess thrust) is done by setting the throttle setting at fixed value below 100 %. The model assumes a linear relationship between the throttle setting and engine power, so the lower the throttle setting the greater the thrust margin is at hover. However, maintaining a large thrust margin decreases the allowable takeoff weight and maximum hovering altitude.

Two cases exist for the hovering trim point; firstly, Table 7.2, the altitude is fixed and the throttle setting is the trim variable; and secondly, Table 7.3, the throttle setting is fixed and the altitude is the variable.

Note, position $z_i < -2\,\text{m}$ (height of CG from un-sprung landing) to ensure that the landing gear is not partially supporting the Jetpack weight.

Figure 7.2 is made by keeping the throttle setting fixed and trimming for

Table 7.2: Throttle setting is the trim variable and height is fixed

State derivative and output requirements	State and input trim variables with initial guess	Non-zero state and input fixed variables
$\dot{w}_f = 0$	$\tau = 90\,\%$	$z_i = -10\,\mathrm{m}$
$\dot{P} = 0$	$P = 120\,\mathrm{kW}$	

Table 7.3: Throttle setting is fixed and height is the trim variable

State derivative and output requirements	State and input trim variables with initial guess	Non-zero state and input fixed variables
$\dot{w}_f = 0$	$z_i = -10\,\mathrm{m}$	$\tau = 90\,\%$
$\dot{P} = 0$	$P = 120\,\mathrm{kW}$	

the unknown air density, which is related to the altitude by equations B.3.1 to B.3.4. This is repeated for a number of different takeoff weights and thrust margins to produce the chart. The *hovering ceiling versus takeoff weight* chart is the primary means of assessing the operating performance for a VTOL aircraft, such as a helicopter or the Jetpack. It shows the relationship between takeoff weight and density altitude, which is used to determine the allowable payload for the given operating altitude. It can be seen from the chart that the hovering altitude quickly diminishes with increasing takeoff weight. For example the maximum altitude of the P-11C, which was typically flown at a weight of 2158 N (thrust margin of $1-2158\,\mathrm{N}/2649\,\mathrm{N} = 19\,\%$), is approximately 800 m at standard atmospheric conditions. It must be noted that at this point there is no additional thrust, hence manoeuvering performance is severely reduced.

7.3 Vertical Climb Trim Points

The vertical climb trim points determine the quasi static equilibrium condition of the Jetpack in pure vertical motion, that is the Jetpack is ascending straight up. The vertical climb trim point is a quasi static trim point, meaning that a true steady state condition does not actually exist. This is because the air density changes with altitude, and hence, the power and thrust also change with altitude. For example, if a given altitude and throttle setting are used to calculate a steady state climb speed, and these conditions are then used as initial conditions in the model, the increase in altitude due to the climbing motion will decrease the power and thrust, thus the climb speed will decrease. This is also true in reality, for the Jetpack, fixed wing, and rotor wing aircraft alike.

The vertical climb trim point can be calculated in three ways. Table 7.4 shows the setting for the vertical climb trim point based on fixed throttle setting and height, z_i, with the climb velocity as the trim variable. This case is useful for calculating the expected climb velocity for a given throttle setting and height. Table 7.5 shows the settings required to determine the height for

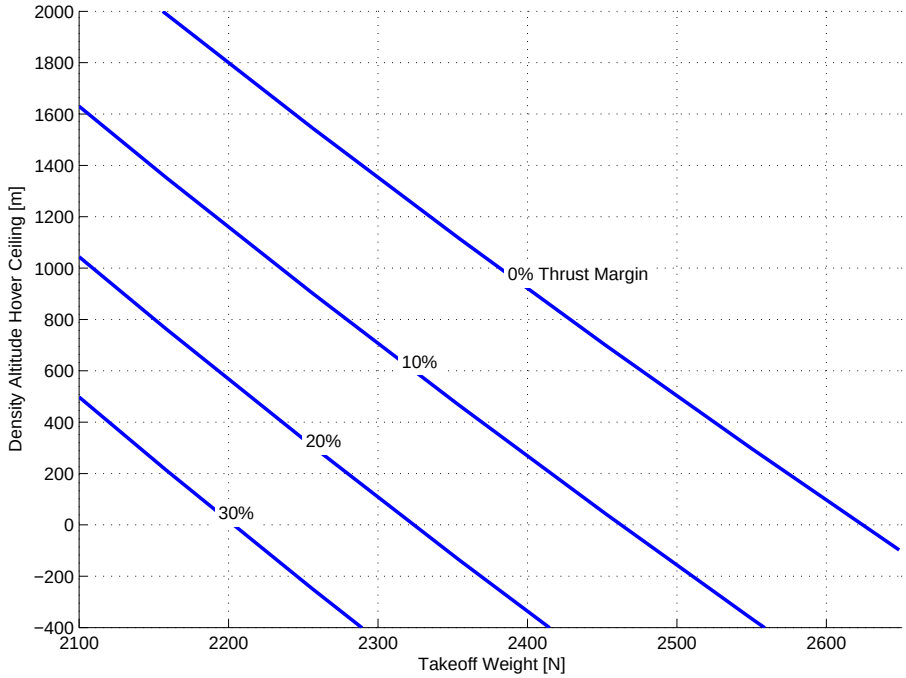

Figure 7.2: Hover ceiling versus takeoff weight for the Martin Jetpack P-11C

a given throttle setting and climb velocity. Table 7.6 evaluates the throttle setting for a given climb speed and height. This case requires the use of the air speed output, V_{air}, as both throttle setting and velocity in body z direction, w_f, need to be trimmed for a given height.

Table 7.4: Throttle and height fixed, w_f (velocity in body z direction) is trim variable

State derivative and output requirements	State and input trim variables with initial guess	Non-zero state and input fixed variables
$\dot{w}_f = 0$	$w_f = -10\,\mathrm{m/s}$	$\tau = 100\,\%$
$\dot{P} = 0$	$P = 120\,\mathrm{kW}$	$z_i = -10\,\mathrm{m}$

Table 7.5: Throttle setting and w_f (velocity in body z direction) fixed, height is trim variable

State derivative and output requirements	State and input trim variables with initial guess	Non-zero state and input fixed variables
$\dot{w}_f = 0$	$z_i = -10\,\mathrm{m}$	$\tau = 100\,\%$
$\dot{P} = 0$	$P = 120\,\mathrm{kW}$	$w_f = -10\,\mathrm{m/s}$

The trim point conditions described in Table 7.5 are used to develop the climb rate versus takeoff weight chart, Figure 7.3. This chart is made by iterating for a range of climb speeds and takeoff weights to obtain the trim altitude. From Figure 7.3, when the Jetpack is operating at high thrust margins (low weight) high climb rates at sea level altitude can be achieved. For example for

Table 7.6: Height fixed, throttle setting and w_f (velocity in body z direction) are trim variables for a given airspeed V_{air}.

State derivative and output requirements	State and input trim variables with initial guess	Non-zero state and input fixed variables
$\dot{w}_f = 0$	$\tau = 100\,\%$	$z_i = -10\,\mathrm{m}$
$V_{air} = 5\,\mathrm{m/s}$	$w_f = -10\,\mathrm{m/s}$	
$\dot{P} = 0$	$P = 120\,\mathrm{kW}$	

a weight of 2158 N at sea level conditions a climb rate of 13 m/s is obtainable, which is a high performing climb rate when compared to general aviation aircraft. However, this climb rate quickly diminishes with altitude. This is due to reductions in both engine power and aerodynamic lift with decreasing air density.

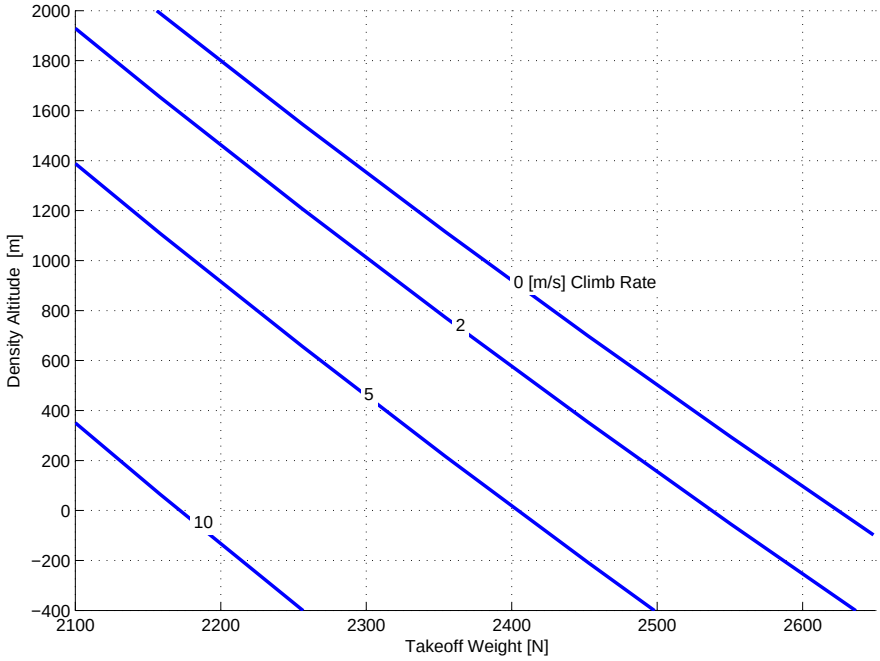

Figure 7.3: Vertical climb rate versus takeoff weight for the Martin Jetpack P-11C

7.4 Longitudinal Level Flight Trim Points

Longitudinal trimmed level flight refers to the aircraft being flown at steady state conditions in the forwards direction maintaining constant: airspeed, attitude, heading, and altitude, as shown on Figure 7.1c. The level flight condition is an important steady state condition as it describes the fundamental function of an aircraft, which is to fly from point A to point B. To maintain level flight trim the sums of all force and moments about the aircraft's centre of gravity must equate to zero. Thus the lift forces opposes the weight, horizontal thrust opposes the drag, and the net moments equate to zero. Typically, to

fly at a different airspeed a change in attitude must be made to the aircraft, which unbalances the aircraft (net moment no longer equates to zero). To regain trimmed flight a means of creating an opposing pitch moment is necessary. The Jetpack uses a similar means as an aeroplane by deflecting the pitch vanes, which are equivalent to the horizontal stabiliser on an aeroplane, to create a lift force and moment about the centre of gravity to oppose any unbalanced moment and trim the aircraft.

An aircraft must be trimmable for level flight over the flyable range of angles of attack [80], otherwise the aircraft would not be flyable. In the case of an aeroplane this implies that the aeroplane can be trimmed from the minimum airspeed (level flight stall airspeed) to the maximum allowable/obtainable airspeed. For the Jetpack the trimmable level flight range begins from hover condition and extends up to the maximum obtainable airspeed, which is limited by either the duct thrust or pitch vane saturation.

The longitudinal level flight trim point for the Jetpack is a function of: power, thrust, airspeed, attitude, pitch vane deflection and altitude. For a given altitude and attitude the thrust vector will have a vertical component to offset the weight and a horizontal component to oppose the drag force, which is a function of the airspeed. The unbalanced aerodynamic moment created by the motion of the Jetpack is opposed by the moment created by the pitch vane deflection.

Three cases for the longitudinal level flight trim conditions have been identified[1]. For each of the longitudinal trim cases the height z_i is fixed and the flight path angle is set to zero, $\gamma = 0$. The trim points are calculated by fixing either the pitch attitude Θ, the pitch vane setting η, or the airspeed V_{air}, and then solving the Jetpack EOM for the two unknown values of either Θ, η, or V_{air}. Refer to Tables 7.9 to 7.8 for the longitudinal level flight trim conditions.

Table 7.7: Longitudinal level flight trim points, height and pitch vane fixed

State derivative and output requirements	State and input trim variables with initial guess	Non-zero state and input fixed variables
$\dot{u_f} = 0$	$u_f = 2\,\mathrm{m/s}$	$z_i = -10\,\mathrm{m}$
$\dot{w_f} = 0$	$w_f = -0.5\,\mathrm{m/s}$	$\eta = 5^\circ$
$\dot{q} = 0$	$\Theta = -0.17\,\mathrm{rad}$	
$\gamma = 0$	$PitchRateLimiter = 5^\circ$	
$\dot{PitchRateLimiter} = 0$	$\tau = 90\,\%$	
$\dot{P} = 0$	$P = 120\,\mathrm{kW}$	

The longitudinal performance of the P11-C Jetpack is shown on Figure 7.4; it is created by iterating the trim point conditions described by Table 7.9 and iterating for a range of attitudes until the EOM become un-trimmable, in this case due to maximum engine power. Figure 7.4 shows how the airspeed, vane deflection, and engine power varies with attitude. Over the trimmable level flight range the airspeed versus attitude relationship is approximately linear,

[1]Note, additional cases can be derived using other parameters.

Table 7.8: Longitudinal level flight trim points, height and airspeed fixed

State derivative and output requirements	State and input trim variables with initial guess	Non-zero state and input fixed variables
$\dot{u_f} = 0$	$u_f = 2\,\mathrm{m/s}$	$z_i = -10\,\mathrm{m}$
$\dot{w_f} = 0$	$w_f = -0.5\,\mathrm{m/s}$	
$\dot{q} = 0$	$\eta = 5°$	
$V_{air} = 5\,\mathrm{m/s}$	$\Theta = -0.17\,\mathrm{rad}$	
$\gamma = 0$	$PitchRateLimiter = 5°$	
$\dot{PitchRateLimiter} = 0$	$\tau = 90\,\%$	
$\dot{P} = 0$	$P = 120\,\mathrm{kW}$	

Table 7.9: Longitudinal level flight trim points, height and pitch attitude fixed

State derivative and output requirements	State and input trim variables with initial guess	Non-zero state and input fixed variables
$\dot{u_f} = 0$	$u_f = 2\,\mathrm{m/s}$	$z_i = -10\,\mathrm{m}$
$\dot{w_f} = 0$	$w_f = -0.5\,\mathrm{m/s}$	$\Theta = -0.17\,\mathrm{rad}$
$\dot{q} = 0$	$\eta = 5°$	
$\gamma = 0$	$PitchRateLimiter = 5°$	
$\dot{PitchRateLimiter} = 0$	$\tau = 90\,\%$	
$\dot{P} = 0$	$P = 120\,\mathrm{kW}$	

which allows for easy prediction of the airspeed based on aircraft attitude. The pitch vane deflection initially increases with airspeed and then decreases to the negative vane deflection limit with increasing attitude.

The large variation of the vane deflection highlights the large change in the centre of pressure of the Jetpack, which is due to the varying duct moment with airspeed and angle of attack. The switch from positive to negative vane deflection shows that the net Jetpack moment, excluding the pitch vane moment, has also changed from positive to negative. A positive pitch moment is favourable as the aircraft has a natural tendency to return to the hover attitude, while a negative pitch moment is unfavourable as it requires increased pitch vane deflection to return the aircraft to hover attitude.

The power versus attitude shows there is an optimum flight speed where the power and the fuel consumption is a minimum, which occurs approximately between 25° to 35°. This occurs due to aerodynamic lift forces sharing the weight of the Jetpack.

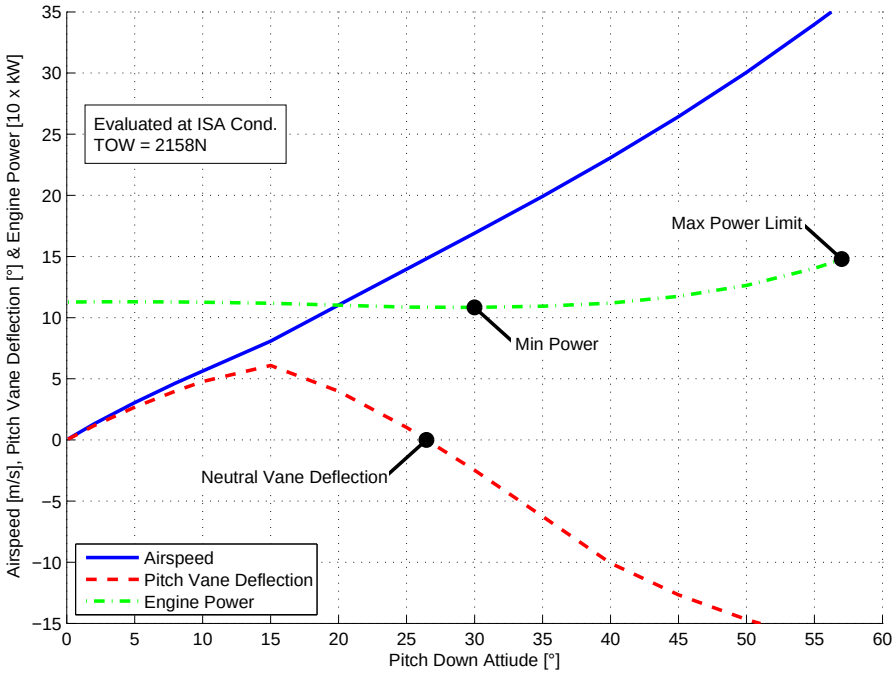

Figure 7.4: Longitudinal performance versus pitch down/forward attitude for the P-11C Jetpack

7.5 Longitudinal Climb Trim Points

The longitudinal climb trim point, Figure 7.1d, calculates the quasi equilibrium condition of a steady state climb with forwards motion. This trim point provides an insight into finding the best rate of climb, which is a useful aircraft performance parameter. This trim point is calculated in a similar way to the longitudinal level trim point with the flight path angle γ set to a none zero value. The settings for the two identified cases are shown in Tables 7.10 and 7.11.

Table 7.10: Longitudinal climb: height, flight path angle and airspeed fixed

State derivative and output requirements	State and input trim variables with initial guess	Non-zero state and input fixed variables
$\dot{u_f} = 0$	$u_f = 2\,\mathrm{m/s}$	$z_i = -10\,\mathrm{m}$
$\dot{w_f} = 0$	$w_f = -0.5\,\mathrm{m/s}$	
$\dot{q} = 0$	$\eta = 5°$	
$V_{air} = 5\,\mathrm{m/s}$	$\Theta = -0.17\,\mathrm{rad}$	
$\gamma = 0.17\,rad$	$PitchRateLimit = 5°$	
$\dot{PitchRateLimit} = 0$	$\tau = 90\,\%$	
$\dot{P} = 0$	$P = 120\,\mathrm{kW}$	

Table 7.11: Longitudinal climb: height, throttle setting, and pitch attitude fixed

State derivative and output requirements	State and input trim variables with initial guess	Non-zero state and input fixed variables
$\dot{u_f} = 0$	$u_f = 2\,\mathrm{m/s}$	$z_i = -10\,\mathrm{m}$
$\dot{w_f} = 0$	$w_f = -0.5\,\mathrm{m/s}$	$\tau = 100\,\%$
$\dot{q} = 0$	$\eta = 5°$	$\Theta = -0.17\,\mathrm{rad}$
$\dot{PitchRateLimit} = 0$	$PitchRateLimit = 5°$	
$\dot{P} = 0$	$P = 120\,\mathrm{kW}$	

The longitudinal climb performance of the P-11C Jetpack is shown on Figure 7.5. Is developed by iterating the conditions described in Table 7.11 for a range of pitch attitudes from hovering to high speed forwards flight. Figure 7.5 shows how the vertical climb speed diminishes with increasing pitch attitude. It can be seen that the best vertical climb speed is achieved at the hovering attitude. The vertical climb speed diminishes quickly with increasing attitude above 30°, this is due to the power being absorbed by the high aerodynamic drag forces at these attitudes/speeds. Interestingly, as the aircraft takeoff weight increases the vertical climb speed versus attitude is nearly constant between 0° to 25°, this is due to the increased lift force with airspeed supplementing the total lift force.

7.6 Lateral Level Flight Trim Points

The lateral level trim point, Figure 7.1e, is the steady state sidewards motion of the Jetpack at a constant height. This trim point is essentially the same as the longitudinal level trim point, 7.4, with the difference being that lateral trim is about the Jetpack's x axis instead of the y axis. Hence, substituting the longitudinal variables (u, q, Θ, η, and $PitchRateLimite$) from Tables 7.7 to 7.9 for the lateral variables (v, p, Φ, ξ, and $RollRateLimit$), respectively, yields the equivalent lateral level trim settings, Tables 7.12 to 7.14.

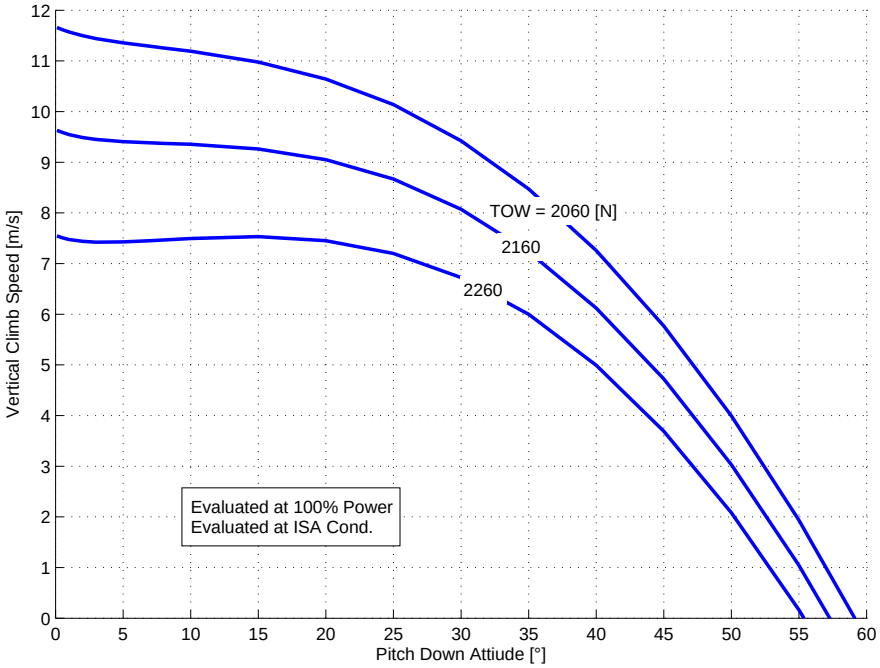

Figure 7.5: Longitudinal climb rate performance for P-11C Jetpack, showing vertical climb speed versus attitude at maximum power at standard ISA conditions.

Table 7.12: Lateral level trim point, height and roll vane setting fixed

State derivative and output requirements	State and input trim variables with initial guess	Non-zero state and input fixed variables
$\dot{v_f} = 0$	$v_f = 2\,\mathrm{m/s}$	$z_i = -10\,\mathrm{m}$
$\dot{w_f} = 0$	$w_f = -0.5\,\mathrm{m/s}$	$\xi = 5°$
$\dot{p} = 0$	$\Phi = -0.17\,\mathrm{rad}$	
$\dot{\gamma} = 0$	$RollRateLimit = 5°$	
$RollRateLimit = 0$	$\tau = 90\,\%$	
$\dot{P} = 0$	$P = 120\,\mathrm{kW}$	

Table 7.13: Lateral level trim point, height and airspeed fixed

State derivative and output requirements	State and input trim variables with initial guess	Non-zero state and input fixed variables
$\dot{v_f} = 0$	$v_f = 2\,\mathrm{m/s}$	$z_i = -10\,\mathrm{m}$
$\dot{w_f} = 0$	$w_f = -0.5\,\mathrm{m/s}$	
$\dot{p} = 0$	$\xi = 5°$	
$V_{air} = 5\,\mathrm{m/s}$	$\Phi = -0.17\,\mathrm{rad}$	
$\gamma = 0$	$RollRateLimit = 5°$	
$\dot{RollRateLimit} = 0$	$\tau = 90\,\%$	
$\dot{P} = 0$	$P = 120\,\mathrm{kW}$	

Table 7.14: Lateral level trim point, height and roll attitude fixed

State derivative and output requirements	State and input trim variables with initial guess	Non-zero state and input fixed variables
$\dot{v_f} = 0$	$v_f = 2\,\mathrm{m/s}$	$z_i = -10\,\mathrm{m}$
$\dot{w_f} = 0$	$w_f = -0.5\,\mathrm{m/s}$	$\Phi = -0.17\,\mathrm{rad}$
$\dot{p} = 0$	$\xi = 5°$	
$\gamma = 0$	$RollRateLimit = 5°$	
$\dot{RollRateLimit} = 0$	$\tau = 90\,\%$	
$\dot{P} = 0$	$P = 120\,\mathrm{kW}$	

Using the conditions described in Table 7.14, Figure 7.6 could be created by solving for the lateral trim points for a range of given roll attitudes. Unlike the longitudinal plane the lateral plane shows that the roll vane deflection increases approximately linearly with both airspeed and attitude. Maximum roll vane deflection becomes the limiting condition that prevents further increases in lateral attitude. However, unlike in the longitudinal plane where the aircraft would experience an unstable negative moment, in the lateral plane if the attitude is increased beyond the roll vane limit, the natural tendency of the aircraft would be to decrease the attitude, which is favourable.

7.7 Lateral Climb Trim Points

The lateral climb trim point, Figure 7.1f, is the quasi steady state sidewards climb of the Jetpack at a given height. This trim point is essentially the same as the longitudinal climb trim point, 7.5, the difference being that lateral trim is about the Jetpack's x axis instead of the y axis. Hence, substituting the longitudinal variables (u, q, Θ, η, and $PitchRateLimit$) from Tables 7.10 to 7.11 for the lateral variables (v, p, Φ, ξ, and $RollRateLimit$), respectively, yields the equivalent lateral level trim settings, Tables 7.15 to 7.16.

The lateral climb performance of the P-11C Jetpack is shown on Figure 7.7. It is developed by iterating the conditions described in Table 7.16 for a range of roll attitudes from hovering to high speed forwards flight. It can be seen on Figure 7.7 that the best vertical climb speed is achieved at the hovering attitude and the vertical climb speed diminishes quickly with increasing roll

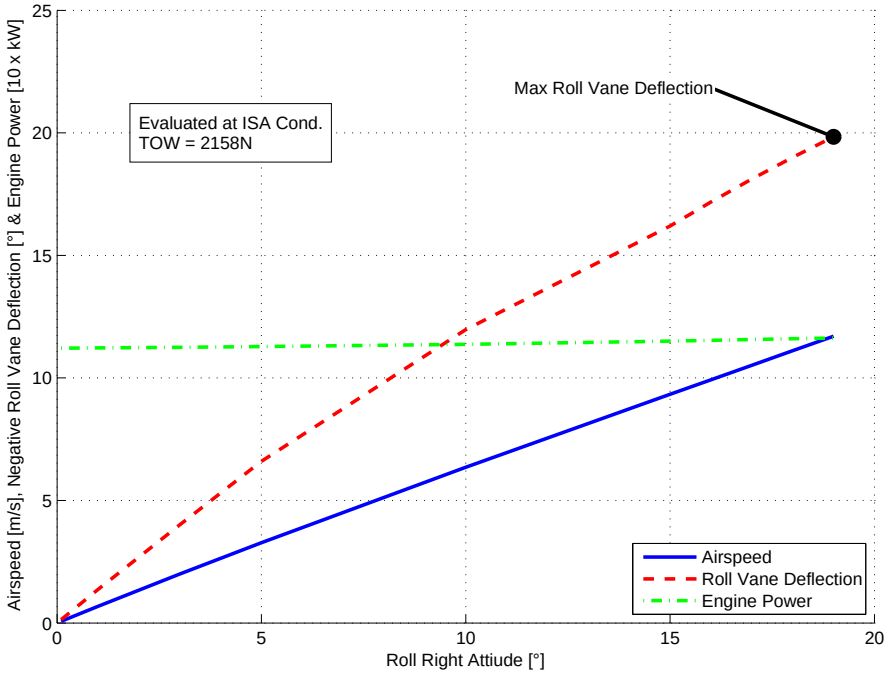

Figure 7.6: Lateral performance versus roll left attitude for the Martin Jetpack P-11C.

Table 7.15: Lateral climb: height, flight path angle and airspeed fixed

State derivative and output requirements	State and input trim variables with initial guess	Non-zero state and input fixed variables
$\dot{vf} = 0$	$v_f = 2\,\mathrm{m/s}$	$z_i = -10\,\mathrm{m}$
$\dot{w_f} = 0$	$w_f = -0.5\,\mathrm{m/s}$	
$\dot{p} = 0$	$\xi = 5°$	
$V_{air} = 5\,\mathrm{m/s}$	$\Phi = -0.17\,\mathrm{rad}$	
$\gamma = 0.17\,rad$	$RollRateLimit = 5°$	
$\dot{RollRateLimit} = 0$	$\tau = 90\%$	
$\dot{P} = 0$	$P = 120\,\mathrm{kW}$	

Table 7.16: Lateral climb: height, throttle setting, and roll attitude fixed

State derivative and output requirements	State and input trim variables with initial guess	Non-zero state and input fixed variables
$\dot{v_f} = 0$	$vf = 2\,\mathrm{m/s}$	$z_i = -10\,\mathrm{m}$
$\dot{w_f} = 0$	$w_f = -0.5\,\mathrm{m/s}$	$\tau = 100\%$
$\dot{p} = 0$	$\xi = 5°$	$\Phi = -0.17\,\mathrm{rad}$
$\dot{RollRateLimit} = 0$	$RollRateLimit = 5°$	
$\dot{P} = 0$	$P = 120\,\mathrm{kW}$	

attitude. This is due to the lower ducted-fan dynamic lift effect as measured and explained in Chapter 6.

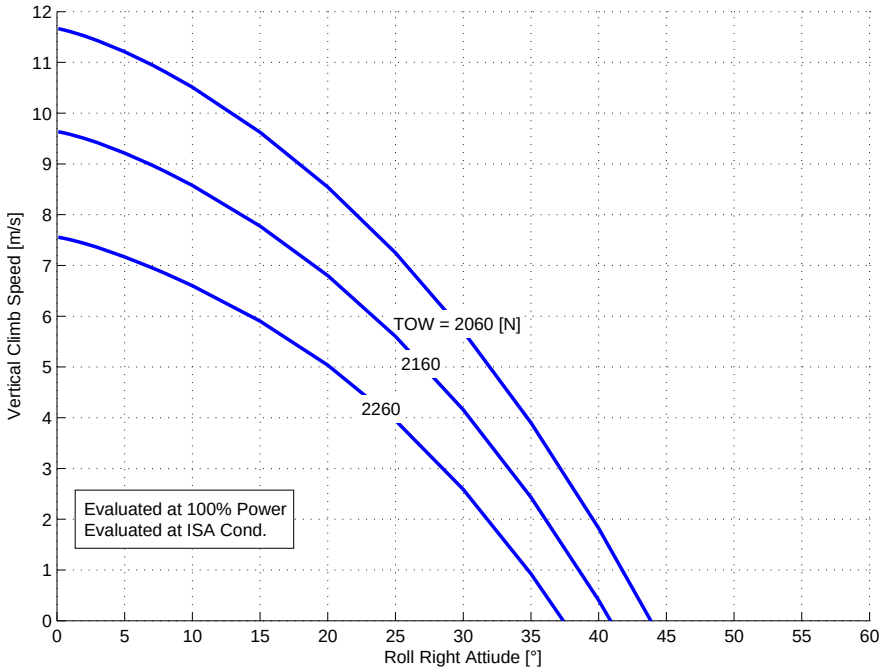

Figure 7.7: Latitudinal climb rate performance for P-11C Jetpack, showing vertical climb speed versus roll attitude at maximum power at standard ISA conditions.

7.8 Longitudinal-Lateral (Skewed) Level Trim Points

Since the Jetpack has the ability to hover it can also fly at mixed roll and pitch attitudes, where the level steady state flight at constant roll and pitch attitudes is described by the combination of longitudinal and lateral level trim points, as shown by the combination of Figures 7.1c, 7.1h, and 7.1g. Similarly to the level longitudinal and lateral, three cases have been identified for this trim point. Table 7.17 shows the settings for fixed roll and pitch attitude. Table 7.18 shows the trim settings for fixed roll and pitch vane values. Table 7.19 shows the trim settings for fixed airspeed and track angle χ.

Figure 7.8 shows the level skewed flight performance of the P-11C Jetpack versus pitch and roll attitude, constructed using the conditions described by Table 7.19 and iterated for a number of flight speeds and track angles. Not all attitude and speed combinations are trimmable, which is shown by the termination of the curves on Figure 7.8, as the roll control vanes lack the ability to trim the aircraft.

Table 7.17: Level longitudinal-lateral trim point, height, roll, and pitch attitude fixed

State derivative and output requirements	State and input trim variables with initial guess	Non-zero state and input fixed variables
$\dot{u_f} = 0$	$v_f = 2\,\mathrm{m/s}$	$z_i = -10\,\mathrm{m}$
$\dot{v_f} = 0$	$v_f = -2\,\mathrm{m/s}$	$\Phi = 0 - 0.17\,\mathrm{rad}$
$\dot{w_f} = 0$	$w_f = -0.5\,\mathrm{m/s}$	$\Theta = -0.17\,\mathrm{rad}$
$\dot{p} = 0$	$\xi = 5^\circ$	
$\dot{q} = 0$	$\eta = 5^\circ$	
$\gamma = 0$	$\tau = 90\,\%$	
$\dot{RollRateLimit} = 0$	$RollRateLimit = 5^\circ$	
$\dot{PitchRateLimit} = 0$	$PitchRateLimit = 5^\circ$	
$\dot{P} = 0$	$P = 120\,\mathrm{kW}$	

Table 7.18: Level longitudinal-lateral trim point, height, roll, and pitch vane fixed

State derivative and output requirements	State and input trim variables with initial guess	Non-zero state and input fixed variables
$\dot{u_f} = 0$	$v_f = 2\,\mathrm{m/s}$	$z_i = -10\,\mathrm{m}$
$\dot{v_f} = 0$	$v_f = -2\,\mathrm{m/s}$	$\xi = 5^\circ$
$\dot{w_f} = 0$	$w_f = -0.5\,\mathrm{m/s}$	$\eta = 5^\circ$
$\dot{p} = 0$	$\Phi = 0 - 0.17\,\mathrm{rad}$	
$\dot{q} = 0$	$\Theta = -0.17\,\mathrm{rad}$	
$\gamma = 0$	$\tau = 90\,\%$	
$\dot{RollRateLimit} = 0$	$RollRateLimit = 5^\circ$	
$\dot{PitchRateLimit} = 0$	$PitchRateLimit = 5^\circ$	
$\dot{P} = 0$	$P = 120\,\mathrm{kW}$	

Table 7.19: Level longitudinal-lateral trim point, height, airspeed, and χ fixed

State derivative and output requirements	State and input trim variables with initial guess	Non-zero state and input fixed variables
$\dot{u_f} = 0$	$v_f = 2\,\mathrm{m/s}$	$z_i = -10\,\mathrm{m}$
$\dot{v_f} = 0$	$v_f = -2\,\mathrm{m/s}$	
$\dot{w_f} = 0$	$w_f = -0.5\,\mathrm{m/s}$	
$\dot{p} = 0$	$\xi = 5^\circ$	
$\dot{q} = 0$	$\eta = 5^\circ$	
$\gamma = 0$	$\tau = 90\,\%$	
$\chi = 0.78\,\mathrm{rad}$	$\Phi = 0 - 0.17\,\mathrm{rad}$	
$V_{air} = 5\,\mathrm{m/s}$	$\Theta = -0.17\,\mathrm{rad}$	
$\dot{RollRateLimit} = 0$	$RollRateLimit = 5^\circ$	
$\dot{PitchRateLimit} = 0$	$PitchRateLimit = 5^\circ$	
$\dot{P} = 0$	$P = 120\,\mathrm{kW}$	

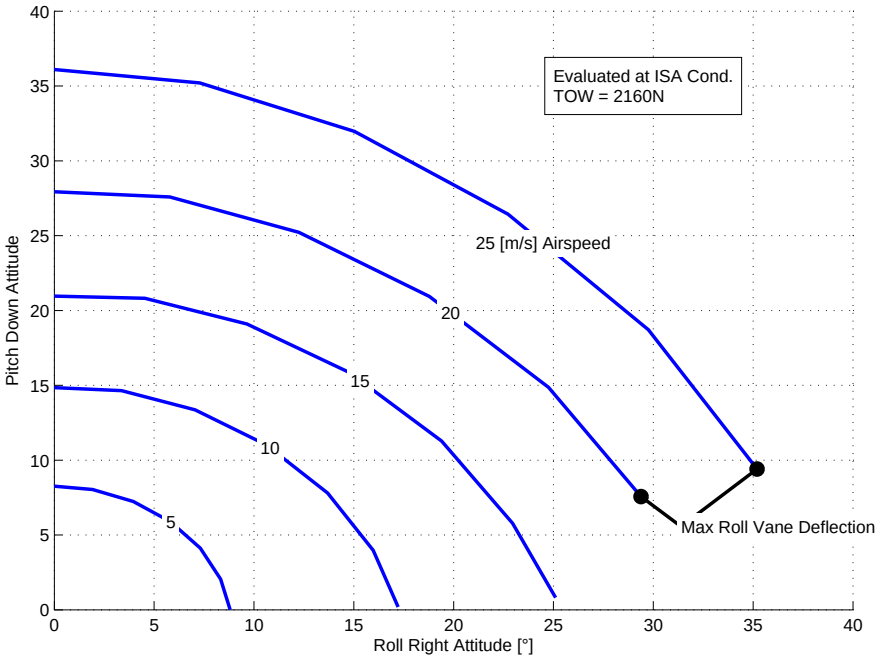

Figure 7.8: Skewed level flight performance for the P-11C Jetpack

7.9 Hover Yaw Turn Trim Points

The Hover yaw turn trim point, Figure 7.1h, is the steady state spinning motion of the Jetpack in a hover. At first glance one would assume that this spinning motion is about the Jetpack's z axis. However, this is not the case, the actual motion is about an axis slightly skewed from z axis. This is due to the antisymmetry of the Jetpack's inertial distribution above and below the Jetpack CG. Mathematically this is shown by the non zero values of the product of inertia terms (non-diagonal terms) of the Jetpack inertia tensor. If the product of inertia terms about the $x-y$ plane are equal to zero, $I_{xz} = I_{zx} = I_{yz} = I_{zy} = 0$, then a trimmed spinning motion aligned to the Jetpack's z axis would be possible. In reality, as the product of inertia terms do exist, small pitch and roll vane inputs are required to dynamically balance the spinning motion of the Jetpack. The maximum rotation speed is limited by the effectiveness of the yaw vanes to counter ram-drag moments created by the ducted-fans during yawing motion.

Three cases for the hover yaw turn have been identified as: Table 7.20 where the yaw rate r has be fixed and the remaining variables are solved, Table 7.21 where the yaw vane ζ has been set and yaw motion solved for, and Table 7.22 where psi-dot $\dot{\Psi}$ has been set and yaw vane setting solved.

Table 7.20: Level yaw turn trim point, height, and yaw rate fixed

State derivative and output requirements	State and input trim variables with initial guess	Non-zero state and input fixed variables
$\dot{u_f} = 0$	$p = 0$	$z_i = -10\,\mathrm{m}$
$\dot{v_f} = 0$	$q = 0$	$r = 6.3\,\mathrm{rad/s}$
$\dot{w_f} = 0$	$\Phi = 0 - 0.17\,\mathrm{rad}$	
$\dot{p} = 0$	$\Theta = -0.17\,\mathrm{rad}$	
$\dot{q} = 0$	$\xi = 5°$	
$\dot{r} = 0$	$\eta = 5°$	
$\dot{\Phi} = 0$	$\zeta = 0°$	
$\dot{\Theta} = 0$	$\tau = 90\,\%$	
$\dot{RollRateLimit} = 0$	$RollRateLimit = 5°$	
$\dot{PitchRateLimit} = 0$	$PitchRateLimit = 5°$	
$\dot{YawRateLimit} = 0$	$YawRateLimit = 0°$	
$\dot{P} = 0$	$P = 120\,\mathrm{kW}$	

Table 7.21: Level yaw turn trim point, height, and yaw vane fixed

State derivative and output requirements	State and input trim variables with initial guess	Non-zero state and input fixed variables
$\dot{u_f} = 0$	$p = 0$	$z_i = -10\,\mathrm{m}$
$\dot{v_f} = 0$	$q = 0$	$\zeta = 15°$
$\dot{w_f} = 0$	$r = 6\,\mathrm{rad/s}$	
$\dot{p} = 0$	$\Phi = -0.17\,\mathrm{rad}$	
$\dot{q} = 0$	$\Theta = -0.17\,\mathrm{rad}$	
$\dot{r} = 0$	$\xi = 5°$	
$\dot{\Phi} = 0$	$\eta = 5°$	
$\dot{\Theta} = 0$	$\tau = 90\,\%$	
$\dot{RollRateLimit} = 0$	$RollRateLimit = 5°$	
$\dot{PitchRateLimit} = 0$	$PitchRateLimit = 5°$	
$\dot{YawRateLimit} = 0$	$YawRateLimit = 15°$	
$\dot{P} = 0$	$P = 120\,\mathrm{kW}$	

Figure 7.9 shows the trimmable yaw turn rate versus yaw vane deflection. At full yaw vane deflection high turn rates are possible. However, in reality these rates may not be obtainable due to the difficultly required to precisely control the aircraft about its rotation axis, which also requires roll and pitch control input.

7.10 Level Banked Turn Trim Points

The level banked turn trim points are the steady state conditions of coordinated banked turns for the Jetpack. A coordinated, or balanced, banked turn for an aircraft involves the aircraft traveling at some speed greater than zero and tilting its lift vector into the direction of the intended turn to achieve a

Table 7.22: Level yaw turn trim point, height and psi-dot fixed

State derivative and output requirements	State and input trim variables with initial guess	Non-zero state and input fixed variables
$\dot{u_f} = 0$	$p = 0$	$z_i = -10\,\mathrm{m}$
$\dot{v_f} = 0$	$q = 0$	
$\dot{w_f} = 0$	$r = 6\,\mathrm{rad/s}$	
$\dot{p} = 0$	$\Phi = 0 - 0.17\,\mathrm{rad}$	
$\dot{q} = 0$	$\Theta = -0.17\,\mathrm{rad}$	
$\dot{r} = 0$	$\xi = 5°$	
$\dot{\Phi} = 0$	$\eta = 5°$	
$\dot{\Theta} = 0$	$\zeta = 5°$	
$\dot{\Psi} = 3\,\mathrm{rad/s}$	$\tau = 90\,\%$	
$\dot{RollRateLimit} = 0$	$RollRateLimit = 5°$	
$\dot{PitchRateLimit} = 0$	$PitchRateLimit = 5°$	
$\dot{YawRateLimit} = 0$	$YawRateLimit = 5°$	
$\dot{P} = 0$	$P = 120\,\mathrm{kW}$	

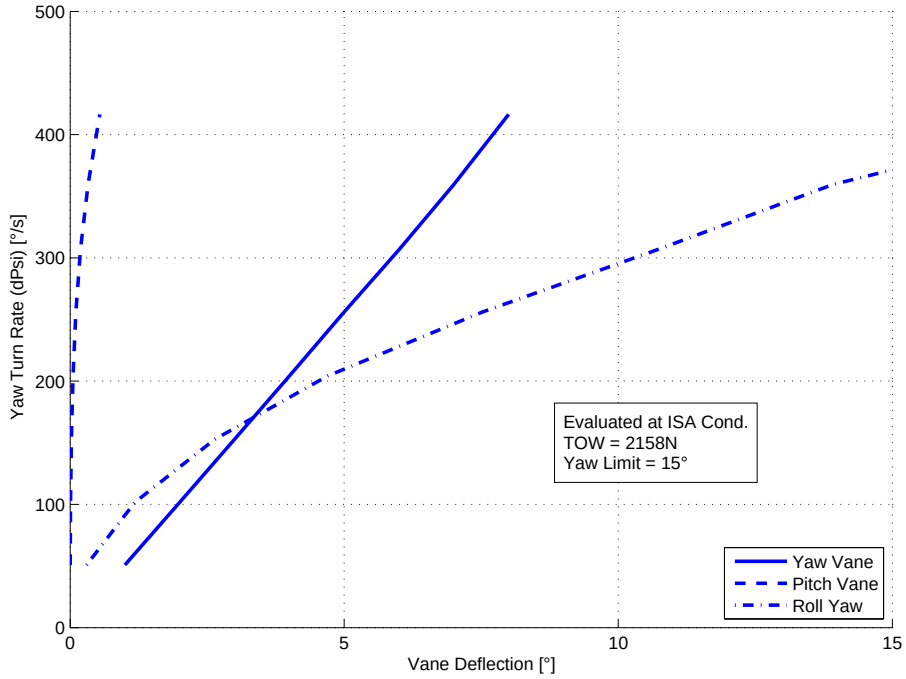

Figure 7.9: Level hovering yaw turn versus yaw vane deflection for the P-11C Jetpack

change in heading Ψ, at a constant radius R, while maintaining no side slip β. This tilting of the lift vector for the banked turn is necessary, since the aircraft is traveling at some speed and needs to generate a centripetal force to create an acceleration towards the direction of the intended turn. To achieve a banked turn an aircraft needs to have a constant angular rotational speed (p, q, and r) about all three axis of the aircraft. For the case the aircraft is traveling forwards the side slip angle needs to be zero $\beta = 0$ to maintain a coordinated turn, which means that the airflow approaching the aircraft is parallel to the aircraft's longitudinal plane, xz plane. The level bank turn is described by the combination of free body diagrams in Figures 7.1c, 7.1e, 7.1h, and 7.1i The Jetpack being a VTOL aircraft is able to achieve steady banked turns for any value of side slip angle β. Hence, the Jetpack can perform a bank turn with the pilot facing towards the centre of the turn throughout the turn manoeuvre. This manoeuvre is accomplished for a side slip value of $\beta = \pm\frac{\pi}{2}$ rad. Table 7.23 shows the trim conditions for a given turn rate $\dot{\Psi}$ value (heading rate change). Table 7.24 shows the trim settings for bank angles derived from a given throttle setting, these conditions can be used to derive maximum possible bank/turn rates.

Table 7.23: Height, airspeed, and psi-dot fixed

State derivative and output requirements	State and input trim variables with initial guess	Non-zero state and input fixed variables
$\dot{u_f} = 0$	$v_f = 2\,\mathrm{m/s}$	$z_i = -10\,\mathrm{m}$
$\dot{v_f} = 0$	$v_f = -2\,\mathrm{m/s}$	
$\dot{w_f} = 0$	$w_f = -0.5\,\mathrm{m/s}$	
$\dot{p} = 0$	$p = 0$	
$\dot{q} = 0$	$q = 0$	
$\dot{r} = 0$	$r = 0$	
$\dot{\Phi} = 0$	$\Phi = -0.17\,\mathrm{rad}$	
$\dot{\Theta} = 0$	$\Theta = -0.17\,\mathrm{rad}$	
$\dot{\Psi} = 1\,\mathrm{rad/s}$	$\xi = 5°$	
$V_{air} = 5\,\mathrm{m/s}$	$\eta = 5°$	
$\beta = 0$	$\zeta = 0°$	
$\gamma = 0$	$\tau = 90\,\%$	
$\dot{RollRateLimit} = 0$	$RollRateLimit = 5°$	
$\dot{PitchRateLimit} = 0$	$PitchRateLimit = 5°$	
$\dot{YawRateLimit} = 0$	$YawRateLimit = 0°$	
$\dot{P} = 0$	$P = 120\,\mathrm{kW}$	

Figures 7.10 shows the forward (side slip $\beta = 0$) level flight banked turn performance for the P-11C, which was produced using the conditions described in Table 7.23. The results show that moderate level flight bank angles of 30° are achievable, but the turn rate quickly diminishes with increasing airspeed. The level flight banked turn performance can be improved by increasing the Jetpack load factor, refer to section 3.4.

The major implication of the low turn rate at high speeds is that the turn radius becomes large, which hinders the ability to operate in confined areas at speed. For example in a search and rescue mission, where searching a large

Table 7.24: Height, airspeed, and throttle fixed

State derivative and output requirements	State and input trim variables with initial guess	Non-zero state and input fixed variables
$\dot{u_f} = 0$	$v_f = 2\,\mathrm{m/s}$	$z_i = -10\,\mathrm{m}$
$\dot{v_f} = 0$	$v_f = -2\,\mathrm{m/s}$	$\tau = 90\,\%$
$\dot{w_f} = 0$	$w_f = -0.5\,\mathrm{m/s}$	
$\dot{p} = 0$	$p = 0$	
$\dot{q} = 0$	$q = 0$	
$\dot{r} = 0$	$r = 0$	
$\dot{\Phi} = 0$	$\Phi = -0.17\,\mathrm{rad}$	
$\dot{\Theta} = 0$	$\Theta = -0.17\,\mathrm{rad}$	
$V_{air} = 5\,\mathrm{m/s}$	$\xi = 5°$	
$\beta = 0$	$\eta = 5°$	
$\gamma = 0$	$\zeta = 0°$	
$\dot{RollRateLimit} = 0$	$RollRateLimit = 5°$	
$\dot{PitchRateLimit} = 0$	$PitchRateLimit = 5°$	
$\dot{YawRateLimit} = 0$	$YawRateLimit = 0°$	
$\dot{P} = 0$	$P = 120\,\mathrm{kW}$	

area in minimal time is the objective, the Jetpack may not be able to directly track a winding road or stream at high speed and will therefore have to fly at a lower speed to follow the road or stream, which increases the flight time and decreases the usefulness of the Jetpack for the mission.

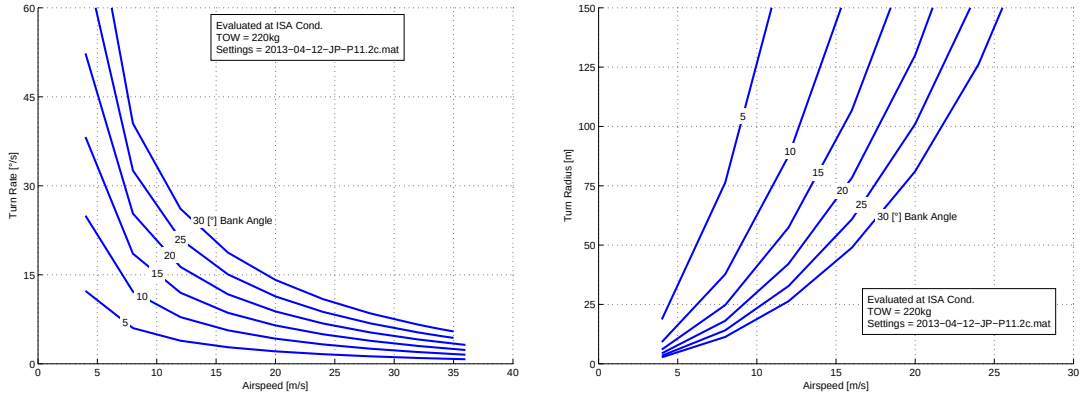

(a) Turn rate versus airspeed

(b) Turn radius versus airspeed

Figure 7.10: Level bank turn performance for the Martin Jetpack P-11C

7.11 Summary

As well as demonstrating the capabilities of the Jetpack the charts shown in this chapter also give insight into how the Jetpack could be improved to further expand the flight envelope. Increasing the thrust margin by either reducing the takeoff weight, or increasing the thrust force, would significantly increase

the flight performance of the Jetpack by allowing flight operations at higher density altitudes. Turbocharging the engine would also reduce the affects on increasing density altitude, as engine power could be maintained.

A constant centre of pressure in both pitch and roll vanes would allow the Jetpack to be trimmed with minimal roll and pitch vane deflection, which reduces vane drag and allows for greater manoeuvrability. A constant centre of pressure also allows the aircraft to be design so that the control vanes do not saturate at maximum deflection, and hence, restrict the aircraft, as was experienced by P-11A Jetpack.

It can be seem from Figure 7.4 that to improve top end speed the Jetpack would need either greater power/thrust or the ability to produce lift in a more horizontal position where the profile and duct induced drag is less. The latter would require the use of a wing to produce the lift force necessary for level flight and also require a transition manoeuvre from one flight phase to the other.

This chapter has explained the various trim conditions that are possible for the Jetpack and how to solve for these trim conditions using the flight model. Performance charts for the P-11C Jetpack were made for the various trim conditions and shown together with the flight capabilities of the P-11C Jetpack, and hence, the flight envelope. Utilizing the Jetpack model these charts can be made for any configuration of the Jetpack; Appendix E contains charts for the P-11E Jetpack. However, the performance predicted by the model in this chapter needs to be validated against Jetpack flight performance, which is the topic of the next chapter.

Chapter 8

Model Validation

"For once you have tasted flight you will walk the earth with your eyes turned skywards, for there you have been and there you will long to return."
Leonardo da Vinci

This Chapter explains how the model described in Chapter 4 is validated using recorded flight data. The Chapter begins with an explanation of the flight testing performed and describes the typical flight profiles used to expand the Jetpack's flight envelope and to obtain flight data needed to validate the model. A summary of the progress made, as a result of this research, from test flying the P-11 series prototypes is explained using flight data recorded from these flights. The method developed by the author used to analyse the flight data is explained. The flight data is then compared to the model in two ways. Firstly, a trim comparison which compares steady state performance, and secondly, a dynamic comparison that uses the recorded flight data from a flight as the model inputs to create a simulated reproduction of the flight.

8.1 Description of Flight Testing

This section gives insight into how the test flying of the Jetpack prototypes is performed.

Location
Various locations have been used for test flying the Jetpack prototypes. Initially the P-11A was flown indoors as it did not have the aerodynamic control to fly in outdoor conditions; even calm wind conditions proved too much for the P-11A. Successor prototypes are all flown outdoors, above spacious level fields, in rural areas due to the excessive loud noise, over 100 dB, created by the Jetpack. The P-11E Jetpack has also successfully hovered and flown at moderate speeds at heights of 4 m to 6 m above water.

Setup
For all the test flying described in this chapter the Jetpack prototypes were flown as unmanned aerial vehicles (UAV) by visual remote control. The remote control system employed to fly the Jetpack is similar to typical remote control hobby aircraft, with the exception that the control inputs from the pilot are

applied via a transmitter backpack that shares the control arrangement of the actual manned Jetpack. For the unmanned prototypes, changes to the airframe were made so it could accommodate ballast to obtain the desired CG positions.

Fight Team Description
The typical flight team for testing the Jetpack prototypes consist of four people: pilot, engine technician, and two handlers. The pilot flies the Jetpack, unmanned, by remote control. Feedback from the pilot is essential for control tuning and elevating the dynamic performance and handling of the Jetpack. The engine technician monitors the engine performance both live (on-line) and off-line, and makes the required modifications and repairs to the aircraft. The two handlers are used to physically assist the Jetpack's attitude by forcing corrective moments into the hovering aircraft during takeoff and landing phases. The author takes the handler role in the flight team, which also requires documenting the Jetpack's performance and assisting control tuning.

Takeoff and Landing
The takeoff is performed with the handlers standing either side of the Jetpack and the pilot standing approximately 10 m behind the Jetpack. During the initial stage of takeoff, below 1 m above the ground, the control vanes have reduced effectiveness as described in section 5.1, this reduced effectiveness makes the Jetpack difficult for the pilot to handle, especially in strong wind and turbulent conditions. The handlers thus help the pilot by physically guiding the aircraft in the intended direction.

The landing phase has greater difficulty than the takeoff as the descent rate must also be controlled and the aircraft must be landed level to avoid crashing the aircraft. Hence, the handlers are actively aiding the pilot by guiding the aircraft to the ground.

Hover
Typically the Jetpack is hovered between 2 m to 4 m above the ground. During hover, the flight speed is keep low, below 10 km/h (2.8 m/s), refer to Figure 8.1 which classifies the flight speeds for the Jetpack. The hover phase is essential for both takeoff and landing, as the aircraft takes-off into the hovering phase and needs to be in the hovering phase before commencing a landing. The hovering phase is also the primary flight phase used for control tuning. Typically, once the aircraft is tuned for hover it only requires minimal fine tuning thereafter. Typically, the fine tuning involves increasing the outer gains to allow for greater airspeeds/attitudes, and increasing inner gains and saturation limits to increase responsiveness and angular motion of the Jetpack.

Straights
Straight flights are the simplest flight involving motion and involve the Jetpack being tilted forwards to a pitch down attitude to increase its forward

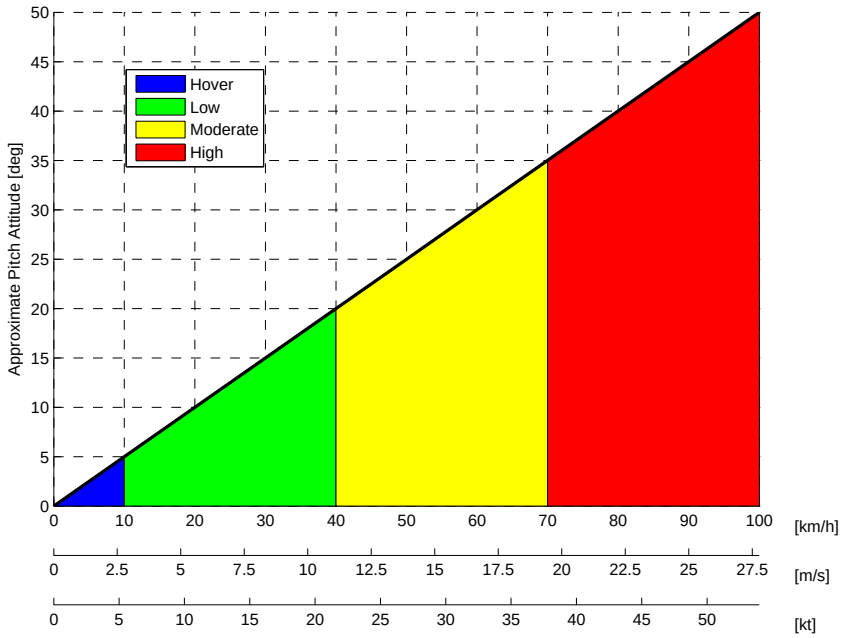

Figure 8.1: Classification of Jetpack flight speeds with approximate pitch forwards/down attitude. The upper limits of the low, moderate, and high speed zones are the Martin Aircraft Company flight speed targets of FP1, FP2, and FP3. Where *FP* is short for *Flight Performance*.

speed. Once it has traveled a set distance, approximately 20 m to 50 m, the forwards motion is decelerated by tilting back to the hover attitude. The aircraft is returned by titling backwards, a pitch up attitude, so the Jetpack flies backwards to the starting position. The heading and drift are maintained by corrective yaw and roll inputs, respectively. Straight flights are also performed in the lateral roll plane by tilting the aircraft left and right. The straight flights allow the aircraft flight envelope to be progressively increased under the flight team supervision by commanding progressively higher attitudes, and hence, airspeeds.

Circuits

Circuits and figure eight patterns are typically flown at heights of 3 m to 8 m above the the ground and involve the aircraft flying with a pitch down attitude, and hence, forwards motion. Typically, the circuits are 100 m to 200 m long (up to 100 m either side of the pilot) and are positioned 20 m to 50 m upwind and in front of the pilot. At the extremity of the circuits the pilot banks the Jetpack to initiate a level bank turn and uses yaw input to coordinate the turn. Circuits are used to expand the flight speed envelope and provide general flight information as these manoeuvres encompass all aspects of flight that a production Jetpack would be required to perform. To date the highest flight speeds obtained are in the moderate speed range where a 15.8 m/s airspeed has been measured on the P-11C Jetpack.

8.2 Analysis of Jetpack Flight Data

The Jetpack prototypes contains an inertial navigation system (Athena INS) that measures the Jetpack's position, attitude, angular rates, translational speeds, and accelerations at approximately 50 Hz. This information along with the joystick command signals is fed into the Jetpack's SAS (stability augmentation system) where the information is used in control algorithms to produced the desired motion of Jetpack. The SAS outputs PWM (pulse width modulation) signals to the servos that control vane deflection and throttle butterfly position. The SAS input and output information is sent to a ground station via blue-tooth telemetry. The ground station converts the information from the Jetpack into a collection of log files that summarize the flight[1].

The multiple files are: attitude data, GPS data, command data, servo data, and system status data. In addition wind data recorded via an ultra sound anemometer is also recorded by the ground station. With exception of the system status data the data files are all time variant files that are recorded at slightly different times; differences of up to 0.006 s occur between the various files. Due to the relatively slow sampling rate of the anemometer (approximately 4 Hz) a larger difference in time occurs between Jetpack data and wind data. For the flight data to be useful and easily analyzed in Matlab®, the data needs to be synchronised and contained in a single file. A synchronisation algorithm was developed by finding the closest time data in each file to the time data in the GPS file, and then saving the data in a single large matrix containing all of the information.

8.3 Flight Testing Progress

This section explains how the flight characteristics have progressed from the P-11A to the P-11E Jetpack prototypes as a direct result from the aerodynamic improvements found from this research. For each prototype examples of the recorded control inputs (pilot commands) are compared to the measured outputs (response of Jetpack) to demonstrate how well the Jetpack follows the pilot commands. It will be shown through the development of the Jetpack prototypes from P-11A to P-11E that better following of outputs to inputs is achieved, which is shown by a reduction of *root mean square errors*, $RMSE$, values and increased commanded values indicating more aggressive improving manoeuvering. In this section $RMSE$ is calculated to indicate the variation of error between the commanded input and the Jeptack's response to provide a metric for well the Jetpack responds to pilot inputs. Although the $RMSE$ provides a quantitative metric of how well the aircraft follows the given inputs, the most important metric is the qualitative pilot rating of how well it flies. Franklin [90] describes that for a pilot to highly rate the handling quality the pilot workload both physical and mental must be minimal. Small precise inputs and/or the requirement for the pilot to lead or anticipate control inputs considerably increases the pilot's mental effort to control the aircraft, thus an aircraft which has these qualities will have low pilot rating and will be deemed

[1]Note, a *flight* in terms of logging, is considered anytime the Jetpack engine is running.

to have poor handling qualities.

P-11A Jetpack

It must be noted that the flight performance shown here for the P-11A is not the performance of the P-11A as designed. The P-11A used to perform these flights was a remote control version that contained a strategically weighted manikin and additional weights above the Jetpack to raise the CG in the order of 150 mm without any significant changes to the airframe. These CG changes were required in order to improve the P-11A handling and performance so it could be flown outside for a length of time to allow for useful flight data to be collected. It must be noted that the during these flight tests the maximum wind speed was less than 1 km/h.

Figure 8.2a shows that roll attitude only loosely ($RMSE = 2.2$) follows the commanded attitude. The roll attitude shows a great deal of oscillation which indicates that the roll control is not effective. Figure 8.2b shows how the Jetpack pitch attitude follows that commanded by the pilot. It can be seen that pitch control is superior to that of roll showing higher attitudes and lower $RMSE$ values, but still contains oscillations. It was found from test flights that the maximum obtainable steady state pitch attitude for the P-11A was 8° of pitch. Any more would cause the P-11A to pitch back with the pitch control vanes saturated. Both yaw and climb rate, as shown on Figures 8.2c and 8.2d, respectively, show good following of the pilot commands. The climb performance chart shows the pilot commands used to climb and descend the P-11A to a height of approximately 30 m above ground, a new record for the Jetpack at the time.

P-11B Jetpack

From the results obtained in Chapter 6 the P-11A airframe was modified to support the inverted engine above the ducted-fans to locate the CG at the approximate ducted-fan centre of pressure. However, this meant that the CG was approximately at the duct lip which is approximately 1.6 m above the ground. The high CG made the P-11B Jetpack very difficult to handle during takeoff and landing and extreme care was necessary. For this reason only a few flights were made to demonstrate that more control was available before committing to further airframe modifications. Hence, control gains were only roughly tuned so the recorded roll and pitch attitude performance, Figures 8.3a and 8.3b, do not show any noticeable improvement compared to P-11A. However, the pilot felt that control had improved so the P-11B was modified into P-11C.

P-11C Jetpack

The P-11C, Figure 8.4, improved on the P-11B by removing a large section of the airframe beneath the ducts to lower the height and CG of the aircraft. This was done to improve the stability of the aircraft while on the ground, which also improves the handling during takeoff and landing. The improved handling and

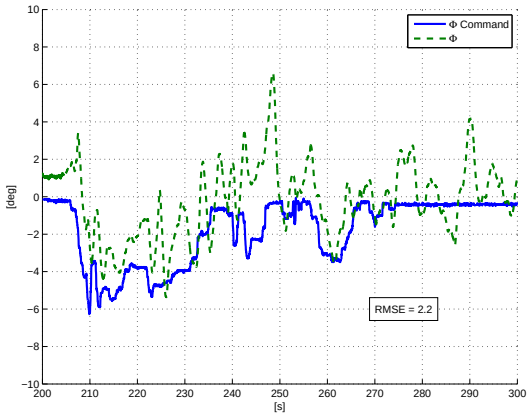

(a) Roll attitude (Φ)

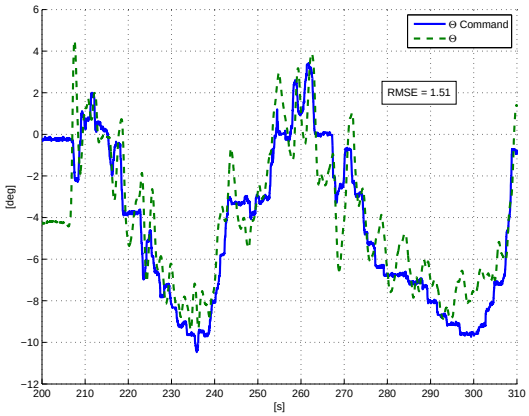

(b) Pitch attitude (Θ)

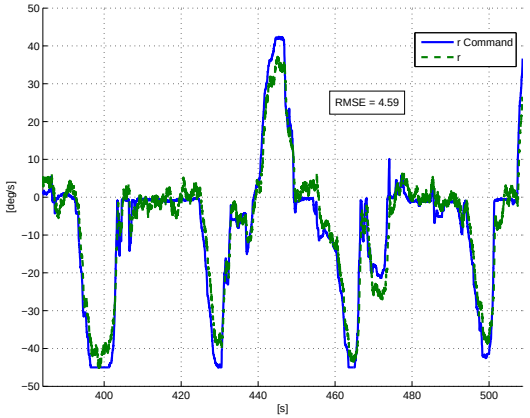

(c) Yaw rate (r)

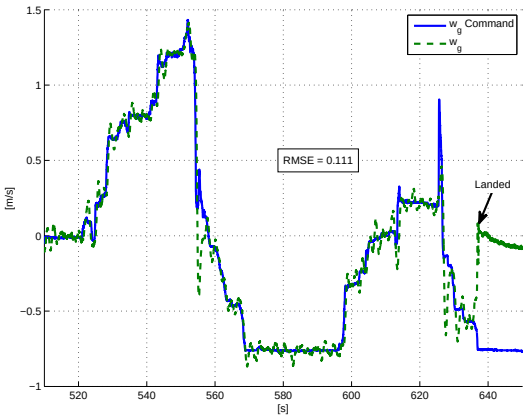

(d) Climb rate (w_g)

Figure 8.2: Comparison between commanded and actual for the P-11A Jetpack.

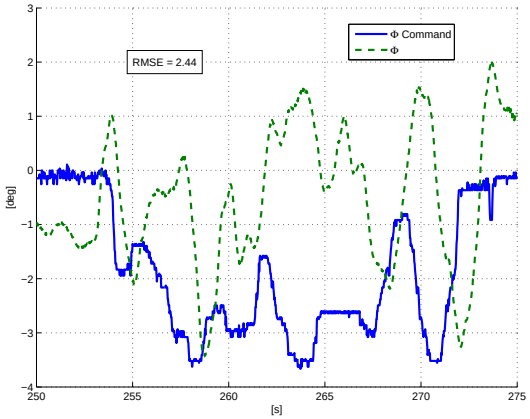

(a) Roll attitude (Φ)

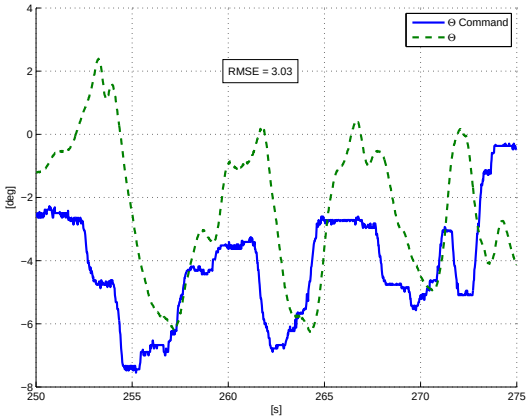

(b) Pitch attitude (Θ)

Figure 8.3: Comparison between commanded and actual for P-11B Jetpack.

control gain tuning allowed for rapid expansion of the flight envelope. Figure 8.5a shows how the roll performance has improved compared to P-11A by showing higher obtainable roll angles. However, this improved roll performance is still not adequate as there remains significant error ($RMSE = 3.66°$). Pitch response has also greatly improved, as shown on Figure 8.5b, but significant error ($RMSE = 8.1$) between pitch command and actual still exists. This error is attributed to the low pitch rate saturation limit within the control loop, which slows the response of the aircraft in pitch motion, and causes lag to develop between command and response. Both yaw rate and climb rate, Figures 8.5c and 8.5d, respectively, show good following to pilot commands.

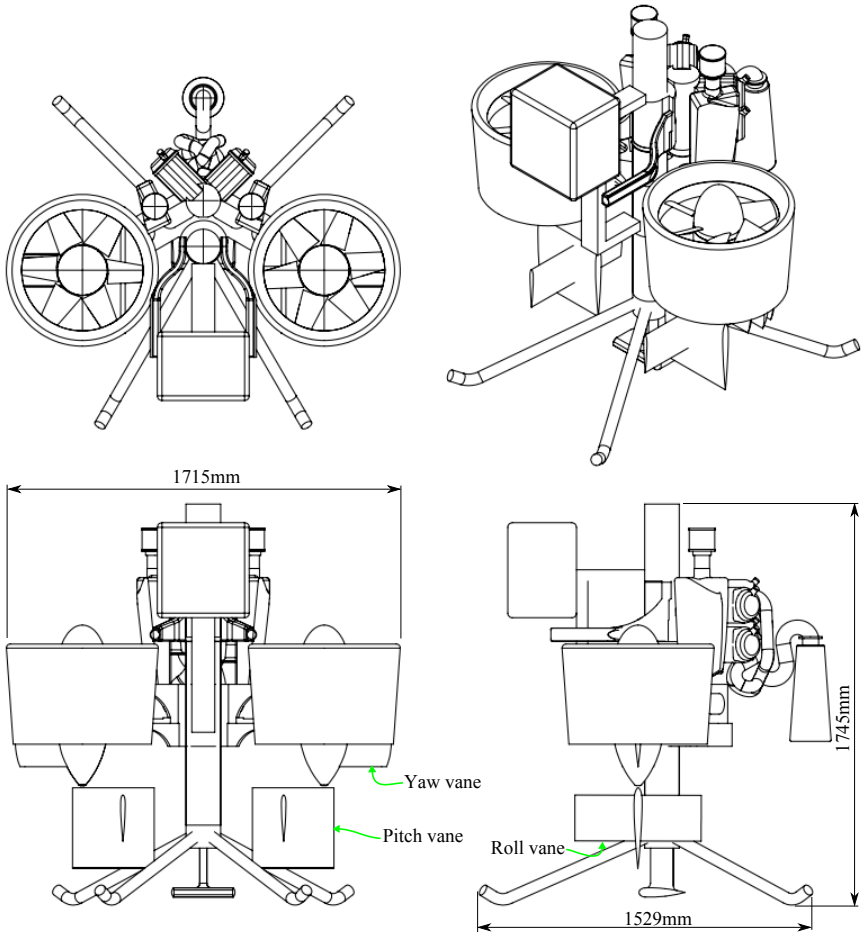

Figure 8.4: P-11C Jetpack projected views, flown September 2011

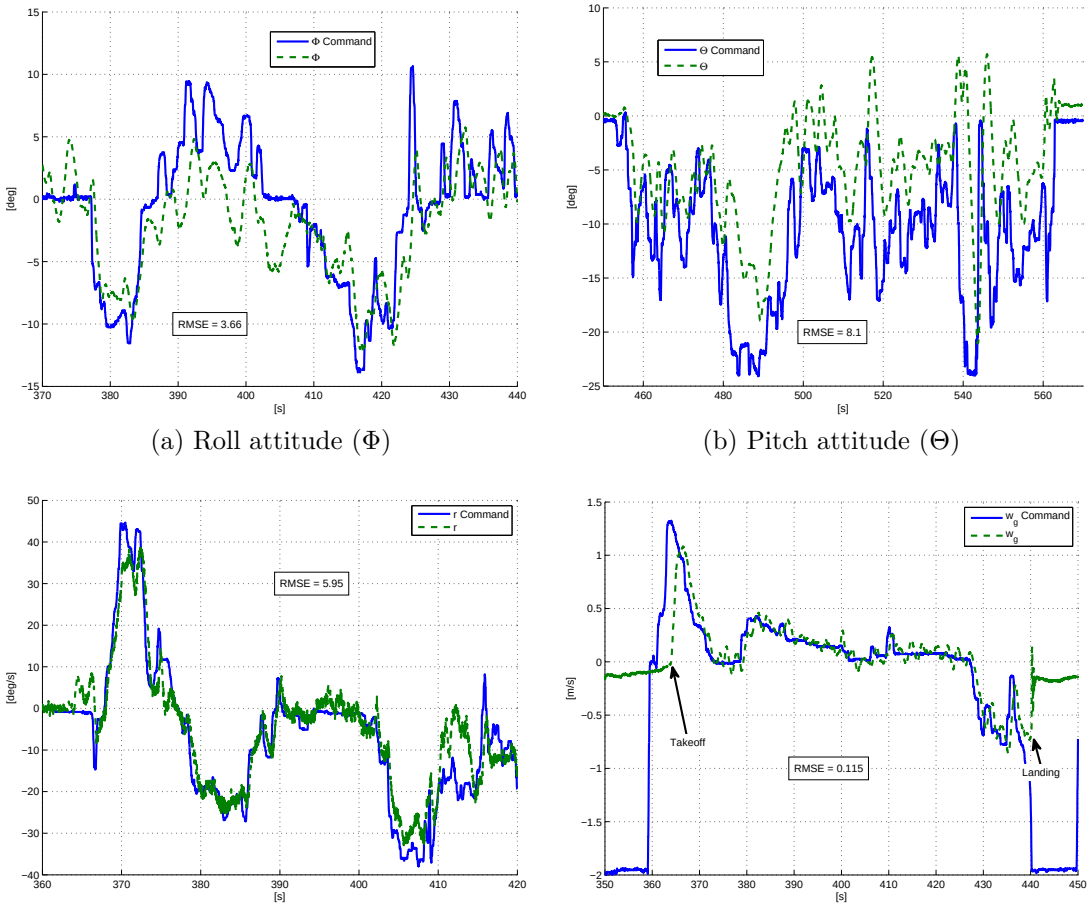

(a) Roll attitude (Φ)

(b) Pitch attitude (Θ)

(c) Yaw rate (r)

(d) Climb rate (w_g)

Figure 8.5: Comparison between commanded and actual for P-11C Jetpack.

P-11D Jetpack

The P-11C showed greatly improved performance by aligning the duct centre of pressure to the CG. However, although roll performance was improved it was still inadequate, as it did not show the ability to achieve high attitudes as per the pitch plane. It was found by visual inspection (by the author) that the position of the roll vanes on the P-11A and subsequent P-11C Jetpacks were subjected to poor airflow due to the high wake turbulence of the belts and hub supports. Also the roll vanes were not symmetrically exposed to the oncoming airflow resulting in the roll vane balancing point being at a deflected position to the oncoming airflow and duct axis.

The P-11D addressed the roll performance problem by repositioning the roll vanes centrally across the duct diameter as shown on Figure 8.7 where they are exposed to high velocity airflow, and hence, are more aerodynamically effective. Comparing the roll performance from Figure 8.5a and 8.6 it can be seen that repositioning the roll vanes enable the P-11D Jetpack to produce a much nicer response to the given roll command, with significantly less oscillation and much increased roll attitude. This result reinforces the positive comments made by the remote control test pilot that the improved control authority has improved the handling qualities of the Jetpack. The large $RMSE$ value in

Figure 8.6 is attributed to the delayed response of the Jetpack to the rapid change in control input. The re-located roll vanes not only produce a superior response, but achieve their response through smaller vane deflections. This has the combined benefit of producing less vane drag and also improving control response as the vanes do not need to deflect to the same extent to achieve the same control force/moment.

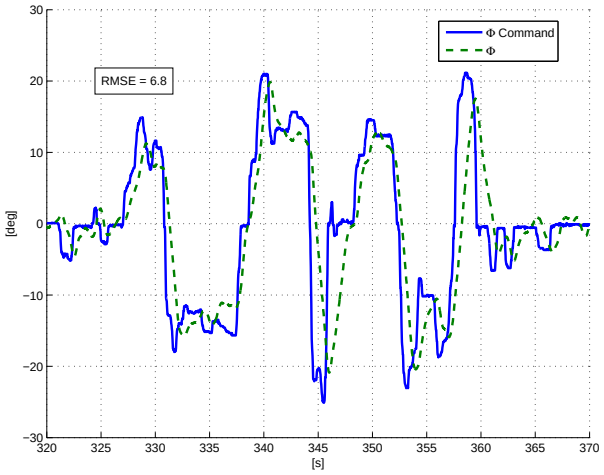

Figure 8.6: Comparison between commanded and actual roll attitude (Φ) for P-11D Jetpack.

P-11E Jetpack

From the success of roll vane re-positioning on the P-11D Jetpack the pitch vanes were also reexamined resulting in the P-11E prototype, Figure 8.7. This led to the pitch vanes being repositioned closer to the ducts and the tri-decker yaw vanes replaced by a single vane positioned below the duct, and used as a combined pitch-yaw vane where the pitch signal was superimposed on the yaw signal. Although the raising of the pitch vane reduced the moment arm, the addition of the mixed pitch-yaw vane increased the overall pitch moment capabilities while presenting a more compact design. This is largely due to the effectiveness of the mixed pitch-yaw vane being exposed to high speed airflow, as the pitch vane is still largely affected by wake of the drive belts and hub support struts.

Figure 8.8a demonstrates the superior roll performance of the P-11E with large and fast roll commands. The pitch performance of the P-11E is shown in Figure 8.8b. The aircraft's response is smooth with reduced oscillations, when compared to P-11C prototype. However, at larger attitudes, the pitch attitude does not match the pitch target. This is because an error is needed between the two signals to generate an appropriate vane deflection to trim the aircraft at these higher attitudes. Both yaw and climb rate, Figures 8.8c and 8.8d also show good response to pilot inputs.

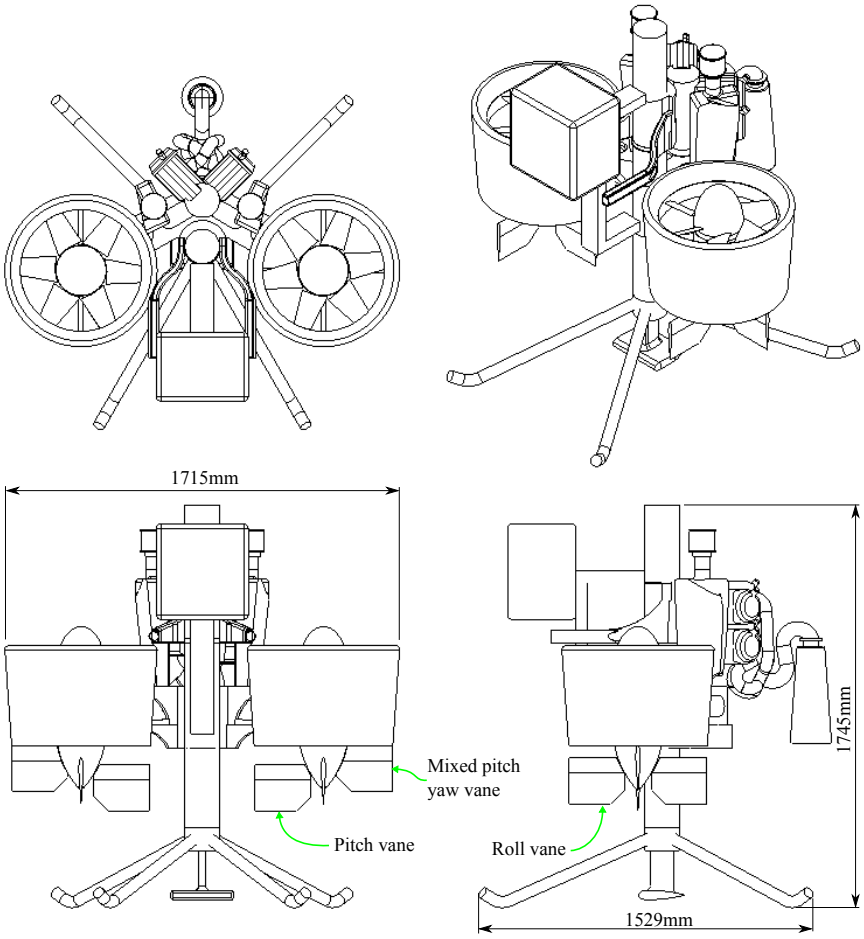

Figure 8.7: P-11E Jetpack projected views, flown March 2012

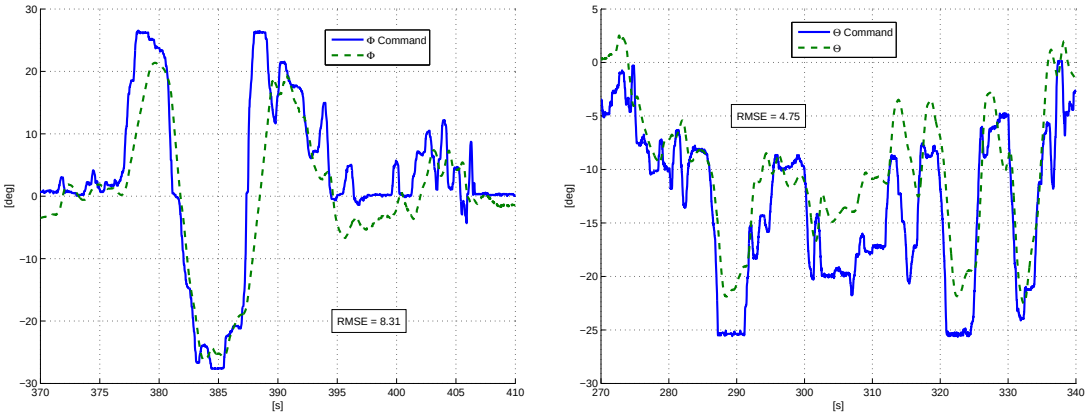

(a) Roll attitude (Φ)

(b) Pitch attitude (Θ)

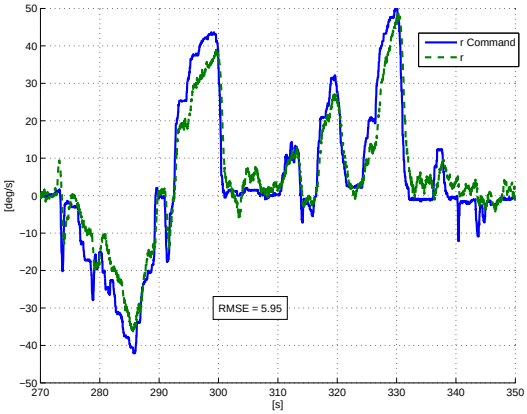

(c) Yaw rate (r)

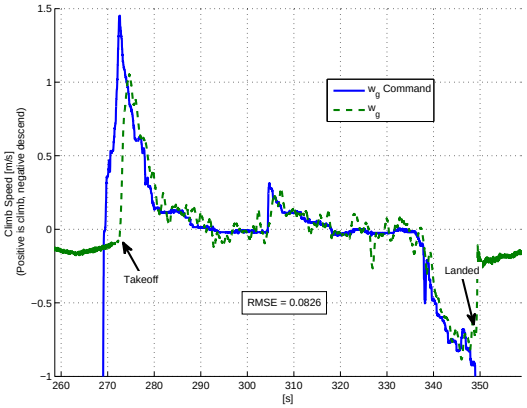

(d) Climb rate (w_g)

Figure 8.8: Comparison between commanded and actual for P-11E Jetpack.

8.4 Longitudinal Trim Validation

The longitudinal trim validation compares the level flight trim performance of the model to the Jetpack in the longitudinal plane (xz plane) for the range of flyable pitch attitudes. Since the trim comparison neglects time varying effects it allows for comparison of forces and moments between model and Jetpack. The comparison, as shown on Figure 8.9, compares the key longitudinal variables of airspeed and pitch vane deflection versus pitch attitude. These variables are used in the comparison as they are measurable quantities that relate to the net forces and moments on the Jetpack. Hence, for the range of attitudes being compared if the model airspeed and vane deflection closely match actual Jetpack values then the model can be considered a successful representation of the Jetpack.

The trim comparison is done by solving for the trim pitch vane deflection and airspeed for a given pitch attitude, as described in section 7.4, and comparing this result with time-averaged steady state values achieved by the Jetpack. The time-averaged values from the flight data are found by manually searching through the recorded flight data and finding time intervals to average the Jetpack attitude, airspeed, and vane deflection over. Time intervals range from 0.5 s to 2 s duration and are taken where the pitch attitude and heading are approximately constant and the roll attitude is close to zero ($\pm 3°$), as this indicates level flight.

It can be seen in Figure 8.9 that the simulated airspeed is in good agreement ($RMSE = 1.16\,\text{m/s}$) to the measured airspeed throughout the range of pitch attitudes measured. However, it must also be noted that the recorded airspeed from the flight data at higher pitch down angles has not reached steady state, as the airspeed is still accelerating. High steady-state airspeeds above 17 m/s have not yet been obtained due to practicality considerations of flying the Jetpack by remote control. The good agreement of airspeeds validates that the modelled sum of forces within the pitch plane represents the forces acting on the Jetpack for pitch down attitudes up to 30°.

The predicted pitch vane deflection shows good relation with that measured from the test flights, ($RMSE = 1.61\,\text{m/s}$) . This indicates that the duct centre of pressure and moment model described by equations6.3.9-6.3.12 is a valid method to predict the ducted-fan, and hence, the Jetpack's behaviour up to a pitch down attitude of 30°. Further flight tests expanding higher pitch down attitudes, beyond 27°, will need to be performed to validate the model for greater attitudes. Both the prototype flight data and model show that the pitch vane deflection initially rises and reaches a maximum at approximately 15° pitch down attitude and decreases passing through neutral vane position at approximately 27° pitch down attitude. This rise in vane deflection corresponds to a negative pitch vane moment (as per sign convention, Figure 1.4) being created by the pitch vanes to oppose the positive pitch moment of the Jetpack, which is due to ducted-fan reactions. The point where the pitch vane deflection is zero (neutral position) indicates that the centre of pressure coincides with the centre of gravity at this pitch attitude and airspeed. Ideally, the pitch vanes should be at their neutral position throughout the flight range to maximize the control authority for manoeuvering. However, as is evident from

the flight test results the centre of pressure changes as a function of attitude and airspeed, hence the control vanes must also deflect to create moments to trim the aircraft.

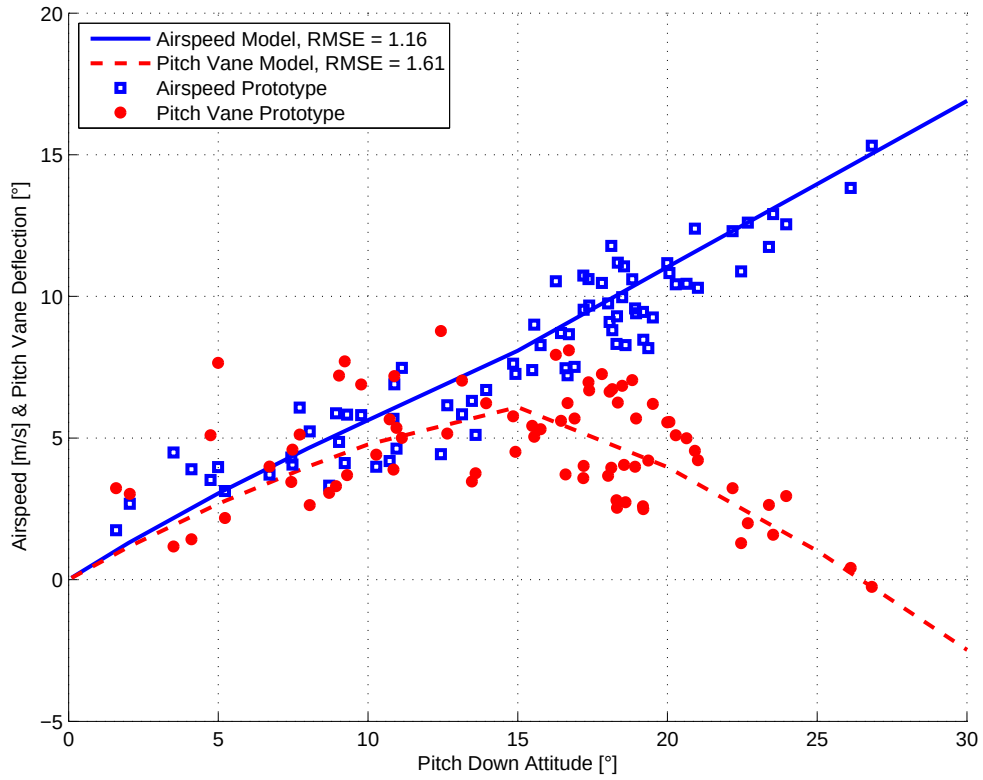

Figure 8.9: Shows the longitudinal level flight trimmed airspeed and vane deflection comparison between simulated and actual flight data for P-11C Jetpack

8.5 Dynamic Validation

The dynamic validation compares the simulated response to the Jetpack's response for the given pilot commands. This comparison uses the recorded pilot commands used to the fly the Jetpack as the transient input into the Jetpack model described in Chapter 4. This method tests the entire Jetpack model as the inputs pass through the model control algorithms and the developed Jetpack equations of motion to determine the simulated Jetpack response. The simulated response is directly compared to the recorded flight data from the Jetpack to validate the model. The dynamic simulations use the ducted-fan centre of pressure models described by equations 6.3.6-6.3.8 and equations 6.3.9-6.3.12 to model the roll and pitch moments respectively.

Method

The following method describes the process used to compare the model with actual flight data.

1. Find a suitable flight data segment from flight logs to use as model inputs and to compare model outputs to. Each flight data segment needs

to begin from a known state so the initial conditions of the model can be matched to the flight data. Since the landing gear ground interaction is included in the model, flight data segments beginning when the Jetpack is on the ground, prior to takeoff, to when the Jetpack has landed again are found. As all takeoffs and landings are made on level ground the initial conditions for the model can be set to zero, with the exception that the CG is approximately 1 m above the ground and the engine power is at idle power level. Flight data segments with minimal wind speed and turbulence are favoured as this avoids having to include the additional affects of wind into the model. Since the wind speed is measured remotely from the Jetpack it becomes difficult to accurately quantify the instantaneous wind speed affecting the aircraft.

2. All four pilot commands/inputs (roll attitude, pitch attitude, turn rate, and climb rate) from the chosen flight segments are loaded into the Simulink® model as model inputs and the model ran for the duration of the flight segment.

3. At the end of the simulation the state-space results and additional internal variables such as inertial velocity and vane deflection, are saved.

4. The simulated results are then directly compared to their flight data counterparts in the time domain; namely, roll and pitch attitude comparisons, yaw and climb rate comparisons.

5. The $RMSE$, defined by equation5.1.3, is calculated to quantify the error between: command and simulation, command and flight data, and simulation and flight data. The time periods between 215 s to 220 s and 255 s to 260 s are not included in the $RMSE$ calculation as during these times the Jetpack is in takeoff and landing phases where the actual Jetpack is exposed to external inputs from handlers and uneven terrain surfaces, which the model does not account for.

Results

Figures 8.10 to 8.14 show the comparisons between the simulated and the actual response of the P-11E Jetpack over a 40 s flight duration from takeoff (215 s) to landing (215 s). For all the plots *Cmd, Sim,* and *FD* represent commanded input, simulation response, and Jetpack flight test response.

Figure 8.10 shows that the roll attitude response of the model and the Jetpack are generally similar ($RMSE = 2.58°$) and show similar overshoot tendencies to pilot commands, such as at $T = 240$ s. The simulation response to the pilot commands is better than the Jetpack's response, $RMSE = 2.52°$ and $RMSE = 3.34°$ respectively. This indicates that the model does not account for all of physics acting on the Jetpack.

The pitch response shown on Figure 8.11 shows good correlation ($RMSE = 3.27°$) between the simulation and Jetpack. The simulated data follows closely to the pilot command ($RMSE = 2.9°$), but typically shows a lagged response to abrupt pilot commands, such as 233 s where the peak commanded pitch attitude leads the peak pitch attitude by 1 s for both the model and Jetpack.

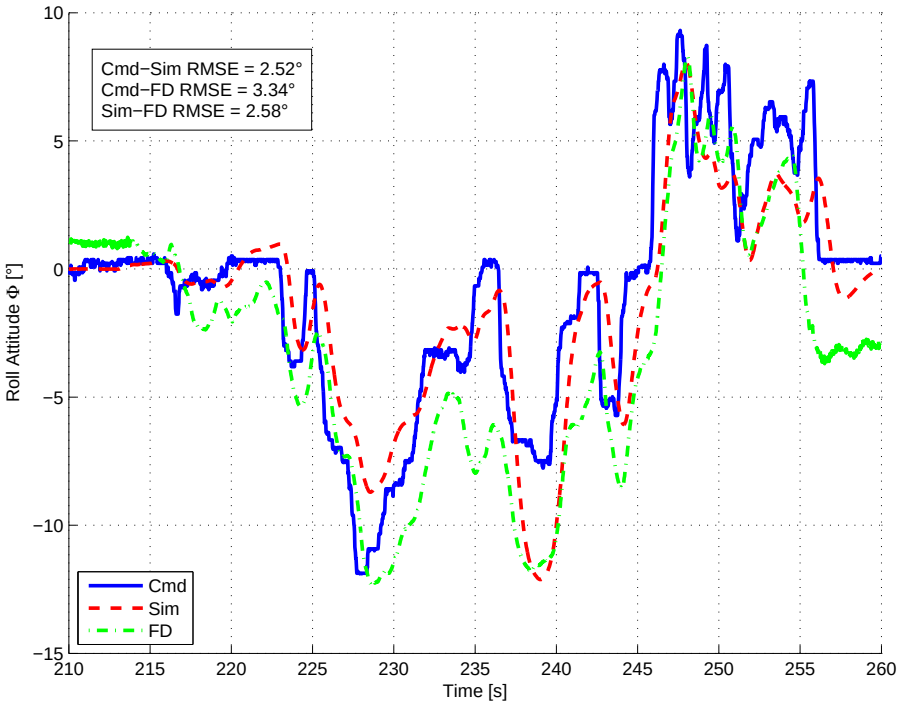

Figure 8.10: Roll attitude comparison for P-11E Jetpack

Both the Jetpack and model should show a slower response than the pilot command as both the roll and pitch axis have rate limits on the joystick commands and also a saturation limit between the outer and inner control loops, which restrict the Jetpack and model from obtaining high roll and pitch rates.

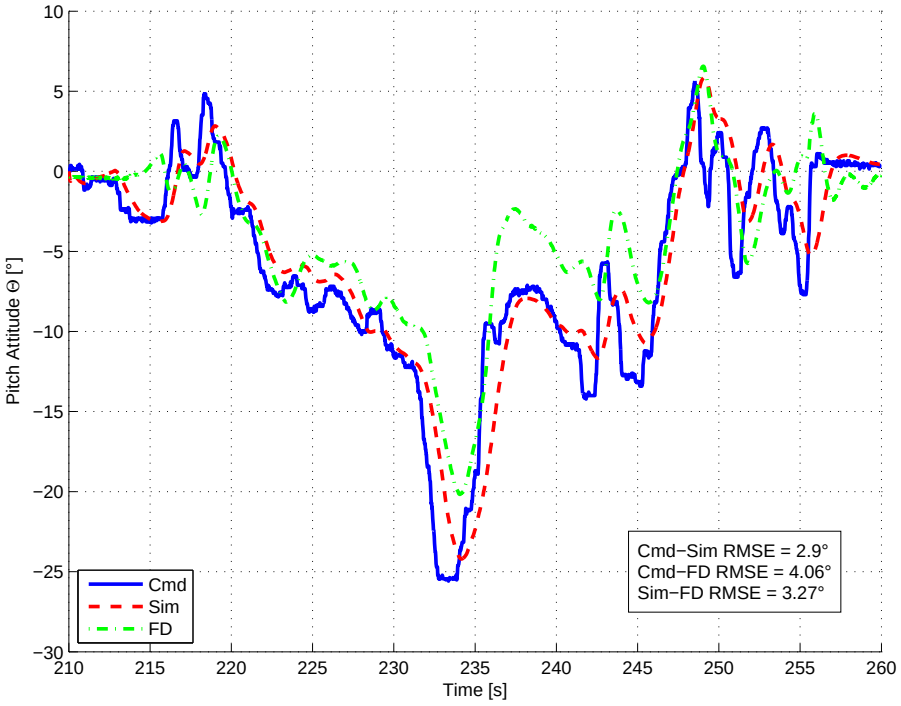

Figure 8.11: Pitch attitude comparison for P-11E Jetpack

The simulated yaw turn, Figure 8.12 matches extremely well ($RMSE = 0.71°$) to the pilot commanded yaw turn rate. The Jetpack yaw rate trend

closely follows the pilot commanded ($RMSE = 4.43°$), and only noticeably differs for turn rate values in excess of $20°/s$. The actual turn rate is also slightly delayed from the commanded turn rate. One of the main contributing factors to way the simulated and actual turn rate differ is that the Jetpack model does not take into account the dynamics from the changing angular momentum from the rotating components of the Jetpack. Hence, every time the engine power setting changes the speed/angular-momentum of the rotating engine components, drive train, and fans change and produce a yaw moment on the aircraft.

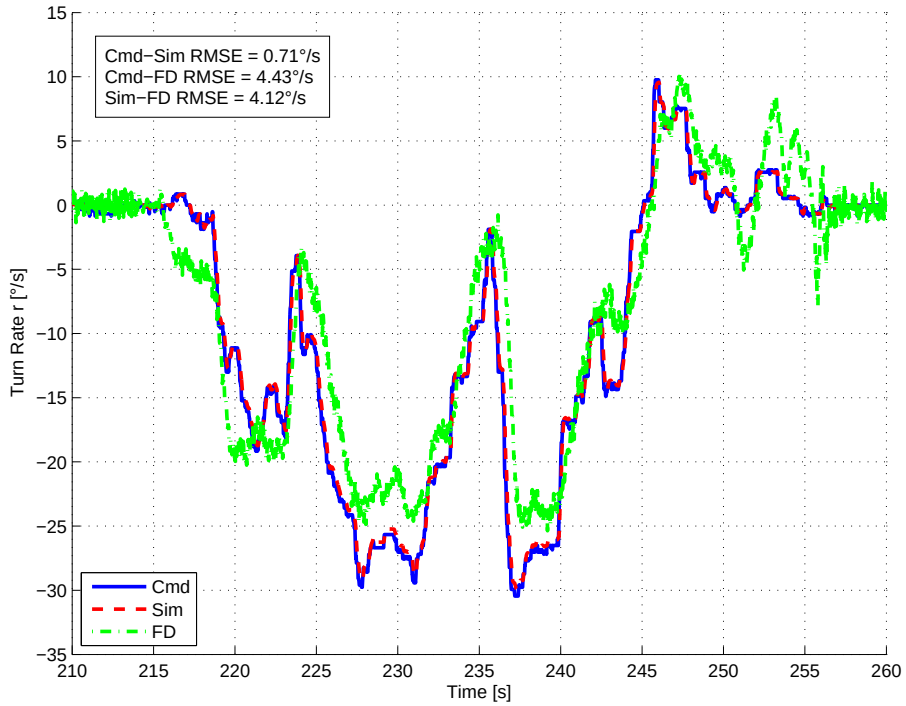

Figure 8.12: Yaw turn rate comparison for P-11E Jetpack

Figure 8.13 shows the climb rate comparison between the pilot commanded, simulated and actual Jetpack. It can be seen that once both the simulation and actual Jetpack are airborne (after 215 s), they both match the commanded signal very well. Typically, the actual Jetpack has more oscillation in climb rate than the simulation. This can be attributed to the model using different gain values and a linear relationship between throttle position and engine power, whereas in reality the relationship is nonlinear. This nonlinearity has the effect that an incremental increase in throttle position is less effective than an incremental decrease in throttle position, which contributes to the oscillation. The non zero climb rate of the Jetpack at the beginning on the simulation is due to error of the Ahtena INU, and the high positive commanded climb rate of is due to the pilot commanding full descent while the Jetpack is on the ground as per flying practices. The difference between the model and Jetpack at the start of the simulation is due to differing initial conditions of engine power. The difference at the end of the simulation is due the simulated result having flown higher than the Jetpack, so the Jetpack lands before the simulated Jetpack does.

Figure 8.14 shows the comparison of the simulated and actual translational positions of the Jetpack during the flight duration. Although the general shape

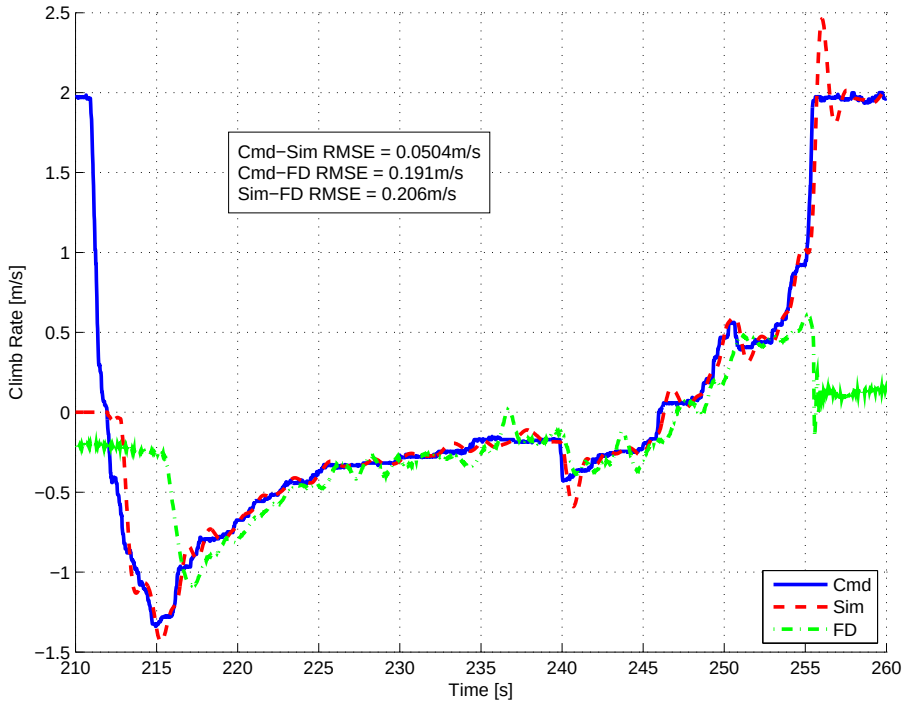

Figure 8.13: Climb rate comparison for P-11E Jetpack

is similar the translational positions are quite different, this is mainly due to the accumulation of error between the model and reality, but the affects of wind drift and GPS accuracy may also become a prevalent factor. The increasingly southeasterly drift of the Jetpack relative to the simulation indicates the present of wind, also it can be seen that the minimal GPS resolution is approximately 3 m.

In general differences between simulation and flight data in decreasing order are attributed to:

- Atmospheric wind conditions. The model assumed no wind, turbulence, or recirculation induced by the Jetpack down wash.
- Aerodynamic expressions not completely taking into account all aerodynamic effects.
- Errors/accuracy of flight data measurements, refer to Athena INS manual [91].
- Over estimation of the Jetpack's inertia, which reduces the response of the model.

8.6 Conclusion

This chapter has described how the flight data from the Jetpack prototypes was obtained and how the flight performance of the Jetpack prototypes has improved. The improvements are shown by better following of the Jetpack response to the command input, and by the increased ability of the Jetpack to perform more aggressive manoeuvres, as shown by the higher obtainable

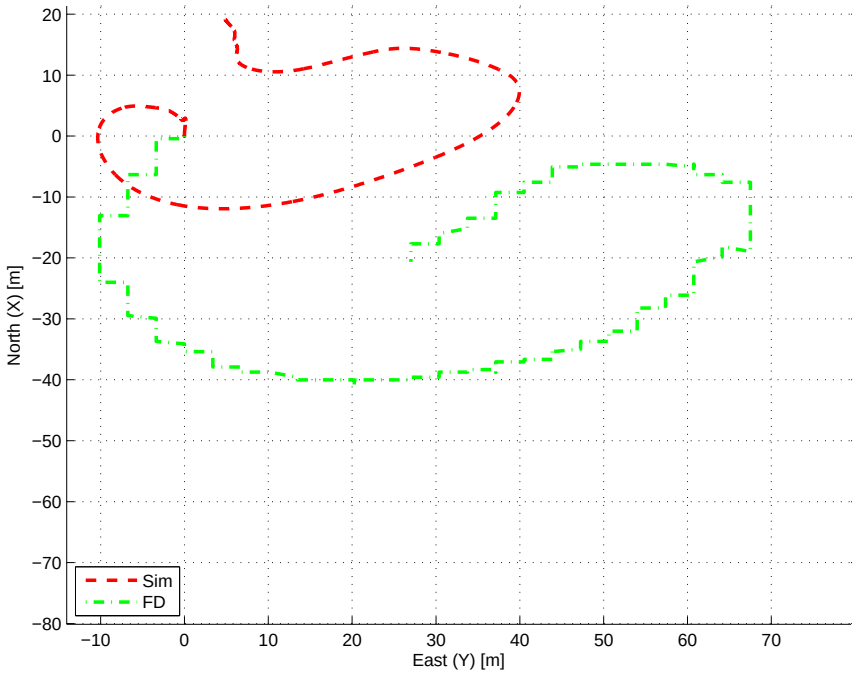

Figure 8.14: Translation position comparison for P-11E Jetpack. Takeoff location is at origin.

roll and pitch angles of the P-11E Jetpack. The Jetpack model, described in Chapter 4, is validated by two means: steady state trim comparison, and direct time domain comparison by using the recorded flight inputs as model inputs. The time domain validation of the roll and pitch attitude, turn rate, and climb rate show that the model dynamics are similar to that of the actual Jetpack thus validating the formulation of the Jetpack model.

Chapter 9

Guide to Jetpack Aerodynamic Design

"Simplicity is the ultimate sophistication."
Leonardo da Vinci

This chapter explains how to design a Jetpack based on the Martin Jetpack twin ducted-fan configuration, and uses the development of the P-12 Jetpack as an example methodology. The P-12 Jetpack, Figure 9.1, is a complete redesign of the predecessor Jetpack airframes based on the aerodynamic knowledge developed from this research and test flying the P-11B to P-11E Jetpack prototypes. The chapter explains the methodology used to design the aerodynamic features of the P-12 Jetpack, which include: larger 800 mm ducts, the rotor and stator blades, optimum CG position, and the design of the tri-decker control vanes. The chapter also documents the experiments made to measure the thrust and efficiency of both the P-11 and P-12 ducted-fans, as well as the lift forces of the developed tri-decker control vanes.

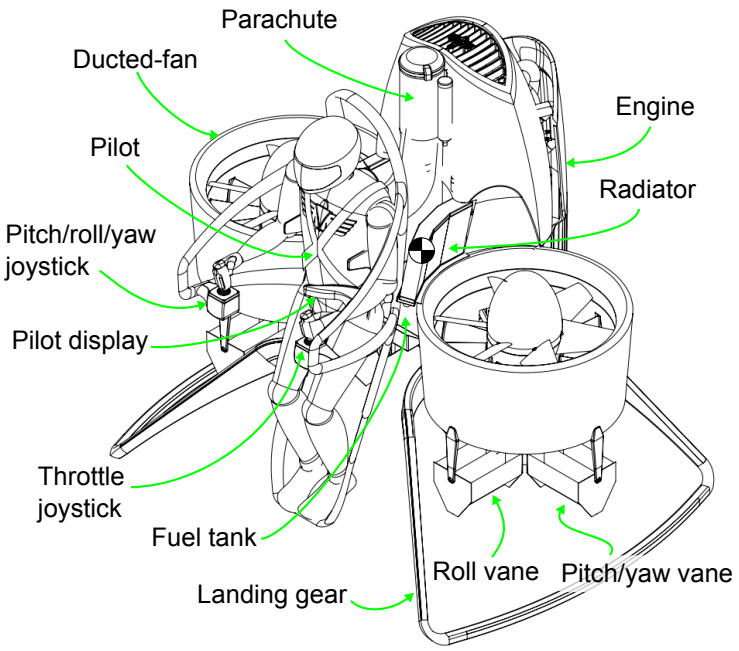

Figure 9.1: The P-12 Jetpack design concept with 800 mm ducted-fans

9.1 Jetpack Design Methodology

This section presents the Jetpack aerodynamic design methodology as used for the P-12 Jetpack. This methodology can be equally well used in the design of any scaled Jetpack concept or single ducted-fan VTOL aircraft.

The aim of the P-12 Jetpack is to demonstrate the flight capabilities of the P-11E Jetpack (unmanned) as a manned aircraft to gain interest of potential investors, and hence, ensure funding for future development to bring the Jetpack concept to market. To achieve this with minimal expense Martin Aircraft Company required that the P-12 Jetpack uses the same engine as that used in P-11 prototypes. For the purpose of the demonstration flights the P-12 Jetpack is required to fly at least 11 m/s, up to moderately windy conditions (winds up to 6 m/s), and have handling qualities equal to that of P-11E, as shown in Figure 8.8.

9.2 Design Thrust

The first step in designing a Jetpack is to determine the design thrust force, which is the maximum required static thrust force developed at maximum engine power. This requires a detailed estimate of the takeoff weight of the aircraft. Using historical weight data from the P-11A and P-11E Jetpacks a detailed weight estimate can be made for the P-12 Jetpack. Table 9.1 shows the actual top level assembly and takeoff weights for the P-11A and P-11E Jetpacks. The table also shows the top level assembly weights as a percentage of the takeoff weight, hence, the component weight fractions. Using the component weight fractions an estimate of the key components and the takeoff weight for the P-12 Jetpack can be made. A similar methodology is employed in [75] to determine the estimated takeoff weight of fixed-wing aircraft.

From Table 9.1 using the P-11A data the payload to maximum takeoff weight fraction can be determined to be:

$$W_p^f = \frac{W_p}{W_{MTOW}} = \frac{922\,\text{N}}{2423\,\text{N}} = 0.38 \tag{9.2.1}$$

where W is weight in kg and the subscript p is payload, which is the sum of pilot, fuel, and baggage masses. The subscript MTOW is the maximum takeoff weight of the Jetpack. The superscript f denotes fraction so that W_p^f means payload weight fraction.

Using equation 9.2.1 and the calculated weight fraction of 0.38 with an assumed payload of $W_p = 100\,\text{kg}$ the MTOW for the P-12 can be estimated to be:

$$W_{MTOW} = \frac{W_p}{W_p^f} = \frac{981\,\text{N}}{0.38} = 2580\,\text{N} \tag{9.2.2}$$

The engine weight for the P-12 is assumed to remain the same as the P-11 prototypes, as no major changes are required. An improved landing gear design that is more stable on the ground and a pilot module that has a built in foot rest are planned for the P-12 concept, hence a greater weight is budgeted for these assemblies. A maximum design takeoff weight of 2650 N is planned

for the P-12 Jetpack to accommodate for the additional weight of the new landing gear.

Using the maximum static thrust fraction from P-11E ($T_m^f = 1.26$), which flight testing has demonstrated to be satisfactory, the maximum static thrust can be determined for the P-12 prototype as:

$$T_{max} = T_m^f W_{MTOW} = 1.26 \times 2650\,\text{N} = 3345\,\text{N} \tag{9.2.3}$$

Table 9.1: Summary of Jetpack top level assembly weights

Description	P-11A Weight [N]	P-11A Weight Fraction [%]	P-11E Weight [N]	P-11E Weight Fraction [%]	P-12 Weight Estimated [N]	P-12 Weight Actual [N]
Engine	824	34	824	39	824	932
Ducted-fans	255	10	98	12	275	265
Fuselage	186	8	186	9	216	284
Control System	98	4	98	5	108	128
Landing gear	59	2	118	6	147	294
Pilot Module	78	3	255	12	98	245
Parachute	0	0	0	0	0	98
Empty Weight	1491	62	1736	82	1668	2080
Max Takeoff Weight W_{MTOW}	2423	100	2109	100	2649	3139
Max Static Thrust T_{max}	2649	109	2649	126	3335	3630
Payload =T_{max}- W_{MTOW}	922	38	373	18	981	1059

Table 9.1 also shows the actual weight of the P-12 Jetpack, as at April 2013, which has significantly increased on what was estimated. This additional weight is due to the increased weight of the components making up the landing gear, pilot module, and engine assemblies, and also the addition of the ballistic parachute. However, the improved efficiency of the P-12 ducted-fans has helped to offset the weight gain, but the maximum static thrust fraction for the P-12, $T_m^f = 3630/3140 = 1.16$, is lower than that of the P-11E. Hence, the additional weight of the P-12 will reduce the flight performance compared to P-11E.

Duct Diameter

For the required maximum static thrust of 3335 N and known engine power of 150 kW (200 HP), the duct exit diameter for the P-12 can be determined by rearranging equation 3.1.34 as:

$$d = \sqrt{\frac{T_d^3}{\rho\pi P_d^2}} = \sqrt{\frac{(3335/2)^3}{1.225\pi(750 \times 100 \times 0.6)^2}} = 0.77\,\text{m} \tag{9.2.4}$$

where T_d and P_d are maximum thrust and power per duct, respectively. A ducted-fan efficiency of $\eta = 0.6$ was assumed, which is slightly higher than the measured efficiency of the P-11 ducted-fan, $\eta = 0.55$, refer to section 9.4. A higher efficiency was assumed for the P-12 ducted-fans, as structural stator blades are used instead of additional struts to support the fan hub. The additional support struts used on the P-11 ducted-fans increased duct internal drag, and hence, reduced the ducted-fan efficiency.

Duct, Rotor, and Stator Blades

With the maximum static thrust, power, and duct diameter known, a detailed design on the rotor and stator blades can begin. Section 9.3 explains how the blade element theory is used to determine the blade profiles for the rotor and stator blades. The rotor blade outer diameter is determined by the duct profile, which for the P-12 duct is identical to that of the P-11 duct. Although the duct profile should be enlarged to maintain correct similarity it was deemed unnecessary as the P-11 duct is not an optimised duct geometry, so no significant thrust loss is assumed to occur by taking the same profile. As a result the P-12 duct has an reduced expansion ration of 1.45 compared to the P-11 duct expansion ratio of 1.56, which is 7.5 % larger.

Jetpack Layout

The Jetpack appearance is driven by the duct size. The duct size not only affects the extent of the Jetpack, namely width, but also dictates the centre of gravity location. As the performance of the Jetpack is greatly affected by the centre of gravity location, care is needed by the designer to position the various Jetpack components so that differences in pilot weight and fuel burn have minimum affect on the overall centre of gravity position during flight. Viewed side on, an initial centre of gravity position located at the intersection of the duct axis and duct leading edge plane should be assumed for conceptual design.

The size of the control vanes are also driven by the ducts, as the vanes should span the duct exit diameter. The position of the vanes should be as far down as possible from the duct trailing edge, ideally 0.75 duct diameters below the duct. However, due to form factor requirements, namely ground interference from landing gear deflection, this value was not achieved.

Other form factor requirements such as Jetpack height and length are not driven by aerodynamic requirements, but rather by functional and practical requirements, hence these are not included in this discussion as they do not significantly affect the aerodynamic performance.

Design Iteration for Performance

Once a basic layout design has been achieved the centre of gravity position and the control vanes can be optimized to ensure the Jetpack performance is optimal. This requires the use of the equations of motion of the Jetpack as described in chapter 4. A procedure was developed using the key design parameters (maximum takeoff weight, position and size of ducts, airframe dimensions, and control vanes) to determine the vertical CG position for the intended airspeed range.

The procedure involves solving the Jetpack pitching moment equations (taken from the equations of motion) for a range of angles of attack and airspeeds. An example of the P-11E moments are shown on Figure 9.2, which shows the pitching moments from the ducted-fans, aerodynamic profile drag, and the control vanes versus airspeed for a range of attitudes, 30° to -40°

(note negative attitude is forwards pitch). Typically, from 0 m/s to 15 m/s airspeed the pitch attitude decreases from 0° to −30°, in an approximately linear manner, which can be extrapolated to higher airspeeds. Using this knowledge the designer has an approximate idea of the Jetpack attitude versus speed. If the Jetpack is disturbed so that the attitude is greater or less than the trimmed attitude, the Jetpack needs to be able to correct this disturbance and return to the trim state. For this to occur the moment developed by the control vanes must be greater than the ducted-fan and profile drag moments. For example if the P-11E Jetpack was flying at trimmed level fight at 15 m/s, which is approximately −30° attitude, and its attitude were to instantly change to 30°, (change of 60°) the net pitching moment of the ducts and profile drag at 30° and 15 m/s would exceed the control vane pitching moment, refer to Figure 9.2. Fortunately, such an abrupt change in attitude is not expected as it has not occurred from test flying to date. However, 10° to 20° abrupt attitude changes are common, so the Jetpack must be able to handle these changes to maintain control.

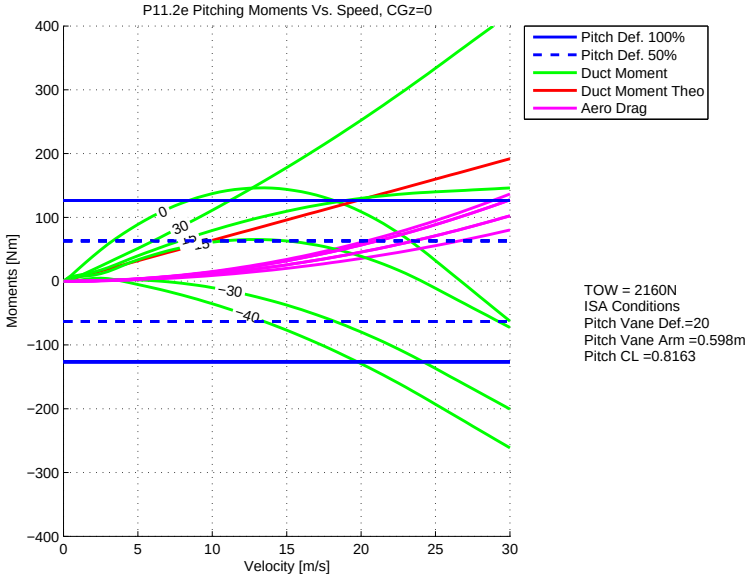

Figure 9.2: P-11E Jetpack calculated steady state duct pitching moments versus airspeed

Control vane moment arm, vane lift force, and centre of gravity position are altered so that throughout the airspeed range the required control moment does not exceed 50 % of the available control moment. Ideally, the moments developed by 50 % pitch vane deflection, as shown by dashed lines on Figures 9.2 to 9.3e, should enclose/bracket the ducted-fan and profile drag pitching moments throughout the entire flight speed range. From test flying the 50 % requirement has been deemed as an acceptable level of control margin for manoeuvering. However, due to the large change in the ducted-fan centre of pressure the bracketing of the ducted-fan pitching moments by the control vanes becomes challenging as an upper limit of control vane size, and hence, moment exists.

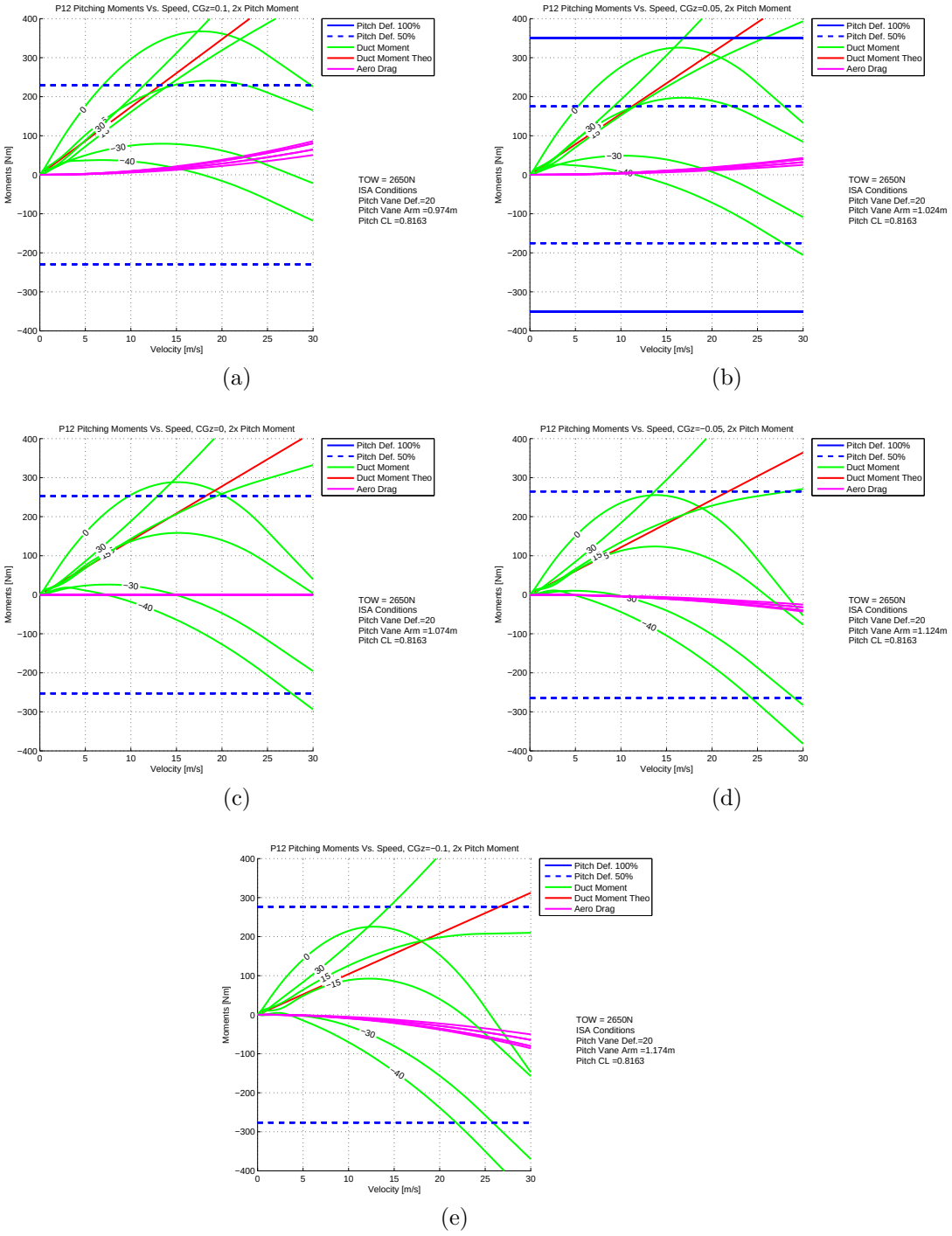

Figure 9.3: P-12 Jetpack calculated steady state duct pitching moments versus airspeed for a range of pitch attitudes from 30 to −40° pitch attitude.

The challenge for the designer is to ensure that the aircraft is trimmable (the control moments from the vane deflection must equal the net aircraft pitching moments) throughout the intended flight envelope and that an adequate control margin exists for manoeuvering. Two options exist: change the CG to change the nature of the duct pitching moments, or increase the available control moment. Using the pitching moments versus speed chart for P-11E, Figure 9.2, as the benchmark for the P-12 design, a range of CG positions from −0.1 m to 0.1 m relative to the duct lip were simulated to de-

termine the expected pitching moments on P-12. Figures 9.3a to 9.3e show how the pitching moments for P-12 vary with changes in control force and CG positions. It can be seen from the figures that when the CG is high (negative CGz values) the duct pitching moment for lower airspeeds (less than 10 m/s) is smaller than when the CG is low. Thus high centre of gravity positions, between 0 m and 0.1 m above the datum (top of duct lip), improve the control margin, as less vane deflection is required for trim allowing more control authority for manoeuvering. Hence, a high CG position is favourable for low speed flight.

Due to the large change in the ducted-fan centre of pressure with airspeed and angle of attack at higher airspeeds, 15 m/s to 30 m/s, Figures 9.3a to 9.3e show that a lower CG position allows for greater control authority. However, for low CG positions low speed handling is reduced as higher vane deflections are required to balance the large duct pitching moments.

Hence, a comprise needs to be made between low speed manoeuverability and high speed flight, as the control authority on the P-12 Jetpack does not have the capability to trim for both while maintaining a 50 % control margin. Referring to the design specifications, the P-12 is required to fly demonstrations up to at least 11 m/s, hence a vertical CG position between 0 m and 0.1 m above the duct lip will ensure that the adequate control margin exists for manoeuvering. A pitch control moment of 280 Nm, which equates to a control force per vane of $280\,\text{Nm}/0.537\,\text{m}/4 = 130\,\text{N}$, is required.

To gain higher airspeeds the large change in ducted-fan centre of pressure movement needs to be addressed.

9.3 Blade Element Theory Applied to P-12 Ducted-Fan

This section describes blade element theory applied to the design of the rotor and stator blades of the P-12 800 mm ducted-fan. Briefly, the purpose of the fan, which is a collection of rotor blades, is to develop a pressure increase across the fan when rotated by the engine. The pressure rise across the fan induces an axial airflow through the fan and creates the thrust force necessary for the Jetpack to fly according to the conservation of momentum, as described in section 3.1. The fan not only induces an axial velocity component, but also a tangential swirl component to the airflow, which deflects the absolute velocity vector of the airflow helically to the duct axis, as shown on Figure 9.4. Stator blades are used to straighten the induced swirl component to recover the energy introduced into the swirling airflow. Stator blades are positioned at an angle of attack to the absolute post fan airflow to re-orientate the airflow. By straightening the airflow the stators produce an equal and opposite torque created by the fan, producing a torque neutral ducted-fan. However, in practice small nonzero torques do exist, which are trimmed for using the yaw vanes on the Martin Jetpack.

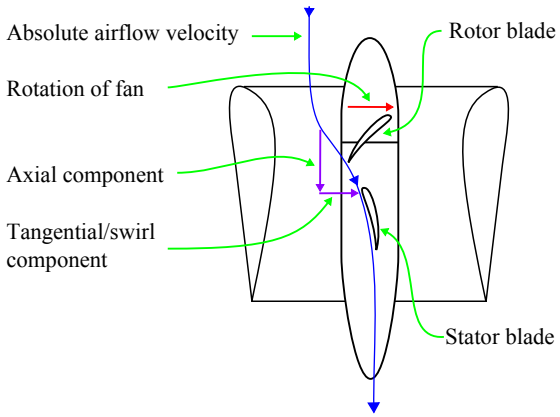

Figure 9.4: Absolute airflow velocity path through a ducted-fan

Determination of the Rotor Blade Profile

The rotor blade is an aerofoil that creates its relative velocity with respect to the free stream velocity by rotation. The relative rotor blade velocity changes in both its magnitude and orientation along the span of the blade. Thus the sectional aerodynamic forces that are a function of the dynamic pressure and angle of attack become a function of the radial position along the blade. An aerofoil cross-section has an optimum angle of attack where maximum lift to drag ratio occurs. To get the best efficiency from a rotor blade the blade cross-section must be positioned at the optimum angle of attack to the relative airflow. If this is done, the blade chord will twist from a coarse to a fine blade setting angle from root to tip, giving the twisted appearance of a rotor blade. The rotor blade setting angle Φ is the angle between the plane of rotation and the aerofoil cross-section chord line.

Blade element theory is a design methodology that determines the blade setting angles, thrust, and torque reactions along the span of the blade. This is done by dividing the blade span into a number of stations, Figure 9.5, where the radial distance between stations is the width of the blade element, dr. The blade element cross-sectional properties are analyzed at each station to determine the thrust and torque produced by this station. The total blade thrust and torque is determined by the sum of individual station thrust and torque reactions, and the total fan blade reactions is the sum of reactions of each blade.

Using blade element theory as described in [92, 93, 33], the following assumptions have been made in the development of the P-12 rotor and stator blades:

- Vortex free flow. Meaning, there is no spanwise airflow, thus the flow is helicoidal to the axis of rotation. In reality there will be spanwise flow, due to the boundary layer and centripetal forces.
- Uniform axial velocity through fan.
- Presence of the duct allows for lift to be generated over the entire blade span, as duct effectively end caps the blade and prevents tip vortices from forming.

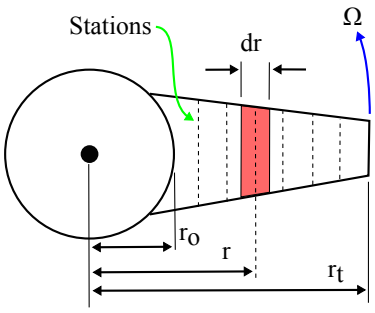

Figure 9.5: Schematic of a blade element

Design Conditions

Before a rotor blade can be designed a number of design conditions must first be determined from momentum considerations using equation 3.1.34, which gives the relation between duct diameter, thrust, and power. In the case of the Jetpack the ducted-fan was designed to achieve best efficiency in the hover condition, thus the free stream velocity $V_0 = 0$, with the design thrust occurring at the maximum engine power for a given duct size.

Rotor Blade Length

The rotor blade outer radius is determined from the duct size and the chosen expansion ratio. The blade inner radius or blade root radius is determined by the recommendations of Wallis [93] where a 40 % blade tip radius was chosen. If the root radius is made smaller, the blade setting angle becomes very coarse as a radial speed of the blade is small at the hub. Hence, it is more effective to have a large hub diameter, as this forces the airflow to flow over the blades at larger radii where the radial speed of the fan blades is greater and the blade pitch setting is finer. However, too large a hub diameter results in the need of a much longer tail cone fairing to diffuse the airflow, which is not practical for the Martin Jetpack design as the tail cone would interfere with the landing gear and the ground.

Blade Tip Speed and Fan Rotational Speed

To maintain high rotor blade efficiency Wallis [93] recommends that the rotor tip speed should be kept below 160 m/s to avoid compressibility effects, which leads to reduced efficiency and increased noise. The P-11 Jetpack at design conditions has a tip speed of 193 m/s, which is higher than recommended, but has been proven to be adequate. Hence, this tip speed limit will be used for the P-12 as well. For a given size duct the blade tip speed criteria determines the maximum fan rotation speed as:

$$\Omega_{max} = \frac{V_{t,max}}{r_t} \tag{9.3.1}$$

where: $V_{t,max}$ is the maximum blade tip speed, Ω_{max} is the maximum fan angular velocity, and r_t is the radius of the rotor blade tip. The calculated maxmium fan rotational speed allows for the gear ratio between the engine, at maximum power/rotational speed, and the fan shaft to be determined.

Blade Relative Velocity

The relative velocity vector, Figure 9.6, is made up of the normal or axial velocity component, fan rotational speed, and half the induced swirl rotational velocity at the radius being analyzed. The relative velocity experienced by the rotor blade cross-section is:

$$V = \sqrt{V_n^2 + (\Omega r - 1/2 \omega r)^2} \tag{9.3.2}$$

where V is the relative velocity with respect to the blade, V_n is the axial velocity component (induced velocity calculated from equation (3.1.32)), Ω is the fan rotation speed, and ω is the unknown swirl velocity that is a function of the radius r. As ω is initially unknown an iterative process is used, with an initial value of $\omega = 0$ that is iterated until ω converges to within a set tolerance for each station, as describe by the criteria:

$$\frac{|\omega - \omega_{-1}|}{\omega} \leq 0.001 \tag{9.3.3}$$

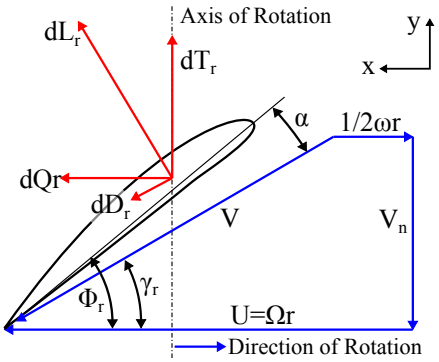

Figure 9.6: Schematic of blade element cross section showing absolute, swirl, rotational, and axial velocity vectors.

The relative velocity angle γ_r between the relative velocity and plane of rotation is:

$$\gamma_r = \arctan\left(\frac{V_n}{(\Omega - \frac{1}{2}\omega)r}\right) \tag{9.3.4}$$

Blade Setting Angle

The blade setting angle Φ_r is the angle between the plane of rotation and the aerofoil chord line. At the blade root Φ_r is large and becomes smaller towards the blade tip as γ_r diminishes due to increasing blade speed with radius. The blade setting angle is calculated as:

$$\Phi_r = \gamma_r + \alpha_{\frac{L}{D}max} \tag{9.3.5}$$

where $\alpha_{\frac{L}{D}max}$ is the maximum lift to drag ratio angle of attack for the aerofoil cross-section.

Blade Inflow, Outflow, and Camber Angles

The inflow angle, which is the angle between the axial velocity and fan rotational velocity, is determined as:

$$\beta_{1,r} = \arctan\left(\frac{\Omega r}{V_n}\right) \tag{9.3.6}$$

The outflow angle, which is the angle between the axial velocity and difference between the fan rotational and swirl velocities, is calculated as:

$$\beta_{2,r} = \arctan\left(\frac{(\Omega - \omega)r}{V_n}\right) \tag{9.3.7}$$

The camber angle is the total deflected angle of the airflow caused by the swirl velocity component and is:

$$\theta_r = \beta_{1,r} - \beta_{2,r} \tag{9.3.8}$$

The F-series camber angle adds an additional angle, ι, to the camber angle to take into account practical considerations such as the viscous effects of the boundary layer. An additional angle of $\iota = 10°$ is recommended by Wallis [93].

$$\theta_{F,r} = \theta_r + \iota \tag{9.3.9}$$

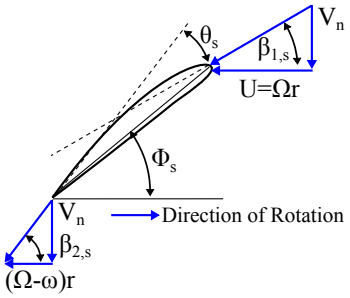

Figure 9.7: Schematic of blade element cross section showing inflow $\beta_{1,r}$, outflow $\beta_{2,r}$, camber θ_r, and blade setting angles Φ_r.

Blade Lift and Drag

With the blade setting angle known the blade lift L calculated for the blade element as:

$$dL_r = \frac{1}{2}\rho(V_n^2 + ((\Omega - \omega)r)^2)C_{l\frac{L}{D}max}c_r dr \tag{9.3.10}$$

where $C_{l\frac{L}{D}max}$ is the best lift to drag ratio of the aerofoil cross-section and c_r is the chord length of the rotor blade at radius r. The elemental rotor drag D is:

$$dD_r = \frac{dL_r}{C_{l\frac{L}{D}max}} \tag{9.3.11}$$

The elemental rotor torque Q and the thrust T is calculated as:

$$dQ_r = (dL_r \sin(\gamma_r) + dD_r \cos(\gamma_r))r \tag{9.3.12}$$

$$dT_r = dL_r \cos(\gamma_r) - dD_r \sin(\gamma_r) \tag{9.3.13}$$

The swirl velocity can now be determined by using the conservation of momentum in the tangential direction:

$$\omega = \frac{dQ_r B_r}{(r^2 V_n \rho \pi[(r + dr/2)^2 - (r - dr/2)^2])} \tag{9.3.14}$$

where B_r is the number of rotor blades. Equations 9.3.4 to 9.3.14 are iterated until the swirl velocity ω converges.

Blade Torque and Thrust

The rotor blade torque Q and thrust T can be calculated by the sum of the incremental torque and thrust between the rotor blade root and rotor blade tip radii as:

$$Q_r = \int_{r_r}^{r_t} (dL_r \sin(\gamma_r) + dD_r \cos(\gamma_r)) r dr \tag{9.3.15}$$

$$T_r = \int_{r_r}^{r_t} dL_r \cos(\gamma_r) - dD_r \sin(\gamma_r) dr \tag{9.3.16}$$

The total fan torque and thrust is calculated by multiplying the rotor blade torque and thrust by the number of rotor blades, B_r, as:

$$Q_{fan} = Q_r B_r$$

$$T_{fan} = T_r B_r$$

Now, the fan thrust and torque are known, as well as the blade geometric parameters at each radial station.

Fan Power

The power required to turn the fan is calculated as:

$$P_{fan} = Q_{fan} \Omega$$

The fan power must match the engine supplied power to insure that the full power of engine is transferred to the fan and consequentially the fluid. This is done by increasing the number of blades and chord length of the rotor blade in an iterative manner.

Fitting the Blade Profile

The Martin Jetpack fan blades use a fan blade profile based on the F-series profile that uses a NACA 230 camber line imposed on top of circular arc C4 aerofoil. The method of fitting the F-series profile onto calculated blades angles is done as described in [93]. Figure 9.8 shows the aerofoil profile for a 15% thick, 2% nose droop, 30° camber angle, and 0° blade setting angle blade section. The aerofoil properties of thickness and nose droop are chosen based

on the expected flow conditions, Reynolds number, and as recommended in [93]. The blade setting and camber angle are determined by solving for the unknown swirl velocity as per section 9.3. With the blade properties known at each radial station the F-series blade profile can be generated for each station. An example of the generated profiles for the Jetpack prototype P-12 fan blade are shown on Figure 9.9. Note that the actual profiles have a spline fitted to the generated profile points during the development of the CAD models to ensure a smooth rounded profile. Also the thickness of the trailing edge is reduced to suit manufacturing of the composite blades to give a trailing edge thickness of approximately 1 mm, which is the combined thickness of the top and bottom laminates.

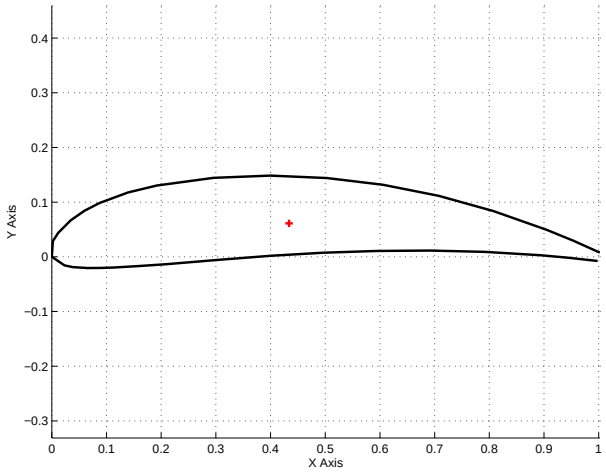

Figure 9.8: F-series aerofoil cross section with 15% thickness, 30° camber angle, and 2% nose droop

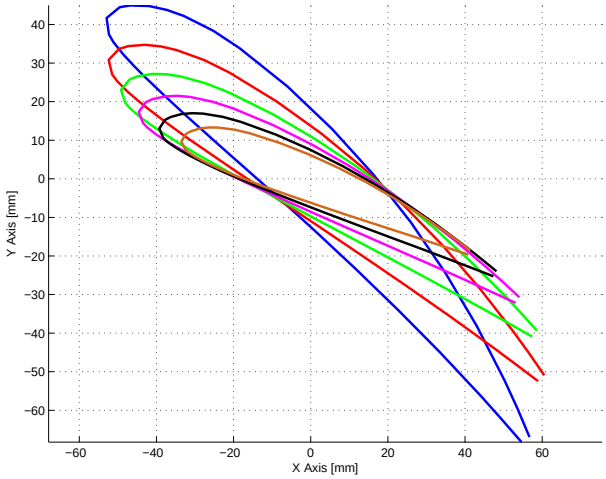

Figure 9.9: Generated F series aerofoil cross sections for P12 rotor blade

The blade thickness as presented in [93] is generated as:

$$y_t = \frac{t}{0.2}(0.3048x^{\frac{1}{2}} - 0.0914x - 0.8614x^2 + 2.1236x^3 - 2.9163x^4 + 1.9744x^5 - 0.5231x^6) \tag{9.3.17}$$

where t is the blade thickness in percentage chord and x is distance along chord in percentage of chord. The circular arc C4 and NACA 230 camber line are generated by the following equation:

$$\begin{cases} y_c = [(\frac{0.5}{\sin\frac{\theta_F}{2}})^2 - (x-0.5)^2]^{\frac{1}{2}} - \frac{0.5}{\tan\frac{\theta_F}{2}} + \\ (120.5 d_{nose}(x^3 - 0.6075x^2 + 0.1147x)) & x < 0.2025 \\ y_c = [(\frac{0.5}{\sin\frac{\theta_F}{2}})^2 - (x-0.5)^2]^{\frac{1}{2}} - \frac{0.5}{\tan\frac{\theta_F}{2}} + d(1-x) & x \geqq 0.2025 \end{cases} \tag{9.3.18}$$

where θ_F is the F-series camber angle and d_{nose} is the percentage of chord nose droop. The upper and lower surface curves are calculated by adding the camber line onto the thickness as:

$$x_u = x - y_t \sin\phi \tag{9.3.19}$$

$$y_u = y_c + y_t \cos\phi \tag{9.3.20}$$

$$x_l = x + y_t \sin\phi \tag{9.3.21}$$

$$y_l = y_c - y_t \cos\phi \tag{9.3.22}$$

where the angle ϕ is the slope of the camber line y_c at the x position being evaluated.

The generated blade profiles are rotated, scaled, and positioned with the centroid of the profile located at the origin of the Cartesian reference frame, as per Figure 9.9. The profiles are then stationed at their respected station, where the three dimensional coordinates of the each station profile are then saved into a text file. The series of profiles are imported into a CAD program such as Solidworks^{TM}, where a surface loft is made through all the blade cross-sections, as shown on Figure 9.10.

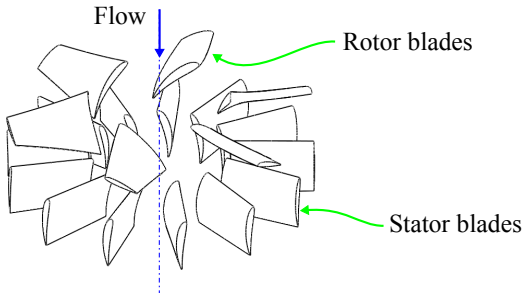

Figure 9.10: Lofted rotor and stator blades for P-12 ducted-fan

Determination of the Stator Blade Profile

The purpose of the stator blades is to remove the swirl velocity component induced into the flow. The process of determining the stator blade angles is a similar process to that of determining the rotor blade angles, with the simplification that the stator blade is stationary and that the swirl component, post fan, is known and is equal to zero ($\omega = 0$).

To determine the thrust and torque of the blade element, lift, drag, and blade setting angle of the aerofoil need to calculated. This begins by calculating the relative velocity angle γ at the blade element as:

$$\gamma_s = \arctan\left(\frac{\frac{1}{2}\omega r}{V_n}\right) \tag{9.3.23}$$

where the orientations of V_n and ω are shown on Figure 9.11.

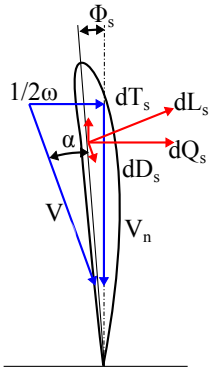

Figure 9.11: Schematic of the stator blade element cross-section and relative velocity

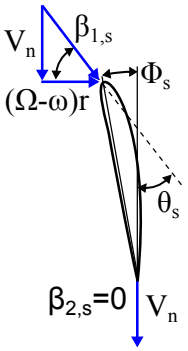

Figure 9.12: Schematic of blade element cross section showing inflow $\beta_{1,s}$, outflow $\beta_{2,s}$, camber θ_s, and blade setting angles Φ_s.

The blade setting angle Φ_s is the angle the between the axis of rotation and the aerofoil chord line. Due to varying swirl velocity the blade setting angle also varies along the span of the blade (blade setting angle Φ_s reduces with increasing radius), and is calculated as:

$$\Phi_s = \gamma_s - \alpha_{\frac{L}{D}max} \tag{9.3.24}$$

The inflow angle, $\beta_{1,s}$, which is the angle between the axial velocity and stator swirl rotational velocity, is determined as:

$$\beta_{1,s} = \arctan\left(\frac{\omega r}{V_n}\right) \tag{9.3.25}$$

Since the stator is designed to remove the swirl flow component the stator out flow angle, $\beta_{2,s}$, is set to zero. Thus the flow leaving the stator is purely axial flow.

$$\beta_{2,s} = 0 \tag{9.3.26}$$

The camber angle is the total deflection of the airflow passing the stator blade and calculated as:

$$\theta_s = \beta_{1,s} - \beta_{2,s} \tag{9.3.27}$$

Similarly to the rotor blade if using an F-series profile an additional angle ι is added to the camber angle. An additional angle of $\iota = 10°$ is recommended in [93].

$$\theta_{F,s} = \theta_s + \iota \tag{9.3.28}$$

With the blade setting angle known the blade lift, drag, thrust, and torque can be calculated for the blade element as:

$$dL_s = C_{l\frac{L}{D}max}\frac{1}{2}\rho(V_n^2 + (\omega r)^2)c_s dr \tag{9.3.29}$$

$$dD_s = \frac{dL_s}{C_{l\frac{L}{D}max}} \tag{9.3.30}$$

$$dQ_s = (dL_s\cos(\gamma_s) + dD_s\sin(\gamma_s))r \tag{9.3.31}$$

$$dT_s = dL_s\sin(\gamma_s) - dD_s\cos(\gamma_s) \tag{9.3.32}$$

The stator blade torque and thrust can be calculated by the sum of the incremental torque and thrust between the stator blade root and tip radii:

$$Q_s = \int_{r_r}^{r_t}(dL_s\cos(\gamma_s) + dD_s\sin(\gamma_s))r dr \tag{9.3.33}$$

$$T_s = \int_{r_r}^{r_t} dL_s\sin(\gamma_s) - dD_s\cos(\gamma_s)dr \tag{9.3.34}$$

The total stator torque and thrust is calculated by multiplying the stator blade torque and thrust by the number of stator blades used, as:

$$Q_{s,assembly} = Q_s B_s$$

$$T_{s,assembly} = T_s B_s$$

The number stator blades and stator blade chord length are chosen to produce a net stator torque equal to the fan torque to produce an overall torque neutral ducted fan. With the stator blade angles and chord length defined the same process described in section 9.3 is used to generate the cross-sectional profiles for the stator blade, as shown on Figure 9.13.

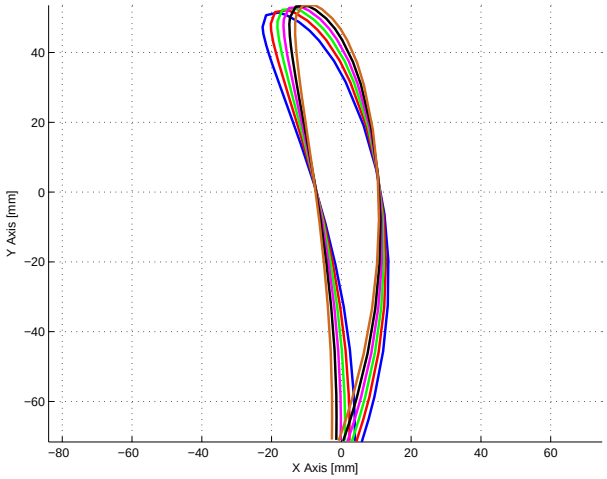

Figure 9.13: Generated F series aerofoil cross sections for P12 stator blade

Limitations of Blade Element Method

One of the major limitations of the blade element theory is obtaining good two dimensional lift and drag data

Assumed uniform axial inlet velocity, which is not case in reality as duct lip and nose cone affect the airflow into the flows blades, also presence of any crosswind means the flow will not be parallel to the duct axis.

Method is limited to attached steady flows

Inlet velocity is parallel to the axis, in reality the closeness of the fan to the duct inlet will mean the airflow entering the fan will be at an angle of

However, for the purpose of designing

9.4 Thrust Measurements on P-11 and P-12 Ducted-Fans

This section presents the static thrust measurements made on the P-11 600 mm and P-12 800 mm diameter ducted-fans using the Martin Aircraft Company static thrust test rig. This thrust rig allows for simultaneous measurement of duct thrust, engine torque, and engine speed. Using these measurements the engine power and the ducted-fan efficiency can be determined. The measurements performed showed that a repeatable maximum thrust of 1240 N and 1710 kg was achieved for the 600 mm and 800 mm ducted-fans, respectively. The P-12 800 mm ducted-fan, which uses the developed blade profiles described in section 9.3, showed a 38 % improvement in thrust and 25 % improvement in efficiency compared to the P-11 600 mm ducted-fan, exceeding expectations.

Aim

The aim of the testing is to quantify the ducted-fan static performance for P-11 600 mm and P-12 800 mm diameter ducted-fans and confirm that the 800 mm ducted-fan produces the equivalent anticipated Jetpack thrust of 3340 N.

Testing Methodology

A P-11 ducted-fan was secured to the Martin Aircraft Company thrust rig and ran at a range of engine speeds from 5000 to 5800 RPM to allow the ducted-fan thrust, engine torque, and engine speed to be simultaneously measured. The thrust rig, shown in Figure 9.14, consists of an engine (75 kW Hirth 3701 ES/VS Engine) and a ducted-fan using the same belt drive assembly as per the P-11 Jetpack. Using linear bearings the thrust rig allows the entire ducted-fan thrust force to pass through a single load cell, which measures the developed thrust force. A second load cell is used to constrain and measure the engine torque. The engine was manually controlled to hold a range of engine speeds between 5000 to 6000 RPM for time interval durations of at least 2 s to obtain steady state data. At each interval the collected data was time-averaged over the period to reduce time variant and signal noise effects.

The time-averaged measurements were used to calculate the engine power by:

$$P_s = Q_{eng}\Omega_{eng} \tag{9.4.1}$$

where P_s is the supplied engine power, Q_{eng} is the engine torque, and Ω_{eng} is the engine rotational speed. Rearranging equation 3.1.34 and using the efficiency ratio of useful power to supplied power, $\eta = \frac{P_d}{P_s}$, the ducted-fan efficiency can be calculated as:

$$\eta = \frac{\sqrt{\frac{T_d^3}{4\rho A_r \epsilon_d}}}{P_s} \tag{9.4.2}$$

Note, this efficiency also includes the unknown, power loss of the drive train. Gates [94] suggests that the synchronous drive belts, as used on the Jetpack can be maintained at 98 % efficient in transmitting power, which gives an indication of the drive train power loss experienced on the Jetpack.

The above methodology was repeated for the P-12 ducted-fan measurements by replacing the 600 mm ducted-fan with the 800 mm ducted-fan and changing the fan to engine gear ratio from 40/34 to 40/48.

Figure 9.14: Static thrust rig with P-12 800 mm ducted-fan in operation

Results

P-11 Ducted-Fan Measurements

Time averaging the performance data at steady engine speeds for the five test runs produces the result shown on Figure 9.15. The maximum thrust results can be seen on Table 9.2. Comparing the results between fine[1] and coarse[2] pitch it can be seen the results are similar with the coarse pitch showing slightly better performance. The main difference between the fine and coarse pitch is the engine speed where the maximum performance occurs, 6000 RPM and 5800 RPM for fine and coarse pitch settings, respectively.

Table 9.2: P-11 600 mm ducted-fan maximum measured static performance

	Engine Speed [RPM]	Thrust[N]	Torque [Nm]	Power[kW]	Efficiency[%]
Fine pitch as per design	6000	1220	107	68	53
Coarse pitch as per P-11	5800	1240	110	68	55

Additional charts showing performance versus time and versus engine speed from the five test runs performed are shown on Figures D.72 to D.76 in Appendix D. Runs one to three, Figures D.72 and D.74, show the performance of the ducted-fan with a coarse blade pitch setting, which has been used for test flying of the P-11 prototypes. Runs four and five, Figures D.75 and D.76, respectively, show the performance of the fan blades set at a finer pitch setting, which was assumed to be close to the original design intent.

P-12 Ducted-Fan Measurements

Seven test runs were performed and plots of performance versus engine speed and performance versus time were produced, refer to Figures D.77 to D.83. Figure 9.16 shows the steady state performance results from the 800 mm ducted-fan over a range of engines speeds from 4000 RPM to 6200 RPM. Table 9.3

[1] Fine refers to blade setting angles as per original design intent.

[2] Coarse refers to steeper blade setting angles used on P-11 prototypes.

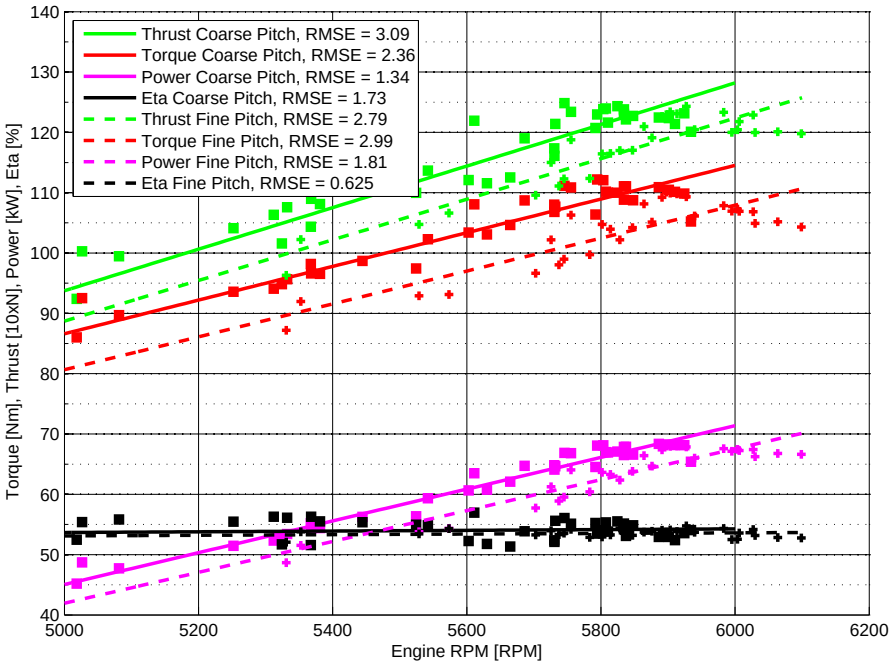

Figure 9.15: Static performance of the P-11 600 mm ducted-fan, measured from five test runs.

summaries the key performance values and compares the P-12 results to that of the P-11 ducted-fan.

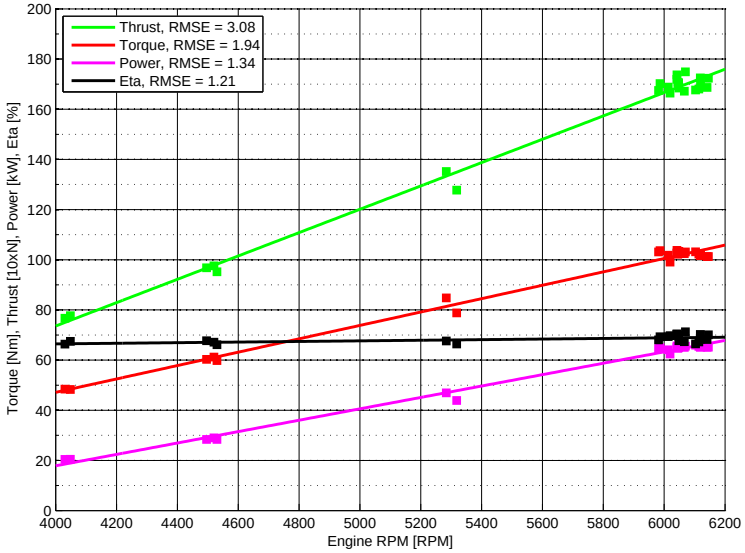

Figure 9.16: P-12 800 mm ducted-fan steady state static performance versus engine speed

Additional test runs were made on the P-12 ducted-fan, refer to Figures D.81 to D.83, to quantify the performance effects by removing the nose and tail cones. It was found that the removal of the tail cone only slightly degraded performance (2 % reduction), but the removal of both the tail and nose

Table 9.3: P-12 800 mm ducted-fan maximum measured static performance compared to P-11 600 mm

	Engine Speed [RPM]	Thrust[N]	Torque [Nm]	Power[kW]	Efficiency[%]	Area [m^2]
P-11 coarse pitch	5800	1240	110	68	55	0.28
P-12 design pitch	6100	1710	103	66	69	0.50
Difference [%]	5	38	−6	−2	25	79

cones had a synergistic effect of reducing the ducted-fan thrust by 11 %, as summarised on Table 9.4.

Table 9.4: Effects of nose and tail cones on P-12 ducted-fan thrust

Description	Thrust [N]	Loss [%]
With nose and tail cones on	1710	-
Tail cone off	1670	2
Nose cone off	1610	6
Nose and tail cones off	1520	11

Discussion

The P-12 rotor and stator blade geometries developed by the author, in section 9.3, and the larger duct diameter have significantly improved the static thrust from that of the P-11 ducted-fan, as summarized in Table 9.3. The static thrust improvements are the result of improved ducted-fan efficiency and a larger duct diameter, which allows for a greater mass flow rate, and hence, a greater change in momentum.

Using the determined ducted-fan efficiencies for both the P-11 and P-12 ducted-fans and equation (3.1.34), Figure 9.17 can be produced, which shows the calculated performance of the ducted-fans versus static thrust[3]. Figure 9.17 can be used to determine the static thrust for a given power. Hence, the figures can be used to determine the maximum static thrust of the P-11 and P-12 Jetpacks by reading thrust value for a given power setting. Figure 9.17 clearly shows the superiority of the larger 800 mm ducted-fan, which used on the Jetpack, powered by a 150 kW engine, can produce a static thrust of 3730 N, (1860 N per duct). This is a 41 % improvement compared to the P-11 600 mm ducted-fans, which produces s thrust force of 2640 N (1320 N per duct) for the same power. For the P-11 Jetpack to obtain the same static thrust maximum static thrust of the P-12 (3730 N) an engine power of 249 kW would be required. The increased weight of a such an engine and the corresponding increased fuel weight reinforces the impracticality of increasing engine power alone to achieve greater thrust performance.

Comparing the measured results to the predicted results from the blade element theory, Table 9.5, it can be seen the differences do exist, which is expected for the simplified theories and numerous assumptions that the blade element method employs, refer to section 9.3. The difference between measured and predicted power can be partially accounted for since the blade element theory does not include the unknown transmission power loss of the belt drive.

[3]Note, the Figure 9.17 shows the ducted-fan performance per duct, these values need to be multiplied by two to equate to performance on the Jetpack.

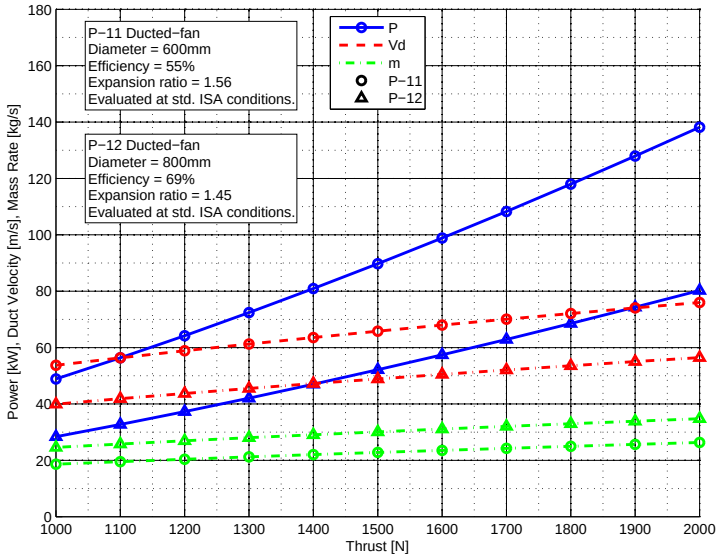

Figure 9.17: Static performance comparison of the P-11 600 mm and the P-12 800 mm ducted-fans

Table 9.5: P-12 800 mm static performance compared to blade element theory

	Fan/ Engine Speed [RPM]	Thrust[N]	Torque [Nm]	Power[kW]
P-12 measured	5083/6100	1710	103	66
BET predicted	5000/6000	1590	112	58.5
Difference [%]	2	7	−8	11
P-12 interpolated	5000/6000	1670	101	63.3
Difference [%]	0	5	−10	8

Conclusion

The static thrust measurement confirms the success of the author's rotor and stator design for the P-12 800 mm ducted-fan. The results show that the maximum static thrust for the P-12 Jetpack is 3730 N, which is 390 kg/12 % more than initially estimated and 1080 N/41 % more the P-11 Jetpack. The improved thrust will greatly improve the performance of the P-12 provided the weight estimated in section 9.2 is accurate. This section proved the lift force for the P-12 Jetpack, but an aircraft must also have control, which is the topic of the next section.

9.5 Control Vane Design for P-12

A new control vane design for the P-12 Jetpack was devised to improve on the aerodynamics, functionality, reliability, and manufacturability of the P-11E and predecessor prototypes. The control vane design of the P-12 involves four identical vanes arranged in a crucifix layout with each vane individually driven by a servo, as shown of Figures 9.1 and A.3. This design achieves control improvements by:

- Crucifix vane arrangement
- Pitch and yaw vane mixing
- Direct drive
- Common vane design

The crucifix position of the vanes allows all the vanes to be submersed in high dynamic pressure airflow with no flow interruptions in front of the vanes. Mixing of yaw and pitch control vanes doubles the pitch force/moment and eliminates the need for separate yaw vanes, which were featured on the original P-11A to C Jetpacks. The reliability of the control vanes has been improved as each individual vane is driven by its own servo via a direct connection to the servo, thus reducing the servo load and enabling a faster response. The direct connection also greatly reduces backlash, which reduces vane flutter and improves aerodynamic performance. Rather than the cantilevered design of predecessors each control vane on the P-12 is supported at both ends by bearings, which significantly reduces vane vibration. The common design of the control vane has improved the manufacturability and maintainability over the P-11 as any vane can be used in any location, roll, pitch or yaw. This reduces the number of unique components and the associated cost.

Control Vane Testing

The aim of the control vane testing was to determine a suitable control vane for the P-12 Jetpack that could deliver 130 N or more of lift, as determined from section 9.2, and to determine a suitable hinge line for the vane. Four control vane designs, Figure 9.18, based on a centrally located 200 mm chord vane were experimentally evaluated. The 200 mm chord vane was chosen as it was

proven on the P-11E Jetpack and readily available. From previous testing and knowledge, end-caps were fitted to all vanes to effectively improve the useful span of the vane, by reducing tip vortices and induced drag. The end-caps also easily allow for tri-decker vane configurations, as the end-caps provide a structure for the additional aerofoils.

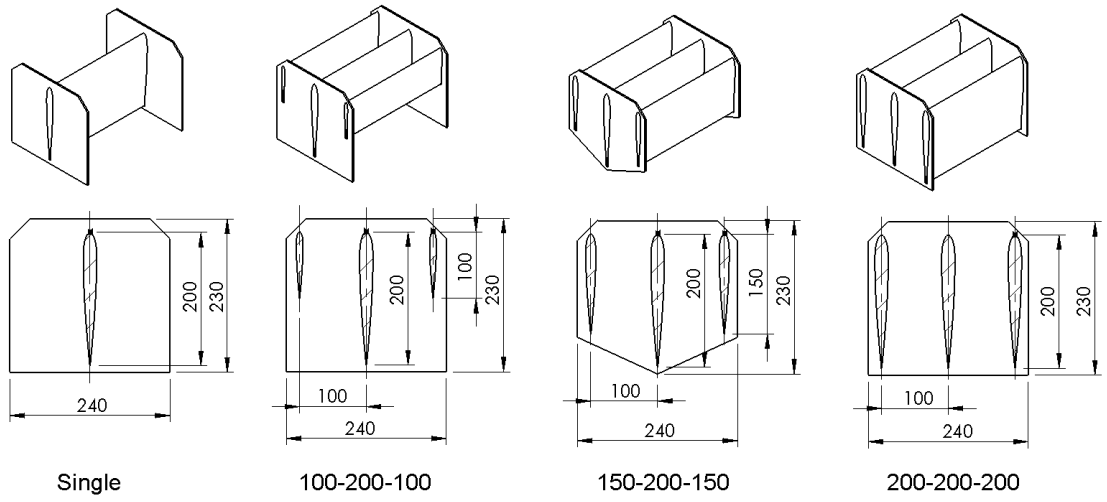

Figure 9.18: Tested control vane designs

Experiment Setup and Methodology

Two types of experimental setup were used. The first held the various control vanes at an angle of attack of 20° to determine the most suitable control vane design. The second setup was essentially a modification of the first to allow the chosen control vane to move under servo load between maximum positive and negative angles of attack to determine the correct vane hinge line.

For both setups control vanes were positioned on the control vane measuring rig, Figures 9.19a and 9.19b , in the duct wake to replicate their intended position on the Jetpack (leading edge of control vane 200 mm from the duct trailing edge). The control vane measuring rig used two load cells to measure vane lift and drag forces, Figure 9.19a. Four control vanes designs, as shown in Figure 9.18 and Table 9.6, were secured onto the vane rig and held at a 20° angle of attack. The ducted-fan was then ran at a nominal power setting and the DAQ system recorded measurements from the vane lift and drag load cells as well as the duct thrust, engine torque, and engine speed. This was repeated for each of the vane designs in Table 9.6. Using the duct thrust measurement and equation 3.1.31, the nominal velocity at the control vane could be determined. This velocity was used to determine the vane lift and drag coefficients, using equations B.1.6 and B.1.5 where the vane area was taken to be the plan-form area of the vane, which for the tri-decker vanes includes the plan-form area of all the individual aerofoils.

For testing purposes the vanes and end-caps were constructed from wood with the exception of the central 200 mm, which is made from carbon fiber. This allowed for rapid evaluation of each vane design.

Once an optimum vane design was determined the chosen vane was fabri-

cated from carbon fiber and the vane test rig modified to include a servo to drive the control vane and a pot to record the vane angle as the control vane was deflected through its range of motion. To maintain simplicity of the experiment, the servo current, hence servo load, was measured to determine the moment on the vane. Using counter weights the servo load was measured for a range of moments until the servo was unable to hold the moment. This data was used to produce a relationship between vane moment and servo current to determine the vane moment under aerodynamic testing.

The testing procedure involved taking the engine up to nominal engine speed and then driving the servo between maximum positive and negative deflections. Approximately after ever 5° of deflection the vane was held steady for approximately 2 s to obtain steady state vane forces and moment. If the vane deflection became unstable, for example deflected to maximum mechanical deflection, the test was halted as the instability highlights the vane centre of pressure is in front of the hinge line, which is unfavourable. The hinge line was systematically brought forward until a suitable hinge line was found.

(a) Rear view (b) Front-side view

Figure 9.19: P-12 control vane test apparatus

Results of the Control Vane Experiment for P-12

Table 9.6 summarizes the results obtained from measuring the vane lift and drag forces for the four control vane designs at an angle of attack of 20°. The single control vane produced the highest lift coefficient of 0.7 although its force was the lowest 79 N, this simply indicates that the single control vane is the most effective design in terms of plane-form area. The 200-200-200 vane produced the largest lift force of 148 N. The 100-200-100 and 150-200-150 vanes produced comparable lift forces of 131 N and 133 N, respectively, and both vanes had same drag force of 50 N.

Moment measurements were taken for a range of hinge line positions from 22 % to 30 % chord, but these positions were all found to be unstable as the vane became stuck at maximum mechanical deflection under aerodynamic load, and the servo was unable to return the vane to neutral position. The hinge line was then brought forward to 13 % chord where an acceptable, stable, response was found where the vane under aerodynamic load was able to drive to 35° without becoming stuck. A summary of the nature of the vane hinge line positions is

Table 9.6: Control Vanes for P-12, description and results at 20° angle of attack. Scaled weight and scaled inertia refer to the weight and inertia data being scaled with respect to the single vane values.

Description	Chord Length [mm]	Span [mm]	Lift [N]	Drag [N]	Lift Coef.	Drag Coef.	Weight [N]	Scaled Weight	Inertia [kg mm^2]	Scaled Inertia
Single vane	200	295	79	24	0.70	0.22	4.8	1	2900	1
Tri-decker	100-200-100	0.285	131	50	0.60	0.23	6.4	1.3	4600	1.6
Tri-decker	200-200-200	0.284	148	48	0.45	0.15	11.0	2.3	11000	3.9
Tri-decker	150-200-150	0.285	133	50	0.52	0.19	8.1	1.7	6419	2.2

shown on Table 9.7.
Table 9.7: Summary of 100-200-100 tri-decker control vane hinge line determination

Hinge Line [mm]	Percentage Chord [%]	Nature
26	13	Stable
43	22	Unstable
52	26	Unstable
60	30	Unstable

Although the servo current increased with the angle of attack, indicating increased aerodynamic moment, it was not identifiable whether the moment was positive or negative. The nature of the moment was confirmed by visual inspection of the vane under load. Figure 9.20a shows a typical plot of 100-200-100 tri-decker vane performance versus angle of attack. The plot shows that the lift force is linear up to 27°. The moment plot shows that the vane is well balanced up 18°, but thereafter increases abruptly requiring greater servo load. Note this is a negative moment, which requires servo load to deflect the vane.

Figure 9.20b shows the current and angle of attack versus time, and shows that the current leads the vane position when the vane returns from maximum deflection to neutral position. This indicates that the vane is experiencing a stable (negative) aerodynamic moment, which favourably returns the vane to the neutral position.

Discussion of Results

Optimum Vane Design

Table 9.6 shows the results of the four control vane designs tested. Although the 100-200-100 tri-decker vane does not produce the most lift it was chosen as the optimum vane as it produced an increase of lift of 66 % compared to the single vane with only an increase of 60 % in inertia. The high inertia of the 150-200-150 and 200-200-200 vanes puts a much higher dynamic load on servo, which is detrimental to servo life and response, hence these have been disregarded. The additional area of the tri-decker vanes did not increase the lift of the vane proportionally, as reflected by the lift coefficients. This is believed to be due to the circulation of the windward aerofoil turning the airflow in front of the leeward aerofoils so that the leeward aerofoils are at a relatively lower angle of attack and thus produce less lift, as shown on Figure 9.21.

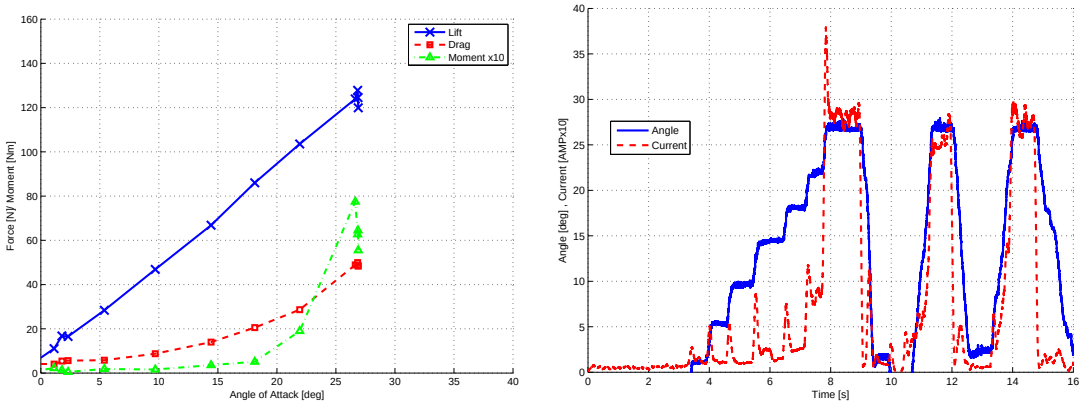

(a) Aerodynamic reactions (b) Deflection and current load

Figure 9.20: Performance of 100-200-100 tri-decker control vane with hinge line at 26 mm from leading edge at an engine speed of 6000 RPM.

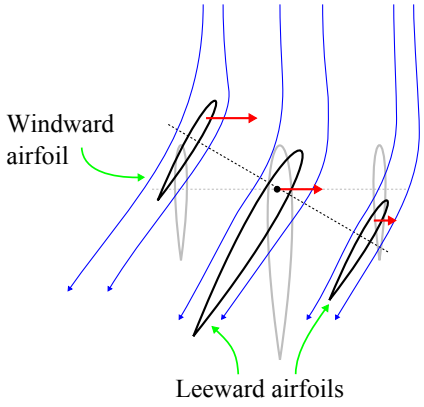

Figure 9.21: Schematic of airflow/streamlines through the cross-section of a tri-decker control vane.

Vane Centre of Pressure

The location of the centre of pressure needs to be determined to find the optimum hinge line for the control vane that allows for the lowest servo load. A minimal servo load is necessary to maintain fast and precise control with minimal servo power consumption. Ideally the hinge line should be slightly in front of the vane centre of pressure, so that in the event of a servo failure the control vane rests in a stable equilibrium at the neutral position and does not contribute to control moments as it is not controllable.

Initially the centre of pressure was assumed to be at 25 % chord, which is that of a single symmetrical two dimensional aerofoil. Hence, a range of hinge line positions from 44 mm to 60 mm from the leading edge, 22 % to 30 % chord, respectively, were tested. All the hinge line positions tested within this range were unstable and exceeded the servo load becoming stuck at maximum mechanical deflection. The unstable nature indicates that the centre of pressure of the tri-decker vane is further fore than initially assumed. It is thought that the windward aerofoil is the most effective, as the circulation produced

from this aerofoil decreases the angle of attack on the leeward aerofoils and thus decreases the lift created from these aerofoils, as shown in Figure 9.21. This results in the windward aerofoil producing a larger moment than the opposing moments of the leeward aerofoils resulting in a centre of pressure that is forward of the hinge line and produces an unstable control vane. Hence, the hinge line needs to move forward to where the moment produced by the leeward aerofoils is greater than the contribution of the windward aerofoil to achieve a centre of pressure behind the hinge line and thus a stable control vane.

A hinge line position of 26 mm, 13 % chord, was tested and showed a satisfactory stable response. The control vane under aerodynamic load moved freely and responsively, hence the hinge line position of 26 mm was chosen for P-12 100-200-100 Tri-decker vane. This result shows that the presence of the additional vanes affects the aerodynamic performance of the other vanes, as illustrated in Figure 9.21.

Improving Control Moments

Control moments in roll and pitch could be further improved by:

- Increasing the vane moment arm
- Modifying duct geometry to obtain a constant centre of pressure location
- Changing the vane layout

Increasing the vane moment arm is the most favourable means of increasing the control moment as this does not require increasing the vane force and consequently the vane drag. However, because of the requirement of maintaining a significant clearance between the control vanes and the ground during landing, there is a limit on how far the vanes can be extended downward. This limit can be increased by increasing the height of the landing gear, but this is detrimental to aircraft's weight as a larger and heavier landing gear would be required.

Modification to the duct by increasing the duct leading edge radius or including a slat on the duct leading edge can be used to prevent or minimise the movement of the duct centre of pressure, as described and shown in [55]. Vortex generators such as those used on the leading edge of aeroplane wings could also be employed to delay leading edge separation, which is the main cause for the movement of the centre of pressure. However, due to the nature of these devices they are best experimentally tested and evaluated.

The layout of the control vanes in the duct wake not only affects the vane effectiveness, but also the net control moments. Using the chosen 100-200-100 tri-decker vane, evaluated at an angle of attack of 20°, the total pitching force per duct can be determined to be 260 N for the crucifix vane layout, see Figure 9.22a. However, greater longitudinal and lateral moments can be developed by positioning the control vanes in an X configuration, Figure 9.22b. This layout enables all vanes to contribute to both lateral and longitudinal moments, at the expense of reduced moments for skewed flights. Using the X configuration a force of 370 N, per duct can be achieved in either the longitudinal (x_f) or the

lateral (y_f) direction, which is a 42 % improvement over the crucifix layout, however the *apparent weight*[4] has increases by 80 %. Using eight single vanes radially positioned, the potential control force can be improved to 380 N, an improvement of 46 %, but this configuration has a heavier weight of 38 N and a slightly heavier apparent weight of 230 N. Even with the increased number of vanes the low aerodynamic drag of the single vanes ensures that the apparent weight is comparable to that of the tri-decker arrangements. This arrangement would also have the least servo load as the single vanes have the lowest inertia. This allows for smaller servos and/or improved servo life, and potentially offer the greatest redundancy in terms of control vane or servo failure. The down side of this arrangement is the increased number of mechanical components and wiring, which may increase the aircraft weight. However, every vane layout must try to avoid locating the control vanes in the wake of the drive belts due to this wake being at lower dynamic pressure, which decreases the effectiveness of the vane in this location.

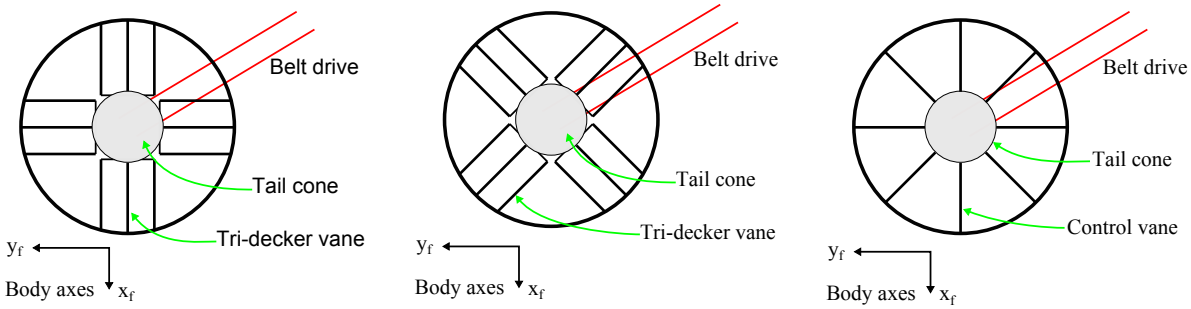

(a) Crucifix layout, as per P-12 (b) X layout (c) Radial layout

Figure 9.22: Various control vane layouts showing vane force contribution in longitudinal direction

Table 9.8: Summary of P-12 control vane layout concepts, evaluated per duct at a vane angle of 20° using values from Table 9.6.

	Lift per Vane [N]	Drag per Vane [N]	Weight [N]	Apparent Weight [N]	Net Pitch/Roll force [N]
Crucifix	131	50	25	125	260
X layout	131	50	25	225	370
Radial	79	24	38	230	380

Conclusion

From the testing, the 100-200-100 tri-decker control vane design has been chosen for the P-12 Jetpack as this vane provides a high lift force, 131 N, for only a small inertia and weight increase compared to that of a single control vane. The 200-200-200 tri-decker vane has the largest lift force, 148 N, but also the largest inertia 390 % greater than the single vane.

Although the crucifix vane layout is the chosen control vane configuration for the P-12 Jetpack an X layout could provide a 41% improvement in pitch

[4]Note, *apparent weight* is the sum of vane weight and vane drag.

and roll force by vectoring all the vanes together.

9.6 P-12 Jetpack Test Flying

This section explains the flight testing performed on the P-12 Jetpack. Although the P-12 Jetpack has been designed to perform manned demonstration flights, the initial testing was done as unmanned to reduce the inherent risk of initial test flights and build confidence in the machine, refer to Figures 9.23 and 9.24 which show the unmanned configuration and the P-12 Jetpack inflight. The P-12 Jetpack's first test flight was on the 1st of November 2012. Using the knowledge from previous test flying the P-12 Jetpack achieved controlled hovers within an hour from first hover. Subsequent test flights focused on in improving flight performance by further control tuning to allow for faster flight speeds.

The improved landing gear design eased takeoff and landing manoeuvres to the point where the remote control pilot did not need the assistance of the ground handlers to achieve flight. It must be mentioned that ground handlers were necessary for the P-11 Jetpack prototypes to get airbourne as the landing gear lacked stability during takeoff and landing.

The P-12 Jetpack also demonstrated greater control during takeoff and landing. The P-12 tri-decker control vanes allow for greater control due to the outer vanes on the tri-decker not being as greatly affected by the airflow stagnation when the ducts are close to the ground. This is also a significant improvement over the P-11 Jetpack prototypes which had little to no control within 1 m from ground due to the stagnation of airflow over the control vanes.

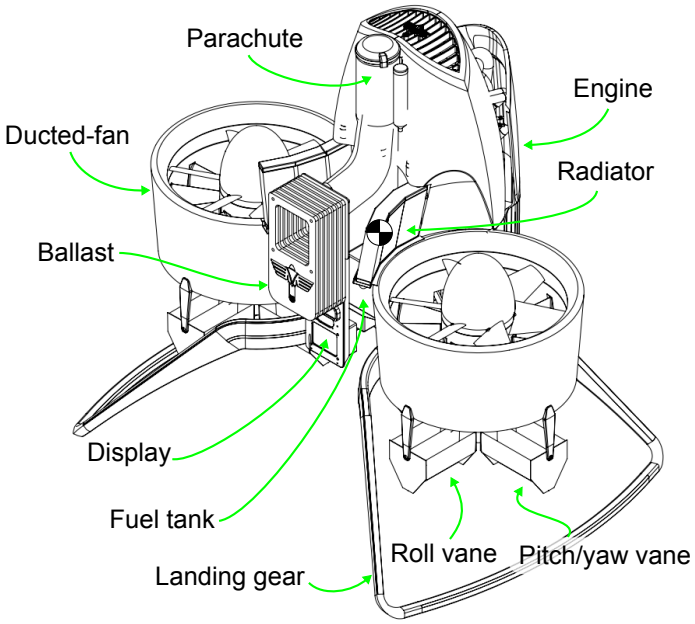

Figure 9.23: Martin Jetpack P-12 design concept with 800 mm ducted-fans

(a) P-12 in flight

(b) P-12 with engine cowlings fitted

Figure 9.24: Unmanned P-12 Jetpack

Figures 9.25a to 9.25d show how the P-12 Jetpack performs to time varying pilot inputs. Both Figures 9.25a and 9.25b show that the roll and pitch command lead the actual roll and pitch attitude with small delay. Although at larger roll and pitch commands the commanded and actual values differ by an error, this error, up to 5°, is not a hindrance to the handling as it is not critical that the aircraft is flying exactly at the commanded attitude. The critical factor is that when the pilot commands a change in attitude that the aircraft responds in the correct sense with minimal delay, and when a steady state attitude is commanded that the aircraft remains at a steady state attitude close to what is commanded. The error at steady state is negligible as the pilot is not concerned about the attitude, but rather about the speed of the aircraft derived from the attitude.

Figure 9.25c shows the commanded and actual yaw rate on the P-12 Jetpack. It can be seen that the actual yaw rate is quite noisy, which is due to yaw gain being set at too high a value. If a rate gain is set too high it will induce a statically stable oscillator motion instead of a damped motion.

Figure 9.25d shows the commanded climb rate versus the actual climb rate. It can be seen that the actual climb rate oscillates slowly (period approximately 1 s), this is similar to the predecessor Jetpacks and indicates that the climb rate control still needs to be fine tuned, or other control method needs to be found.

9.7 Comparison of P-11A and P-12

This section compares the P-11A Jetpack to the P-12 Jetpack and highlights the superiority of the P-12 Jetpack. This comparison is made to show and quantify the improvements this research has made on the Martin Jetpack concept. Using the Jetpack flight model, described in Chapter 4, for the Jetpack parameters describing the P-11A and P-12 Jetpacks Figures 9.26 to 9.27 have been created. Refer to Section E.2 for additional P-12 performance charts.

Figure 9.26 show how the hovering performance has been improved from the P-11A Jetpack to the P-12 Jetpack. The larger ducts and improved ro-

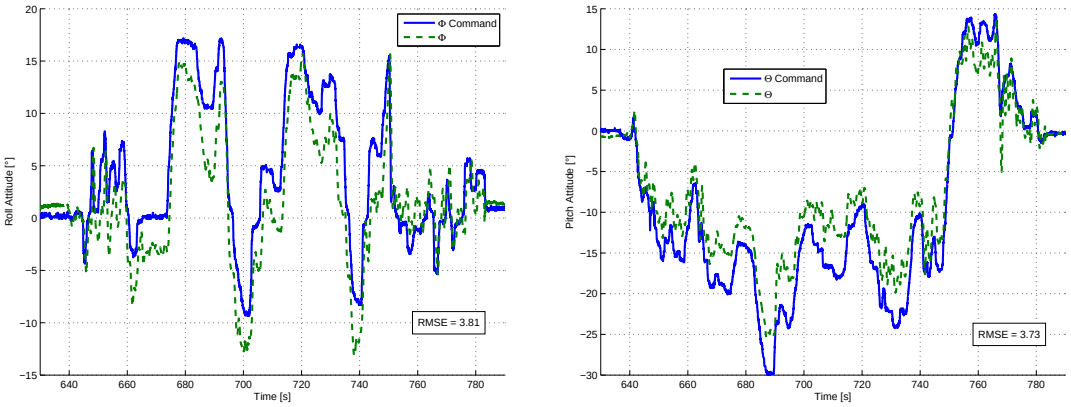

(a) Roll attitude (Φ)

(b) Pitch attitude (Θ)

(c) Yaw rate (r)

(d) Climb rate (w_g)

Figure 9.25: Comparison between commanded and actual for P-12 Jetpack.

tor and stator design has allowed to significantly increase the takeoff weight. Theoretically the P-12 Jetpack could sustain an out of ground effect hover at standard sea level conditions with a takeoff weight of 3700 N, which is 42 % larger than the P-11 Jetpack maximum takeoff weight of 2630 N. The maximum takeoff weight of the P-12 Jetpack is limited to 3140 N to ensure that a reasonable thrust margin exists for manoeuvering, which at sea level conditions is 29 %, compared to 8 % for the P-11A Jetpack with a takeoff mass of 2450 N. The higher thrust margin of the P-12 Jetpack allows for improved performance, as more engine power is available for manoeuvering and altitude compensation. The high thrust margin also means that the engine is running at lower power, which equates to lower fuel burn rates and less strain/wear on the engine.

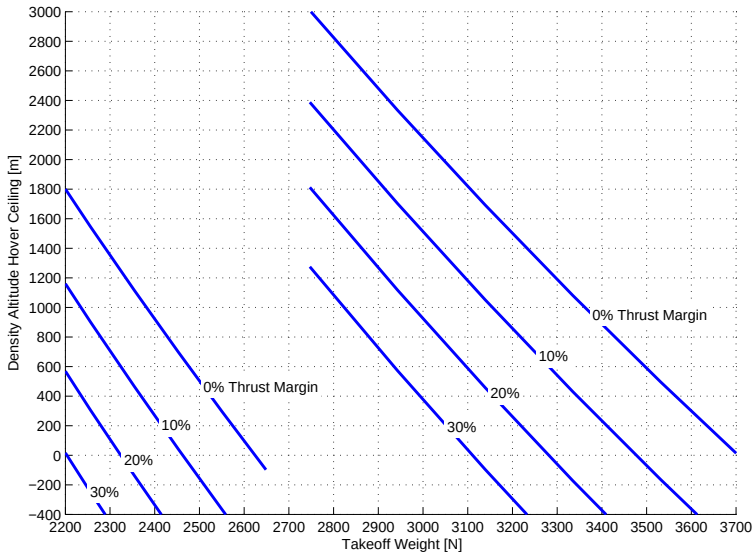

Figure 9.26: Hover height performance comparison between P-11A and P-12.

Figure 9.27 compares the trimmed longitudinal level flight performance between the P-11A and P-12 Jetpacks. It can be seen that the P-11A Jetpack has a maximum trimmed level flight speed of only 3.2 m/s, which is quite impractical. The reason for the poor flight performance is due to the ducted-fan aerodynamics not being correctly taken into account in the development of the P-11A Jetpack, hence the pitch vanes of the P-11A Jetpack become saturated trying to trim the aircraft. Using the findings of this research the centre of gravity is correctly aligned to the centre of pressure on the P-12 Jetpack resulting in the level flight performance shown on Figure 9.27, which shows that the maximum level flight speed is 27 m/s. However, this speed is also limited by pitch vane saturation due to the large change in centre of pressure movement.

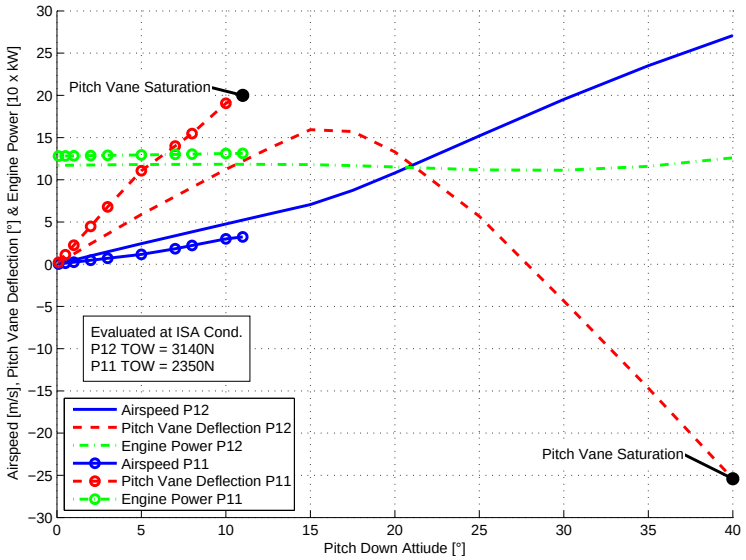

Figure 9.27: Longitudinal level trimmed flight performance comparison between P-11A and P-12.

9.8 Conclusion

Using the theories and methodologies developed by this research the aerodynamic design of the Martin Jetpack was imporved as explained within this chapter. The test flights performed between November 2012 and April 2013 have demonstrated the improved flying characteristics of the P-12 compared to the predecessor prototypes, validating the engineering methodology presented in this chapter and the research described in this thesis. Table 9.9 summarises the key performance values of the P-12 to date. While the P-12 Jetpack has to yet demonstrate extensive manned flight operations it has proven manned hovering flight, as shown in Figure 9.28.

Table 9.9: Jetpack P-12 performance April 2013

Performance	Value
Max speed	12.5 m/s
Wind/turbulence tolerance	Moderate $\approx$ 7 m/s
Max demonstrated takeoff weight	3140 N
Handling quality	Very Good

Figure 9.28: P-12 in hovering flight, flown by James Bowker, 25^{th} June 2013

Chapter 10

Remaining Issues and Future Research for the Jetpack

"It is possible to fly without motors, but not without knowledge and skill."
Wilbur Wright

This Chapter highlights the author's opinions of the major technical issues facing the development of the Martin Jetpack. The Chapter also explains the author's suggestions for future research topics on the Jetpack.

10.1 Remaining Issues Facing the Jetpack

For the Martin Jetpack concept to become a commercial success many technical barriers need to be overcome. Foremost the Jetpack must be able to fly well enough to meet the intended mission requirements. The purpose of this thesis has been to understand the unique aerodynamics of the Martin Jetpack to allow the development of a flight model to quantify the aerodynamics of the Jetpack. The validated model has become a successful tool to predict and study existing and future Jetpack prototypes. The prediction and simulation ability of the model allows the aerodynamics to be inexpensively optimized, hence achieving a Jetpack configuration that has sound aerodynamic qualities that allow the Jetpack to successfully meet mission specific performance goals.

Jetpack Control

The ideal control for a VTOL aircraft uses movement of the lift vector relative to the centre of gravity. This method produces powerful moment couples, which are naturally scaled to the aircraft, as the moments are created by the separation of the lift and weight forces. Helicopters and multi-rotor copters are prime examples of this type of control.

For the Jetpack, control moments are made from deflection of control vanes, which for pitch and roll produce unbalanced force reactions as well as moments. This is not ideal as only moments are desired, but translation accelerations also occur in the opposite direction to the intended attitude change. In flight, this form of control is adequate. However as the Jetpack approaches the ground, control authority decreases to the point when the Jetpack contacts the ground

there is no longer any effectiveness from the control vanes to control the Jetpack. The low to no control effectiveness makes the takeoff and particularly the landings phases difficult to perform, as little control exists to maintain the aircraft in the correct attitude and zero ground speed condition, which is needed for a successful landing.

The inability of the Jetpack to move its thrust vector relative to its CG requires the Jetpack to be operated from level ground. Operations from sloped terrain must be avoided as the thrust vector on takeoff and landing will be perpendicular to the slope surface, which greatly increases the chance of the Jetpack from tipping over due to the moment produced by the thrust force and the landing gear, as illustrated on Figure (10.1). The Jetpack is unstable on the ground when the vertical component of the thrust is less than the weight force and the moment of the thrust force and landing gear is greater than the moment of the weight force and landing gear. This is mathematical shown as:

$$W > T\cos\theta \tag{10.1.1}$$

$$Tl_{xLG} > Wl_{xLGi} \tag{10.1.2}$$

where l_{xLG} and l_{xLGi} are the x positions of the landing gear from the CG in body and inertial frames respectively. This ground stability is made worse by the presence of wind, turbulence, and any Jetpack momentum.

A better option for the Jetpack would be direct control of the lift vector relative to the CG. This could perhaps be accomplished through the use of moveable slats, or use of ejectors as described in [7] with or without the current control vanes.

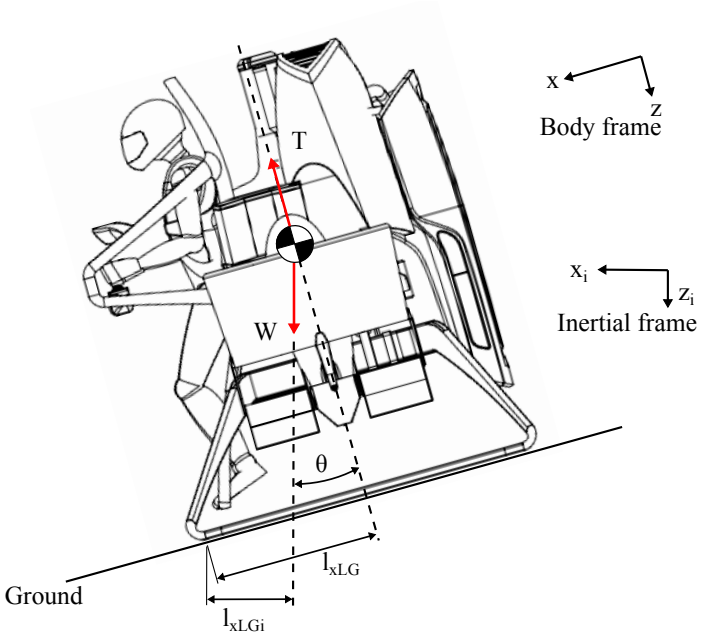

Figure 10.1: Free body diagram of P-12 Jetpack demonstrating tipping hazard during takeoff and landing from sloped terrain.

Acoustic Noise

The current Jetpack is far too loud, decibel readings in excess of 100 dB have been measured, which is far from acceptable for both military and civilian use.

The military require a quiet aircraft to avoid detection by enemy forces and to allow close proximity surveillance. The civilian uses of the Jetpack such as search and rescue, first response and urban commuter will also require the quietest possible Jetpack as these intended uses by their nature will require the Jetpack to be flying at low elevation and most often over urban and suburban areas where noise restrictions are often in place. For both military and civilian use the noise level needs to be significantly reduced from the current level to prevent hearing loss for the pilot and ground crew, particularly when hearing protection is not worn. The noise on the Jetpack is made up from: exhaust, aerodynamic, and vibration.

The exhaust noise is extremely loud due the inherent pulsation of the two stroke engine. This pulsation occurring in exhaust manifold/expansion chamber has speeds in excess of the local speed of sound, thus breaking the sound barrier and producing sonic booms. This physically produces a high pitched/frequency cracking sound. Two solutions exits to decrease this sound, an improved muffler design, or changing the engine type from two stroke engine to another form of combustion engine.

Aerodynamic noise on the Jetpack is largely produced by turbulent flow of the high speed air through the ducts. This can be decreased by removing and aerodynamically smoothing as many of the obstructions and protrusions as possible within the ducts. Increasing the duct diameter size would also decrease the aerodynamic noise as for the same thrust force a lower disc loading (thrust force over duct area) is achieved, which means the flow rate thought the duct is decreased so the intensity of the turbulence is reduced, and hence, the noise. Increasing the size and number of rotor blades would allow for a slower blade tip speed, which would reduce compressibility effects on the fan blades and consequently noise. Future work exists to optimize the design of the fan rotor and stator via computational techniques to minimise the noise produced from the fan rotor and stator interaction.

Vibration

Vibration noises are due to the large amplitude high frequency vibrations experienced by the Jetpack during operation. The source of these vibrations is due to the large unbalanced secondary vibration mode of the V4 engine. A V4 engine is inherently unbalanced, but can be dynamically balanced by adding two counter rotating balancing shafts at twice the engine speed. This however adds significant weight and further complexity to the engine, both of which are detrimental to an aircraft.

Vibration not only produces significant amount of noise on the Jetpack, as explained above, but also greatly decreases the reliability of the hardware and the performance of the inertial navigation unit (INU). The hardware reliability and particularly those of the numerous aluminium parts is greatly reduced by the vibration as these parts might prematurely crack due to the fatigue stress of the vibrational loading. Typically, components have been oversized to increase their useful life, but this has the effect of increasing the takeoff weight of the Jetpack. The vibration effects the performance of the INU and decreases its ability of accurately measure the motion of the Jetpack as the vibration motion is also partially measured. This has been mitigated by mounting the

INU on isolators, but it is always more advantageous to remove the source of the vibration. Solving the issue of the unbalanced V4 engine would greatly improve the reliability of the hardware and the INU.

Fuel Burn and Emissions
The inherently high disc loading of the Martin Jetpack requires a large power source, 150 kW, which means that the fuel burn rate, typically in excess of 1.5 L/min, and carbon emissions are also high. This power source is large compared to small helicopters such as the Robinson R-22. In a time where sustainability and carbon emissions are a prevalent social matter, the Martin Aircraft Company needs to adequately address the matter and ensure they have the cleanest burning Jetpack possible. The operation of the two stroke engine inherently burns more fuel compared to a similarly powered four stroke engine − and the addition of lubricating oil into the fuel mix means that the emissions of a two stroke engine contain greater quantities of particulate matter in addition to the hydrocarbons and carbon monoxide than a similar sized four stroke engine. These gases and practicals are all detrimental to the health of people and the environment.

Reliability
Currently the Jetpack V4 two stroke engine requires overhauls every 20 hours of operation, where key engine components such as the crank bearings are replaced. This time is far less than the time between services of a similar powered aeroplane engine and two orders of magnitude less than time between overhauls. The reason for this is two fold, the Jetpack engine for normal operation is operating at very close to maximum power, where most aircraft engines spend the majority of their time operating at cruise power, typically 75 % of the maximum power. The other reason is due to the vibration of the current Jetpack engine. This vibration severely shortens the life of the engine components and also requires these components to be heavier, which decreases aircraft performance.

Pilot Comfort
The nature of the Jetpack requires the Jetpack to fly through a large range of attitudes from hover to high speed flight. For the intended flight speeds of 28 m/s the Jetpack will have an attitude of 45°to 50° from the vertical. At this high attitudes the pilot will be hanging from the harness, and will require their head to be arched back to allow forward visibility As this is not a natural position and if found to be uncomfortable it may lead to suspension trauma, which will require attention as it can seriously distract the pilot's airmanship.

Safety
The Martin Jetpack without the ability to autorotate is inherently less safe than a helicopter, and also factoring the minimal pilot protection the survivability in the event of a system failure is low. A ballistic parachute (rocket propelled parachute) has been proposed by Martin Aircraft Company and development has been began. However, a ballistic parachute still requires time

to open which translates in free fall distance, which when close to the ground is not able available. Hence, even with the best ballistic parachute a significant height fall still occurs before the Jetpack is slowed to the terminal velocity of the parachute. This makes the transition from takeoff until a safe parachute height is reached life threatening for the pilot.

This technical barrier may not be possible to overcome, which requires that the chance of a system failure be a very minute. Even though the hardware of the Jetpack is simple compared to a helicopter, it has an additional level of complexity due to the electrical fly-by-wire system, which if fails leads to instant loss of control of the aircraft. Hence, great care must be taken in the design and implementation of the various Jetpack systems to ensure that the occurrence of a failure is minimised, as any failure threatens lives.

10.2 Future Research

Control of Duct Centre of Pressure

Reducing the movement of the duct centre of pressure would mean that the net centre of pressure of the Jetpack would have less variation, thus less trim moments would be required by the control vanes leaving greater control authority throughout the flight envelope. Leading edge devices are a potential means of controlling the duct centre of pressure. Implementing devices like the double duct [63], duct inlet slat [55], and leading edge vortex generators could delay or prevent duct leading edge stall from occurring, which is the main instigator of the duct centre of pressure movement. This would significantly decrease the demands on the control vanes to trim the aircraft allowing greater control authority throughout the flight envelope. These devices are yet to be proven on actual VTOL ducted-fan aircraft. Further research and experimentation is recommended.

The use of vortex generators on the duct leading edge has been conceived by the author. These vortex generators, Figure 10.2c, would function in a similar means to vortex generators on the top surface of the leading edge of an aeroplane's wing. The vortex generators are small aerofoils at an angle of attack to the flow, which due to their low aspect ratio make large tip vortices. The formed vortex keeps the flow attached by circulating high energy flow into the boundary layer.

The duct leading edge slat as shown in Figure 10.2b could also be made dynamic so when it is open it produces a positive pitch moment and when closed a negative pitch moment as shown in Figure 10.3. An experimental investigation is recommended to prove this concept and measure the pitching moments to validate its feasibility.

Louvre Style Control Vanes

The developed tri-decker control vanes for the P-12 Jetpack could be improved by designing the vane so that the leading edges of all individual vanes remain a constant position from the duct trailing edge. The current design of the tri-decker, which is mechanically simple, rotates all three vanes about the centre of pressure position of the three vanes, at 15 % chord of the central vane.

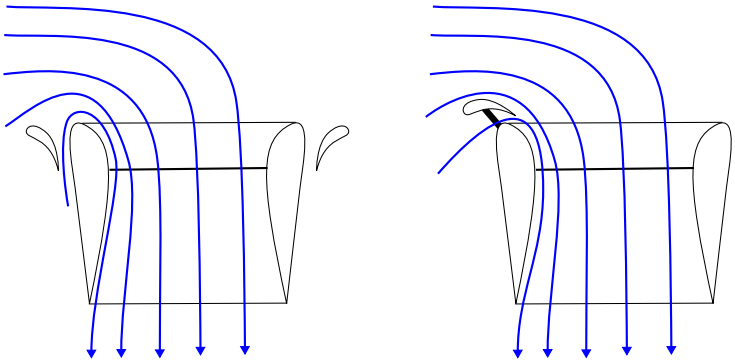

(a) Double duct concept [63]

(b) Duct leading edge slat concept [55]

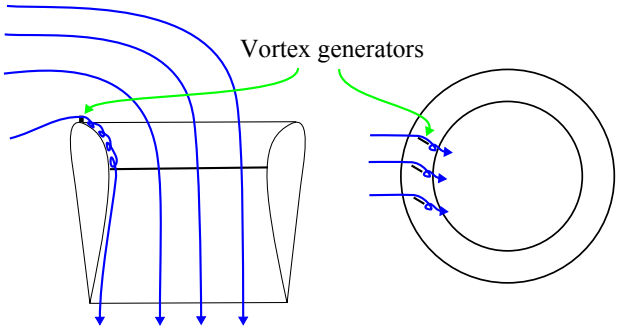

(c) Duct leading edge vortex generators concept

Figure 10.2: Potential duct devices to control duct centre of pressure

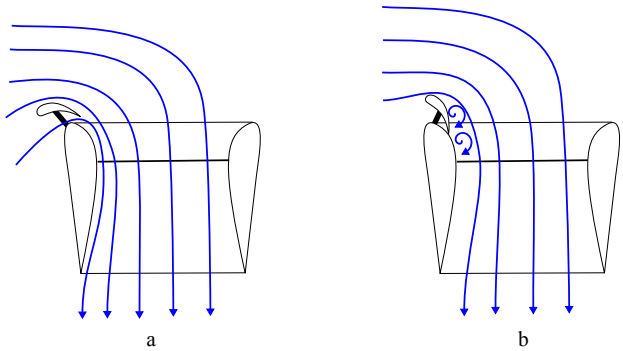

Figure 10.3: Duct inlet dynamic slat, showing slat open (a) and slat closed (b).

This rotation raises and lowers the leading edge of the outer vanes. Due to the closeness of the vanes to one another the airflow from the leading vane will disturb the airflow of leeward vanes, which reduces their effective angle of attack and thus their lift generating capability.

Louvre style control vanes would reduce this negative effect as all the vanes would experience equal angles of attack. However, a louvre style system is mechanically more complex and may add more weight into the aircraft.

Control Vane Layout

Instead of the crucifix configuration of the control vanes, as used on the P-12, the control vanes could be used rotated by 45° from the current P-12 layout, so the vanes would no longer be pure pitch and roll, but rather all mixed together. Such a system with correct vane mixing algorithms, would allow greater pitch or roll moments to be created allowing for improved control authority in both roll and pitch flight. However, control authority in skewed flight may be diminished.

CFD Simulation of Duct Design

The design of the duct inlets on the Martin Jetpack prototypes could be improved by enlarging and smoothing the inlet radius. This would increase the mass flow rate through the ducts, and hence, the thrust. Using computational fluid dynamics (CFD) software a range of duct inlet designs could be simulated to find an optimum design, which could be done in a similar manner as described in [95, 64].

CFD Simulation of Rotor and Stator Design

The presented theory used for the design of the P-12 Jetpack rotor and stator blades as well as those rotor blades of other ducted-fan VTOL aircraft has been done using blade element theory. Potential improvements could be made to the performance of the ducted-fans by using CFD simulations. An investigation into non-uniform axial flows through the fan rotor using CFD simulations could be made to improve ducted-fan performance. A basis for this research are the findings by [86], which showed thrust improvements for non-uniform axial flows, and the fan blade designs of state-of-the-art high by pass gas turbine engines.

Chapter 11

Conclusion

"To invent an airplane is nothing. To build one is something. But to fly is everything."
Otto Lilienthal

This section summaries the major findings presented within this research.

Contributions to State-of-the-Art
This research has contributed to the current state-of-the-art by the development of an aerodynamic flight model and equations of motion for the unique aircraft layout of the Martin Jetpack, which has twin ducted-fans with control vanes located in the duct wakes. The developed equations of motion describe the contributions of: the two ducted-fans, the aircraft body, the control vanes, and the landing gear. The ducted-fan normal force was modelled based on the conservation of momentum through the duct as per the state-of-the-art.

However, the current state-of-the-art lacks the ability to model the ducted-fan pitching and rolling moments, as well as the accurately account for the inflight lift and drag forces. This inability to easily model the ducted-fan moments is particularly problematic in the early design stage where it is necessary to have this information to ensure that the conceived aircraft layout has the ducted-fan centre of pressure correctly position relative to the centre of gravity.

An experimental Jetpack tow test setup (refer to Chapter 6) was developed to measure the inflight aerodynamic reactions occurring on the P-11A Jetpack and the ducted-fans. The results were used to develop a model for the ducted-fan centre of pressure movement along the duct axis, which for the roll plane is modelled by equations(6.3.6) and (6.3.7), and for the pitch plane is modelled by equations(6.3.9), (6.3.10), and (6.3.11). The developed ducted-fan centre of pressure models are used to model the ducted-fan rolling and pitching moments as a function of the airspeed, angle of attack, thrust and duct diameter, by equations (6.3.8) and (6.3.12) respectively. This new formulation of the ducted-fan centre of pressure movement and moment allows for a more accurate prediction of the behaviour of VTOL ducted-fan aircraft at the early design stage than what is currently available. However, for accurate results the formulation is limited to speeds below 25 m/s, and in the roll plane for angles of attack greater than 90° limited to speeds below 17 m/s.

Validation of the various parameters used in the model was achieved by a series of experiments to measure the aerodynamic responses of the key features.

The experiments presented show how the control vanes, the Jetpack, and duct lift, drag, and pitching moments were obtained using the actual aircraft as the test specimen. The novel experimental methodologies allowed for these features to be determined under actual design loading conditions with minimal experimental cost.

The combination of theory and experimental data developed by this research has driven the unique aerodynamic design layouts of the P-11C and P-12 aircraft. These new layouts have made a significant improvement on the flight envelope and handling qualities of the original P-11A Jetpack, as shown in Table 11.1, which compares the key performance values between the P-11A, P-11C, and P-12 Jetpacks. The improvements are due to:

Better Understanding of Flight Mechanics
This research has provided a detail description of the flight mechanics involved with the Martin Jetpack. It is now understood the Jetpack, like other VTOL aircraft, shows no natural stability in roll and pitch attitude and is also dynamically unstable due to no inherent damping. All of the major reactions acting on the Jetpack are now accounted for and include the contributions from: the ducted-fans, Jetpack body, control vanes, gyration of rotating parts, and landing gear reactions. Before this research the inflight mechanics of the Martin Jetpack were understood, particularly the contribution of the ducted-fan normal force. This force and its associated moment are now accounted for in the Jetpack design, which has led to the significant improvement in flight performance, as shown in Table 11.1. This was done by measuring the centre of pressure movement and developing formulation to model the centre of pressure movement. Using this model the optimum centre of gravity for the P-11C, P-11E, P-12 was determined to be between 0 to $0.125d$ above duct lip, where d is the duct diameter.

Increased Effectiveness of Control Vanes
The effectiveness of the Jetpack control vanes and particularly the roll and pitch vanes have increased from those that were originally on the P-11A Jetpack to the vanes that are now on the P-12 Jetpack, as a result of this research. The improved effectiveness of the vanes to produce control moments has helped improve the Jetpack's handling and manoeuvering qualities, and also the tolerance to wind turbulence. The increased effectiveness of the control vanes is due to:

- increased moment arms
- revised vane design
- addition of end-caps to the control vanes
- improved vane location within duct wake

Control Laws
The development of the Jetpack model (Chapter 4) allowed new control laws to be simulated, analysed, and compared to the original control algorithms.

The nested control algorithm for attitude control showed superior response over the original controller, and as a result has become the standard attitude control algorithm for Jetpacks.

Increased Thrust Performance

The rotor and stator blades were redesigned for the larger P-12 800 mmducted-fan. Not only was a more thrust produced, but efficiency of the ducted-fan significantly improved from 55 % to 69 %. The methodology of the balding design was proven by test flying the P-12 where no noticeable yaw vane deflection was shown in hover indicating that the stator blades are correctly removing the swirl flow produced by the fan.

Table 11.1: Performance summary of the Jetpack prototypes

Performance	P-11A	P-11C	P-12
Date	June 2009	September 2011	April 2013
Max speed	$< 3\,\mathrm{m/s}$	$15.8\,\mathrm{m/s}$	$12.5\,\mathrm{m/s}$
Wind/turbulence tolerance	Nil	Moderate $\approx 6\,\mathrm{m/s}$	Moderate $\approx 7\,\mathrm{m/s}$
Handling quality	Poor	Good	Very Good

"We are shaped by our thoughts; we become what we think. When the mind is pure, joy follows like a shadow that never leaves"

Buddha

Appendix A

Jetpack Projected Views

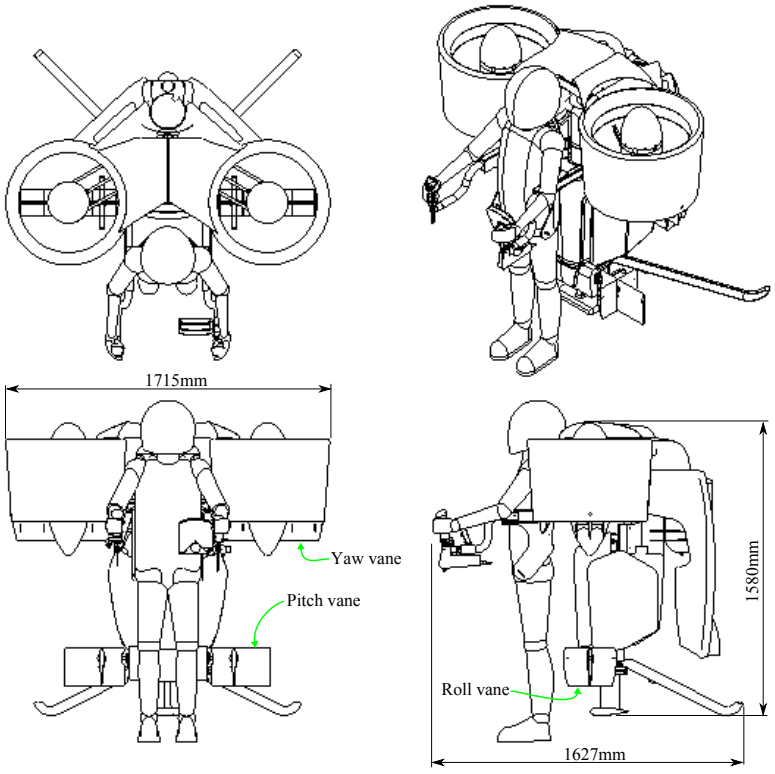

Figure A.1: P-11A Jetpack projected views, designed and flown before commencement of this research, pinnacle flight 26^{th} April 2009

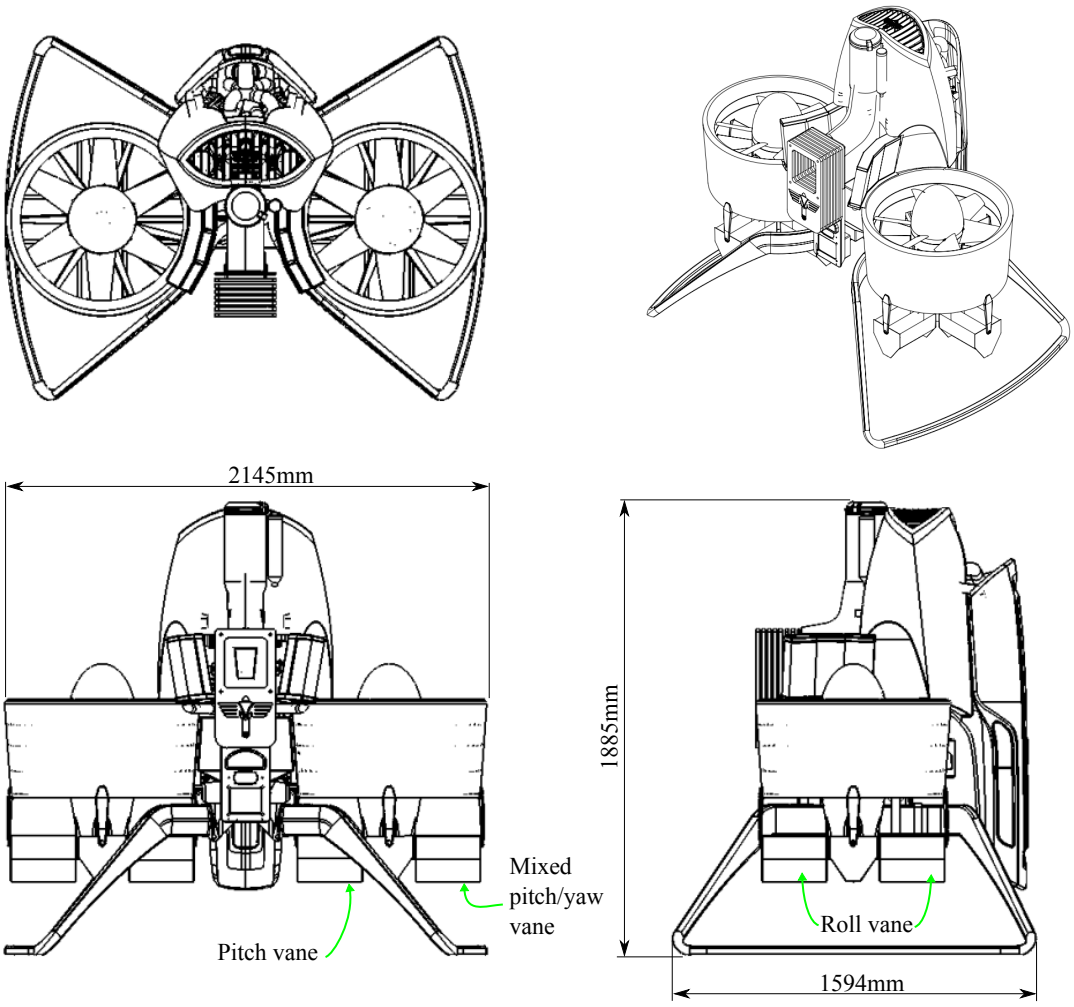

Figure A.2: P-12 remote controlled Jetpack projected views, first flight 1^{st} November 2012

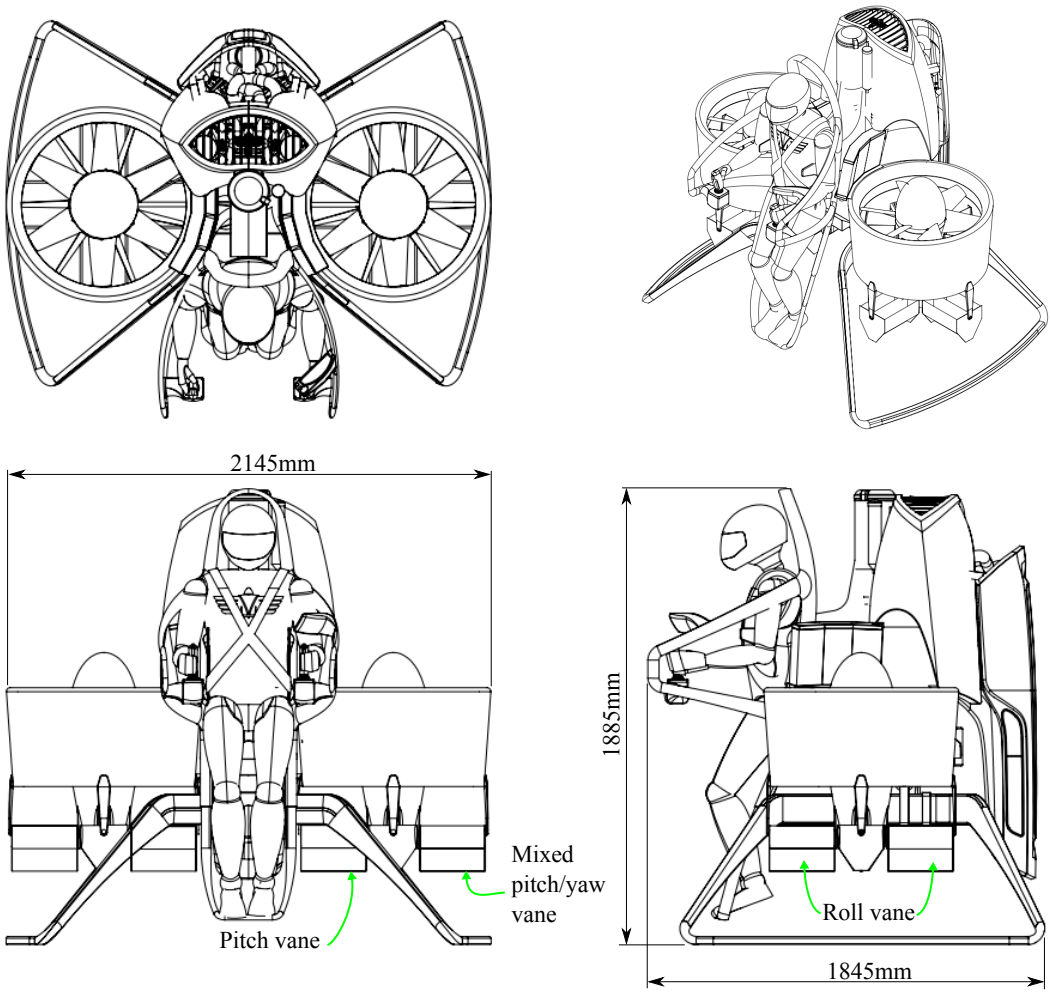

Figure A.3: P-12 manned Jetpack projected views

Appendix B

Additional Background Information

This appendix chapter provides the reader with basic aerodynamic concepts and terminology, from types of flows through to definition of aerodynamic reactions. The chapter progresses with an explanation of what keeps conventional heavier than air aircraft such as aeroplanes and helicopters aloft, how these aircraft are controlled, and the nature of the stability of these aircraft.

B.1 Aerodynamics

This section briefly introduces the key points of aerodynamics. Aerodynamics is the study of how a body behaves when immersed in a gaseous substance with relative motion between the body and gas. From here on, the gas can be assumed to be air, which is a mixture of 78 % nitrogen, 21 % oxygen, and 1 % of other gases. Air is invisible to the human eye, but has a mass and hence a density of 1.225 kg/m^3 at International Standard Atmospheric (ISA) conditions [96].

When a body and an air mass experience relative motion, either by the body moving through the air or the air moving around the body, the passing airflow must move out of the body's path. The forced movement of the airflow requires that the airflow needs to accelerate and decelerate, hence, a change in momentum of the airflow occurs to move around the body. The forces required for changing the airflow's momentum to move around the body create equal and opposite forces acting on the body, according to Newton's third law of motion. The forces from the airflow acting on the body can only be transferred via normal pressures and shear stresses. Normal pressures act perpendicularly to the surface while shear stresses act parallel to the surface, as per Figure B.1.

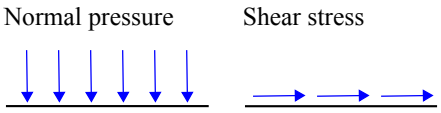

Figure B.1: Schematic of normal pressure and shear stress acting on a surface

The net effect of the normal pressures and shear stresses acting on the

body's surface are the aerodynamic reactions: lift, drag, and moment, as shown in Figure B.2. The lift force is the net force acting perpendicular to the free stream velocity. The drag force is the net reaction acting parallel to the free stream velocity. The moment is the torque reaction about any chosen point on the body.

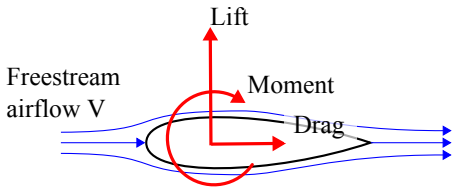

Figure B.2: Aerodynamic reactions of a body

Streamlines and the Bernoulli Equation

Figure B.3 shows how streamlines move around a cylinder and a streamlined body. Streamlines are the lines that are tangent to the instantaneous velocity vector of the flow [97]. Streamlines cannot cross one another, but can move around bodies and themselves. The point where a streamline terminates is said to be a stagnation point. At the stagnation point the momentum of the air has been transferred to a build up of static pressure. Streamlines may also break away from the surface of the body, the point at which this occurs is called the separation point. Separation occurs either at an abrupt change in geometry or due to the centrifugal accelerations exceeding the pressures acting on the air particle and pulling the particle away from the surface.

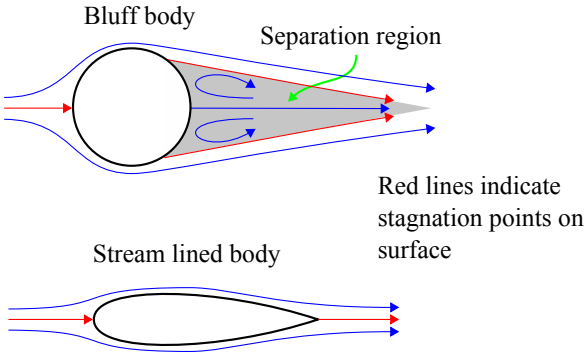

Figure B.3: Schematic of flow around bluff and streamlined bodies

The energy at any point along the streamline may be related to that at any other point by Bernoulli's equation B.1.1 as follows:

$$const. = p_1 + \frac{1}{2}\rho V_1^2 + \rho g h_1 = p_2 + \frac{1}{2}\rho V_2^2 + \rho g h_2 = p_{total} \tag{B.1.1}$$

where p is the static pressure, ρ is the density of air, V is the velocity, g is acceleration due to gravity, and h is the height. The subscripts 1 and 2 indicate two arbitrary points along a streamline. The Bernoulli equation is only valid for irrotational and inviscid flows.

Assuming a constant height, $h_1 = h_2$, it can been seen from Bernoulli's equation that at the stagnation point $V_2 = 0$ and the static pressure is $p_2 =$

$p_1 + \frac{1}{2}\rho V_1^2$. Hence, the static pressure at point 2 is equal to the total pressure of the fluid at point 1. Thus the static or stagnation pressure p_2 is proportional to velocity squared, hence, doubling the speed quadruples the stagnation pressure. The sum of the static pressures acting on a body parallel to the free stream velocity equates to the *Profile drag* force. Favourable aerodynamic shapes minimise stagnation areas on the leading or windward surfaces and allow pressure recovery to occur on trailing or lee surfaces to avoid high profile drag forces.

Deflection of a Stream Tube

A streamline by definition has an infinitely small cross section, however a group of streamlines enclosing an area can from a *stream tube*, which has a finite cross section. As an example; the flow inside a pipe represents a stream tube with a diameter equal to that of the pipe and would represent the mean flow through the pipe.

Suppose a stream tube enters and leaves a control volume, refer to Figure B.4. Applying the conservation of mass law - the mass flow rate entering the control volume must equal the mass flow rate leaving the control volume:

$$\dot{m}_{in} = \dot{m}_{out} = \dot{m} \tag{B.1.2}$$

If the stream tube leaves the control volume at an angle to which it entered a momentum exchange must have occurred within the control volume, as $\mathbf{V}_{in} \neq \mathbf{V}_{out}$. Applying the conservation of momentum, Newton's First and Second Law of Motion, it can be shown that the change in the vertical momentum, $\dot{m}\Delta V_y$, produces a lift force L (perpendicular to the free stream velocity):

$$\dot{m}\Delta V_y = F_y = L \tag{B.1.3}$$

A change in the horizontal momentum, $m\dot{\Delta}V_x$, produces a drag force D (parallel to the free stream velocity[1]).

$$\dot{m}\Delta V_x = F_x = D \tag{B.1.4}$$

It can be seen from the conservation of mass and momentum that if a lift force is produced by deflecting a stream tube a drag force is also produced. This drag force is termed lift induced drag, and is directly related to how much lift is produced.

Fluid Viscosity

The viscosity of a fluid is an important fluid property that describes resistance of the fluid to flow due to an applied stress. High viscosity fluids such as honey require a much greater stress to deform than low viscosity fluids such as water or air. Consequently, bodies travelling through high viscosity fluids will have much higher skin friction.

[1] *Free stream velocity* is the undisturbed flow velocity far in front of a body

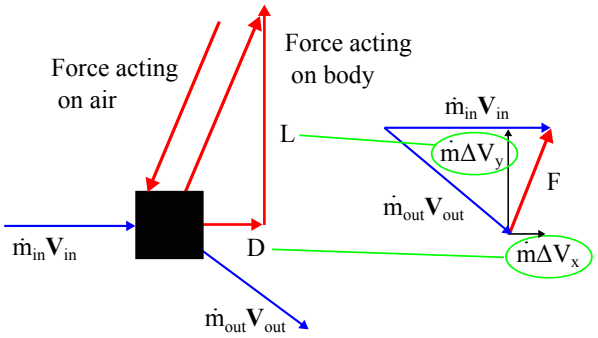

Figure B.4: Free body diagram of a stream tube passing through a control volume

The ideal fluid has no viscosity and is refer to as inviscid fluid [97], however, in practice the ideal fluid does not exist[2], but in many situations air may be treated as an ideal/inviscid fluid for simplified analysis using the Bernoulli equation.

Boundary layer

The boundary layer is a zone next to the surface where the velocity changes from zero at the surface to the ambient velocity with increasing distance from the surface. This zone exists on all real surfaces with relative fluid motion due to the fluid's viscosity. The viscosity of the air retards the motion of the airflow from the ambient speed to zero speed at the surface of the body the airflow is passing over. Hence, it is the viscosity that creates the boundary layer.

The thickness of the boundary layer is a function of the fluid viscosity, the flow type - laminar or turbulent (Figure B.5), the velocity of the ambient flow, the length (distance from the leading), and the roughness of the surface.

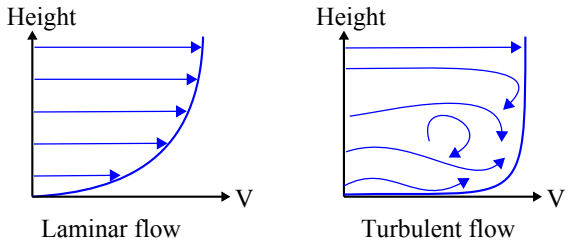

Figure B.5: Boundary layer flow types

Laminar Boundary Layer

To minimise wall or surface shear stress, which creates skin friction, it is desirable to have a laminar boundary layer, as the laminar boundary layer has a reduced velocity gradient near the surface compared to a turbulent boundary layer. In a laminar boundary layer each subsequent layer of air above the

[2]Ideal fluids do exist in special labouratory conditions, typically at extremely low temperatures, and are referred to as superfluidity fluids.

surface moves slightly faster than the one beneath until the top layer is at the same speed as the ambient airflow, as shown in Figure B.5.

Turbulent Boundary Layer

The nature of the turbulent boundary layer greatly increases the mixing within the boundary layer, which makes the velocity near the surface much higher than in the laminar case. This results in the skin friction being much higher for a turbulent boundary layer than a laminar one. However, there are situations where a turbulent boundary layer is favourable. Flow containing a turbulent boundary layer is more able to adhere to the surface in positive-pressure-gradient flow regimes, due to the turbulence induced mixing. This can delay or prevent separation from occurring.

A positive or adverse pressure gradient occurs when the static pressure increases in the flow direction, which generally occurs on the lee side of the body's maximum thickness, (Figure B.6). A laminar airflow on the other hand is more likely to separate over an adverse pressure gradient. This separation creates an increase in profile drag, as the difference in normal pressures between the leading and trailing surfaces is greatly increased. Profile drag, typically, being much greater than the skin friction drag, should be avoided to minimise the overall drag. Thus, a turbulent boundary layer, even with its higher skin friction can actually reduce the overall drag by reducing or preventing the effects of separation. For this reason the surface of golf balls are covered with dimples to encourage a turbulent boundary layer to delay flow separation.

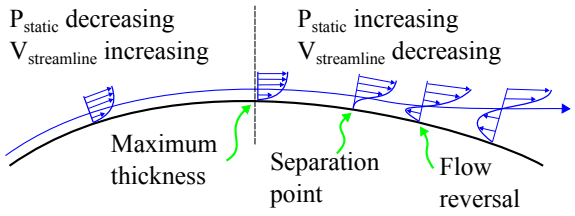

Figure B.6: The effect of shape on pressure gradients

The Centre of Pressure and Aerodynamic Centre

A key aerodynamic reaction of a body in an airflow is the aerodynamic moment generated. The moment is the result of the net normal pressures and shear stresses acting on the surface about an arbitrary reference point. The moment is calculated by the multiple of the elemental surface pressure with the perpendicular distance from the element to the reference point. The reference point can be any convenient point, which for aerofoils is typically taken at the quarter chord point.

The *centre of pressure* is defined as the point where the net normal pressures and shear stresses acting on a body's surface equate to a resultant force and a zero moment. The *aerodynamic centre* is defined as the point where the moment remains constant for changes in angle of attack. The aerodynamic centre for an aerofoil typically remains constant only for angles of attack between positive and negative stall angles. For symmetric aerofoils, such as the

NACA 0012, the centre of pressure and aerodynamic centre coincide at the quarter chord point.

Bluff and Streamlined Bodies

The shape of the body exposed to the airflow directly affects how the airflow moves around the body and subsequently the reaction forces experienced by the body. The aerodynamic shape of the body can be split into two classes: bluff and streamlined.

Bluff bodies, as shown in Figure B.3, can be characterized as shapes that have a large thickness to length ratio. The consequence of the large thickness to length ratio is that lee side of the object has steep or abrupt angles that cause the airflow to break away from the surface, which is referred to as separation. In the separated zone the static air pressure is relatively low, and hence, the leeward facing surfaces experience low normal pressure, while the windward surfaces experience high normal pressure due to flow stagnation. The large difference in the normal pressures creates the profile drag force experienced by the body. For a bluff body the normal pressures far exceed the viscous shear stresses, hence the effect of shear stresses can be ignored and the fluid can be treated as inviscid in analyzing a bluff body shape.

Streamlined shapes have low thickness to length ratios, typically less than $\frac{1}{3}$, and have smooth curved surfaces with their thickness portion typically located $\frac{1}{3}$ of the length back from the front edge. The smooth curves are chosen to closely match how the airflow would naturally move around the body without flow separation. Streamlining a body has the effect of reducing or eliminating flow separation, which results in much smaller pressure differential between the windward and leeward faces of the body, and hence, greatly reduces the profile drag when compared to a bluff body. For streamlined bodies the shear stresses, which are the result of the viscosity of air (the ability of a layer of air to slide pass the neighbouring layer), can become more significant and may even exceed the normal pressures. Hence for streamlined bodies close attention is paid to minimizing the skin friction drag. This can done by encouraging the airflow to remain laminar for as long as possible over the shape. Laminar type aerofoils such as the NACA 6 digit series achieve this by placing the maximum thickness of the aerofoil closer to mid chord, (middle of the aerofoil), which extends the length of the negative pressure gradient, which encourages laminar flow and delays the onset of the transition to turbulent flow.

Summary of Drag Types

To summarize, the types of drag can be classed as one of the three following types:

1. Profile drag is due to difference in static pressures, and is a function of the geometric shape exposed to the airflow and increases with airspeed.

2. Skin friction drag is due to the viscous property of the flow, and is a function of the flow condition, the size of the boundary layer, and the airspeed.

3. Lift induced drag is due to changes in flow momentum, and is a function of flow deflection, and increases with flow deflection and speed.

The total drag acting on the body is the sum of the all three. Since profile and skin friction drag increase with airspeed their combination is referred to as *parasite drag*.

Practically Dealing With Body Reactions

To model the flow paths and boundary layer interactions around real bodies is a very complex and time consuming problem. To date, analytical solutions for the Navier-Stokes equations exist only for the simplest flow problems, which consist of laminar flow around simple shapes. Flow over complex shapes can be solved by numerically applying the Navier-Stokes equations to these problems, this is known as Computational Fluid Dynamics (CFD). Computational fluid dynamics is typically done by discretization of a flow domain surrounding the body of interest and numerically solving the Navier-Stokes equations for each discretized volume, commonly referred to as a finite volume.

Most real world flows contain turbulence so using the Navier-Stokes equations without any additional turbulent models requires the Navier-Stokes equations to be numerically solved at all spatial and temporal scales. This is referred to as *direct numerical simulation*, which is computationally expensive. However, methods have been developed where the Navier-Stokes equations are time averaged and turbulence fluctuations are modelled by additional turbulence equations to provide a means to model the complex turbulent flow at an acceptable cost.

However, CFD methods are still time consuming and often need numerous simplifying assumptions in order for them to produce meaningful results in an acceptable time frame.

Traditionally, the method to determine the aerodynamic reactions of a body has been to measure the reactions via physical experimentation. Experimentation involves immersing the body of interest into a known flow and measuring the physical reactions experienced by the body. This can either be done at full or scaled size. Direct measurement of the body reactions can produce high quality results as the body of interest is being subjected to the same or similar flow conditions as it is designed for, and no or few simplifying assumptions need to be made.

Reynolds Number

The *Reynolds Number* is a non-dimensionalized number used to measure the relative importance of inertia and viscosity for flows involving shapes that are geometrically similar. Flows around shapes that have similar Reynolds numbers have similar characteristics. The Reynolds Number is calculated as the ratio of inertial forces to viscous forces as:

$$RE = \frac{V \rho l}{\mu}$$

where V is the characteristic velocity, ρ is the density, l is the characteristic length, and μ is the viscousity of the fluid.

The Reynolds number for a body immersed in a flow allows for classification of the type of flow. For example, a high Reynolds Number, above 10^6, is a good indication that flow along a flat plate will quickly develop a turbulent boundary layer, whereas a low Reynolds number, below 10^4, indicates that viscous forces are more significant, and hence, laminar is more likely to prevail. For most practical aircraft, larger than birds, the Reynolds Number is in the order of magnitude of 10^5 to 10^8, refer to Figure B.7. In this range of Reynolds numbers the flow conditions are dominated by the inertial forces, and remain relatively constant with Reynolds number, provided the flow remains subsonic and thus in-compressibility can be assumed. This independence of Reynolds number allows constant aerodynamic coefficients to be determined.

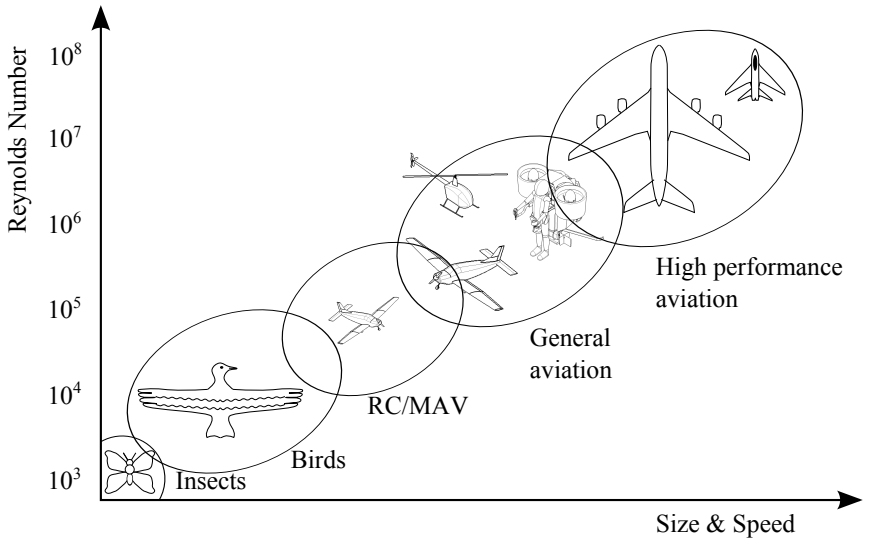

Figure B.7: Reynolds numbers for various flying items

Aerodynamic Coefficients

For subsonic airflows with high Reynolds number constant aerodynamic coefficients can be found for bluff and streamlined shapes that relate the dynamic pressure, $\frac{1}{2}\rho V^2$, the geometric form and the force/moment reaction experienced by the body. These coefficients are the drag coefficient:

$$C_D = \frac{D}{\frac{1}{2}\rho V^2 A} \tag{B.1.5}$$

the lift coefficient:

$$C_L = \frac{L}{\frac{1}{2}\rho V^2 A} \tag{B.1.6}$$

and the moment coefficient:

$$C_M = \frac{M}{\frac{1}{2}\rho V^2 A l} \tag{B.1.7}$$

where A is the reference area, typically the frontal area of a bluff body and planform area for an aerofoil, and l is the characteristic length, typically the

chord line for an aerofoil.

Neglecting the effects of viscosity (inviscid assumption), the lift force is the difference in static pressure between the top and bottom surfaces. Similarly, the drag force, for a bluff body, is the difference in static pressure between the forward and rearward facing surfaces of a body. For a streamlined body viscosity effects must be included in determination of the drag force, as the viscous drag, skin friction, is the predominate drag force.

The Aerofoil

An aerofoil is a specially designed streamlined shape that maximises the lift force, which acts perpendicularly to the free stream airflow. The aerofoil can either be symmetrical or asymmetrical about the *chord line*, which is a reference line connecting the *leading edge* (front most edge of aerofoil) to the *trailing edge* (rear most edge of aerofoil). A symmetrical aerofoil, Figure B.8, will only produce a lift force when the chord line is at some angle to the free stream velocity. This angle between the free stream velocity vector and the chord line is known as the *angle of attack.* An asymmetrical aerofoil has a curved *camber line* which is a reference curve that is half way between the top and bottom surfaces of the aerofoil and spans from the leading edge to the trailing edge, refer to Figure B.9. The degree of the camber effectively alters the angle of attack of the airflow while maintaining the same geometric angle. Where the *geometric angle* is the angle between the chord line and the free stream airflow in front of the aerofoil.

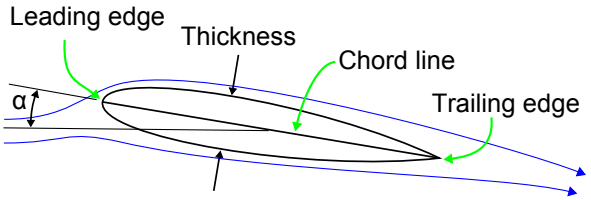

Figure B.8: Symmetric aerofoil at an angle of attack

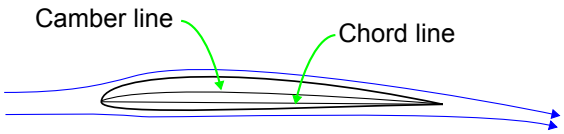

Figure B.9: Asymmetric aerofoil at zero angle of attack

Other aspects that are important to an aerofoil are the thickness of the aerofoil, the chord-wise location of the maximum thickness and the roundness of the leading edge. The maximum thickness, expressed in percentage of chord length, in general defines the maximum lift the aerofoil can produced. However, increasing aerofoil thickness also increases the profile drag of the aerofoil. So an aerofoil thickness needs to be designed for the correct operation of the aerofoil. Typically slow flying fixed wing aircraft have an aerofoil thickness of 15 % to 18 % of the chord length, medium speed aircraft 12 % to 15 of the chord length, and high speed aircraft less than 10 % of the chord length.

The chord-wise location of the maximum thickness plays an important role

on determining the extent of the laminar flow over the aerofoil. As explained in section B.1 a laminar boundary layer favours negative pressure gradients, thus by positioning the point of maximum thickness of the aerofoil closer towards the rear the extent of laminar flow over the aerofoil is increased and consequentially the total drag produced by the aerofoil is decreased. However, the roundness of the leading edge plays a very important role on the condition of the stall of an aerofoil.

An aerofoil is in the stalled condition when the airflow begins to separate from the aerofoil, so the streamlines no longer move tangential to the aerofoil surface. As separation increases the lift force decreases and the drag force increases rapidly, due to increasing profile drag. The centre of pressure of the aerofoil also abruptly changes as the aerofoil begins to stall, which can have large influences on the handling of an aircraft. Flow separation can begin to occur at the trailing edge (favourable), or at the leading edge (unfavourable), or occur simultaneously at the both the leading and trailing edges. The flow is more likely to separate at the leading edge if the leading edge has a small radius of curvature. Leading edge stall is less favourable as the separating flow in this region struggles to reattach onto the aerofoil, thus once the leading edge begins to stall the entire top surface typically stalls as well, in an abrupt fashion. Aerofoil designers for general aviation aircraft typically design aerofoils to stall from the trailing edge first, and then progress forwards as the stall deepens; this results in a smoother stable stall (stall occurs over a wider range of angle of attacks), which is easier for a pilot to correct for.

Aerofoil Coefficients

Aerofoil data is general presented in terms of aerodynamic coefficients, as explained in section B.1, as a function of the airfoil angle of attack and the flow Reynolds number, as presented in [74]. Referring to Figure B.10 it can be seen that the lift coefficient curve C_L is essentially linear until an angle is reached where a maximum lift coefficient occurs, C_{Lmax}. At this angle of attack the aerofoil ceases to increase lift as the stalled condition establishes. Increasing the angle of attack further deepens the stall causing lift to rapidly decay and drag to rapidly increase, as shown by the drag coefficient line, C_D. The drag coefficient curve is the sum of lift induced and parasitic drag. It can be seen at zero angle of attack the aerofoil produces no lift, thus the drag acting on the aerofoil is at a minimum, C_{Do}, and is purely parasite drag. As the wing angle of attack increases the induced drag begins to increase proportional to the lift coefficient squared. Once the wing stalls and the airflow separates the drag force rapidly increases as profile drag becomes the most significant from of drag. For a symmetric aerofoil the pitching moment about the quarter chord, which also happens to be the location of mean aerodynamic centre, remains zero with increasing angle of attack. Once stall occurs the pitching moment, typically, becomes negative as the centre of pressure moves reward.

The ratio of the lift to drag coefficients is equal to the ratio of lift to drag forces and is a function of angle of attack:

$$L_D = \frac{C_L}{C_D} = \frac{L}{D} \tag{B.1.8}$$

The angle of attack where the maximum lift to drag ratio occurs is an important concept. At this point the aerofoil works most efficiency, it produces the most amount of lift for the least amount of drag. For optimum efficiency (longest range for minimum fuel burn or height lost in the case of a sailplane) the aeroplane or sailplane needs to be flown so that the wings are at the best lift to drag ratio angle of attack. This point is defined as:

$$\frac{dL_D}{d\alpha} = 0 \tag{B.1.9}$$

where the maximum lift to drag ratio is denoted as L_{Dmax} and occurs at an angle of attack of α_{LDmax}.

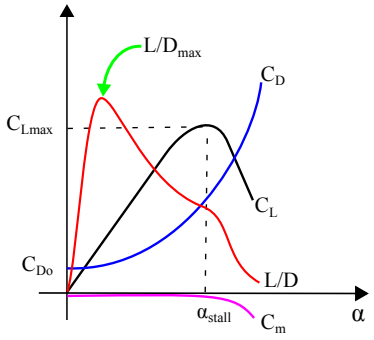

Figure B.10: Aerodynamic coefficient curves versus angle of attack for a general symmetric aerofoil

Stability

A system is said to be statically stable, if when it is disturbed, it moves back towards its predisturbed state without the aid of any external influence. Figure B.11 shows the three cases of static stability for a ball on a surface. In the stable case, if the ball is displaced left or right the horizontal component of the contact force between the ball and the surface will create a restoration force to move the ball back to the bottom of the bowl. The presences of this restoration force makes the ball in the bowl scenario stable. However, if the ball is placed on a flat surface and moved to a disturbed state the ball will remain at that disturbed position as no restoration force exits, this is termed neutral static stability. A third case exists where the ball is initially on top of a convex surface or upside down bowl and moved slightly to a disturbed position. At this disturbed position the horizontal component of the contact force moves the ball further away from the initial position, this is effectively a negative restoration force, which is referred to as statically unstable.

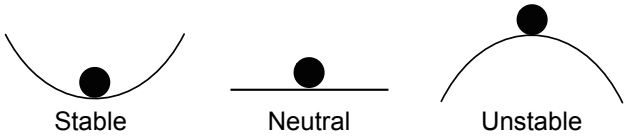

Figure B.11: Three cases of static stability

Dynamic stability refers to the motion of a body when disturbed. For a system to have dynamic stability it must have static stability (a restoration

force). However, even with the restoration force the system may not be dynamically stable. Similarly to static stability there are three cases for dynamic stability: stable, neutral and unstable, as shown on Figure B.12. Referring to the stable case of the ball in a bowl the ball is only dynamically stable if it comes to rest back in the predisturbed position. To achieve this, it requires a restoration force to move the ball in the correct direction and a damping force to decay the kinetic energy of the ball's motion. If no damping forces exist the ball would not come to rest at the bottom of on the bowl, as each time it passes the predisturbed position the restoration force has transferred the restoration energy into kinetic energy, thus the ball oscillates about its predisturbed state. If energy is somehow added to the ball during this oscillation the oscillation will grow and the amplitude of the disturbance will become larger. This is referred to as dynamically unstable.

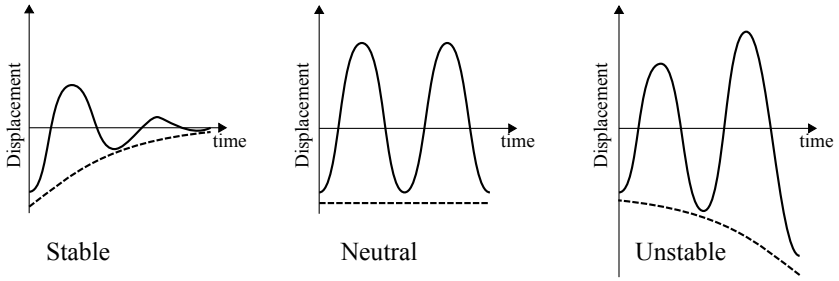

Figure B.12: Three cases of dynamic stability, showing motion versus time. Solid lines represent oscillatory motion and dash lines over-damped motion.

Since aircraft are a form of transport, and as such move from one location to another, they cannot be positionally stable or else they would not function as an aircraft. However, aircraft need to be have stability in orientation and motion to function. Stability for aircraft can be achieved by two means: it can be passive, inherent to the design; or it can be active, requires external feedback loops to introduce stability into the system.

Three static stability cases exist for how an aircraft responds to a disturbance:

1. Stable: The aircraft restores back to predisturbed attitude and velocity
2. Neutral stable: The aircraft remains at disturbed state
3. Unstable: The aircraft diverges from predisturbed state

Dynamic stability involves the motion of an aircraft after it has been disturbed. For dynamic stability to exist the motion of the aircraft must decay with time.

B.2 Common Aircraft Types

A brief explanation of the three most predominant aircraft types, the hot air balloon, the aeroplane, and the helicopter are presented to explain how the lift and thrust forces are developed and how the control and stability are achieved for each aircraft type.

For an aircraft to successfully fly it needs the following three attributes:

1. A controllable lift force to overcome the weight of the aircraft
2. Control moments about the three rotational axes: roll, pitch and yaw
3. Stability, either passive (built into the airframe) or active (artificially induced)

The Hot Air Balloon

Lighter than air aircraft such as the hot air balloon, which uses heated air, and the airship, which uses lighter than air gases such as hydrogen and helium, are the simplest forms of flying vehicles. These aircraft obtain their lift by physically displacing the surrounding higher density air with a lower density gaseous volume. The difference in mass between the displacement and the entrapped air within the balloon creates a buoyant lift force, allowing for ascent.

In the case of a hot air balloon, Figure B.13, the difference in density between the entrapped and the surrounding air is created by heating of the air inside the balloon, commonly referred to as the envelope. Air within the envelope is typically heated to 100°C to 120°C. The upper temperature is limited by the material properties of the envelope, which is typically made from Nylon or Nomex fabric. The heated air is significantly less dense than the cool surrounding air outside of the envelope. For a surrounding air temperature of 10°C and a temperature of 100°C inside the balloon the density inside the balloon is 76% of that outside. This equates to a lift force of 300 g for every cubic meter of volume in the balloon envelope. Hence, balloon envelope sizes range from 600 m^3 to 17000 m^3 depending the payload weight. A typical three to five person balloon has an envelope volume of 2800 m^3.

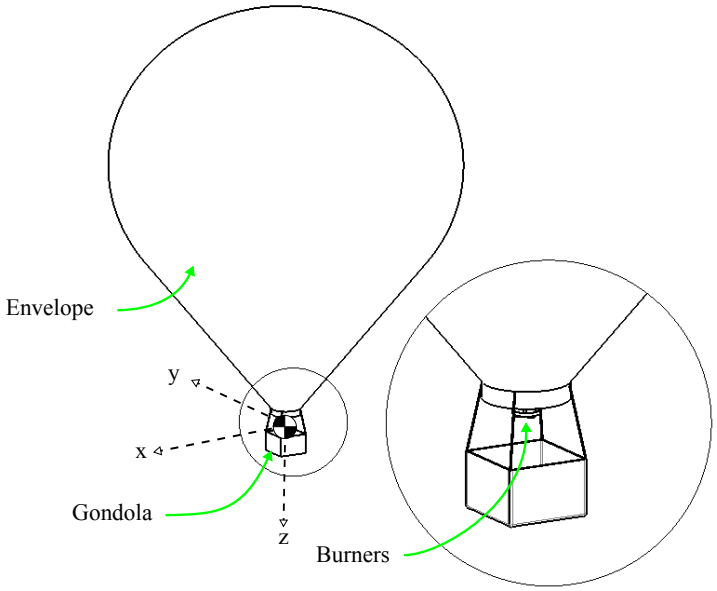

Figure B.13: Key features of a hot air balloon

Hot Air Balloon Control

The control of a modern hot air balloon is limited to height control. Climb rate is controlled by varying the burn rate of the burners, which varies the

heating and thus the density of the air mass inside the envelope. The balloon begins to descend as air within the envelope begins to cool. The rate of decent can be accelerated by venting hot air from the top of the balloon allowing cool air to enter from the bottom of the balloon.

Some balloons have additional vents around the circumference of the balloon which when opened allow the balloon to turn about normal z axis. However, hot air balloons have no horizontal motion control. They are completely passive and move essentially at the same speed as the prevailing wind. Airships have an advantage over balloons as they carry propulsion devices, typically ducted-propellers, to allow motion in the desired direction by orientating the thrust in the desired direction of travel.

Hot Air Balloon Stability

Lighter than air vehicles have the unique advantage that they are inherently stable irrespective of airspeed. This is because the lift force on these types of aircraft is generated by means of buoyancy. The buoyant lift vector always opposes gravity and is approximately located at the centre of volume of the envelope, while the centre of gravity of a balloon is located within the basket or gondola, refer to Figure B.14, with the weight force acting downwards regardless of the orientation of the balloon. Hence, a stable restoration moment always exist. For example if the hot air balloon is tilted to the side, a stabilising moment couple is made due to the perpendicular distance between the lift and weight vectors, as per Figure B.14. The moment induces a correcting motion which realigns the lift and weight vectors, in similar fashion to a pendulum. The shear size of the envelope, in excess of 15 m diameter, effectively dampens the restoring motion.

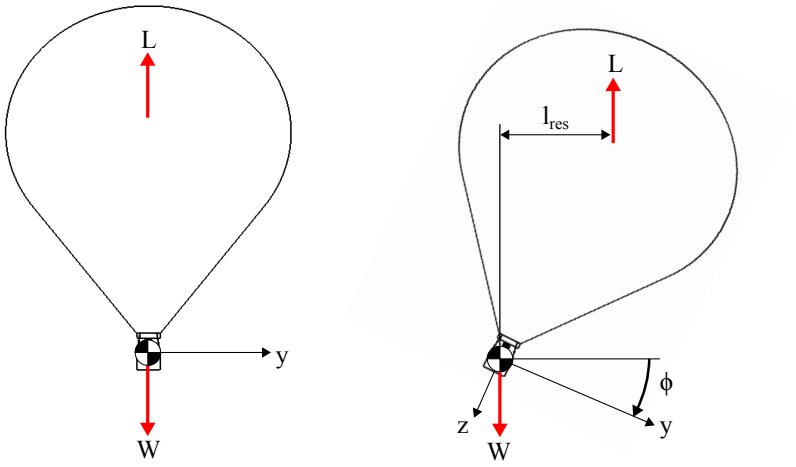

Figure B.14: Hot air balloon restoration moment

The Aeroplane

The aeroplane, classed as a fixed wing aircraft, was the first heavier than air aircraft to achieve sustained flight. Figure B.15 shows the physical layout of a typical general aviation aeroplane. The typical aeroplane primarily consists of:

a wing, large aerofoil surface; control surfaces, smaller aerofoils; a propulsive device, propeller or jet engine; and a fuselage to connect the key components and contain the pilot, passengers, and payload.

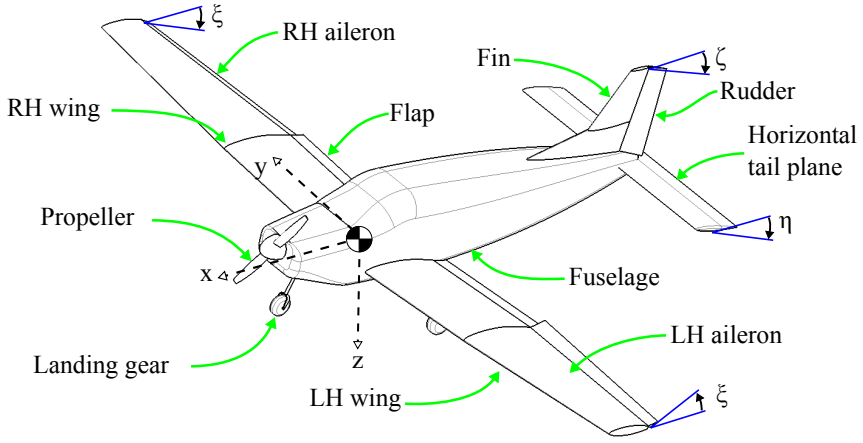

Figure B.15: Key features of a conventional aeroplane with coordinate system and positive deflections of control surfaces, as defined in Cook [81].

Aeroplane Lift Force

For the aeroplane to fly at equilibrium at level altitude (termed *level flight*) the weight force of the aircraft must be opposed by the lift force. This lift force is created by the wings deflecting the free stream airflow downwards as the aeroplane moves through the air. This downwards deflection of the air creates a change in momentum of the air in the vertical direction that creates the upward lift force, refer to equation B.1.3. The momentum is also changed in the horizontal direction, creating a drag force, refer to equation B.1.4. If this drag force is not balanced the aircraft would slow down and the lift force decrease, hence the aeroplane would no longer maintain level flight. To overcome this, a thrust force, created by a propeller or similar device and powered by an engine, is used to oppose the drag force on the aeroplane. Thus an aeroplane can fly at level flight when the lift opposes the weight and thrust opposes the drag, as per Figure B.16.

Since the lift force is dependent on the change in momentum of air downwards it requires that the aircraft must travel at a relative airspeed to the air mass for change in momentum to occur. Hence, for an aeroplane to fly at level flight it requires a minimum airspeed to generate the required amount of lift to overcome the weight force. At this minimum airspeed the aeroplane is flying at the maximum value of the wing lift coefficient, which corresponds to the maximum angle of attack of the wing. If the wing angle of attack is increased further stall will occur, wing lift will abruptly decrease, and drag rapidly increase. Hence, for level flight the aeroplane can only fly between the maximum obtainable airspeed and the level flight stall airspeed, limited by maximum power and maximum angle of attack, respectively.

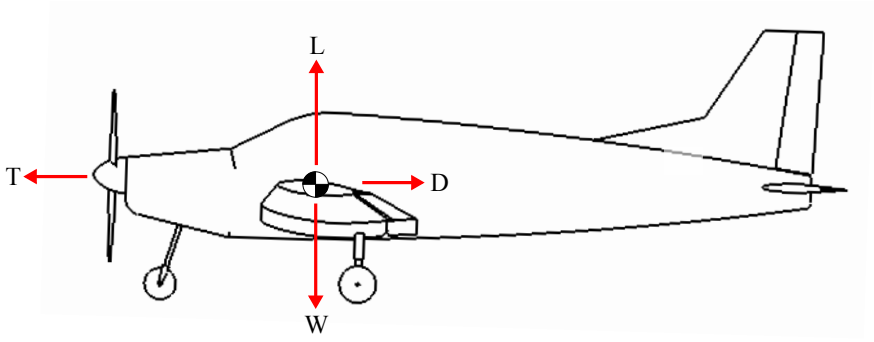

Figure B.16: Aeroplane in trimmed level flight

Aeroplane Control

An aeroplane has four degrees of primary control: roll, pitch, yaw, and thrust. Roll, pitch, and yaw refer to aeroplane's motion about the x, y, and z axes, see Figure B.15. The moments required to rotate the aeroplane about an axis are created by varying the deflection of the aeroplane's control surfaces. When these control surfaces are deflected the effective angle of attack and camber of the aerofoil changes, thus altering the lift and drag forces of the aerofoil. The force multiplied by the perpendicular distance between the control surface and centre of gravity creates the control moment, which induces angular motion about the aeroplane's axes. The aeroplane's control forces and moments are directly dependent on the dynamic pressure experienced by the aerofoil section of the control surfaces. Hence, the control forces are proportional to the aeroplane's airspeed. At low airspeeds, large deflections of the control surfaces are necessary to create the desired control moments, whereas at high airspeeds smaller deflections of the control surfaces can achieve the same control rate. If the airspeed is low the control surfaces will have redcued effect.

Roll Control

Roll or lateral control is created by the deflection of the aileron control surfaces. These surfaces are located on the outer trailing edges of the wing to maximize the moment from the ailerons to the centre of gravity. The aileron deflection and corresponding control moment is shown on Figure B.17.

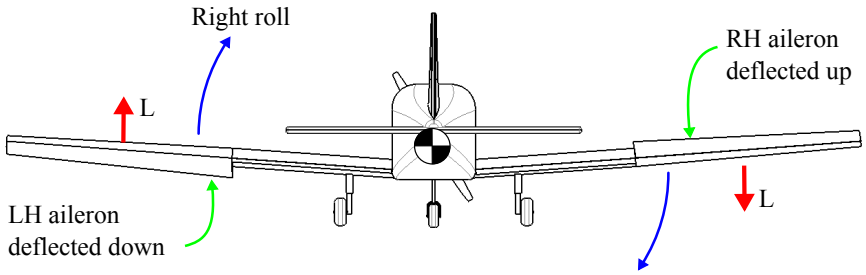

Figure B.17: Aeroplane in right hand roll turn

Pitch Control

The purpose of pitch or longitudinal control is to control the pitch attitude and motion of the aeroplane. This is done by the deflection of the elevator,

which is a trailing edge flap located on the horizontal stabiliser. The horizontal stabiliser is a small aerofoil, in comparison to the wing, located at the rear of an aeroplane. The large distance between the horizontal stabiliser and the centre of gravity improves the effectiveness of the elevator to produce pitch control moments. Note that it is common for small general aviation aeroplanes to deflect the entire horizontal stabiliser for pitch control, which is referred to as a *flying tailplane*. Figure B.18 shows the pitch force created by the horizontal tail to create a positive nose up moment.

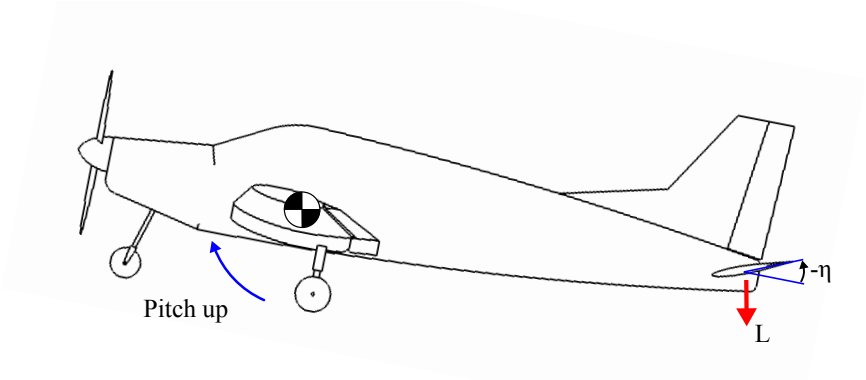

Figure B.18: Aeroplane in pitch up motion created by negative deflection of the horizontal stabiliser.

Yaw Control

Yaw control of the aeroplane is obtained through the deflection of the rudder, which is a trailing edge flap located on the vertical stabiliser. Similarly to the elevator and horizontal tail plane it becomes more effective at creating control moments as the lever arm between the centre of gravity and vertical stabiliser is increased. The yaw motion from rudder deflection is illustrated on Figure B.19.

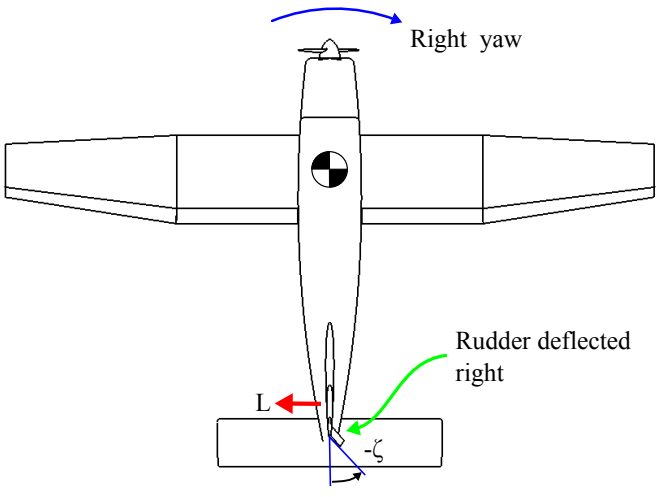

Figure B.19: Aeroplane in right hand yaw turn

Thrust Control

Thrust control is used to control the airspeed of an aeroplane. As the wings are a passive lift device (i.e. they do not add energy into the passing airflow) they require the aeroplane to have a forward airspeed for the airflow to flow around the wings. The thrust control force is set by the pilot setting the engine to operate at desired power output. The engine power is used to drive a propeller or a jet turbine propulsion device to aerodynamically create a thrust force in the forward direction of the aircraft.

To fly at higher airspeeds greater thrust is required to overcome the parasite drag. At higher airspeeds, level flight is achievable at lower wing angles of attack due to the increased dynamic pressure. The lower angle of attack of the wing reduces the angle the airflow is deflected through and decreases the lift induced drag. Hence, there is an optimum airspeed to fly at. This airspeed is known as the *best rate of climb airspeed*, as at this airspeed the aeroplane requires the least amount of power to fly, hence, the greatest amount of excess power is available for maneuvering and climbing. This airspeed is also the best glide ratio airspeed as it is the best lift to drag ratio attitude for the aeroplane.

Aeroplane Stability

Similar to the lift force, the restoration forces and moments on a conventional inherently stable aeroplane are dependent on airspeed. Both static and dynamic stability about all three axes, x, y, and z, is achieved by the wings, horizontal stabiliser and vertical stabiliser, respectively. An aeroplane, like every other aircraft, needs to be stable in orientation for a pilot to fly; where stability can be either inherent or artificially introduced. Many disturbances alter an aeroplane's orientation as it flies through the air. Disturbances are caused by influences external and internal to the aircraft.

External or atmospheric disturbances result from the dynamically changing atmosphere. Changes in the atmosphere are the result of weather, which is driven by local and global thermal gradients. The intensity of weather affects the movement of the air mass. If the movement of the air mass itself is very abrupt and constantly changing it can be said to be turbulent. Turbulence and wind gusts affect the aircraft by changing the aerodynamic forces on the aircraft as it flies through the air mass. An aeroplane is particularly sensitive to vertical wind gusts and turbulence, because changes in vertical airspeed changes the angle of attack of the wing and thus the wing lift and pitching moment.

Internal disturbances are introduced by changes of the aircraft itself. These can be the result of a changing centre of gravity position due to fuel burn and movement of payload. Both intentional and unintentional pilot control inputs can cause disturbances that alter the orientation the aircraft.

Stability About the Lateral Y Axis

When an aeroplane is disturbed in pitch, about the y axis, the fuselage and wing pitching moments change as they are function of the angle of attack of the wing. Typically, the changes in fuselage and wing moments with angle of attack are positive, as the angle of attack increases so does the moment produced by the wing and fuselage. This is destabilising as the moment produced by the

wings and fuselage are further increasing the angle of attack and thus pitch attitude. According to the stability definitions of section B.1 a stable system is one that restores itself to its predisturbed state.

The horizontal stabiliser on an aeroplane creates the stabilising restoration moment about the lateral y axis on an aeroplane. Figure B.20 shows an aeroplane at a disturbed angle of attack α. Since the stabilising moment from the horizontal stabiliser is larger than the destabilising moment of the wing and fuselage a net stabilising moment is created that produces a rotation q towards the predisturbed attitude.

The effectiveness of the horizontal stabiliser in creating the restoration moment is a function of the moment arm from the centre of gravity to the horizontal stabiliser and the size of the horizontal stabiliser. Increasing the size of the horizontal stabiliser increases the lift force and hence the moment. However, it also increases the aircraft's net parasitic drag. Increasing the moment by extending the horizontal stabiliser further aft allows for a smaller sized stabiliser and thus lower drag while still maintaining the desired restoration moment.

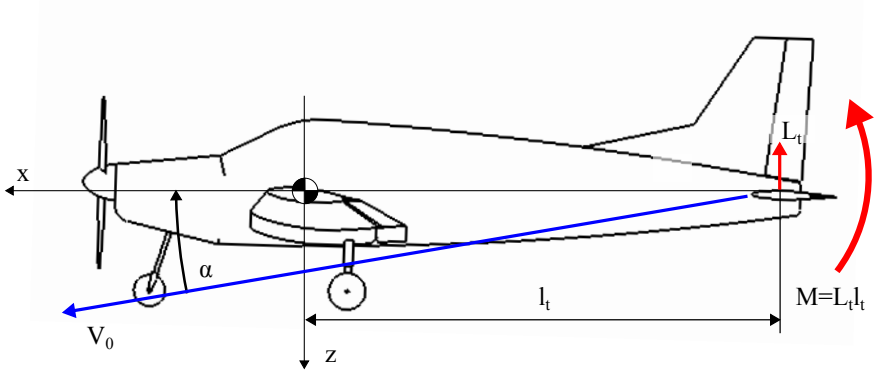

Figure B.20: Aeroplane at a positive angle of attack showing positive pitch restoration contribution from horizontal stabiliser.

The horizontal stabiliser is the largest contributor to damping motion about the lateral y axis. Figure B.21 shows how the pitching motion q induces a damping lift force on the horizontal stabiliser and therefore a damping moment.

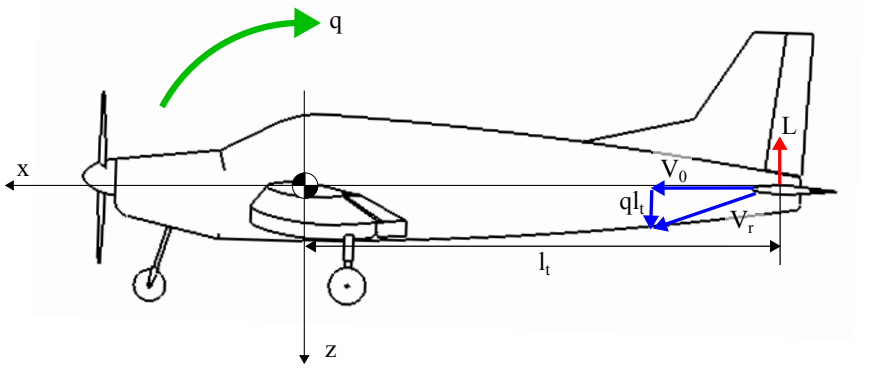

Figure B.21: Aeroplane in positive pitching motion showing pitch damping contribution from horizontal stabiliser.

Stability About the Normal Z Axis

The vertical stabiliser functions similarly to the horizontal stabiliser, but stabilises the aeroplane about z axis instead. The vertical stabiliser is necessary to maintain directional stability to ensure that the aeroplane flies directly into the airflow for optimized flight (sideslip angle $\beta = 0$). Thus the explanation of the horizontal stabiliser can be used to describe the function of the vertical stabiliser. The yaw restoration moment is created whenever the aeroplane is experiencing a sideslip angle, β, Figure B.22. The vertical stabiliser is also the most significant contributor to damping motion about the z axis, as shown on Figure B.23.

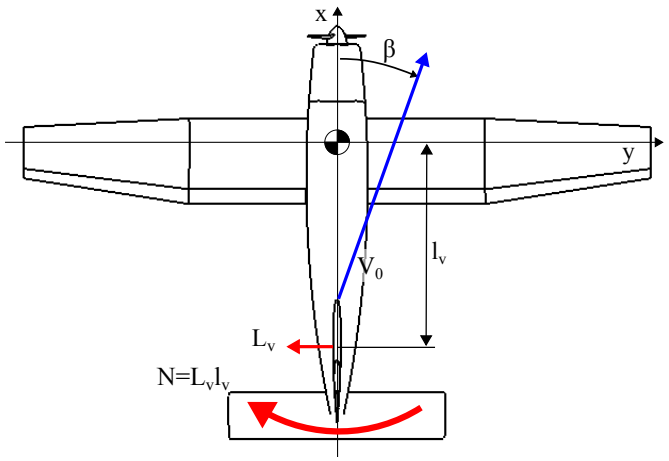

Figure B.22: Aeroplane in negative side slip showing positive yaw restoration contribution from vertical stabiliser.

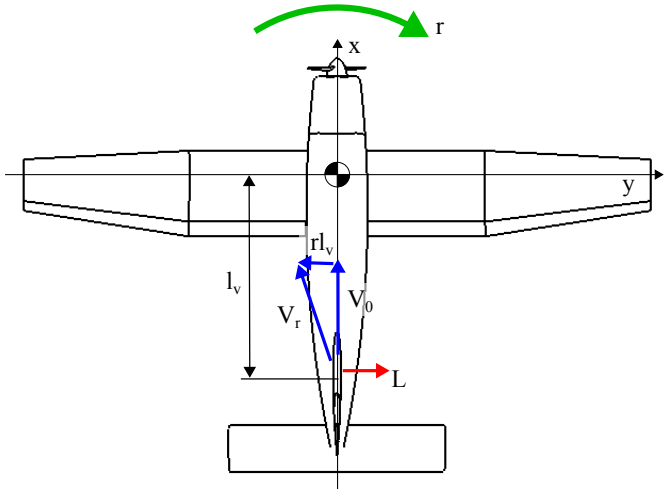

Figure B.23: Aeroplane in positive yawing motion showing yaw damping contribution from vertical stabiliser.

Stability About the Longitudinal X Axis

Referring to Figure B.24 it can be seen there is no direct passive restoring moment when an aeroplane is disturbed in roll by ϕ. Thus an aeroplane is only neutral stable in roll. However, it is also shown on Figure B.24 that the aeroplane is no longer in equilibrium as the lift force is tilted by ϕ. Referring to

the aircraft fixed axis the weight force now has an unbalanced force component in the positive y direction. This induces a side slip motion and a side slip angle β coupling the longitudinal and directional stability.

Depending on the geometry of an aeroplane the side slip motion can create stable, neutral or unstable response as a function of the side slip angle. Briefly, aeroplanes that have wing dihedral (wings that are angled upward from the wing root to the wing tip) experience a stable response to roll disturbance. Swept wing and high winged aeroplanes also create a stable response to roll disturbance. While the opposite, wing anhedral, low wing and forward swept wings create a destabilising moment in roll.

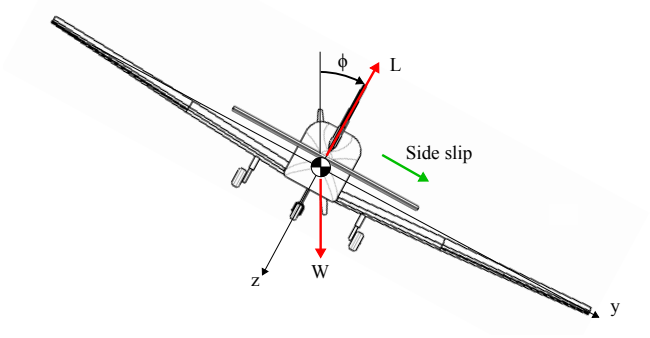

Figure B.24: Aeroplane in a disturbed roll position showing development of side slip motion.

The wings are the largest contributor to damping the roll motion p. The roll motion induces an upward lift force on the down going wing and a downward force on the up going wing creating a strong damping moment, as shown on Figure B.25. Both the vertical and horizontal stabiliser also contribute to roll damping. Generally, the greater the wing span the greater the roll damping. For this reason aerobatic and fighter aircraft have smaller span wings.

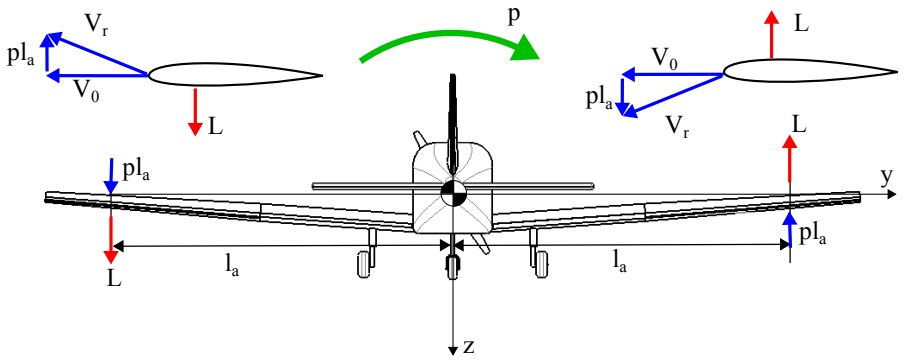

Figure B.25: Aeroplane in positive rolling motion showing roll damping contribution from wings.

Aeroplane Summary

Concluded from Cook [81], Pamadi [80], and Raymer [75], the conventional aeroplane is:

- Limited to fly at an airspeed greater than stall speed (angle of attack less than stall angle of attack).

- Limited to fly in a flight path defined by a cone, refer to Figure B.33.

- Controlled by force and moment reactions created by the deflection of control surfaces.

- Both statically and dynamically stable in pitch, roll and yaw.

The Helicopter

The helicopter or rotor-wing aircraft [88], is the most successful heavier than air VTOL aircraft. The helicopter allows for rapid point to point air transportation and does not require a runway to land or takeoff as the helicopter has the ability to hover/fly at zero airspeed. The helicopter is used in a wide variety of roles in both military and civilian applications. Typical civilian roles are air ambulance, search and rescue, police duties, tourism, and transportation. The helicopter is predominantly used where the ability to hover and takeoff and land vertically is required.

The conventional helicopter, as shown in Figure B.26, contains one or more engines that power the main rotor blades to rotate creating a relative airspeed over the rotor-blade aerofoils. A smaller anti-torque rotor located on the end of a tail boom is required to balance the torque needed to spin the main rotor.

To control the lift force, rolling moments, and pitching moments on a helicopter a mechanically complex system is used to change the angle of attack of each rotor blade as they rotate. This system is achieved by having two swash plates, an upper swash plate that rotates with the rotor and a lower swash plate that does not rotate, but can be move up and down and also tilted. Connecting links from the upper swash plate to the rotor blades constrain the angle of attack of the rotor blades. Hence, the angle of attack of the rotor blades is changed by the pilot moving the lower swash up and down with the collective joystick and tilting the swash plate with the cyclic joystick.

By varying the thrust of the tail rotor the pilot can control the rotation of the helicopter about the vertical axis, this is done by the pilot manipulating the rudder/foot pedals. To obtain translational flight the helicopter tilts its thrust vector into the direction of the intended motion. The horizontal component of the thrust force is used to overcome the aerodynamic drag forces experienced the moving helicopter. The thrust vector can be tilted forwards, backwards, left and right allowing the helicopter to move in all directions.

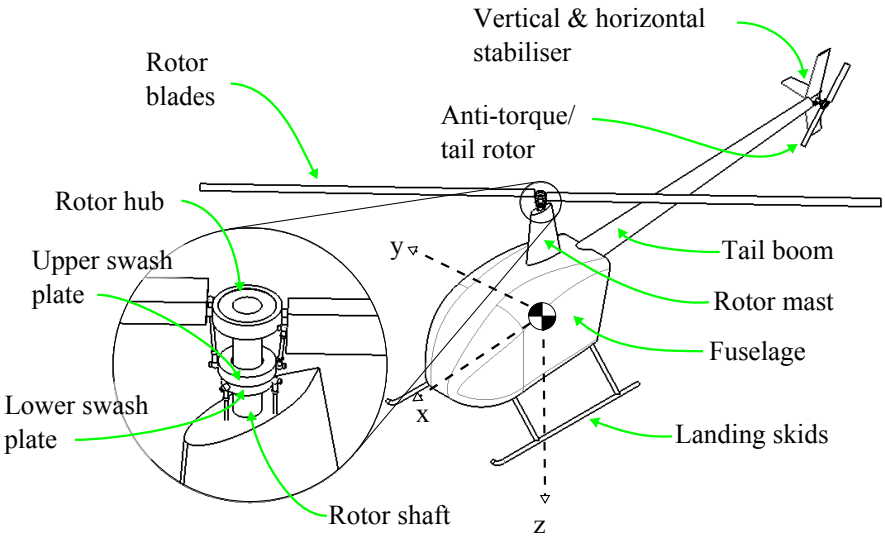

Figure B.26: Key features of a conventional single rotor helicopter

Helicopter Lift Force

The rotor blade has an aerofoil cross section similar to that of an aeroplane's wing or propeller. The lift force for a helicopter is created by rotating the rotor blades to create a relative airspeed over the rotor blade. Hence, lift can be created when the blade is at an angle of attack with respect to the relative airflow. If the blades are spun fast enough the high relative airspeed combined with the rotor blade angle of attack can create a lift force to overcome the weight of the helicopter, Figure B.27, and thus allow the helicopter to fly at zero airspeed, referred to as hovering. During flight the rotor blades generally stay at a fixed angular velocity and the angle of attack of the rotor blades is altered to control the lift force. This is done as it is not practical to change rotational speed of the rotor blades due to the high rotational inertia of the blades, which would cause a very delayed response. To control the rate of climb or descent the pilot operates the collective stick which moves the lower stationary swash plate up or down, which has the effect of changing all the rotor blades angles of attack together in a collective manner, refer to Figures B.28a and B.28b.

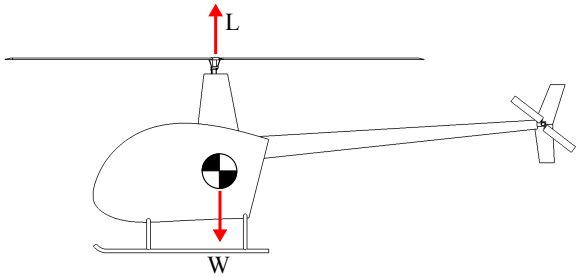

Figure B.27: Lift force of helicopter in hovering flight

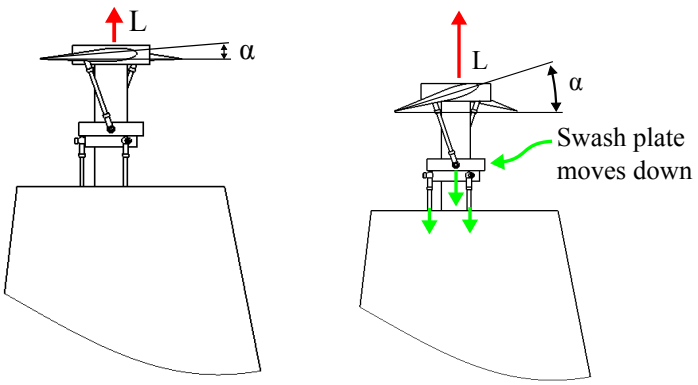

(a) Rotor head in hover showing low blade angle of attack

(b) Rotor head in climb showing increased blade angle of attack

Figure B.28: Collective movement on helicopter rotor blade

Pitch and Roll Control

To fly the helicopter in a desired direction the lift or thrust force of the helicopter needs to be tilted into the desired direction. This is done by the pilot using the cyclic joystick to tilt the lower swash plate. The tilting of the lower swash plate alters/cycles the rotor blade angle of attack as the rotors rotate around the shaft. Hence, when the swash plates are tilted the blades opposite each other have differing angles of attack to one another so create differing amounts of lift. This differential in lift effectively moves the combined lift vector away from the central hover thrust line. This creates a moment about the centre of gravity and causes the helicopter to tilt which tilts the thrust vector and creates a force and motion in the desired direction.

The cyclic can tilt the swash plates forwards and rearwards for pitching the helicopter about the y axis to move the helicopter forwards and rearwards, refer to FigureB.29. Similarly tilting the swash plate left and right causes a rolling moment about the x axis, which causes the helicopter to move sidewards, refer to Figure B.30.

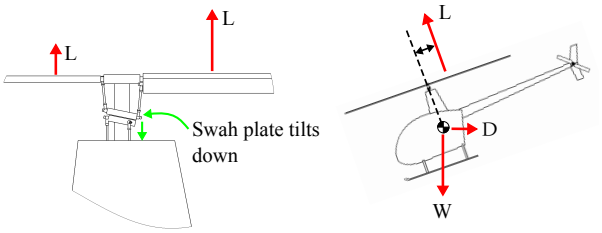

Figure B.29: Forces acting on a helicopter in forward flight and pitch control

Yaw Control

Yaw control of a conventional helicopter is done by altering the angle of attack of the anti torque rotor (also known as the tail rotor), refer to Figure B.31. The torque required to spin the main rotor must be balanced by an opposing torque to prevent the helicopter from spinning about the yaw, z, axis. The pilot can alter the angle of attack of tail rotor blade by operating the yaw

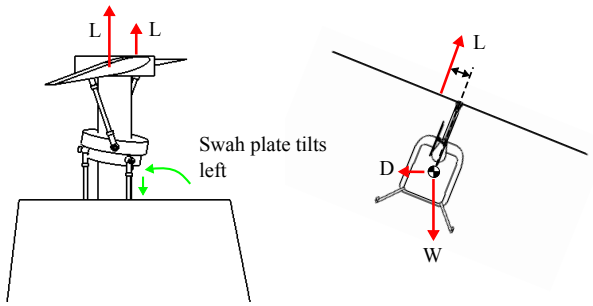

Figure B.30: Forces acting on a helicopter in sidewards flight and roll control

foot pedals, (similar to an aeroplane). A decreased angle of attack of the tail rotor reduces the thrust of the tail rotor and decreases the anti torque effect, hence the helicopter begins to spin in the opposite direction to the main rotor rotation. By increasing the angle of attack of the tail rotor the thrust force increases and the anti torque effect becomes greater than the torque of the main rotor the helicopter begins to spin in the same direction as the main rotor. Generally it is easier for a helicopter to spin in the opposite direction to the main rotor rotation as this requires less work from the tail rotor.

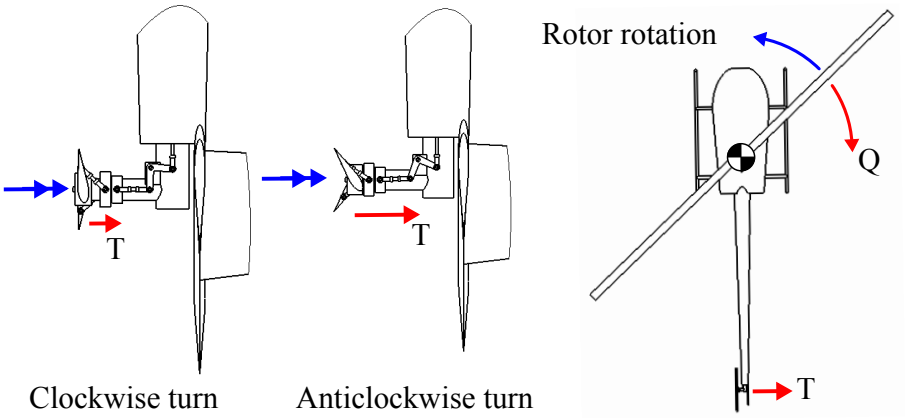

Figure B.31: Tail rotor force and yaw control

Helicopter Stability

The stability of a helicopter is dependent on a range of parameters from helicopter size, flight condition (hovering or fast moving flight), geometric layout, and rotor blade design. A brief description of the stability for a conventional single main rotor helicopter is presented.

As helicopter rotor blades are free to hinge, at rotor blade root, the rotor blade tip plane is mechanically free from the rotor shaft and fuselage. If the rotor shaft is tilted, either in roll or pitch, the rotor blades will remain in their original plane of rotation due to inertia. Since the rotor blades angle of attack is linked to the tilt of the swash plate, for cyclic control, the angle of attack of the rotor blades will change as the swash plate tilts with the rotor shaft. The cyclic change in rotor blade angle of attack will realign the rotor blade tip plane and the rotor shaft to be normal to one another. Hence, the orientation of the fuselage and rotor tip plane are coupled together.

Pitch and Roll Stability in Hover

The helicopter stability in both pitch and roll is analogous to the stability of an aeroplane in roll [98]. If a helicopter is tilted in roll or pitch, the thrust vector that can be assumed to act normal to the blade tip plane is also tilted with the helicopter, so that the thrust line passes through the centre of gravity. Hence, no moment exists to either restore the helicopter or diverge the helicopter in angular position, this equates to neutral stability. However, when tilted there is an unbalanced force component that causes the helicopter to accelerate in the direction of the unbalance force, Figure B.32 step 1. This motion causes the rotor blade tip plane to tilt in the opposite direction to the motion, which creates a restoring moment, Figure B.32 step 2. This restoring moment induces an angular velocity so that when the helicopter passes through level the helicopter fuselage has an angular rotational velocity and zero translational velocity, Figure B.32 step 3. The helicopter continues with the angular motion and causes the rotor blade tip plane to tilt away from level direction and induces an acceleration in the opposite direction completing one half of the hover oscillation, Figure B.32 step 4. As the oscillation typically diverges for helicopters it demonstrates that helicopters are statically stable, but dynamically unstable for pitch and roll attitude in hovering flight.

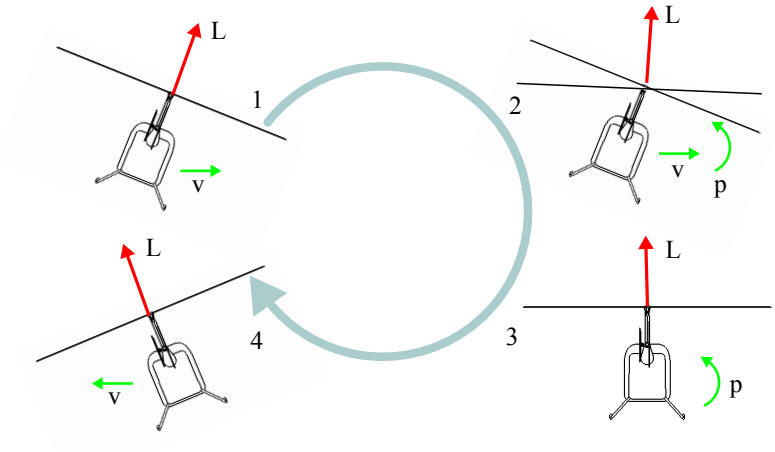

Figure B.32: Oscillation of a helicopter in hover due to attitude disturbance.

Directional Stability in Hover

In hover the helicopter has neutral static directional stability and dynamic directional stability. The tail rotor provides the dynamic stability by the change in thrust of the tail rotor due the increase or decrease in tail rotor angle of attack due to yawing motion.

Stability in Forward Flight

Due to the aerodynamics of the rotor blades, the stability of a helicopter in forward flight is dependent on airspeed as well as pitch attitude. An increase in airspeed, at a constant angle of attack, will produce a nose pitch up moment that will reduce the airspeed, as the thrust vector is tilted back creating a stabilising moment.

Helicopter static stability for changes in angle of attack result in non-linear destabilising moments. The degree to of this destabilising moment is depen-

dent on the design of the helicopter, but in similar fashion to an aeroplane horizontal stabilisers are located on the tail boom to increase both static and dynamic stability.

The directional stability of a helicopter in forwards flight is both static and dynamically stable, due to the vertical stabiliser functioning in the same manner as on an aeroplane.

Helicopter Summary

In summary, the conventional helicopter is:

- Able to generate lift independent of airspeed
- Controlled by altering rotor blade angle of attack via the mechanically complex swash plate mechanism. Yaw is controlled by blade angle of attack of the tail rotor.
- Both statically and dynamically stable in pitch, roll and yaw in forward flight.
- At best, statically stable in hover but only neutral dynamic stability. Most helicopters tend to have neutral statical stability and unstable dynamic stability in the hover/low speed flight regime.

Aeroplane Versus Helicopter

From the brief overview of the three most common types of aircraft the aeroplane and the helicopter far exceed the practicality of lighter than air aircraft for transportation roles. For this reason the following discussion will focus only on the advantages and disadvantages of the helicopter and the aeroplane.

Cruise Performance

The lift to drag ratio is a measure an of aircraft's transport efficiency. The ratio simply shows the how much an aircraft can lift and for a given thrust force in level flight. With this parameter in mind, the aeroplane is much more efficient than the helicopter as it has a much higher lift to drag ratio, typically in order of 6 to 20 for a general aviation fix-wing. In contrast to a modern helicopter has a maximum lift to drag ratio of approximately 4.5, [99]. The higher lift to drag ratio of aeroplanes means that for the same weight as a helicopter the aeroplane has less drag, requiring less power, resulting in less energy consumption and thus higher transport efficiency.

The maximum flight speed of a helicopter is less than that of an aeroplane due to the inefficiencies of the helicopter's rotor blades in fast forward flight. This occurs as the retreating blade has lower dynamic pressure and increased angle of attack. This leads to blade stall occurring at the blade root and progressing towards the blade tip with increasing flight speed on the retreating blade. Once a critical portion of the blade has stalled the drag can no longer be overcome and the maximum airspeed of the helicopter has been reached.

Low Speed Flight/Hover

The helicopter has the advantage over the aeroplane that it can take off and land vertically, as hence, it can fly in all directions, forwards, backwards and sidewards. The hovering ability does not restrict the helicopter to operate from costly runways, which allows the helicopter to fly from point A to point B, where point A and B only need to be large enough for the helicopter to safely operate from. Using winches, helicopters can even operate over hazardous environments lowering and raising people and supplies without the need to land.

An aeroplane's minimum level flight speed is limited to the stall speed of the aircraft, as such the aeroplane must fly at airspeeds higher than the stall speed to safely perform its mission objectives. Any aeroplane can only tolerate a small component of sidewards velocity as the airflow must be largely parallel to the chord of the wing (aerofoil cross-section) for the wing to produce lift. Thus, the airspeed vector (V_0) must have a magnitude greater than the stall speed and be constrained between minimum and maximum angles of attack and between negative and positive side slip angles as shown in Figure B.33.

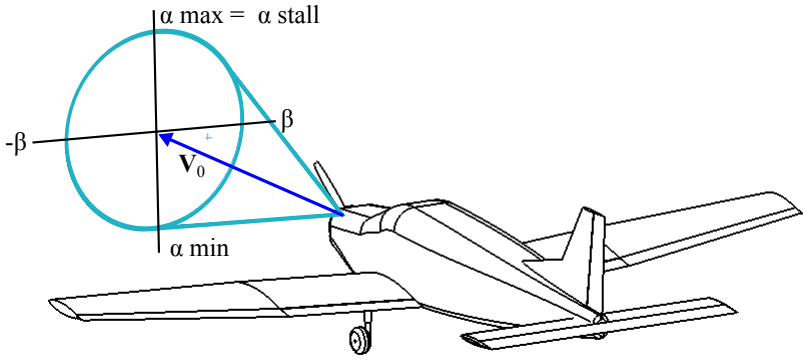

Figure B.33: Constraints of the aeroplane's airspeed vector. Typical aeroplane angle of attack range is from $\alpha_{min} = 2°$ to $\alpha_{max} = 20°$ and side slip range of $\beta_{max} = \pm 15°$ and $\mathbf{V}_0$ is level flight stall airspeed.

Mechanical Complexity

In terms of mechanical complexity the aeroplane is far simpler than the helicopter. The aeroplane is essentially a collection of stationary aerofoils with hinged controlled surfaces, which when deflected orientate the aeroplane. Typically, one or more engines directly drive a propeller or fan, providing a reliable source of propulsion. The helicopter requires a complex mechanical control system to provide both lift and control. Reduction gear boxes are necessary to reduce the high shaft speed of the engine(s) to that of the slower rotor speed. Gearing, power transmission, and control is also required for the helicopter's tail rotor. The extra mechanical complexity of a helicopter greatly increases the number of failure modes when compared to an aeroplane. For this reason, helicopters require more intensive maintenance than fixed-wing aircraft, and as a consequence are more expensive to procure and operate.

The Ideal Solution - The Hybrid of the Skies
It has long been the dream of many aircraft designers to combine the advantages of an aeroplane, namely cruise performance, with the VTOL capabilities of a helicopter [20]. History shows that such an aircraft would look similar to an aeroplane with an additional means of providing lift for hovering flight. Whatever the hybrid aircraft will resemble, its resemblance towards either aircraft type will be greatly determined upon the mission objectives of the aircraft. If high speed cruise is necessary, the aircraft will resemble an aeroplane. If hover efficiency is a higher priority, the aircraft will have a large rotor diameter and resemble a helicopter, such as the Eurocopter X-3 (Figure 1.2d). Either way, the economic restraints will dictate the outcome whether the aircraft will ever reach production. Hence, any contender will need to be: cost effective, mechanically simple and reliable.

Ducted-fan technology has long been thought of as a key technology to develop the hybrid VTOL aircraft, as the ducted-fan offers greater static thrust than a propeller of equal size and power [68]. Thus a ducted-fan could be used to supply the thrust force for both hovering and horizontal flight. Although the Martin Jetpack in current form is intended for low speed flight, up to 100 km/h, this research is valuable for the successful implementation of the ducted-fan for VTOL flight.

B.3 The Atmosphere

This section introduces the atmospheric model, used to calculate atmospheric properties, and the wind models used to create steady, gusty, and turbulent conditions in the simulation environment.

Atmospheric Model

The lower region of atmosphere that the majority of aircraft fly in is the *troposphere.* This region extends from the surface of the earth up to the *tropopause,* which is the boundary between the *troposphere* and *stratosphere.* Within this layer the temperature decays at approximately a linear rate. The pressure and density decay at non linear rates, but are related to the temperature and gravitational acceleration. As the atmospheric density is an important property for the design and modelling of an aircraft, it is thus important to accurately model how the density varies within the atmosphere that the intended aircraft is to fly in.

The International Standard Atmosphere (ISA) is an atmospheric model based on linear temperature lapse rates to model atmospheric properties throughout the various regions within the atmosphere. The International Organization for Standardization publishes the ISA model as ISO 2533:1975 [96]. Table B.1 shows the standard ISA conditions used in equations (B.3.1) to (B.3.4) that are used to model the atmospheric properties of temperature, pressure, air density, and speed of sound within the troposphere.

The local ISA air temperature is calculated as:

$$T = -hL + T_0 \tag{B.3.1}$$

Table B.1: International Standard Atmosphere properties

Property	ISA Value
Temperature lapse rate	$L = 0.0065\,K/m$
Mean sea level temperature	$T_0 = 288.15\,K = 15°C$
Mean sea level pressure	$P_0 = 101325\,Pa$
Mean sea level density	$\rho_0 = 1.225\,kg/m^3$
Height of tropopause	$11000\,m$
Temperature tropopause	$T_{tropopause} = 216.65\,K = -56.5°C$
Ratio of specific heats	$\gamma = 1.4$
Gas constant for air	$R = 287.0531\,\mathrm{J/kg/K}$
Acceleration of gravity	$g = 9.80665\,\mathrm{m/s^2}$
Mean sea level speed of sound	$a_0 = 340\,\mathrm{m/s}$

where h is the height above sea level, L is the temperature lapse rate, and T_0 is the standard sea level temperature. The local speed of sound of air is a function of the local temperature, and is calculated as:

$$a = \sqrt{\gamma R T} \tag{B.3.2}$$

where γ is the ratio of specific heats for air and R is the universal gas constant for air. The local air pressure is calculated as:

$$P = P_0 \left(1 - \frac{h.L}{T_0}\right)^{\frac{g}{LR}} \tag{B.3.3}$$

where P_0 is the ISA sea level pressure and g is the acceleration due to Earth's gravity. The key aerodynamic property of air density is calculated using the ideal gas model as:

$$\rho = \frac{P}{T} \tag{B.3.4}$$

Using equations (B.3.1) to (B.3.4) Figure B.34 can be created, which shows how the atmospheric air temperature, relative air pressure (RAP), relative air density (RAD), and relative speed of sound (RSS) decrease with increasing altitude within the troposphere. RAP, RAD, and RSS are defined as:

$$RAP = \frac{P}{101325\,\mathrm{Pa}} \tag{B.3.5}$$

$$RAD = \frac{\rho}{1.225\,\mathrm{kg/m^3}} \tag{B.3.6}$$

$$RSS = \frac{a}{340\,\mathrm{m/s}} \tag{B.3.7}$$

Wind Model

It is evident, when one looks at the atmosphere, that it is never perfectly still. The movement of the air, termed wind, is driven by pressure gradients. The pressure gradients themselves are produced by differences in pressure as

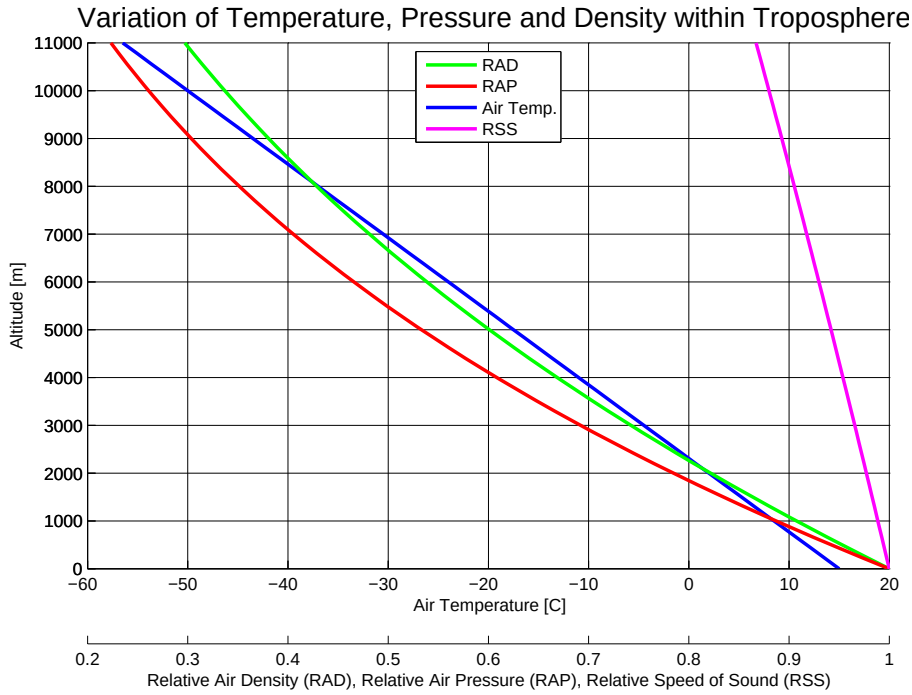

Figure B.34: Variation of temperature, pressure, and density within the troposphere

a results of thermal processes in the atmosphere. Heating of an air mass from the sun's radiation causes the density within an air mass to decrease creating a buoyant lift force, which forces the warm air to ascend and drawing in cool air to fill its space creating a convection process. In areas where air is rising the pressure is lower, while is areas where the air is subsiding the pressure is higher than average. This difference in pressure forces air to flow from high to low pressure, creating wind.

The wind phenomena occurs at a range of scales from global size, trade winds, to micro size, heat convention within a building. Consequently, the strength and frequency of wind also changes with scale, and is a function of numerous local conditions.

The wind velocity and particularly dynamic wind velocity can strongly affect an aircraft by changing aerodynamic reactions in flight, often drastically. Hence, it is prudent to include wind effects into an aircraft flight model to be able to assess an aircraft's response to wind. A six degree of freedom wind model can be developed by combining: steady state wind (S), wind gust (G), and wind turbulence (T) models.

Steady State Wind

Steady state wind is simply what the name implies, a constant wind velocity.

$$\mathbf{V}_{wind}^{S} \tag{B.3.8}$$

where $\mathbf{V}$ is a vector representing three translation degrees of freedom of the wind.

Wind Gust
A wind gust is an increase and decay of wind velocity over a short time frame [100], typically 1 - 10 s. A simple wind gust model was formulated based on a sinusoidal function as a function of time:

$$\mathbf{V}_{wind}^{G} = -\frac{\mathbf{G}}{\mathbf{2}}\left(1 - \cos\left(\frac{2\pi t}{T_G}\right)\right) + \frac{\mathbf{G}}{\mathbf{2}} \tag{B.3.9}$$

where $\mathbf{G}$ is a three dimensional vector of peak gust velocity, t is the simulation time, T_G is the gust period. This formulation is similar to that described by MathWorks$^{\text{TM}}$ [101], which shows a discrete gust model for the implementation of the U.S. Military Specification F-8785C [102].

Wind Turbulence
Wind turbulence is the random change in wind velocity over a short period of time [100]. A wind turbulence model was developed from a white noise signal passed through a first order low pass filter to model the inertial effects of the air mass for each of the six wind degrees of freedom:

$$\mathbf{V}_{wind}^{T} = f(p, \tau_T) \tag{B.3.10}$$

where p is the power density of the white noise and τ_T is the filter time constant for the first order low pass filters. These variables are chosen to represent realistic wind turbulence, and range from 0.1 to 100 and from 0.2 to 2 for p and τ_T respectively. This is a similar formulation to that described by MathWorks$^{\text{TM}}$ [103], which is implements the turbulence models described in the U.S. Military Specification F-8785C [102] and the U.S. Military Handbook 1797 [104].

Total Wind
The total wind velocity with respect to the inertial reference frame is calculated as the sum of steady, gust, and turbulent wind speeds as:

$$\mathbf{V}_{wind} = \mathbf{V}_{wind}^{S} + \mathbf{V}_{wind}^{G} + \mathbf{V}_{wind}^{T} \tag{B.3.11}$$

Similarly as the translational wind components rotational wind components also exist, where the sum of the rotational wind is:

$$\boldsymbol{\Omega}_{wind} = \boldsymbol{\Omega}_{wind}^{S} + \boldsymbol{\Omega}_{wind}^{G} + \boldsymbol{\Omega}_{wind}^{T} \tag{B.3.12}$$

Airspeed
The airspeed of the aircraft is calculated as the difference between inertial and wind velocities as:

$$\mathbf{V}_0 = \mathbf{V} - \mathbf{V}_{wind} \tag{B.3.13}$$

and similarly for the rotational case:

$$\boldsymbol{\Omega}_0 = \boldsymbol{\Omega} - \boldsymbol{\Omega}_{wind} \tag{B.3.14}$$

Appendix C

First Tow Test Experiment

C.1 Methodology

The aim of the first tow test experiment is to validate that the tow testing method can quantify the aerodynamic behaviour of the Martin P-11A Jetpack under flying conditions.

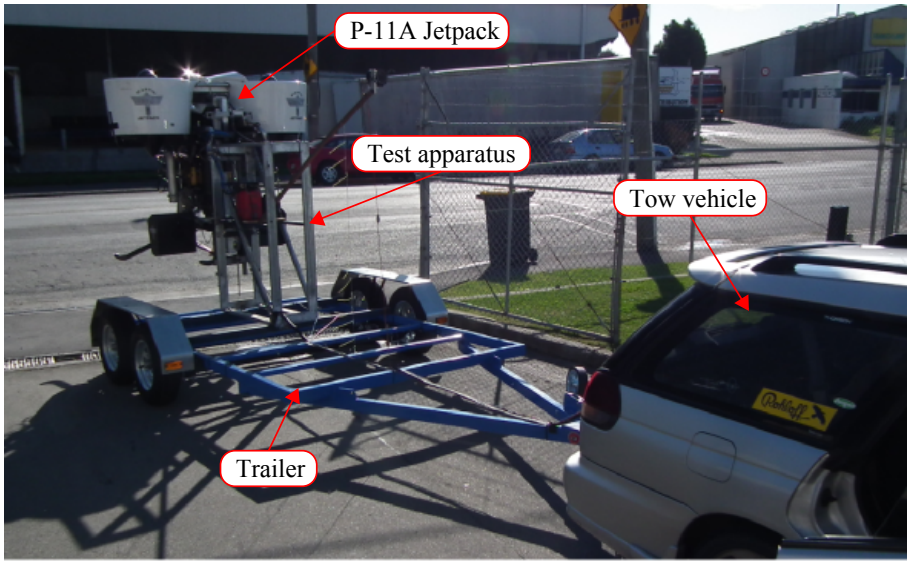

Figure C.1: Experimental setup used for tow testing

Test Apparatus Design

A tandem axial trailer was used to carry the Jetpack and the test apparatus, as shown on Figure C.1. The apparatus, Figure C.2, used three load cells to measure the lift, drag, and pitching moment reactions. Linear bearings were used to allow for freedom in the vertical plane, where the lift load cell was used to constrain the motion in the vertical plane allowing the entire lift force to pass through the load cell. The pitching moment was measured by using the moment load cell force F_{Mlc} to constrain the angular motion about the moment pivot, and is calculated as:

$$M_{pivot} = l_{Mlc} F_{Mlc} \tag{C.1.1}$$

where l_{Mlc} is the moment arm between the moment load cell and the pivot.

Due to the design of the apparatus both the drag, F_{Dlc}, and moment load cell, F_{Mlc}, measurements were required to be summed together to give the drag force acting on the Jetpack as:

$$D = F_{Dlc} + F_{Mlc} \tag{C.1.2}$$

This measurement of the drag force is not ideal, as the experimental uncertainty is doubled due to the addition of the load cells, and a small amount of the drag force is leaked through the lever mechanism, as the lever is not perfectly vertical.

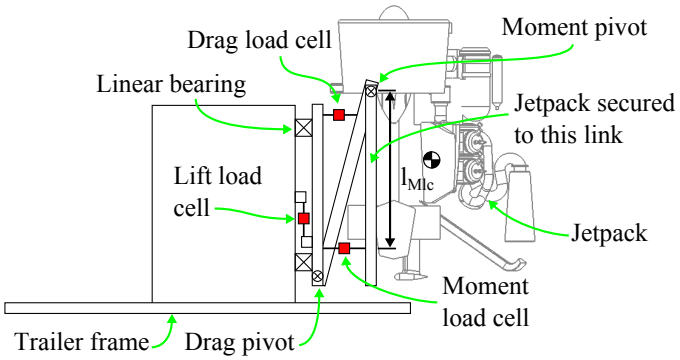

Figure C.2: Schematic of test apparatus

Testing Procedure

To obtain the desired results, a detailed test methodology was developed and strictly followed for each of the test runs. Before each test run was commenced the Jetpack engine was warmed to operating temperature, once warmed it was then shutdown to allow the DAQ system to begin logging from a steady zero reading. Lead bricks were added on top of the Jetpack exhaust to provide a known loading into the load cell, and were then removed. The Jetpack was then started again and brought up to 5750 RPM to obtain a steady state static thrust measurement. The tow vehicle was then driven to the target tow speed. At the desired test speed the engine was ran up to 5750 RPM, and held steady for a minimum of 2 s before returning to idle power; this was repeated three times for each test speed, with the exception of the 60 km/h and 80 km/h test speeds, where it was repeated twice, as the required test space for three samples was not available. The engine was then shutdown and the tow vehicle continued driving at the tow speed for a minimum of 5 s to allow for the recording of engine off data to complete the test run. The test was repeated for tow speeds of 20, 30 km/h, 40 km/h, 60 km/h, and 80 km/h to obtain data for a range of flight speeds at a duct angle of attack of 90°.

C.2 Results and Discussion

The DAQ system was continuously ran at a high sampling rate (83 Hz), recording the load cell forces and engine speed for each test run. Using the recorded engine speed data to identify the sample periods, the data points were obtained by time averaging the recorded samples. The results are shown on Figures C.3 to C.7, which show the body aerodynamic drag force, ducted-fan drag force, ducted-fan lift force, ducted-fan pitching moment, and ducted-fan centre of pressure movement. All results are shown with their experimental uncertainty, which is based on the variation of the results and measurement accuracy, which is ±1 kg per load cell. Note, the ducted-fan drag, lift, and pitching moments shown on Figures C.4 to C.6 are the net forces and moment for both left and right hand ducted-fans on the P-11A Jetpack.

Aerodynamic Forces

The theoretical aerodynamic body drag force has been added to Figure C.3 using equation (B.1.5) with a drag coefficient of 0.6 and a frontal area of 1.8 m^2. The theoretical line closely matches the measured result, indicating that the drag coefficient is appropriately chosen. This value of drag coefficient is on the lower end of bluff body shapes [84], which the Jetpack airframe is. However, it is believed that the actual aerodynamic drag coefficient on the Jetpack would be higher, due to the Jetpack being partially submerged in the wake of the tow vehicle during testing, which would reduce the measured drag force acting on the Jetpack.

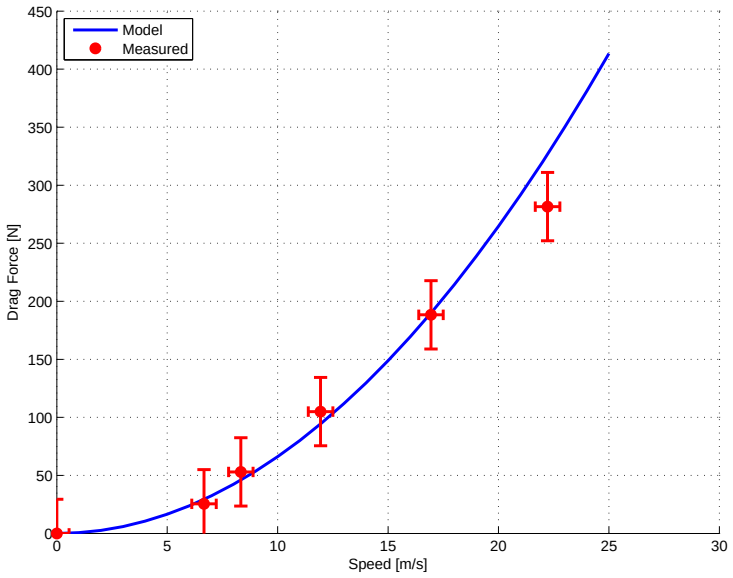

Figure C.3: Measured compared to theoretically predicted body drag force

Ducted-Fan Drag

Figure C.4 shows that the theoretical ducted-fan drag closely matches the measured ducted-fan drag force. The theoretical ducted-fan drag force is cal-

culated using equation (3.1.33) to determine the axial velocity and mass flow rate of the duct for the measured static force of 238 kg from Figure C.5. With the calculated mass flow rate the ducted-fan drag force can be calculated using equation (3.2.1).

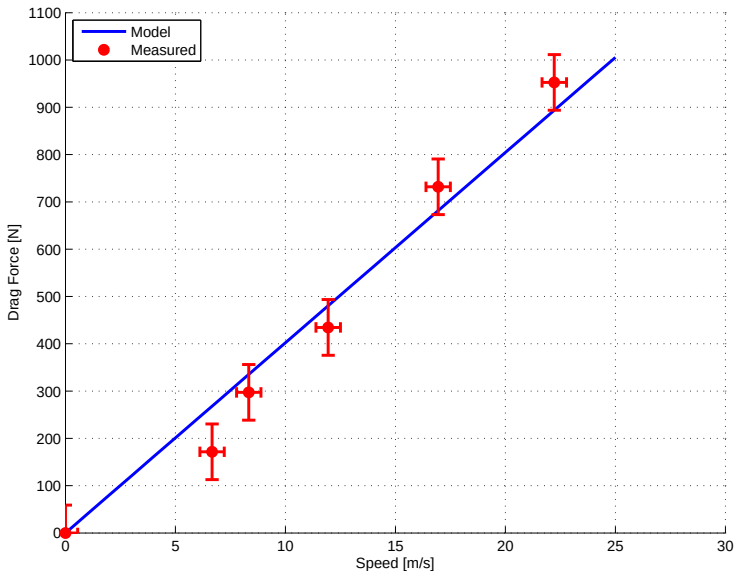

Figure C.4: Measured compared to theoretical predicted Ducted-fan drag force

Ducted-Fan Lift

Favourably, the measured ducted-fan lift force (Figure C.5) increases with airspeed and shows a trend that is proportional to velocity squared. Figure C.5 shows that at 80 km/h an additional 57 kg of lift is produced from the static lift/thrust force at an engine speed of 5750 RPM. Provided that this lift force is still available when the Jetpack is at a trimmed angle of attack, the Jetpack will experience an optimum flight speed where the engine power is less than the power required for takeoff/hover. The theoretical lift or duct thrust force remains constant with increasing velocity, as the ducted-fan thrust equation (3.1.48) only accounts for axial velocity, so an additional equation needs to be developed to include this effect into the Jetpack model. This increase in lift force is attributed to the increase in down wash experienced as shown on by the wool tuft photographs Figure 6.30b and explained in section 6.3.

Ducted-Fan Pitching Moment

The measured ducted-fan pitching moment (Figure C.6) is similar to that predicted by the fixed centre of pressure theory in section 3.2 for speeds from 0 km/h to 60 km/h. However, at 80 km/h the measured moment result differs from that predicted. This is believed to be due to separation occurring over the duct leading edge, which results in the fan thrust force moving leeward from

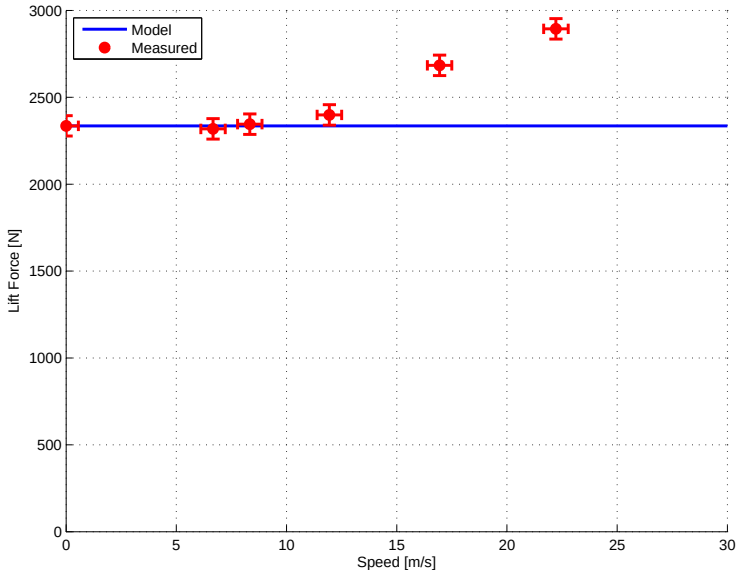

Figure C.5: Measured compared to theoretical ducted-fan lift force

the duct axis, and creating a moment that counter acts the positive moment produced by the ducted-fan normal force.

Figure C.6 also shows the maximum pitch moment available from the pitch control vanes for the P-11A Jetpack, as measured in Chapter 5 and shown on Figure 5.8. It can be seen that the ducted-fan pitching moment dominates the maximum pitch vane moment. At approximately 15 km/h the total available pitch moment opposes the ducted-fan pitching moment. If the airspeed were to increase above this, due to a disturbance, the control vanes would no longer be able to maintain the aircraft in trimmed flight, resulting in loss of control. This result reflects what has been experienced flying the P-11A Jetpack, where the top obtainable airspeed is approximately 10 km/h (indoors) before the pitch control vanes become saturated.

Centre of Pressure

Figure C.7 shows how the centre of pressure along the duct axes measured from the duct quarter chord changes with velocity. The constant centre of pressure theory described in section 3.2 is close to that measured at low velocities, but differs with increasing velocity as the duct centre of pressure moves towards the duct quarter chord with increasing velocity.

The high ducted-fan centre of pressure combined with the centre of gravity located 0.527 m below the duct quarter chord means there is an excessive separation between the ducted-fan centre of pressure and the centre of gravity on the P-11A Jetpack. This separation combined with the large ducted-fan normal force results in the large positive pitching moment that prevents the Jetpack from obtaining trimmable flight speeds greater than approximately 15 km/h. Hence, to improve the Jetpack's flight performance, the ducted-fan centre of pressure must be positioned in such a way that it coincides as best

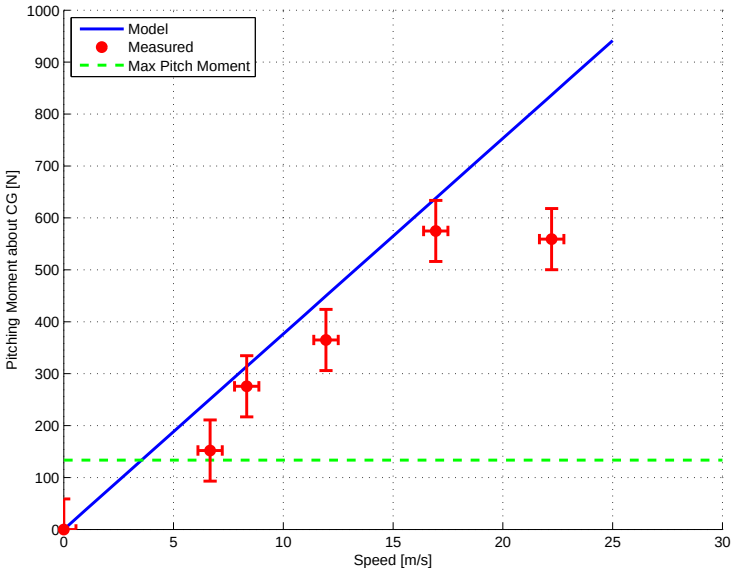

Figure C.6: Measured compared to theoretical predicted ducted-fan pitching moment and compared to maximum pitch vane moment.

as possible with the centre of gravity. The results in Figure C.7 suggest that a centre of gravity position between 0.1 m to 0.2 m above the duct quarter chord would significantly improve the Jetpack performance.

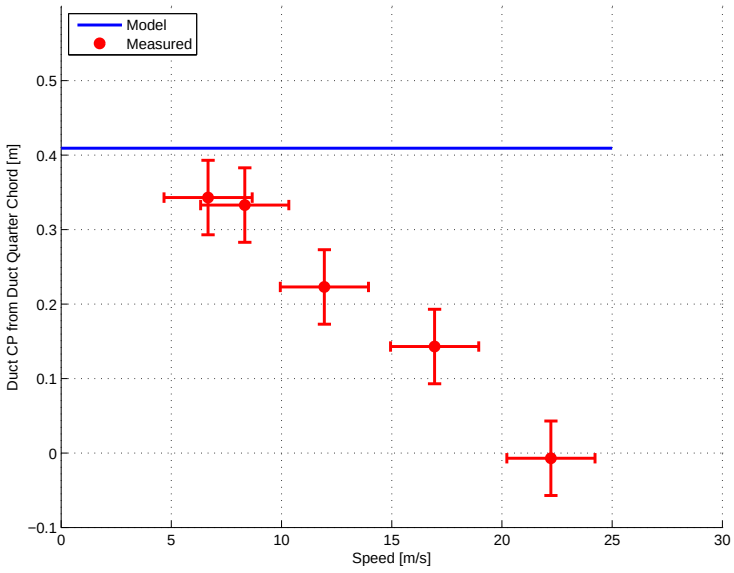

Figure C.7: Ducted-fan centre of pressure, measured from duct quarter chord

C.3 Conclusions

The experimental procedure of towing the P-11A Jetpack, at flying power, to measure the ducted-fan reactions and to determine the ducted-fan centre of

pressure movement has been successful. The results from the test have shown that the Jetpack body has a drag coefficient of 0.6, and that the drag predicted from ducted-fan normal force closely relates to the measured ducted-fan drag. Favourably, as the airspeed increased the ducted-fans produced an increased lift force, which at 80 km/h equates to an additional 57 kg of lift. It was found that the fixed centre of pressure model does not accurately model the duct-fan centre of pressure as the centre of pressure shows a non-constant relationship with velocity, which reflects the non-linear ducted-fan pitching moment with velocity.

In order to understand how the ducted-fan centre of pressure moves during flight conditions, the centre of pressure needs to be measured for a range of angles of attack in both the pitch and roll planes. Using the proven methodology of the first tow test, the following section explains in detail how the ducted-fan reactions are measured for a range of angles of attack in both the pitch and roll planes to obtain a more comprehensive understanding of the centre of pressure movement. The improved understanding will allow for a more sophisticated model of the ducted-fan centre of pressure, and hence the ducted-fan moment, to be developed, which will improve the realism of the Jetpack model.

Appendix D

Results from Experiments

D.1 Tow Test Experiment Results

Note, for the following Figures *ducted-fan* refers to the aerodynamics of both ducted-fans, hence to obtain results for an individual ducted-fan divide the data shown data by two.

Jetpack Drag at 0º and 180ºAngles of Attack

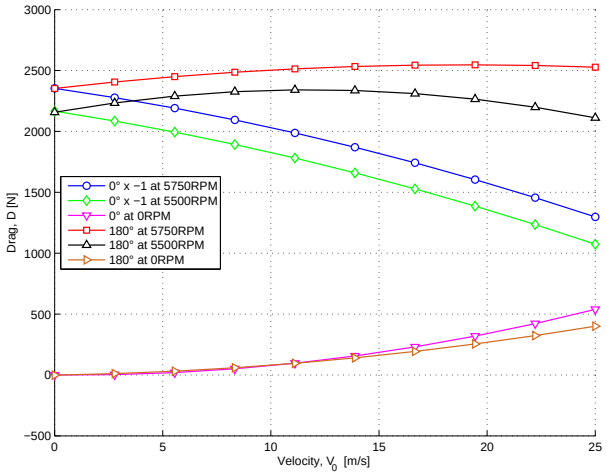

Figure D.1: Pitch

Ducted-Fan Drag at 0º and 180º Angles of Attack

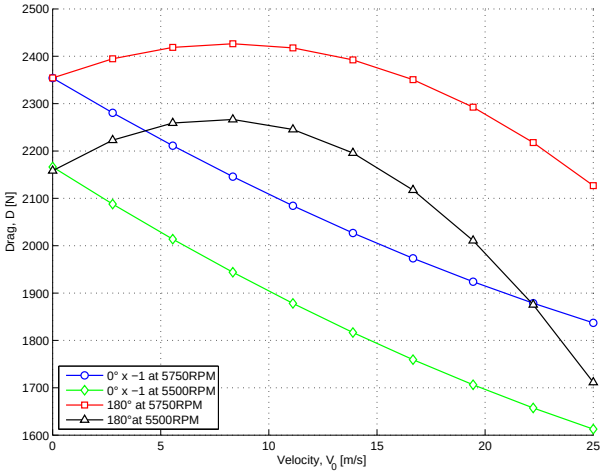

Figure D.2: Pitch

Jetpack Measurements at 5500 RPM

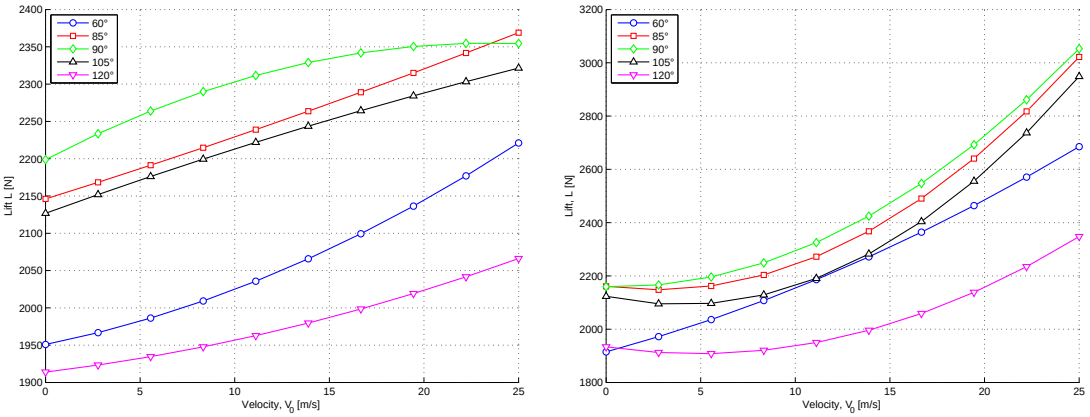

(a) Roll (b) Pitch

Figure D.3: Jetpack lift for various angles of attack at 5500 RPM

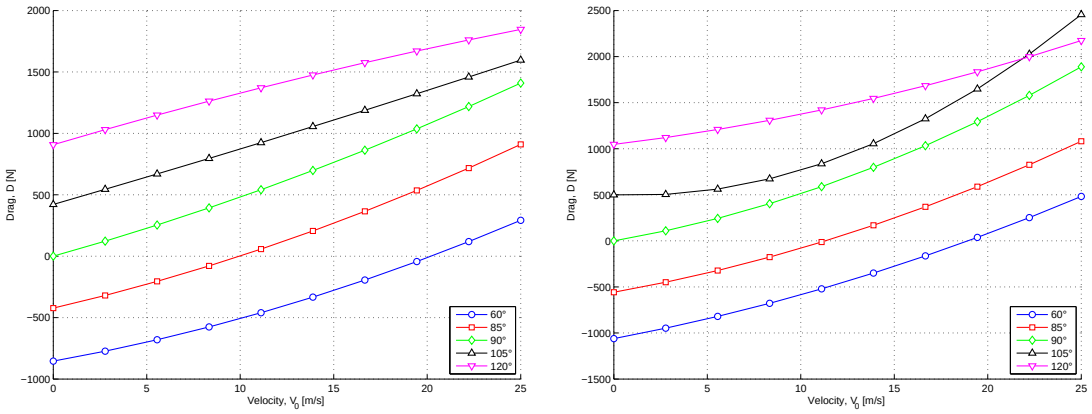

(a) Roll (b) Pitch

Figure D.4: Jetpack drag for various angles of attack at 5500 RPM

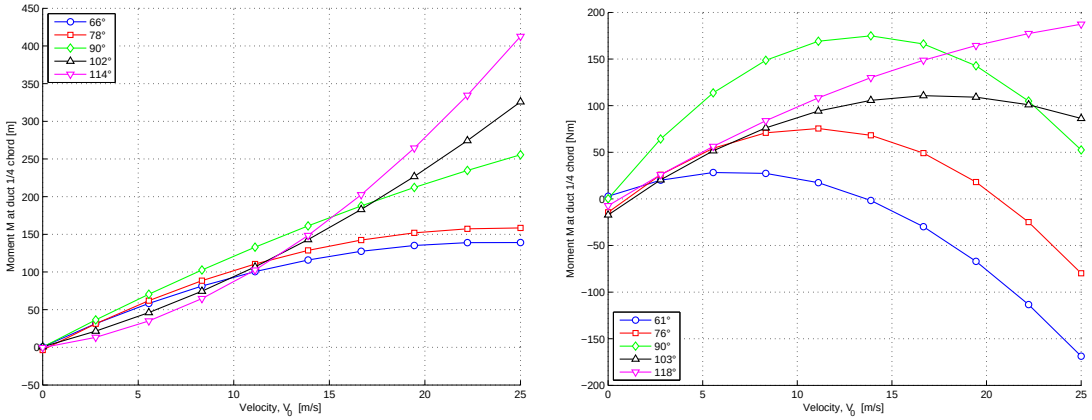

(a) Roll (b) Pitch

Figure D.5: Jetpack moment for various angles of attack at 5500 RPM about the duct quarter chord point

Jetpack Measurements at 5750 RPM

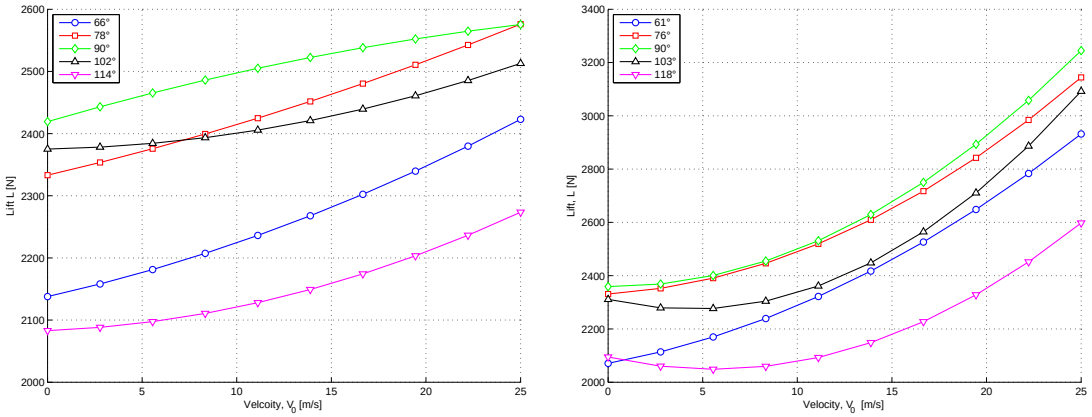

(a) Roll (b) Pitch

Figure D.6: Measured Jetpack lift for various angles of attack at 5750 RPM

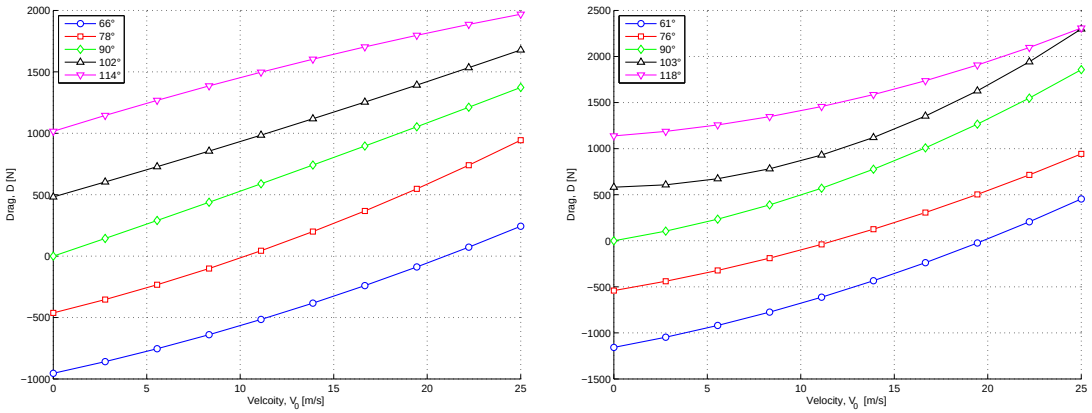

(a) Roll (b) Pitch

Figure D.7: Measured Jetpack drag for various angles of attack at 5750 RPM

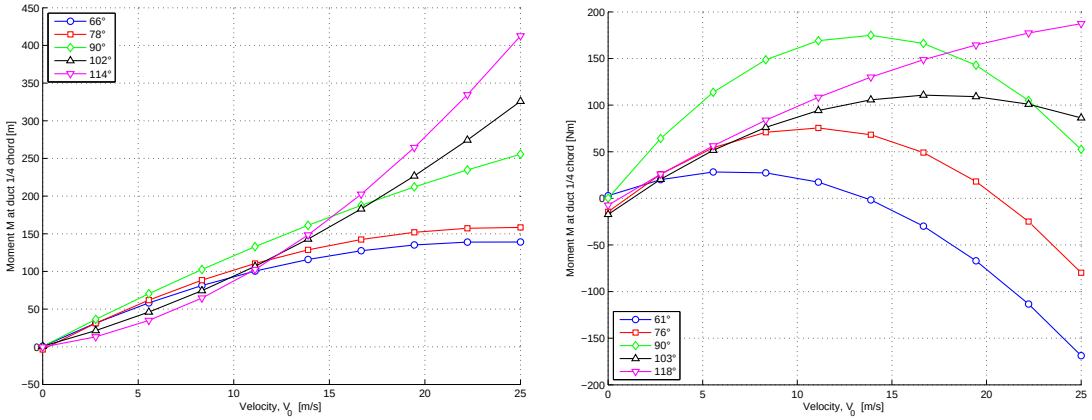

(a) Roll (b) Pitch

Figure D.8: Measured Jetpack moment for various angles of attack at 5750 RPM about the duct quarter chord point

Ducted-Fan Measurements at 5500 RPM

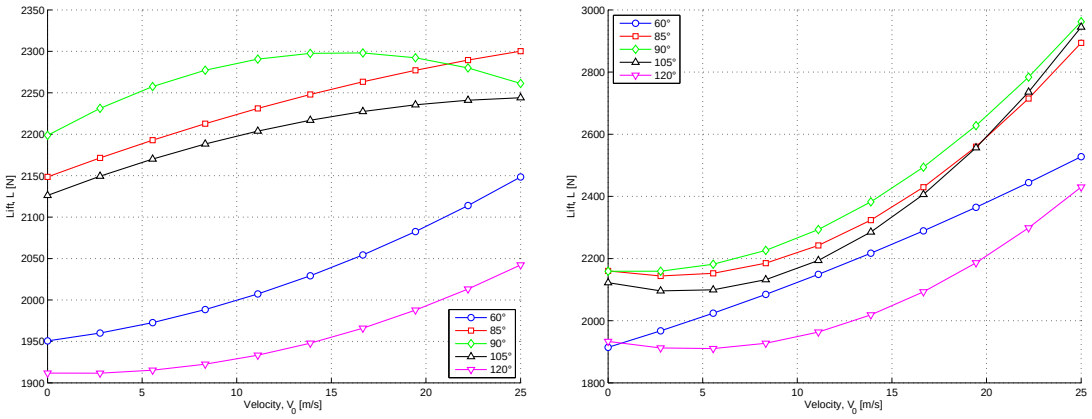

(a) Roll (b) Pitch

Figure D.9: Duct lift for various angles of attack at 5500 RPM

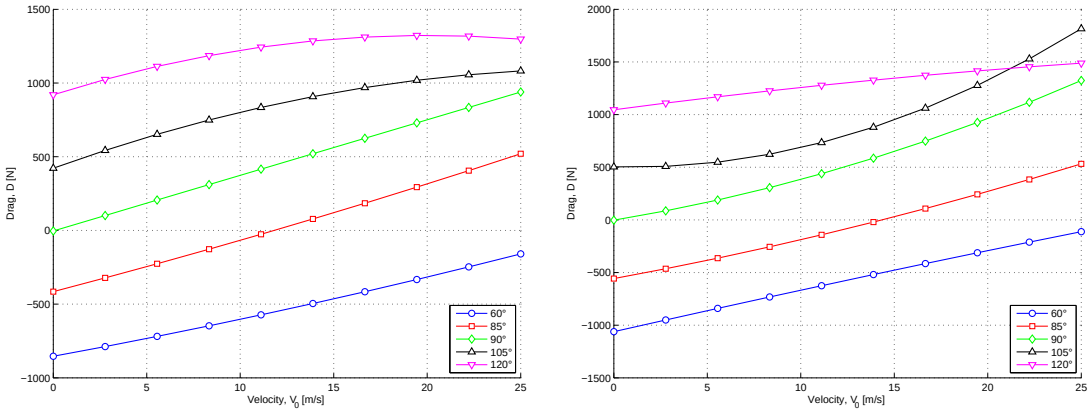

(a) Roll (b) Pitch

Figure D.10: Duct drag for various angles of attack at 5500 RPM

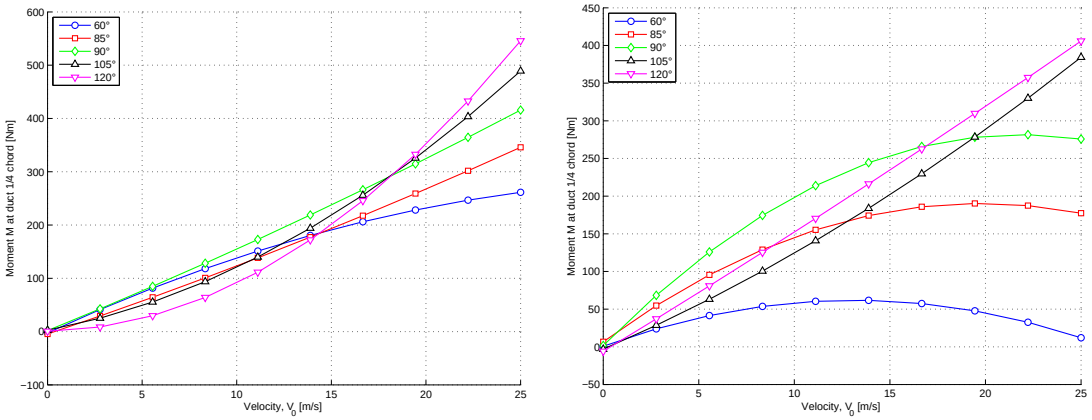

(a) Roll (b) Pitch

Figure D.11: Duct moment for various angles of attack at 5500 RPM about the duct quarter chord point

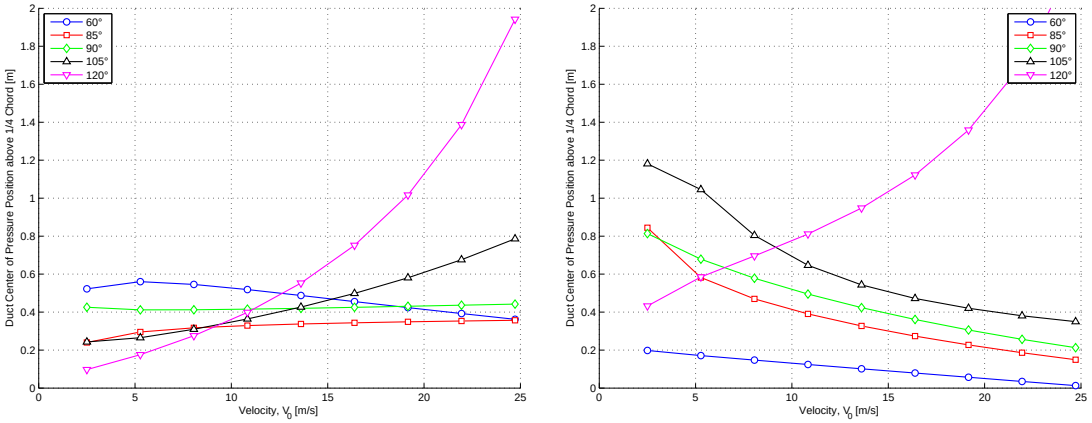

(a) Roll (b) Pitch

Figure D.12: Duct centre of pressure movement from the the duct quarter chord point for various angles of attack at 5500 RPM

Non-Dimensionalised Jetpack Measurements at 0 RPM

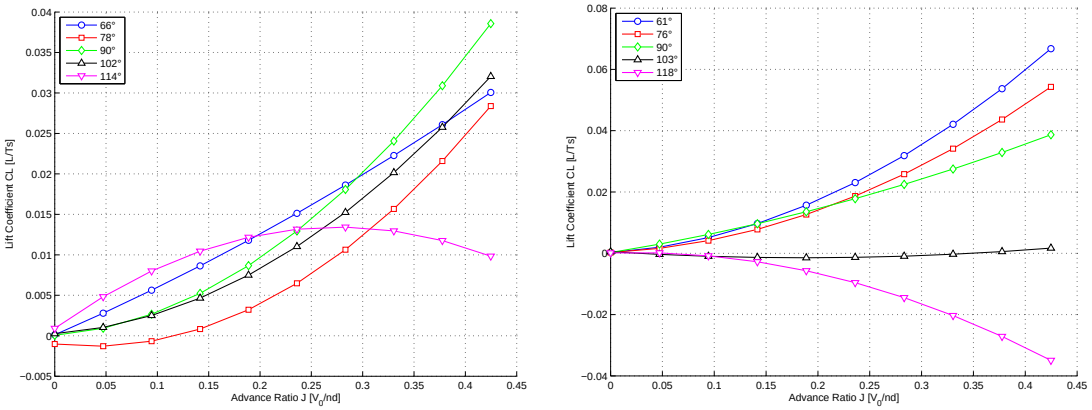

(a) Roll (b) Pitch

Figure D.13: Jetpack lift for various angles of attack at 0 RPM

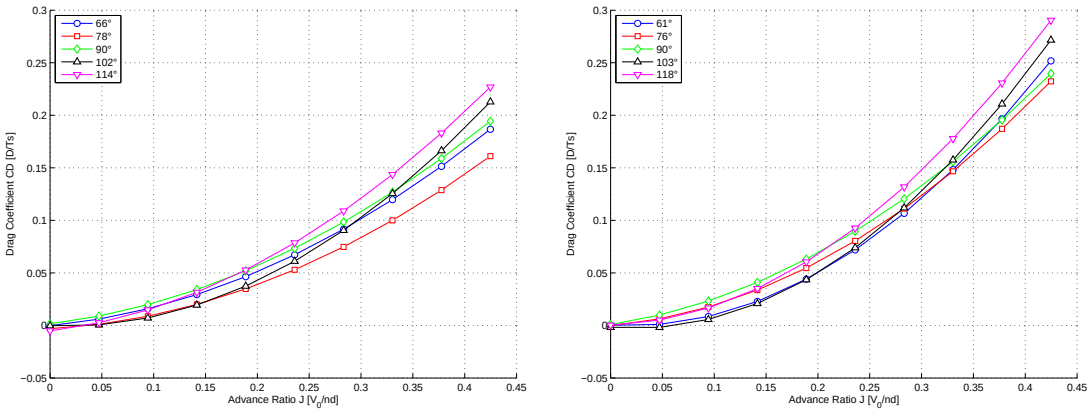

(a) Roll (b) Pitch

Figure D.14: Jetpack drag for various angles of attack at 0 RPM

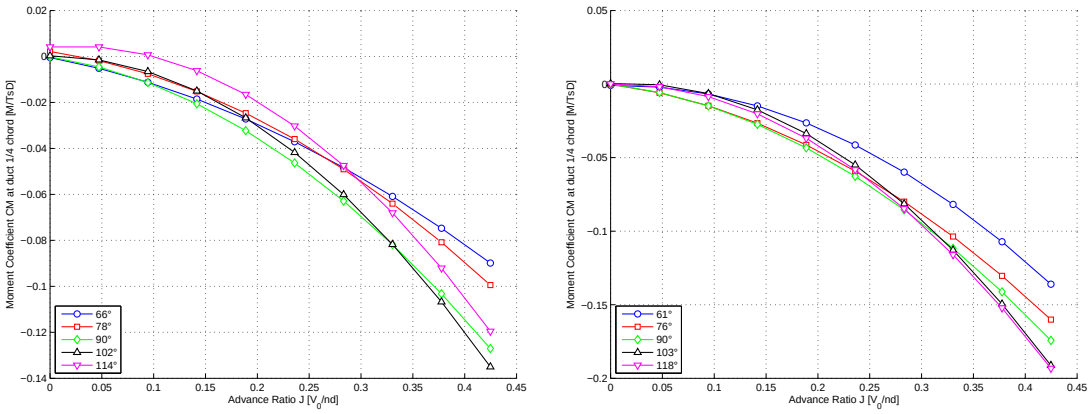

(a) Roll (b) Pitch

Figure D.15: Jetpack moment for various angles of attack at 0 RPM about the duct quarter chord point

Non-Dimensionalised Jetpack Measurements at 5750 RPM

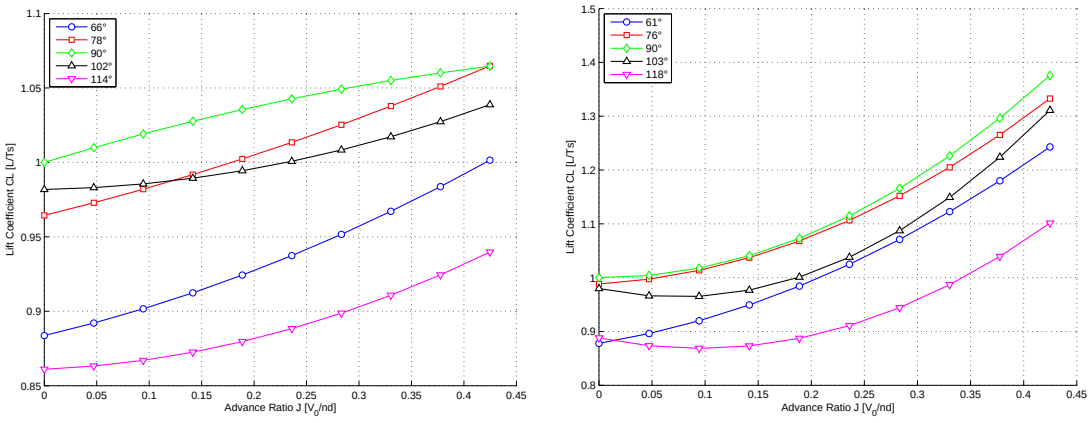

(a) Roll (b) Pitch

Figure D.16: Jetpack lift for various angles of attack at 5750 RPM

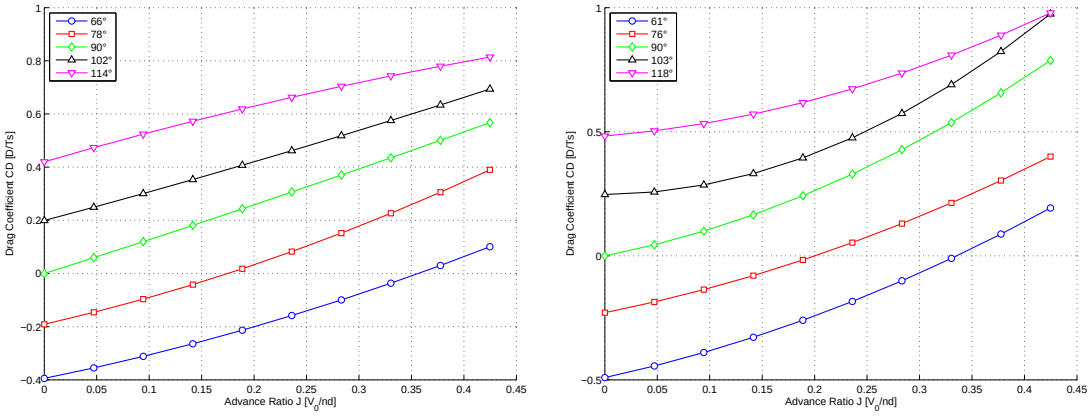

(a) Roll (b) Pitch

Figure D.17: Jetpack drag for various angles of attack at 5750 RPM

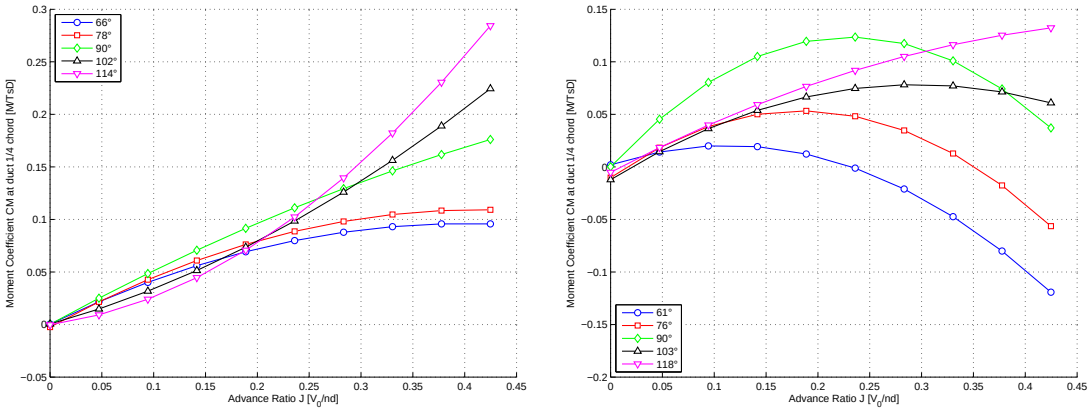

(a) Roll (b) Pitch

Figure D.18: Jetpack moment for various angles of attack at 5750 RPM about the duct quarter chord point

Non-Dimensionalised Ducted-Fan Measurements at 5750 RPM

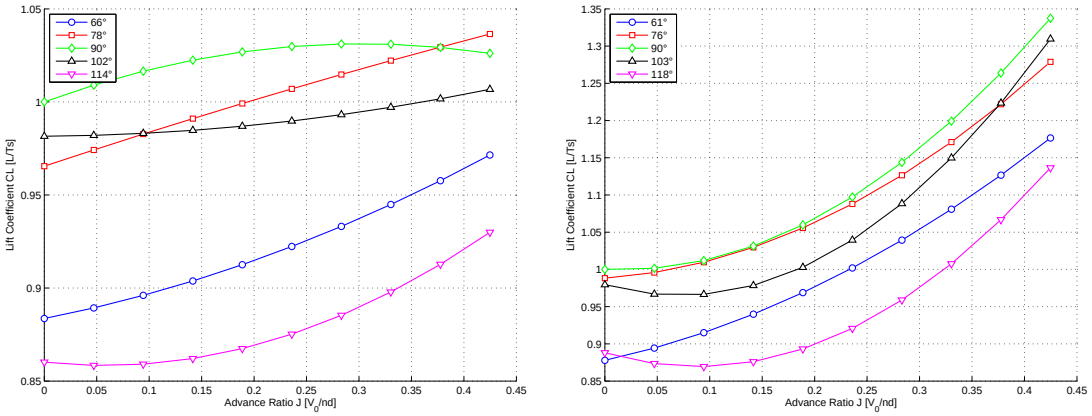

(a) Roll (b) Pitch

Figure D.19: Duct lift for various angles of attack at 5750 RPM

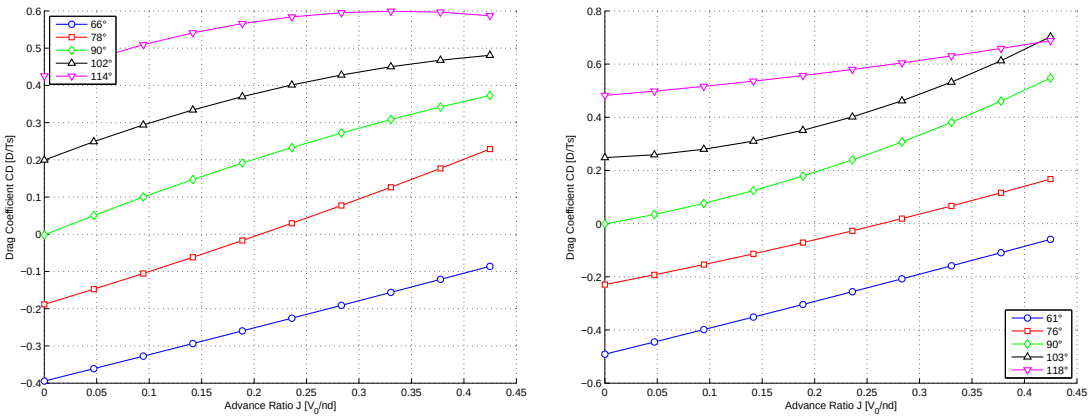

(a) Roll (b) Pitch

Figure D.20: Duct drag for various angles of attack at 5750 RPM

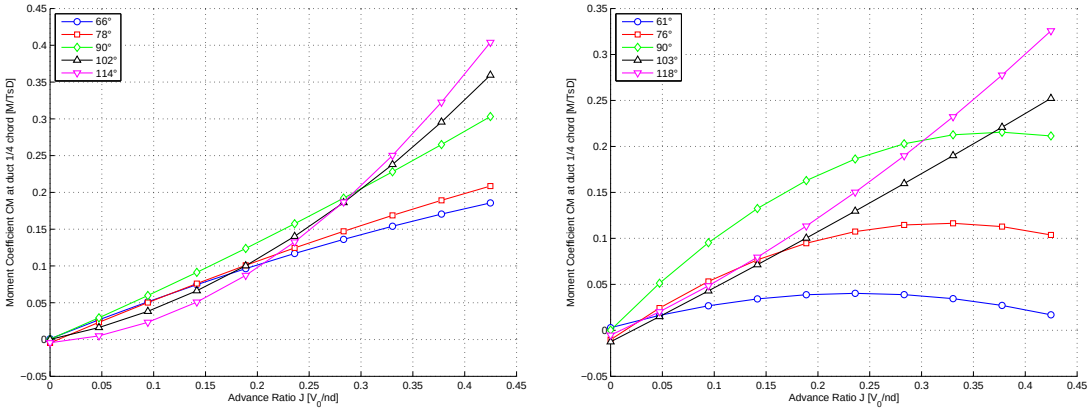

(a) Roll (b) Pitch

Figure D.21: Duct moments for various angles of attack at 5750 RPM about the duct quarter chord point

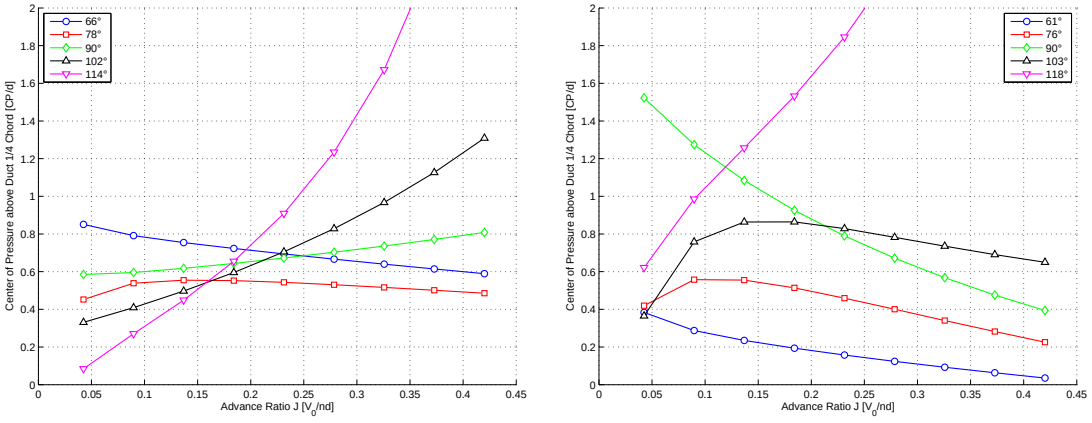

(a) Roll (b) Pitch

Figure D.22: Duct centre of pressure movement from the the duct quarter chord point for various angles of attack at 5750 RPM

D.2 Tow Testing Wool Tuft Pictures

Pitch 60°Angle of Attack

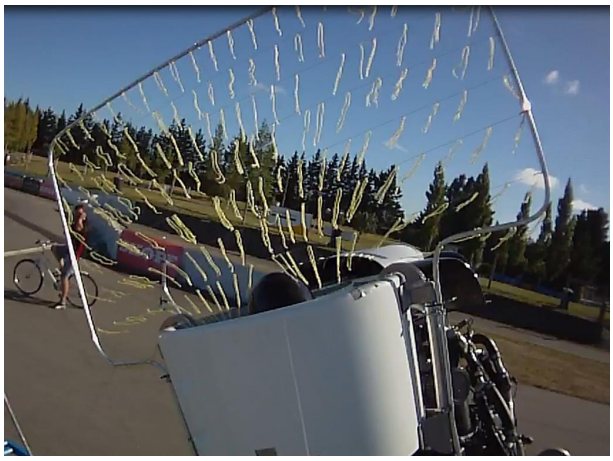

Figure D.23: Tuft rig 60° angle of attack, 0 m/s, engine on

(a) Engine on (b) Engine off

Figure D.24: Tuft rig 60° angle of attack, 6 m/s

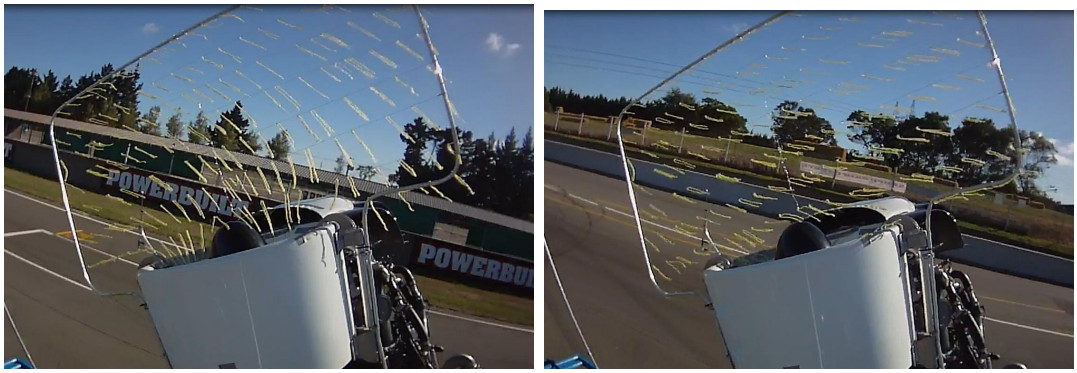

(a) Engine on (b) Engine off

Figure D.25: Tuft rig 60° angle of attack, 11 m/s

(a) Engine on (b) Engine off

Figure D.26: Tuft rig 60° angle of attack, 17 m/s

(a) Engine on (b) Engine off

Figure D.27: Tuft rig 60° angle of attack, 22 m/s

Pitch 75°Angle of Attack

Figure D.28: Tuft rig 75° angle of attack, 0 m/s, engine on

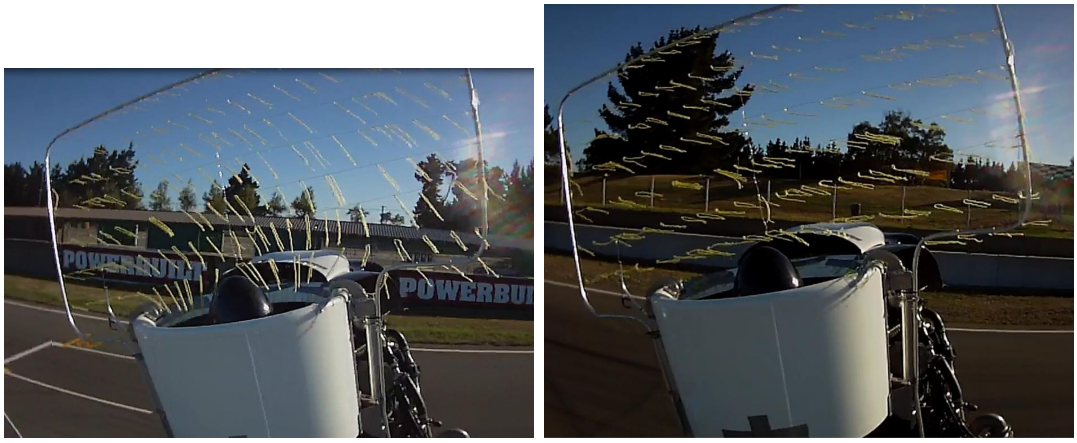

(a) Engine on (b) Engine off

Figure D.29: Tuft rig 75° angle of attack, 6 m/s

(a) Engine on (b) Engine off

Figure D.30: Tuft rig 75° angle of attack, 11 m/s

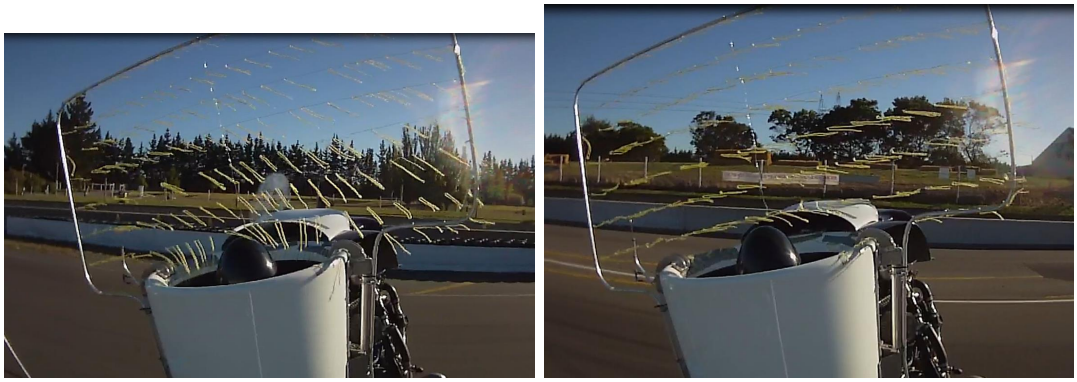

(a) Engine on (b) Engine off

Figure D.31: Tuft rig 75° angle of attack, 17 m/s

(a) Engine on (b) Engine off

Figure D.32: Tuft rig 75° angle of attack, 22 m/s

Pitch 90°Angle of Attack

Figure D.33: Tuft rig 90° angle of attack, 0 m/s, engine on

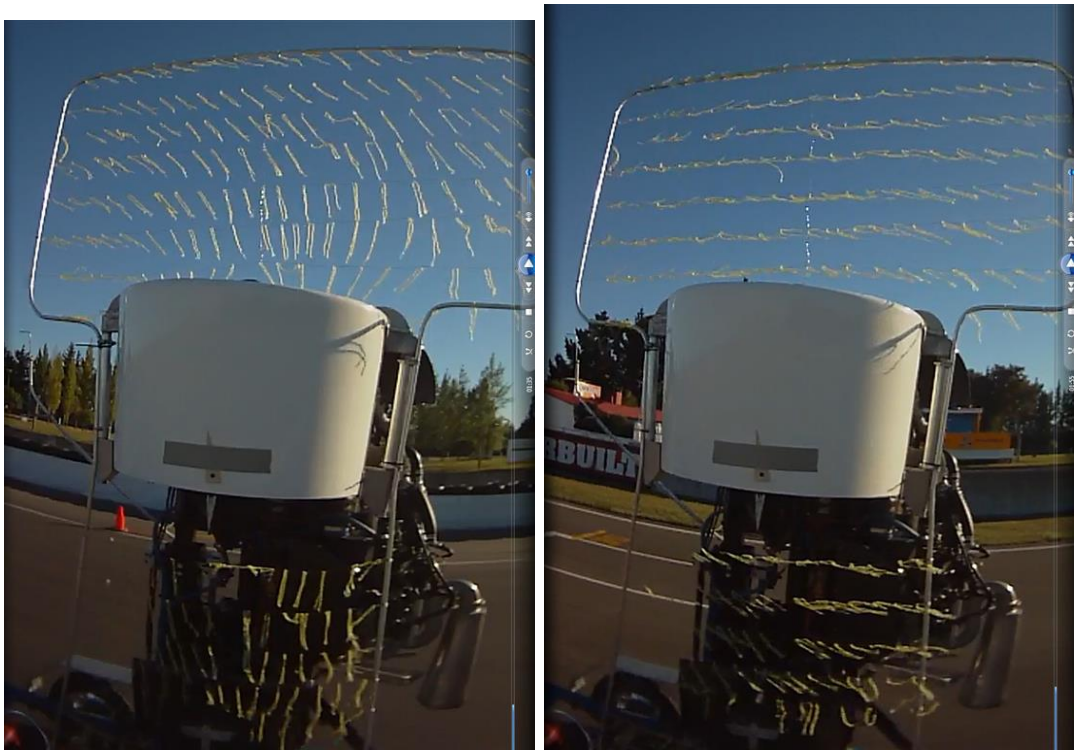

(a) Engine on (b) Engine off

Figure D.34: Tuft rig 90° angle of attack, 6 m/s

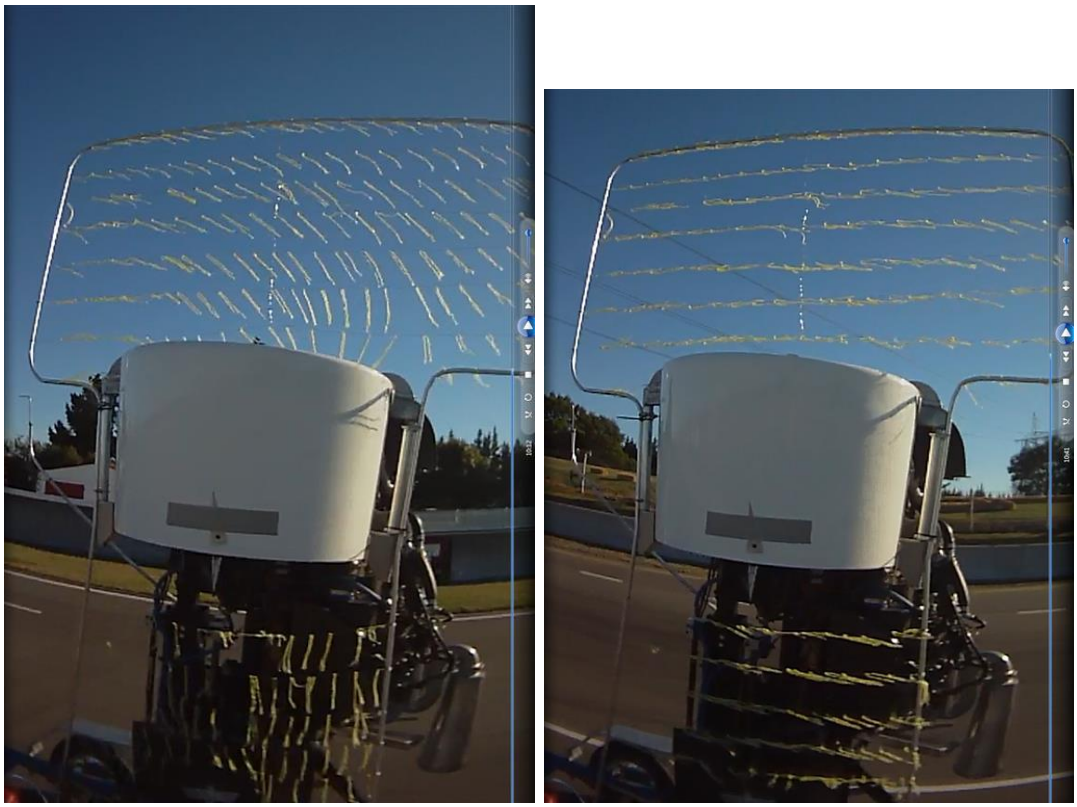

(a) Engine on (b) Engine off

Figure D.35: Tuft rig 90° angle of attack, 11 m/s

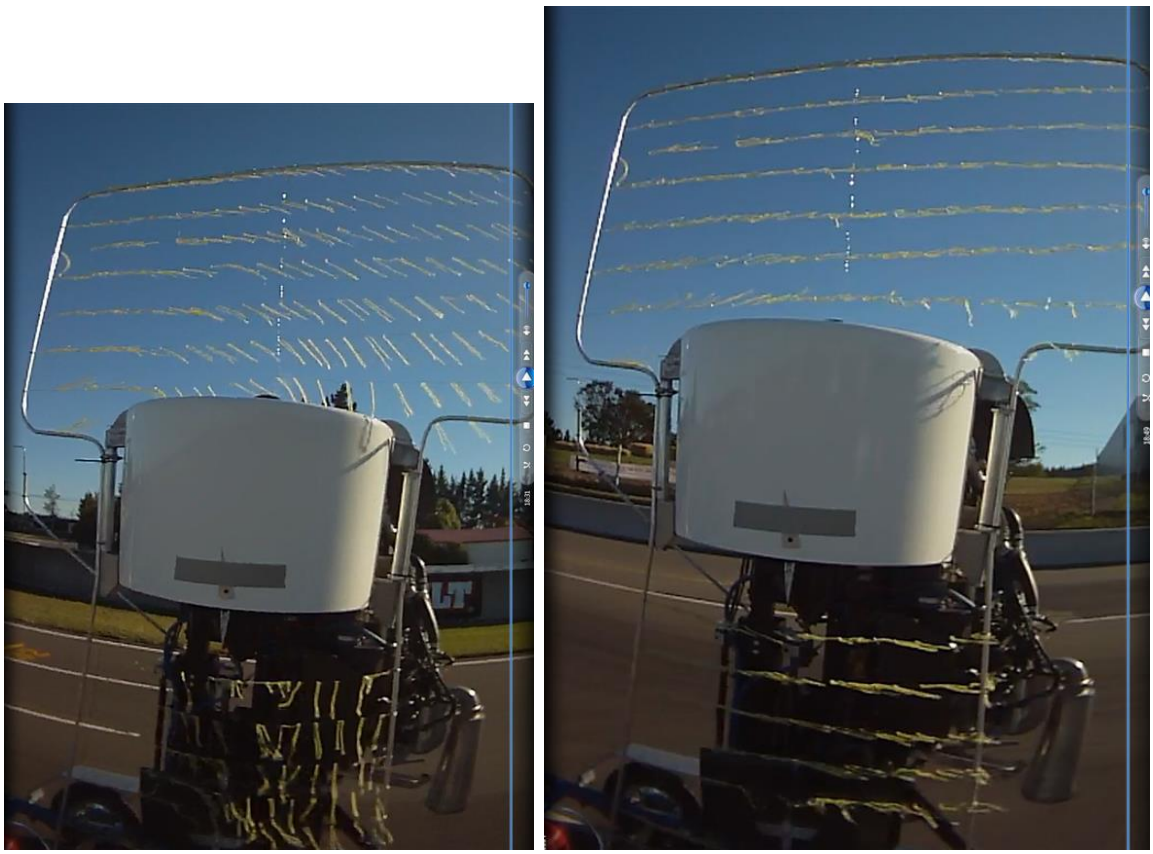

(a) Engine on (b) Engine off

Figure D.36: Tuft rig 90° angle of attack, 17 m/s

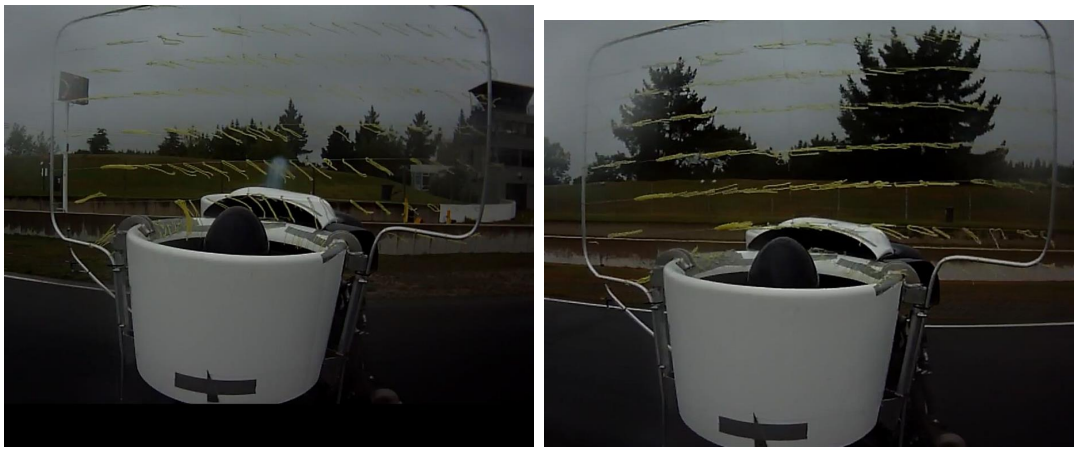

(a) Engine on (b) Engine off

Figure D.37: Tuft rig 90° angle of attack, 22 km/h

Pitch 105° Angle of Attack

Figure D.38: Tuft rig 105° angle of attack, 0 m/s

(a) Engine on

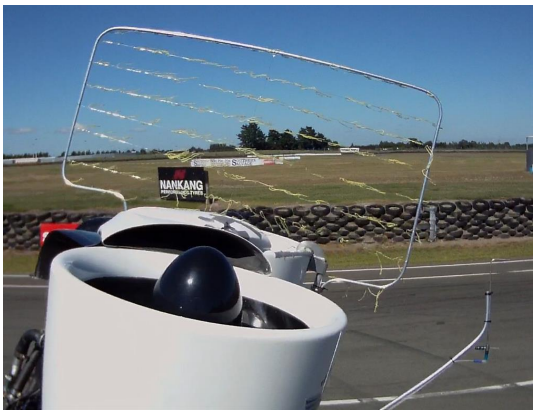

(b) Engine off

Figure D.39: Tuft rig 105° angle of attack, 6 m/s

(a) Engine on

(b) Engine off

Figure D.40: Tuft rig 105° angle of attack, 11 m/s

(a) Engine on (b) Engine off

Figure D.41: Tuft rig 105° angle of attack, 17 m/s

(a) Engine on (b) Engine off

Figure D.42: Tuft rig 105° angle of attack, 22 m/s

Pitch 120º Angle of Attack

Figure D.43: Tuft rig 120° angle of attack, 0 m/s

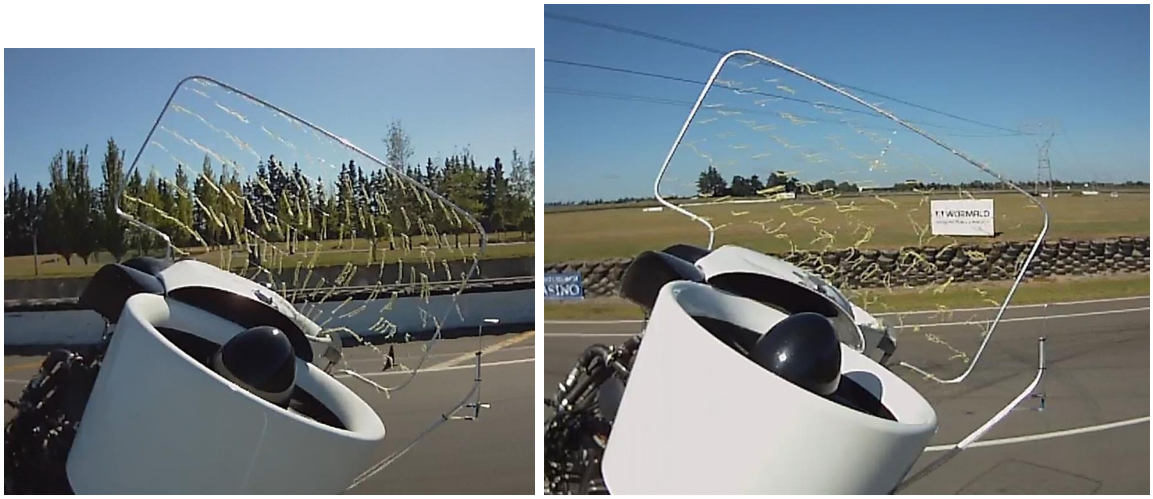

(a) Engine on (b) Engine off

Figure D.44: Tuft rig 120° angle of attack, 6 m/s

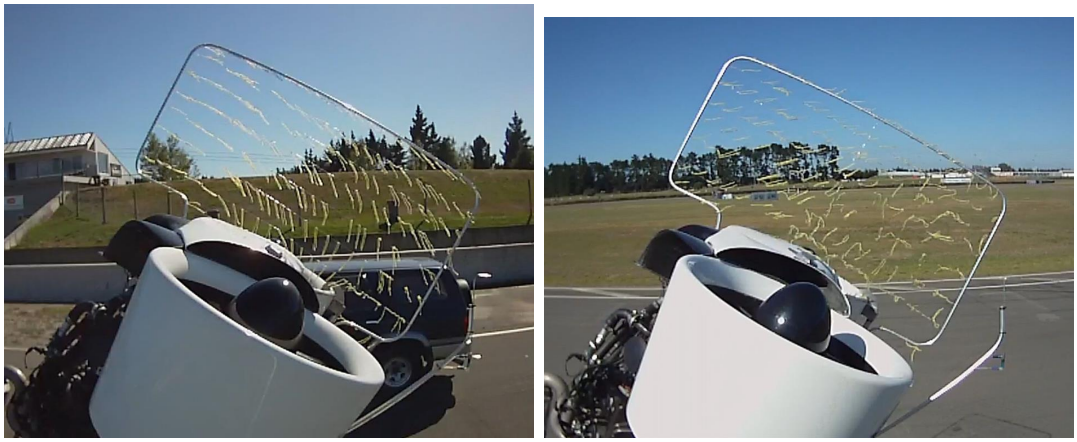

(a) Engine on (b) Engine off

Figure D.45: Tuft rig 120° angle of attack, 11 m/s

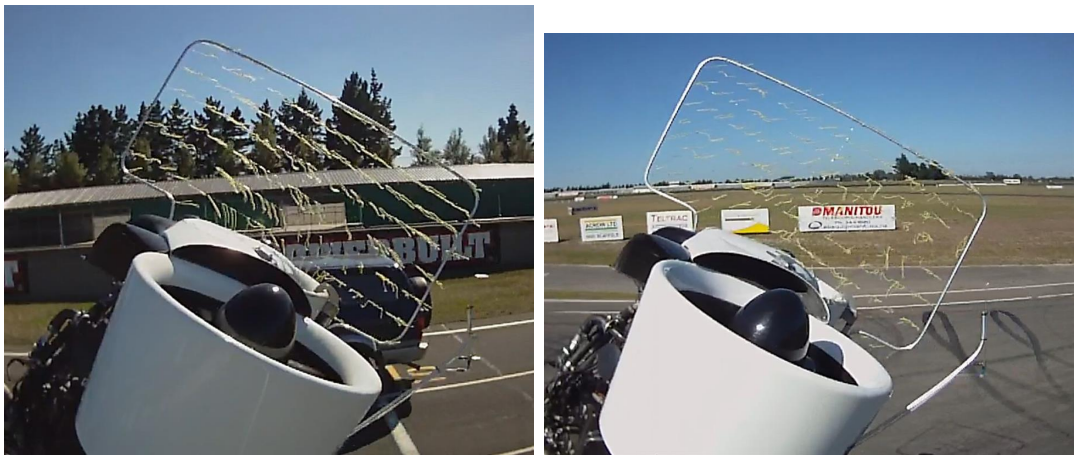

(a) Engine on (b) Engine off

Figure D.46: Tuft rig 120° angle of attack, 17 m/s

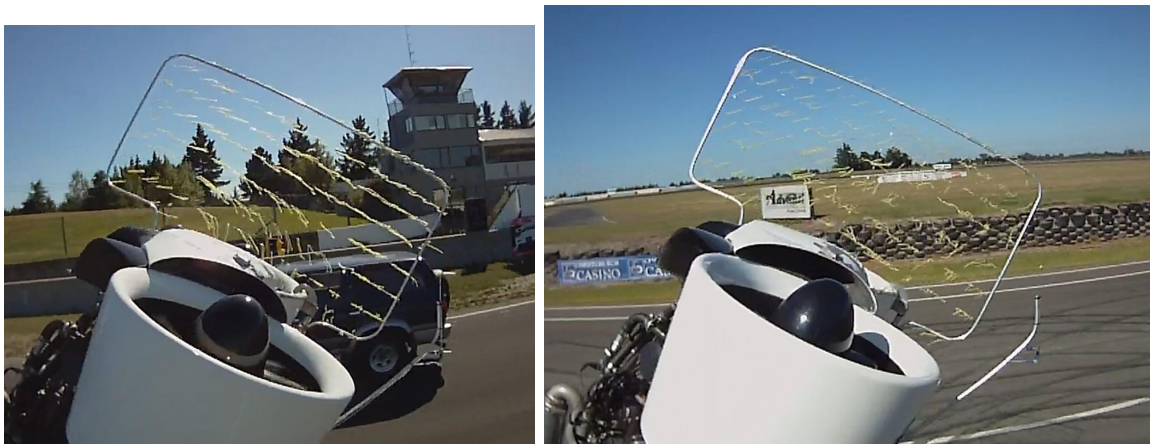

(a) Engine on (b) Engine off

Figure D.47: Tuft rig 120° angle of attack, 22 m/s

Pitch 0º Angle of Attack

Figure D.48: Tuft rig 0° angle of attack, 0 m/s

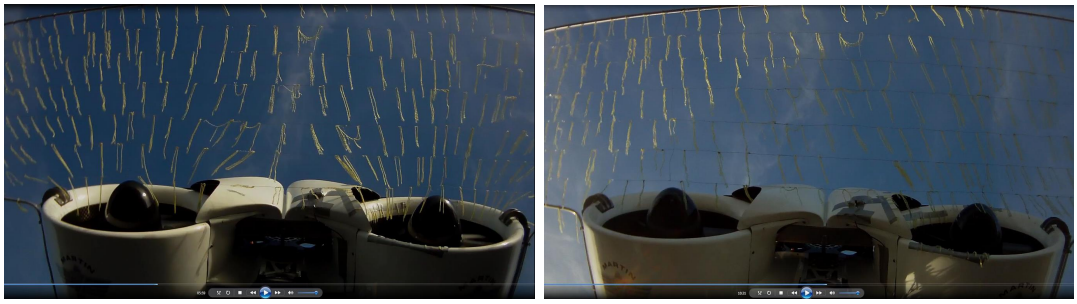

(a) Engine on (b) Engine off

Figure D.49: Tuft rig 0° angle of attack, 6 m/s

(a) Engine on (b) Engine off

Figure D.50: Tuft rig 0° angle of attack, 11 m/s

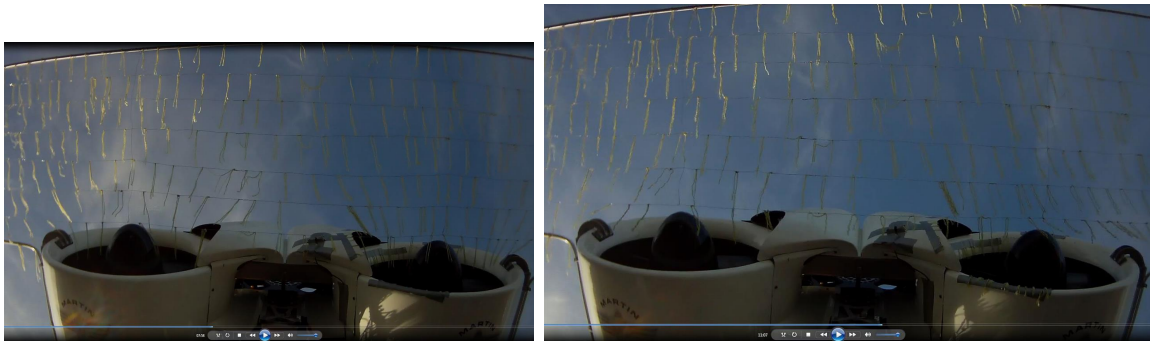

(a) Engine on (b) Engine off

Figure D.51: Tuft rig 0° angle of attack, 17 m/s

(a) Engine on

Figure D.52: Tuft rig 0° angle of attack, 22 m/s

Pitch 180° Angle of Attack

Figure D.53: Tuft rig 180° angle of attack, 0 m/s, engine on

Figure D.54: Tuft rig 180° angle of attack, 6 m/s, engine on

Figure D.55: Tuft rig 180° angle of attack, 8 m/s, engine on

Figure D.56: Tuft rig 180° angle of attack, 11 m/s, engine on

Figure D.57: Tuft rig 180° angle of attack, 17 m/s, engine on

Roll 60°Angle of Attack

Figure D.58: Tuft rig 60° angle of attack, 0 m/s, engine on

(a) Engine on

(b) Engine off

Figure D.59: Tuft rig 60° angle of attack, 6 m/s

(a) Engine on

(b) Engine off

Figure D.60: Tuft rig 60° angle of attack, 11 m/s

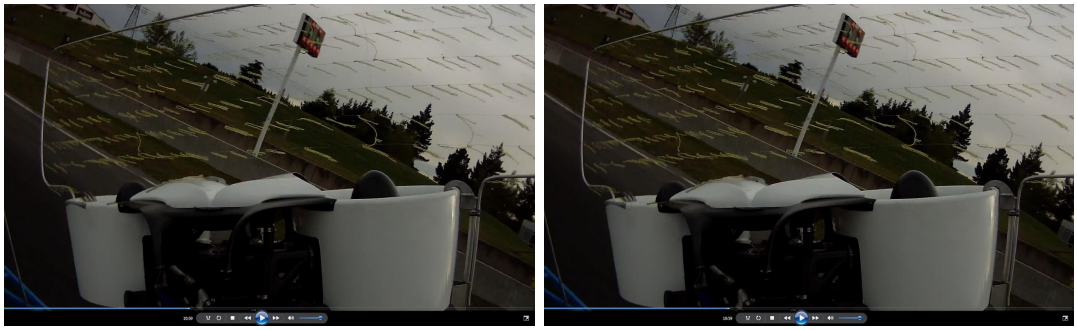

(a) Engine on (b) Engine off

Figure D.61: Tuft rig 60° angle of attack, 17 m/s

(a) Engine on (b) Engine off

Figure D.62: Tuft rig 60° angle of attack, 22 m/s

Roll 105° Angle of Attack

Figure D.63: Tuft rig 105° angle of attack, 0 m/s, engine on

(a) Engine on (b) Engine off

Figure D.64: Tuft rig 105° angle of attack, 6 m/s

(a) Engine on (b) Engine off

Figure D.65: Tuft rig 105° angle of attack, 11 m/s

(a) Engine on (b) Engine off

Figure D.66: Tuft rig 105° angle of attack, 17 m/s

(a) Engine on (b) Engine off

Figure D.67: Tuft rig 105° angle of attack, 22 m/s

Roll 120º Angle of Attack

Figure D.68: Tuft rig 120° angle of attack, 0 m/s, engine on

Figure D.69: Tuft rig 120° angle of attack, 6 m/s, engine on

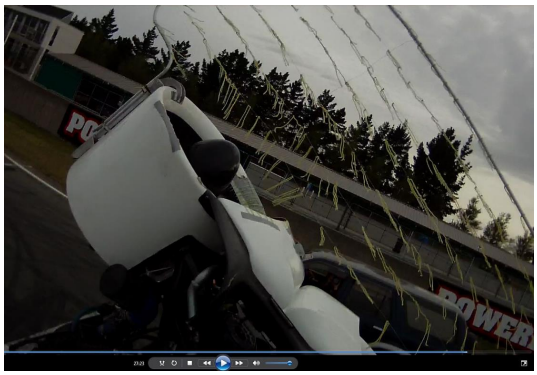

Figure D.70: Tuft rig 120° angle of attack, 11 m/s, engine on

Figure D.71: Tuft rig 120° angle of attack, 17 m/s, engine on

D.3 600 mm Duct Static Thrust Measurements

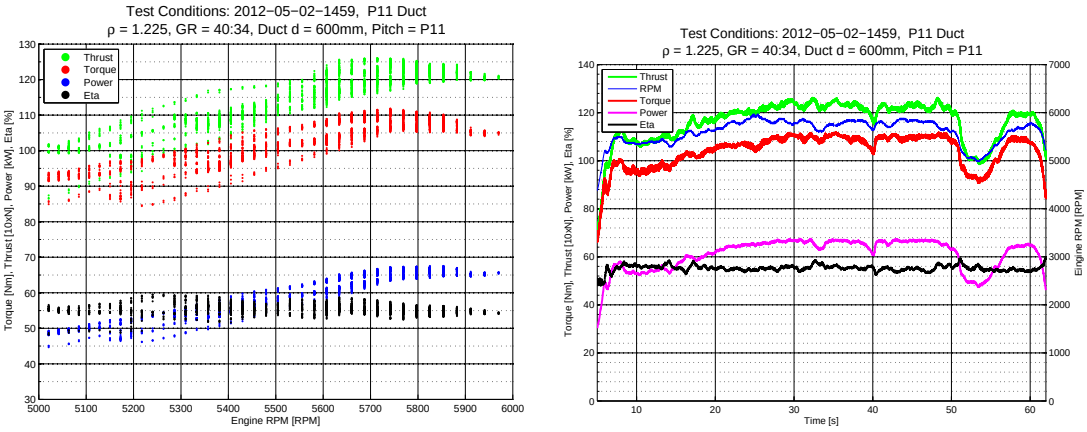

(a) Performance versus engine speed

(b) Performance versus time

Figure D.72: Static performance of the P-11 600 mm ducted-fan

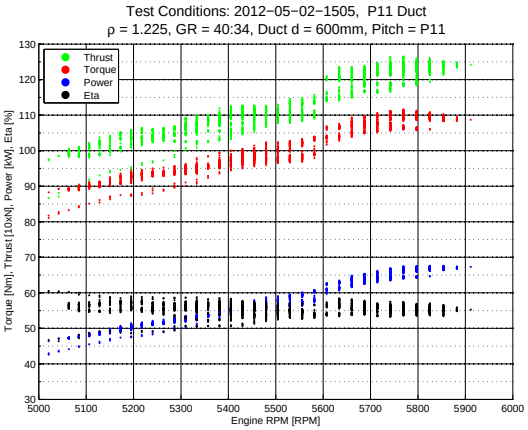

(a) Performance versus engine speed

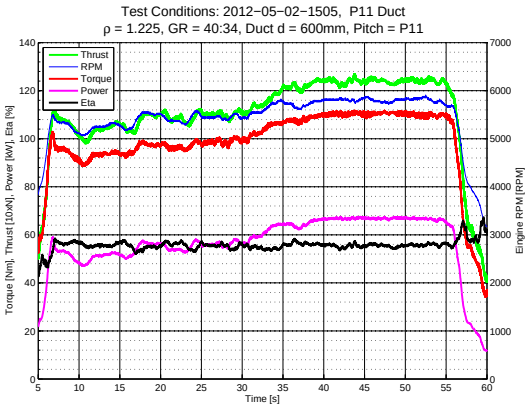

(b) Performance versus time

Figure D.73: Static performance of the P-11 600 mm ducted-fan

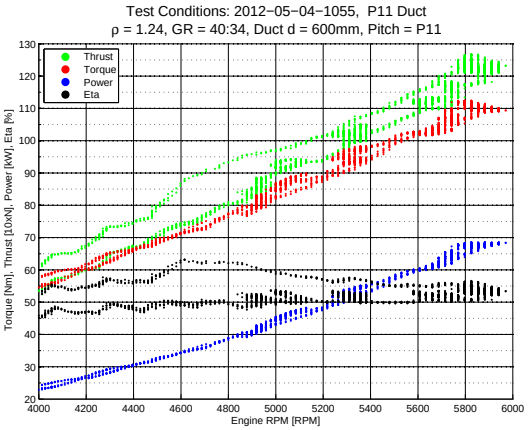

(a) Performance versus engine speed

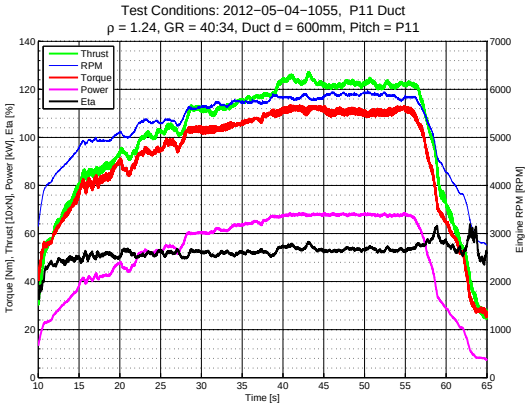

(b) Performance versus time

Figure D.74: Static performance of the P-11 600 mm ducted-fan

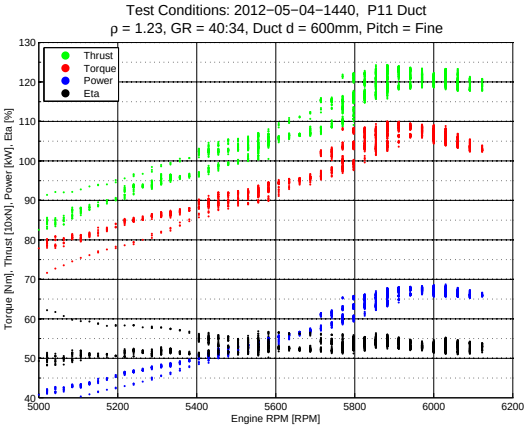

(a) Performance versus engine speed

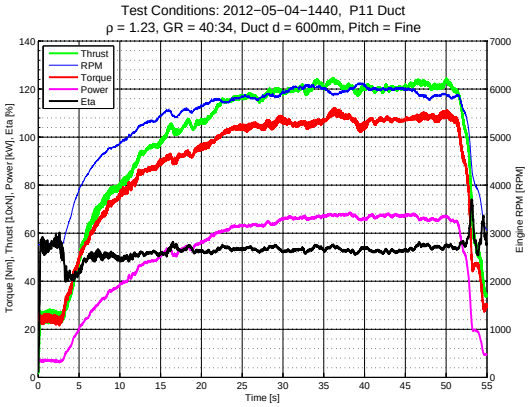

(b) Performance versus time

Figure D.75: Static performance of the P-11 600 mm ducted-fan

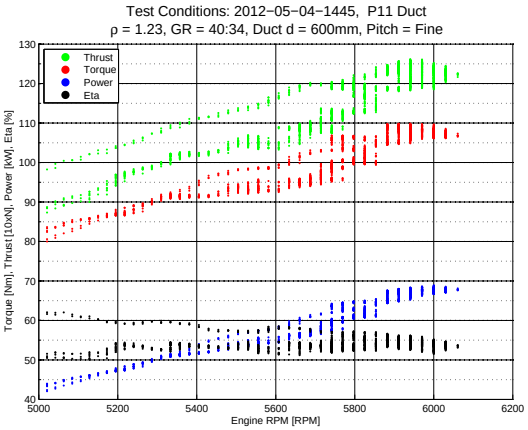

(a) Performance versus engine speed

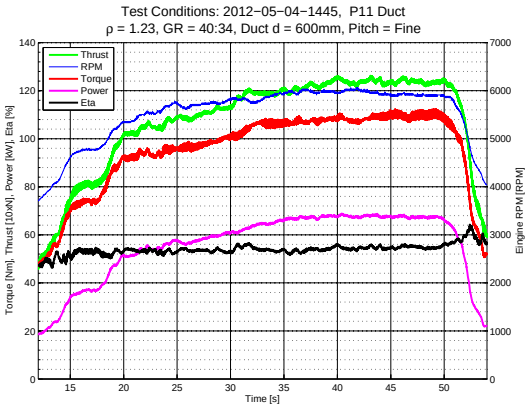

(b) Performance versus time

Figure D.76: Static performance of the P-11 600 mm ducted-fan

D.4 800 mm Duct Static Thrust Measurements

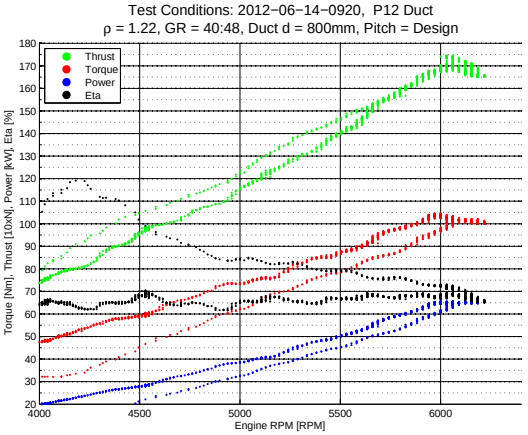

(a) Performance versus engine speed

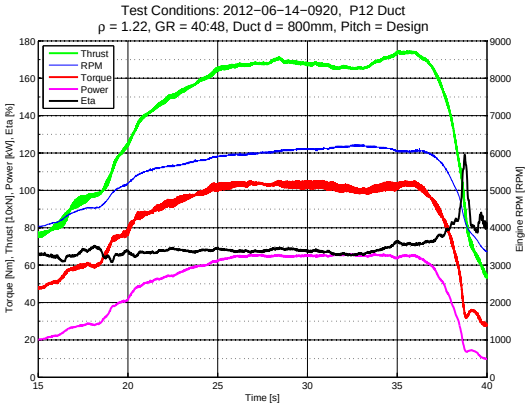

(b) Performance versus time

Figure D.77: Static performance of the P-12 800 mm ducted-fan

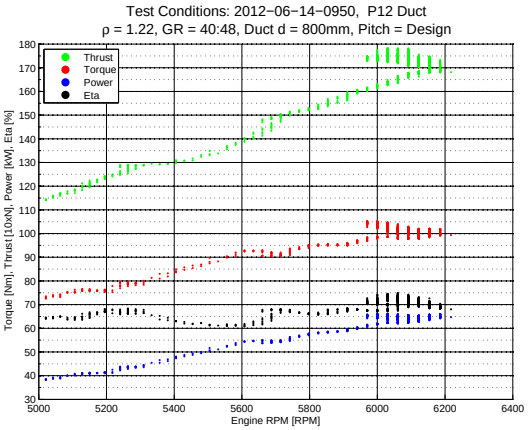

(a) Performance versus engine speed

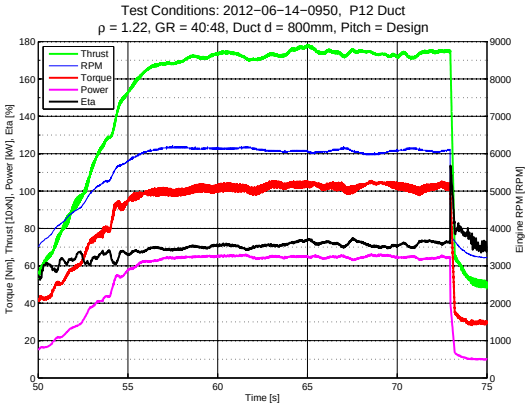

(b) Performance versus time

Figure D.78: Static performance of the P-12 800 mm ducted-fan

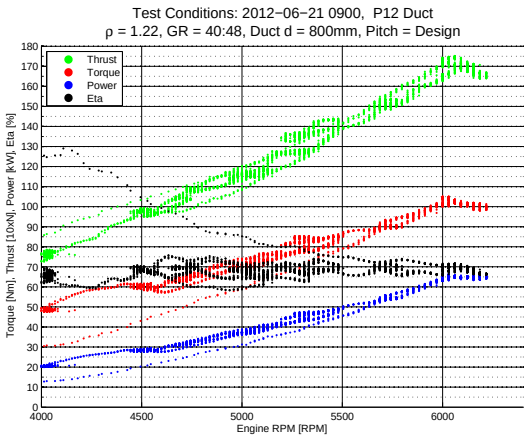

(a) Performance versus engine speed

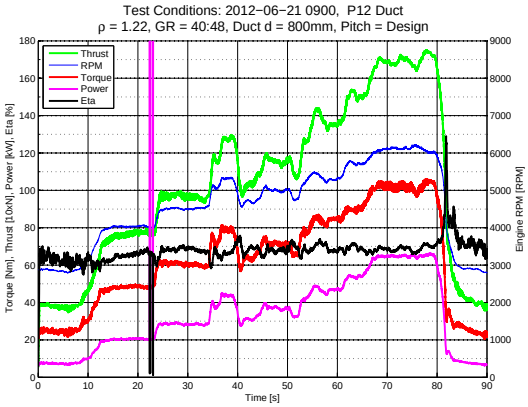

(b) Performance versus time

Figure D.79: Static performance of the P-12 800 mm ducted-fan

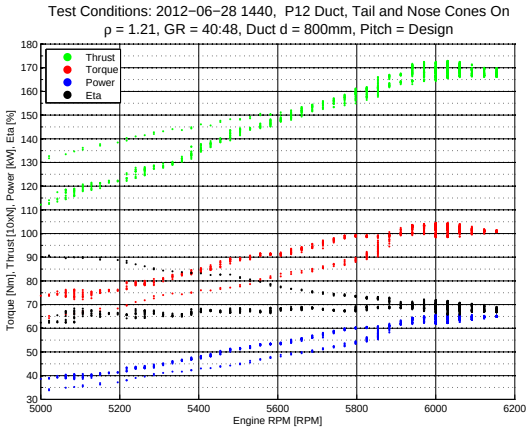

(a) Performance versus engine speed

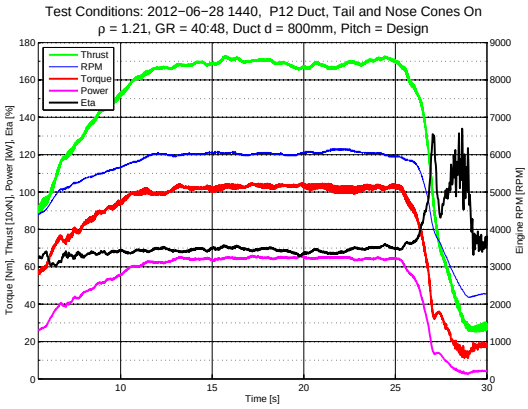

(b) Performance versus time

Figure D.80: Static performance of the P-12 800 mm ducted-fan

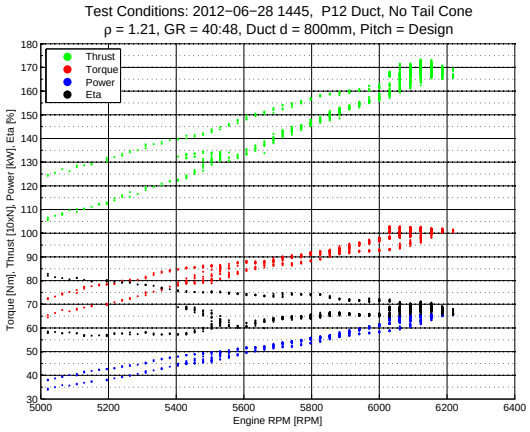

(a) Performance versus engine speed

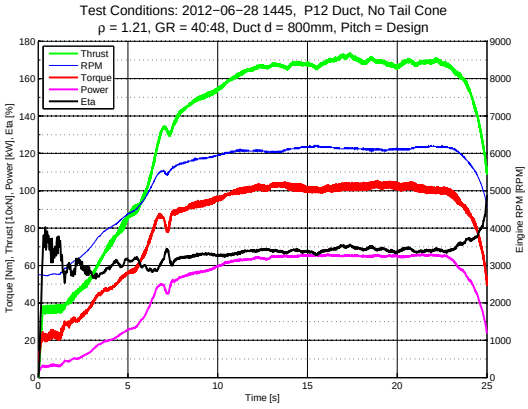

(b) Performance versus time

Figure D.81: Static performance of the P-12 800 mm ducted-fan with nose cone but no tail cone

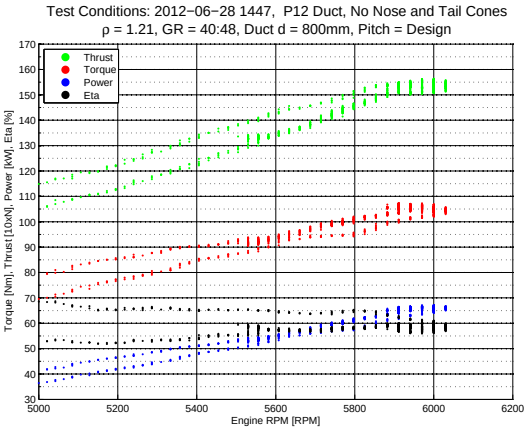

(a) Performance versus engine speed

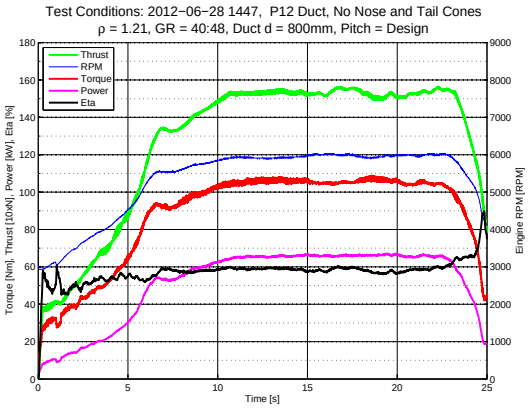

(b) Performance versus time

Figure D.82: Static performance of the P-12 800 mm ducted-fan, with no nose and tail cones

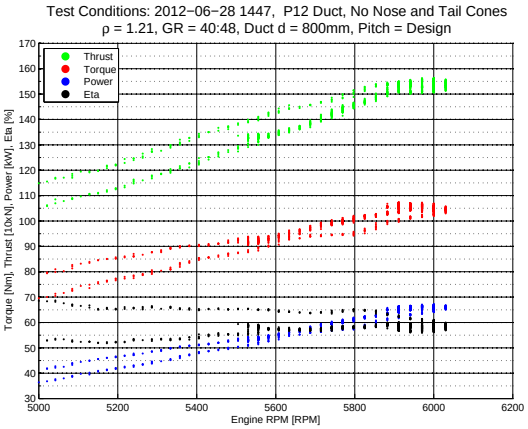

(a) Performance versus engine speed

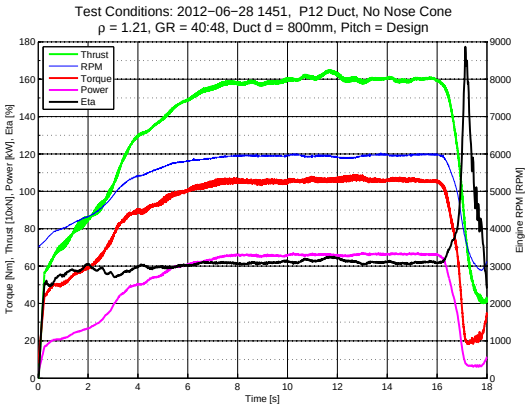

(b) Performance versus time

Figure D.83: Static performance of the P-12 800 mm ducted-fan, with tail cone but no nose cone

Appendix E

Additional Items

E.1 P-11E Performance Charts

Figures E.1 to E.4 describe the trim performance of the P-11E Jetpack, which is the pinnacle of the P-11 series prototypes.

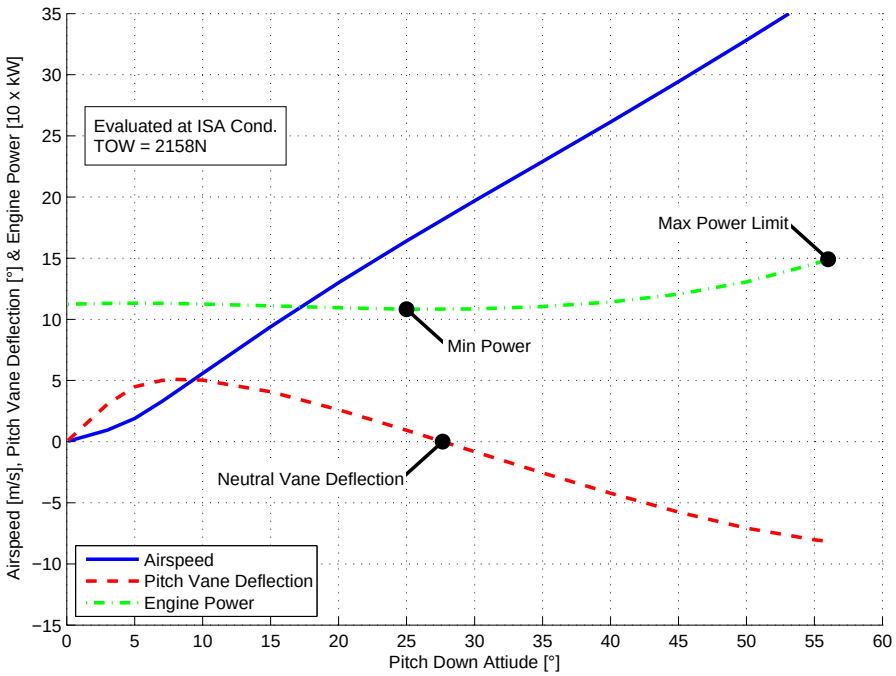

Figure E.1: Longitudinal performance versus pitch down/forward attitude for the Martin Jetpack P-11E

E.2 P-12 Performance Charts

This section presents the trimmed performance charts produced by the flight model, described in Chapter 4, for the P-12 Jetpack. The theoretical variable centre of pressure model, (section 3.2) has been used to model the ducted-fan reactions. The methodology used to find the trim points to developed the performance charts is that described in Chapter 7.

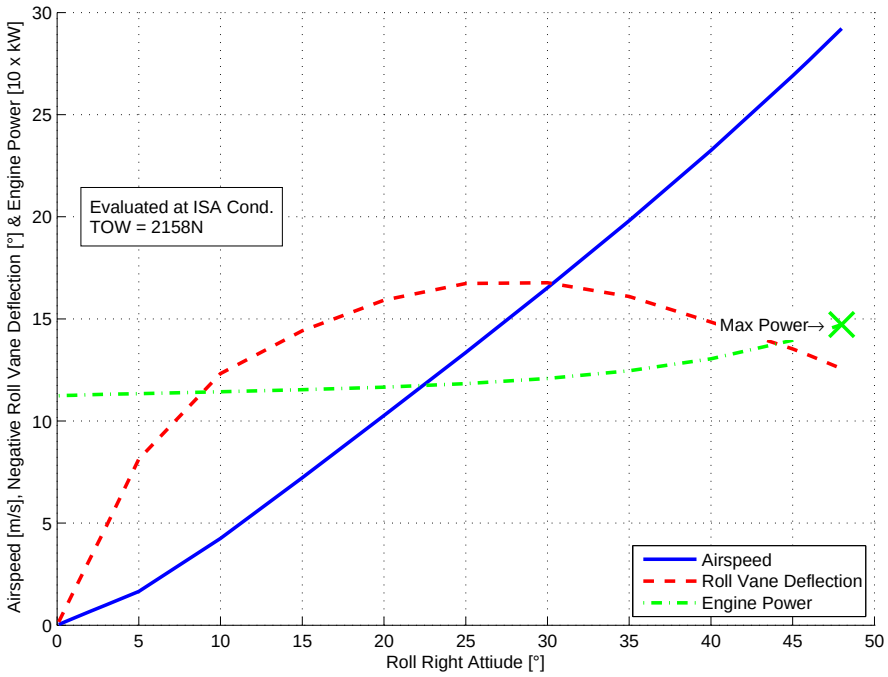

Figure E.2: Lateral performance versus roll right attitude for the Martin Jetpack P-11E

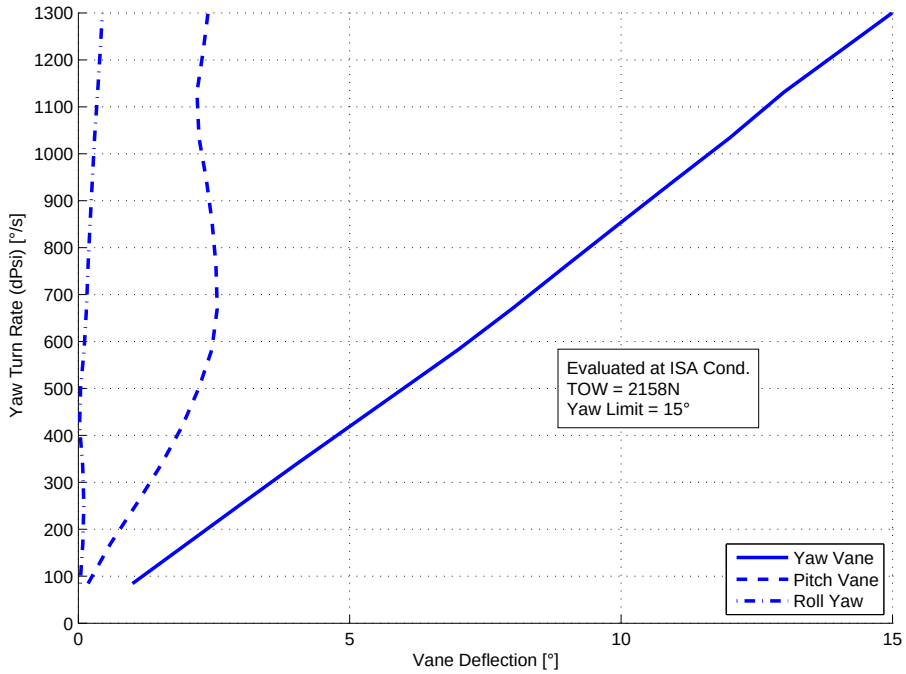

Figure E.3: Hover yaw turn performance versus yaw vane deflection for the Martin Jetpack P-11E

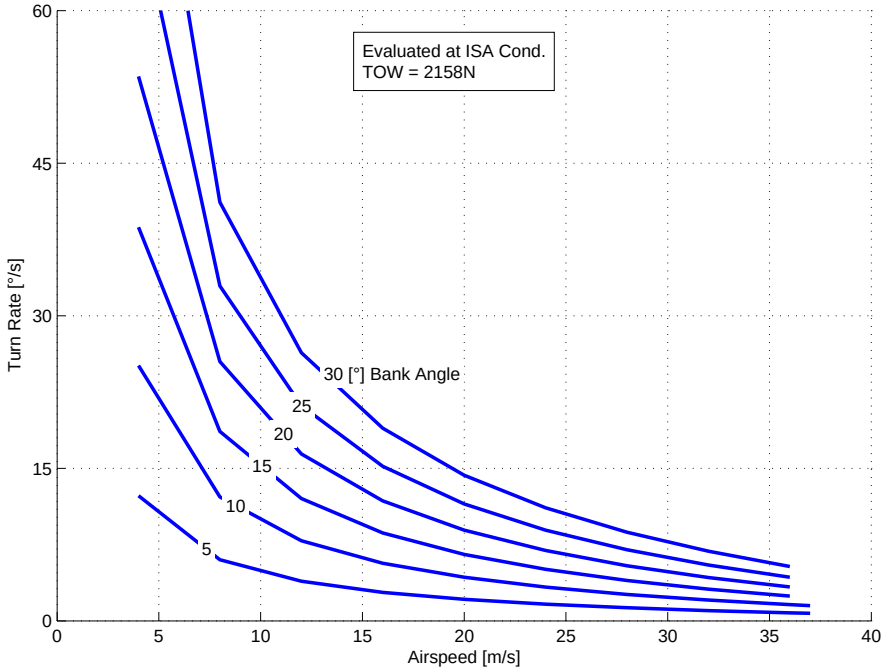

(a) Turn rate versus airspeed

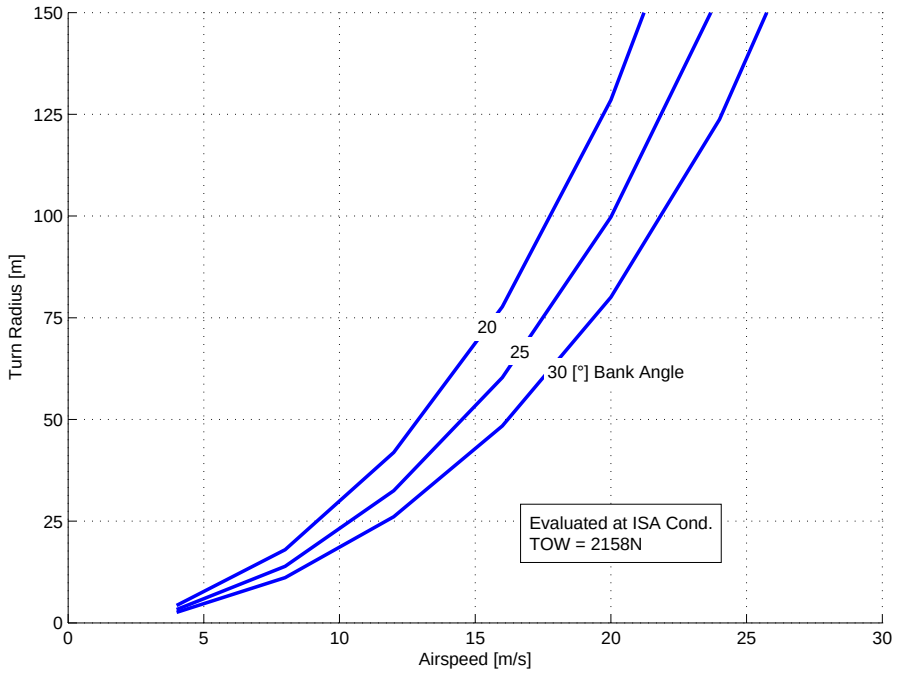

(b) Turn radius versus airspeed

Figure E.4: Level bank turn performance for the Martin Jetpack P-11E

Hover Ceiling Versus TOW

Figure E.5 shows the hover ceiling versus takeoff weight for the P-12 Jetpack. The Figure shows that increasing the thrust margin decreases the hover ceiling, and increasing the takeoff weight decreases the hover ceiling and vice versa. This result is expected as the decreasing air density with altitude has the double effect of decreasing engine power and ducted-fan aerodynamic performance.

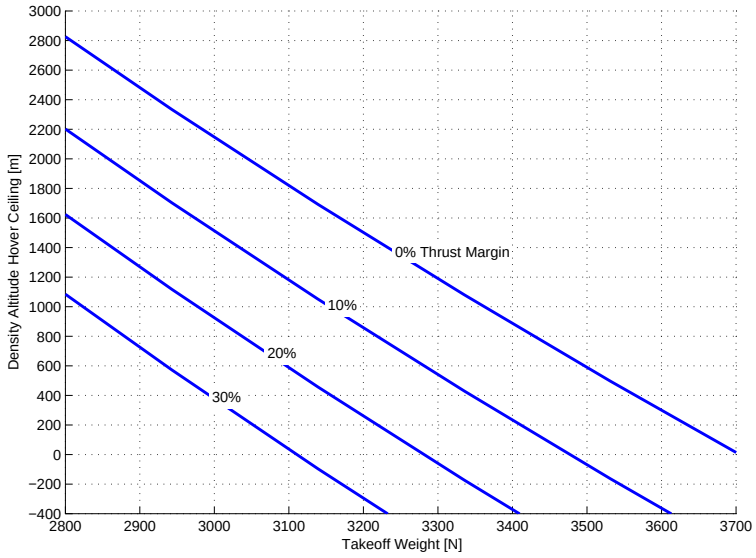

Figure E.5: P-12 Jetpack hover ceiling versus takeoff weight for various thrust margins

Climb Rate

Similarly, the hover ceiling versus takeoff weight the climb rate performance, shown on Figure E.6, deceases with altitude and takeoff weight. At the maximum takeoff weight of 3140 N the model predicts that P-12 should have a sea level climb rate of 8 m/s (1600 ft/min), which is comparable to a light general aviation aircraft.

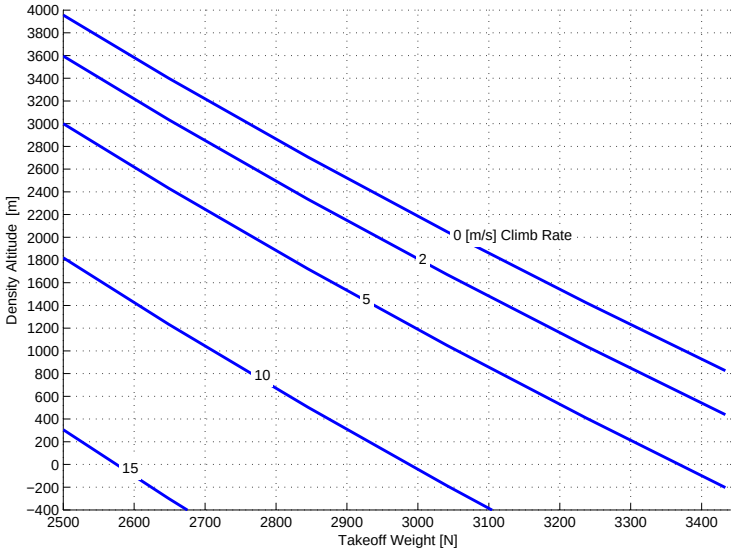

Figure E.6: P-12 Jetpack vertical climb performance versus takeoff weight

Longitudinal Performance

The level flight longitudinal performance of the P-12 Jetpack is shown on Figure E.7, and shows a similar trend to that of the P-11C Jetpack (Figure 7.4). Figure E.7 shows that the level performance of the P-12 Jetpack is limited by pitch vane saturation, which is unfavourable compared to being limited by engine power. The model shows that the maximum level flight speed of the P-12 Jetpack is 27 m/s. A minimum engine power occurs at an attitude of 30°. At this attitude/speed the P-12 Jetpack will have its best endurance (flight time), best cruise efficiency (zero-wind), and best rate of climb. The reduced power occurs as a result of the translational aerodynamic lift forces contributing to the overall lift force. Table E.1 summaries the key longitudinal performance conditions of maximum speed and minimum power.

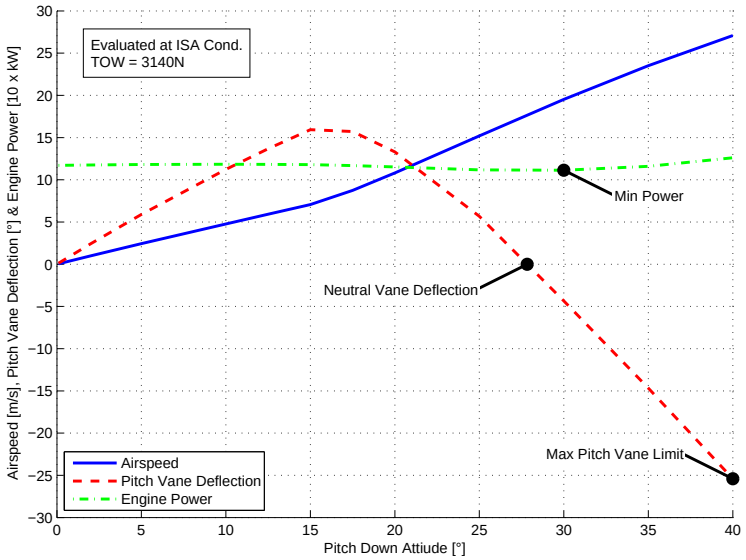

Figure E.7: Longitudinal performance versus pitch down/forward attitude for the Martin Jetpack P-12

Table E.1: Longitudinal Performance Summary for the P-12 Jetpack

Condition	Attitude	Speed	Limitation
Maximum Speed	40°	27 m/s	Pitch limit
Minimum Power	30°	19.5 m/s	-
Neutral Vane Position	28	17.5 m/s	-

Lateral Performance

The lateral level flight performance of the P-12 Jetpack is shown on Figure E.8. The Figure shows that the maximum lateral speed of the Jetpack is 14 m/s and occurs at an attitude of 29°. The maximum roll vane deflection is the limiting constraint on the lateral velocity. The large negative roll vane deflection indicates the centre of pressure in lateral flight is above the centre of gravity. Hence, to improve the lateral speed increasing the centre of gravity position with respect to the ducted-fans needs to be done. However, this is detrimental to longitudinal performance.

The minimum engine power in lateral flight occurs at hover and progressively increases with roll attitude. This result reinforces that the Jetpack with the ducted-fans in a twin arrangement is more efficient than a tandem arrangement.

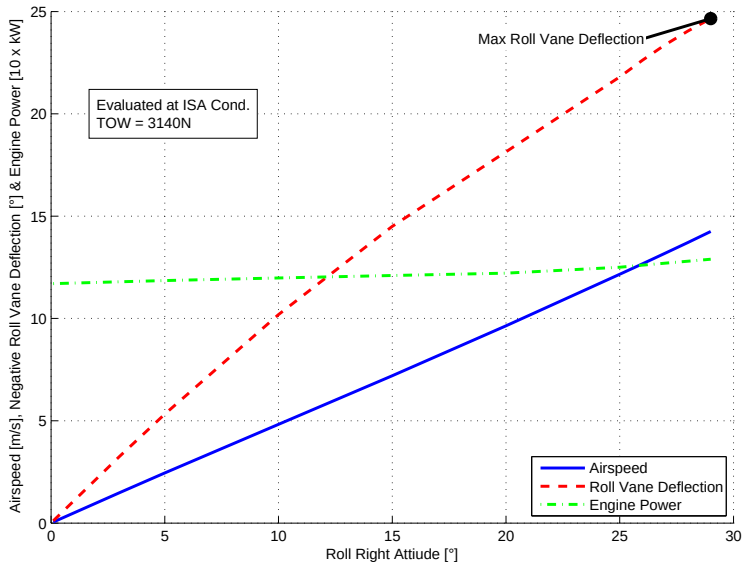

Figure E.8: Lateral performance versus roll right attitude for the Martin Jetpack P-12

Hover Yaw Turn

The hover yaw turn performance of the P-12 Jetpack is shown on Figure E.9. Due to the inertia imbalance of the P-12 Jetpack, large pitch vane deflections are also required in the hover yaw turn as the Jetpack does not spin perfectly about its z axis, but rather at an axis slightly offset from the z axis. Since the yaw and pitch vanes are mixed together on the P-12 Jetpack, the yaw vane deflection becomes the sum of the pitch and yaw vane signals and saturates at 25°, which is the maximum vane deflection on the P-12 Jetpack.

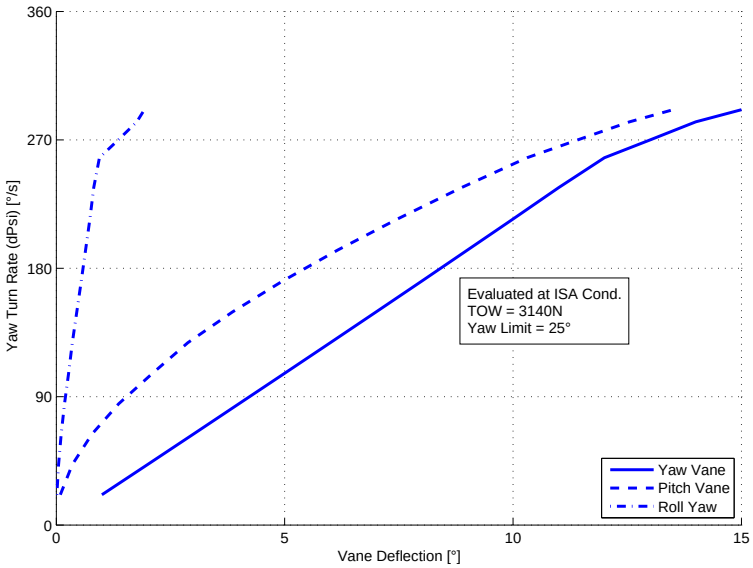

Figure E.9: Hover yaw turn performance versus yaw vane deflection for the Martin Jetpack P-12

Bank Turn

The level bank turn performance of the P-12 Jetpack is shown on Figures E.10b and E.10a, and as expected for a given bank angle the turn rate decreases and the turn radius increases rapidly with increasing airspeed. The Figures show that a maximum bank angle of 25° is obtainable for the P-12 Jetpack at 3140 N takeoff weight. Higher bank angles would be obtainable for lower takeoff weights as this increases the thrust margin.

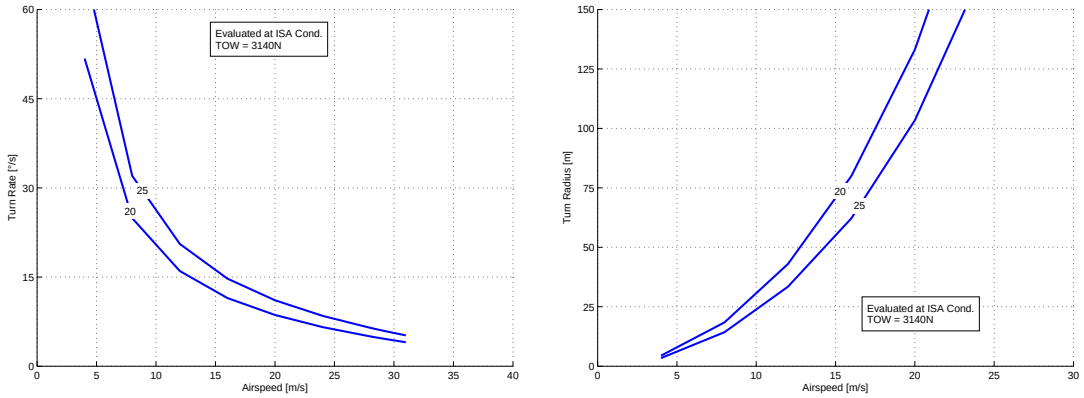

(a) Turn rate versus airspeed

(b) Turn radius versus airspeed

Figure E.10: Level bank turn performance for the Martin Jetpack P-12

E.3 P-11C Dynamic Validation

This section contains additional dynamic model validation plots for the P-11C Jetpack.

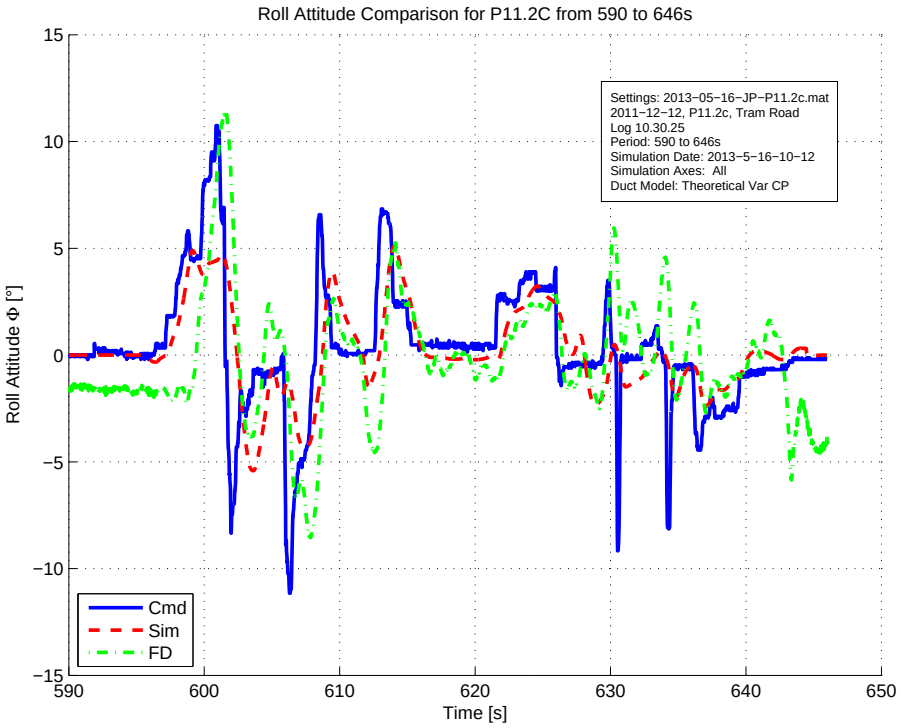

Figure E.11: Roll attitude comparison

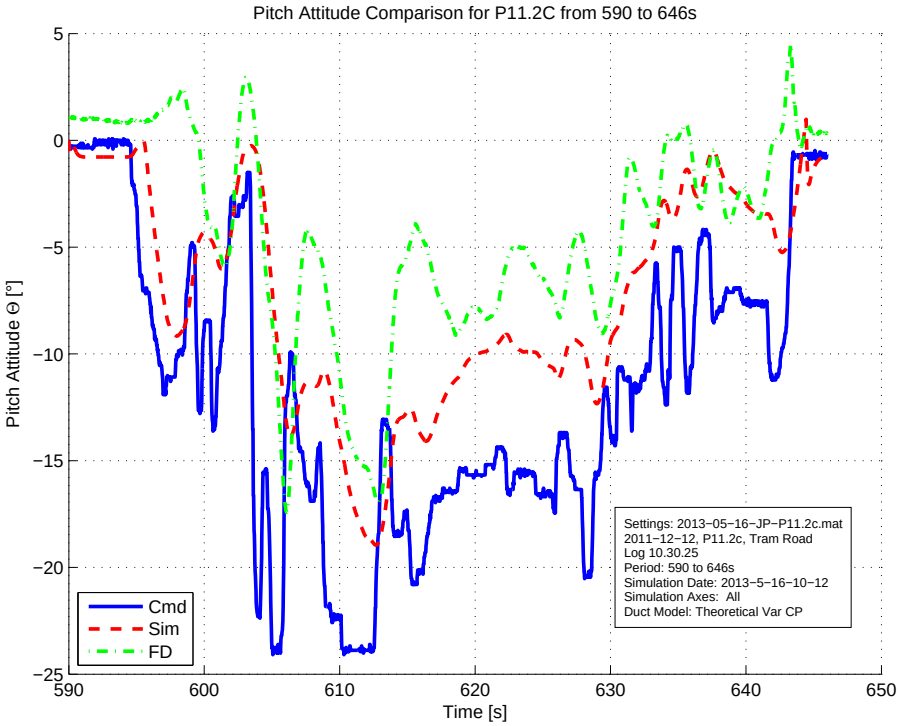

Figure E.12: Pitch attitude comparison

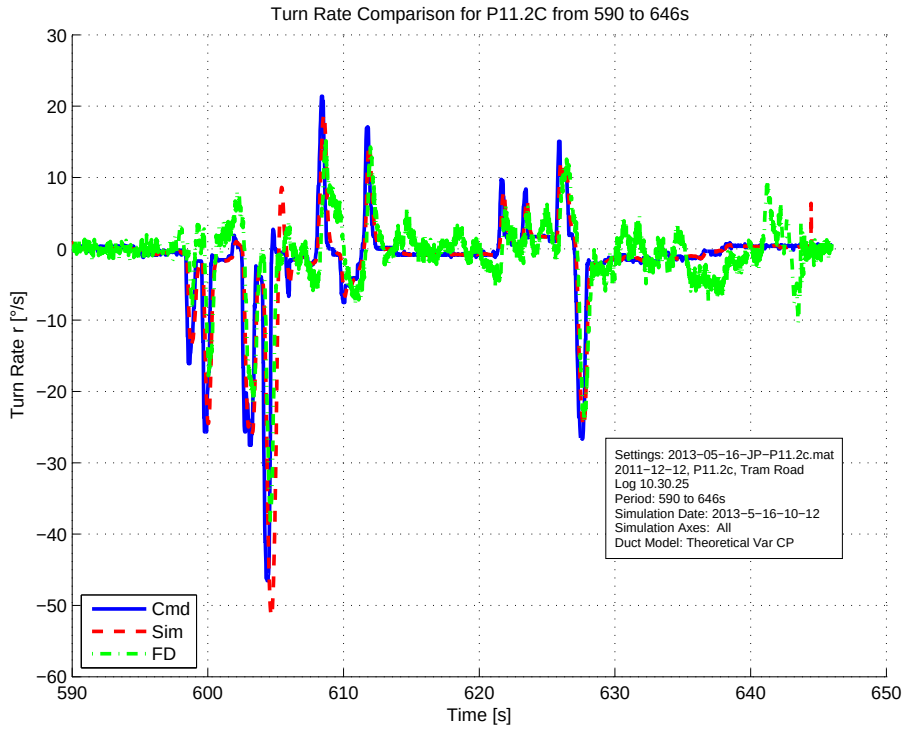

Figure E.13: Turn rate comparison

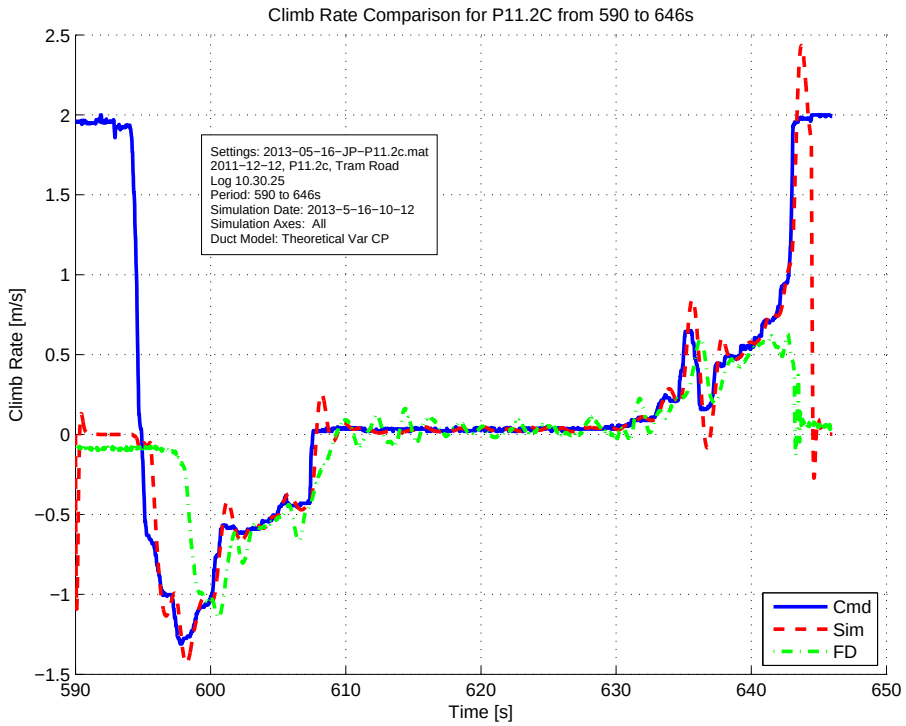

Figure E.14: Climb rate comparison

E.4 P-12 Dynamic Validation

This section contains additional dynamic model validation plots for the P-12 Jetpack

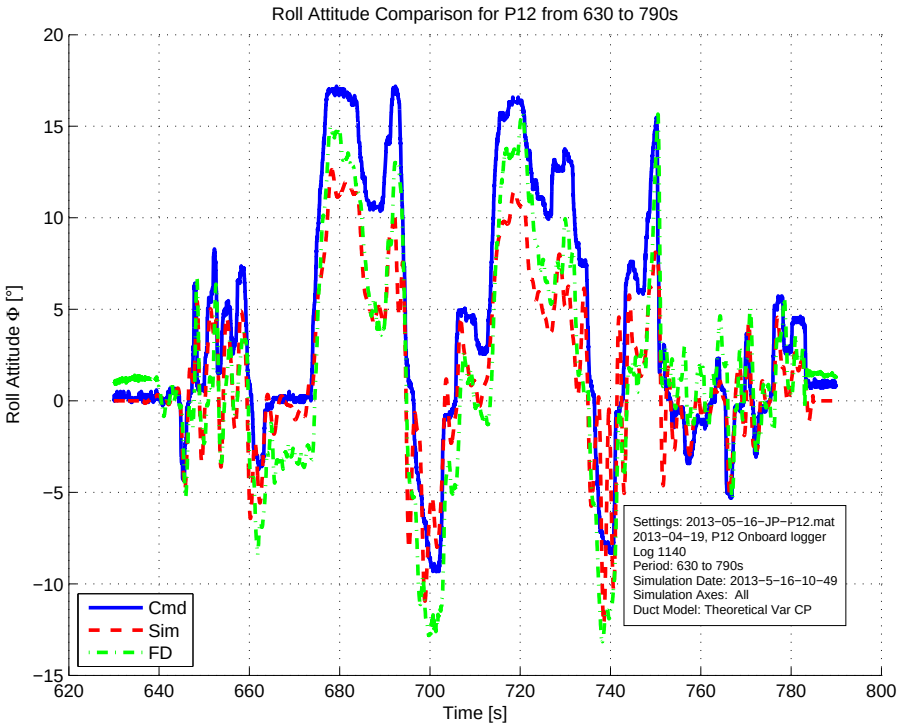

Figure E.15: Roll attitude comparison

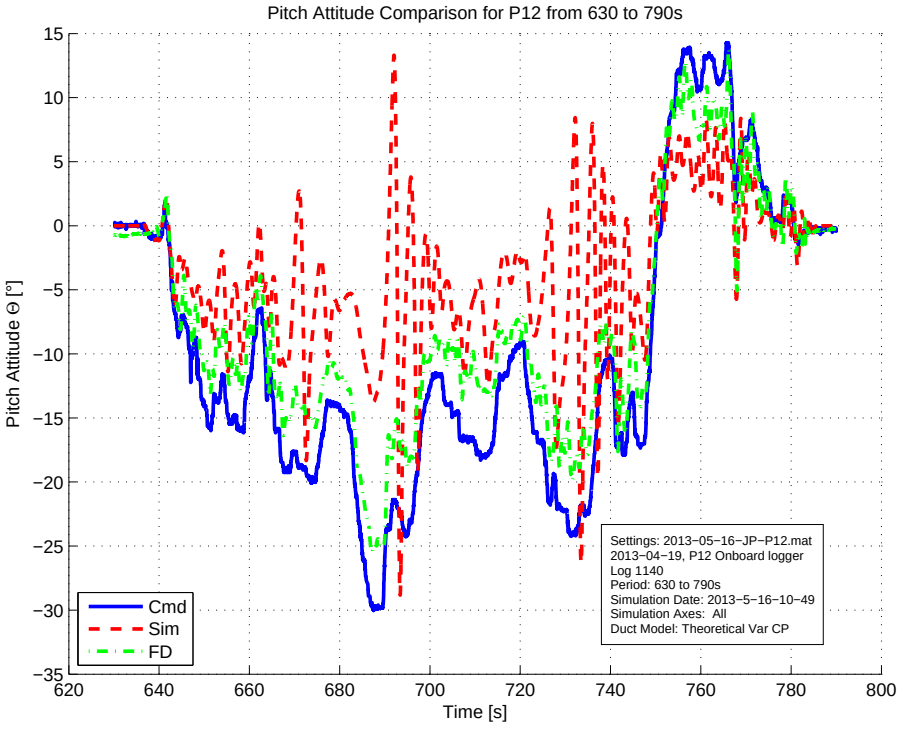

Figure E.16: Pitch attitude comparison

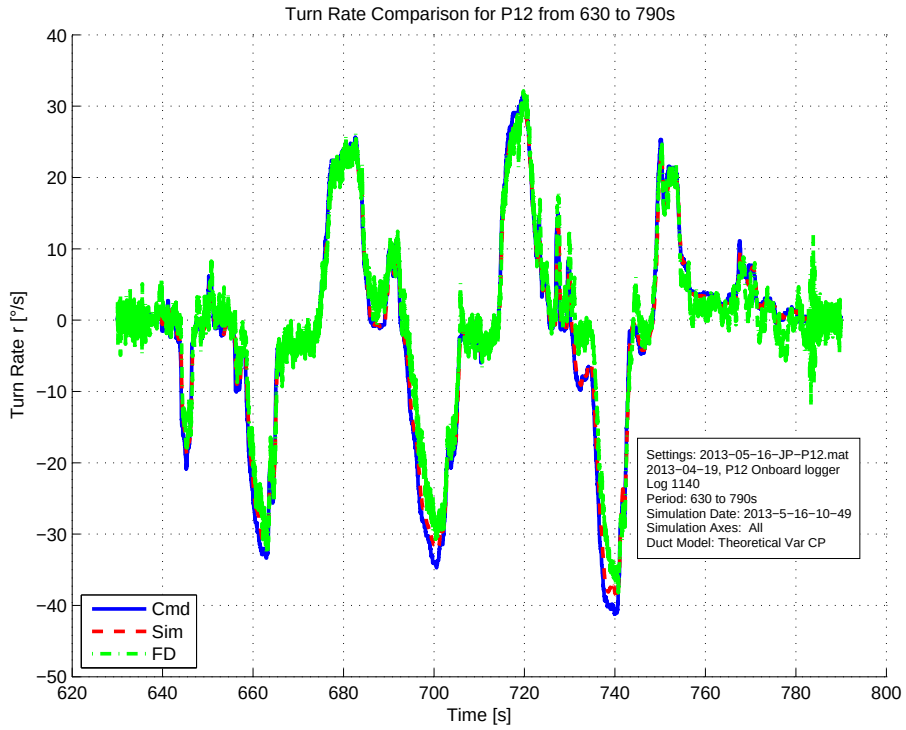

Figure E.17: Turn rate comparison

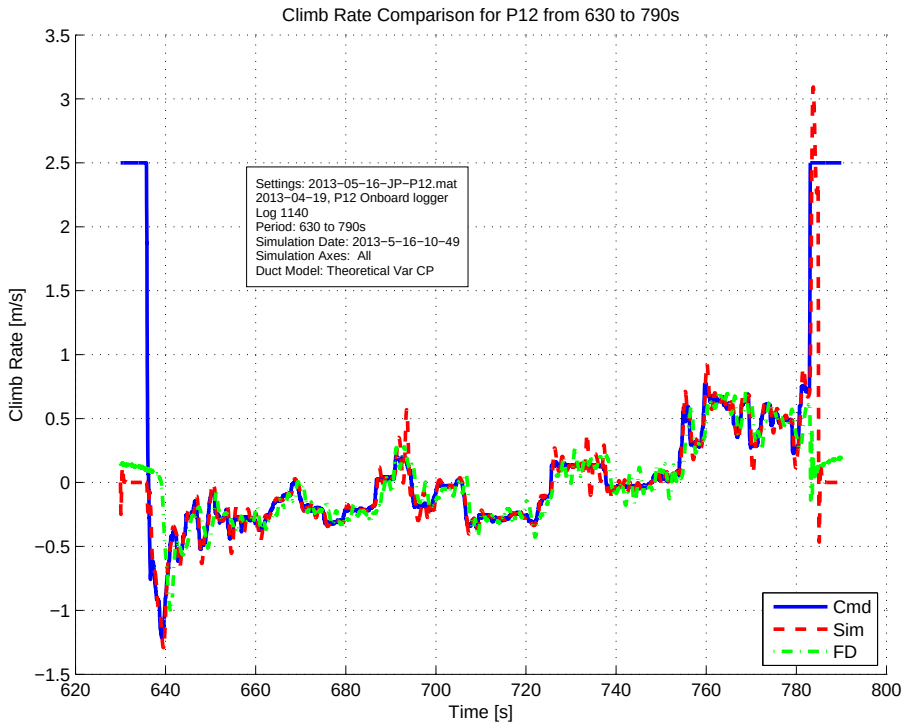

Figure E.18: Climb rate comparison

E.5 Modelled Ducted-Fan Reactions

The following modelled ducted-fan reactions are calculated using the aerodynamic equations developed in Chapter (6), and show the combined reactions for two ducted-fans in twin configuration, as per the Martin Jetpack design.

Model Predictions for Combined 600 mm Diameter Duct Reactions at 110kW (5500 RPM)

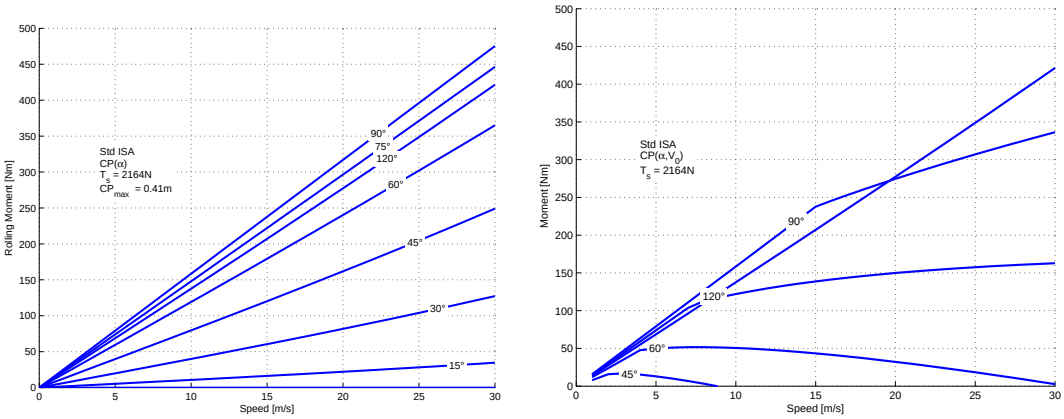

(a) Roll (b) Pitch

Figure E.21: Ducted-fan moment for various angles of attack at 110 kW

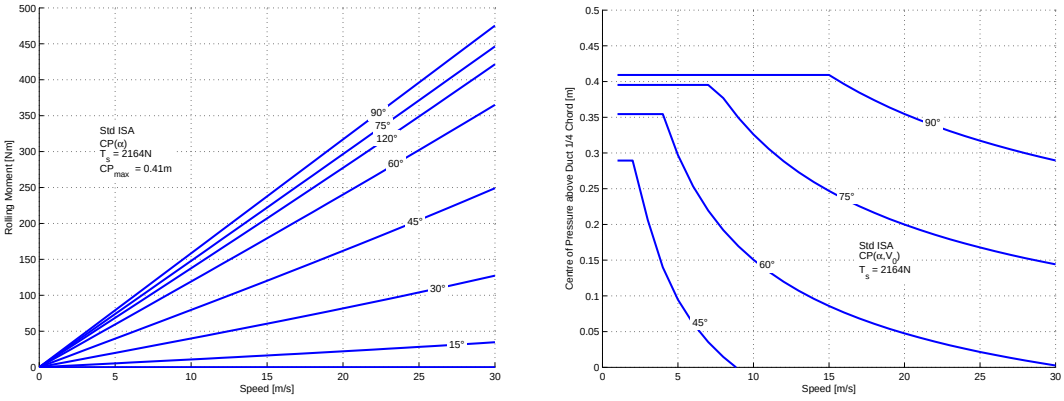

(a) Roll (b) Pitch

Figure E.22: Ducted-fan centre of pressure movement for various angles of attack at 110 kW

Non-Dimensionalised Combined 600 mm Diameter Ducted-Fan Reaction Predictions

Figures E.23 to E.26 show the model non-dimensional results of the duct reactions modelled at 110 kW. The reactions have been non-dimensionalized by the static thrust force of 2164 N, duct diameter of 0.6 m, and a fan speed of 6470 RPM, which is equivalent to an engine speed of 5500 RPM on the P-11 Jetpack.

Combined 800 mm Diameter Duct Reaction Predictions at 115 kW

The plots shown on Figures E.27a to E.30 given an indication of the expected in-flight reactions acting on the P-12 Jetpack. to P-12 Jetpack.

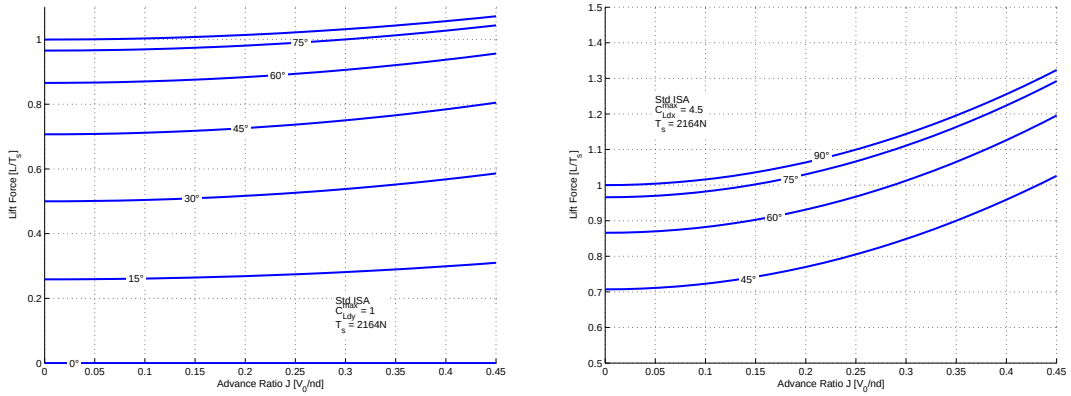

(a) Roll (b) Pitch

Figure E.23: Ducted-fan lift force for various angles of attack at 110 kW

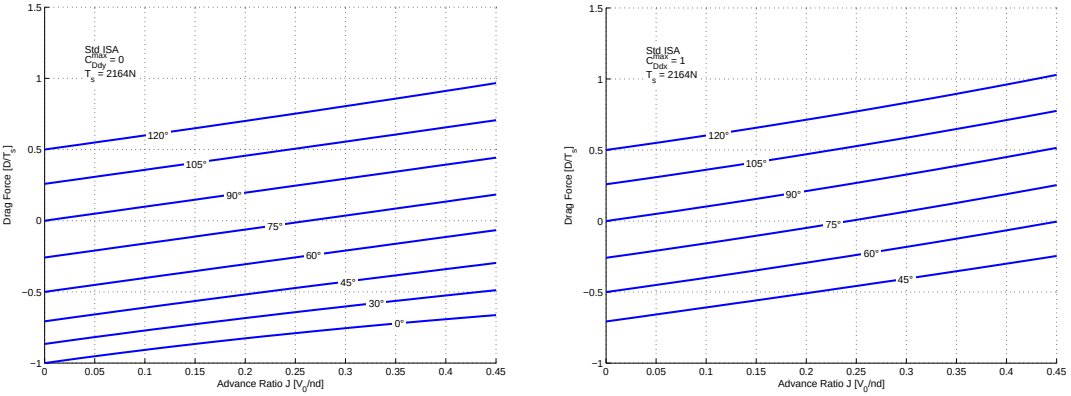

(a) Roll (b) Pitch

Figure E.24: Ducted-fan drag force for various angles of attack at 110 kW

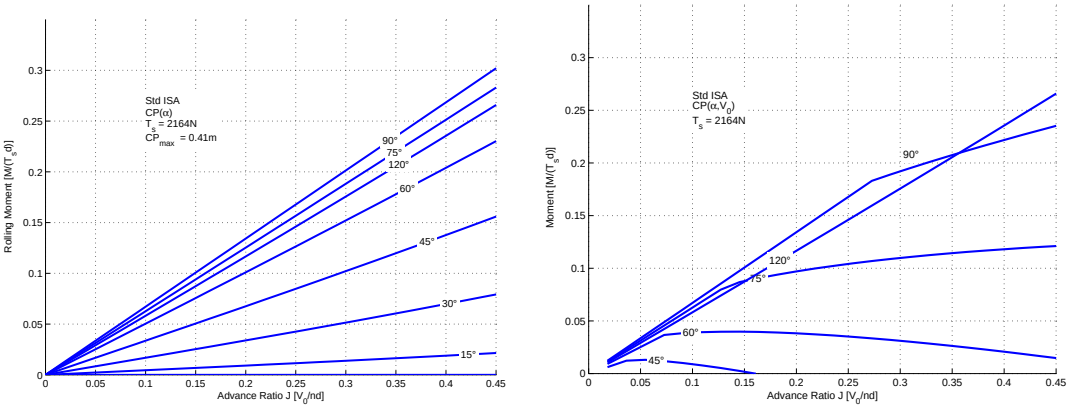

(a) Roll (b) Pitch

Figure E.25: Ducted-fan moment for various angles of attack at 110 kW

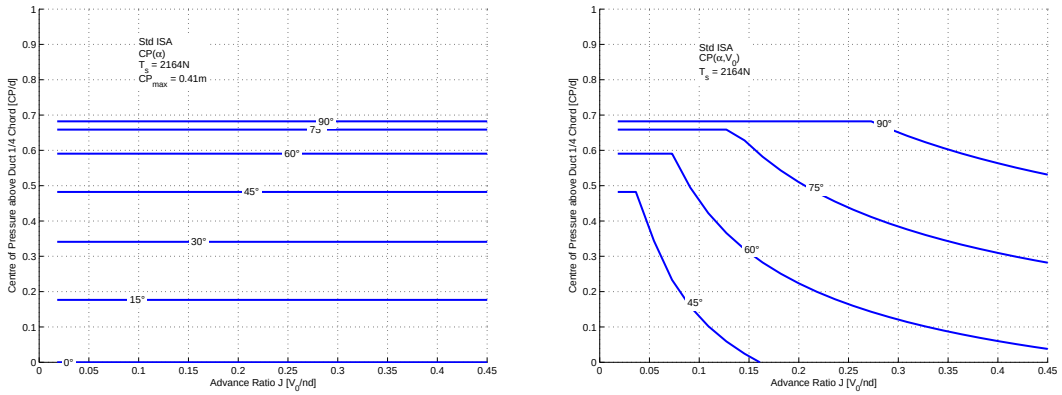

(a) Roll (b) Pitch

Figure E.26: Ducted-fan centre of pressure movement for various angles of attack at 110 kW

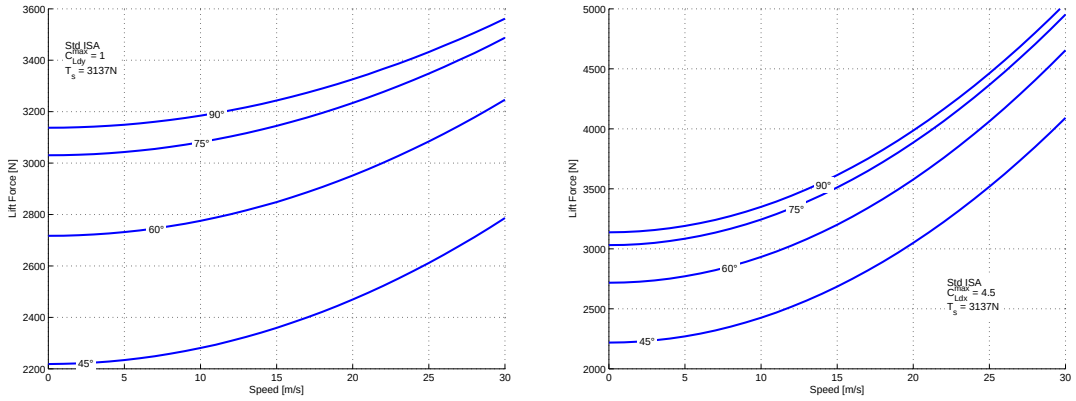

(a) Roll (b) Pitch

Figure E.27: Ducted-fan lift force for various angles of attack at 115 kW

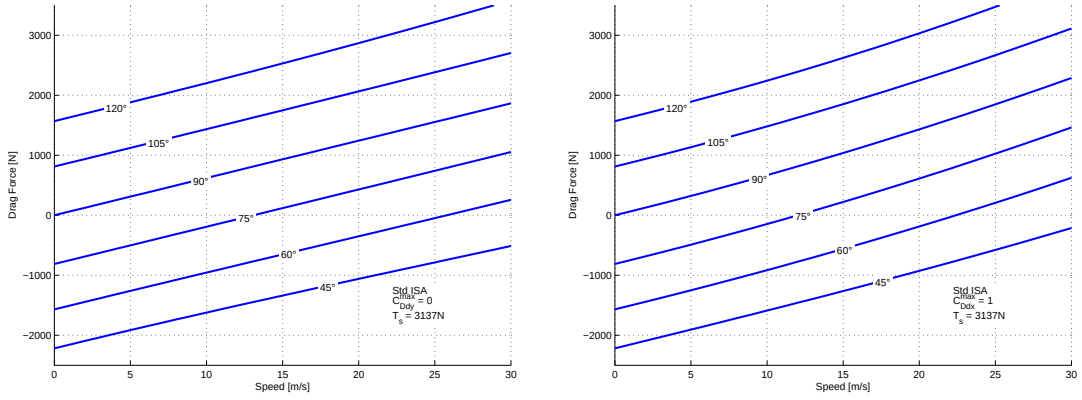

(a) Roll (b) Pitch

Figure E.28: Ducted-fan drag force for various angles of attack at 115 kW

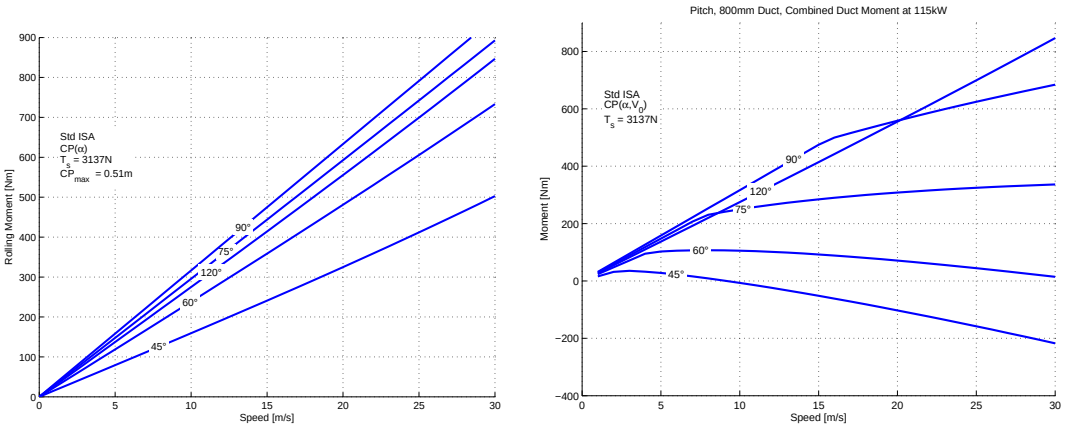

(a) Roll (b) Pitch

Figure E.29: Ducted-fan moment for various angles of attack at 115 kW

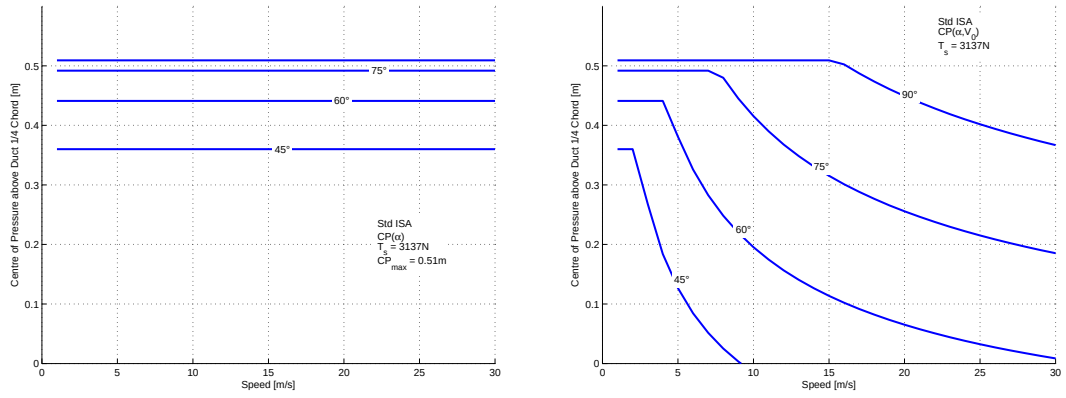

(a) Roll (b) Pitch

Figure E.30: Ducted-fan centre of pressure movement for various angles of attack at 115 kW

E.6 Hypothetical Wing for Jetpack

With a few assumptions the hypothetical size of a wing for the P-11C Jetpack can be found using the lift coefficient equation B.1.6 as:

$$A_{wing} = \frac{F_L}{C_L \frac{1}{2} \rho V^2} = \frac{220 \times 9.81}{1.5 \times \frac{1}{2} \times 1.225 \times 30^2} = 2.6\,\mathrm{m}^2 \tag{E.6.1}$$

where the lift force F_L is equal to the weight of the Jetpack, the velocity V is the assumed minimum velocity where the wing carries the weight of the Jetpack, and C_L is the assumed wing lift coefficient. Referring to Figure 7.4 it can be seen that the P-11C achieves a 30 m/s flight speed at an attitude of 50°. This angle equates to an angle of attack of 40°, which is much higher than the typical stall angle for a wing. By making the wing have a low aspect ratio, a higher stall angle can be reached, which has the benefit that lift produced from the wing and from the ducted-fans overlap during the transition phase from duct lift to wing lift. Ideally, the wing would be mounted with the thrust line and chord line approximately parallel, so when the Jetpack is at an attitude of 90° (angle of attack 0°) the thrust from the ducted-fans is only producing a propelling force, and the lift force is produced entirely from the wing. This concept would allow for maximum obtainable speed for the Jetpack.

Appendix F

Model Studies

This chapter summarizes two investigations into the Jetpack performance. The first study is an analysis of the P-11A Jetpack's response to wind turbulence. It was performed to highlight that changing the duct centre of pressure to a more favourable position not only improves the trim performance but also the dynamic performance of the Jetpack.

The second study looks at how the aircraft centre of pressure can be kept more constant by increasing the profile drag centre of pressure location further above the centre of gravity to produce a positive pitching moment to counter the negative duct pitching moment at high attitudes and airspeeds.

F.1 Investigation on the Effect of Turbulence on the P-11A Jetpack in Hovering Flight

Overview

Using the flight model an investigation was made of how wind turbulence affects the Jetpack's dynamic response. Two configurations were compared to demonstrate that locating the ducted-fan centre of pressure at the centre of gravity improves the Jetpack's response to handle wind turbulence.

Background

Turbulence is random fluctuations in wind speed that can produce random aerodynamic forces and moments which can significantly affect aircraft position and attitude. If any aircraft is dynamically stable the turbulence will have little effect on the aircraft's orientation, but the Martin Jetpack which is unstable requires a feedback system (via fly-by-wire) to artificially introduce stability. This requires control algorithms to compute the corrections and control vanes to produce the forces and moments to control the aircraft. To reduce the efforts required by the control vanes the aircraft designer positions the major aerodynamic features in such a way that the net centre of pressure acts as close as possible to the CG; this reduces the magnitude of aerodynamic moments acting on the aircraft, and hence, improves its ability to cope with turbulence.

Method

The simulation procedure involved running the model described in Chapter 4 for two Jetpack configurations for a duration of 15 s. Each run began at a trimmed hovering position and used a proportional rate controller on the roll, pitch, and yaw axes. The rate controller was manually tuned for the P-11A Jetpack configuration and the same gains were used for other configurations. The model employed the constant duct centre of pressure model, as described in section 3.2. The configurations simulated are:

1. The P-11A as flown by Martin Aircraft Company from 2010-2011.

2. A hypothetical version of P-11A with the ducts lowered so that the duct centre of pressure aligns to the CG, as proposed by the author.

Turbulence was modelled using a time dependent white noise signal (random number generator) filtered with a low pass filter to give a realistic inertia to the air mass, as explained in Appendix B.3. This was done for each of the three wind speed components x, y, and z in the global reference frame. The noise power density and low pass filter were modified to produce wind turbulence that ranged between the nominal values of $\pm 10\,\mathrm{m/s}$, $\pm 2\,\mathrm{m/s}$, and $\pm 1\,\mathrm{m/s}$ for x, y, and z, respectively to produce the ground wind speed shown in Figure F.1.

A similar methodology is used by the United States Military Standards [102, 104], where band-limited white noise is passed through turbulence forming filters. However, these models use a frozen turbulence field with the assumption that the mean wind speed and the root-mean-square turbulence velocity must be small compared to aircraft's speed. The frozen turbulence field means the turbulence is spatially dependent, so the turbulence frequency depends on how fast the aircraft flies through the turbulence field. Since the Jetpack is intended to operate at low airspeeds, in comparison to fixed-wing aircraft, not only is the aforementioned assumption not valid, but in the case of the Jetpack at hover the frozen turbulence field results in zero turbulence, which is unrealistic. Hence a time dependent turbulence model is used instead.

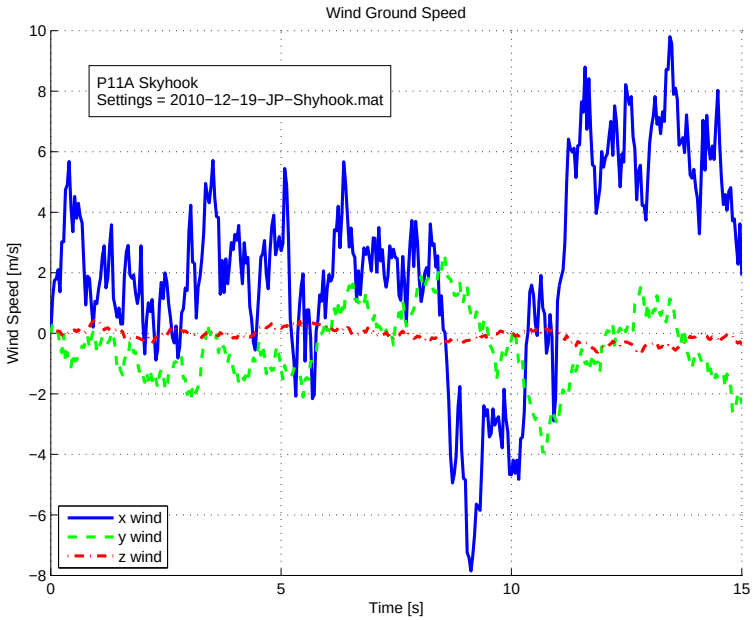

Figure F.1: Wind speed with respect to the inertial reference frame used for the Jetpack turbulence handling investigation

Results

P-11A Jetpack

For the P-11A Jetpack configuration, divergence in pitch attitude, Θ, of 10° occurs after approximately 9 s, with control loss happening soon after, refer to Figure F.2b. Loss of control occurs due to the Jetpack not having adequate control authority, as seen on Figure F.2a where the pitch vane, η, saturates at approximately 8.5 s in an attempt to correct the large pitching moment produced by the ram-drag force and the associated ram-drag moment.

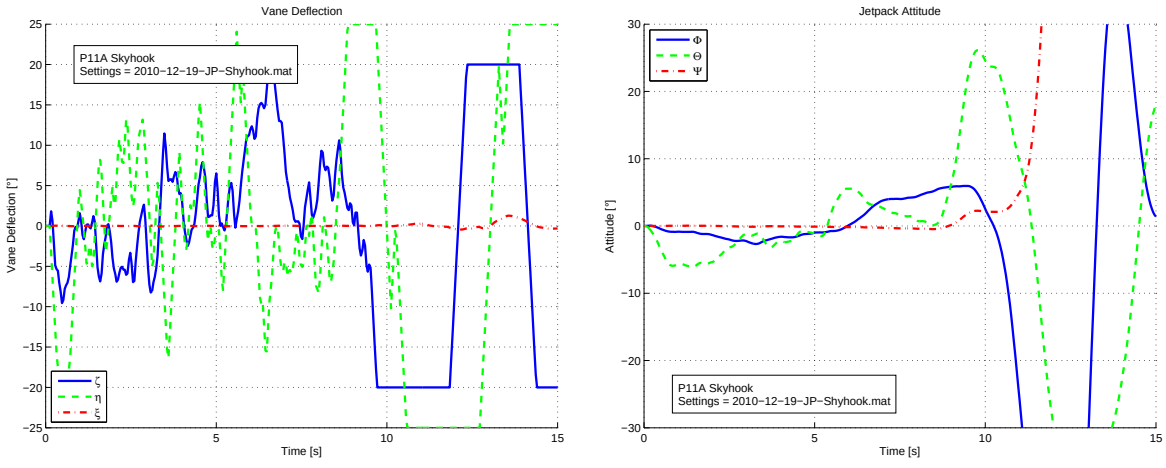

(a) Vane deflection (b) Attitude

Figure F.2: Simulated response of the P-11A Jetpack to wind turbulence

P-11A with the Centre of Pressure Located at CG

Figure F.3 shows that by positioning the duct centre of pressure at the CG of the Jetpack the adverse effect of the ducted-fan normal force moment on the

Jetpack's attitude is eliminated. With the ducted-fan normal force moment eliminated, the control vanes only need to correct for inertial and form-drag moments, both of which are far smaller in magnitude than the ram-drag moment on the P-11A. Figure F.3 also shows that the size and speed of the current pitch and roll vanes are adequate to control the Jetpack for the turbulence shown in Figure F.1.

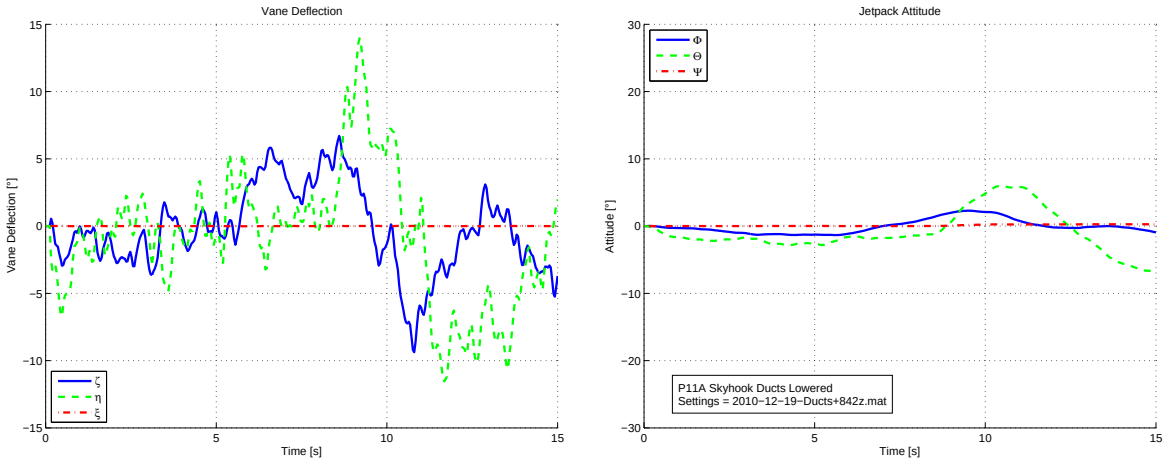

(a) Vane deflection

(b) Attitude

Figure F.3: Simulated response of P-11A Jetpack with CP located at CG to wind turbulence with CG located close to approximate centre of pressure position

Conclusion

The P-11A Jetpack resulted in loss of control, due to inadequate control authority from the applied wind turbulence in hovering flight. Repositioning the duct centre of gravity near the centre of pressure eliminates ram-drag moment, and hence, greatly improves the controllability of the Jetpack by reducing the effort required by the control vanes.

F.2 Jetpack P-11C Centre of Pressure Study

Overview

Using the flight model an investigation on the effects of moving the body centre of pressure upward on the Jetpack has been made. Moving the body centre of pressure upward has been proposed by the author as a means of obtaining a neutral pitch vane deflection throughout the longitudinal trimmed flight envelope.

Background

Figure 7.4 shows how the pitch vane deflection varies for longitudinal trimmed flight. It is seen that at low speeds the vane deflection is positive, but as speed increases the vane deflection reaches a maximum positive deflection before decreasing and becoming increasingly negative. Ideally, the vane deflection should remain neutral throughout the flight speed range, as this maximises

the use of vane deflection for manoeuvering the aircraft. The reason for the varying vane deflection is that the duct centre of pressure varies with airspeed and angle of attack, as experimental results show on Figure 6.24b. This results in the duct producing a positive pitching moment at low speeds and a negative pitching moment at high speeds which requires the pitch vanes to be deflected positively and negatively, respectively, as is shown on Figures F.4.

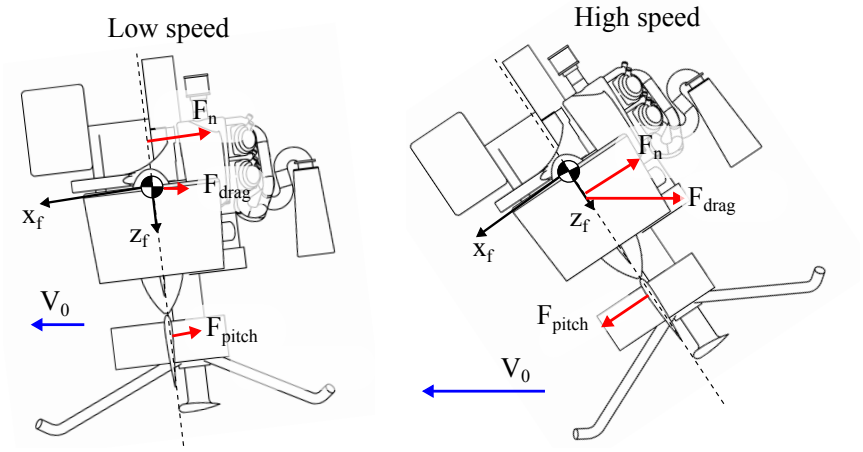

(a) Low speed (b) High speed

Figure F.4: Free body diagram of P-11C showing ram-drag, profile drag, and pitch vane force for P-11C at low and high speed longitudinal flight.

It is proposed by the author that the position of the Jetpack centre of pressure be moved above the CG so that a positive moment is produced by the drag force which counter acts the negative duct moment at high speeds. The advantage of this concept is that the body drag force is proportional to the velocity squared; so at low velocity the drag force is small and does not adversely effect the Jetpack. At high velocities the drag force equals or exceeds the ram-drag force, and produces an opposing moment to the ram-drag moment resulting in less pitch vane deflection required for trim, as shown by the free body diagram on Figure F.5.

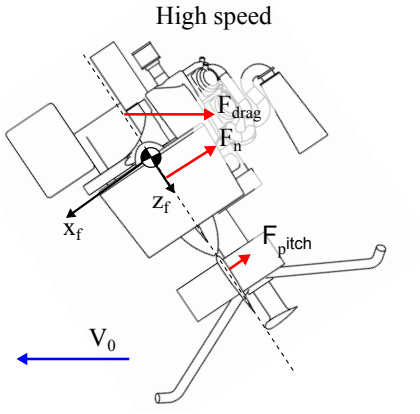

Figure F.5: Free body diagram proposed solution with body centre of pressure above the CG

The purpose of this study is to determine by how much the body centre of pressure has to move above the CG in order to minimise pitch vane deflection variation throughout the longitudinal flight envelope.

Method

The flight model in chapter 4 is solved for longitudinal level flight trim conditions described in section 7.4 for a range of body centre of pressure locations from 0 m to 0.5 m above the centre of gravity. This study was performed on the P-11C Jetpack configuration.

Results

Figure F.6 shows simulated level flight trimmed vane deflection for various body centre of pressure locations above the centre of gravity for the P-11C Jetpack. The approximate airspeed versus attitude for all configurations is also shown for reference. Note, negative z is physically an upward direction on the Jetpack.

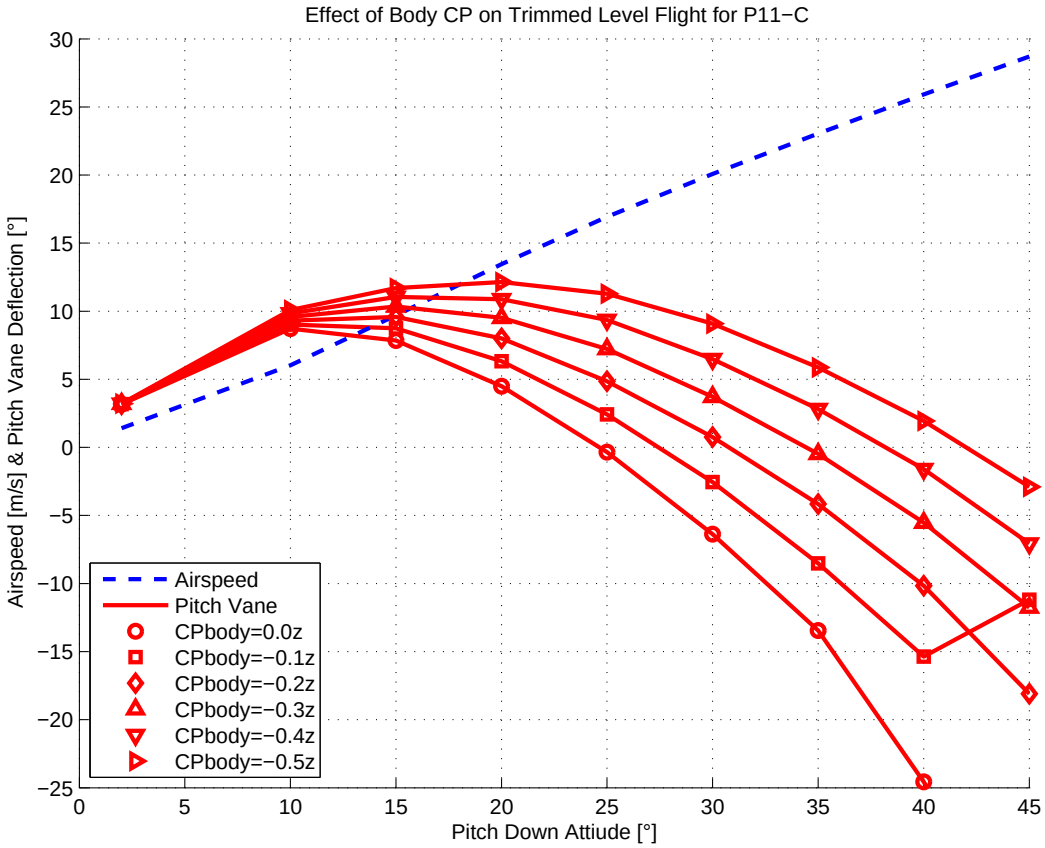

Figure F.6: Effect of the body profile drag position on longitudinal flight performance for the P-11C Jetpack.

Discussion

It can be seen on Figure F.6 that increasing the centre of pressure location above the centre of gravity flattens the pitch vane deflection curve so that less variation in pitch vane deflection is required for trim throughout the flight range. This has a twofold benefit on performance. Firstly, pitch vane saturation of $\pm 25^\circ$ is avoided until higher attitudes, if it occurs at all, which allows for higher attitudes and airspeeds to be obtained. Secondly, vane deflection remains positive for a greater range of attitudes. This is favourable as this means the Jetpack has a natural positive pitching moment to return the

Jetpack towards hovering attitude.

Ideally maximum speed should occur at the point of maximum power developed by the engine. This way the pitch vanes maintain control authority to manoeuvre the Jetpack throughout the entire flight envelope. If level flight speed is limited by pitch vane authority a condition can occur that the Jetpack has no more pitch control available to manoeuvre the Jetpack or counter any atmospheric induced pitching moments from turbulence, thus loss of control occurs, which must be avoided. This phenomena plagued the earlier Jetpack prototypes such as P11-A Jetpack.

The effective location of the body centre of pressure can be increased by increasing the exposed surface area above the CG, which increases the positive aerodynamic drag moment. Likewise the exposed surface area beneath the CG should be minimised and/or streamlined to reduced the negative aerodynamic drag moment produce by these features.

The addition of a canard wing above the CG would also help, especially at higher attitudes where the profile drag moment is reduced due to decreasing moment arm.

Conclusion

It has been shown that by altering the design of the P-11C Jetpack so that the body centre of pressure is between 0.3 m to 0.5 m above the centre of gravity, the variation in pitch vane deflection with increasing attitude is reduced. This has the benefit of improving the performance of the Jetpack as pitch vane saturation is avoided, allowing the Jetpack to be trimmed for a larger range of attitudes, and hence, flight speeds.

Appendix G

Jetpack Model Parameters

This appendix documents the Jetpack model parameters shown on Table G.1 used in the developed Jetpack model described in Chapter 4.

Table G.1: Jetpack model parameters

Variable	Description	P-11A	P-11C	P-11E	P-12
TOM	Takeoff mass [kg]	240	220	215	320
$\mathbf{I}$	Inertia tensor [kgm^2]	$\begin{bmatrix} 63.4 & -0.09 & -1.19 \\ -0.09 & 63.6 & -0.03 \\ -1.19 & -0.03 & 38.9 \end{bmatrix}$	$\begin{bmatrix} 47.1 & 0.83 & -0.06 \\ 0.83 & 45.1 & 6.35 \\ -0.06 & 6.35 & 54.1 \end{bmatrix}$	$\begin{bmatrix} 63.4 & -0.09 & -1.19 \\ -0.09 & 63.6 & -0.03 \\ -1.19 & -0.03 & 38.9 \end{bmatrix}$	$\begin{bmatrix} 66.0 & 0.07 & 6.67 \\ 0.07 & 65.0 & 0.06 \\ 6.67 & 0.06 & 58.6 \end{bmatrix}$
$\mathbf{I}_{rot}$	Angular momentum [kgm^2/s]	$\begin{bmatrix} 0 & 0 & 50.37 \end{bmatrix}$	$\begin{bmatrix} 0 & 0 & 50.37 \end{bmatrix}$	$\begin{bmatrix} 0 & 0 & 50.37 \end{bmatrix}$	$\begin{bmatrix} 0 & 0 & 40.4 \end{bmatrix}$
$\mathbf{l}_{d,RH}$	Vector from CG to RH ducted-fan [m]	$\begin{bmatrix} 0 & 0.5265 & -0.529 \end{bmatrix}$	$\begin{bmatrix} 0 & 0.5265 & 0.109 \end{bmatrix}$	$\begin{bmatrix} 0 & 0.527 & 0.139 \end{bmatrix}$	$\begin{bmatrix} 0 & 0.6380 & 0.109 \end{bmatrix}$
$\mathbf{l}_{d,LH}$	Vector from CG to LH ducted-fan [m]	$\begin{bmatrix} 0 & -0.5265 & -0.529 \end{bmatrix}$	$\begin{bmatrix} 0 & -0.5265 & 0.109 \end{bmatrix}$	$\begin{bmatrix} 0 & -0.527 & 0.139 \end{bmatrix}$	$\begin{bmatrix} 0 & -0.638 & 0.109 \end{bmatrix}$
$\mathbf{l}_{roll,RH}$	Vector from CG to RH roll vane [m]	$\begin{bmatrix} 0 & 0.351 & 0.5240 \end{bmatrix}$	$\begin{bmatrix} 0 & 0.35 & 0.727 \end{bmatrix}$	$\begin{bmatrix} 0 & 0.527 & 0.568 \end{bmatrix}$	$\begin{bmatrix} 0 & 0.638 & 0.537 \end{bmatrix}$
$\mathbf{l}_{roll,LH}$	Vector from CG to LH roll vane [m]	$\begin{bmatrix} 0 & -0.351 & 0.524 \end{bmatrix}$	$\begin{bmatrix} 0 & -0.35 & 0.727 \end{bmatrix}$	$\begin{bmatrix} 0 & -0.527 & 0.568 \end{bmatrix}$	$\begin{bmatrix} 0 & -0.638 & 0.537 \end{bmatrix}$
$\mathbf{l}_{pitch,RH}$	Vector from CG to RH pitch vane [m]	$\begin{bmatrix} 0 & 0.3905 & 0.524 \end{bmatrix}$	$\begin{bmatrix} 0 & 0.4530 & 0.727 \end{bmatrix}$	$\begin{bmatrix} 0 & 0.35 & 0.598 \end{bmatrix}$	$\begin{bmatrix} 0 & 0.385 & 0.537 \end{bmatrix}$
$\mathbf{l}_{pitch,LH}$	Vector from CG to LH pitch vane [m]	$\begin{bmatrix} 0 & -0.3905 & 0.524 \end{bmatrix}$	$\begin{bmatrix} 0 & -0.4530 & 0.727 \end{bmatrix}$	$\begin{bmatrix} 0 & -0.35 & 0.598 \end{bmatrix}$	$\begin{bmatrix} 0 & -0.385 & 0.537 \end{bmatrix}$
$\mathbf{l}_{yaw,RH}$	Vector from CG to RH yaw vane [m]	$\begin{bmatrix} 0 & 0.7275 & -0.237 \end{bmatrix}$	$\begin{bmatrix} 0 & 0.8 & 0.462 \end{bmatrix}$	$\begin{bmatrix} 0 & 0.705 & 0.513 \end{bmatrix}$	$\begin{bmatrix} 0 & 0.891 & 0.537 \end{bmatrix}$
$\mathbf{l}_{yaw,LH}$	Vector from CG to LH yaw vane [m]	$\begin{bmatrix} 0 & -0.7275 & -0.237 \end{bmatrix}$	$\begin{bmatrix} 0 & -0.8 & -0.462 \end{bmatrix}$	$\begin{bmatrix} 0 & -0.705 & 0.513 \end{bmatrix}$	$\begin{bmatrix} 0 & -0.891 & 0.537 \end{bmatrix}$
$\mathbf{l}_{LG,front,RH}$	Vector from CG to front RH landing gear [m]	$\begin{bmatrix} 0.603 & 0.155 & 0.822 \end{bmatrix}$	$\begin{bmatrix} 0.73 & 0.69 & 1.22 \end{bmatrix}$	$\begin{bmatrix} 0.73 & 0.69 & 1.25 \end{bmatrix}$	$\begin{bmatrix} 0.769 & 0.928 & 1.1 \end{bmatrix}$

Variable	Description	P-11A	P-11C	P-11E	P-12
$\mathbf{l}_{LG,front,LH}$	Vector from CG to front LH landing gear [m]	$\begin{bmatrix} 0.603 & -0.155 & 0.822 \end{bmatrix}$	$\begin{bmatrix} 0.73 & -0.69 & 1.22 \end{bmatrix}$	$\begin{bmatrix} 0.73 & -0.69 & 1.25 \end{bmatrix}$	$\begin{bmatrix} 0.769 & -0.928 & 1.1 \end{bmatrix}$
$\mathbf{l}_{LG,rear,RH}$	Vector from CG to rear RH landing gear [m]	$\begin{bmatrix} -0.569 & 0.602 & 0.822 \end{bmatrix}$	$\begin{bmatrix} -1 & 0.78 & 1.22 \end{bmatrix}$	$\begin{bmatrix} -1 & 0.78 & 1.25 \end{bmatrix}$	$\begin{bmatrix} -0.769 & 0.928 & 1.1 \end{bmatrix}$
$\mathbf{l}_{LG,rear,LH}$	Vector from CG to rear LH landing gear [m]	$\begin{bmatrix} -0.569 & -0.602 & 0.822 \end{bmatrix}$	$\begin{bmatrix} -1 & -0.78 & 1.22 \end{bmatrix}$	$\begin{bmatrix} -1 & -0.78 & 1.25 \end{bmatrix}$	$\begin{bmatrix} -0.769 & -0.928 & 1.1 \end{bmatrix}$
$\mathbf{l}_{LG,top}$	Vector from CG to top contact point [m]	$\begin{bmatrix} 0 & 0 & -0.876 \end{bmatrix}$	$\begin{bmatrix} 0 & 0 & -0.362 \end{bmatrix}$	$\begin{bmatrix} 0 & 0 & -0.332 \end{bmatrix}$	$\begin{bmatrix} 0 & 0 & -0.6 \end{bmatrix}$
$\mathbf{l}_{CP,body}$	Vector from CG to body centre of pressure[m]	$\begin{bmatrix} 0 & 0 & 0 \end{bmatrix}$	$\begin{bmatrix} 0 & 0 & 0.02 \end{bmatrix}$	$\begin{bmatrix} 0 & 0 & -0.17 \end{bmatrix}$	$\begin{bmatrix} 0 & 0 & 0 \end{bmatrix}$
C_z	Landing gear damping coefficient	800			
C_x	Landing gear surface damping coefficient	200			
K	Landing gear spring constant	8000			
$A_{x,y,z}$	Front, side, and top area projections [m^2]	$\begin{bmatrix} 1.8 & 1.2 & 1.123 \end{bmatrix}$	$\begin{bmatrix} 1.8 & 1.2 & 1.123 \end{bmatrix}$	$\begin{bmatrix} 1.8 & 1.2 & 1.123 \end{bmatrix}$	$\begin{bmatrix} 1.93 & 1.73 & 2.21 \end{bmatrix}$
$C_{D,x,y,z}$	Front, side, and top drag coefficients	$\begin{bmatrix} 0.81 & 1.05 & 0.94 \end{bmatrix}$	$\begin{bmatrix} 1.9 & 1.05 & 0.94 \end{bmatrix}$	$\begin{bmatrix} 0.81 & 1.05 & 0.94 \end{bmatrix}$	$\begin{bmatrix} 0.81 & 1.05 & 0.94 \end{bmatrix}$

Variable	Description	P-11A	P-11C	P-11E	P-12
	Vane lift factor versus height		$\begin{bmatrix} \text{m} & factor \\ 0 & 0 \\ 0.409 & 0.66 \\ 0.669 & 0.86 \\ 1.269 & 1 \end{bmatrix}$		
d	Duct exit diameter [m]	0.6			0.8
d_{ro}	Rotor diameter [m]	0.528			0.728
d_h	Hub diameter [m]	0.22			0.3
d_c	Duct chord length [m]	0.437			0.437
A_e	Duct exit area [m^2]	0.2447			0.432
A_{ro}	Duct rotor area [m^2]	0.1809			0.3456
A_d	Duct area [m^2]	0.2827			0.503
η_d	Duct efficiency	0.55			0.69
ϵ_d	Duct expansion ratio	1.56			1.45
$C_{L,d,max,x,y}$	Duct Lift Coefficient	$\begin{bmatrix} 4.5 & 1 \end{bmatrix}$			$\begin{bmatrix} 4.5 & 1 \end{bmatrix}$
$C_{D,d,max,x,y}$	Duct Drag Coefficient	$\begin{bmatrix} 1.5 & 1.5 \end{bmatrix}$			$\begin{bmatrix} 1.5 & 1.5 \end{bmatrix}$
$d_{CPF,x,y}$	Duct Turning Factor	$\begin{bmatrix} 0.45 & -0.2 \end{bmatrix}$			$\begin{bmatrix} 0.45 & -0.2 \end{bmatrix}$
	Roll vane type	Single vane			Tri-decker
ξ_s	Roll vane max speed [°/s]	80	80	80	80
ξ_{max}	Roll vane max angle [°]	20	20	20	25
	Roll vane data		$\begin{bmatrix} \alpha^\circ & C_L & C_D \\ 0 & 0 & 0.038 \\ 5 & 0.21 & 0.067 \\ 10 & 0.39 & 0.090 \\ 15 & 0.64 & 0.16 \\ 20 & 0.82 & 0.22 \\ 25 & 0.99 & 0.33 \\ 30 & 1.1 & 0.41 \end{bmatrix}$		$\begin{bmatrix} \alpha^\circ & C_L & C_D \\ 0 & 0 & 0.02 \\ 20 & 0.42 & 0.12 \\ 25 & 0.47 & 0.2 \end{bmatrix}$

Variable	Description	P-11A	P-11C	P-11E	P-12
ξ_c	Roll vane chord [m]	0.2	0.2	0.2	0.4
ξ_b	Roll vane span [m]	0.2650	0.2650	0.24	0.294
ξ_A	Roll area [m^2]	0.0530	0.0530	0.048	0.1176
ξ_f	Roll vane modifying factor	0.36	0.36	1	1
	Pitch vane type	Single vane with end cap			Tri-decker
η_s	Pitch vane max speed [°/s]	80	80	80	80
η_{max}	Pitch vane max angle [°]	20	20	20	25
	Pitch vane data	$\begin{bmatrix} \alpha^\circ & C_L & C_D \\ 0 & 0 & 0.038 \\ 5 & 0.21 & 0.067 \\ 10 & 0.39 & 0.090 \\ 15 & 0.64 & 0.16 \\ 20 & 0.82 & 0.22 \\ 25 & 0.99 & 0.33 \\ 30 & 1.1 & 0.41 \end{bmatrix}$			$\begin{bmatrix} \alpha^\circ & C_L & C_D \\ 0 & 0 & 0.02 \\ 20 & 0.42 & 0.12 \\ 25 & 0.47 & 0.2 \end{bmatrix}$
η_c	Pitch vane chord [m]	0.35	0.35	0.2	0.4
η_b	Pitch vane span [m]	0.35	0.35	0.24	0.294
η_A	Pitch vane area [m^2]	0.1225	0.1225	0.048	0.1176
η_f	Pitch vane modifying factor	0.5	1	0.25	1
	Yaw vane type	Tri-decker vane			Tri-decker
ζ_s	Yaw vane max speed [°/s]	40	40	80	80
ζ_{max}	Yaw vane max angle [°]	15	15	20	25

Variable	Description	P-11A	P-11C	P-11E	P-12
	Yaw vane data		$\begin{bmatrix} \alpha^\circ & C_L & C_D \\ 0 & 0 & 0.038 \\ 5 & 0.21 & 0.067 \\ 10 & 0.39 & 0.090 \\ 15 & 0.64 & 0.16 \\ 20 & 0.82 & 0.22 \\ 25 & 0.99 & 0.33 \\ 30 & 1.1 & 0.41 \end{bmatrix}$		$\begin{bmatrix} \alpha^\circ & C_L & C_D \\ 0 & 0 & 0.02 \\ 20 & 0.42 & 0.12 \\ 25 & 0.47 & 0.2 \end{bmatrix}$
ζ_c	Yaw vane chord [m]	0.1	0.1	0.2	0.4
ζ_b	Yaw vane span [m]	0.19	0.19	0.24	0.294
ζ_A	Yaw vane area [m^2]	0.057	0.057	0.048	0.1176
ζ_f	Yaw vane modifying factor	0.91	0.91	0.91	1
τ_e	Engine time constant [s]	0.2			
P_e, τ	Engine data, power and throttle position	$\begin{bmatrix} \text{kW} & \% \\ 0 & 15 \\ 15 & 10 \\ 150 & 100 \end{bmatrix}$			
	Roll Control Description	Nested attitude and rate controller			
Roll Joystick	Joystick gain [°]	10	28	30	35
Roll V1	Inner P gain [μs^2/°]	2	9.5	20	4.2
Roll V2	Feed forward [μs/°]	1	0	1.2	1.2
Roll V3	Outer P gain [1/s]	1	1.5	1.5	2.5
Roll V4	Outer saturation [°/s]	10	12	12	35
Roll V5	Joystick rate limit [°/s]	8	8	8	20
Roll V6	Vane gradient [μs/°]	0.0526	0.0526	0.0526	0.01

Variable	Description	P-11A	P-11C	P-11E	P-12
Roll V7	Vane y intercept [μs]	-78.9	-78.9	-78.3	-150
Roll V8	Vane neutral position [μs]	1500	1500	1500	1500
	Pitch Control Description	Nested attitude and rate controller			
Pitch Joystick	Joystick gain [°]	40	28	30	35
Pitch V1	Inner P gain [$\mu s^2/°$]	2	6	12	2.5
Pitch V2	Feed forward [$\mu s/°$]	0	0	1.2	1.2
Pitch V3	Outer P gain [1/s]	1	1.1	1.3	5
Pitch V4	Outer saturation [°/s]	10	10	10	40
Pitch V5	Joystick rate limit [°/s]	8	8	8	25
Pitch V6	Vane gradient [μs/°]	0.1029	0.1029	0.1029	0.01
Pitch V7	Vane y intercept [μs]	-154.35	-154.35	-156.2	-150
Pitch V8	Vane neutral position [μs]	1500	1500	1500	1500
	Yaw Control Description	Rate controller			
Yaw Joystick	Joystick gain [°/s]	120	70	70	70
Yaw V1	P gain [$\mu s^2/°$]	0.5	10	10	7
Yaw V5	Yaw-pitch mixing gain	0	0	1	0.8
Yaw V6	Vane gradient [μs/°]	0.0713	0.0713	0.0713	0.01
Yaw V7	Vane y intercept [μs]	-107	-107	-107	-150
Yaw V8	Vane neutral position [μs]	1500	1500	1500	1500

Variable	Description	P-11A	P-11C	P-11E	P-12
	Throttle Control Description	Velocity PID controller			
Throttle Joystick	Joystick gain [m/s]	−4	−4	−4	−4
Throttle V1	P gain	50	50	50	50
Throttle V2	I gain	2	2	2	2

Bibliography

[1] Wright flyer of 1903. 2013. Encyclopaedia Britannica Online. Retrieved 26 December, 2013, from http://www.britannica.com/EBchecked/topic/649596/Wright-flyer-of-1903.

[2] balloon. 2013. Encyclopaedia Britannica Online. Retrieved 26 December, 2013, from http://www.britannica.com/EBchecked/topic/50696/balloon.

[3] balloon: Montgolfier brothers demonstration. [Photograph]. Encyclopaedia Britannica Online. Retrieved 26 December, 2013, from http://www.britannica.com/EBchecked/media/110557/Jean-Francois-Pilatre-de-Rozier-and-Francois-Laurent-marquis-dArlandes.

[4] Wright flyer of 1903. [Photograph]. Encyclopaedia Britannica Online. Retrieved 26 December, 2013, from http://www.britannica.com/EBchecked/media/3789/Orville-Wright-beginning-the-first-successful-controlled-flight-in-history.

[5] Igor Sikorsky. 2013. Encyclopaedia Britannica Online. Retrieved 26 December, 2013, from http://www.britannica.com/EBchecked/topic/543984/Igor-Sikorsky/6671/Work-in-the-United-States.

[6] Thunderbolt Aerosystems Inc. Wendell F. Moore. Online. Retrieved 26 December, 2013, from http://www.thunderman.net/about/scientific-team-moore.php.

[7] M. De Roche. Thrust Augmentation and Control of a Ducted-Fan VTOL Air Vehicle. In *AHS Future Vertical Lift Aircraft Design Conference*, San Francisco, CA., USA, 18-20 January 2012.

[8] NASA. The Puffin: A Passion for Personal Flight. Online. Retrieved 26 December, 2013, from http://www.nasa.gov/topics/technology/features/puffin.html.

[9] GEN Corporation. Gen H-4. Retrieved 26 December, 2013, from http://www.gen-corp.jp/product/categories/p2.html.

[10] Martin Aircraft Company. P-11 Jetpack Performance. Online. Retrieved 8 June, 2010, from http://martinjetpack.com/.

[11] Federal Aviation Regulation Part 103 - Ultralight Vehicles.

[12] W. Krueger. On Wind Tunnel Tests and Computations Concerning the Problem of Shrounded Propelllers. Technical Report 1202, NACA, February 1949. Translation of ZWB Forschungsbericht Nr. 1949, January 21, 1944.

[13] G. N. Patterson. Ducted Fans: Design for High Efficiency. Technical Report ACA-7, Australian Council for Aeronautics, July 1944.

[14] G. N. Patterson. Ducted Fans: Approximate Method of Design for Small Slipstream Rotation. Technical Report ACA-8, Australian Council of Aeronautics, August 1944.

[15] G. N. Patterson. Ducted Fans: Effect of the Straightener on Overall Efficiency. Technical Report ACA-9, Australian Council of Aeronautics, September 1944.

[16] C. H. Zimmerman. Preliminary Experiental Investigation of the Flight of a Person Supported by a Jet Thrust Device Attached to His Feet. Technical report, NACA, 1953.

[17] A. C. Robertson, J. Stuart III, P. Alto, and R. A. Wagner. Vertical Take-Off Flying Platform. Patent, US2953321, September 1960.

[18] L. P. Parlett. Hovering Flight Investigation of Two Methods of Controllong a Man-Carrying Ducted-Fan Vehicle of the Flying-Platform Type. Technical report, NASA, 1961.

[19] S. Ando. A Simple Theory on Hovering Stability of One Ducted-Fan VTOL. Technical report, Nagoya University, Nagoya Japan, 1986.

[20] J. P. Campbell. *Vertical Takeoff and Landing Aircraft.* The MacMillan Company New York, 1962.

[21] L. P. Parlett. Stability and Control Characteristics of a Small-Scale Model of an Aerial Vechicle Supported by Two Ducted Fans. Technical Report D-920, NASA, 1961.

[22] L. P. Parlett. Stability and Control Characteristics of a Small-Scale Model of an Aerial Vechicle Supported by Four Ducted Fans. Technical Report D-937, NASA, 1961.

[23] R. J. Tapscott and H. L. Kelley. A Flight Study of the Conversion Manoeuver of a Tilt-Duct VTOL Aircraft. Technical Note D-372, NASA, November 1960.

[24] P. F. Yaggy and K. W. Goodson. Aerodynamics of a Tilting Ducted Fan Configuration. Technical Note D-785, NASA, March 1961.

[25] K. W. Goodson and K. J. Grunwald. Aerodyanmic Characteristics of a Powered Semispan Tilting Shrouded Propeller VTOL Model in Hovering and Transition Flight. Technical Report D-981, NASA, January 1962.

[26] K. W. Mort and P. F. Yaggy. Aerodynamic Characteristics of a 4-Foot-Diamter Ducted Fan Mounted on the Tip of a Semispan Wing. Technical Report D-1301, NASA, Ames Research Center, Moffett Field, CA, USA, April 1962.

[27] K. W. Mort. Performance Characteristics of a 4-Foot-Diamter Ducted Fan at Zero Angle of Attack for Several Fan Blade Angles. Technical Report TN D-3122, NASA, Ames Research Center, December 1965.

[28] D. J. Giulianetti, J. C. Biggers, and R. L. Maki. Longitudinal and Lateral-Directional Aerodynamic Characteristics of a Large- Scale, V/STOL Model with Four Tilting Ducted Fans Arranged in a Dual Tandem Configuration. Technical Report D-3490, NASA, June 1966.

[29] K. P. Spreemann. Wind-Tunnel Investigation of Longitudinal Aerodynamic Characteristics of a Powered Four-Duct-Propeller VTOL Model in Transition. Technical report, NASA, 1966.

[30] J. C. Biggers D. J. Giulianetti and R. L. Maki. Longitudinal Aerodynamic Characteristics in Ground Effect of a Large- Scale, V/STOL Model with Four Tilting Ducted Fans Arranged in a Dual Tandem Configuration. Technical Report D-4218, NASA, October 1967.

[31] A. I. Abrego and R. W. Bulaga. Performance Study of a Ducted Fan System. In *AHS Aerodynamics, Acoustics, and Test and Evaluation Technical Specialists Meeting*, January 2002.

[32] M. De Roche. Air-Vehicle Augmented Kinesthetic Control System. Patent, US8056866B2, November 2011.

[33] R. J. Weir. Aerodynamic Design Considerations for a Free Flying Ducted Propeller. In *AIAA Atmospheric Flight Mechanics Conference*, Minneapolis, Minnesota, USA, 15-17 August 1998.

[34] M. De Roche. Peripheral Control Ejector. Patent, US20110250066A1, 2011.

[35] M. De Roche. Air-Vehicle Integrated Kinesthetic Control System. Patent, US20120032032A1, February 2012.

[36] J. Fleming and T. Jones. Improved Control of Ducted Fan VTOL UAVs in Crosswind Turbulence. In *AHS 4th Decennial Specialists Conference*, San Francisco, 21-23 January 2004.

[37] R. Yoeli. Ducted Fan Vechicles Particularly Useful as VTOL Aircraft. Patent, US64641, October 2002.

[38] R. Yoeli. Ducted Fan Vechicles Particularly Useful as VTOL Aircraft. Pantent, US6817570, November 2004.

[39] R. Yoeli. Ducted Fan Vechicles Particularly Useful as VTOL Aircraft. Patent, US6883748, April 2005.

[40] R. Yoeli. Ducted Fan Vechicles Particularly Useful as VTOL Aircraft. Patent, US7246769, July 2007.

[41] R. Yoeli. Ducted Fan Vechicles Particularly Useful as VTOL Aircraft. Patent, US7275712, October 2007.

[42] R. Yoeli. Flight Control System Especially Suited for VTOL Vehicles. Pantent, US7946528, May 2011.

[43] R. Yoeli. Apparatus for Generating Horizontal Forces in Aerial Vechicles and Related Method. Patent, US7717368, May 2010.

[44] R. Yoeli. Ducted Fan Vehicles Particularly Useful as VTOL Aircraft. Patent, US7918416, April 2011.

[45] R. Yoeli. Ground Effect Vanes Arrangment. Patent, US8020804, September 2011.

[46] W. E. Graf. Effects of Duct Lip Shaping and Various Control Devices on the Hover and Forward Flight Performance of Ducted Fan UAVs. Masters Thesis, Virginia Polytechnic Institute and State University, May 2005.

[47] O. J. Ohanian III. *Ducted Fan Aerodynamics and Modeling, with Applications of Steady and Synthetic Jet Flow Control*. PhD thesis, Virginia Polytechnic Institute and State University, 2011.

[48] O. J. Ohanian III, E. D. Karni, W. K. Londenberg, and P. A. Gelhausen. Ducted-Fan Force and Moment Control via Steady and Synthetic Jets. In *27th AIAA Applied Aerodynamics Conference*, San Antonio, Texas, USA, 22-25 June 2009. AIAA.

[49] A. Ko, O. J. Ohanian, and P. Gelhausen. Ducted Fan UAV Modeling and Simulation in Preliminary Design. In *AIAA Modeling and Simulation Technologies Conference and Exhibit*, Hilton Head, South Carolina, USA, 20-23 August 2007.

[50] E. N. Johnson and M. A. Turbe. Modeling, Control, and Flight Testing of a Small Ducted Fan Aircraft. *Journal of Guidance, Control, and Dynamics*, 29:769–779, July-August 2006.

[51] H. W. Zhao. Development of a Dynamic Model of a Ducted Fan VTOL UAV. Masters Thesis, School of Aerospace, Mechanical and Manufacturing Engineering, RMIT University, Australia, August 2009.

[52] H. W. Zhao and C. Bil. Aerodynamic Design and Analysis of a VTOL Ducted Fan UAV. In *26th AIAA Applied Aerodynamics Conference*, Honolulu, Hawaii, USA, 18-21 August 2008.

[53] J. Fleming, T. Jones, and W. Ng. Improving Control System Effectiveness for Ducted Fan VTOL UAVs Operating in Crosswinds. In *2nd AIAA "Unmanned Unlimited" Systems, Technologies, and Operations*, San Diego, CA., USA, 15-18 September 2003.

[54] P. Martin and C. Tung. Performance and Flowfield Measurements on a 10-inch Ducted Rotor VTOL UAV. In *60th Annual Forum of the American Helicopter Society*, Baltimore, MD., USA, 7-10 June 2004.

[55] W. E. Graf, J. Fleming, and W. Ng. Improving Ducted Fan UAV Aerodynamics in Forward Flight. In *AIAA Aerospace Sciences Meeting and Exhibit*, Reno, Nevada, USA, 7-10 January 2008.

[56] T. A. Ducan. VTOL Aircraft Control Method. Patent, US5419514, May 1995.

[57] P. J, Weitz. A Qualitative Discussion of the Stability and Control of VTOL Aircraft During Hover (Out of Ground Effect) and Transition. Masters Thesis, United States Naval Postgraduate School, October 1965.

[58] L. P. Parlett. Aerodyanmic Characteristics of a Small Scale Shrouded Propeller at Angles of Attack from 0 to 90 degrees. Technical Report 3547, NACA, 1955.

[59] R. T. Taylor. Experimental Investigation of the Effects of Some Shroud Design Variables on the Static Thrust Characteristics of a Small Scale Shrouded Propeller Submerged in a Wing. Technical Report 4128, NACA, January 1958.

[60] K. W. Mort and B. Gamse. A Wind-Tunnel Investigation of a 7-Foot-Diameter Ducted Propeller. Technical Report D-4142, NASA, August 1967.

[61] J. L. Pereira. *Hover and Wind-Tunnel Testing of Shrouded Rotors for Improved Micro Air Vehicle Design*. PhD Thesis, University of Maryland, USA, 2008.

[62] A. Shavalikul A. Akturk and C. Camci. PIV Measurements and Computational Study of a 5-Inch Ducted Fan for V/STOL UAV Applications. In *47th AIAA Aerospace Sciences Meeting and Exhibit*, Orlando, Florida, USA, 5-8 January 2009.

[63] A. Akturk and C. Camci. Double Ducted Fan (DDF) as a Novel Ducted Fan Inlet Lip Separation Control Device. In *AHS International Powered Lift Conference*, Philadelphia, PA. USA., 5-7 October 2010.

[64] I. Chang, R. Rajagopalan. CFD Analysis for Ducted Fans with Validation. In *21st Applied Aerodynamics Conference*, Orlando, Florida, USA, 2003.

[65] A. Akturk and C. Camci. A computational and experimental analysis of a ducted fan used in vtol uav systems. Turbomachinery Aero-Heat Transfer Laboratory Department Aerospace Engineering Pennsylvania State University University Park, PA 16802, January 2011.

[66] Froude, W. Discussion on Paper by WJM Rankine. *Trans Inst Naval Architecture*, 6:35–37, 1865.

[67] K. Dyer. Aerodynamic Study of a Small Ducted VTOL Aerial Vehicle. Masters Thesis, Massachusetts Institute of Technology, USA, June 2002.

[68] B. W. McCormick, Jr. *Aerodynamics of V/STOL Flight*. Academic Press INC., Dover Edition edition, 1967.

[69] E.L. Houghton, and A.E. Brock. *Aerodynamics for Engineering Students*. Edward Arnold (Publishers) lTD., 1960.

[70] S. F. Hoerner. *Fluid-Dynamic Lift*. Hoerner Fluid Dynamics, Second Edition, 1985.

[71] B. Berry, G. Bowen-Davies, K. Gluesenkamp, Z. Kaler, J. Schmaus, W. Staruk, E. Weiner, B. Woods. Design Optimization of Gamera II: Human Powered Helicopter. In *AHS 68th Annual Forum*, May 2012.

[72] I. Guerrero, K. Londenberg, P. Gelhausen, and A. Myklebust. A Powered Lift Aerodynamic Analysis for the Design of Ducted Fan UAVs. In *2nd AIAA "Unmanned Unlimited" Systems, Technologies, and Operations*, September 2003.

[73] C. H. Zimmerman. Characteristics of Clark Y Airfoils of Small Aspect Ratios. Technical Report 431, NACA, 1932.

[74] I. H. Abbott and A. E. von Doenhoff. *Theory of Wing Sections*. McGraw Hill, 1959.

[75] D. Raymer. *AIRCRAFT DESIGN: A Conceptual Approach*. AIAA, fourth edition, 2006.

[76] Federal Aviation Regulations Part 23 - Airwothiness Standards: Normal, Utility, Acrobatic, and Commuter Category Airplanes.

[77] Federal Aviation Regulation Part 25 - Airworthiness Standards: Transport Category Airplanes.

[78] Federal Aviation Regulation Part 27 - Airworthiness Standards: Normal Category Rotorcraft.

[79] ADS-33E-PRF AERONAUTICAL DESIGN STANDARD PERFORMANCE SPECIFICATION HANDLING QUALITIES REQUIREMENTS FOR MILITARY ROTORCRAFT, 2000.

[80] B. N. Pamadi. *Performance, Stability, Dynamics, and Control of Airplanes*. AIAA, Second Edition, 2004.

[81] M. V. Cook. *Flight Dynamics Principles*. Elsevier, 2007.

[82] H. S. Fletcher. Experimental Investigation of Lift, Drag, and Pitching Moment of Five Annular Airfoils. Technical Report TN 4117, NACA, October 1957.

[83] E. R. Johnston Jr F. P. Beer. *Vector Mechanics for Engineers: Dynamics*. Boston: McGraw-Hill, Seventh Edition, 2004.

[84] M. C. Potter and D. C. Wiggert. *Mechanics of Fluids*. Thompson Learning, Third Edition, 2001.

[85] W. H. Rae Jr. and A. Pope. *Low-Speed Wind Tunnel Testing*. John Wiley & Sons, Inc., Second Edition, 1984.

[86] B. Neal. The Design and Testing of Three 6-Foot Diameter Ducted Propellers With Their Rotational Axes Normal to the Free Stream. Technical Report LR-426, National Research Council of Canada, National Aeronautical Establishment Flight Research Section, Ottawa, Canada, June 1965.

[87] O. J. Ohanian III, P. A. Gelhausen, and D. J. Inman. A Compact Method for Modeling the Aerodynamics of Ducted Fan Vehicles. In *48th AIAA Aerospace Sciences Meeting Including the New Horizons Forum and Aerospace Exposition*, Orlando, Florida, USA, 4-7 January 2010.

[88] W. Wagtendock. *Principles of Helicopter Flight*. Aviation Supplies and Academics, Inc., 1996.

[89] K. J. Grunwald and K. W. Goodson. Aerodynamic Loads on an Isolated Shrouded Propeller Configuration for Angles of Attack From -10 to 110 Degrees. Technical Report D-995, NASA, January 1962.

[90] J.A. Franklin. *Dynamics, Control, and Flying Qualities of V/STOL Aircraft*. AIAA, 2002.

[91] Inc. Athena Technologies. *Micro INS User Manual*, May 2008.

[92] T. W. Sheehy. Computer Aided Shrouded Propeller Design. In *AIAA 9th Annual Meeting and Technical Display*, Washington D.C. USA, 8-10 January 1973.

[93] R. A. Wallis. *Axial Flow Fans and Ducts*. A Wiley-Interscience publication, 1983.

[94] Julie I. Harrington. Saving Energy With Synchronous Belts, January 1991.

[95] G. Blair and M. Cahoon. Best bell, Special Investigation: Design of Intake Bellmounth. Online. Retrieved 19 February, 2014, from http://www.profblairandassociates.com/pdfs/RET-Bellmouth-Sept.pdf.

[96] International Organization for Standardization, ISO 2533:1975 Standard Atmosphere.

[97] J. D. Anderson Jr. *Fundamentals of Aerodynamics Fourth Edition*. McGraw Hill, 2007.

[98] A. Gessow and G. C. Myers Jr. *Aerodynamics of the Helicopter*. Fredrick Ungar Publishing Company, Fourth Printing Edition, 1967.

[99] J. G. Leishman. *Principles of Helicopter Aerodynamics*. Cambridge University Press, 2006.

[100] W. Wagtendock. *Meterorology for Professional Pilots*. Aviation Theory Centre NZ Ltd, Eight Edition, 2003.

[101] MathWorks. Discrete Wind Gust Model. Online. http://www.mathworks.com.au/help/aeroblks/ discretewindgust-model.html, February 2014.

[102] U.S. Military Specification MIL-F-8785C, November 1980.

[103] MathWorks. Dryden Wind Turbulence Model (Continuous). Online. http://www.mathworks.com.au/help/aeroblks/ drydenwindturbulence-modelcontinuous.html, February 2014.

[104] U.S. Military Handbook MIL-HDBK-1797, December 1997.